



PACIFIC EARTHQUAKE ENGINEERING RESEARCH CENTER

An Assessment to Benchmark the Seismic Performance of a Code-Conforming Reinforced Concrete Moment-Frame Building

Curt B. Haselton
Stanford University

Christine A. Goulet
University of California, Los Angeles

Judith Mitrani-Reiser
California Institute of Technology

James L. Beck
California Institute of Technology

Gregory G. Deierlein
Stanford University

Keith A. Porter
California Institute of Technology

Jonathan P. Stewart
University of California, Los Angeles

Ertugrul Taciroglu
University of California, Los Angeles

An Assessment to Benchmark the Seismic Performance of a Code-Conforming Reinforced Concrete Moment-Frame Building

Curt B. Haselton

Stanford University

Christine A. Goulet

University of California, Los Angeles

Judith Mitrani-Reiser

California Institute of Technology

James L. Beck

California Institute of Technology

Gregory G. Deierlein

Stanford University

Keith A. Porter

California Institute of Technology

Jonathan P. Stewart

University of California, Los Angeles

Ertugrul Taciroglu

University of California, Los Angeles

PEER Report 2007/12
Pacific Earthquake Engineering Research Center
College of Engineering
University of California, Berkeley

August 2008

ABSTRACT

This report describes a state-of-the-art performance-based earthquake engineering methodology that is used to assess the seismic performance of a four-story reinforced concrete (RC) office building that is generally representative of low-rise office buildings constructed in highly seismic regions of California. This “benchmark” building is considered to be located at a site in the Los Angeles basin, and it was designed with a ductile RC special moment-resisting frame as its seismic lateral system that was designed according to modern building codes and standards. The building’s performance is quantified in terms of structural behavior up to collapse, structural and nonstructural damage and associated repair costs, and the risk of fatalities and their associated economic costs. To account for different building configurations that may be designed in practice to meet requirements of building size and use, eight structural design alternatives are used in the performance assessments.

Our performance assessments account for important sources of uncertainty in the ground motion hazard, the structural response, structural and nonstructural damage, repair costs, and life-safety risk. The ground motion hazard characterization employs a site-specific probabilistic seismic hazard analysis and the evaluation of controlling seismic sources (through disaggregation) at seven ground motion levels (encompassing return periods ranging from 7 to 2475 years). Innovative procedures for ground motion selection and scaling are used to develop acceleration time history suites corresponding to each of the seven ground motion levels. Structural modeling utilizes both “fiber” models and “plastic hinge” models. Structural modeling uncertainties are investigated through comparison of these two modeling approaches, and through variations in structural component modeling parameters (stiffness, deformation capacity, degradation, etc.). Structural and nonstructural damage (fragility) models are based on a combination of test data, observations from post-earthquake reconnaissance, and expert opinion. Structural damage and repair costs are modeled for the RC beams, columns, and slab-column connections. Damage and associated repair costs are considered for some nonstructural building components, including wallboard partitions, interior paint, exterior glazing, ceilings, sprinkler systems, and elevators. The risk of casualties and the associated economic costs are evaluated based on the risk of structural collapse, combined with recent models on earthquake fatalities in collapsed buildings and accepted economic modeling guidelines for the value of human life in loss and cost-benefit studies.

The principal results of this work pertain to the building collapse risk, damage and repair cost, and life-safety risk. These are discussed successively as follows.

When accounting for uncertainties in structural modeling and record-to-record variability (i.e., conditional on a specified ground shaking intensity), the structural collapse probabilities of the various designs range from 2% to 7% for earthquake ground motions that have a 2% probability of exceedance in 50 years (2475 years return period). When integrated with the ground motion hazard for the southern California site, the collapse probabilities result in mean annual frequencies of collapse in the range of $[0.4 \text{ to } 1.4] \times 10^{-4}$ for the various benchmark building designs. In the development of these results, we made the following observations that are expected to be broadly applicable:

(1) The ground motions selected for performance simulations must consider spectral shape (e.g., through use of the epsilon parameter) and should appropriately account for correlations between motions in both horizontal directions;

(2) Lower-bound component models, which are commonly used in performance-based assessment procedures such as FEMA 356, can significantly bias collapse analysis results; it is more appropriate to use median component behavior, including all aspects of the component model (strength, stiffness, deformation capacity, cyclic deterioration, etc.);

(3) Structural modeling uncertainties related to component deformation capacity and post-peak degrading stiffness can impact the variability of calculated collapse probabilities and mean annual rates to a similar degree as record-to-record variability of ground motions. Therefore, including the effects of such structural modeling uncertainties significantly increases the mean annual collapse rates. We found this increase to be roughly four to eight times relative to rates evaluated for the median structural model;

(4) Nonlinear response analyses revealed at least six distinct collapse mechanisms, the most common of which was a story mechanism in the third story (differing from the multi-story mechanism predicted by nonlinear static pushover analysis);

(5) Soil-foundation-structure interaction effects did not significantly affect the structural response, which was expected given the relatively flexible superstructure and stiff soils.

The potential for financial loss is considerable. Overall, the calculated expected annual losses (EAL) are in the range of \$52,000 to \$97,000 for the various code-conforming benchmark building designs, or roughly 1% of the replacement cost of the building (\$8.8M). These losses are dominated by the expected repair costs of the wallboard partitions (including interior paint)

and by the structural members. Loss estimates are sensitive to details of the structural models, especially the initial stiffness of the structural elements. Losses are also found to be sensitive to structural modeling choices, such as ignoring the tensile strength of the concrete (40% change in EAL) or the contribution of the gravity frames to overall building stiffness and strength (15% change in EAL).

Although there are a number of factors identified in the literature as likely to affect the risk of human injury during seismic events, the casualty modeling in this study focuses on those factors (building collapse, building occupancy, and spatial location of building occupants) that directly inform the building design process. The expected annual number of fatalities is calculated for the benchmark building, assuming that an earthquake can occur at any time of any day with equal probability and using fatality probabilities conditioned on structural collapse and based on empirical data. The expected annual number of fatalities for the code-conforming buildings ranges between 0.05×10^{-2} and 0.21×10^{-2} , and is equal to 2.30×10^{-2} for a non-code conforming design. The expected loss of life during a seismic event is perhaps the decision variable that owners and policy makers will be most interested in mitigating. The fatality estimation carried out for the benchmark building provides a methodology for comparing this important value for various building designs, and enables informed decision making during the design process.

The expected annual loss associated with fatalities caused by building earthquake damage is estimated by converting the expected annual number of fatalities into economic terms. Assuming the value of a human life is \$3.5M, the fatality rate translates to an EAL due to fatalities of \$3,500 to \$5,600 for the code-conforming designs, and \$79,800 for the non-code conforming design. Compared to the EAL due to repair costs of the code-conforming designs, which are on the order of \$66,000, the monetary value associated with life loss is small, suggesting that the governing factor in this respect will be the maximum permissible life-safety risk deemed by the public (or its representative government) to be appropriate for buildings.

Although the focus of this report is on one specific building, it can be used as a reference for other types of structures. This report is organized in such a way that the individual core chapters (4, 5, and 6) can be read independently. Chapter 1 provides background on the performance-based earthquake engineering (PBEE) approach. Chapter 2 presents the implementation of the PBEE methodology of the PEER framework, as applied to the benchmark building. Chapter 3 sets the stage for the choices of location and basic structural design. The

subsequent core chapters focus on the hazard analysis (Chapter 4), the structural analysis (Chapter 5), and the damage and loss analyses (Chapter 6). Although the report is self-contained, readers interested in additional details can find them in the appendices.

ACKNOWLEDGMENTS

This work was supported primarily by the Earthquake Engineering Research Centers Program of the National Science Foundation, under award number EEC-9701568 through the Pacific Earthquake Engineering Research Center (PEER). Any opinions, findings, and conclusions or recommendations expressed in this material are those of the authors and do not necessarily reflect those of the National Science Foundation.

Supplementary funding was also provided to Christine Goulet from the National Sciences and Engineering Research Council of Canada and from Le Fonds Québécois de la Recherche sur la Nature et les Technologies.

The primary lead institutions for the seismic hazard analysis, the structural analysis, and the damage and loss analysis, in this PEER project are, respectively, the University of California at Los Angeles (J. Stewart [P.I.] and C. Goulet), Stanford University (G. Deierlein [P.I.] and C. Haselton) and the California Institute of Technology (J. Beck [P.I.] , J. Mitrani-Reiser, and K. Porter). The authors would also like to acknowledge the valuable input from Professors Helmut Krawinkler, C. Allin Cornell, Eduardo Miranda, and Jack Baker; architect and professional cost estimator, Gee Hecksher; graduate student Abbie Liel; and undergraduate interns Sarah Taylor Lange and Vivian Gonzales at Stanford and Caltech, respectively.

CONTENTS

ABSTRACT	iii
ACKNOWLEDGMENTS	vii
TABLE OF CONTENTS	ix
LIST OF FIGURES	xvii
LIST OF TABLES	xxv
1 INTRODUCTION	1
1.1 Performance-Based Earthquake Engineering (PBEE): Current State of Practice	1
1.2 Limitations of Current PBEE Assessment.....	4
1.2.1 Limitations for Seismic Hazard Analysis and Ground Motion Record Selection.....	4
1.2.2 Limitations in Structural Modeling: Comparisons of FEMA 356 Component Models with Test Data	5
1.2.3 Limitations for Damage and Loss Modeling	7
1.3 PEER’s PBEE.....	10
1.4 Motivation for Benchmark Study	10
1.5 Overview of Benchmark Study	11
2 STUDY OVERVIEW	13
2.1 Introduction	13
2.2 PEER Methodology Overview	13
2.3 Facility Definition.....	17
2.3.1 Site Definition	17
2.3.2 Building Design: Structural.....	17
2.3.3 Building Design: Nonstructural	18
2.4 Hazard Analysis and Ground Motion Selection	19
2.5 Structural Analysis	20
2.5.1 Introduction and Purpose	20
2.5.2 Structural Modeling	21
2.5.3 Structural Analysis Methodology	22
2.5.4 Effects of Structural Uncertainties	24

2.6	Damage Analysis.....	25
2.7	Loss Analysis.....	25
2.7.1	Repair Cost.....	26
2.7.2	Other Decision Variables: Downtime, Injuries, and Fatalities	27
3	BENCHMARK SITE AND BUILDING DESCRIPTION.....	29
3.1	Introduction	29
3.2	Site Selection and Description.....	29
3.3	Structural Design.....	31
3.3.1	Design Basis Codes.....	31
3.3.2	Review of Practitioner Designs.....	32
3.3.3	Site Hazard.....	32
3.3.4	Building Layout	34
3.3.5	Design Variants.....	36
3.4	Nonstructural Components.....	41
3.4.1	Wallboard Partitions.....	43
3.4.2	Exterior Glazing.....	43
3.4.3	Elevators.....	43
3.4.4	Sprinklers	44
3.4.5	Ceiling.....	44
3.5	Summary of Damageable Building Components	46
4	HAZARD ANALYSIS AND GROUND MOTION CHARACTERIZATION	47
4.1	Site Hazard Characterization.....	47
4.1.1	Project Specific Parameters and Mean PSHA Results.....	48
4.1.2	Estimation of Epistemic Uncertainty Associated with Mean Uniform Hazard Results	51
4.2	Record Selection Methodology	56
4.2.1	Criteria Definition for Record Selection and Interpretation of Disaggregation Results.....	58
4.2.3	Record Selection Procedure	66
4.2.4	Other Considerations.....	69
5	STRUCTURAL MODELING AND SIMULATION	71

5.1	Introduction	71
5.2	Overview of Structural Model	72
5.2.1	Frame Configuration and Components	72
5.2.2	Overview of Fiber-Element Beam-Column Model	76
5.2.3	Overview of Lumped-Plasticity Structural Model	77
5.3	Fiber-Spring Model for Pre-Collapse Simulation	79
5.3.1	Overview	79
5.3.2	Fiber-Spring Model Strengths and Limitations	79
5.3.3	Section and Material Models	80
5.3.4	Joint Model Including Panel Shear and Bond-Slip	86
5.3.5	Bond-Slip Model for Column Footings	86
5.4	Lumped-Plasticity Model for Collapse Simulation	86
5.4.1	Overview of Hysteretic Hinge Model	86
5.4.2	Lumped-Plasticity Model Strengths and Limitations	88
5.4.3	Initial Stiffness of Reinforced Concrete Element (Chord Rotation at Yielding)	89
5.4.4	Post-Yield Stiffness of Reinforced Concrete Element	91
5.4.5	Flexural Strength of Reinforced Concrete Element	91
5.4.6	Plastic-Rotation Capacity of Reinforced Concrete Element	92
5.4.7	Post-Capping Stiffness	96
5.4.8	Cyclic Deterioration	97
5.4.8.1	Calibration of Cyclic Deterioration	97
5.4.9	Bond-Slip Model	97
5.4.10	Joint Model	98
5.5	Joint Model	98
5.5.1	Overview	98
5.5.2	Shear Panel Spring Model	99
5.6	Modeling Gravity-Frame Contribution	105
5.6.1	Gravity-Column Modeling	105
5.6.2	Slab-Beam Modeling	106
5.6.3	Coupling of Gravity and Primary Frames	108
5.7	Effects of Nonstructural Element on Response Predictions	109

5.8	Soil-Foundation-Structure Interaction (SFSI)	109
5.8.1	Overview of Soil-Foundation-Structure Interaction (SFSI) Mechanisms	109
5.8.2	Modeling Parameters to Account for SFSI	110
5.8.3	Modeling Variants for OpenSees Analyses and Data Post-Processing	121
5.8.4	Summary of Results from OpenSees Simulations	123
5.8.5	General Interpretation and Discussion of Results	128
5.9	Numerical and Damping Considerations	130
5.9.1	Numerical Solution Algorithm	130
5.9.2	Other Numerical Issues	131
5.9.3	Damping	132
5.10	Nonlinear Static Pushover Analysis and Fundamental Period for Each Design Variant	132
5.10.1	Fundamental Period	132
5.10.2	Static Pushover Analyses	133
5.11	Prediction of Structural Responses before Collapse	138
5.11.1	Methodology	138
5.11.2	Interstory Drift Predictions	139
5.11.3	Residual Drift Predictions	140
5.11.4	Peak Floor Acceleration Predictions	141
5.11.5	Element Plastic-Rotation Predictions	142
5.11.6	Damage Patterns for 2%-in-50-Years Ground Motion	143
5.11.7	Comparison of Response Predictions Using Fiber-Spring and Lumped-Plasticity Models	146
5.12	Collapse Capacity Prediction	150
5.12.1	Collapse Methodology and Three-Dimensional Considerations	150
5.12.2	Collapse Predictions	151
5.13	Illustration of Element Responses from Low Ground Motion Levels to Collapse	160
5.14	Performance-Based Design Study for Beam to Column Strength Ratio	166
5.15	Summary and Conclusions	169
5.15.1	Summary and Conclusions on Structural Modeling	169
5.15.2	Summary of Responses before Collapse	170
5.15.3	Summary of Predicted Collapse Capacity	170

5.15.4	Generalizing Conclusions beyond Building Configurations Considered in Study	171
6	LOSS ANALYSIS	173
6.1	Fragility and Cost Distribution Functions	173
6.1.1	Structural Components: Beams and Columns.....	173
6.1.2	Structural Components: Column-Slab Connections	177
6.1.3	Nonstructural Components: Drywall Partitions and Finish	178
6.1.4	Nonstructural Components: Interior Paint	179
6.1.5	Nonstructural Components: Exterior Glazing.....	181
6.1.6	Nonstructural Components: Acoustical Ceiling.....	181
6.1.7	Nonstructural Components: Automatic Sprinklers	182
6.1.8	Nonstructural Components: Elevators	183
6.2	MDLA: MATLAB Damage and Loss Analysis Toolbox	184
6.2.1	MDLA Input: Table of Damageable Assemblies.....	185
6.2.2	MDLA Input: Fragility and Cost-Distribution Functions	185
6.2.3	MDLA Input: Structural Analysis Results	186
6.2.4	MDLA Architecture	191
6.2.5	MDLA Output: Damage and Loss Results	192
6.3	Damage Results	193
6.4	Loss Results: Seismic Vulnerability Functions	201
6.4.1	Vulnerability Functions: Design Comparisons	204
6.4.2	Vulnerability Functions: Modeling Comparisons.....	207
6.5	Loss Results: MDF, PML, and EAL	210
6.5.1	MDF and PML for All Design Variants	210
6.5.2	EAL for All Design Variants	212
6.6	Loss Results: Expected Annual Loss due to Fatalities	214
6.6.1	History of Fatality Modeling.....	215
6.6.2	Methodology for Fatality Estimation	220
6.6.3	Methodology for Loss Estimation due to Fatalities	226
6.7	Summary and Conclusions	228
7	SUMMARY AND CONCLUSIONS	231

7.1	Overview	231
7.2	Collapse Safety	232
7.3	Damage and Repair Costs.....	235
7.4	Life-Safety Risks and Costs	237
7.5	Future Research Needs	237
REFERENCES.....		241
APPENDIX A: REVIEW OF PRACTITIONER DESIGNS.....		253
APPENDIX B: DESIGN DOCUMENTATION FOR EACH DESIGN VARIANT.....		267
APPENDIX C: CALIBRATION OF BEAM-COLUMN ELEMENT MODEL.....		275
APPENDIX D: DOCUMENTATION OF ELEMENT PLASTIC-ROTATION CAPACITIES FOR EACH DESIGN VARIANT		281
APPENDIX E: STRUCTURAL SENSITIVITY STUDY AND PROPAGATION OF STRUCTURAL UNCERTAINTIES AFFECTING COLLAPSE CAPACITY.....		283
APPENDIX F: QUANTIFICATION OF STRUCTURAL MODELING UNCERTAINTIES FOR LUMPED-PLASTICITY MODEL.....		325
APPENDIX G: APPROXIMATE METHOD FOR ESTIMATING EFFECTS OF CORRELATIONS BETWEEN ELEMENTS.....		335
APPENDIX H: SAMPLE FIRST-ORDER SECOND-MOMENT CALCULATION FOR COLLAPSE CAPACTIY OF DESIGN A.....		339
APPENDIX I: FRAGILITY FUNCTIONS AND COST OF COLUMN-SLAB CONNECTION DAMAGE		345
APPENDIX J: TABLES OF DAMAGEABLE ASSEMBLIES.....		353
APPENDIX K: COMPARING LOSS PREDICTIONS TO OTHER STANDARD METHODOLOGIES		357

LIST OF FIGURES

Figure 1.1	Recommended seismic performance objectives for buildings. Mean recurrence intervals of 43 yrs, 72 yrs, 475 yrs, and 949 yrs correspond to Poisson arrival events with 50% probability of exceedance in 30 yrs, 50% in 50 yrs, 10% in 50 yrs, and 10% in 100 yrs, respectively (after SEAOC 1995).....	2
Figure 1.2	Superposition of FEMA 356 backbone prediction with test results for conforming RC column tested by Saatcioglu and Grira, specimen BG-3 (1999) (Haselton et al. 2006; PEER 2005).....	6
Figure 2.1	Framework of PEER PBEE methodology as applied to benchmarking (after Porter 2003).....	15
Figure 2.2	Depiction of information flow between research groups	16
Figure 2.3	IDA results using fiber-spring model (Design A)	23
Figure 2.4	Collapse IDA using lumped-plasticity element model (Design A, record Bins 4A and 4C, controlling horizontal direction)	24
Figure 3.1	Location map for Los Angeles Bulk Mail site. Red and blue lines, respectively, correspond to strike-slip faults and oblique faults controlling hazard at site. White lines are other faults also contributing to hazard but to lesser extent. Freeways shown for spatial reference (thin yellow lines). More details on faults and site hazard presented in Chapter 4	30
Figure 3.2	Summary of soil profile (simplified) and seismic wave velocities at Los Angeles Bulk Mail site	31
Figure 3.3	Plan view of perimeter frame benchmark building	35
Figure 3.4	Elevation view of frame along column line 1	36
Figure 3.5	Plan view of space-frame benchmark building	40
Figure 3.6	Floor plan of ground floor	42
Figure 3.7	Floor plan of floors 2–4	42
Figure 3.8	Automatic sprinkler piping system of ground floor	45
Figure 3.9	Automatic sprinkler piping system of floors 2–4	45
Figure 4.1	Mean hazard curves for three spectral periods for the LA Bulk Mail site	50
Figure 4.2	Mean uniform hazard spectra (5% damping) for the LA Bulk Mail site for seven hazard levels	51

Figure 4.3	Logic tree for epistemic uncertainty estimation. Numbers correspond to weights. We assume a $\pm 2\sigma$ truncation. Attenuation relationship abbreviations (all 1997): A&S: Abrahamson & Silva, BJJ: Boore, Joyner & Fumal, C: Campbell, S: Sadigh.....	53
Figure 4.4	Confidence intervals around mean 1.0 s hazard curve (5% damping), estimated from epistemic uncertainty (including choice of attenuation relationship and variability of slip rate)	54
Figure 4.5	Contributions from slip rate and choice of attenuation relationship to coefficient of variation from mean hazard curve, for all seven faults listed in Table 4.	55
Figure 4.6	Confidence intervals around mean uniform hazard curve (5% damping) for selected hazard levels, at 1.0 sec. Confidence intervals estimated from epistemic uncertainty (including choice of attenuation relationship and variability of slip rate).....	56
Figure 4.7	Illustration of ϵ at $T=0.8$ s modified from Baker and Cornell (2005a)	59
Figure 4.8	Disaggregation of hazard at $T=1.0$ s for LA Bulk Mail site. Numbers above each figure represent hazard level and (return period).	61
Figure 4.9	Disaggregation of mean hazard for fault source with distance at $T=1.0$ s using attenuation relationships and weights from Table 4.1	63
Figure 4.10	Spatial distribution of faults controlling mean hazard at $T=1.0$ s for LA Bulk Mail site. Figure modified from SCEDC (2005)	64
Figure 4.11	Hazard disaggregation according to directivity parameter $X*\cos(\theta)$	65
Figure 5.1	Plan view of perimeter-frame building.....	73
Figure 5.2	Elevation views of perimeter (lateral-load-resisting moment frame) and interior gravity frame idealized in two-dimensional structural analysis	74
Figure 5.3	Overview of fiber element structural model. Figure shows fiber layers two directions; however, since frame model in study is only two dimensional, fiber layers are oriented only parallel to axis of bending.....	77
Figure 5.4	Overview of lumped-plasticity element structural model	78
Figure 5.5	Concrete model (a) backbone and (b) hysteretic behavior	80
Figure 5.6	Tension stiffening effect illustration (after Feenstra 1993).....	81
Figure 5.7	Concrete tension material model (after Kaklauskas and Ghaboussi 2001).....	82
Figure 5.8	Hysteretic behavior of Guiffre-Menegotto-Pinto steel material model.....	83

Figure 5.9	Shear demand and capacities predicted by several researchers, showing normalized shear demand and capacity (shear divided by shear demand at ultimate flexural strength) plotted against normalized displacement demand (displacement divided by yield displacement)	85
Figure 5.10	Element backbone defining backbone parameters and notation	87
Figure 5.11	Illustration of cyclic deterioration effects.....	88
Figure 5.12	Monotonic response of RC beam to yielding, showing various methods to represent initial stiffness of element (data from Ingham 2001)	91
Figure 5.13	Comparison of model calibration and experimental results from Tanaka and Park (Tanaka 1990), specimen 2 (TestID 19) (PEER 2005; Eberhard 2005)	96
Figure 5.14	Schematic diagram of joint model (after Altoontash 2004, Chapter 2)	98
Figure 5.15	Joint shear panel backbone curve.....	100
Figure 5.16	Joint shear panel cyclic behavior.....	101
Figure 5.17	Penetration of strains into joint or footing (after Lowes 2004).....	102
Figure 5.18	Relationship between rebar stress and slip (ex. for BS1 of Design A)	103
Figure 5.19	Relationship between moment and rotation (ex. for BS1 of Design A); (a) predictions from directly integrating strains, (b) bilinear approximation.....	104
Figure 5.20	Amplitude of transfer function between free-field motion and FIM for vertically incident incoherent waves. Modified from Veletsos and Prasad (1989) and Veletsos et al. (1997)	112
Figure 5.21	Effect of kinematic interaction on foundation input motion for sample motion, (a) in time domain, (b) in spectral acceleration space, and (c) in ratio of response spectral acceleration space, including transfer function.....	114
Figure 5.22	Schematic diagram for inertial SSI modeling in OpenSees	116
Figure 5.23	Empirical relationships for SPT blow count and internal angle of friction for sandy soils, mean values. All SPT values made uniform to represent N_{60}	118
Figure 5.24	Vertical stiffness modeling for shallow bearing footings (FEMA 356).....	119
Figure 5.25	Simplified Gazetas equations as presented in ATC-40 (1996). Refer to Gazetas (1991) for complete and detailed procedure.....	120

Figure 5.26 Schematic of model variants for OpenSees simulations. Example of run names: C0 would consider using FFM records with fixed-base building, while D2 would be FIM records applied to flexible base system with mean valued parameters.....	122
Figure 5.27 IDA plots comparing <i>EDP</i> response for fixed-base and flexible models	124
Figure 5.28 IDA plots comparing maximum roof (floor 5) acceleration for 3 estimates of soil strength properties ϕ . Run D2: \bar{x} or mean soil strength (black), run D3: $\bar{x} - \sqrt{3}\hat{S}$ (red) and run D4: $\bar{x} + \sqrt{3}\hat{S}$ (blue). All analyses performed for FIM	125
Figure 5.29 IDA plots comparing maximum roof (floor 5) acceleration for 3 estimates of soil shear modulus G_s . Run D2: \bar{x} or mean G_s (black), run D3: $\bar{x} - \sqrt{3}\hat{S}$ (red) and run D4: $\bar{x} + \sqrt{3}\hat{S}$ (blue). All analyses performed for FIM.....	126
Figure 5.30 IDA plots comparing response to FIM (blue) to FFM (red) as input motions	127
Figure 5.31 Transfer function for kinematic SFSI computed using Kim and Stewart (2003), for mean benchmark building.....	129
Figure 5.32 Period lengthening ratio for single degree-of-freedom structure. Simplified case for rigid circular foundation on viscoelastic halfspace (Veletsos and Nair 1975).....	129
Figure 5.33 Pseudo-code for solution convergence algorithm for nonlinear dynamic analysis	133
Figure 5.34 (a) Static pushover curves, using inverted triangular load pattern, for Design A with and without including gravity frame in structural model; (b) story drift profiles for each model at point building has degraded to 1200 kip base shear	134
Figure 5.35 (a) Static pushover curves, using inverted triangular load pattern, for Design D with and without including gravity frame in structural model; (b) story drift profiles for each model at end of pushover shown in part (a)	134
Figure 5.36 Static pushover curves for both lumped-plasticity and fiber-spring models (using inverted triangular load pattern, for Design A including gravity frame in structural model).....	135

Figure 5.37	Static pushover curves, using inverted triangular load pattern and including P-delta effects. Curves are for perimeter-frame designs A, C, and D, without including gravity frame in structural model	136
Figure 5.38	Static pushover curves, using inverted triangular load pattern and including P-delta effects. Curves are for space-frame designs E, F, G, and H.....	137
Figure 5.39	Nonlinear dynamic analysis predictions of roof drift ratio for Design A; fiber-spring model with seven ground motion sets selected specifically for each of eight intensity levels.....	139
Figure 5.40	Nonlinear dynamic analysis predictions of interstory drift ratios (stories 1-4) for Design A; fiber-spring model with seven ground motion sets selected specifically for each of eight intensity levels	140
Figure 5.41	Nonlinear dynamic analysis predictions of residual interstory drift ratios (stories 1–4) for Design A; fiber-spring model with seven ground motion sets selected specifically for each of eight intensity levels	141
Figure 5.42	Nonlinear dynamic analysis predictions of peak absolute floor accelerations (floors 2-roof) for Design A; fiber-spring model with seven ground motion sets selected specifically for each of eight intensity levels	142
Figure 5.43	Nonlinear dynamic analysis predictions of maximum column and beam plastic rotation demands for Design A (fiber-spring model with eight ground motion sets selected specifically for each of intensity levels). Reported plastic rotation demand is peak demand for any column or any beam in frame; element with maximum demand differs with ground motion input.....	143
Figure 5.44	Damage patterns for Design A subjected to 2% in 50-years ground motion. Response predictions completed using lumped-plasticity model (legend by A.B. Liel of Stanford University)	146
Figure 5.45	Comparison of peak roof drift demand predictions using fiber-spring and lumped-plasticity models for Design A.....	146
Figure 5.46	Comparison of peak interstory drift demand predictions using fiber-spring and lumped-plasticity models for Design A.....	147
Figure 5.47	Comparison of residual interstory drift demand predictions using fiber-spring and lumped-plasticity models for Design A.....	148

Figure 5.48	Comparison of peak floor acceleration demand predictions using fiber-spring and lumped-plasticity models for Design A	149
Figure 5.49	Comparison of plastic rotation demand predictions using fiber-spring and lumped-plasticity models for Design A; for (a) columns and (b) beams	149
Figure 5.50	Collapse IDAs for Design A not considering beneficial effects of gravity frame, using lumped-plasticity model and ground motion Bins 4A and 4C (36 ground motions with two components each); figure showing (a) all ground motion components (36x2) and (b) only ground motion components that first cause collapse for each record (36x1)	153
Figure 5.51	Collapse CDFs for Design A	154
Figure 5.52	Collapse CDFs for Design A, both excluding and including effects of modeling uncertainty	156
Figure 5.53	Peak drifts just prior to side-sway collapse	159
Figure 5.54	Diagrams showing collapse modes for Design A, and percentage of ground motion records that caused each collapse mode	160
Figure 5.55	Diagrams showing progression of peak interstory drift and damage from low levels of ground motion to collapse. Record causes damage to localize in second and third stories and causes collapse at $S_a(T=1\text{sec}) = 3.5g$	161
Figure 5.56	Diagrams showing column responses for various levels of ground motion	163
Figure 5.57	Diagrams showing beam hinging responses for various levels of ground motion	164
Figure 5.58	Diagrams showing joint shear panel responses for various levels of ground motion	165
Figure 5.59	Static pushover diagram (inverted triangular loading) showing effect of reducing beam strength in Design A by 40%	167
Figure 5.60	Diagrams showing collapse mechanism for earthquake records 941052 for various levels of beam strength. Ground motion causes side-sway collapse at: 2.6g for 100% beam strength, 2.6g for 60% beam strength, and 2.2g for 40% beam strength	168
Figure 5.61	Diagrams showing effects of beam strength on collapse capacity	169
Figure 6.1	Fragility curves for RC moment-frame members	176
Figure 6.2	Fragility curves for column-slab connections	177

Figure 6.3	Fragility curves for wallboard partitions	179
Figure 6.4	Fragility curve for interior paint.....	180
Figure 6.5	Fragility curves for exterior glazing.....	181
Figure 6.6	Fragility curve for acoustical ceiling.....	182
Figure 6.7	Fragility curve for braced automatic sprinklers.....	183
Figure 6.8	Fragility curve for hydraulic elevators	184
Figure 6.9	Input and output parameters for MDLA toolbox	185
Figure 6.10	Fitted probability and observed step-function distributions of peak roof drift ratio (EW-dir) results for four levels of <i>IM</i>	188
Figure 6.11	<i>EDP</i> numbering for structural components in N-S and E-W directions	189
Figure 6.12	Approximations for <i>DDI</i> for biaxially loaded columns	190
Figure 6.13	Biaxial moment relationship for columns (ACI 1990).....	191
Figure 6.14	Schematic of MDLA toolbox	192
Figure 6.15	Average probabilities of damage per story level for Variant 1	196
Figure 6.16	Average probabilities of damage per story level for Variant 2	196
Figure 6.17	Average probabilities of damage per story level for Variant 3	197
Figure 6.18	Average probabilities of damage per story level for Variant 6	197
Figure 6.19	Average probabilities of damage per story level for Variant 9	198
Figure 6.20	Average probabilities of damage per story level for Variant 11	198
Figure 6.21	Average probabilities of damage per story level for Variant 12	199
Figure 6.22	Average probabilities of damage per story level for Variant 13	199
Figure 6.23	Average probabilities of damage per story level for Variant 14	200
Figure 6.24	Average probabilities of damage per story level for Variant 15	200
Figure 6.25	Contributions to mean total repair cost for (a) Variant 1 and (b) Variant 2.....	202
Figure 6.26	Contributions to mean total repair cost for (a) Variant 3 and (b) Variant 6.....	202
Figure 6.27	Contributions to mean total repair cost for (a) Variant 9 and (b) Variant 11.....	203
Figure 6.28	Contributions to mean total repair cost for (a) Variant 12 and (b) Variant 13.....	203
Figure 6.29	Contributions to mean total repair cost for (a) Variant 14 and (b) Variant 15.....	204
Figure 6.30	Vulnerability functions for (a) Variants 1 and 2 and (b) Variants 1 and 3.....	206
Figure 6.31	Vulnerability functions for (a) Variants 1 and 6 and (b) Variants 2 and 9.....	207
Figure 6.32	Vulnerability curves for (a) Variants 1 and 11 and (b) Variants 1 and 12.....	209
Figure 6.33	Vulnerability curves for Variants 1, 13, 14, and 15	210

Figure 6.34 Fractional office building occupancy throughout day224

Figure 6.35 Event tree model for fatality estimation of specific building, considering
probabilities of local and global collapse at every hazard level *im*227

LIST OF TABLES

Table 1.1	Target building performance levels, reproduced from Table C1-2 in FEMA 356 (ASCE 2000) describing range of damage of structural and nonstructural components for various target building performance levels	3
Table 1.2	Criteria for assigning structural performance level to concrete frame members, reproduced from Table C1-3 in FEMA 356 (ASCE 2000)	8
Table 1.3	Criteria for assigning nonstructural performance level to concrete frame members, reproduced from Table C1-5 in FEMA 356 (ASCE 2000)	9
Table 2.1	Damageable structural components in benchmark building	18
Table 2.2	Damageable nonstructural components in benchmark building	19
Table 3.1	Summary of code provisions and application to building design.....	33
Table 3.2	Summary of design decisions	37
Table 3.3	Table of damageable assemblies for perimeter-frame design	46
Table 3.4	Table of damageable assemblies for space-frame design.....	46
Table 4.1	Ground motion prediction equations used for the PSHA.....	49
Table 4.2	Uniform mean hazard results.....	51
Table 4.3	Slip rates for faults significantly contributing to site hazard at T=1 sec. Faults selected for consideration of effect of slip rate variability on results if they contribute > 5% of site hazard.....	52
Table 4.4	Coefficients of variation from epistemic uncertainty for mean uniform hazard spectral accelerations at T=1s.....	54
Table 4.5	Criteria for ground motion record selection	57
Table 4.6	Bin definitions based on disaggregation of hazard.....	62
Table 4.7	Earthquake events available in the database	68
Table 5.1	Contributions to chord rotation at onset of flexural yielding (Design A)	90
Table 5.2	Predictions of plastic rotation capacity and onset of rebar buckling (Design A).....	94
Table 5.3	Recommended values of shear wave velocity reduction factor n_2 (FEMA 356 2005)	113
Table 5.4	Bearing capacity (Q_{ult}) properties utilized with Qzsimple1 elements. Q_{ult} is computed with Vesic's bearing capacity equations (Coduto 2001)	118
Table 5.5	<i>EDPs</i> tracked through incremental dynamic analysis (IDA)	122

Table 5.6	Fundamental periods for each of eight design variants and various structural models (initial stiffness terminology defined in Fig. 5.12 of Section 5.4.3.1).....	133
Table 5.7	Summary of collapse capacity predictions for all design variants	155
Table 5.8	Summary of collapse predictions (mean estimates) for all design variants; showing probability of collapse, annual frequency of collapse, and effects of modeling uncertainty	157
Table 5.9	Summary of collapse predictions (at given levels of prediction confidence) for all design variants; showing probability of collapse and annual frequency of collapse.....	158
Table 6.1	Williams et al. (1997) damage states and consequences for concrete columns	174
Table 6.2	Stone and Taylor (1993) damage states and consequences for concrete columns.....	175
Table 6.3	Summary of assembly fragility and cost distribution parameters	186
Table 6.4	Summary of benchmark building designs and structural models.....	193
Table 6.5	Design variant descriptions and corresponding MDF results at <i>IM</i> having 10% exceedance probability in 50 years ($S_a = 0.55g$), and PML results.....	212
Table 6.6	Design variant descriptions and corresponding EAL results	214
Table 6.7	Death and injury ratios from some major U.S. earthquakes. (All entries but last modified from NOAA [1972]. Last entry calculated from Loma Prieta mortality data [Eberhart-Phillips et al. 1994] and from 1980 population of seven Bay Area counties [U.S. Census 2006])	217
Table 6.8	Comparison of fatality models disaggregated by building type and damage quantity (modified from Table 19 in Shoaf and Seligson 2005).....	219
Table 6.9	Mean and variance of fatality models for local collapse (LC) and global collapse (C) of building.....	225
Table 6.10	Design variant descriptions and corresponding expected annual number of fatalities (EANF) and expected annual loss due to fatalities (EALF)	228

1 Introduction

1.1 PERFORMANCE-BASED EARTHQUAKE ENGINEERING (PBEE): CURRENT STATE OF PRACTICE

Performance-based earthquake engineering (PBEE) can be defined as the assessment of system-level performance of a building, bridge, or other individual structural system subjected to seismic excitation, and the detailed design of its structural features to achieve prescribed performance goals. In a broad sense, performance-based earthquake engineering has existed since the beginning of the twentieth century: seismic design provisions of early U.S. building codes, beginning with the 1927 Uniform Building Code (PCBO 1927), sought to “permit structures to withstand earthquakes without collapse or endangerment of life safety,” (Hamburger and Moehle 2000). In the 1970s, code requirements were added to enhance damage control for important facilities. Modern building codes (e.g., ICC 2003; ASCE 2006) provide design guidelines intended to achieve a similar performance objective (life safety and some degree of damage control) under a specified ground motion hazard.

New documents have been published in recent years that seek to provide for more-robust performance-based seismic design. The first of these was Vision 2000 (SEAOC 1995), which articulated the goal to “embrace a broader scope of design and construction quality assurance issues and ... yield more predictable seismic performance over a range of earthquake demands.” Vision 2000 describes various hazard levels: the *frequent* or 50%-in-30-years earthquake event, the *occasional*, or 50%-in-50-years earthquake event, *rare*, or 10%-in-50-years earthquake event, and the *very rare*, or 10%-in-100-years earthquake event. Vision 2000 also defines various structural performance levels: *fully operational*, *operational*, *life safe*, and *near collapse* in terms of damage to structural and nonstructural components and in terms of consequences to the occupants and functions carried on within the facility. Vision 2000 offers relationships between these hazard and performance levels for various building categories (e.g., hospitals are

considered to be critical facilities). This relationship is shown in Figure 1.1, which indicates that the performance level that should be satisfied for the given hazard level and the type of structure.

Performance-based approaches were further codified with publication of the *Seismic Evaluation and Retrofit of Concrete Buildings* (ATC-40, 1996) and the *National Earthquake Hazards Reduction Program (NEHRP) Guidelines for the Seismic Rehabilitation of Buildings* and associated *Commentary* (FEMA 273 and 274, 1997). These documents addressed the rehabilitation of existing structures, and led to the most comprehensive guidelines for PBEE to date: the *Prestandard and Commentary for the Seismic Rehabilitation of Buildings* (FEMA 356; ASCE 2000).

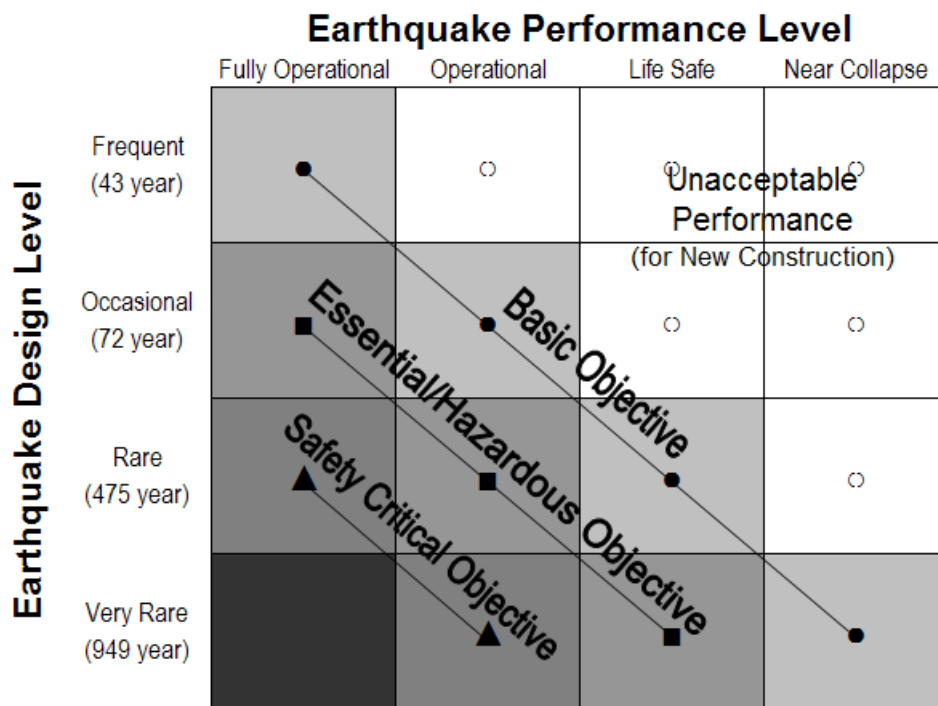


Fig. 1.1 Recommended seismic performance objectives for buildings. Mean recurrence intervals of 43 yrs, 72 yrs, 475 yrs, and 949 yrs correspond to Poisson arrival events with 50% probability of exceedance in 30 yrs, 50% in 50 yrs, 10% in 50 yrs, and 10% in 100 yrs, respectively (after SEAOC 1995).

Table 1.1 Target building performance levels, reproduced from Table C1-2 in FEMA 356 (ASCE 2000), describing range of damage of structural and nonstructural components for various target building performance levels.

Damage Control and Building Performance Levels				
	Target Building Performance Levels			
	Collapse Prevention Level (5-E)	Life-safety Level (3-C)	Immediate Occupancy Level (1-B)	Operational Level (1-A)
Overall Damage	Severe	Moderate	Light	Very Light
General	Little residual stiffness and strength, but load-bearing columns and walls function. Large permanent drifts. Some exits blocked. Infills and unbraced parapets failed or at incipient failure. Building is near collapse.	Some residual strength and stiffness left in all stories. Gravity-load-bearing elements function. No out-of-plane failure of walls or tipping parapets. Some permanent drift. Damage to partitions. Building may be beyond economical repair.	No permanent drift. Structure substantially retains original strength and stiffness. Minor cracking of facades, partitions, and ceilings as well as structural elements. Elevators can be restarted. Fire protection operable.	No permanent drift. Structure substantially retains original strength and stiffness. Minor cracking of facades, partitions, and ceilings as well as structural elements. All systems important to normal operation are functional.
Nonstructural components	Extensive damage.	Falling hazards mitigated but many architectural, mechanical, and electrical systems are damaged.	Equipment and contents are generally secure, but may not operate due to mechanical failure or lack of utilities.	Negligible damage occurs. Power and other utilities are available, possibly from standby sources.
Comparison with performance intended for buildings designed under the NEHRP provisions, for the Design Earthquake	Significantly more damage and greater risk.	Somewhat more damage and slightly higher risk.	Less damage and lower risk.	Much less damage and lower risk.

The FEMA 356 report was intended to encourage wider use of FEMA 273 by converting it into mandatory language, and to provide a basis for a future, nationally recognized, ANSI-approved standard that incorporates its approaches and technologies into mainstream design and construction practice. It defines various target building performance levels and earthquake

hazard levels similar to those presented in Vision 2000. A target building performance for a specific earthquake hazard is selected by the designer and the client together, and the building is designed according to the specifications of this standard. Performance levels are defined for structural and nonstructural systems, whose approximate damage is described in *some* detail. The performance levels and descriptions of corresponding physical damage are shown in Table 1.1. There are many tables in the standard for specific structural performance levels (e.g., for concrete frames, braced steel frames, metal deck diaphragms, etc.) and nonstructural performance levels (e.g., for glazing, piping, cladding, etc.). These tables also include some engineering limit states (e.g., drift values) believed to correspond to the various performance levels for a particular component. These limit states are not intended to be used as acceptance criteria or in the post-earthquake evaluation of damage, but are instead indicative of the range that exists for the limit states that typical structures undergo.

1.2 LIMITATIONS OF CURRENT PBEE ASSESSMENT

The PBEE approach applied in this study was developed through research by the Pacific Earthquake Engineering Research (PEER) Center in response to some perceived limitations of current PBEE assessment guidelines, such as presented in FEMA 356. As summarized below, a few of the more notable limitations are related to ground motion hazard characterization, nonlinear structural modeling, and incomplete loss modeling.

1.2.1 Limitations for Seismic Hazard Analysis and Ground Motion Record Selection

The FEMA 356 (ASCE 2000) document proposes simplified procedures to define the design spectrum based on seismic hazard maps but does not provide guidance on how to conduct more detailed probabilistic site-specific analyses or how to select ground motion records. The recommendations for time-history analyses are that three or seven sets (each set having two horizontal and one vertical component) of ground motions should be selected. If only three motions are selected, then the largest response results should be used as the design basis. If seven sets of motions are selected, then the response for design should be the average from all the analyses. The only recommendation for ground motion record selection is that the records should

be representative of the site hazard with consistent magnitude, fault distance and source mechanism. Guidance provided with regards to the scaling of the records is as follows:

“The data sets shall be scaled such that the average value of the SRSS spectra does not fall below 1.4 times the 5%-damped spectrum for the design earthquake for periods between $0.2T-1.5T$ sec (where T is the fundamental period of the building).”

In a practical context, the FEMA 356 requirements leave considerable, what many consider as too much, latitude for interpretation by seismologists and project engineers. Based on these very general guidelines, there is little chance that two independent teams would select the same motions or would obtain similar response from their set of motions. The procedure as it is, requires judgment and is subjective. Furthermore, one could easily define the hazard or select the motions in such a way as to minimize the response. The subjective nature of this approach can lead to undesirable bias and liability issues.

In this study, our approach is to select a large enough number of ground motion records to obtain statistically robust results, which are less dependent on the specific choice of records. Given the limited availability of recorded ground motions within relatively narrow magnitude and distance ranges appropriate to a given site conditions, we have relaxed these constraints (magnitude and distance) in favor of other parameters that we believe are better predictors of the nonlinear response. Our approach, choices, and assumptions regarding the site hazard and the ground motion record selection are presented in Chapter 4.

1.2.2 Limitations in Structural Modeling: Comparisons of FEMA 356 Component Models with Test Data

Many of the default modeling and acceptance criteria in FEMA 356 are deliberately conservative and overly simplistic. Figure 1.2 provides an example of this, where the idealized FEMA 356 backbone curve is superimposed over test data for a conforming RC column. The particular column in this example has a transverse confinement area ratio of 0.8%, an axial load equal to 20% of the nominal compression strength, and 76 mm stirrup spacing. As shown in Figure 1.2, the FEMA 356 backbone curve underpredicts the tests element deformation capacities by a large margin.¹ In addition, the negative post-failure slope of the FEMA backbone curve is not defined,

¹ It should be noted that these backbone curves are a single component of an assessment procedure, so they are not necessarily meant to represent true element behavior.

yet this slope is of critical importance for realistic collapse simulation (Ibarra 2005, 2003 Chapter 4).

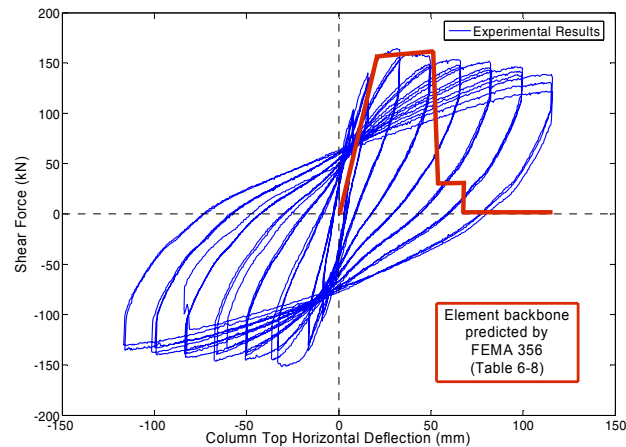


Fig. 1.2 Superposition of FEMA 356 backbone prediction with test results for conforming RC column tested by Saatcioglu and Grira, specimen BG-3 (1999) (Haselton et al. 2006; PEER 2005).

The current research employs ideas similar to the FEMA 356 approach, but with the goal of modeling mean behavior (as opposed to the intentionally conservative modeling assumptions of FEMA 356) over a range of ground motion levels, from low intensity through to levels causing collapse. This study utilizes new element models and nonlinear dynamic analyses for structural response prediction. The notable differences between the element models being used in this study and those in FEMA 356 are: (1) element models include cyclic degradation behavior, (2) model parameters are based on *expected* (mean) behavior (with appropriate statistical measures of variability) instead of a conservative lower bound, and (3) post-failure negative stiffness is explicitly defined and based on test data.

The comments of this section are based on the default backbone curves provided in the FEMA 356 document, which deals with specific materials and types of structural systems. An alternative approach is outlined in Section 2.8 of FEMA 356, in which a user can create improved backbone curves based on test data. While this alternative approach aims to obtain more realistic structural modeling, it fails to account for the distinction between strength deterioration that occurs within a single cycle and between two cycles. Section 5.4 of this report and Chapter 4 of FEMA 440 (FEMA 2005) discuss the differences in these two modes of

strength deterioration and the critical importance of keeping these two modes separate in structural modeling.

1.2.3 Limitations for Damage and Loss Modeling

Beyond issues associated with ground motion hazard characterization and accurate simulation of structural elements, perhaps the most notable limitation of existing PBEE methods is the over-reliance on discrete component-level acceptance criteria, as opposed to probabilistic system-level performance metrics. In FEMA 356, overall performance (i.e., immediate occupancy, life safety, collapse prevention) is evaluated solely on the basis of structural component criteria, where the system performance is judged based on the most critical (localized) component in the structure. As such, this method does not account for the nonlinear interaction of structural components and their influence on the building system performance. By contrast, the methodology used by the authors of this study seeks to quantify performance using probabilistic measures that are of direct relevance to building stakeholders, namely: repair costs, life safety, and post-earthquake operability (“dollars, deaths, and downtime”).

Although FEMA 356 does not attempt to quantify the probability of achieving a given performance level or to quantify repair costs, number or likelihood of fatalities, or loss-of-use duration, it does address component-level and system-level damage states and relates them to life-safety and post-earthquake operability, as shown in Table 1.1. While qualitatively these performance metrics are useful, they do not provide a direct way to quantify dollars, deaths, and downtime. Rather, the damage states given in FEMA 356 tend to be qualitative and open to interpretation. For example, Tables 1.2 and 1.3, reproduced from FEMA 356, illustrate the qualitative language used to describe damage states for concrete frame systems, cladding, glazing, partitions, and ceilings. Some examples of this language are: *minor*, *distributed*, *some*, *many*, *extensive*, and *most*. Such qualitative language is difficult to employ in a quantitative, probabilistic model of damage and loss, especially considering the sometimes broad categories of building components addressed in the tables.

It is necessary to better quantify these component damage states, as done with the fragility functions used in this study (Chapter 6). These fragility functions not only match up values of structural response to specific damage states, but they do so in a probabilistic way—reflecting the inherent uncertainties in the evaluation. In general, a fragility function gives the

probability of an undesirable outcome as a function of input excitation. As used here, a fragility function quantifies the probability that a particular type of component will reach or exceed a clearly defined damage state as a function of the structural response to which it is subjected.

Table 1.2 Criteria for assigning structural performance level to concrete frame members, reproduced from Table C1-3 in FEMA 356 (ASCE 2000).

Table C1-3 Structural Performance Levels and Damage 1, 2, 3—Vertical Elements				
Structural Performance Levels				
Elements	Type	Collapse Prevention (S-5)	Life Safety (S-3)	Immediate Occupancy (S-1)
Concrete Frames	Primary	Extensive cracking and hinge formation in ductile elements. Limited cracking and/or splice failure in some nonductile columns. Severe damage in short columns.	Extensive damage to beams. Spalling of cover and shear cracking (<1/8" width) for ductile columns. Minor spalling in nonductile columns. Joint cracks <1/8" wide.	Minor hairline cracking. Limited yielding possible at a few locations. No crushing (strains below 0.003).
	Secondary	Extensive spalling in columns (limited shortening) and beams. Severe joint damage. Some reinforcing buckled.	Extensive cracking and hinge formation in ductile elements. Limited cracking and/or splice failure in some nonductile columns. Severe damage in short columns.	Minor spalling in a few places in ductile columns and beams. Flexural cracking in beams and columns. Shear cracking in joints <1/16" width.
	Drift	4% transient or permanent	2% transient; 1% permanent	1% transient; negligible permanent

Table 1.3 Criteria for assigning nonstructural performance level to concrete frame members, reproduced from Table C1-5 in FEMA 356 (ASCE 2000).

Nonstructural Performance Levels and Damage 1—Architectural Components				
Nonstructural Performance Levels				
Component	Hazards Reduced N-D	Life Safety N-C	Immediate Occupancy N-B	Operational N-A
Cladding	Severe distortion in connections. Distributed cracking, bending, crushing, and spalling of cladding elements. Some fracturing of cladding, but panels do not fall in areas of public assembly.	Severe distortion in connections. Distributed cracking, bending, crushing, and spalling of cladding elements. Some fracturing of cladding, but panels do not fall.	Connections yield; minor cracks (<1/16" width) or bending in cladding.	Connections yield; minor cracks (<1/16" width) or bending in cladding.
Glazing	General shattered glass and distorted frames in unoccupied areas. Extensive cracked glass; little broken glass in occupied areas.	Extensive cracked glass; little broken glass.	Some cracked panes; none broken.	Some cracked panes; none broken.
Partitions	Distributed damage; some severe cracking, crushing, and racking in some areas.	Distributed damage; some severe cracking, crushing, and racking in some areas.	Cracking to about 1/16 width at openings. Minor crushing and cracking at corners.	Cracking to about 1/16 width at openings. Minor crushing and cracking at corners.
Ceilings	Extensive damage. Dropped suspended ceiling tiles. Moderate cracking in hard ceilings.	Extensive damage. Dropped suspended ceiling tiles. Moderate cracking in hard ceilings.	Minor damage. Some suspended ceiling tiles disrupted. A few panels dropped. Minor cracking in hard ceilings.	Generally negligible damage. Isolated suspended panel dislocations, or cracks in hard ceilings.

Another limitation of damage and loss assessment in current PBEE procedures is the lack of a standard methodology for the systematic development of new fragility functions. Every damageable building component considered in the damage assessment needs a clear definition of its damage states and its corresponding fragility functions. Similarly, the damageable components considered in the loss assessment need clear definitions of the repair efforts and

probabilistic repair costs associated with damage states. The loss assessment tools presented in Chapter 6 provide a compilation of available fragility functions, which provides a model for development of more comprehensive databases that describe damage in a systematic way so that it may be useful for loss estimators.

1.3 PEER'S PBEE

The performance-based earthquake engineering methodology employed in this study consists of PEER's second-generation methodology. This methodology estimates the mean frequency with which a particular performance metric will exceed various levels for a given location (Porter 2003). This methodology provides a framework with which many of the limitations presented above can be overcome. Chapter 2 provides further details on the PEER methodology as applied in this study.

1.4 MOTIVATION FOR BENCHMARK STUDY

This study was motivated by the question, "What is the seismic performance of buildings that are designed and built according to modern building codes?" While engineers generally have a sense that modern building codes provide adequate performance, in fact the engineering profession does not know quantitatively how these buildings will perform during future earthquakes in terms of dollars, deaths, or downtime. Observations from past earthquakes have shown that code-conforming buildings generally perform well in terms of structural safety, although conformance with building-code requirements does not guarantee zero probability of loss of life or life-threatening damage. From the standpoint of damage, monetary loss, and building closure, code-conforming building performance might vary widely and thus far is poorly understood.

One example that highlights the limitations of current building code provisions to limit losses and downtime is damage that occurred to the Olive View Hospital in Sylmar, California. During the 1994 Northridge earthquake, this recently constructed hospital experienced little structural damage, despite strong shaking of almost 0.9g free-field PGA. Even so, nonstructural damage to fire-sprinkler piping, chilled-water lines, and HVAC equipment caused the closure of the hospital for several days following the earthquake.

Research in PBEE has progressed to the point that we now have the tools necessary to begin answering some of the questions about how buildings will perform in future earthquakes.

1.5 OVERVIEW OF BENCHMARK STUDY

This study applies the latest PBEE methodology and tools, developed by the PEER Center, to evaluate the seismic performance of eight alternative designs of a four-story reinforced concrete (RC) special-moment-resisting-frame (SMRF) building. Situated at a site in southern California, this so-called “benchmark” building is intended to represent the seismic performance of a broad class of low-rise office building construction in the highly seismic regions of coastal California. The study objectives were both to illustrate the application of the PBEE methodology and to evaluate the expected performance of similar structures designed and constructed in accordance with modern building code provisions, thus answering the question “How well do code-conforming buildings perform?” The performance estimates considered in this study include structural collapse, damage to structural and nonstructural components, the risk of fatalities, and expectations of monetary losses. The important uncertainties are included and propagated through each step of the PBEE assessment process. Included are uncertainties in the ground motion hazard, structural response (including record-to-record variability and uncertainty associated with structural modeling), damage states of building components, and monetary loss functions.

This benchmarking effort provides performance predictions that are envisioned to serve a standard of performance against which other systems can be judged. We envision this information to have many uses, including the following:

- Provide information to code committees that will allow them to calibrate building-code provisions to produce desired levels of societal protection.
- Provide information for engineers and building code officials in establishing policies and making decisions on retrofit requirements.
- Provide a standard of performance that can be used to judge innovative systems.

For these benchmark results to be useful, they must be calculated using a clear methodology, with models and analyses that are well calibrated, believable, and readily duplicated. With this objective in mind, much of the present effort focused on refining and standardizing the newly developed PBEE methodology, exploring uncertainties related to ground

motion hazard and structural modeling, calibrating structural element models, expanding a library of fragility functions and cost distributions, and developing open-source software to perform damage and loss analyses. This project served as a mechanism to standardize and package the models and methods needed to complete a PBEE assessment. The collaboration effort between the research team further facilitated streamlining of the procedure and the interface between the different fields involved (engineering seismology, geotechnical engineering, structural engineering, and damage and loss modeling).

2 Study Overview

2.1 INTRODUCTION

The performance-based earthquake engineering (PBEE) methodology developed by the Pacific Earthquake Engineering Research (PEER) Center is broadly applicable for predicting seismic performance of bridges, buildings, and lifeline systems. Several recent publications have presented the general framework of this methodology (Deierlein et al. 2003; Porter 2003; Deierlein 2004; Krawinkler and Miranda 2004; Moehle and Deierlein 2004). The purpose of this chapter is not to repeat a general explanation of the methodology; rather, the intent is to summarize specifically how we applied the methodology to assess the seismic performance of a new code-conforming reinforced concrete (RC) special moment-resisting frame (SMRF) building. Further details of the implementation follow in the remainder of this report.

2.2 PEER METHODOLOGY OVERVIEW

The PEER PBEE methodology breaks the seismic performance assessment into four primary steps: (1) ground motion hazard characterization, (2) structural response analysis, (3) damage analysis, and (4) loss assessment. To treat each step rigorously, this research involves collaboration between research groups at the University of California, Los Angeles (UCLA), Stanford University, and the California Institute of Technology (Caltech). Figure 2.1 shows each of the steps, a brief description of each step, and the role of each research group.

In its most generic sense, the PBEE methodology is used to estimate the mean annual frequency with which a particular performance metric will exceed various levels for a specified facility and location (Porter 2003). The methodology has been expressed in various forms of a framing equation, e.g., a double integral (Cornell and Krawinkler 2000), a quadruple integral (Baker and Cornell 2003), and a triple integral (Cornell 2004), with the last apparently its final

form, expressed mathematically in Equation 2.1. The triple integral appears with various notations in Cornell 2004 and elsewhere, typically with conditioning on D (facility and location) implicit. In both the figure and the equation, $p[x|y]$ denotes the probability density function of X conditioned on Y (i.e., the derivative with respect to x of $P[X \leq x | Y = y]$), $G[x|y] = P[X > x | Y = y]$ denotes the complementary cumulative distribution of X conditioned on Y (i.e., $1 - P[X \leq x | Y = y]$), $\lambda[x|y]$ denotes the mean exceedance rate of X given Y (i.e., the mean occurrence rate of events $X > x$ given $Y = y$), $\lambda'[x|y]$ denotes its first derivative with respect to x , IM denotes an intensity measure, EDP denotes a vector of engineering demand parameters, DM denotes a vector of damage measures, and DV denotes decision variables.

$$\lambda[DV | D] = \iiint G[DV | DM, D] p[DM | EDP, D] p[EDP | IM, D] \lambda'[IM | D] dIM dEDP dDM \quad (2.1)$$

Or in an equivalent form:

$$\lambda[DV | D] = \lambda_0 P[DV > DV | D]$$

where

$$P[DV > DV | D] = \iiint P[DV > DV | DM, D] p(DM | EDP, D) p(EDP | IM, D) p(IM | D) dIM dEDP dDM$$

and λ_0 is the mean occurrence rate of events of interest.

The first step in this approach is the hazard analysis, in which one evaluates the seismic hazard for a particular facility, considering nearby faults, site distance, source-to-site conditions, facility location, facility design, etc. The ground shaking at the site is parameterized in terms of an intensity measure, IM . The hazard curve, $\lambda[IM|D]$, is the estimated mean rate at which events will occur that produce shaking at the site that exceeds IM . The IM in this study is the damped elastic spectral acceleration response at the estimated small-amplitude fundamental period of the structure.

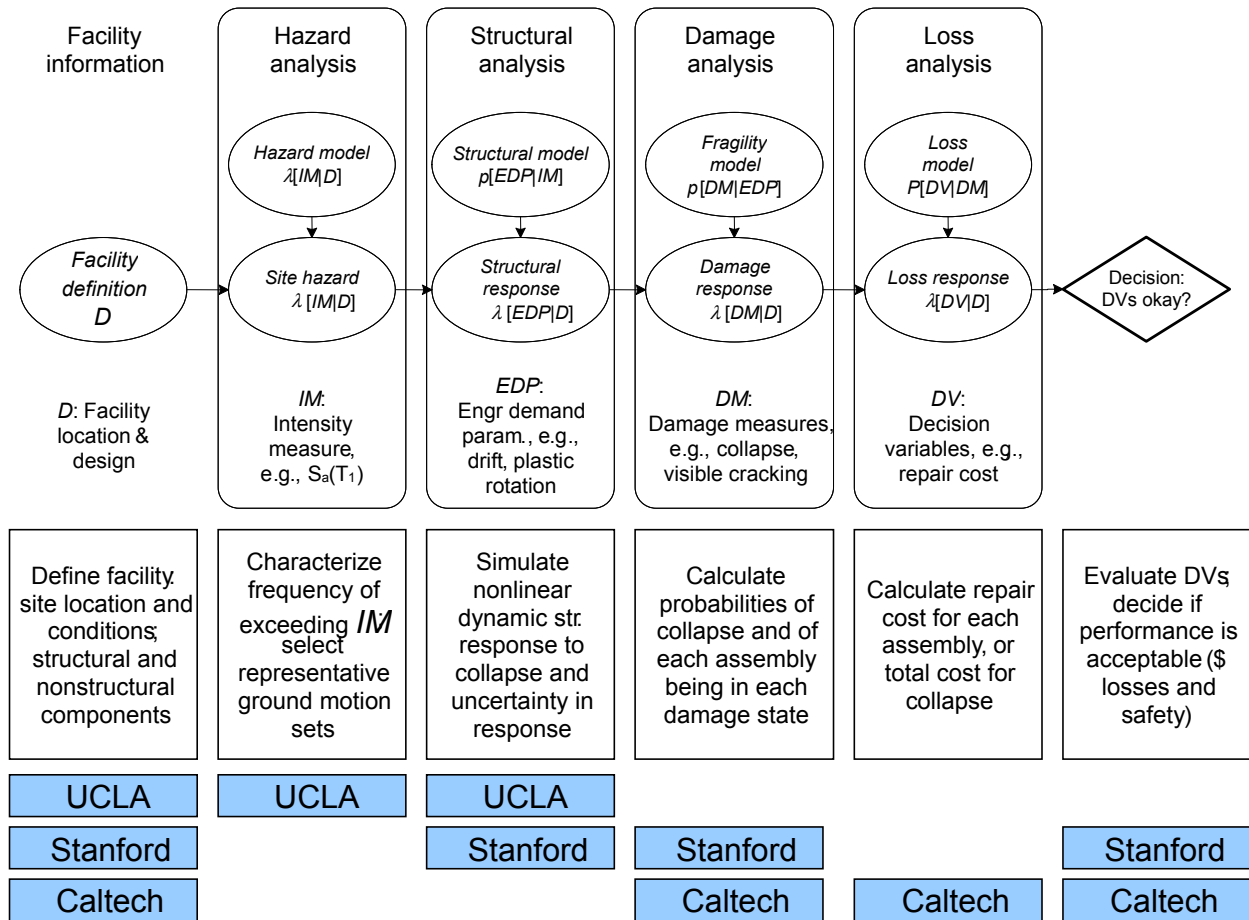


Fig. 2.1 Framework of PEER PBEE methodology as applied to benchmarking (after Porter 2003).

The second step is the structural analysis, which is evaluated through an inelastic time-history analysis of a structural model, including soil-foundation-structure and other effects as appropriate. The response is measured in terms of a vector of engineering demand parameters ($EDPs$), conditioned on the intensity measure IM and the design. The $EDPs$ considered in this study are directional peak transient interstory drift, directional peak diaphragm acceleration, and peak plastic-hinge rotation in beams and columns. The methodology allows for uncertainty in the structural models.

The first consideration in the damage analysis is to distinguish between instances of collapse and non-collapse, based on the EDP results from structural analysis. For instances of non-collapse, the damage is assessed through component fragility functions to estimate the

probability of various components (e.g., beam, column, wall partition, etc.) to reach or exceed a particular damage state, as a function of the calculated *EDP*. The different damage states, *DM*, are indicative of the corresponding repair efforts needed to restore a facility component to an undamaged state. Although shown as continuous variables in Equation 2.1, as implemented here, the *DMs* are discrete variables corresponding to discrete damage states. These fragility functions, compiled based on laboratory experiments, analytical investigation, expert opinion, or some combination, are used to create a probabilistic array of damage measures.

The probabilistic assessment of the *DMs*, calculated for the non-collapse cases, are combined with the likelihood of collapse in the loss analysis. This analysis is the probabilistic estimation of system performance measures, referred to here as decision variables (*DV*), conditioned on damage. This study focuses on two *DVs*: (1) monetary loss due to the cost of repair (non-collapse) or replacement (collapse) and (2) the risk of fatalities due to collapse. These *DVs* are described in terms of mean annual frequencies with which various levels of *DV* are exceeded.

As the four stages of the PBEE assessment methodology are treated as conditionally independent, each stage can be conducted separately—provided that the exchange of information is organized carefully. Figure 2.2 shows how we structured this flow of information.

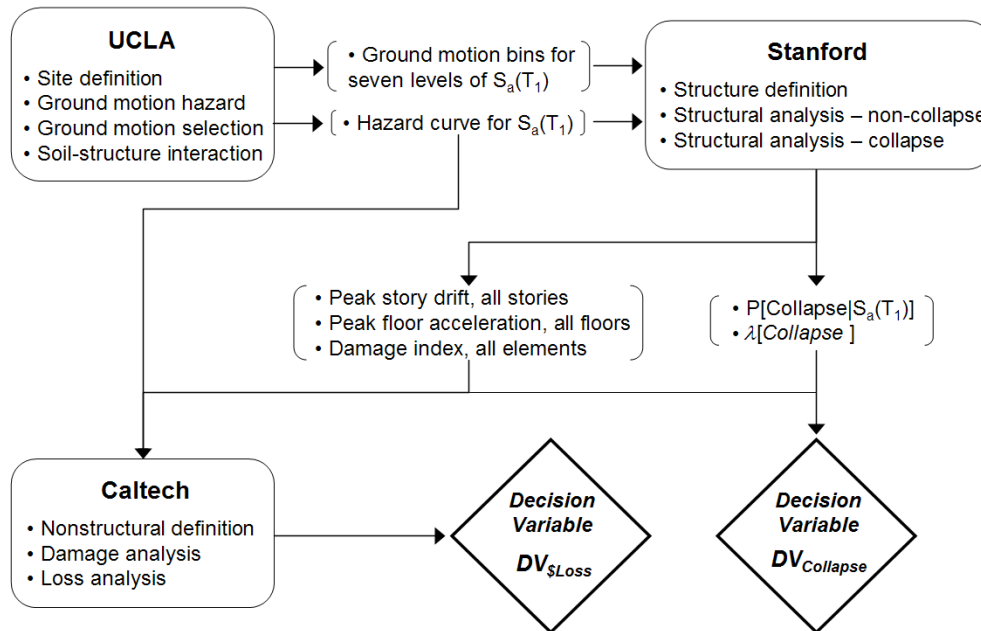


Fig. 2.2 Depiction of information flow between research groups.

The following sections of this chapter give more detailed explanation of how we executed each step of the PBEE assessment process for benchmarking the performance of typical low-rise RC office building construction that is designed and constructed according to current building code provisions.

2.3 FACILITY DEFINITION

The first step in the performance assessment is to define the building, including its geographic location, its configuration, and its structural and nonstructural characteristics.

2.3.1 Site Definition

For the benchmark project, the goal was to locate the building on a site with conditions typical of a highly seismic region in urban California. The selected site is located at the Los Angeles Bulk Mail Facility in Bell, approximately 6 km south-east of the center of downtown Los Angeles. Chapter 3 presents the criteria used for the site selection.

2.3.2 Building Design: Structural

With the ultimate goal to contribute toward understanding the seismic performance implied by modern building codes, this study presents a detailed assessment of a four-story RC SMRF office building with a fairly standard floor plan configuration. Eight different design variants were investigated to help assess the variability in performance that results from various design decisions. The design variants included perimeter-frame and space-frame configurations. To ensure that these designs are representative of current practice, we reviewed two practitioner-designed RC SMRF buildings and consulted with structural engineers to understand their design intent and the factors that affected decisions regarding framing configurations, member sizing, etc.

The building was designed according to the 2003 International Building Code for the site in the Los Angeles basin (Section 2.3.1). The design strength demand for the perimeter-frame designs was: $S_1 = 0.9g$, $S_s = 1.5g$, and $C_s = 0.094$ (base shear coefficient). Using a simple centerline structural model and the code-drift-determination method (ASCE 7-02 Section

9.5.5.7.1), the member sizes were primarily controlled by minimum strength requirements as determined using the design base shear and capacity design provisions. Seismic drift demands did not govern the designs (see Appendix B).

2.3.3 Building Design: Nonstructural

The structural and nonstructural components of a real, constructed building are (approximately) revealed by as-built drawings, site investigations, or both. The benchmark building examined here is *not* a real facility, so we were free to design its structural and nonstructural components constrained only by the code and common practice. We designed it as if it were an office building, and rendered realistic architectural plans, as shown in Chapter 3. These are used to quantify the nonstructural components of the building—the exterior closure, interior finishes, and selected mechanical, electrical, and plumbing features that would most likely account for most of the repair cost. Loss analysis results from other PBEE studies (e.g., Beck et al. 2002) have suggested that the building components for this facility that would contribute the most to repair cost are its structural members, drywall partitions and interior paint. Thus, this benchmark study focuses on these specific building components. The building structural and nonstructural components considered for the damage and loss analyses are listed in Tables 2.1 and 2.2, respectively.

Table 2.1 Damageable structural components in benchmark building.

Components	EDP	Reference
RC SMRF beams	Displacement Damage Index (DDI)	Williams (1997)
RC SMRF columns	Displacement Damage Index (DDI)	Williams (1997)
Gravity Frame: Slab-Column Joints	Peak Transient Drift Ratio (PTDR)	Aslani (2005)

Table 2.2 Damageable nonstructural components in benchmark building.

Components	EDP	Reference
Exterior Walls	Peak Transient Drift Ratio (PTDR)	Behr et al. (1998); Porter et al. (2001)
Interior Partitions	Peak Transient Drift Ratio (PTDR)	Porter et al. (2001); Rihal (1982)
Conveying Systems¹	Peak Ground Acceleration (PGA)	Benuska (1990); Finley et al. (1996); Porter (2006)
Plumbing² and Fire Protection³	Peak Diaphragm Acceleration (PDA)	Porter et al. (2001); Sprinkler Fitters U.A. (1989)
Ceiling Systems	Peak Diaphragm Acceleration (PDA)	Porter et al. (2001)
¹ Elevators and escalators. ² Domestic water distribution, sanitary waste system, and specialty plumbing. ³ Sprinkler systems and standpipes.		

2.4 HAZARD ANALYSIS AND GROUND MOTION SELECTION

Following PEER’s PBEE methodology, we assessed the site hazard through a probabilistic seismic hazard analysis (PSHA) for the LA Bulk Mail site. The ground motion intensity measure IM is the 5% damped spectral acceleration response at the four-story building’s estimated fundamental period of 1 sec, $S_a(T_1=1.0 \text{ sec})$. For each hazard level and for this fundamental period, the PSHA results are disaggregated by magnitude, distance, epsilon, fault rupture mechanism, and directivity, to determine which combinations of these dominate the hazard. Further discussion is presented in Chapter 4.

Recorded ground motions are selected and scaled for the structural analyses to be consistent with the disaggregation results. Ground motion record selection and scaling techniques are still evolving and there is still debate as to which method is the most appropriate. Chapter 4 addresses some of these issues while explaining the choices made for this project.

Another product of the PSHA is a series of hazard curves expressing the probability of exceedance of a given ground shaking level for different spectral periods. As it will be shown, these curves are used at all the subsequent steps of the methodology where they are integrated with the simulation results.

2.5 STRUCTURAL ANALYSIS

2.5.1 Introduction and Purpose

The purpose of the structural analysis is twofold: (1) to relate IM (5%-damped, 1-sec spectral acceleration response) to $EDPs$ (peak drifts, peak floor accelerations, and inelastic deformations of each reinforced concrete component) and (2) to estimate the collapse probability as a function of IM , i.e., to create a collapse fragility function. Although this second task can be seen as part of the damage analysis (depicted as such in Fig. 2.1), it is more naturally included with the structural analysis and so it is discussed here. The inputs and outputs of this step, for each structural design realization, are:

- Input
 - Ground motion hazard curve (Section 4.1.1)
 - Bin of ground motions for each of seven distinct hazard levels (Section 4.2)
- Outputs
 - $EDPs$ for each ground motion record at each hazard-level bin
 - $EDPs$ for mean structural model (all modeling variables set to their respective expected values) (Section 5.11)
 - Collapse capacity
 - Collapse capacity for mean structural model (all modeling variables set to their respective expected values) (Section 5.12.2)
 - Total uncertainty in collapse capacity estimates, including uncertainties from record-to-record variability and structural modeling uncertainties (Sections 5.12.2, E.5.2)
 - Probability of collapse at a given ground motion intensity level, denoted here by $P[C | im]$ (Section 5.12.2.2)
 - Collapse hazard, $\lambda_{\text{collapse}}$ (mean annual rate of collapse) (Sections 5.12.2.2, E.7.1)

2.5.2 Structural Modeling

To produce accurate and dependable benchmark results that include the assessment of nonstructural damage, the structural model needs to accurately predict structural response from *low* deformation levels (where cracking and tension-stiffening phenomena are important) up to the *extremely high* deformation levels (where deterioration leading to collapse is important). To achieve these goals requires a structural model that accurately represents behavior from initial cracking up through collapse.

The structural analyses for this study are run using PEER's Open System for Earthquake Engineering Simulation (OpenSees 2005). Based on our assessment of the available modeling features in OpenSees (as of 2005), we concluded that *no single model* would accurately capture the structural response over the full ranges of ground motion intensity. Models that could capture the initiation of cracking well did not accurately simulate strain softening at large deformations, and models that captured deterioration at large deformations did not simulate the initial loading stages well. Therefore, we used the following two different models to simulate the full range of response: (1) a fiber model for low-intensity levels (where cracking behavior governs) and (2) a lumped-plasticity model to deal with high intensities at which structural collapse can occur. Both models incorporate bond-slip (Section 5.5.2.4), element shear flexibility (Section 5.3.3.3), and the gravity system (Section 5.6) effects.

The fiber model is a force-based beam-column element implementation by Filippou (1999) that captures the cracking behavior of the concrete section using a uniaxial concrete constitutive law, and tracks the spread of plasticity through the element cross section and along the element length. This model is termed the "fiber-spring model" because the fiber elements include an uncoupled shear degree-of-freedom that is used in conjunction with rotational springs at the ends of each element to model bond-slip behavior. Section 5.3 discusses this model in more detail. The current fiber-element model in OpenSees (2005) cannot capture rebar buckling and low-cycle fatigue, and hence cannot accurately model side-sway system collapse of a ductile RC frame. (This is not an inherent limitation of the fiber-element formulation, but comes from an inability of the existing steel models to simulate rebar degradation.)

The lumped-plasticity model consists of elastic beam-column elements that are combined with concentrated hinge springs, which employ the peak-oriented material model (called "Clough" in OpenSees). The "Clough" spring implementation in OpenSees includes

modifications introduced by Ibarra and Krawinkler (Ibarra 2003) to capture strain softening at large deformations. The model is composed of a trilinear backbone and is capable of modeling four types of cyclic deterioration of strength and stiffness (OpenSees 2005). Section 5.4 discusses this model in more detail.

2.5.3 Structural Analysis Methodology

We employed incremental dynamic analysis (IDA) (Vamvatsikos 2002) with the lumped-plasticity model to estimate collapse probability as a function of IM , denoted here by $P[C | im]$. In an IDA, a set of ground motions is systematically scaled and applied to the structural model over a broad range of IM levels. At each IM level, the input ground motions are scaled to the desired value of IM , and the resulting $EDPs$ from the structural analysis are recorded. For the purpose of assessing collapse, the ground motion record set corresponding to largest earthquake magnitude bin was applied over the IDA. On the other hand, for evaluating the onset of damage at lower-intensity values, we employed a related method to IDA called stripe analysis with the fiber-element model, where separate ground-motion-record bins are applied for each IM level. This is in contrast to the conventional IDA, where records from one ground motion bin are scaled over the full range of intensities, the rationale being that there may be differences in the record bins that should be reflected in the various hazard intensity levels.

Stripe analysis. Figure 2.3 illustrates the results of the stripe analysis for one of the fiber models of the benchmark building. This figure shows the individual drift responses for each earthquake record with lines for the median, 16th and 84th percentile responses, assuming that the drift is lognormally distributed for a given S_a level (Krawinkler and Miranda 2004). This shows the uncertainty in drift response due to the variability between ground motion records, conditioned on the S_a intensity. Since different ground motion bins are used at each stripe level, the variation in response reflects both the record-to-record variability within a bin (at a given strip) and variations between record sets at the various intensity stripes.

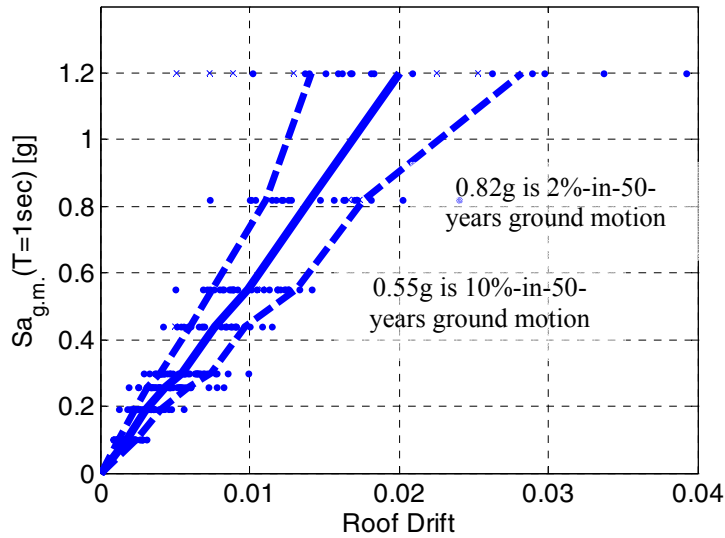


Fig. 2.3 IDA results using fiber-spring model (Design A).

IDA. As noted above, the stripe analysis is used to estimate losses prior to collapse, whereas IDA is used to model collapse. There are several potential local and global collapse mechanisms, notably (a) loss of gravity-load-carrying capacity of a column, (b) local collapse of a gravity slab system, and (c) global side-sway collapse caused by dynamic instability in one or more stories. We assume that the detailing provisions of the current building code (ICC 2003) will effectively prevent local collapse modes (a) and (b), so this study focuses on global side-sway collapse.

Figure 2.4 shows the collapse behavior of the structural model when subjected to each of the 36 earthquake records. None of the 36 records cause collapse near the 2%-in-50-years hazard level (0.82g), thus demonstrating that the simulation model predicts high collapse capacities, with a corresponding low associated probability of collapse at the 2%-in-50-years hazard level. Section 5.12 discusses how information of the type shown in Figure 2.4 is used to evaluate the collapse probability as a function of IM and the mean annual collapse frequency.

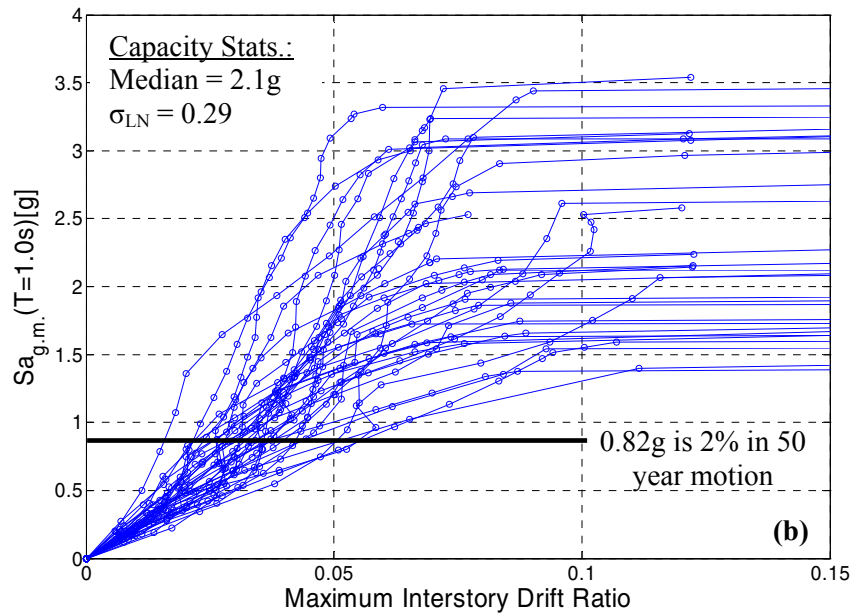


Fig. 2.4 Collapse IDA using lumped-plasticity element model (Design A, record Bins 4A and 4C, controlling horizontal direction).

2.5.4 Effects of Structural Uncertainties

Despite the apparently low collapse probability in the 2%-in-50-years event suggested by Figure 2.6, consideration of structural and modeling uncertainties can increase the collapse probability by an order of magnitude. Uncertainties in the structural behavior and modeling include those in element plastic-rotation capacities, cyclic deterioration modeling parameters, and other variables. These uncertainties affect both the structural behavior before collapse and the collapse capacity, but we have considered only their effect on the more sensitive collapse capacity.

Details of the modeling uncertainty analysis are presented in Appendix E of this report. Briefly, the process involved (1) quantifying uncertainties in structural modeling parameters, using both previous research and calibration to experimental data (Table E.4, Appendix C) and (2) applying the first-order second-moment (FOSM) approximation (Baker and Cornell 2003) to integrate the modeling uncertainties with the record-to-record uncertainties to evaluate the collapse capacity (Section E.5.1). A significant observation from this exercise was that the degree of correlation between variables strongly affects the final uncertainty in collapse capacity.

2.6 DAMAGE ANALYSIS

The structural analysis results are input to component fragility functions to compute the probability of reaching or exceeding damage state j , for a component of type i , conditioned on the structure not collapsing and on IM :

$$P[DM_{ij} | NC, im] = \int_{edp_i} P[DM_{ij} | edp_i] p(edp_i | NC, im) dedp_i \quad (2.2)$$

The first component of the integrand, $P[DM_{ij} | edp_i]$, is the probability of reaching or exceeding the damage state j for a given building component, conditioned on EDP i appropriate for component of type i (this probability comes directly from the corresponding fragility function). The second component of the integrand, $p(edp_i | NC, im)$, is the probability density of EDP i , conditioned on the structure not collapsing (NC) and on a given IM level. To evaluate this component, a lognormal distribution is used to fit the structural response data, as is done by other researchers (e.g., Miranda and Aslani 2003). As mentioned in Section 2.5, the probability of collapse given IM is estimated as part of the structural analysis results.

2.7 LOSS ANALYSIS

The framework of the PEER methodology (Fig. 2.1) allows for modular software development. A MATLAB damage and loss analysis toolbox (MDLA) was created for this study to perform the damage and loss analyses. Its inputs are a database of generic fragility and cost distribution functions (generic in the sense that they are applicable to other buildings and analyses as well), tables of the damageable components of the benchmark building, and the hazard and structural analysis results. The outputs of the toolbox are the probability of exceedance of damage states for all damageable components in the structure; the first two moments of the repair cost to restore the building to an undamaged state as functions of IM (referred to here as the vulnerability function); and the expected annualized loss (EAL), which is the amount one could expect to pay on average every year to repair earthquake damage, considering the uncertain occurrence and severity of earthquakes. Note that this study, like most others, employs a Poisson occurrence model for seismic events and damage events. This probability model is reasonable, for example, if for design purposes it is assumed that the building is restored to its initial

condition after each damaging event. (Der Kiureghian, 2005, treats some implications of this model.)

2.7.1 Repair Cost

The vulnerability functions, a product of the last step of the performance assessment, establish the relationship between repair costs and shaking intensity level. The vulnerability functions are given by:

$$\begin{aligned}
 E[TC | im] &= E[TC | NC, im] \cdot (1 - P[C | im]) + E[TC | C, im] \cdot P[C | im] \\
 E[TC^2 | im] &= P(NC | im) \cdot E[TC^2 | im, NC] + P(C | im) \cdot E[TC^2 | im, C] \\
 Var[TC | im] &= E[TC^2 | im] - (E[TC | im])^2
 \end{aligned} \tag{2.3}$$

where $E[TC | im]$ is the expected total repair costs conditioned on $IM=im$, $E[TC | C, im]$ is the replacement cost of the structure, and $P[C | im]$ is the probability of collapse, as estimated from the structural response simulation. Similarly, $E[TC^2 | im]$ is the mean-square of the total repair costs conditioned on $IM=im$, and $Var[TC | im]$ is the variance conditioned on $IM=im$. The expected total repair cost conditioned on the structure not collapsing and on IM , $E[TC | NC, im]$, is calculated by:

$$\begin{aligned}
 E[TC | NC, im] &= (1 + C_{OP}) \cdot C_I \cdot C_L \sum_{i=1}^{na} Nu_i \cdot E[RC_i | NC, im] \\
 E[RC_i | NC, im] &= \sum_{j=1}^{nds_i} E[RC_i | DM_{ij}] \cdot P[DM_{ij} | NC, im]
 \end{aligned} \tag{2.4, 2.5}$$

where C_{OP} , C_I , and C_L are factors to account for contractor overhead and profit, inflation, and location, respectively; na is the number of damageable assembly groups; Nu_i is the number of units in assembly group i ; Ri_{ca} is the repair cost for one unit in assembly group i ; and nds_i is the number of damage states for damageable component group i . We define an assembly group as the set of damageable components of the same type that are sensitive to the same EDP . Their damage states and repair costs are modeled as perfectly correlated and conditionally independent given EDP from all other assembly groups.

The expected annual loss (EAL) is calculated consistently with other researchers (e.g., Porter et al. 2000; Baker and Cornell 2003) as the product of the mean total rate of occurrence of

events of interest and the mean loss conditional on an event of interest occurring, which may be expressed as:

$$EAL = \lambda_0 \int E[TC | im] p(im | im \geq im_0) dim \quad (2.6)$$

where im_0 refers to a value of IM below which repair cost is probably negligible (here taken as 0.1g), λ_0 is the mean annual rate of events with $IM \geq im_0$; $E[TC | im]$ is calculated as in Equation 2.4; and $p(im | im \geq im_0)$ is the probability density function of damaging IM values, i.e., $p(im | im \geq im_0)dim$ is the probability that the building will experience $IM = im$, given that it experiences an event with $IM \geq im_0$.

2.7.2 Other Decision Variables: Downtime, Injuries, and Fatalities

Fatalities and monetary losses associated with fatalities are estimated as part of this study, as discussed in Chapter 6. Downtime and injuries could also be used as decision variables in the PEER PBEE methodology, but these are outside the scope of the present benchmark study. Even so, for those readers interested in these decision variables, a brief overview of the approach is given in Chapter 6.

3 Benchmark Site and Building Description

3.1 INTRODUCTION

The benchmark building consists of a (hypothetical) four-story office building designed to comply with the 2003 International Building Code. The building is designed at a site located in the Los Angeles basin, which was selected to represent a typical urban site high seismic region of California but without unusually strong, localized near-fault effects dominating the hazard. Eight alternative structural designs are developed to reflect the “design variability,” i.e., how different member proportions could result for the same basic building geometry designed for a given configuration, site, and based on the same building code provisions. This chapter summarizes some key details of the building design, including the site selection and architectural (nonstructural) features that contribute to damage and losses from earthquakes.

3.2 SITE SELECTION AND DESCRIPTION

Our goal was to locate the building on typical urban California site conditions, avoiding unusual site-specific features. Our site-selection criteria were therefore:

- California urban location
- Within a fault transition zone, defined per in IBC 2003 Design Maps (ICC 2003)
- Far from the ends of major strike-slip faults (to avoid directivity issues)
- Not at basin edges (to avoid localized basin effects)
- Not having lens-shaped underlying sediment (to avoid resulting local site amplification)
- Representative site class (NEHRP class C or D, not B or E)
- ROSRINE site (with high-quality geotechnical data; see <http://geoinfo.usc.edu/rosrine>, viewed August 2005)

The selected site is the LA Bulk Mail facility in Bell, California (33.996N, 118.162 W), south of downtown Los Angeles. The site is located on deep sediments, mostly Quaternary alluvial deposits, near the middle of the Los Angeles basin (Fig. 3.1). The basin depth at the site is $z_{1.5} = 1960$ m (Magistrale et al. 2000). One would expect some effect of near-source ground motions, since the site is within 20 km of 7 faults. However, as will be shown in Chapter 4, no single major fault produces near-fault motions that dominate the site hazard, and the contributions of near-fault motions from the other faults are actually very typical of the Los Angeles area. Hence, the essence of the selection criteria is captured with this benchmark site.

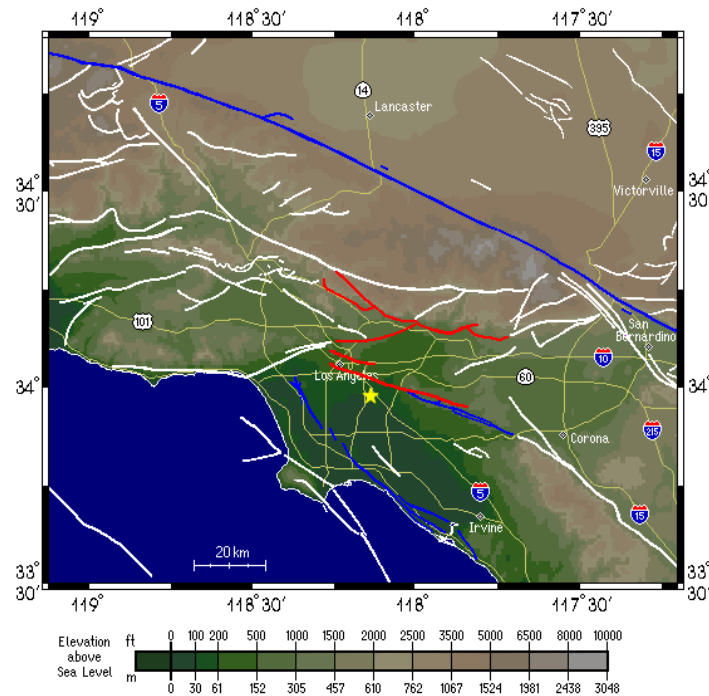


Fig. 3.1 Location map for Los Angeles Bulk Mail site. Red and blue lines, respectively, correspond to strike-slip faults and oblique faults controlling hazard at site. White lines are other faults also contributing to hazard but to lesser extent. Freeways shown for spatial reference (thin yellow lines). More details on faults and site hazard presented in Chapter 4.

The following information is available for the LA Bulk Mail site on the ROSRINE project website (<http://geoinfo.usc.edu/rosrine>): boring logs showing lithology and penetration resistance (SPT blow count), seismic wave velocities from suspension logging, and laboratory index test results. Figure 3.2 summarizes the soil profile and geophysical data. The site is underlain by deep seated alluvial deposits. The upper 30 m consist of sands and silts with traces

of clay and cobbles. These surface materials are underlain by successive layers of clay, sand and silt until relatively stiff material is reached at a depth of approximately 100 m. The shear wave velocity data also shown in Figure 3.2 indicate an average velocity in the upper 30 m of $V_{s-30} = 285$ m/s, which corresponds to NEHRP Category D. The standard penetration test N_{60} blow counts range from 33 to 42 for the upper 30 m (overburden-corrected blow counts, $N_{1(60)}$, range from 14 to 29).

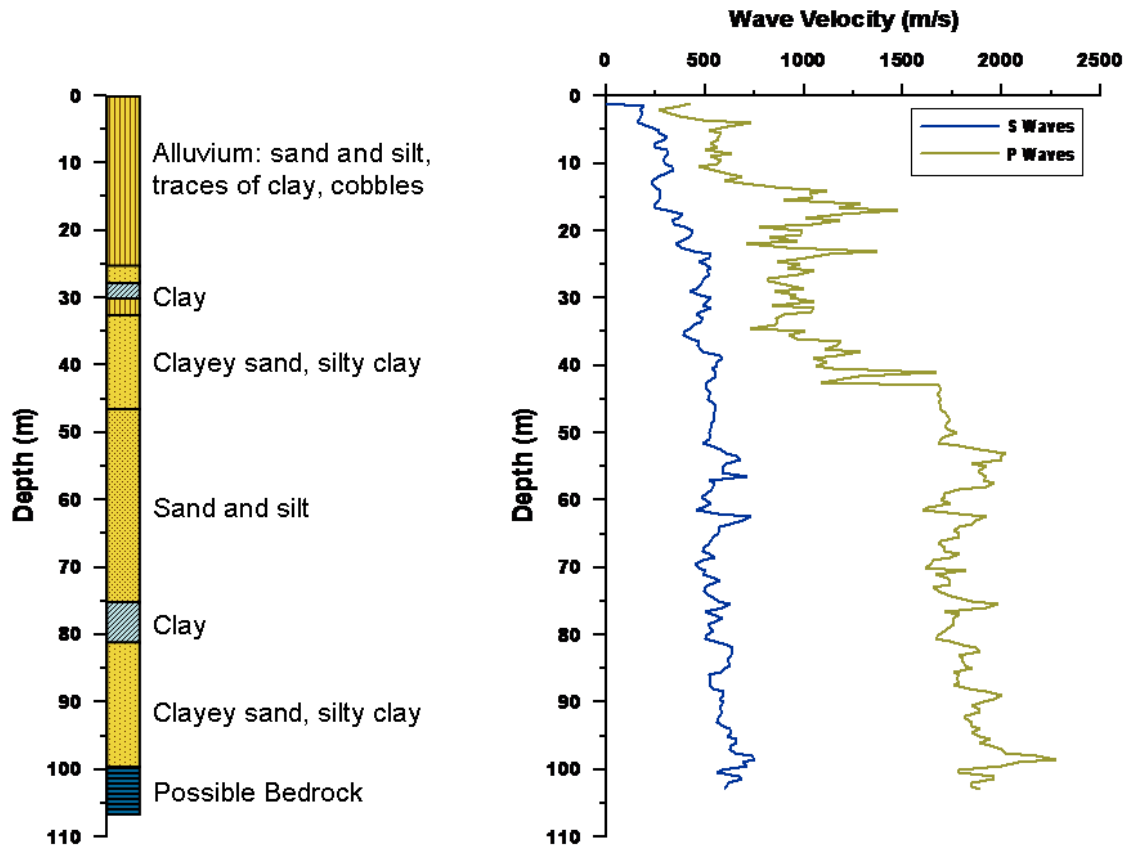


Fig. 3.2 Summary of soil profile (simplified) and seismic wave velocities at Los Angeles Bulk Mail site.

3.3 STRUCTURAL DESIGN

3.3.1 Design Basis Codes

We designed the benchmark building as a special moment-resisting frame according to the 2003 International Building Code (ICC 2003). This provision makes reference to publication ASCE

7-02 *Minimum Design Loads for Buildings and Other Structures* and ACI 318-02 *Building Code Requirements for Structural Concrete*. Table 3.1 identifies important code criteria that controlled the design of the benchmark building, compares 1997 UBC and 2003 IBC code provisions, and summarizes the relevance of each criterion to the benchmark building.

It is interesting to note the effects of the code provisions related to joint horizontal shear limitations. The intention of this requirement is to control the shear demands in the joint region, but this provision affects much more about the design. To meet the joint shear check, the designer often needs to do one or more of three things: (1) add more columns and reduce the bay widths (which adds redundancy), (2) increase the cross-sectional area of the column (which reduces column gravity stresses and increases ductility), or (3) increase the beam depth (which adds lateral stiffness to the frame). Thus, the provision substantially increases the design conservatism.

3.3.2 Review of Practitioner Designs

To make the benchmark building reflect current practice, we collaborated with two San Francisco Bay Area structural engineering firms. We reviewed two building designs in detail and met with the practitioners on multiple occasions to learn how they designed buildings (what assumptions they make, how conservative they are, etc.). Appendix A describes this review in detail and shows how we used this information to ensure that we applied code requirements in a manner consistent with practitioners.

3.3.3 Site Hazard

The complete hazard curve (the mean frequency of exceeding various levels of S_a) is detailed in Chapter 4. However, the design spectral response accelerations according to the building code can be presented here. The benchmark site has mapped short-period and 1-sec period spectral acceleration values of $S_s = 1.50g$ and $S_1 = 0.90g$, respectively, according to the 2003 IBC design maps (ICC 2003). The 5%-damped design spectral response accelerations at short period and at 1-sec period (denoted by S_{DS} and S_{D1} , respectively) are two-thirds of $F_a S_s$ and $F_v S_1$, respectively, where F_a and F_v are site coefficients that depend on site class and S_s , according to the 2003 IBC and ASCE 7-02 (ASCE 2002). Here, $F_a = 1.0$ and $F_v = 1.5$, so $S_{DS} = 1.0g$ and $S_{D1} = 0.90g$.

Table 3.1 Summary of code provisions and application to building design.

<u>Design Requirements</u>	<u>Code References</u>	<u>Comments on 2003 IBC and 1997 UBC Provisions</u>	<u>Application of 2003 IBC Provisions to Design of Benchmark Frame</u>
Strength and Force Demand Provisions:			
Load Combination Requirements	IBC 1605, UBC 1612		
Site Hazard and Lateral Load Demands	IBC 1615, ASCE7 9.4.1.2, ASCE7 Table 9.5.2.5.1, UBC 1630.2	The site hazard maps are significantly changed between the UBC and IBC provisions. The upper bound for building period (for strength design) is different. Both codes adjust the design strength based on the strength reduction and importance factors, as well as the site conditions.	As permitted by ASCE7 Table 9.5.2.5.1, the Equivalent Lateral Force Procedure was used in the design of the benchmark frames.
Distribution of Lateral Forces to Structure	IBC 1617.4, ASCE7 9.5.5, UBC 1630.5		
Required Redundancy	ASCE7 9.5.2.4, UBC 1630.1.1	The requirements are identical for the UBC and IBC. Both provisions require that $\rho < 1.25$ for a SMRF.	In the design of the perimeter frame that spans from A-1 to E-1, $\rho = 1.03$, so the design was slightly altered by this provision. This provision essentially causes the perimeter frame design to include a minimum of four bays in each perimeter frame.
Stiffness Provisions:			
Method Of Computing Drift Demand	ASCE7 9.5.5.7, UBC 1630.9.2	The drift computation differs between the two codes. For a RC SMRF structure, the UBC calculation leads to approximate 10% lower design drifts.	
Drift Limitations	ASCE7 9.5.2.8, UBC 1630.10	The IBC drift limitations are based on the type of structure and the seismic use group, with limitations ranging from 0.7-2.5% drift. The UBC drift limitations are based on the period of the structure and are 2.0% drift for short period structures and 2.5% drift for longer period structures.	The drift limitation did not control the design of the four-story benchmark frame.
Ductility Provisions:			
Detailing	ACI 21.4.4, 21.3.3, 7.10.5.3, UBC 1921.4.3, 1921.3.3, 1907.10.5.3	The provisions are nearly the same for both codes. The only difference is that for beam-column members, the transverse reinforcement spacing requirement was 4" in the UBC, but was relaxed in the ACI to allow for spacing of up to 6" in some cases.	For beam-columns, intermediate ties engaging each longitudinal bar is required by ACI 21.4.4.1, in order to provide concrete confinement and lateral support to the longitudinal bars. The cross-ties for intermediate longitudinal bars is required by 21.4.4.3 in order to provide adequate concrete confinement. Provision 21.4.4.2 did not control the stirrup spacing of the benchmark frame, but the spacing was controlled by the confinement requirements of 21.4.4.1. In the beams, stirrup spacing was controlled by 21.3.3.2 and one cross-tie for longitudinal bars was required by 7.10.5.3.
Reinforcing Ratio Limitations	ACI 21.3.2.1, ACI 21.4.3.1 and ASCE7-02 9.5.2.4	This provision is a limitation for the reinforcing ratio in beam and beam-column members.	The minimum column reinforcing ratio controlled in the designs that involved weaker columns. In these cases, the column size could not be reduced due to the joint shear provision (ACI 21.5.3).
Members not Proportioned to Resist Lateral Loads (Gravity Columns)	ACI 21.11	The provisions are the same for both codes. The provisions allow different design and detailing requirements based on whether the element force demands were checked at the design displacements.	Gravity columns were sized based on meeting the slab shear provisions of ACI 11.12. The detailing of the column was done for the case that the forces were not explicitly checked for the design displacements (21.11.1 and 21.11.3). As the factored axial force in the gravity column is large 21.11.3.3 requires that the gravity column be detailed according to many of the provisions that apply for the beam-column members of the lateral force resisting system.

Table 3.1—Continued

Capacity Design Provisions:			
Strong-Column Weak Beam	ACI 21.4.2, UBC 1921.4.2.2	This provision has changed significantly. In the IBC, the girder strength in negative bending is required to include slab steel effects. Additionally, the moments are summed at the faces of the joint. The IBC approach is 25-35% more conservative than the UBC approach.	This provision controlled the strength of all columns of the benchmark building.
Shear Demands in Elements	ACI 21.3.4 and 21.4.5, UBC 1921.3.4 and 1921.4.5	These provisions are the same for both codes.	These provisions controlled the amount of transverse steel in areas of the elements other than the plastic hinge region. In multiple cases, this provision also required that the spacing of the transverse reinforcing be reduced beyond that required by ACI 21.3.3.4 and 21.4.4.6. The requirement in 21.3.4.2 did not apply to the design, because even though the axial column axial demands were low, the earthquake induced shear force was less than one-half of the maximum required shear strength.
Joint Horizontal Shear Limitations	ACI 21.5, UBC 1921.5	These provisions are the same for both codes.	This provision ended up controlling much of the structural design. Similarly to the redundancy provision, these provisions controlled the number of bays required in the frame to keep the joint shear below the prescribe threshold. Meeting this provision often required using a larger column cross-sectional area or increasing the beam depth. By providing a lower bound to the column size, this provision effectively limits the column axial load ratio and thus increases the column ductility.
Continuity Provisions:			
Splice Requirements	ACI 12.14, 21.2.6, 21.3.2.3, and 21.4.3.2, UBC 1921.3.2.3 and 1921.4.3.2	Lap splices are only permitted in the center half of the member length for beam-columns, and are precluded from the hinge regions for beams. All lap splices are required to be enclosed transverse reinforcement.	The splices of the benchmark building were not designed, as the splice details will have no impact on the performance assessment that is to follow the design. This is based on the assumption that a splice failure mode is not likely in newly designed RC SMRF frame buildings. This assumption will be researched shortly, to ensure that a splice failure mode is not probably for this type of design.
Reinforcing Continuity	ACI 21.3.2.1, UBC 1921.3.2.1	For flexural members, it is required that at least two bars be provided continuously, both top and bottom. This provision is identical for both codes.	This provision did not impact the design of the benchmark building.
Slab-Column Joints	ACI 13.3.8.5, UBC 1913.3.8.6	At least two of the column strip bottom bars are to pass through the column core and be continuous and anchored to exterior supports. All other bottom bars must be spliced with a as per ACI 13.3.8.5. This provision is identical for both codes.	This provision was met for the design of the benchmark building. This provision is important for later performance assessments, as the continuity of bottom rebar will delay local collapse hazards due to failure of the slab-column joint.

3.3.4 Building Layout

The structural layout of the benchmark building is depicted in Figure 3.3, and represents a four-bay by six-bay plan with 30-ft span lengths. Figure 3.4 shows the elevation of the frame with a 14-ft first story and three 13-ft stories above. The layout is consistent with the practitioners’

guidance on how they would design an office building with this general architectural arrangement. Figure 3.3 represents the design variants that incorporate a perimeter-frame system (Section 3.3.6.1). We also examine space-frame designs (Section 3.3.6.2) which have similar plan layout, but with a lateral moment-resisting frame on every framing line.

For the purpose of the seismic performance assessment of the benchmark building, we use two-dimensional nonlinear dynamic response history analyses (Section 5.2.1). To complete these analyses for the perimeter-frame buildings, the frame along column line 1 is assessed with the appropriate tributary load and mass.

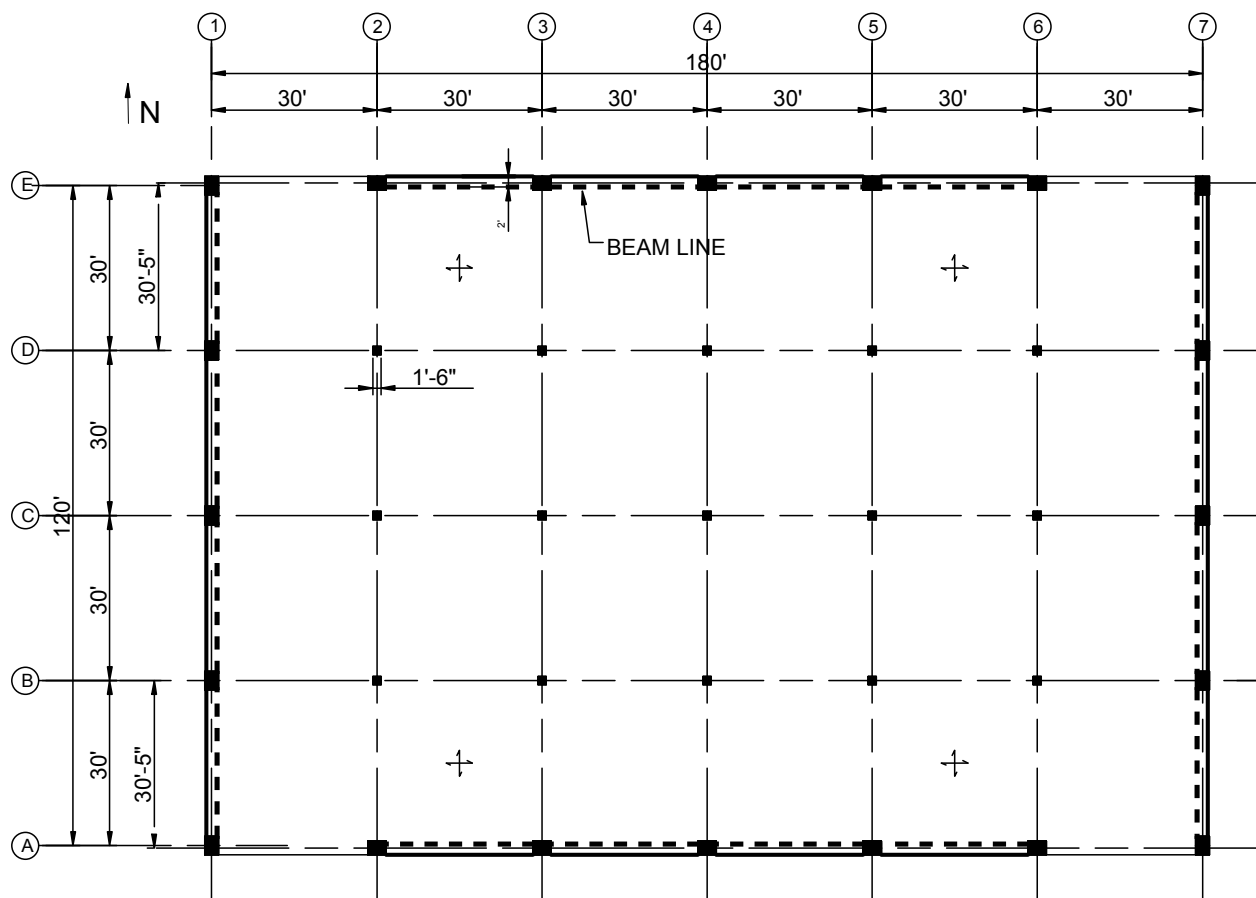


Fig. 3.3 Plan view of perimeter-frame benchmark building.

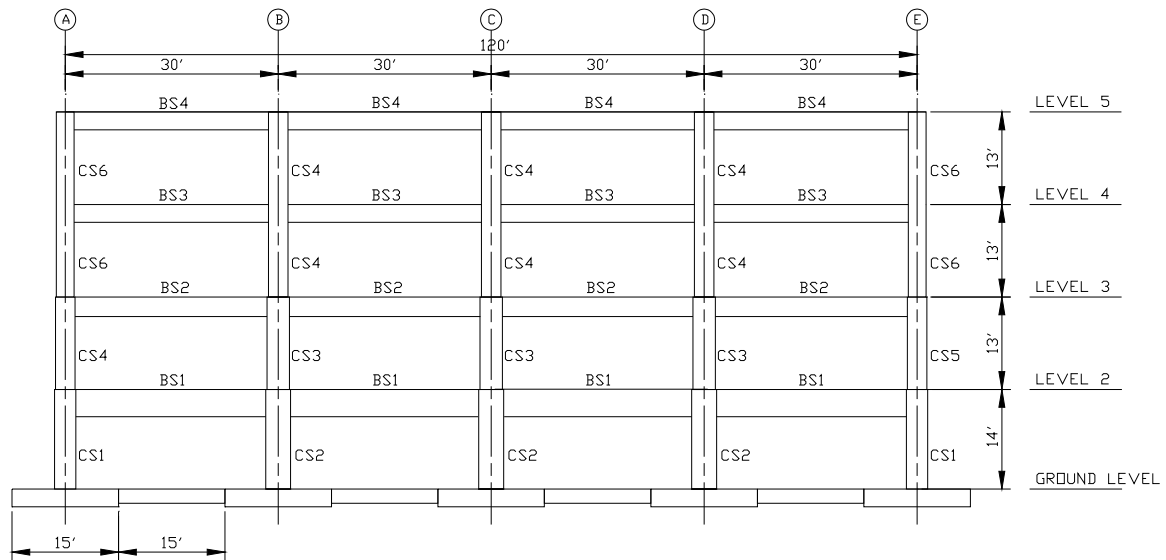


Fig. 3.4 Elevation view of frame along column line 1.

3.3.5 Design Variants

3.3.5.1 Motivation to Examine Design Variants

Within the constraints of the building code, important design variables included:

- System:
 - Building system: space frame or perimeter frame
 - Plan and elevation strength and stiffness irregularities
 - Floor heights
 - Bay widths
 - Frequency of reducing beam and column sizes over the building height
- Structural members:
 - Level of conservatism in applying the element strength requirements
 - Consideration of slab steel in design (i.e., possible T-beam design)
 - Application of the strong-column weak-beam (SCWB) provision even if code does not require it (ACI 318-02, Section 21.4.2.1)
 - Column sizes and resulting axial load ratios (important for column ductility)
 - Foundation design (footing sizes, link beam sizes, detailing, etc.)
- Modeling (Section 5.2.1 provides an overview of the element types used in the structural model):

- Member stiffness assumed in design
- Column base rotational stiffness assumed in the design

These design decisions can significantly affect the building performance, so to reflect some of the variability in the performance due to these design decisions, we created multiple design variants that test the sensitivity of performance to alternative choices of many (but not all) of the variables listed above. For those variables not reflected with alternative variants, we attempted to be consistent with current engineering practice, often referring to the practitioners' design documents (Appendix A), and periodically consulting with the practitioners. As summarized in Table 3.2, seven variants of the basic design were developed to probe the sensitivity of performance to four of the variables:

- Building system: space frame and perimeter frame examined (column 2 of Table 3.2)
- Level of conservatism in applying the element strength requirements (columns 3 and 5)
- Consideration of slab steel in design (i.e., possible T-beam design; columns 6 and 8)
- Application of the strong-column weak-beam (SCWB) provision even if code does not require it (ACI 318-02, Section 21.4.2.1; columns 4 and 7)

Other design variables, such as strength and stiffness irregularities may impact performance, but these were outside the scope of this study. Also note that the design variability, which affects the physical properties of the model, are distinct from modeling uncertainty, which reflects how the structural properties are modeled in the nonlinear time-history simulations.

Table 3.2 Summary of design decisions.

Design	Frame System	Beam Design Strength Factor ($\phi M_n / M_u$)	SCWB Factor (code requirement is 1.2)	Provided ratio of positive to negative beam flexural capacity (ACI 318-05 21.3.2.2)	Beams Designed as T-Beams?	SCWB Provision Applied in Design	Slab Steel
A	Perimeter	1.25	1.3	0.75	No	2003 IBC / ACI 318-02	2 #4 @12" o.c.
B	Perimeter	1.0	1.2	0.5	No	2003 IBC / ACI 318-02	2 #4 @12" o.c.
C	Perimeter	1.25 ^a	1.3 ^a	0.5	No	2003 IBC / ACI 318-02	2 #4 @12" o.c.
D	Perimeter	1.0	n/a	0.5	No	none ^b	2 #4 @12" o.c.
E	Space	1.0	1.2	0.5	No	2003 IBC / ACI 318-02	2 #4 @12" o.c.
F	Space	1.0	1.2	0.5	Yes	2003 IBC / ACI 318-02	2 #4 @12" o.c.
G	Space	1.0	1.2	0.5	No	1997 UBC	2 #4 @12" o.c.
H	Space	1.0	1.2	0.5	No	1997 UBC	#5, #6 @16" o.c.

a - only the second floor beam and first story columns were proportioned for these ratios
b - not a code-conforming design; columns designed for strength demand, not considering strong-column weak-beam design provisions

3.3.5.2 Perimeter-Frame Design Variants

As shown in Figures 3.3 and 3.4, the lateral system of the perimeter-frame design variants consists of two exterior frames in each direction. For the convenience of this study, we designed the frame along line A1–E1 and then used this same frame design for A7–E7, A2–A6, and E2–E6 (notice in Fig. 3.3 that the beam does not continue between A1–A2). This design simplification allows us to use a two-dimensional finite-element model (Section 5.2.1).

The gravity system consists of 18-in.-sq concrete columns spaced at 30-ft centers and an 8-in. post-tensioned two-way slab. The slab was not explicitly designed, so the slab reinforcement was taken to consist of #4 reinforcing bars at the top and bottom of the slab spaced at 12-in. centers, which is generally consistent with the practitioner designs (Appendix A). Based on the practitioner designs, the likely slab steel could be up to 50% greater; however, we used the lower amount to be conservative and because a modest increase in slab would not markedly change the structural response in the perimeter-frame system. Note that this trend is not always true for the space-frame design variants, where an increase in slab steel was considered in design Variant H (see Section 3.3.6.2).

As outlined in Table 3.2, we examine four variants of the perimeter moment frame. Key aspects of these four variants are described below, with further details in Appendix B. All designs are based on the 2003 IBC (and ACI 318-03, ASCE7-02) provisions, and the beam strength design does not consider the strength due to the adjacent slab.

Design A. Design A represents an average “practitioner” design, which tends to exceed the minimum building code requirements. This design includes 25% beam flexural strength above code minimum, an average SCWB ratio of 1.3 (as compared to the 1.2 requirement), and an average of $[M_{n, \text{pos}} / M_{n, \text{neg}}] = 0.75$ (as compare to the code prescribed limit of 0.50, i.e., ACI 2005, Section 21.3.2.2). Figures B.5–6 of Appendix B show the actual strength ratios and SCWB ratios for this design.

Design B. Design B meets the code force requirements, as closely as possible to the minimum values. It includes no flexural strength in beams above the code minimum and an average SCWB ratio of 1.2.

Design C. Design C is meant to be easily constructible (use of same forms, etc.). For Design C, we designed the level-2 beam and first-story columns (BS1, CS1, CS2 in Fig. 3.4) and

used these same member dimensions, reinforcing schedule, and material properties, in upper-story beams and columns.

Design D. Design D has columns that are designed based on strength demands and do not adhere to the SCWB capacity design requirements of the building code. Design D is not a code-conforming design, but was done just to quantify the effects of the SCWB requirement. To proportion the members in Design D, we started with Design B and reduced the column strengths to be based on strength demands, while still leaving 20% additional strength to account for steel material over strength of 10% (Table F.1) and the over strength from $\phi = 0.9$. Note that when using small columns and still meeting the joint shear requirements (which often cause the column cross-sectional size to be increased), the minimum reinforcement ratio of 0.01 may control the design and provide additional column over strength. This potential source of over strength was not considered in Design D.

3.3.5.3 Space-Frame Design Variants

Figure 3.5 shows the plan view of the space-frame variants. The elevation of these designs is the same as for the perimeter frames (Fig. 3.4). Other than the change to the structural system, the space-frame building is identical to the perimeter-frame building (dimensions, site, loading, slab system, usage, etc.). The designs of the space-frame and perimeter-frame buildings are similar, except that the beam design strengths in the space frame are more affected by the gravity loading, which causes the space-frame designs to have much higher over strength (Section 5.9.2).

Analysis of the space-frame variants raised the issue of modeling building collapse where the columns would be subjected to large biaxial bending under earthquake effects. Since there does not appear to be a consensus among researchers on how to address this problem, and since modeling of biaxial response would require a more involved three-dimensional model, we made the simplifying assumption to treat the space frames as uncoupled in each of the two loading directions. This is a significant simplification but a necessary one, because well-calibrated element models that can capture the three-dimensional collapse behavior of an RC column do not exist. Even if they did, test data on biaxially loaded columns, needed to calibrate such a model, are limited. For more detailed discussion of this three-dimensional problem and the approach that we take in this study, see the modeling and analysis Section 5.11.1.

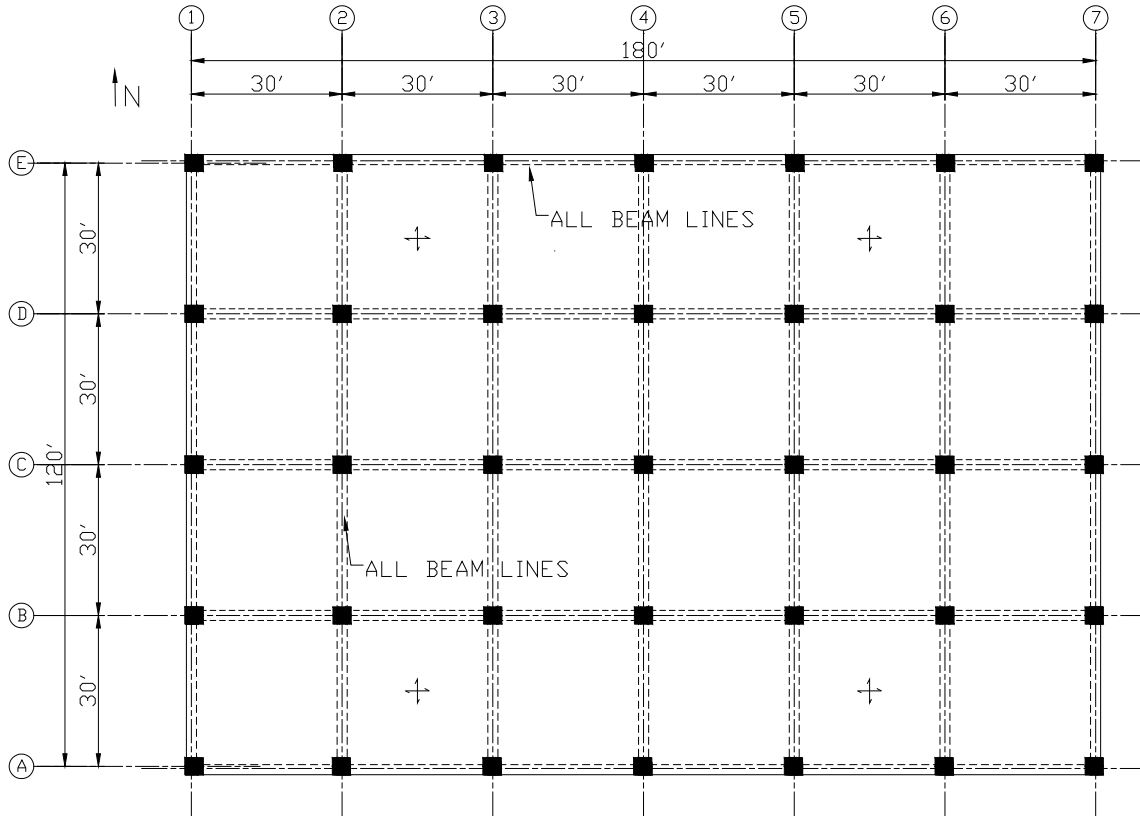


Fig. 3.5 Plan view of space-frame benchmark building.

To help compensate for the simplification of biaxial column response in analysis, the space-frame design variants were designed based on strength demands and capacities along a single framing line, neglecting biaxial bending. Thus, by neglecting the additional strength that would have been provided in the design for biaxial bending, the assumption is that this will partially compensate for neglecting the out-of-plane effects that are not considered in the two-dimensional analysis.

As shown in Table 3.2, four space-frame variants are considered. Included below is an overview of the designs; further details are provided in Appendix B. All designs are based on the minimum force requirements of the 2003 IBC (similarly to Design B), and the minimum SCWB ratio of 1.2 (from the code used for the specific design, see Table 3.2).

Design E. Design E was based on the provisions of the 2003 IBC and ACI 318-02. The beam reinforcement required for the minimum strength design was calculated without considering the contribution of the slab steel. However, the slab steel was considered when

evaluating the minimum column strength, as required by the SCWB provision of the ACI 318-02 Section 21.4.2.2.

Design F. Design F was based on the provisions of the 2003 IBC and ACI 318-02. In the beam strength design, the beams were designed as T-beams where the slab steel was considered to contribute to the strength of the beams. Thus, the beam steel in Design F is less than in Design E.

Design G. Design G is similar to Design E, except the minimum column strengths were determined according to the SCWB provision of the 1997 UBC, as opposed to the IBC 2003. Other than this SCWB provision, the design conforms to the provisions of the 2003 IBC and ACI 318-02. We used this design variant to examine the effects that the change in SCWB provision has on the performance of buildings with significant contributions of slab steel, such as space-frame buildings.

Design H. Design H is identical to Design G except that the slab steel is increase by approximately 50%. The intent of this variant is to investigate the extent to which the less conservative SCWB provision of the 1997 UBC could potentially lead to a story mechanism when the slab steel is over-designed and not included in the SCWB check.

3.4 NONSTRUCTURAL COMPONENTS

This hypothetical benchmark building was designed assuming office occupancy. As shown in Figures 3.6 and 3.7, architectural floor plans were created, sufficient for damage and loss calculations. They depict several conference rooms, a mailroom, private and cubicle offices ranging in plan area between 125–300 ft². Drywall partitions are 5/8" wallboard on 3-5/8" metal studs at 16" centers with screw fasteners. Exterior walls are 5-ft by 6-ft lightweight glazed aluminum panels. Hydraulic elevators provide vertical transport, as is typical for two- to five-story buildings. Automatic sprinklers provide fire suppression. Ceilings are suspended aluminum grid with 2-ft by 4-ft tile. These components are discussed in more detail in the following sections.

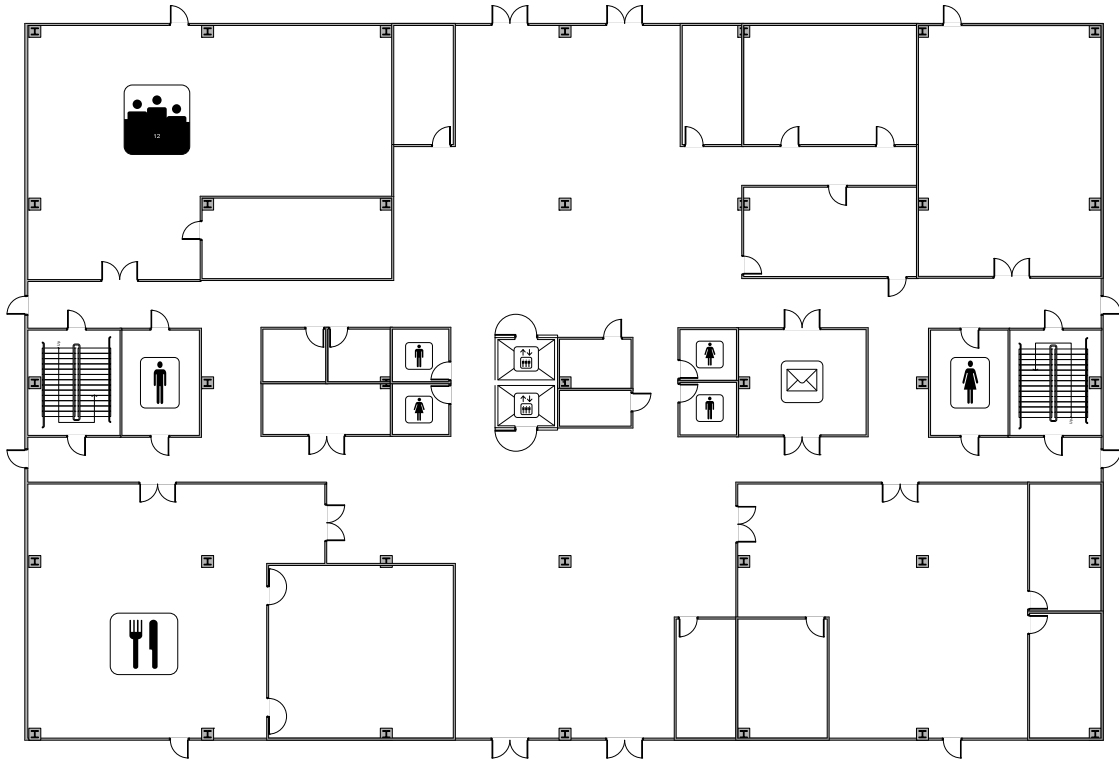


Fig. 3.6 Floor plan of ground floor.

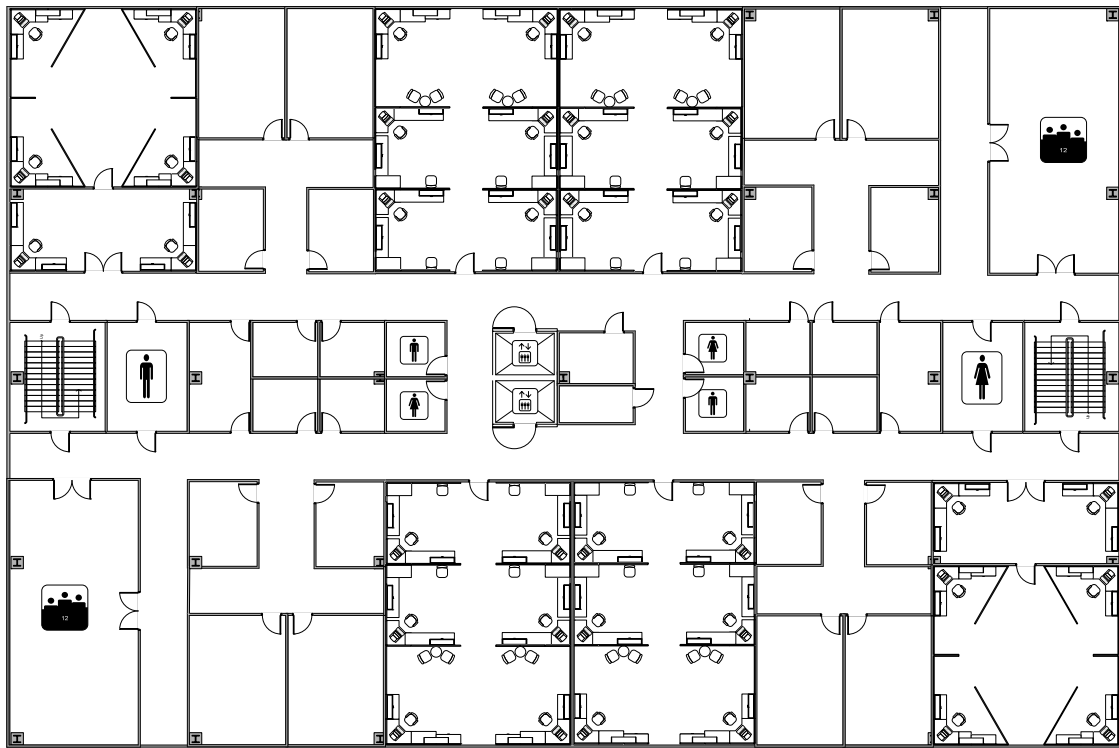


Fig. 3.7 Floor plan of floors 2-4.

3.4.1 Wallboard Partitions

Interior full-height non-fire-rated walls of the benchmark building use a single layer of 5/8-in. gypsum wallboard fixed with drywall screws to 3-5/8-in. metal studs with fixed (rather than sliding) top plates. Fire-rated walls (2-hour rating at elevator shafts and stairwells) use multiple layers of wallboard. These additional layers make the walls more resistant to interstory displacements (Pardoen 2000). Therefore, these walls are considered to be robust and are not included in the loss analysis. Modular office furniture is used for partial-height partitions, which are assumed to be anchored to the slab and thus rugged (not damageable) and therefore excluded from the damage and loss analysis.

3.4.2 Exterior Glazing

Damageability data are limited for exterior glazing. We used fragility functions developed earlier (Porter 2001) based on analysis of laboratory tests by Behr et al. (1998) for Horizon Wall glazing. The exterior cladding system is composed of 5-ft by 6-ft architectural glass assemblies with aluminum framing. A total of 1,060 glass assemblies make up the cladding for the benchmark building.

3.4.3 Elevators

The benchmark building has two passenger hydraulic elevators that serve all story levels and comply with the 2003 International Building Code (ICC 2003) and the *American Society of Mechanical Engineers Safety Code for Elevators and Escalators* (ASME 1997). Also, the benchmark building abides by the *Americans with Disabilities Act Design Requirements for Accessible Egress* (ADAAG 2002), which requires at least one passenger elevator for private facilities that have more than 3000 sq ft per story and that are at least three stories tall. The dimensions of the elevator cars in the benchmark building are 81" wide and 114" deep, as required to meet wheelchair access requirements (ADAAG 2002).

3.4.4 Sprinklers

The benchmark building uses an active fire protection system (or wet automatic sprinklers), shown in Figures 3.8 and 3.9, to protect against damaging fires. Each floor of the benchmark building has an area of 21,600 ft², within the allowable range for sprinkler-protected area for office buildings and categorized as “light hazard” according to the *National Fire Protection Association’s Automatic Sprinkler Systems Handbook* (NFPA-13 2002). The area/density approach of the NFPA handbook (NFPA-13 2002) is used to design the sprinkler system. The minimum required area of sprinkler operation for an office building is 1,500 ft² and an area of operation of 2,000 ft² is assumed for the design of the sprinkler system. Assuming that each sprinkler provides 125 ft² of coverage, the hydraulic calculation assumes that a minimum of 16 sprinklers operate simultaneously during a fire emergency. The piping necessary for these requirements is 2,241 linear feet in the first story and 2,418 linear feet for all stories above. The sprinkler pipe weight is supported by hanger rods and the pipes are braced every 12 feet to restrain lateral and longitudinal displacements.

3.4.5 Ceiling

The ceiling consists of a grid-work of aluminum channels in the shape of an upside-down “T,” connected to the diaphragm above with splay wires that, in theory, provide lateral-force bracing along with vertical compression struts. These channels are in a regularly spaced pattern made up of a 2-ft by 4-ft grid and support lightweight acoustical ceiling tiles. A total of 81,000 sq ft of acoustical tiles make up the ceiling for the four-story building.

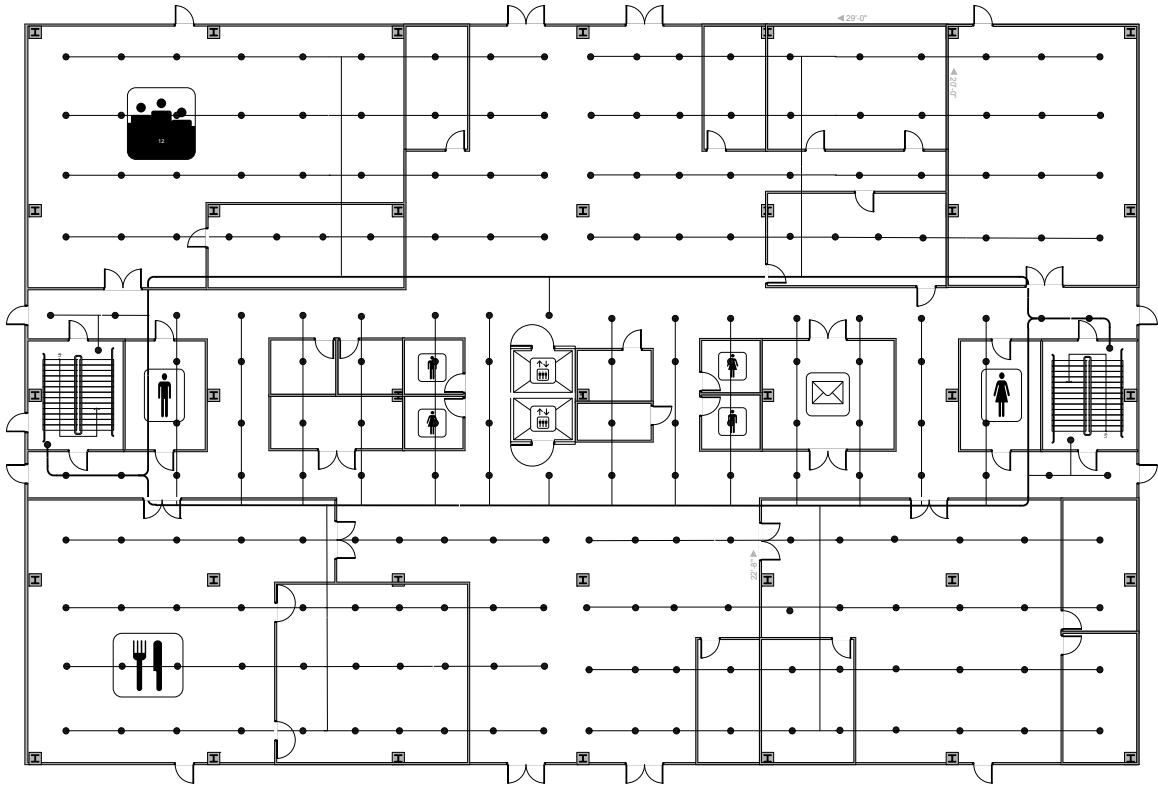


Fig. 3.8 Automatic sprinkler piping system of ground floor.

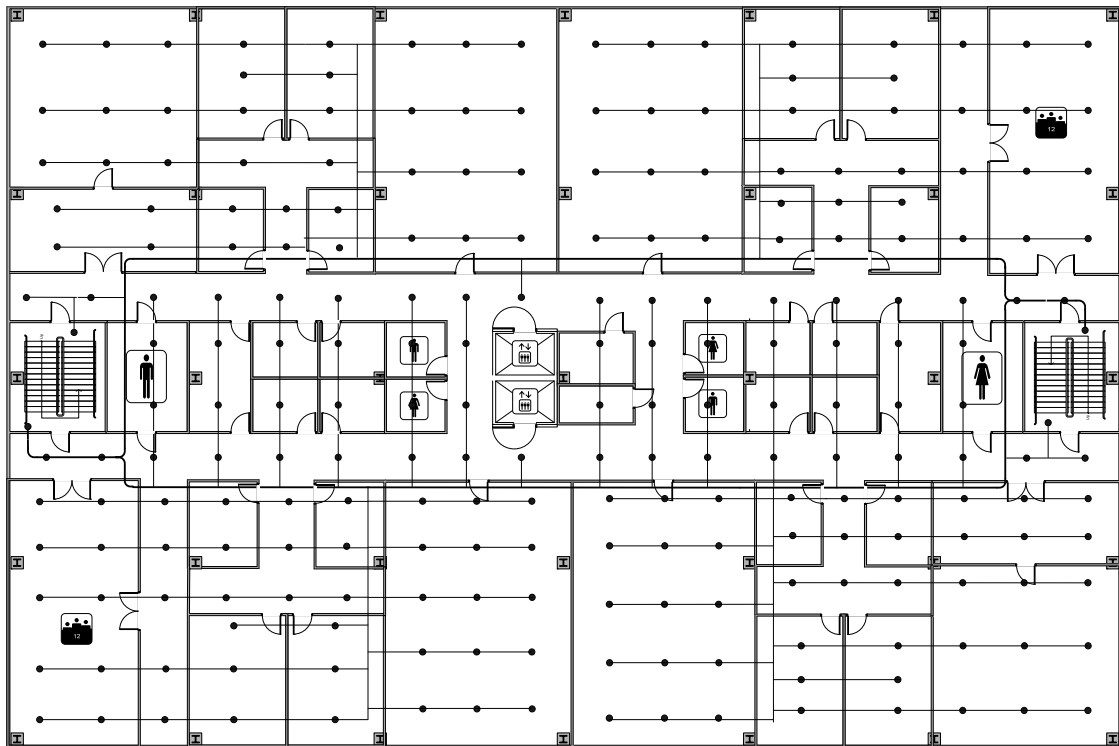


Fig. 3.9 Automatic sprinkler piping system of floors 2-4.

3.5 SUMMARY OF DAMAGEABLE BUILDING COMPONENTS

A table of the components considered in the damage and loss analyses, including brief descriptions and quantities, is given below for the perimeter-frame designs in Table 3.3 and for the space-frame designs in Table 3.4.

Table 3.3 Damageable assemblies for perimeter-frame design.

Assembly Designation	Assembly Description	Unit	Quantity
3.5.190.1102.01	Ductile cast-in-place reinforced concrete beams	ea	64
3.5.180.1101.01	Ductile cast-in-place reinforced concrete columns	ea	80
B1045.003	Column-slab connections	ea	80
6.1.500.0001.01	Drywall partition, 5/8-in., 1 side, on metal stud	64 sf	1,293
6.1.500.0002.01	Drywall finish, 5/8-in., 1 side, on metal stud	64 sf	1,293
4.7.100.0001.01	Exterior glazing, 5'x6' pane Al frame	pane	1,060
6.7.100.5800.01- 6.7.100.5800.31	Acoustical ceiling, 2'x4' light Al grid attached	sf	81,000
8.2.110.0000.02	Automatic sprinklers, braced	12 lf	793
7.1.100.0000.01	Hydraulic elevators	ea	2

Table 3.4 Damageable assemblies for space-frame design.

Assembly Designation	Assembly Description	Unit	Quantity
3.5.190.1102.01	Ductile cast-in-place reinforced concrete beams	ea	232
3.5.180.1101.01	Ductile cast-in-place reinforced concrete columns	ea	140
6.1.500.0001.01	Drywall partition, 5/8-in., 1 side, on metal stud	64 sf	1,293
6.1.500.0002.01	Drywall finish, 5/8-in., 1 side, on metal stud	64 sf	1,293
4.7.100.0001.01	Exterior glazing, 5'x6' pane Al frame	pane	1,060
6.7.100.5800.01- 6.7.100.5800.31	Acoustical ceiling, 2'x4' light Al grid attached	sf	81,000
8.2.110.0000.02	Automatic sprinklers, braced	12 lf	793
7.1.100.0000.01	Hydraulic elevators	ea	2

4 Hazard Analysis and Ground Motion Characterization

4.1 SITE HAZARD CHARACTERIZATION

One of the objectives of this project is to quantify uncertainties at each stage of the PBEE methodology, from hazard analysis to loss analysis (*IM* to *DV*). The objectives of the hazard analysis are twofold. First, we provide hazard curves that express the probability of exceeding various values of *IM* within a given time period. Of particular interest are *IM* values for selected hazard levels (the definition and justification for those hazard levels is provided later in this chapter). Second, we compile suites of ground motion records that are compatible with the selected hazard levels for use in structural response analyses.

The analysis of ground motion hazards is affected by aleatory and epistemic uncertainties. These two fundamental types of uncertainty are defined as (BESR 1997):

- Aleatory: the uncertainty inherent in a nondeterministic (stochastic, random) phenomenon.
- Epistemic: the uncertainty attributable to incomplete knowledge about a phenomenon that affects our ability to model it.

Epistemic uncertainty can possibly be reduced with further research, better knowledge, and improved models. The remaining uncertainty is considered aleatory. One could argue that all uncertainty is epistemic and that it could be reduced if all the physics of a phenomenon was understood. For the purpose of this report, the epistemic uncertainty is addressed at the model level and the term “epistemic uncertainty” is equivalent to “model uncertainty.”

The evaluation of hazard curves for *IM* (sometimes called “Probabilistic Seismic Hazard Analysis,” or PSHA) formally accounts for ground-motion prediction uncertainty conditional on an attenuation model (e.g., McGuire 2004; Stewart et al. 2001) through the use of a lognormal

probability density function on the *IM* level conditional on magnitude, distance, and other source/path/site parameters.

The *IM* selected for this project is the 5% damped spectral acceleration response at the building's estimated first-mode period $S_a(T_1=1.0\text{ s})$. According to Shome and Cornell (1998) and Luco and Cornell (2005), $S_a(T_1)$ is a useful *IM*, with efficiency and sufficiency comparable or superior to other available scalar *IMs* such as PGA that can be calculated independently of the structure. Moreover, many ground motion prediction equations are available for spectral acceleration, which makes $S_a(T_1)$ convenient to use as the *IM* for this project. It will also be shown in Section 4.2 that when $S_a(T_1)$ is combined with the parameter ϵ for record selection, it represents a more sufficient *IM*.

Epistemic uncertainty for this *IM* is considered by using alternative feasible models for critical components of the hazard analysis. Specifically, we consider alternative ground motion prediction equations and alternative estimates of fault slip rate. More information on the treatment of epistemic uncertainty is provided in Section 4.1.2.

The interest in performing a site-specific analysis for this project comes from the desire to utilize additional information to improve the hazard estimates and to estimate the uncertainty of those estimates. An alternative to performing a site-specific analysis would have been to use PSHA data from the U.S. Geological Survey's National Seismic Hazard Mapping project (<http://eqint.cr.usgs.gov/eq-men/html/custom2002.html>). Although maps provided by the USGS are helpful, they provide inadequate detail for present purposes on fault definitions and their treatment. More specifically, we can not obtain results for a specific set of parameters or for certain hazard levels as we can by running hazard analysis software. This has important implications for the selection of records and consistency of results.

4.1.1 Project Specific Parameters and Mean PSHA Results

As described in Section 3.1, the chosen building site is the LA Bulk Mail site consisting of alluvial sediments with $V_{s30} = 285\text{ m/s}$, which indicates NEHRP category D (FEMA 1997). Accordingly, soil-site ground-motion attenuation relationships were used in the present analyses.

A PSHA was performed for the selected site using computer code HAZ (versions 3.1 and 3.6) developed by Abrahamson (2004). The HAZ code was used with the four attenuation relationships listed in Table 4.1. The Next Generation Attenuation (NGA) models were

unavailable at the time these calculations were performed (Boore and Atkinson 2006, Campbell and Bozorgnia 2006, Chiou and Youngs 2006). The weights given in Table 4.1 reflect the authors' judgment; the down-weighting of the Boore et al. (1997) equations is based on their use of a linear site term, which may bias near-fault ground motion estimates. The site term is set where most of the data lie—which is at large distance (hence, weak motion and nearly linear site response). Projecting this linear term to the near field introduces bias, hence the down-weighting.

Table 4.1 Ground motion prediction equations used for PSHA.

Ground Motion Prediction Equation	Weight	Site Condition	Horizontal ground motion prediction	Directivity Estimation
Abrahamson and Silva (1997)	0.3	Soil or rock	Geometric mean	Yes*
Campbell (1997)	0.3			No
Sadigh et al. (1997)	0.3			
Boore, Joyner, and Fumal (1997)	0.1	V_{s30}	Geometric mean or Individual component	

* With Somerville directivity (Somerville et al. 1997)

We used a source model for California by the California Geological Survey (Frankel et al. 2002 and Bryant 2005). This model updates the widely used source model of the Working Group on California Earthquake Probabilities (1995). Preliminary mean hazard curves were developed by considering variations in attenuation relations (per Table 4.1). Later we also considered variations in source parameters (details provided in next section) and re-computed a mean hazard curve for 5%-damped elastic spectral acceleration response at a 1-sec period. The preliminary mean hazard curves obtained from the PSHA are presented in Figure 4.1 for various spectral periods.

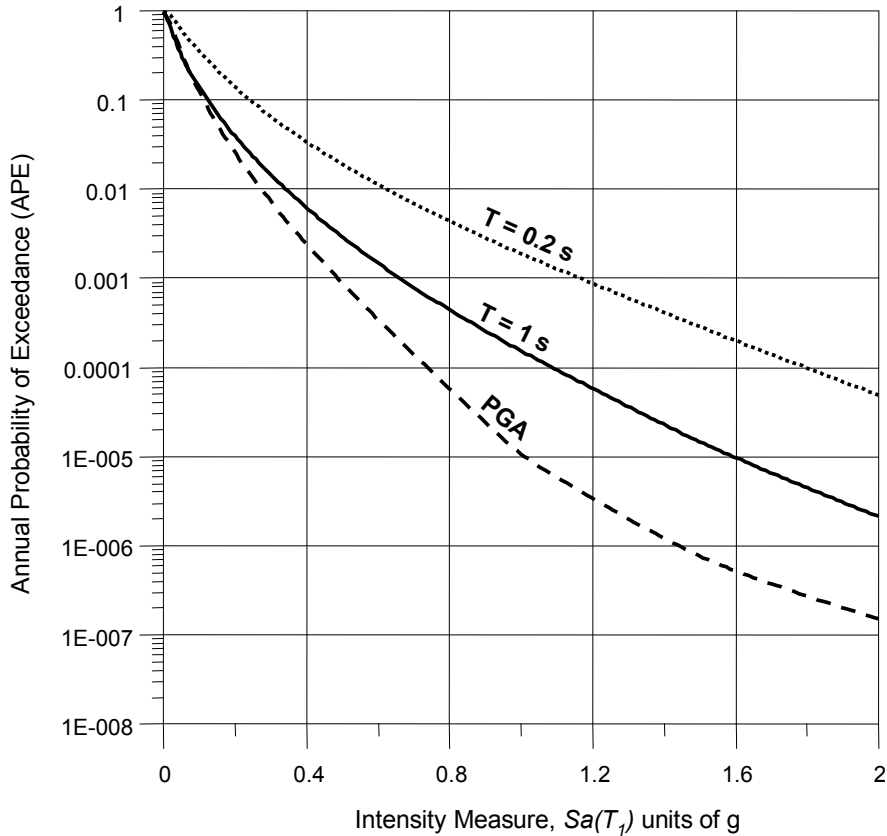


Fig. 4.1 Mean hazard curves for three spectral periods for LA Bulk Mail site.

Table 4.2 shows the values of the mean ground motions for the seven hazard levels selected. The interest in selecting a wide range of hazard levels (from 50% probability of exceedance in 5 years to 2%-in-50-years) was to provide a broad range of ground motion levels for the site (with their associated probabilities) for use in structural damage and loss estimates. This is critical for a performance-based estimate of structural performance. Even modest ground motions can generate nonstructural damage. The larger ground motions having lower annual probabilities (e.g., 2% exceedance probability or less in 50 years) are used to evaluate collapse probabilities. Uniform hazard spectra are plotted in Figure 4.2 for the hazard levels identified in Table 4.2.

Table 4.2 Uniform mean hazard results.

Spectral acceleration (units of g) for each hazard level							
Hazard level (Equivalent mean return period in yr)	50% in 5 yrs (7)	20% in 5 yrs (22)	10% in 5 yrs (47)	50% in 50 yrs (72)	20% in 50 yrs (224)	10% in 50 yrs (475)	2% in 50 yrs (2475)
Period (s)							
0.01 (PGA)	0.10	0.17	0.21	0.25	0.34	0.41	0.58
0.2	0.21	0.36	0.49	0.57	0.81	0.99	1.46
1.00	0.10	0.19	0.26	0.30	0.44	0.55	0.82

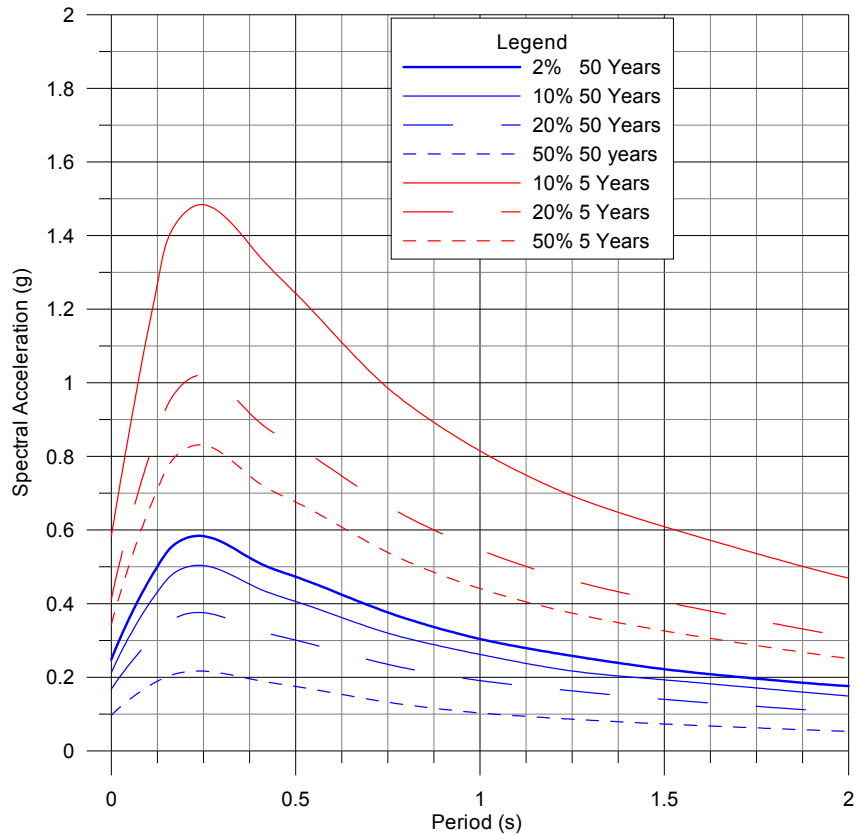


Fig. 4.2 Mean uniform hazard spectra (5% damping) for LA Bulk Mail site for seven hazard levels.

4.1.2 Estimation of Epistemic Uncertainty Associated with Mean Uniform Hazard Results

A key uncertain parameter in the fault rupture models for many faults is the fault slip rate. Changes in the slip rate significantly affect the rate of future earthquakes expected on the fault and hence the hazard attributable to that fault. Accordingly, we also performed PSHA for various

realizations of fault slip rate for several key faults in the study area. The faults for which slip rate was varied, and the values of slip rate considered, are given in Table 4.3.

Table 4.3 Slip rates for faults significantly contributing to site hazard at T=1 sec. Faults selected for consideration of effect of slip rate variability on results if they contribute > 5% of site hazard.

Fault Name	Slip rate (mm/year) (Bryant 2005)	
	μ	σ
Elsinore-Whittier	2.5	1.0
Sierra Madre	2.0	1.0
Newport-Inglewood	1.0	0.5
San Andreas-Mojave	30.0	7.0
San Andreas-1857 Rupture	34.0	10.0
Puente Hills	0.7	0.4
Raymond	1.5	1.0

Hazard analyses were repeated for three possible realizations of slip rate for each of the faults listed in Table 4.3, as well as for each of the attenuation relationships listed in Table 4.1, as illustrated in Figure 4.3. This resulted in 12 realizations per fault (three slip rates and four attenuation relationships), or 84 realizations in total (12 per each of 7 faults). From these 84 results, we then computed a new hazard curve for T=1 sec along with the standard deviation of the hazard, assuming a normal (Gaussian) distribution of the hazard. The means and standard deviations were calculated for the probabilities corresponding to particular levels of ground motion.

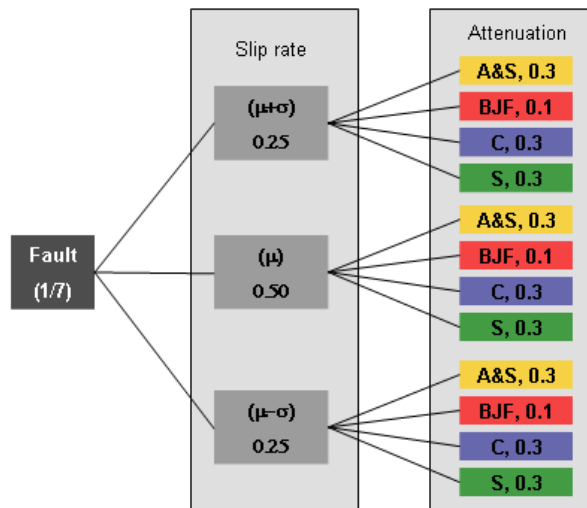


Fig. 4.3 Logic tree for epistemic uncertainty estimation. Numbers correspond to weights. We assume $\pm 2\sigma$ truncation. Attenuation relationship abbreviations (all 1997): A&S: Abrahamson and Silva, B&J: Boore, Joyner and Fumal, C: Campbell, S: Sadigh.

The weights given for slip rate in Figure 4.3 represent a balance between theoretical rigor and practical considerations. The theoretical optimal three-point representation of a normal distribution would involve sampling the distribution at the mean (μ) and $\mu \pm \sqrt{3}\sigma$, and then providing the samples with weights of 2/3 and 1/6 (twice). Those sample points and weights preserve the first (mean), second (variance), and fourth central moments of the underlying distribution (Rosenblueth 1975; Ching et al. 2006). In practice, the above sample points cannot be used for many faults in California because a reduction of $\sqrt{3}\sigma$ below the mean would result in very small slip rates. Accordingly, we elected to sample at $\mu \pm \sigma$ with the weights given in Figure 4.2, which provides a good match to a normal distribution truncated at two standard deviations. We recognize that this assumption may underestimate the epistemic uncertainty of ground motion due to slip rate.

We have estimated the coefficients of variation (COV) using a standard logic tree analysis (Baecher and Christian 2003). The estimated COV at each hazard level for 1.0 s spectral accelerations are given in Table 4.4. In Figure 4.4 we show the 95% confidence intervals around three of the mean hazard curves (assuming normal distribution of the hazard). The width of these confidence intervals reflects the epistemic uncertainty in the estimated hazard.

Table 4.4 Coefficients of variation from epistemic uncertainty for mean uniform hazard spectral accelerations at T=1s.

Hazard level (Equivalent return period in years)	$S_a(T_1)$ (g)	COV = σ/μ
50% in 5 years (7)	0.10	0.25
20% in 5 years (22)	0.19	0.25
10% in 5 years (48)	0.26	0.24
50% in 50 years (72)	0.30	0.24
20% in 50 years (224)	0.44	0.22
10% in 50 years (475)	0.55	0.20
2% in 50 years (2475)	0.82	0.15

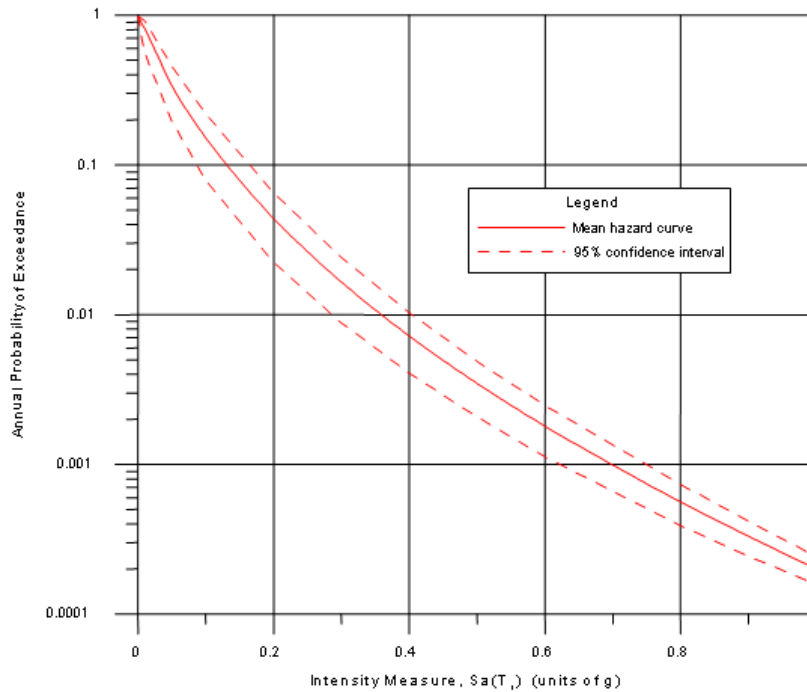


Fig. 4.4 Confidence intervals around mean 1.0 s hazard curve (5% damping), estimated from epistemic uncertainty (including choice of attenuation relationship and variability of slip rate).

The relative significance of the epistemic uncertainty associated with the fault slip rates and the attenuation model is investigated by calculating COVs for suites of runs where slip rates are fixed at their mean values (this provides the COV attributable to variations in the attenuation model only) and for suites of runs for a single attenuation relationship with variable slip rates (this provides the COV attributable to variations in slip rate).

The results are shown in Figure 4.5, and indicate that for the LA Bulk Mail site, variability due to the attenuation model is comparable to the variability due to slip rates. It is important to note that the seven faults considered for the uncertainty estimation contribute to an increasing proportion of the hazard as the hazard level increases (from 27.5% for the 50%-in-5-years hazard to 72.2% for the 2%-in-50-years hazard). Overall, when considering the combination of all the hazard levels, the selected faults contribute to 51% of the hazard (based on hazard disaggregation results by fault). It is reasonable to expect that if the slip rate variability were considered for all the faults contributing to the hazard, the COV due to slip rate would be significantly higher for low hazard levels, but would not change as much for the high hazard levels. This occurs because of the numerous faults that contribute to the site hazard, especially at low hazard levels. Cao et al. (2005) observed a similar reduction in dispersion with increase of hazard level. The dispersion in hazard level was converted to an uncertainty in spectral acceleration on the uniform hazard spectra at $T=1.0$ sec. The confidence intervals are shown on Figure 4.6.

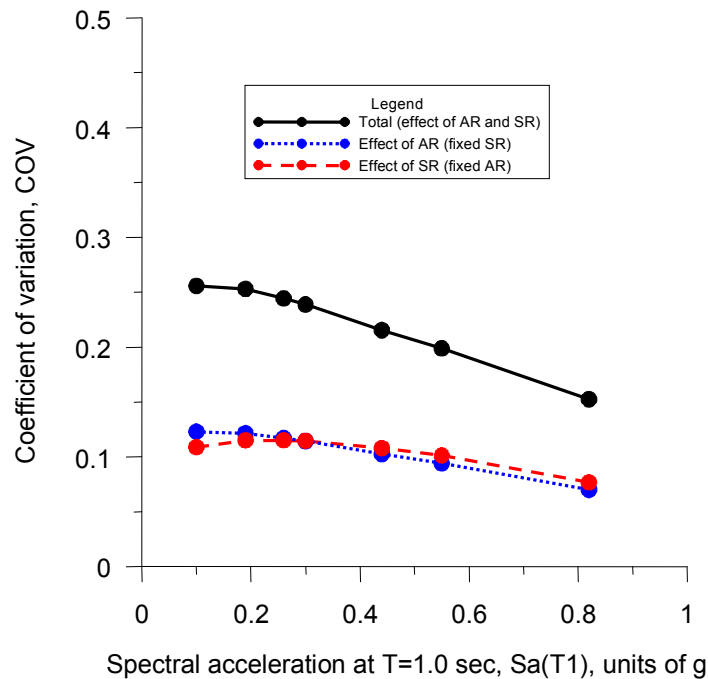


Fig. 4.5 Contributions from slip rate and choice of attenuation relationship to coefficient of variation from mean hazard curve, for all seven faults listed in Table 4.2.

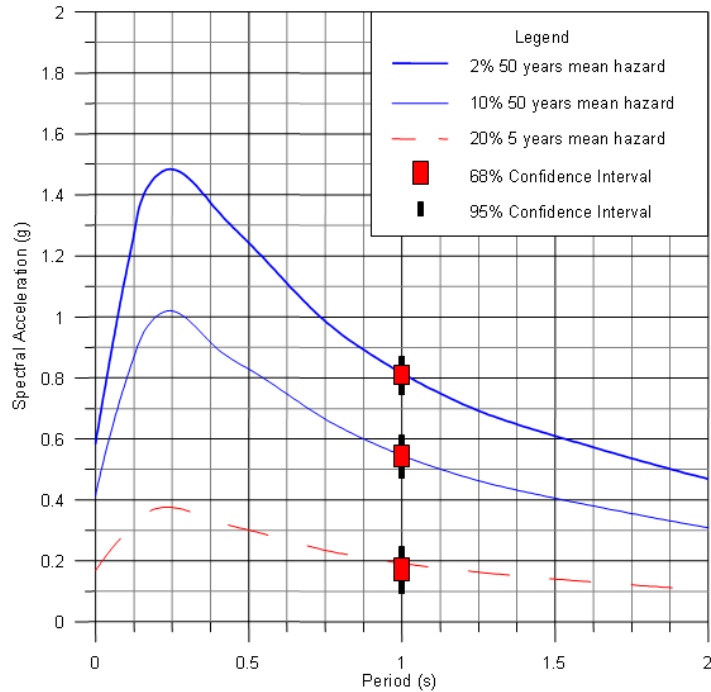


Fig. 4.6 Confidence intervals around mean uniform hazard curve (5% damping) for selected hazard levels, at 1.0 sec. Confidence intervals estimated from epistemic uncertainty (including choice of attenuation relationship and variability of slip rate).

It is important to note at this point that the values of uniform hazard spectral accelerations obtained from the second estimate mean hazard curve (the one that considers the slip rate uncertainty) differ by approximately 5% for all the hazard levels considered. The uncertainty in slip rate therefore has only a modest effect on the mean hazard for this specific site.

4.2 RECORD SELECTION METHODOLOGY

The estimation of *EDPs* for the benchmark structure conditional on *IM* involves nonlinear response history analysis, so the *IM* hazard is represented in terms of accelerogram suites. The suites of ground motions are compatible with the mean estimate of *IM* determined above and represent a reasonable range of possible future ground motions at the site for the given hazard level. In order to capture and quantify the variability of future ground motions conditional on *IM*, 20 to 30 records were selected for each hazard level (whenever possible).

Our objective was also to select records that are appropriate for the site location, considering both site soil conditions and the fault magnitudes and distances that contribute to the

hazard. Identification of the most critical source conditions is accomplished through disaggregation of the seismic hazard (e.g., McGuire 1995; Bazzurro and Cornell 1999), which separates the contributions from different magnitudes and site-source distances. In addition, the seismic sources controlling the hazard can be identified, which provides useful information on the focal mechanism affecting the hazard. Based on these considerations, records having similar magnitude, site-source distance, causative fault focal mechanism, and site-source azimuths (for near-fault effects) to target values were selected per the criteria summarized in Table 4.5. The target values of a parameter, such as magnitude, are taken from the disaggregation analysis. The criteria listed in Table 4.5, as well as the criteria-specific disaggregation results, are discussed in more detail in the following section.

Site conditions at the recording station have an impact on the frequency content of the recorded motion. Hence, we select records only from soil sites known to be either NEHRP C or D, which is consistent with the LA Bulk Mail facility location. When V_{S30} information was not available, judgment was applied regarding the applicability of the record based on the site lithology. A systematic review of the available site information (lithology and its age) was performed for each record.

Records were selected from a database of 1495 3-channel recordings (each having two horizontal and one vertical component) (Stewart et al. 2001). However, since records with rock site conditions or poorly-defined estimates of magnitude and distance were not considered, the effective database size for record selection was reduced to 789.

Table 4.5 Criteria for ground motion record selection.

Criterion	Restriction	Interest
Magnitude range	Hazard level dependent, refer to disaggregation results.	Duration and frequency content
Site-source distance range		Frequency content and near-fault characteristics
Epsilon range		Structural response predictor.
Fault mechanism	Based on disaggregation.	Affects amplitude of ground motion, given M , r , ϵ . Also controlling factor for near-fault characteristics.
Scaling factor	Minimize	See text for discussion.

4.2.1 Criteria Definition for Record Selection and Interpretation of Disaggregation Results

4.2.1.1 Source Magnitude, Distance, and ε

We utilize two different hazard disaggregation schemes. The results from both types of disaggregation are used to guide record selection. The first disaggregation scheme groups the relative contribution of earthquakes into bins of magnitude (M), distance (r), and epsilon (ε). Reasons for considering M and r are summarized in Table 4.5. Unfortunately, records with similar M and r can exhibit significant variability in phasing and frequency content. This variability in the records leads to substantial variability in the calculated nonlinear response of structures. Baker and Cornell (2005a) proposed the parameter ε (epsilon) as an effective indicator of whether a particular record will cause a relatively large or relatively modest nonlinear response (as quantified by EDP). Epsilon is a property of the ground motion record defined by:

$$\varepsilon = \frac{\ln(S_a)_{data} - \ln(\mu_{S_a})}{\sigma_{S_a}} \quad (4.1)$$

where $(S_a)_{data}$ is spectral acceleration of the recording and μ_{S_a} and σ_{S_a} are predicted values of the median and logarithmic standard deviation of S_a from a ground motion prediction equation (calculated using the distance, site, and source parameters particular to the subject recording). All of the above quantities are evaluated at the period of interest, in this case 1.0 s. The physical interpretation of ε is the offset (in number of standard deviations) between the value of the record's IM and the expected value from a ground motion prediction equation. Parameter ε is obviously model-dependent, although the differences between models are small. In the present study we used the Abrahamson and Silva (1997) attenuation relationship to quantify ε for recordings in the database.

An IM evaluated from PSHA with a very low probability of exceedance will tend to have high epsilon values, whereas IM s frequently exceeded could have negative epsilon. Figure 4.7 illustrates examples of positive ε (called a peak record) and negative ε (a valley record) at $T=0.8s$.

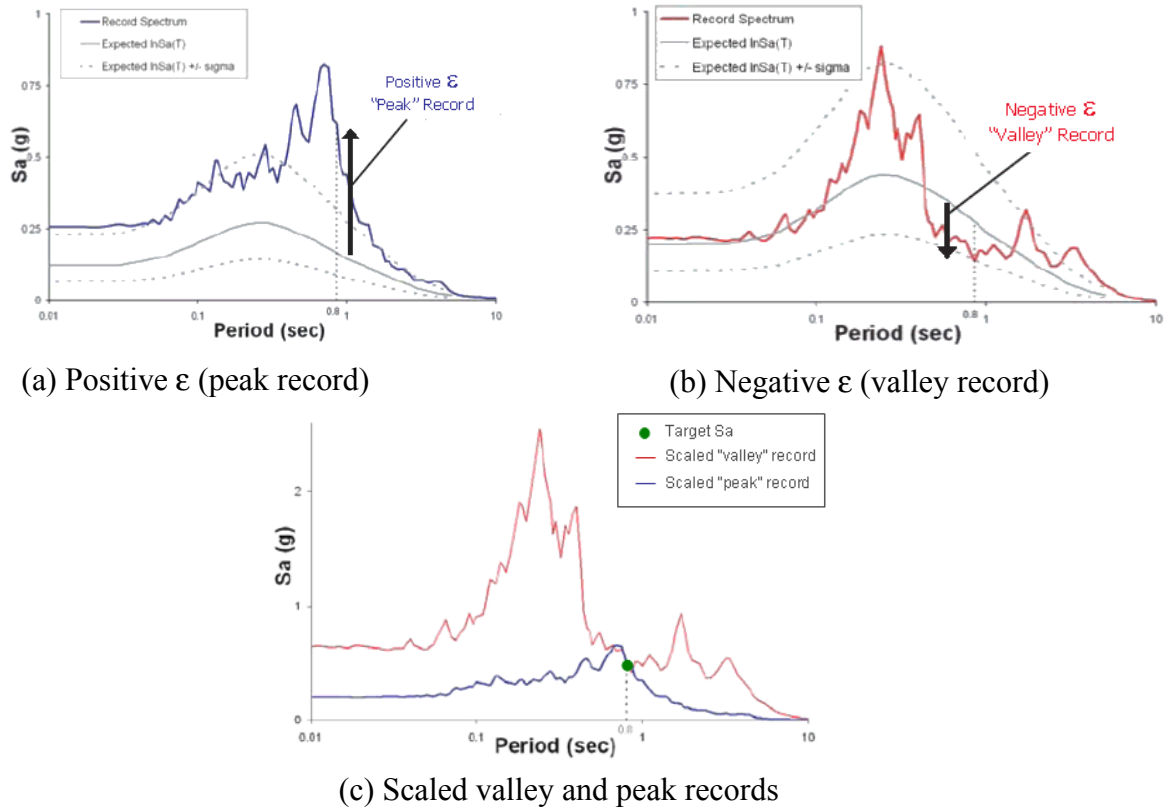


Fig. 4.7 Illustration of ϵ at $T=0.8$ s, modified from Baker and Cornell (2005a).

The benefit of using ϵ as a parameter to guide record selection can be illustrated when records with high and low epsilon are scaled to the same value of $S_a(T_I)$ ($T_I=0.8$ s for the example shown above). As shown in Figure 4.7, the spectral content of a negative epsilon record (i.e., a valley record) is often relatively rich for $T > T_I$. As a structure accumulates damage during earthquake shaking, its natural period at the first mode lengthens. As the building softens, the valley record will subject the building to relatively large seismic demand. In contrast, the spectral content of a positive epsilon (a peak record) is typically relatively low for $T > T_I$, leading to reduced seismic demand as the building softens.

The hazard disaggregation based on M , r , and ϵ is shown in Figure 4.8 for the seven hazard levels considered in this study. Note that the bin numbers are arbitrary. For most hazard levels, the computed IM is dominated by two clusters (A and B) of magnitude-distance combinations. We define sub-Bin A as the small r and small M grouping and sub-Bin B as the large r and large M grouping, associated with the San Andreas fault. There is an exception to this nomenclature for Bin number 3 where three sub-Bins, A, B, and C were used to represent the full

hazard. The need for this subdivision in magnitude and distance sub-bins will become clear when the record selection procedure is addressed in Section 4.2.3. Sub-Bin B contributes significantly at all hazard levels, because earthquakes occur relatively frequently on the San Andreas fault because of its high slip rate.

As shown in Figure 4.8, at low hazard levels, many magnitude and distance bins contribute similarly to the estimated ground motion. This is consistent with the observation made in Section 4.1.2 concerning the controlling faults used for the epistemic uncertainty evaluation. At low ground motion levels, nearby sources with higher magnitudes are characterized by relatively low, often negative, ϵ values. This occurs because large magnitude earthquakes on nearby faults are very likely to exceed a low ground motion level (associated with the low hazard level or short return period), resulting in negative epsilon. Sources at larger distances with lower magnitudes are associated with larger ϵ values because the ground motions from these events would need to be significantly larger than average to exceed even a low ground motion level. This trend can be observed on Figure 4.8, especially (a), for which the range of ϵ is visually easier to discriminate (presence of both negative and positive ϵ values). For the other hazard levels (b–g), we note no—or a very low—contribution from negative ϵ values.

As hazard level increases, particular magnitude and distance ranges begin to dominate. This “specialization” of sources can be explained by only particular sources (at particular M and r combinations) creating large ground motions. Another observation is that the increase in ground motions is due not only to larger magnitudes but also to an increase in the ground motions for a given earthquake source. That phenomenon is expressed by the ϵ parameter: as the ground motions for a given M and r increase with hazard level, ϵ experiences a corresponding increase.

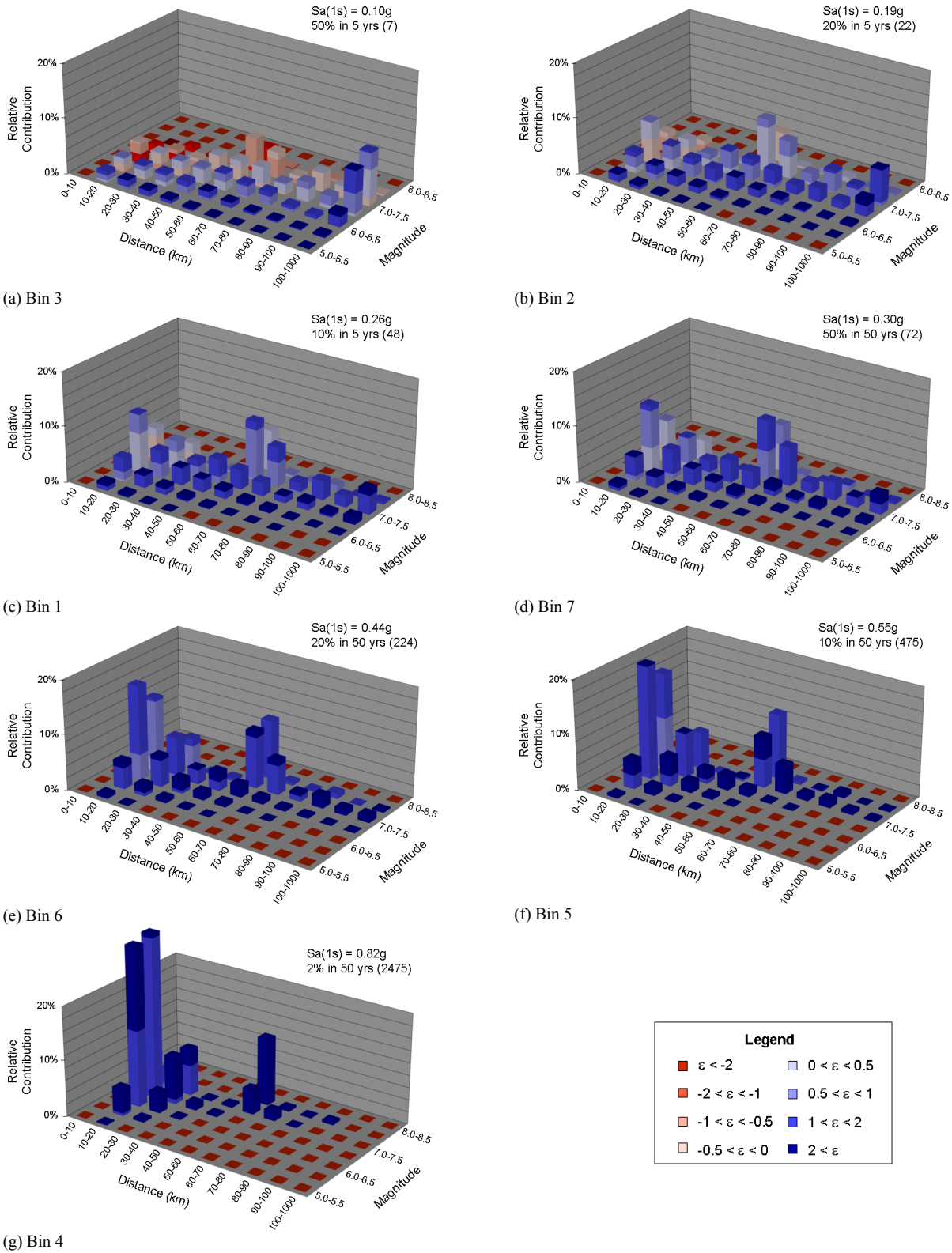


Fig. 4.8 Disaggregation of hazard at $T=1.0s$ for LA Bulk Mail site. Numbers above each figure represent hazard level and return period.

The importance of sub-Bin A grows as the return period lengthens, because longer return periods imply more earthquakes on proximate faults with low slip rates. The importance of the relative contribution of the A and B sub-bins varies with the hazard level, but together these two sub-bins represent the hazard in an average sense. Target values of magnitude, distance, and ϵ were determined based on the disaggregation specific to each hazard level. As shown in Table 4.6, the bins for acceleration history selection were then selected, with the width of the bin (e.g., the range of magnitudes in the bin) affected both by the disaggregation results and the need to “cast the net” widely enough to provide a sufficient number of records for each bin.

Table 4.6 Bin definitions based on disaggregation of hazard.

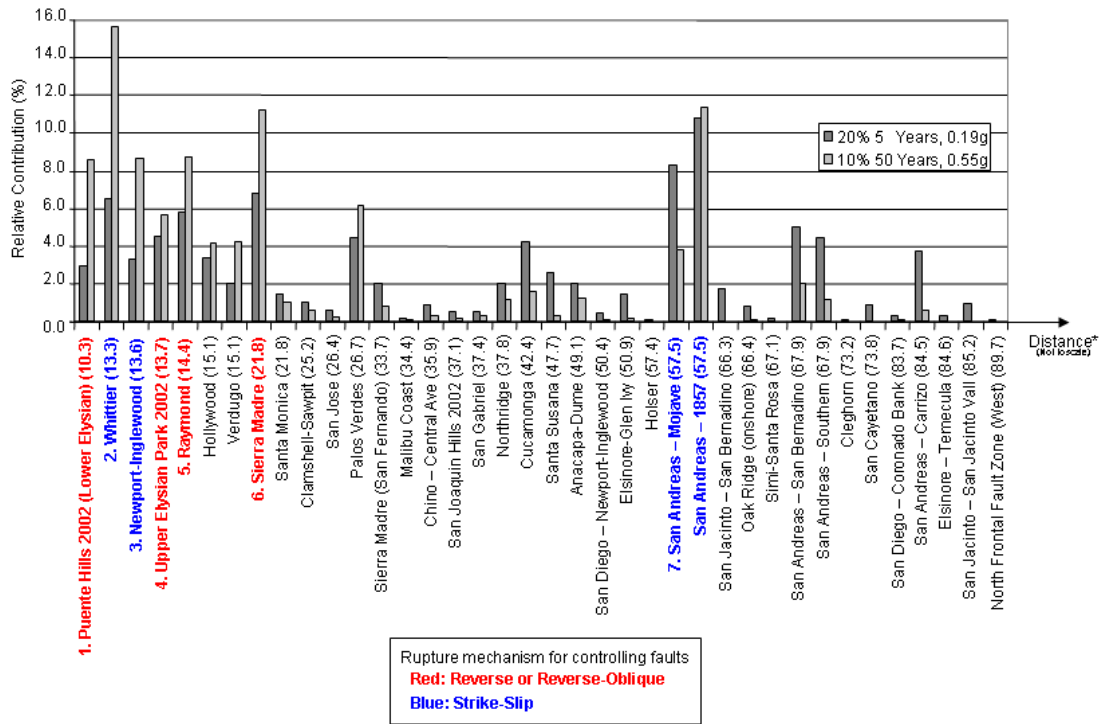
Hazard level	$S_a(1 \text{ sec})$ (g)	Bin	Min M	Max M	Min r	Max r	Min ϵ	Max ϵ
10%/5 yr	0.26	1A	5.9	7.1	5	35	-0.5	1.0
		1B	6.9	8.0	40	80	-1.0	1.0
20%/5 yr	0.19	2A	5.9	6.6	5	35	-0.5	1.0
		2B	6.9	8.0	40	80	-0.5	1.0
50%/5 yr	0.10	3A	5.9	6.5	5	35	-2.0	-0.5
		3B	6.4	8.0	50	80	-2.0	0.5
		3C	6.4	7.6	100	∞	0.0	∞
2%/50 yr	0.82	4A	5.9	7.1	5	35	1.0	2.0
		4B	6.9	8.0	40	80	2.0	∞
10%/50 yr	0.55	5A	5.9	7.1	5	35	0.5	2.0
		5B	6.9	8.0	40	80	1.0	∞
20%/50 yr	0.44	6A	5.9	7.1	5	35	0.5	2.0
		6B	6.9	8.0	40	80	1.0	2.0
50%/50 yr	0.30	7A	5.9	7.1	5	35	0.0	2.0
		7B	6.9	8.0	40	80	0.0	2.0

The bins sizes for magnitude and distance are large, but this is a compromise that is required to obtain a sufficient number of records when binning on three parameters simultaneously (M , r , ϵ). Baker and Cornell (2005a) suggest that this practice is acceptable because M and r are relatively weak at predicting EDP when compared to their combination with ϵ values.

The procedure we have used, selecting a single-valued IM , $S_a(T_1)$, and conditioning the record selection based on the additional parameter ϵ , is sometimes referred to as a vector-valued IM composed of $S_a(T_1)$ and ϵ (Baker and Cornell 2005a).

4.2.1.2 Source Mechanism and Directivity

We also have performed a fault-specific disaggregation in which the relative contribution to the computed hazard of earthquakes on each fault is evaluated. The results of this de-aggregation for two representative hazard levels of $S_a(T=1.0s)$ are shown in Figure 4.9.



*Numbers in parenthesis represent the rupture distance (km).

Fig. 4.9 Disaggregation of mean hazard for fault source with distance at T=1.0s using attenuation relationships and weights from Table 4.1.

As shown in Figure 4.9, the hazard for the LA Bulk Mail site is most strongly influenced by seven sources (the same faults considered for the epistemic uncertainty analyses, Section 4.1.2), with roughly half having a strike-slip rupture mechanism and half reverse or reverse-oblique slip. Accordingly, ground motion time histories were selected in proportion to their observed contribution. Figure 4.10 shows the location of these faults.

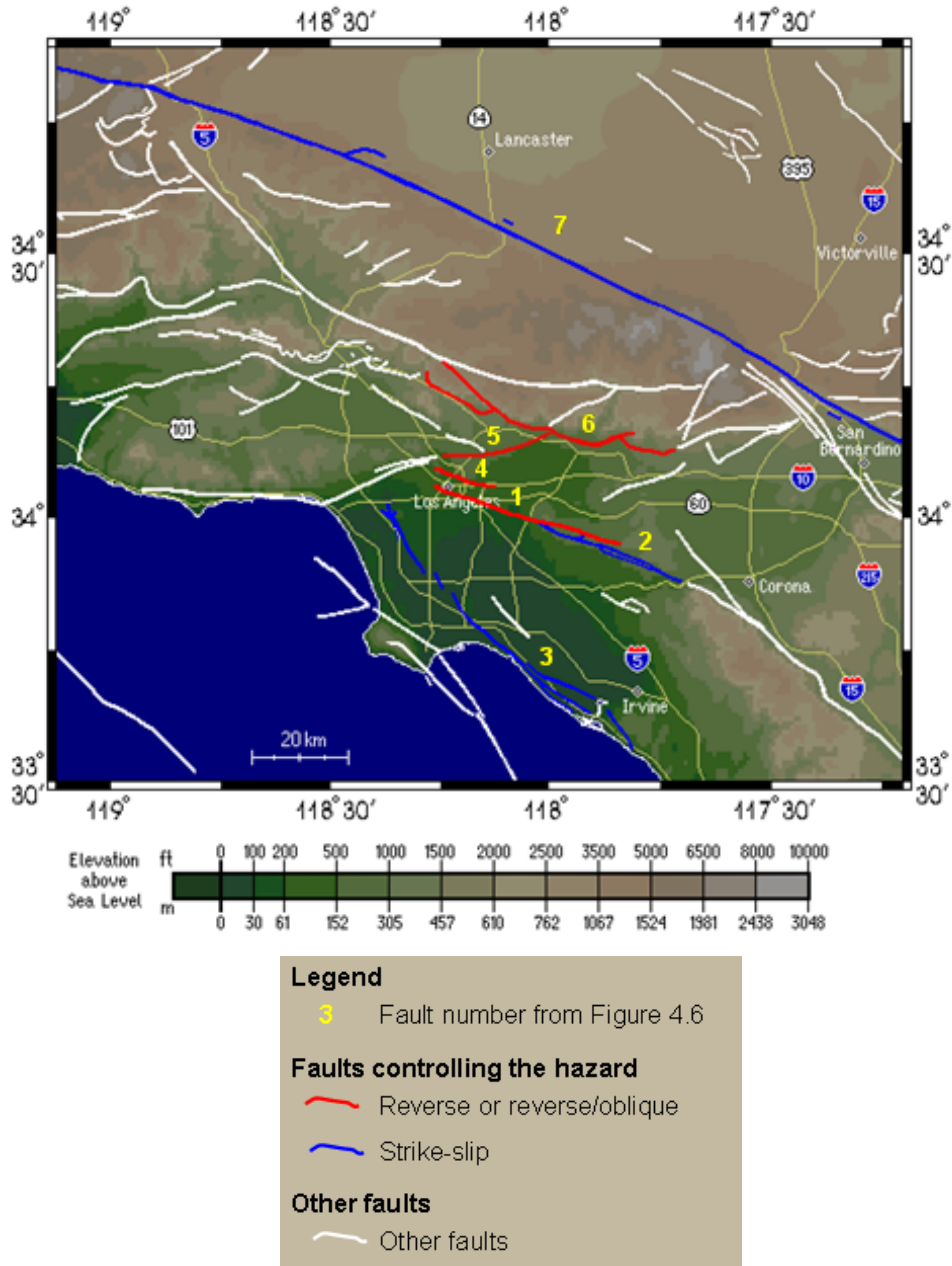


Fig. 4.10 Spatial distribution of faults controlling mean hazard at T=1.0s for LA Bulk Mail site. Figure modified from SCEDC (2005).

Directivity appears not to be a major issue in the hazard for this site. The faults near the site (the A sub-Bins) are oriented in such a way that they do not produce large directivity effects at the site, and more-distant sources (B and C sub-Bins) in general do not produce strong directivity because of their distance. We investigated the actual contribution of three bins of rupture directivity parameters through disaggregation. HAZ 3.6 allows the disaggregation relative to $X \cdot \cos(\theta)$ (directivity parameter used for strike-slip sources) and $Y \cdot \cos(\phi)$ (used for

reverse and reverse/oblique faults), as defined in Somerville (1997). Figure 4.11 illustrates the disaggregation results according to $X \cdot \cos(\theta)$.

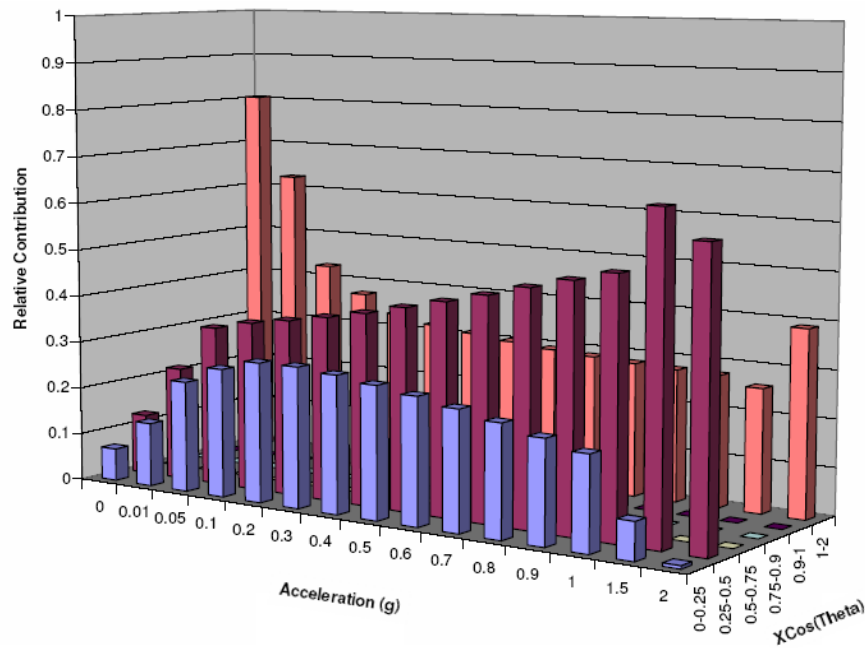


Fig. 4.11 Hazard disaggregation according to directivity parameter $X \cdot \cos(\theta)$.

A shortcoming to disaggregation results based on rupture directivity parameters such as $X \cdot \cos(\theta)$ is their inability to distinguish between strike-slip and reverse focal mechanisms. This is important because strike-slip near-fault effects are stronger. This can be overcome using a parameter called the rupture directivity index (RDI), which was defined by Baturay and Stewart (2003) as the amplification or deamplification of the geometric mean of the two horizontal components at 3.0 s spectral acceleration due to rupture directivity effects as computed by the empirical model of Somerville et al. (1997), later modified by Abrahamson (2000). Even though RDI is evaluated for a 3.0 s spectral acceleration, it is simply an indication of rupture directivity effects that is equally applicable at any period. A site experiencing no rupture directivity effect has $RDI = 1.0$. For strike-slip faults, RDI varies from 1.48 (forward directivity) to 0.55 (backward directivity), while the range for dip-slip faults is from 1.16 to 0.72.

To guide record selection, we defined three RDI levels. RDI_1 represents the case of no directivity effects ($RDI=1.0$), RDI_3 represents relatively large directivity effects, while RDI_2 represent intermediate cases. If a group of records meets the criteria for M , r , and ϵ , we attempt to include equal number of records from each category. This is based on the disaggregation

results we obtained that showed roughly equal contributions of earthquakes with small and large values of the geometric rupture directivity parameter.

4.2.3 Record Selection Procedure

Records compatible with the disaggregation results were selected from the PEER Strong Motion Database (Silva 2000), which contained 789 recordings on soil (2 horizontal components each) from 41 earthquakes of magnitude larger than 5.

The earthquakes in the database are listed in Table 4.7. Records were selected based on the geometric mean of the two horizontal components, which is consistent with the PSHA results for geometric mean. From this reduced database, the selection procedure was as follows:

- (a) For each hazard level, extract records that match the target M , r , ε listed in Table 4.6.
- (b) Records with similar source, path, and site condition, per the criteria given in Table 4.5, still exhibit considerable variability. Accordingly, scaling is needed to enforce a consistent value of the target IM (which is the mean uniform hazard value determined from hazard analysis). Since the ground motion prediction equations utilized in PSHA provide the geometric mean of the two horizontal components, the scaling factor utilized here for record selection is also based on the geometric mean of the two horizontal recordings. This scaling factor is defined as

$$SF = \frac{(S_a(T_1))_{tar}}{(S_a(T_1))_{rec}} \quad (4.2)$$

where $(S_a(T_1))_{tar}$ is the hazard-specific target value from PSHA and $(S_a(T_1))_{rec}$ is the value from the geometric mean (horizontal components) from a single recording. From the group of records identified in (a), we select records that require scaling by a factor of 5.0 or less (up or down, or from 0.2 to 5) to match the “target” value of $S_a(T_1)$. This choice of scaling factor was based on engineering judgment and the standard of practice at the time. Because we have considered ε , allowing scaling factors as large as 5.0 is not likely to introduce significant bias into the analysis of EDP (Luco and Bazzurro 2007).

- (c) The final selection of records from the group identified in (a) is made in consideration of: (1) selecting matching records from various earthquake events; (2) favoring records that are from earthquakes with focal mechanisms compatible with the disaggregation results (i.e.,

combination of strike-slip and reverse for sub-Bin A; preference for strike-slip for sub-Bin B); and (3) for near-fault situations (sub-Bin A), selecting recordings with a level of rupture directivity compatible with the de-aggregation results. For criterion 3, records were classified as having high, intermediate, or no directivity to guide record selection, as defined earlier, and we selected approximately a third in each case whenever possible, following the disaggregation results discussed above.

The results of record selection for a given bin are a group of recorded pairs (for the two horizontal directions). Each pair is utilized in the bidirectional nonlinear structural response analyses discussed in Chapter 5.

Table 4.7 Earthquake events available in database.

Earthquake Location	year-month-day	Magnitude
Imperial Valley	1940-05-19	7
Kern County	1952-07-21	7.4
Parkfield	1966-06-28	6.1
Borrego Mtn	1968-04-09	6.8
Lytle Creek	1970-09-12	5.4
San Fernando	1971-02-09	6.6
Point Mugu	1973-02-21	5.8
Santa Barbara	1978-08-13	6
Tabas, Iran	1978-09-16	7.4
Coyote Lake	1979-08-06	5.7
Imperial Valley	1979-10-15	6.5
Imperial Valley	1979-10-16	5.5
Livermore	1980-01-24	5.8
Livermore	1980-01-27	5.4
Taiwan SMART1(5)	1981-01-29	6
Westmorland	1981-04-26	5.8
Coalinga	1983-05-02	6.4
Coalinga	1983-07-22	5.8
Morgan Hill	1984-04-24	6.2
Bishop (Rnd Val)	1984-11-23	5.8
Hollister	1986-01-26	5.4
Taiwan SMART1(40)	1986-05-20	6.4
N. Palm Springs	1986-07-08	6
Chalfant Valley	1986-07-20	5.9
Chalfant Valley	1986-07-21	6.2
Chalfant Valley	1986-07-21	5.6
Chalfant Valley	1986-07-31	5.8
Whittier Narrows	1987-10-01	6
Superstittn Hills(A)	1987-11-24	6.3
Superstittn Hills(B)	1987-11-24	6.7
Loma Prieta	1989-10-18	6.9
Cape Mendocino	1992-04-25	7.1
Landers	1992-06-28	7.3
Big Bear	1992-06-28	6.4
Northridge	1994-01-17	6.7
Northridge Aftershock	1994-01-17	5.9
Kobe	1995-01-16	6.9
Hector Mine	1999-10-16	7.1
Izmit	1999-08-17	7.51
Duzce	1999-11-12	7.2
ChiChi Taiwan	1999-09-20	7.62

4.2.4 Other Considerations

4.2.4.1 Target Spectral Period for Scaling of Records

All the selected records were scaled to their hazard-specific target $\{S_a(T_1)\}_{tar}$. In this report, the term “scaling” refers to this intra-bin matching of the target $IM, S_a(T_1)$. Scaling according to Equation 4.2 matches the spectral acceleration at a specified period instead of a range of periods beyond T_1 . Such a range might better represent the system response as it softens during strong shaking. The effect of the choice of scaling scheme on the *EDP* dispersion was not investigated as a part of this project. However, Shome and Cornell (1998) showed that for an MDOF structure with $T_1 = 1.05$ sec (similar to $T_1 = 1$ sec for this project), the *EDP* dispersion was not reduced when input records were scaled to match the target over a range of periods versus at $S_a(T_1)$ only. They did note such an *EDP* dispersion reduction however for a stiffer structures ($T_1 = 0.25$ sec). They have concluded that for long-period structures, intra-bin scaling to the spectral acceleration at the fundamental frequency (for higher damping (e.g., 5%)) is the most convenient to use and the best among the considered alternatives. This was the rationale guiding our approach to scale using S_a at the first-mode period.

4.2.4.2 Consistency of PSHA Results and Record Selection

When selecting records, one has to be consistent regarding which value of S_a is used; that is, if the attenuation relationships used to perform the PSHA provide geometric mean spectral accelerations (which is typically the case), records should also be selected based on the geometric mean of the horizontal components (e.g., as reflected by Eq. 5.4). More typically, records are selected on an individual component basis and then scaled to match a PSHA result representing the geometric mean. This practice is accurate for a 2D system analysis only if the ground motion prediction equations used in the PSHA apply not to the geometric mean condition but a random horizontal component condition (ground motion prediction equations provide similar medians for the two cases, but higher standard deviation for the latter case; Boore et al. 1997). The common practice of using PSHA from ground motion equations based on the geometric mean and then selecting individual components can introduce bias, due to the incorrect standard deviation in the PSHA (Baker and Cornell 2006). A 3D analysis requires a pair of orthogonal horizontal motions with reasonable proportionality between the two

components. Scaling both horizontal motions to $\{S_a(T_I)\}_{tar}$ would provide an unrealistic seismic demand, as would scaling so that the maximum direction provides $S_a(T_I)_{tar}$.

The use of epsilon in time-history selection is also affected by whether motions are scaled on a component or geometric-mean basis. There are two contributing factors. The first is that epsilon would need to be computed for the geometric mean of the records if scaling is based on the geometric mean. Second, the larger standard deviation for individual components would need to be taken into account in the analysis of epsilon for individual components. The common practice of calculating individual component epsilon using the standard deviation for the geometric mean would systematically overestimate epsilon. We calculated epsilon based on the geometric mean of the two horizontal components.

5 Structural Modeling and Simulation

5.1 INTRODUCTION

To permit the accurate assessment of nonstructural damage, monetary losses, and casualty risks, the structural model needs to accurately simulate structural response from *low* deformation levels (where cracking and tension-stiffening phenomena are important) up to *large* deformation levels (where deterioration leading to collapse is important). For loss modeling, Porter et al. (2004) and Krawinkler et al. (2005) have shown that frequent lower-intensity ground motions are major contributors to financial losses due to earthquake damage over time. On the other hand, for fatality risks, collapse under rare high-intensity earthquake ground motions is important. Thus, for performance-based assessments, the structural analyses need to provide high-fidelity response simulations over the full range of performance. To interrogate the performance over the expected range of earthquake ground motion intensities, nonlinear time-history analyses are conducted at seven hazard levels, ranging from *IM* levels that have a 50%-in-5-years exceedance probability (7.2 years recurrence) to high-intensity motions that have a less than 2%-in-50-years exceedance probability (2475-years recurrence). Beyond the 2%-in-50-years hazard, ground motion intensities are incremented up to the collapse point.

The structural analyses are run using the Open Source for Earthquake Engineering Simulation (OpenSees 2006) software developed by the PEER Center. A few notable aspects of the structural modeling are that (a) we used both a fiber and lumped-plasticity model and compare results of the two, (b) in the fiber model, we included nonlinear bond-slip behavior and nonlinear panel shear behavior, (c) we calibrated the lumped-plasticity element model to account for the important deterioration modes that precipitate side-sway collapse (the plastic-rotation capacities are much higher than some may expect), (d) we directly predicted the collapse capacity and mechanism using the lumped-plasticity model, and (e) we quantified the effect of

structural modeling uncertainty on collapse capacity estimation (for collapse, this so-called modeling uncertainty turns out to be as important as record-to-record variability). The structural models described in this chapter are intentionally made as detailed and accurate as practically feasible to help ensure accuracy of the seismic benchmarking study. This level of detail in structural modeling may not be practical for routine design situations, but we believe such detail is necessary to meet the goals of accurately assessing structural and nonstructural performance.

This chapter summarizes the development and calibration of the structural models, including the predicted structural responses for each structural design (static pushover results, incremental dynamic analysis results, collapse capacities, etc.). Sections 5.2–5.5 begin with an overview of the models used in this study, followed by more details about the fiber-spring and lumped-plasticity models. Sections 5.5–5.7 then summarize the modeling topics that are the same for both the fiber-spring and the lumped-plasticity models (e.g., gravity-frame, nonstructural elements, numerical algorithms); and Section 5.8 covers soil-foundation-structure interaction. Sections 5.9–5.11 present the characteristics of each structural model (e.g., fundamental period, static pushover response), the structural responses prior to collapse, and the predictions of collapse capacity and behavior. Sections 5.12–5.14 conclude with illustrations of structural response, thoughts on alternative design criteria to improve collapse performance, and then a summary and conclusions.

5.2 OVERVIEW OF STRUCTURAL MODEL

5.2.1 Frame Configuration and Components

Shown in Figure 5.1 is the plan layout of the building with the perimeter-frame system. Figure 5.2 shows the elevation views of the perimeter and gravity frames, where the perimeter frame constitutes the primary lateral system and the gravity frame provides incidental lateral resistance. Models of the perimeter and gravity frames are combined in a two-dimensional analysis where models of the two frames are connected by a rigid kinematic link to enforce lateral deformation compatibility at the floors. The gravity frame in the analysis model has properties to represent the 2-1/2 gravity frames that are supported by each perimeter frame. The structural model used for the space-frame designs is similar, except that the space-frame models do not include a separate gravity framing system, since by definition all of the space framing lines participate in

both the lateral and gravity systems. For convenience, a mathematical “leaning column” is included in the analysis model to account for the additional P-delta effects that come from the gravity loads tributary to the gravity system. The yield strengths of all the nonlinear component models (beams, columns, beam-column joints) are based on the expected material strengths, which are typically about 1.1–1.3 times the minimum nominal specified values.

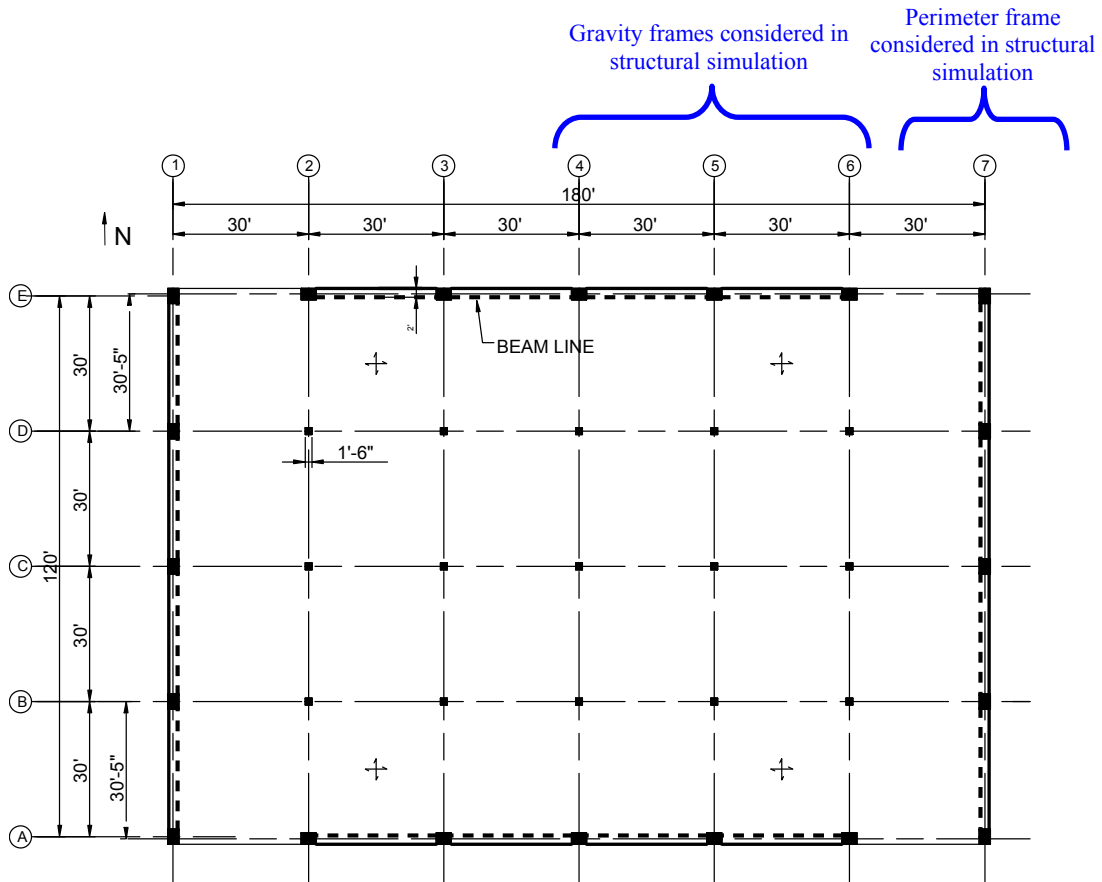


Fig. 5.1 Plan view of perimeter-frame building.

- ii The lumped-plasticity model is composed of beam-column elements that include an elastic element and nonlinear rotational springs at each end (*OpenSees commands: Clough material, Elastic element*).
- (b) RC Beams: Beams are modeled with either fiber or elastic elements with lumped plastic hinges at each end. Where included, the lumped-plasticity hinges are defined as part of the beam-column joint at the ends of each element. The beam model includes the strength and stiffness contribution of the slab, as detailed later (*OpenSees commands: nonlinearBeamColumn element, Steel02 material, Concrete02 material for beam, Concrete01 material for slab, elasticBeamColumn element, Clough material*).
- (c) RC Beam-Column Joint: The joint panel zone model accounts for the finite geometry of the joint, the joint panel shear behavior, and a portion of the bond-slip behavior for beam and column longitudinal bars. The shear panel simulates cracking and has a pinched hysteretic response. The shear panel has finite strength and post-failure negative stiffness, although these are not important for this frame because the capacity-design rules prevent the joints from failing in shear. The moment-rotation bond-slip springs are nonlinear and have a pinched response; however, these springs never lose strength because it is assumed that complete pullout will not occur for modern designed buildings (*OpenSees commands: joint2D element, Clough material*).
- (d) Column Bases—Perimeter Frame: The column bases of the perimeter (or primary) frame are connected to two springs in series. One spring is elastic and represents the rotational flexibility of the footing. The other represents bond-slip and is similar to the bond-slip springs used in the joint model (*OpenSees commands: zeroLength element, Elastic material, Clough material*).
- (e) Column Bases—Gravity Frame: The column bases of the gravity frame are connected to a single elastic spring to represent the rotational flexibility of the footing. Because of footing size, this spring is more flexible than the spring at the base of the columns in the perimeter frame. Given the low base-fixity, bond-slip is not modeled at the bases of the gravity-frame columns (*OpenSees commands: zeroLength element, Elastic material*).

5.2.2 Overview of Fiber-Element Beam-Column Model

Shown in Figure 5.3 is a schematic diagram of the fiber model used to simulate the beams and columns in the RC frames. Each element is assigned five integration points along its length where the nonlinear axial-flexural behavior of the cross section is monitored. Each section is composed of 50 core fibers and 15 cover fibers for each of the two cover areas. While computationally expensive, the large number of fibers were used because they were found to improve numerical convergence. The fibers in each cross section are assigned material properties to represent either unconfined concrete, confined concrete, or steel reinforcement. Beam elements include an effective width of the slab in the section definition, including the bonded (non-prestressed) reinforcement present in the slab. An elastic shear spring (not shown in Fig. 5.3) is incorporated into each section to represent shear deformations. Note that the bond-slip springs discussed in the last section are external to the fiber elements and are added at each location where the fiber element connects with a joint or foundation element.

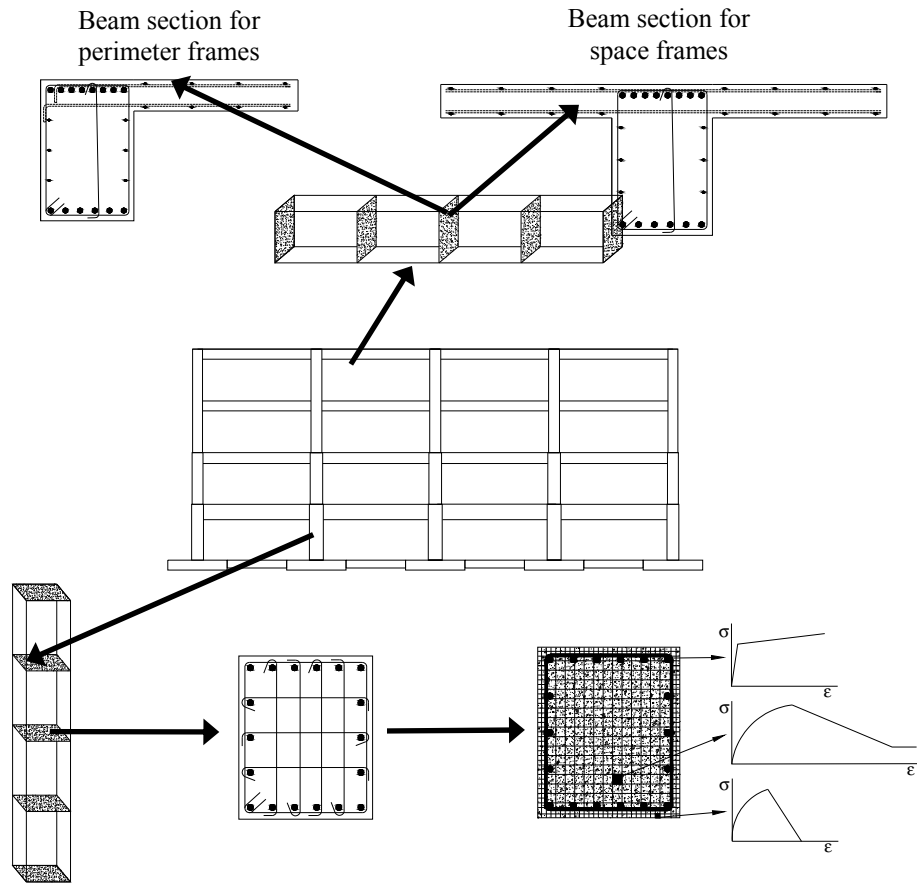


Fig. 5.3 Overview of fiber-element structural model. Figure shows fiber layers two directions; however, since frame model in study is only two dimensional, fiber layers oriented only parallel to axis of bending.

5.2.3 Overview of Lumped-Plasticity Structural Model

Figure 5.4 shows a simple schematic diagram of the lumped-plasticity model. The element model is composed as elastic elements with plastic hinges at each end. The elastic stiffness of the plastic hinge is large ($11 \cdot K_e$, where K_e is the elastic stiffness of the element) but not perfectly rigid. To account for the finite stiffness, the elastic element stiffness is increased to $1.1K_e$ following an approach suggested by Zareian (2006, Appendix D).

The trilinear moment-rotation diagram shown in Figure 5.4 is common to all of the inelastic hinges used in the lumped-plasticity analysis. The defining parameters of the moment-rotation relationship are the elastic stiffness, yield moment, ultimate moment, capping rotation

(the rotation at the ultimate moment) and the negative slope of the post-peak response. The rotation quantities are calibrated to test data based on the chord rotation between the inflection point and the end of the element (typically assuming double-curvature), including only the plastic deformations of the plastic hinge.

For the four-story benchmark building, the yield point chord rotation angles range from 0.0065 to 0.008 radians in the columns and roughly 0.005–0.008 radians in the beams. The column values vary primarily due to axial compression loads, and the beam values vary due to changes in beam section depths over the height of the building. The plastic-rotation capacity to the capping point (i.e., the plastic rotation to the onset of strain softening) ranges between 0.034–0.065 for the columns and 0.067–0.073 for the beams. The smaller capping rotations occur in the space-frame columns, which have larger axial load ratios compared to the perimeter-frame columns. The post-capping stiffness is assumed to be the same for beams and columns, equal to -7.5% of the initial elastic stiffness of each element.

Further details regarding the concentrated hinge element are summarized in Section 5.4 and Appendix D.

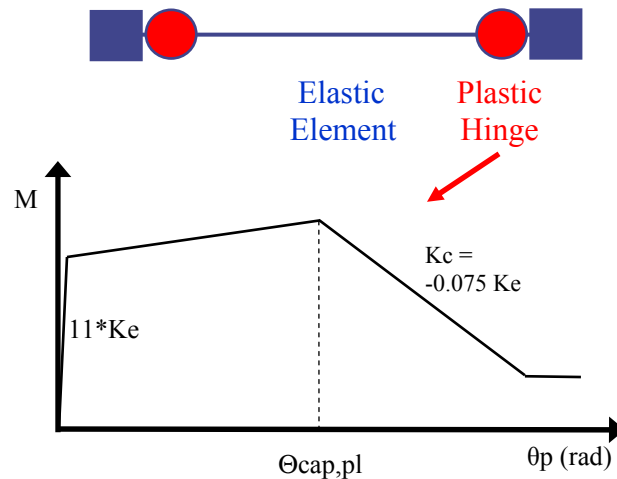


Fig. 5.4 Overview of lumped-plasticity element structural model.

5.3 FIBER-SPRING MODEL FOR PRE-COLLAPSE SIMULATION

5.3.1 Overview

The fiber-element model is based on a force-based formulation by Filippou (1999), which captures the spread of plasticity throughout the element cross section and along its length. The term “fiber element” refers to the fact that the cross-section response is evaluated in terms of uniaxial material properties. We refer to this element as the “fiber-spring” model to reflect the addition of rotational springs at each end of the element to account for bond-slip flexibility. The model also includes a shear degree of freedom at each integration point.

5.3.2 Fiber-Spring Model Strengths and Limitations

The key advantages of the fiber-spring model are its ability to (a) capture the axial-flexural interaction (for both strength and stiffness), (b) incorporate the effects of the concrete tensile strength and tension stiffening, (c) account for the nonlinearity in the bond-slip behavior, and (d) model elongation (dilation) of the concrete under reverse cyclic loading and the resulting forces introduced into the frame due to end restraint. Another benefit of the fiber model is that it is relatively intuitive, yet still allows the user to model inelastic behavior without extensive calibration (e.g., axial flexural interaction is captured automatically).

A significant limitation of the current fiber-element model is its inability to capture deterioration of the steel reinforcing bars due to rebar buckling and low-cycle fatigue. This is not an inherent limitation of the fiber-element formulation; rather, the limitation arises from an inability of the currently available steel models to simulate reinforcing bar degradation. Early in this project, we attempted to capture the effects of rebar buckling by using a steel model that softens as a function of strain. However, this worked poorly because of the difficulty in calibrating the onset of rebar buckling to the fiber strain, whose calculation is known to be very sensitive to the model idealization (Filippou 1999).

Because of these limitations, the fiber model (using the currently available material models) in OpenSees cannot simulate the collapse behavior of a ductile RC frame. Therefore, the fiber model is not used to simulate response for high levels of ground motion that may cause collapse. Instead, to model the collapse behavior we use the lumped-plasticity beam-column model with hinges. PEER researchers are currently working on a model to simulate buckling

and fracture of the steel reinforcing bars, which may enable direct collapse modeling with fiber-type elements in the future.

5.3.3 Section and Material Models

5.3.3.1 Concrete Material Model Including Tension-Stiffening Effect

This study employs the OpenSees (2005) concrete material model Concrete02 by Filippou (2005), which captures the compressive and tensile behavior of concrete and can be calibrated to include the tension-stiffening effect. Figure 5.5 shows the material model backbone and its hysteretic behavior. To quantify confinement effects, we used the compressive concrete model by Scott et al. (1982), which accounts for the effects that confinement has on the concrete strength and ductility. Figure 5.5 shows the resulting material backbone curves for confined and unconfined concrete that has a nominal compressive strength of 5 ksi. The initial stiffness is defined as twice the secant stiffness through the capping point (the point where strain-softening begins), and the stiffness is reduced according to the model by Scott et al. More detailed information regarding this model and compression response parameters is available in the OpenSees documentation (2006) and Filippou (2005).

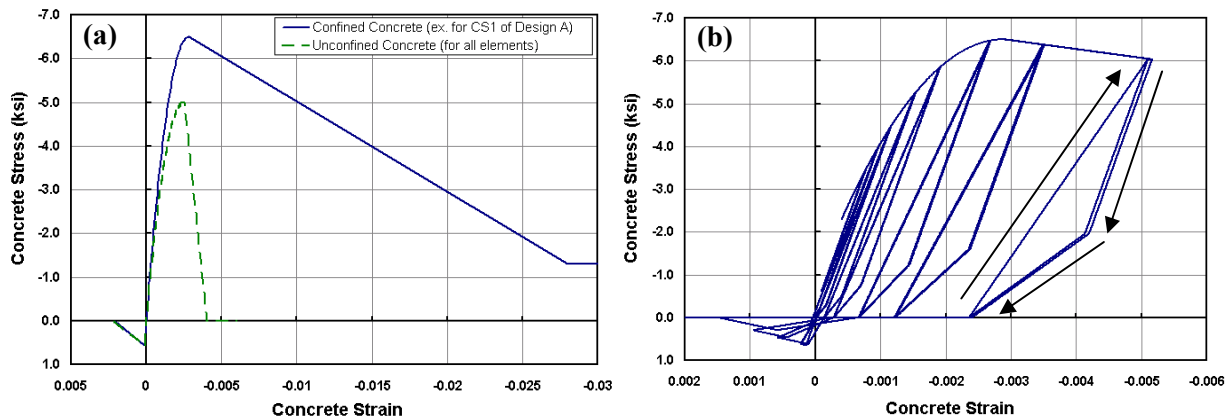


Fig. 5.5 Concrete model (a) backbone and (b) hysteretic behavior.

The concrete tensile strength is based on the standard modulus of rupture (Nilson 1997), which is related to the compressive strength as follows: $f_r = \sigma_{cr} = 10\sqrt{f'_c}$. The descending concrete tensile slope is calibrated to account for tension stiffening. The slab concrete of the beam section is conservatively assumed to have no tensile strength, since the cracking strength of

the full slab width is unlikely to develop due to shear-lag and nonlinear stress/strain fields in the slab that are not represented by the idealized beam theory (plane sections) assumption inherent in the beam-column formulation.

The tension-stiffening effect comes from the fact that once reinforced concrete begins to crack, the uncracked portions of the concrete continue contributing to the total stiffness through bond stress transfer to the reinforcement. Figure 5.6 illustrates an example of a single rebar cast in concrete. Even after initial cracking, the concrete between cracks carries stress. This causes the stiffness of the rebar and concrete to be higher than that of the rebar alone (Kaklauskas 2001). The tension-stiffening effect can add significant flexural stiffness, which can lead to reduced displacements—particularly at lower deformation levels.

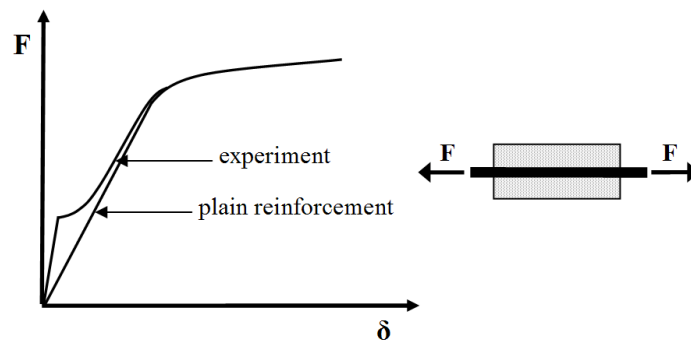


Fig. 5.6 Tension-stiffening effect illustration (after Feenstra 1993).

The tension-stiffening effect is really not a property of either the steel or the concrete separately, but a behavior that occurs from the interaction of both materials. Even so, to model the effect, we adjust only the tensile concrete material behavior (i.e., the tensile strain at zero stress, $\alpha_2 \epsilon_{cr}$, where α_2 is a calibration coefficient and ϵ_{cr} is the cracking strain). Figure 5.7 shows the tensile branch of the concrete model, as proposed by Kaklauskas and Ghaboussi (2001).

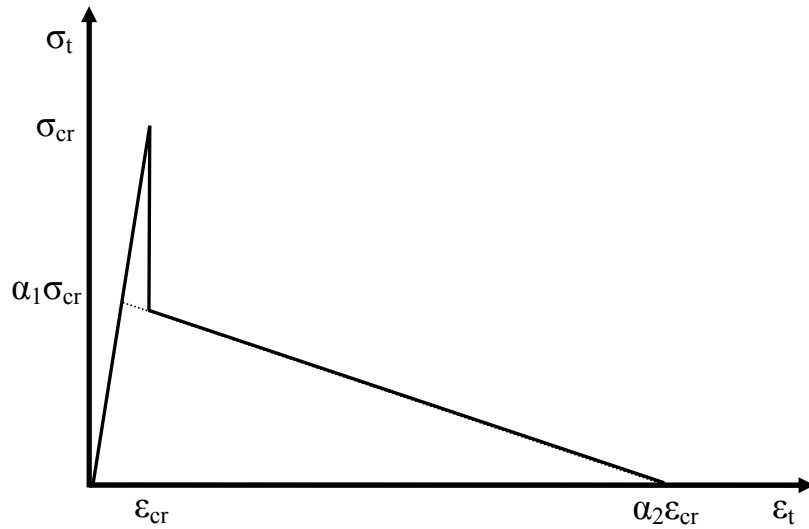


Fig. 5.7 Concrete tension material model (after Kaklauskas and Ghaboussi 2001).

Kaklauskas and Ghaboussi (2001) compared data from 14 experimental beam tests to fiber model predictions and calibrated the α_2 parameter of the concrete model (see Fig. 5.7) for each experimental test. They found that α_2 is highly dependent on the reinforcement ratio, with higher values of α_2 associated with lower reinforcement ratios. Their calibration was done only for beams without axial loads, and they apply the same tensile concrete model for all concrete fibers in the section. Lacking further data to either account for axial load effects on α_2 or the nonlinear distribution of tension stiffening through the cross section, we have applied these same assumptions that are inherent in their calibrations.

For lightly reinforced concrete members ($0.5\% < \rho < 1.0\%$) Kaklauskas and Ghaboussi predict $12 < \alpha_2 < 22$ ($0.0017 < \alpha_2 \epsilon_{cr} < 0.0031$, for $f'_c = 5$ ksi). Work by Torres et al. (2004) predicts similar values of α_2 . For simplicity, we used $\alpha_2 \epsilon_{cr} = 0.002$ ($\alpha_2 = 14$) for all concrete models, independent of reinforcement ratio (ρ). Another important calibration parameter, α_1 (as shown in Fig. 5.7), describes the effective immediate stress loss after cracking. Kaklauskas and Ghaboussi use $0.6 < \alpha_1 < 0.7$, whereas Torres et al. recommend a lower value of 0.4. We used a value of $\alpha_1 = 0.5$.

The currently available concrete models in OpenSees are only bilinear in the tension region, so the sharp stress drop upon cracking (see Fig. 5.8) cannot be captured. Therefore, we have decided to use the bilinear tensile concrete material model, shown by the dotted line in Figure 5.7.

5.3.3.2 Steel Material Model

This study employs the Guiffre-Menegotto-Pinto steel material (Steel02) implemented in OpenSees by Filippou (2005). This model is capable of capturing both kinematic and isotropic hardening. Figure 5.8 shows the cyclic behavior of this material model, as calibrated for this study, using values recommended by Filippou and excluding isotropic hardening.

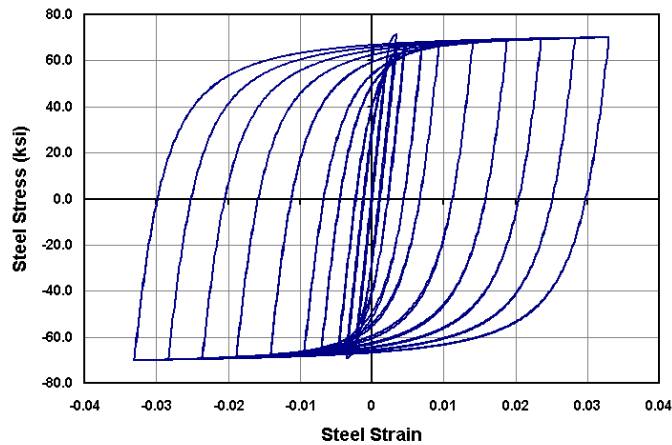


Fig. 5.8 Hysteretic behavior of Guiffre-Menegotto-Pinto steel material model.

The model yield strength is set equal to the expected yield strength of 67 ksi (for Grade 60 steel) as recommended by Melchers (1999). The elastic modulus is set to $E_s = 29,000$ ksi.

Wang (1978) suggests use of an average strain-hardening modulus of approximately $0.018 * E_s$, where E_s denotes the Young's modulus for steel; however, this value does not account for the additional post-yield flexibility coming from bond-slip and shear deformations. Note that the discrete bond-slip springs discussed elsewhere only account for the bond-slip deformations up to flexural yielding, and do not account for the fact that the post-yield stiffness should be reduced to account for bond-slip and shear flexibilities. To approximately account for these additional post-yield flexibilities, we reduced the hardening stiffness of the steel material model. Fardis and Biskinis (2003) estimate that approximately 35% of the plastic-rotation capacity comes from bond-slip deformations. The relative contribution of shear deformations to the post-yield flexibility is not entirely clear. As an approximation, we assume that 50% of the post-yield deformations come from bond-slip and shear, while the other 50% come from flexural deformations. Therefore, we use a steel material strain-hardening value of $0.01 * E_s$.

5.3.3.3 Element Shear Model

For newly designed special moment-resisting reinforced concrete frames (SMFs), the shear strength is based on capacity design provisions (ACI 318-02, 21.4.5) with the intent that no element of an SMF should experience shear failure. Even so, shear deformations will occur. To model shear flexibility, we included a shear degree-of-freedom in the fiber-element sections. We used a simple linear-elastic spring, based on recommendations by Mehanny (1999) and by Park and Paulay (1975), where the stiffness is calibrated based on the intensity of shear demand. Using this approach for the members in the four-story benchmark building, the predicted shear deformation angle (γ) at yielding is about 0.0004–0.0006 radians for beams and 0.0008–0.0016 radians for columns. As a point of comparison, Panagiotakos and Fardis (2001) empirically estimate shear distortions for RC members on the order of 0.0025 radians. These values relate to extremely small effective shear stiffnesses, in the range of about $0.07GA$ – $0.15GA$, where G is the shear modulus of the concrete and A is the cross-sectional area.

To verify that the capacity design provisions meet their goal of prohibiting shear failure, we looked at a summary of shear strength predictions by Elwood (2002, Chapter 2). This includes models by three studies (Sezen 2002; Yoshikawa 2001; Pujol 1999) that considered the effects of shear strength reduction with increased ductility demands. Figure 5.9 shows the shear strength predictions from the three studies as well as a plot of the normalized shear demand (shear demand divided by shear demand at ultimate flexural strength) in an RC column as it yields in flexure (this example is for column CS5 of Design A, as discussed in Sections 3.3.4–3.3.5, which has a low axial load ratio of $P/A_g f'_c < 10\%$). Also shown is the expected shear strength calculated according to the ACI 318-02 (ACI 2002), which is approximately 1.5 times the maximum shear strength demand. The ACI margin results from a 25% strength adjustment between the nominal and expected strength from ACI 318-02 provision 21.4.5.1, an increase of 1.33 associated with the resistance factor $\Phi_{\text{shear}} = 0.75$, an adjustment of 12% between the nominal and expected flexural strength (and associated shear demand). Of all four models, only the Sezen (2002) model predicts that flexure-shear failure would occur, and this would only occur at large displacements where the member strength is already limited by flexural yielding. Based on this evidence, our performance assessment is based on the assumption that column shear failure would not significantly affect the calculation of side-sway collapse capacities.

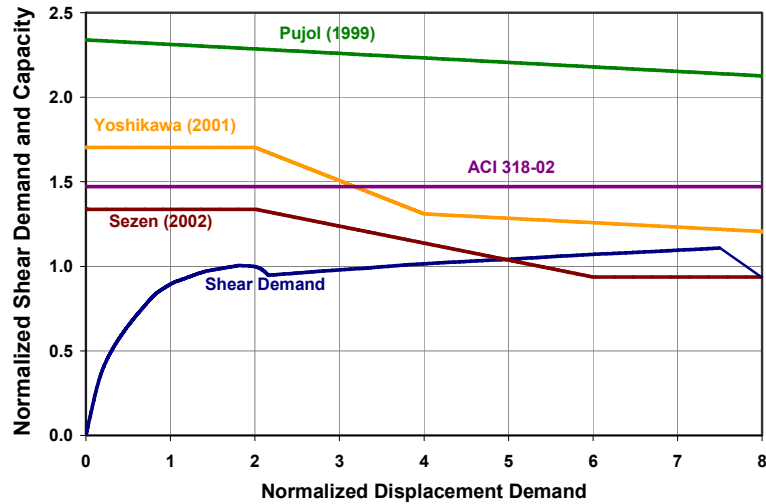


Fig. 5.9 Shear demand and capacities predicted by several researchers, showing normalized shear demand and capacity (shear divided by shear demand at ultimate flexural strength) plotted against normalized displacement demand (displacement divided by yield displacement).

5.3.3.4 Effective Slab Width for Beam Sections

The beam section includes an effective slab width that is established considering its likely effect on strength and stiffness. The provisions of FEMA 356 procedure (FEMA 2000a, Section 6.4.1.3) are utilized for the effective width for beam strength estimation; this results in an effective slab width of 64 in. for perimeter frames and 72 in. for space frames, so for simplicity 70 in. was used in both models.

To assess the effective stiffness, Robertson (2002) recommends a using a larger effective slab width of $l_2/3$, where l_2 is the span length of the slab. Robertson’s work was focused on slab-beam connections, so these recommendations are most applicable to space-frame buildings. For the space-frame designs, this would result in an effective width of 120 in.—about 1.7 times the value calculated for strength. For the simulation model we defined the effective slab width based on the strength provisions (neglecting the additional width that contributes to stiffness) and included slab steel within that width. For the space frame, this difference between 70–120 in. of slab width makes the lateral stiffness be underpredicted by approximately 15–20%.

We computed the cracked stiffness of the slab section, considering axial stresses from post-tensioning, to be $0.5E_cI_g$. For simulation, the slab is modeled using an elastic element with plastic hinges at each end. This method is utilized in both the fiber and plastic-hinge versions of

the model because this approach is simpler than modeling the slab with fiber elements and manually adding pre-compression to represent post-tensioning effects.

5.3.4 Joint Model Including Panel Shear and Bond-Slip

The joint model captures the effects of bond-slip and panel shear deformations. Section 5.5 describes the joint model and explains how this model is used for both the fiber-spring and lumped-plasticity models.

5.3.5 Bond-Slip Model for Column Footings

Bond-slip springs are used at the base of each column to account for the rebar strains penetrating into the footing. These springs are developed the same way as for the bond-slip springs in the joints, with nonlinear pinched response. This model is explained in Section 5.5.2.4.

5.4 LUMPED-PLASTICITY MODEL FOR COLLAPSE SIMULATION

5.4.1 Overview of Hysteretic Hinge Model

Ibarra and Krawinkler (Ibarra 2003; Ibarra et al. 2005) recently developed a concentrated hinge model to capture the important modes of deterioration of beams and columns that can lead to side-sway collapse in frames. Figure 5.10 shows the monotonic trilinear backbone of the element model, which is described by five parameters: yield moment (M_y), yield chord rotation (θ_y), hardening stiffness (K_s), capping rotation (θ_{cap}), and post-capping stiffness (K_c). Figure 5.11 shows the associated cyclic behavior, which is governed by several additional parameters. Altoontash (2004) implemented this model into OpenSees (2006) as a material model that is accessed through the “Clough” material model command. Note that this name “Clough” is a misnomer, as the actual model is based on the work by Ibarra and Krawinkler (Ibarra 2003; Ibarra et al. 2005).

The model captures four modes of cyclic deterioration (Ibarra et al. 2005): basic strength deterioration, post-capping strength deterioration, unloading stiffness deterioration, and accelerated reloading stiffness deterioration. Each mode of cyclic deterioration is based on an energy index that has two parameters: normalized energy-dissipation capacity (normalized by

yield strain and stress) and an exponent term to describe how the rate of cyclic deterioration changes with accumulation of damage. Each of the cyclic deterioration modes can be calibrated independently, for a total of eight cyclic deterioration parameters. To reduce complexity and make the calibration tractable, we use simplifying assumptions to consolidate the cyclic deterioration parameters from eight to two (following the guidelines in Ibarra 2003, Chapter 3).

An important aspect of Ibarra’s model is that it allows separation of strength deterioration that occurs in a single cycle and strength deterioration that occurs between two consecutive cycles. Haselton (2006, Chapter 4) discusses these types of deterioration in more detail and shows that careful separation of these two types of strength deterioration is critical for accurate collapse simulation.

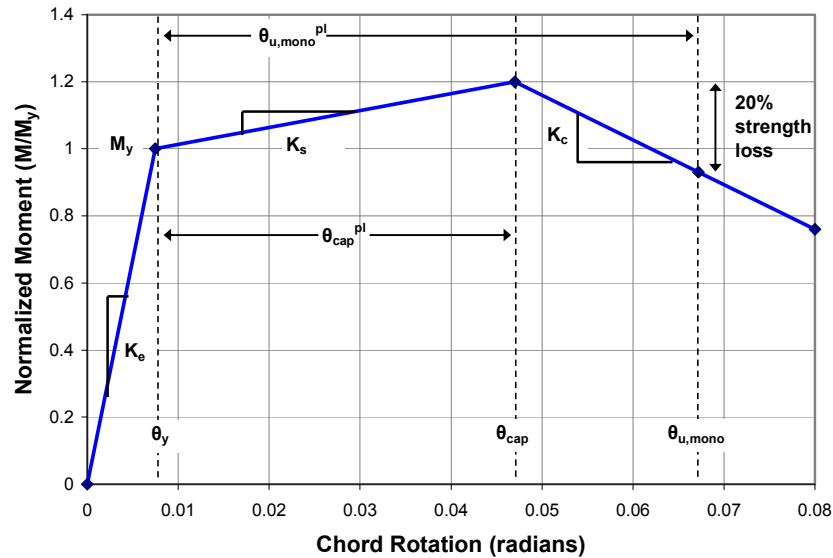


Fig. 5.10 Element backbone defining backbone parameters and notation.

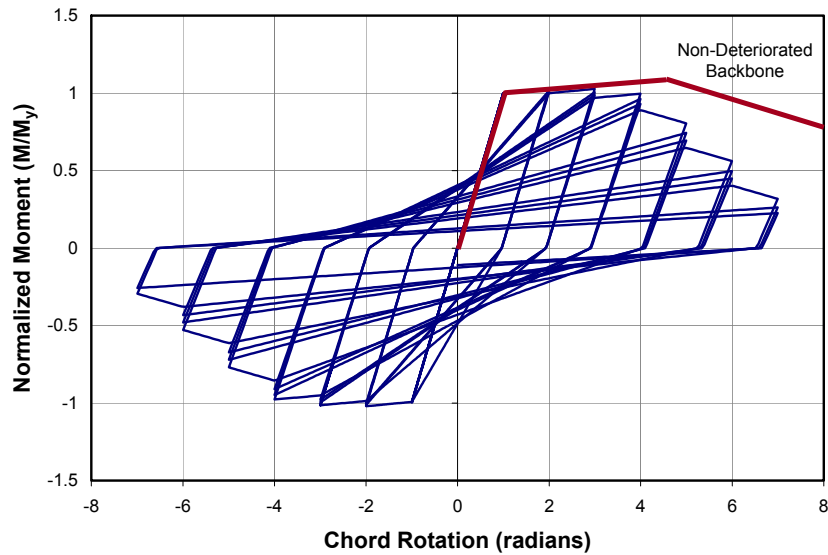


Fig. 5.11 Illustration of cyclic deterioration effects.

As described later, the trilinear hinge model was calibrated for this study using a number of means: through fiber moment-curvature analyses, through empirical relationships published in past research, and through calibrations of the model to 30 cyclic beam-column tests (Appendix C). Since completion of this benchmark study, the authors have undertaken a more extensive calibration of the trilinear element model, and recommendations from the study have been published in Haselton et al. (2007, 2006 Chapter 4). While the member properties from this more recent calibration are not significantly different from the values assumed for this study of the four-story building, guidelines from the new calibration are more generally applicable to a wider range of member properties.

5.4.2 Lumped-Plasticity Model Strengths and Limitations

The main incentive for using the lumped-plasticity model is that it can capture strength and stiffness deterioration that are necessary to assess global side-sway collapse of moment-frame buildings. However, the present formulation of the lumped-plasticity model has a number of limitations relative to the fiber-spring element model. In particular, the lumped-plasticity model does not explicitly simulate axial-flexural interaction effects, concrete cracking behavior, tension-stiffening, and other spread-of-plasticity effects. As such, it requires careful calibration

to simulate response at low deformations, where the onset of cracking and other inelastic effects are more significant than the strain softening at large deformations.

5.4.3 Initial Stiffness of Reinforced Concrete Element (Chord Rotation at Yielding)

Referring to Figure 5.15, the “initial” stiffness of reinforced concrete members is usually defined on the basis of a secant stiffness to some load or deformation level. At the point of flexural yielding, there are three important components of deformation: flexure, bond-slip, and shear. Many times only the flexural, and possibly the shear, component is considered. Using a database of results of over 1800 experimental tests, Fardis et al. (Fardis 2003; Panagiotakos 2001) created empirical equations that predict the chord rotation at the onset of flexural yielding, incorporating all three contributors mentioned above. The equation proposed by Fardis for θ_y is given below:

$$\theta_y = \phi_y \frac{L_s}{3} + 0.00275 + a_{sl} \frac{\varepsilon_y}{(d-d')} \frac{0.2d_b f_y}{\sqrt{f'_c}} \quad (5.1)$$

where θ_y is the chord rotation at yield, ϕ_y is yield curvature, L_s is distance from point of maximum to zero moment, a_{sl} is a bond-slip indicator (1 if boundary conditions allow bond-slip past point of maximum moment), ε_y is longitudinal steel yield strain, $(d-d')$ is distance from top to bottom longitudinal steel, d_b is the beam depth, f_y is longitudinal steel yield strength, and f'_c is concrete strength.

Table 5.1 summarizes the predicted values (Eq. 5.1) of θ_y for the members of frame Design A (see Fig. 3.4 for element locations within the frame). This shows shear deformation predictions from both Fardis and Mehanny; we judged Fardis’s predictions to be too large, so we used Mehanny’s predictions when developing the structural model. For future studies, we recommend using the Fardis model for all aspects of deformation, for consistency, because his regression analysis predicts the total deformation and not the various components of deformation.

Comparing the total yield rotation, θ_y (given in the seventh column of Table 5.1) to the flexural deformation (column 3), the flexural deformation comprises only about 60% of the total yield deformation. Effective stiffness values are back-calculated from the total yield rotation and reported in the table. The resulting average effective stiffness is equal to $EI_{\text{eff}} = 0.25EI_{\text{gross}}$. The final column of Table 5.1 clearly shows how the flexural deformations only represent about 60% of the total deformations at yield.

Table 5.1 Contributions to chord rotation at onset of flexural yielding (Design A).

Section	Expected Axial Load (kips)	$\Theta_{y,flexure}$ (rad)	$\Theta_{y,bond-slip}$ (rad)	$\Theta_{y,shear, Fardis}$ (rad)	$\Theta_{y,shear, Mehanny}$ (rad)	$\Theta_{y,total}$ (rad)	EI_{eff} / EI	$\Theta_{y,flexure} / \Theta_{y,total}$
CS1	-218	0.0031	0.0016	0.0028	0.0014	0.0062	0.21	50.3%
CS2	-410	0.0025	0.0013	0.0028	0.0014	0.0052	0.19	47.7%
CS3	-298	0.0028	0.0016	0.0028	0.0018	0.0062	0.18	44.3%
CS4	-190	0.0027	0.0014	0.0028	0.0008	0.0049	0.19	54.6%
CS4	-87	0.0027	0.0014	0.0028	0.0008	0.0049	0.17	54.6%
CS5	-156	0.0028	0.0016	0.0028	0.0011	0.0055	0.19	50.3%
CS6	-99	0.0035	0.0016	0.0028	0.0007	0.0058	0.20	59.8%
CS6	-45	0.0035	0.0016	0.0028	0.0007	0.0058	0.20	59.8%
BS1	0	0.0037	0.0011	0.0028	0.0006	0.0054	0.39	68.4%
BS2	0	0.0043	0.0013	0.0028	0.0005	0.0061	0.39	69.4%
BS3	0	0.0051	0.0015	0.0028	0.0005	0.0072	0.32	71.6%
BS4	0	0.0049	0.0015	0.0028	0.0005	0.0070	0.31	70.7%
Average:						0.25	58.5%	

The test results from a RC beam, show in Figure 5.15, illustrate the strongly nonlinear response from zero to the yield point. Several options for defining the effective initial stiffness are also shown, based on secant stiffness values defined at loading equal to 0.4, 0.5, and 1.0 times the yield force. As described later, our comparisons using K_{stf_2} (secant at 0.4 yield) and K_{yld} (secant to yield) indicate that 0.4 is shown to provide the best *compromise* for modeling the full range of performance (from small deformations up to collapse). However, this is a compromise and the significance of the initial stiffness assumption is investigated in the loss analyses of Chapter 6, where comparisons are made between analyses with the fiber-spring element model, which explicitly models concrete cracking, tension-stiffening effect, and nonlinear bond-slip, and the lumped-plasticity model. All comparisons do rely on the lumped-plasticity model for assessing collapse.

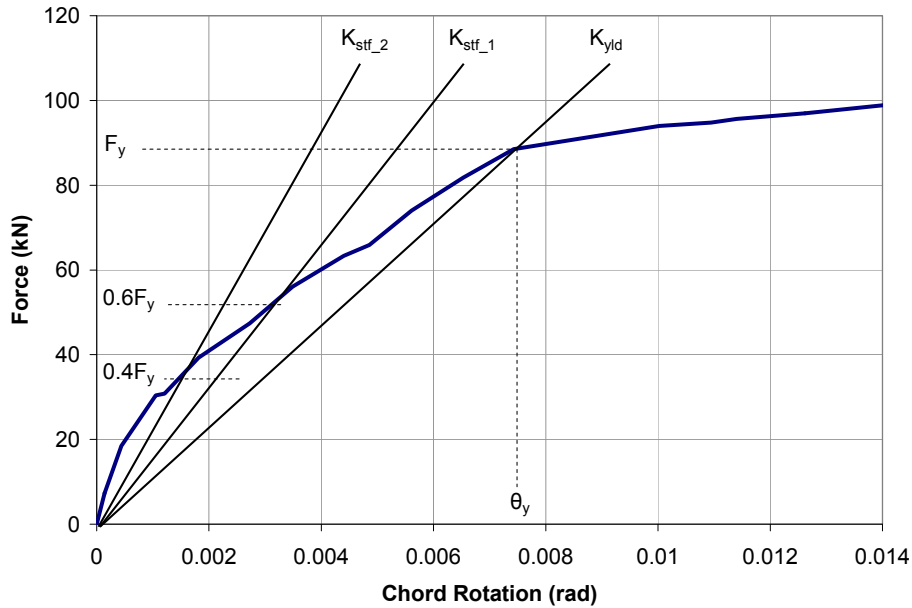


Fig. 5.12 Monotonic response of RC beam to yielding, showing various methods to represent initial stiffness of element (data from Ingham 2001).

5.4.4 Post-Yield Stiffness of Reinforced Concrete Element

The post-yield stiffness values of the beams and columns were determined by integrating curvatures from a fiber moment-curvature analysis at the expected axial load level over plastic-hinge lengths predicted by Priestley et al. (1996). The calibrations in Appendix C substantiate this approach, with post-yield stiffness values ranging from 1% to 7% of the pre-yield stiffness values, with a mean ratio of 5%.

5.4.5 Flexural Strength of Reinforced Concrete Element

Hinge flexural strengths are based on fiber moment-curvature analyses at the expected axial load of the element. Since the fiber-element model uses expected material properties, the calculated strengths similarly correspond to the expected strength. In general, the fiber moment-curvature results are expected to agree with flexural strengths calculated through use of traditional stress-block approaches or the closed-form predictive equations developed by Panagiotakos and Fardis (2001).

5.4.6 Plastic-Rotation Capacity of Reinforced Concrete Element

5.4.6.1 Importance for Collapse Modeling

Ibarra (Ibarra 2003, Chapter 6; Ibarra et al. 2005) shows that the plastic-rotation capacity is the parameter that most impacts the collapse capacity, especially for ductile systems. Our collapse sensitivity study also verifies this for one of the buildings used in this study.

For newly designed structural elements, the plastic-rotation capacity (θ_{cap}^{pl}) is typically dictated by the onset of rebar buckling or loss of confinement of the concrete core (Fardis 2003; Panagiotakos 2001). Berry and Eberhard (2005, 2003) developed empirical functions to predict the plastic rotation at the onset of rebar buckling. Independently, Fardis, Panagiotakos, and Biskinis (Fardis 2003; Panagiotakos 2001) developed empirical functions to predict the plastic-rotation capacities (defined by the point where 20% strength loss occurs) under both monotonic and cyclic loading. This section reviews both studies as related to the determination of plastic-rotation capacities.

5.4.6.2 Predictions of Onset of Rebar Buckling

Berry and Eberhard (2005, 2003) assembled a database (PEER 2005) of cyclic test results of rectangular and circular RC columns. Of the 253 rectangular columns in the data base, the 199 are classified as having a flexural failure mode. From these data, Berry and Eberhard created empirical equations to predict the plastic rotations at the onset of concrete spalling and reinforcing bar buckling. As described later, data from the empirical equations for reinforcing bar buckling are used to check the calibration of the capping point rotation where the RC members begin to strain soften (degrade).

5.4.6.3 Predictions of Plastic-Rotation Capacity

Fardis, Panagiotakos, and Biskinis (Fardis 2003; Panagiotakos 2001) assembled a comprehensive database of experimental results of RC element tests. The database currently includes a total of 1802 tests, 727 of which are cyclic tests of rectangular columns having conforming detailing and failing in a flexural mode. From these data Fardis and Panagiotakos created empirical equations to predict the chord rotation of RC elements at yield and “ultimate,” where “ultimate” is defined

as a 20% reduction in lateral load resistance. These equations distinguish the plastic rotation at “ultimate” between monotonic and cyclic loading. The equation proposed by Fardis for monotonic loading, $\theta_{u,mono}^{pl}$, is as follows:

$$\theta_{u,mono}^{pl} = \alpha_{st}^{pl} (1 + 0.55a_{sl})(1 - 0.4a_{wall})(0.2)^v \left(\frac{\max(0.01, \omega')}{\max(0.01, \omega)} f'_c \right)^{0.225} \left(\frac{L_s}{h} \right)^{0.375} 25^{\left(\alpha \rho_s \frac{f_{yw}}{f'_c} \right)} 1.3^{100\rho_d} \quad (5.2)$$

where L_s is distance from point of maximum to the point of zero moment,

a_{sl} is a bond-slip indicator (1 if boundary conditions allow bond-slip past point of maximum moment),

$f_{y,w}$ is longitudinal steel yield strength of stirrups (MPa),

f'_c is concrete strength (MPa),

$\theta_{u,mono}^{pl}$ is monotonic plastic rotation from yield to point of 20% strength loss,

α_{st} is a coefficient for type of steel,

a_{wall} is a coefficient to indicate if the member is a wall,

v is the axial load ratio ($P/A_g f'_c$),

ω and ω' are longitudinal reinforcement ratios in tension and compression,

h is the height of the section,

α is a confinement effectiveness factor,

ρ_s is the area ratio of transverse steel parallel to direction of loading, and

ρ_d is ratio of diagonal reinforcement.

As shown in the backbone plot of Figure 5.12, Equation 5.2 predicts the plastic rotation corresponding to a 20% strength loss for monotonic loading ($\theta_{u,mono}^{pl}$). To translate this point to the plastic rotation at capping, θ_{cap}^{pl} (which is needed as input into the backbone curve model), we extrapolated back to a strength increase of 20% of the yield moment using the post-capping stiffness (Section 5.4.7), K_c , i.e., $\theta_{cap}^{pl} = \theta_{u,mono}^{pl} - 0.2M_y/K_c$.

Table 5.2 summarized the resulting plastic capping rotation capacity predictions for building Design A as well as the underlying $\theta_{u,mono}^{pl}$ from Equation 5.2 and Berry’s predictions of the plastic rotation at the onset of rebar buckling. Overall, the predicted capping point plastic rotations (on the order of 0.05 radians for columns and 0.07 radians for beams) are much higher than values suggested by FEMA 356 (FEMA 2000a) and other publications. These large plastic-rotation capacities result from the high transverse confinement ratios required for new code-conforming designs and the low axial load levels of the columns of this low-rise perimeter-frame

building (Design A). In addition, the beam plastic-rotation capacities reflect their large span to depth ratio. These plastic-rotation capacities would be reduced for smaller transverse confinement ratios and/or higher axial load levels. Appendix D provides the plastic-rotation capacity estimates for all eight structural designs used in this study.

Table 5.2 Predictions of plastic-rotation capacity and onset of rebar buckling (Design A).

Section	Expected Axial Load (kips)	Fardis	Computed	Berry
		$\theta_{u,mono}^{pl}$ (rad)	θ_{cap}^{pl} (rad)	$\theta_{p,bb}$ (rad)
CS1	-218	0.067	0.047	0.055
CS2	-410	0.064	0.047	0.048
CS3	-298	0.062	0.043	0.054
CS4	-190	0.066	0.047	0.052
CS4	-87	0.068	0.050	0.054
CS5	-156	0.066	0.047	0.059
CS6	-99	0.070	0.049	0.059
CS6	-45	0.072	0.051	0.061
BS1	0	0.087	0.067	n/a
BS2	0	0.089	0.067	n/a
BS3	0	0.092	0.070	n/a
BS4	0	0.092	0.070	n/a

Data in Table 5.2 from Berry’s predictions for the onset of rebar buckling are consistently about halfway between Fardis’s prediction of $\theta_{u,mono}^{pl}$ and our computed value of θ_{cap}^{pl} . This is consistent with the fact that reinforcing bar buckling is one of the primary contributors to strength degradation of well confined RC members. This consistency between the Fardis and Berry predictions gives further strength and validity to the collapse predictions that follow in this chapter.

5.4.6.4 Strengths and Limitations

Fardis’s models are among the few substantiated studies to determine the mean and dispersion of the plastic-rotation capacity of a reinforced concrete member. However, any model of this kind is limited because the majority of available test data are for tests run with traditional loading protocols that have 2–4 cycles per displacement level, and typically having many post-yield displacement levels before the specimen fails. This is not a specific limitation of the Fardis model, but is a limitation of any model created using such test data. Whether such models are

accurate for collapse assessment is not clear, since structural collapse under earthquakes may occur under just a few large deformation cycles. The effects that loading protocol have on element behavior has received relatively little research attention and could impact significantly the results of the collapse studies. Fardis addressed this issue by separating cyclic and monotonic test results and using an indicator variable to differentiate these two types of data. Even so, this approach still assumes that the trends in the data are similar for both cyclic and monotonic tests.

Ingham (2001) conducted a recent study that addresses this topic for RC elements, in which he subjected the same column to various loading protocols. However, most tests were not continued to deformations large enough to observe the capping point, so these results did not provide information on how the plastic-rotation capacity may be affected by loading protocol.

5.4.6.5 Calibration of Plastic-Rotation Capacity Using Test Data

To provide further verification of Fardis's prediction of $\theta_{u,mono}^{pl}$ and our computed value of θ_{cap}^{pl} , Appendix C presents the results of calibrations to 30 tests of rectangular concrete columns. Figure 5.13 shows the results of one of these calibrations. This appendix shows that for conforming elements, the predictions of θ_{cap}^{pl} are still an average of 25% lower than observed values. It is notable that the "observed values" of plastic-rotation capacity are often a lower-bound estimate because the test was not continued to failure of the element. The models used in this study are based on the Fardis predictions, so the collapse capacities reported in this study are still slightly conservative.

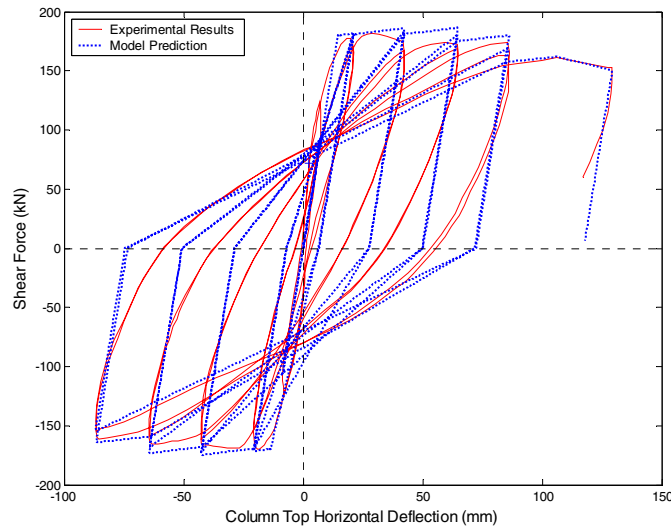


Fig. 5.13 Comparison of model calibration and experimental results from Tanaka and Park (Tanaka 1990), specimen 2 (TestID 19) (PEER 2005; Eberhard 2005).

5.4.7 Post-Capping Stiffness

Ibarra also identified post-capping stiffness (shown in Fig. 5.10), K_c , as a key parameter for modeling side-sway collapse (Ibarra 2003, Chapter 4; Ibarra et al. 2005). To quantify the post-capping stiffness, we used the calibrations to 30 conforming concrete columns (Appendix C). The available test data show that conforming elements maintain strength and positive stiffness to high levels of deformation and, unfortunately, few tests are loaded to deformation levels that are large enough to accurately reveal the post-capping behavior. From the calibrations in Appendix C, only 4 of the 30 conforming column experiments were continued to deformation levels adequate to show the post-capping stiffness.

Figure 5.13 shows one of the four tests that were loaded far enough to show post-capping stiffness. Even though a negative stiffness is evident in the test data, accurate estimation of this stiffness is difficult. From the four tests that showed in-cycle strain softening, the median post-capping stiffness is estimated to be $K_c = -0.075K_e$. This value is used for the structural models of this report. Due to highly limited test data, we applied a large uncertainty (c.o.v. = 60%) to the degrading stiffness, which is consistent with that assumed by Ibarra (2003). The lack of data on post-capping response and the importance of this response on simulating collapse indicate the need for further research to quantify this aspect of behavior.

5.4.8 Cyclic Deterioration

5.4.8.1 Calibration of Cyclic Deterioration

The effects of cyclic deterioration on the strength and stiffness of an RC component are illustrated in Figure 5.14. Research by Ibarra (Ibarra 2003, Chapter 4) indicates that cyclic deterioration is important but generally not dominant for collapse capacity prediction, especially when the energy-dissipation capacity is large, as is the case for conforming elements.

Ibarra's model (Ibarra 2003, Chapter 3) assumes that cyclic deterioration is a function of the energy dissipated in the element. He uses two calibration parameters to capture this effect: (1) γ (also called λ by Altoontash (2004)), the normalized cyclic energy-dissipation capacity (hysteretic energy-dissipation capacity = $E_t = \gamma F_y \delta_y = \gamma M_y \theta_y$), and (2) c , an exponent that controls the rate of deterioration ($c = 1.0$ causes deterioration to be proportional to dissipated energy and $c > 1.0$ retards early deterioration and accelerates later deterioration). To calibrate the cyclic deterioration parameters we used the experimental data set in Appendix C and determined a mean value of $\gamma = \lambda = 110$ (c.o.v. = 0.39) with $c = 1.0$. However, the models used for many of the analyses in this report are based on a preliminary calibration exercise that showed $c = 1.0$ and $\gamma = \lambda = 120$. Based on Ibarra's observations and our own sensitivity analysis (see Appendix E), the 10% difference in γ (110 versus 120) is inconsequential to the collapse assessment.

5.4.9 Bond-Slip Model

To account for bond-slip in the context of the lumped-plasticity model, we simply lump the bond-slip flexibility (as described in Section 5.4.3) with the other flexibilities (flexural and shear) when determining the initial stiffness of the element and post-yield stiffness of the plastic hinge. As noted previously, since the conforming elements are not expected to experience pullout and given the lack of data on post-peak strain softening, the effects of bond-slip are not explicitly considered for modeling post-peak (capping point) response.

5.4.10 Joint Model

The joint model is described in Section 5.5, where the joint response is distinguished between a joint-panel spring and four “bond-slip” springs. When used with lumped-plasticity models, the “bond-slip” spring properties account for both bond-slip and element plastic hinging behavior. These effects are lumped into a single spring for computational convenience and because the kinematic constraint features used in the joint and spring model implementations in OpenSees do not permit the definition of two springs in series. Nevertheless, the total response is theoretically the same whether the beam and joint bond-slip springs are modeled separately or as a single spring.

5.5 JOINT MODEL

5.5.1 Overview

This study employs a two-dimensional joint model developed and implemented by Altoontash et al. (Altoontash 2004 Chapter 2; Lowes 2004, 2003). Named “Joint2D” in the OpenSees scripting language, this model accounts for the finite joint size, and uses rotational springs and systems of constraints to model the shear panel behavior and the bond-slip behavior. Figure 5.14 shows a schematic diagram of this model.

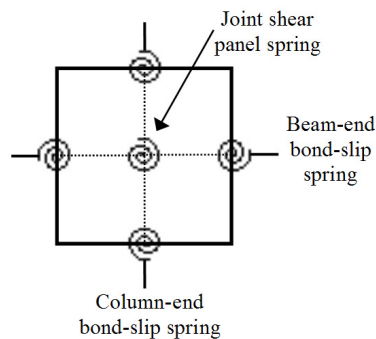


Fig. 5.14 Schematic diagram of joint model (after Altoontash 2004, Chapter 2).

5.5.2 Shear Panel Spring Model

5.5.2.1 Introduction and Overview

Current building code provisions (ACI 21.5) require that the joint shear capacity be based on capacity design principles, so the joint shear demand will never exceed the capacity. We have briefly reviewed research on joint shear strength and did not find any evidence to suggest that the joint shear capacity design provisions (ACI 21.5) will not meet the intent of preventing joint shear failure. This observation is supported by Brown and Lowes (2006) who reviewed results of 45 experimental test of conforming joints and found that none exhibited damage requiring joint replacement. This supports the premise that severe damage is highly unlikely in conforming joints and that, therefore, nonlinear (strength-degrading) joint shear modeling is not a critical aspect of simulating collapse performance. For these reasons, we have opted for a relatively simple approach to evaluating the joint shear response. For readers interested in more details on modeling of joint response, the modified compression field theory (MCFT) (Vecchio 1986; Stevens 1991; Altoontash 2004; Lowes 2004; Lowes 2003; Mitra 2004) has been shown to work well for conforming joints and not as well for non-conforming joints (Mitra and Lowes 2004).

5.5.2.2 Shear Panel Backbone

For simplicity, we modeled the pre- and post-cracked stiffnesses of the joint shear backbone based on simple mechanics (Umemura 1969) up to the yield point.

Since we do not expect joint shear failure for new buildings, we did not carefully quantify the strength or the post-capping stiffness of the joint shear panel. The estimate of joint shear strength is based on work by Meinheit and Jirsa (Meinheit 1981), with the stress capacity for interior joints being approximately $22\sqrt{f'_c}$. We then conservatively assume that a negative stiffness will initiate just after yield. This post-capping stiffness shown in Figure 5.15 is based on the results of a single experimental test of an older un-reinforced joint tested by Walker (Altoontash 2004, Fig. 4.25). Note that this value is a conservative approximation that is not intended to influence the response of RC frames configured according to capacity design principles where joint shear failure is not expected.

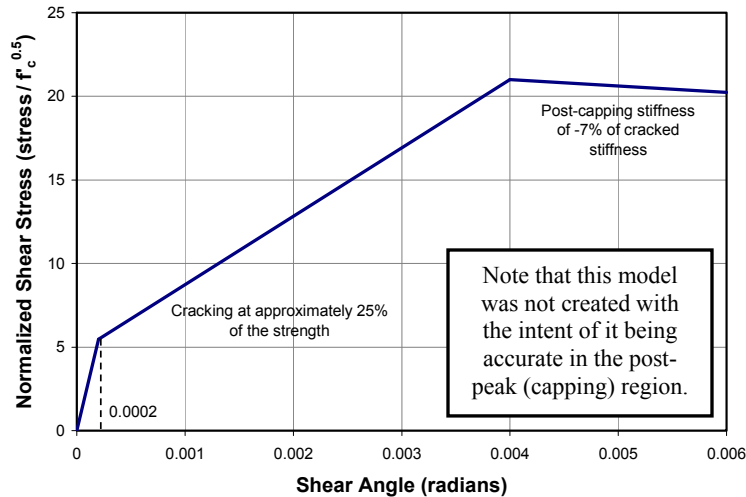


Fig. 5.15 Joint shear panel backbone curve.

In the analyses completed for this study, we verified that joint shear failure is not a controlling mechanism. The only exception is when we used an extremely large plastic-rotation capacity (170% of the mean capacity) during the sensitivity study; this allowed the elements to harden unrealistically and caused joint shear failure to govern the response (Fig. E.4).

5.5.2.3 Shear Panel Hysteretic Behavior

The cyclic behavior of the joint shear panel is based on recommendations by Altoontash (Altoontash 2004, Chapter 4), who proposes that the hysteretic behavior be pinched and have the pinch-point at 25% of the maximum historic stress and 25% of the maximum historic rotation. Figure 5.16 shows the cyclic behavior of the model, which is calibrated excluding cyclic strength or stiffness deterioration. We feel that this simplification is appropriate because we do not expect joint shear failure in this code-conforming building.

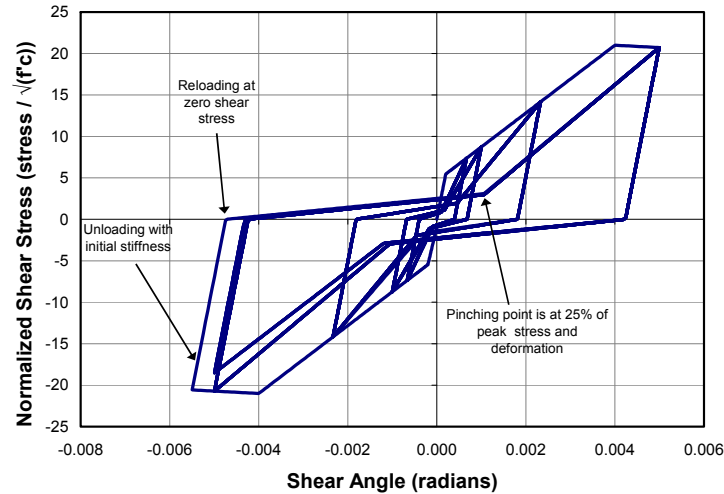


Fig. 5.16 Joint shear panel cyclic behavior.

5.5.2.4 Bond-Slip Spring Model

Bond-slip adds additional flexibility both before and after the onset of flexural yielding. For those interested in better understanding the phenomenon, Eligehausen, Popov, and Bertero (Eligehausen 1983) give a clear and thorough explanation of bond-slip (and potential for pullout) before yielding of reinforcement. Recent work by Lowes, Mitra, and Altoontash (Lowes 2004, 2003) propose a bond-slip model, based on the approach of integrating the strains into the joint or footing. Additionally, Fardis et al. (Fardis 2003; Panagiotakos 2001) used test data to empirically quantify the bond-slip deformations at the yield and ultimate chord rotations. In this work, we draw on the work by Lowes et al. and Fardis et al. to develop a model for bond-slip using a discrete rotational spring. This discrete spring does not yield, so this spring accounts only for the bond-slip flexibility up to the onset of flexural yielding. This discrete spring is used only as part of the fiber-spring model. In the lumped-plasticity model, a single spring is used to represent both plastic deformation and bond-slip deformation.

Lowes primarily focused on non-conforming joints and developed a bond-slip model to capture both element flexibility associated with bond-slip and the strength loss associated with rebar pullout. In this work focused on new buildings, we assume that the combination of code required development length and the minimum joint dimensions (to limit the bond stress demand) will prevent strength loss associated with rebar pullout. This assumption is substantiated by the work of Brown and Lowes (2006) as mentioned previously.

Figure 5.17 shows how the reinforcing bar strains penetrate into the joint or footing. This strain integration approach is used by Lowes et al. (Lowes 2004, 2003) and others (Filippou et al. 1999; Mazzoni and Moehle 2001) to evaluate bar-slip deformations.

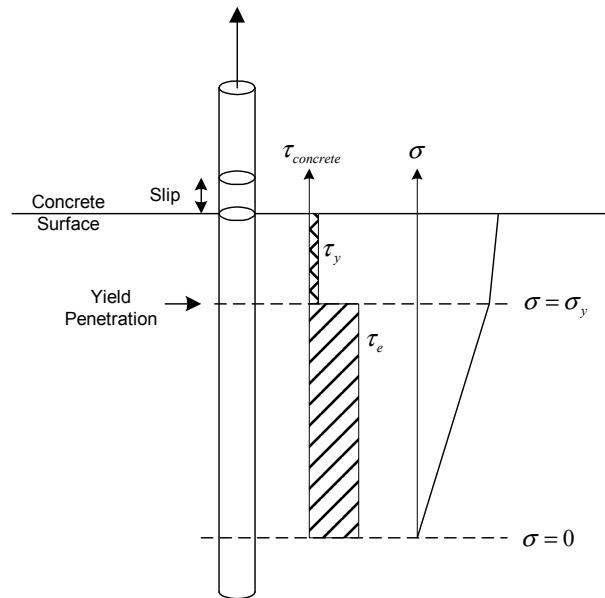


Fig. 5.17 Penetration of strains into joint or footing (after Lowes 2004).

As shown, when as the reinforcing bar strains penetrates into the concrete, bond stresses are developed between the rebar and the concrete. The bond transfer reduces during tension bar yielding due to a combination of damage to the concrete-steel interface and the negative Poisson effect of the bar. Bond stresses do not deteriorate as much under compression loading, where the Poisson effect is positive. Moreover, since reinforcing bar slip in tension dominates the rotations from bond-slip, the effect of bond transfer in compression can usually be ignored (Filippou 1999). We verified this by calculation and showed that neglecting the compressive rebar slip overpredicts the final rotational bond-slip stiffness by less than 10%, based on the conservative assumption that the concrete in the compression zone is flexible enough to allow the compression rebar to push into the footing or joint.

To integrate the strains and compute the bond-slip deformations, we must predict the bond strengths, τ_e and τ_y . Lowes et al. (Lowes 2004) proposes a bond strength of $\tau_e = 21\sqrt{f'_c}$ (f'_c and τ_e in psi) for the interface between concrete and elastic rebar and a much lower and more uncertain bond strength of $\tau_y = 0.6\sqrt{f'_c}$ to $4.8\sqrt{f'_c}$ (f'_c and τ_y in psi) between concrete and

yielded rebar. Fardis (Fardis 2003; Panagiotakos 2001) inferred the effective bond strength, τ_e , from regression analysis using data from over 1800 tests (primarily with cyclic loading) and determined a value of $\tau_e = 7.5\sqrt{f'_c}$ (f'_c and τ_e in psi). Figure 5.18 shows a comparison of bond-slip results obtained by integrating the strains using values of τ_e from both Lowes and Fardis. This example of stress-slip response is for a longitudinal #9 rebar in the second floor beam of Design A (see Fig. 3.4). The discrepancy between the bond-slip models by Lowes and Fardis is likely due to the many assumptions made when interpreting the experimental data, such as what portion of the deformation to allocate to bond-slip versus other effects, and how to account for the effects of cyclic loading. For consistency with other modeling parameters that we have assumed by Fardis et al., we have assumed his recommendations for τ_e .

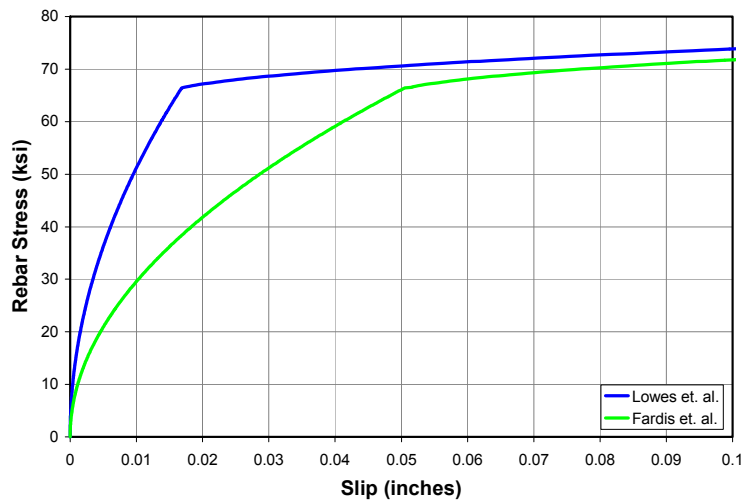


Fig. 5.18 Relationship between rebar stress and slip (ex. for BS1 of Design A).

To relate the bond-slip deformation to the hinge rotation, we need to assume an effective lever arm through the cross section. Following Fardis’s assumption that the compression steel does not contribute to bond slip, we have adopted his proposal to use the dimension $(d-d')$ as the effective lever arm, where d is the depth to the tension steel and d' is the depth to the compression steel. Figure 5.19a shows the resulting estimates for the moment versus bond-slip rotation, using Fardis’s recommendation for τ_e .

This process shows that we can predict the relationship between moment and rotation due to bond-slip for both the pre-yield and post-yield regions. However, a yielding bond-slip spring

in series with a fiber element will cause all of the plastic deformations to localize in only one of the two elements. Therefore, in this work we use a bond-slip spring in series with the fiber element only to capture the bond-slip behavior in the pre-yield regime. We then adjust the steel strain-hardening stiffness to capture bond-slip flexibility in the post-yield regime (Section 5.3.3.2).

Figure 5.19b shows how we use a bilinear idealization of the bond-slip behavior in the pre-yield regime, with a stiffness change of $\frac{1}{4}$ at 40% of the flexural strength. For the fiber-element models, we use this bilinear idealization when creating the bond-slip springs.

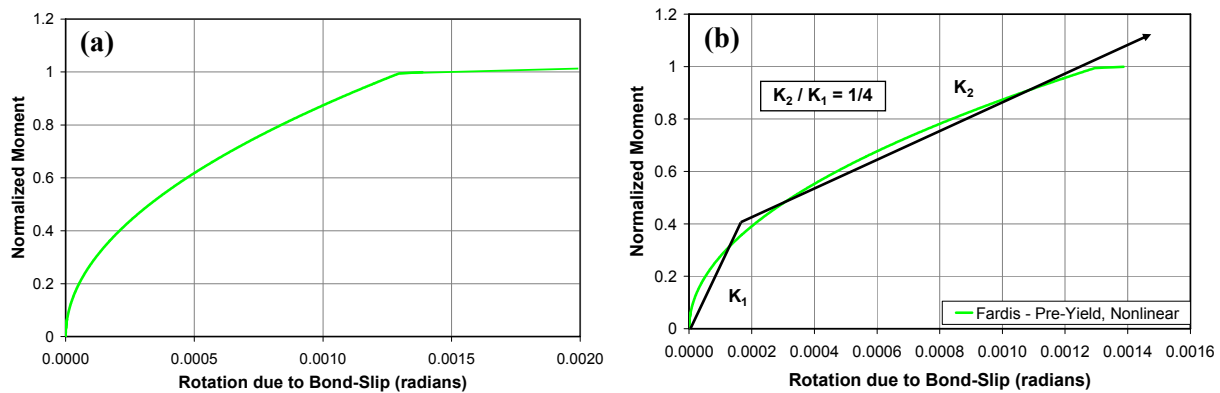


Fig. 5.19 Relationship between moment and rotation (ex. for BS1 of Design A); (a) predictions from directly integrating strains, (b) bilinear approximation.

This illustration of integrating strains to determine the moment-rotation response due to bond-slip was for a single element, namely beam section one of Design A. To generalize the bond-slip model, we use the simplified expression developed by Fardis (Panagiotakos 2001; Fardis 2003) to predict the bond-slip rotation at yield (third term of Eq. 5.1 in Section 5.4.3) and then adopt the stiffness approximation of Figure 5.19b.

To model the cyclic behavior of the bond-slip spring, we use recommendations by Mitra and Lowes (Mitra 2004) who suggest unloading with the initial stiffness and pinching behavior that has a “pinching point” at 25% of the flexural yield strength and 25% of the stiffness. This cyclic behavior is similar to that previously shown for the joint shear panel in Figure 5.16, with the exception that the bond-slip spring is bilinear and never has negative stiffness.

For the lumped-plasticity models, the bond-slip flexibility is simply lumped together with the flexural and shear flexibilities when defining the initial hinge stiffness. When applied in this

way, the pre-yield bilinear bond-slip behavior is not captured and the bond-slip pinching response is not incorporated into the model (Section 5.4.3).

5.6 MODELING GRAVITY-FRAME CONTRIBUTION

As illustrated in Figure 5.2, for perimeter-frame buildings, the gravity frames are composed of a flat-slab supported by gravity columns. Although not typically considered to provide lateral resistance, the gravity frame is likely to provide additional strength and stiffness to the primary perimeter moment frame. Where included in the analysis, the gravity-frame columns and slab-beams are modeled with centerline connections, and the gravity load tributary to the gravity frame is applied directly to the gravity frame. When the gravity frame is not included in the perimeter-frame models, a fictitious “leaning column” is introduced into the structural model to account for the additional P-delta forces that the gravity system imposes on the perimeter frame. This “leaning column” is composed of pin-connected truss elements and connected to the primary frame at each floor level.

5.6.1 Gravity-Column Modeling

The columns of the gravity system are modeled in a similar manner as the columns of the primary frame, meaning that they are modeled using fiber elements in the fiber version of the model and plastic-hinge elements in the plastic-hinge version of the model. The differences are as follows:

- The connection between the column and slab is modeled as a center-line connection, and the finite size of this connection region is neglected.
- Bond-slip is not modeled in the slab-column connection region, since it is assumed that the moment transfer between the slab and column is not large enough to develop appreciable bond-slip of the column reinforcement. Similarly, with the exception of localized nonlinear behavior of the slab-column connection, it is assumed that bond-slip will not be a significant issue in the slab.
- The footing rotational stiffness at the base of the gravity column is less than for the primary frame, due to the difference in footing size. This stiffness is computed considering the soil stiffness and stiffness of the attached grade beams.

We assume that the minimum confinement requirements for gravity columns (ACI 318-02, Section 21.11) will be sufficient to prevent vertical collapse (premature shear failure or axial failure) after flexural hinging. A similar assumption was made for columns of primary lateral-force-resisting system (Section 5.11.1).

5.6.2 Slab-Beam Modeling

The slab-beam model is based on stiffness and strength guidelines by Enomoto and Robertson (2001) and on punching shear predictions by Aslani and Miranda (2005). The following sections discuss each component of the slab-beam model. In both the fiber and plastic-hinge versions of the model, the slab-beam is modeled using an elastic element and plastic hinges at each end. The plastic hinge connects the elastic slab beam to the column, and captures the strength and stiffness loss associated with punching shear failure. This method of modeling is utilized because it is much simpler than using a fiber element and manually applying axial load to account for post-tensioning effects.

5.6.2.1 Slab-Beam Strength

The slab yield strength is computed using a fiber analysis at the expected axial load level due to post-tensioning effects and neglecting concrete tensile capacity. For effective slab width, we use recommendations from Robertson (2002). This procedure utilizes an effective slab width for strength, of $c_2 + 5h$, where c_2 is the width of the column perpendicular to the applied lateral load and h is the thickness of the slab. For the gravity frame of the perimeter-frame buildings, the effective slab width is 70". Robertson also recommends using $1.25 \cdot f_y$, but for consistency with other aspects of our model, we use $f_{y, \text{expected}} = 67$ ksi (for Grade 60 reinforcement).

5.6.2.2 Slab-Beam Pre-Yield Stiffness

The stiffness of the gravity system is an important consideration, especially for drift induced losses at low ground motion levels. The effective slab width for stiffness is much larger than for strength. Robertson (2002) proposes computing the cracked section stiffness of the slab using an

effective slab width of $l_2/3$, where l_2 is the span length of the slab. For the perimeter-frame designs, this effective width for stiffness is 120". The cracked stiffness of the slab section, computed considering the axial stress from post-tensioning, was computed to be $0.5E_cI_g$.

5.6.2.3 Slab-Beam Post-Yield Stiffness

The moment curvature response of the slab exhibited slight post-yield hardening behavior. Based on this observation, we defined the post-yield stiffness of the slab-beam to be 1% of the initial pre-yield stiffness.

5.6.2.4 Punching Shear and Onset of Strain Softening

Much work has been done to quantify the onset of punching shear. Experimental work by Pan and Moehle (1986), and many other researchers were reviewed by Hueste and Wight (1999). Hueste and Wight developed a punching shear model that accounts for the effects of the shear in the connection due to gravity loads; this concept was further improved by Aslani and Miranda (2005). Aslani developed a relationship to predict the mean and variability of story drift level at the onset of punching shear failure, as a function of gravity load.

The research by Aslani and Miranda was specific to older reinforced concrete construction that did not have continuous bottom slab reinforcing bars. To determine whether their findings may also be applied to slabs with continuous bottom slab reinforcing bars, we refer to Robertson (2002) who reviewed test data for slab-column connections with and without continuous bottom slab reinforcing. Robertson observed that for both types of construction the *onset* of punching shear occurs at the same drift level, but the behavior after punching shear is much different. He found that vertical collapse will occur soon after punching for slabs without continuous bottom bars, but that collapse will be postponed (and was actually never observed in the tests) when continuous bottom reinforcing bars are provided. Based on this observation, we use the fragility function by Aslani and Miranda to quantify the mean story drift ratio of 3.3% and a coefficient of variation of 0.3 for the onset of punching shear. The plastic-rotation capacity of the slab-beam hinges was set equal to 0.023 radians, which caused the punching shear failure to occur in the model at the proper level of interstory drift.

After the structural models were completed, Porter looked more closely at the behavior of slab-column connections and determined that when conforming slabs have post-tensioning, the onset of punching shear is delayed. Porter's findings are included in Appendix I, which shows that a more appropriate estimate of the onset of punching shear is a mean interstory drift ratio of 4.5%, with a $\sigma_{LN} = 0.6$. This updated information was considered in the loss analyses presents in Chapter 6.

5.6.2.5 Strain-Softening Stiffness after Punching Shear

In this work, we assume that once punching shear occurs, the slab-column connection strain-softens. In recent research, the primary focus has been to capture the onset of punching shear and less attention was given to the slope after punching shear occurs.

Before spending time to accurately quantify the softening behavior after punching shear failure, we checked the impacts that this negative stiffness has on the response of the frame. To quantify this impact, we completed structural analyses at a ground motion level that caused punching shear in the slab, then varied the strain softening of the slab to be both -10% and -100% of the initial stiffness of the slab. These analyses showed that such a drastic difference in the slab softening slope only caused a maximum of 7% difference in the interstory drift response. Due to the small impact that this parameter has on drift response, we simply assumed that the slope was -30% of the initial slab stiffness, which we felt was appropriate and slightly conservative.

5.6.2.6 Considering Vertical Collapse of Slab System after Punching Shear

We also assume that the code-required two continuous bottom reinforcing bars will be sufficient to prevent vertical collapse of the slab after punching shear. Therefore, we focus on predicting side-sway collapse of the building and do not focus on vertical collapse of the slab.

5.6.3 Coupling of Gravity and Primary Frames

The connection between the gravity frame and primary frame is composed of the slab system which transfers the loads and provides partial axial restraint to the beams of the primary frame.

Under cyclic loading, the beams elongate, so the level of axial restraint that the slab imposes on the beams can significantly increase the beam axial force, and the resulting increase in beam strength and stiffness. This beam elongation effect is captured by the fiber model but not by the lumped-plasticity model.

In this study, we chose to connect the gravity frame and perimeter frame with one axial strut at each floor level. This approach neglects the axial restraint that the slab will provide to the beam, and the associated increase in strength and stiffness caused by axial load accumulating in the beam. The connecting struts were assigned approximately the same axial stiffness as a column in compression, in order to avoid causing any possible numerical problems with the stiffness matrix. Another approach to modeling the linkage would have been to apply a rigid kinematic constraint between all of the nodes at each floor; however this was not used as it would likely overestimate the axial constraint that the slab will provide to the beam.

5.7 EFFECTS OF NONSTRUCTURAL ELEMENT ON RESPONSE PREDICTIONS

As will be shown in Chapter 6, much of the nonstructural damage and loss occurs at low levels of deformation, when nonstructural elements of the building may be significant contributors to the lateral resistance of the building. However, due to constraints of time and other resources, the influence of nonstructural components on response was not considered in the structural model. This simplification is conservative and may lead to an overprediction of drifts, and resulting losses, especially at lower levels of ground motion.

If one wanted to be more accurate and remove this conservative simplification, the contribution of the nonstructural elements could be added to the structural model. One of the common nonstructural elements are gypsum drywall partitions and an analytical model has recently been developed by Kanvinde and Deierlein for such an element (Kanvinde et al. 2005).

5.8 SOIL-FOUNDATION-STRUCTURE INTERACTION (SFSI)

5.8.1 Overview of Soil-Foundation-Structure Interaction (SFSI) Mechanisms

In conventional structural analysis, the assumption of fixed-base is generally used. For seismic analysis, this means that ground motions are applied directly to the bottom of the structure. In

reality soil-foundation-structure interaction (SFSI) affects the ground motions and the response of the foundation-building system in a way that is not captured by fixed-base analyses. Two mechanisms contribute to SFSI: *inertial SFSI* and *kinematic SFSI*. As part of the benchmark project, there was an interest in investigating the effects of both types of SFSI on the distribution of *EDPs* for the mean benchmark (perimeter Design A) structure as defined earlier in Chapter 3.

The kinematic SFSI characterizes the variation between the free-field and foundation input motions (FFM and FIM, respectively). Free-field motion refers to a recorded ground motion at the ground surface away from any structure. The FIM is the theoretical motion at the base of the structure if the foundation and structure had no mass. At the building location, if free-field motions were recorded at various locations within the footprint of the building, there would be differences in the records due to the incoherence of ground motions as they reach the surface. The presence of the stiff foundation impedes this and what is observed is an averaged ground motion. This base-slab averaging combined with embedment effects lead to an effective foundation input motion (or FIM) different from the FFM.

The *inertial SFSI* relates to the foundation stiffness and damping. When a structure is subjected to ground motions, inertia from the masses above the foundation lead to development of base shear and moments at the foundation level. The foundation reacts to these forces by displacement and rotation, which in turn affect the building's motion. The motion of the foundation on the soil also allows dissipation of energy through radiation damping (the foundation motion acts as a source of waves that are moving away from the structure) and hysteretic damping from the near-field soil nonlinear dynamic response.

Before we applied SFSI models to this structure, we designed square RC footings linked together with grade beams. The structural design for shear and flexure follows the ACI guidelines (2002). The grade beams were modeled as elastic beam-columns to improve the simulation convergence.

5.8.2 Modeling Parameters to Account for SFSI

5.8.2.1 Kinematic SSI Modeling

This section presents simple models used for the analysis of ground motion variations between the FFM and FIM. In general, these models account for base slab averaging, embedment effects,

and pile-soil interaction effects. For the current project, the structure is supported by shallow foundations with small embedment. The main contribution to kinematic SFSI comes from base slab averaging, which will be the focus here. Much of the material presented here was originally presented by Stewart et al. (2004) and is applied in the present study.

Theoretical models for kinematic interaction effects are expressed as frequency-dependent ratios of the Fourier amplitudes (i.e., transfer functions) of FIM to FFM. Base-slab averaging results from inclined or incoherent incident wave fields. In the presence of those wave fields, translational base-slab motions are reduced relative to the free-field (rotational motions are also introduced, but are not considered here). The reductions of base-slab translation tend to become more significant with decreasing period. The period-dependence of these effects is primarily associated with the increased effective size of the foundation relative to the seismic wavelengths at low periods. In addition, ground motions are more incoherent at low periods.

Veletsos and co-workers (Veletsos and Prasad 1989; Veletsos et al. 1997) developed useful models for theoretical base slab averaging that combine an analytical representation of the spatial variation of ground motion with rigorous treatment of foundation-soil contact. The transfer function amplitudes computed by the Veletsos group are presented in Figure 5.20 for circular and rectangular foundations subject to vertically incident, incoherent shear waves. Similar curves are available for other wave fields. The transfer functions in Figure 5.20 are plotted against the dimensionless frequency parameter \tilde{a}_0 , defined as follows for circular and rectangular foundations subject to vertically incident waves, respectively,

$$\tilde{a}_0 = \kappa a_0 \text{ (circular); } \tilde{a}_0 = \frac{\omega b_e \kappa}{2V_{s,r}} \text{ (rectangular)} \quad (5.3)$$

where $a_0 = \omega r / V_{s,r}$, $V_{s,r}$ is the strain-reduced shear-wave velocity; r is the radius of the circular foundation; $b_e = \sqrt{ab}$, where $a \times b$ is the full footprint dimensions of rectangular foundation; κ is a ground motion incoherence parameter. This type of transfer function can be effectively described as a (frequency-dependent) high-frequency filter of the Fourier amplitude spectrum that depends on the foundation dimensions and geometry.

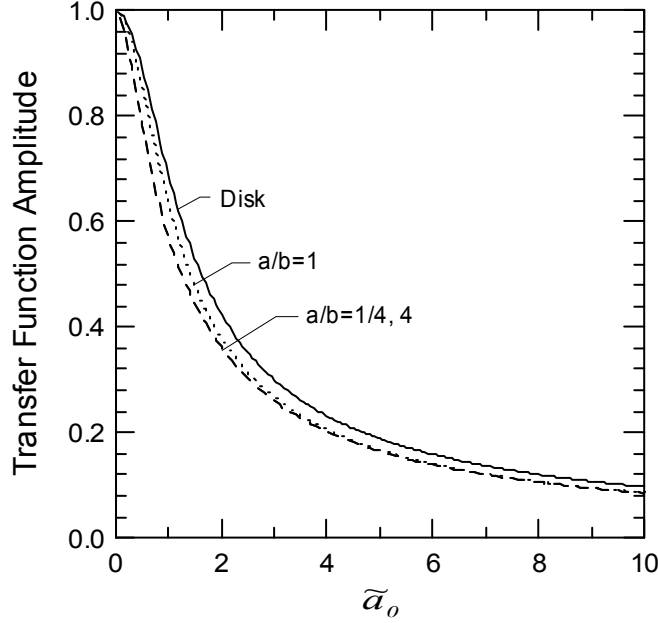


Fig. 5.20 Amplitude of transfer function between free-field motion and FIM for vertically incident incoherent waves. Modified from Veletsos and Prasad (1989) and Veletsos et al. (1997).

Kim and Stewart (2003) calibrated Veletsos' analysis procedure against observed FIM and FFM variations as quantified by frequency-dependent transmissibility function amplitudes, $|H|$. Veletsos' models were fit to $|H|$ and apparent κ -values (denoted κ_a) were fit to the data. Those κ_a values reflect not only incoherence effects, but necessarily also include average foundation flexibility and wave inclination effects for the calibration data set. The structures in the calibration data set generally have shallow foundations that are interconnected (i.e., continuous mats or footings interconnected with grade beams). Parameter κ_a was found to be correlated to average soil shear-wave velocity approximately as follows:

$$\kappa_a = -0.037 + 0.00074V_s \quad \text{or} \quad \kappa_a \approx 0.00065V_s \quad (5.4)$$

where V_s is the small strain shear-wave velocity in m/s.

The fact that κ_a is nearly proportional to V_s (Eq. 5.4) causes dimensionless frequency term $\tilde{\alpha}_0$ to effectively reduce to a function of frequency and foundation size (b_e). This is shown by the following, which is written for vertically propagating waves ($\alpha_v = 0$):

$$\tilde{\alpha}_0 = \frac{\omega b_e \kappa}{2V_{s,r}} \approx \frac{\omega b_e n_1 V_s}{2n_2 V_s} = \frac{\omega b_e n_1}{2n_2} \quad (5.5)$$

where $n_1 \approx 6.5 \times 10^{-4}$ s/m and n_2 is the square root of the soil modulus reduction factor, which can be estimated as shown in Table 5.3 (FEMA 2005).

Table 5.3 Recommended values of shear wave velocity reduction factor n_2 (FEMA 356 2005).

<u>Shear Wave Velocity Reduction Factor, n_2</u>			
Site Class	Peak Ground Acceleration, PGA (g)		
	0.1	0.4	0.8
A	1.00	1.00	1.00
B	1.00	0.97	0.95
C	0.97	0.87	0.77
D	0.95	0.71	0.32
E	0.77	0.22	*
F	*	*	*

Note: Use straight line interpolation for intermediate values of PGA

* = should be estimated from site-specific analysis

The model for transfer function amplitude is represented by the ordinates in Figure 5.20 coupled with Equation 5.5 to relate \tilde{a}_0 to site-specific parameters. For this study, before the motions were applied at the base of the foundation, each free-field (FFM) acceleration history was converted to a foundation input motion (FIM) acceleration history. This was done by calculating the Fourier amplitude of the free-field record, scaling the Fourier amplitude by the transfer function (resulting in a reduced Fourier amplitude), and performing a reverse Fourier transformation with the modified amplitude and the original phase to return to an acceleration history. Ideally, the phase should also have been modified (particularly at high frequencies), but no model or practical guidelines for this adjustment currently exists. Figure 5.21 illustrates the effect of kinematic SFSI for the benchmark structure for one sample motion (Chalfant 07/20/86, Benton 270 motion), which is representative of the overall results. It can be observed that for the benchmark structure, the kinematic interaction has only a mild impact of the free-field record and that for very short periods (less than 0.2 s) only (Fig. 5.21).

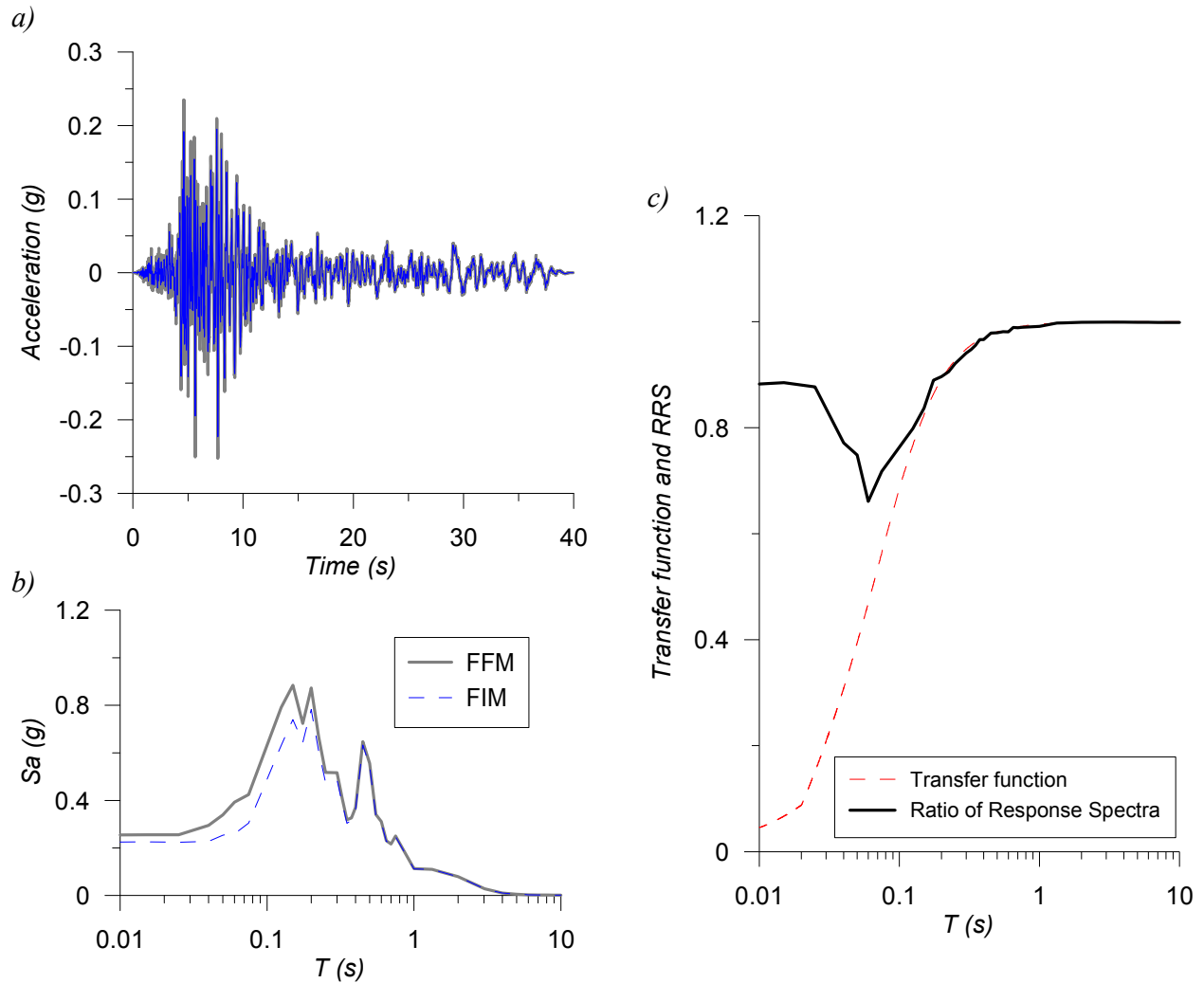


Fig. 5.21 Effect of kinematic interaction on foundation input motion for a sample motion, (a) in time domain, (b) in spectral acceleration space and (c) in ratio of response spectral acceleration space, including transfer function.

5.8.2.2 Inertial SSI Modeling

To perform the inertial SFSI analysis, we have used the mean building (perimeter Design A) to which we have attached nonlinear soil-foundation-interaction elements. The resulting model is a structural system that will allow the direct analysis of SFSI effects, accounting for the nonlinearity of both structural and SFSI elements.

The interaction elements that are considered include a combination of springs and dashpots at the foundation level as shown in Figure 5.22. Elements were added to account for the vertical and horizontal compliance and damping at the foundation-soil interface. Our interest is

two-fold: (1) to use the available OpenSees (OpenSees 2005) elements and tools to test whether or not they allow such analyses to be performed efficiently and (2) to investigate the effect of SFSI and the variability of soil properties on the distribution of *EDPs* for the mean benchmark building.

The first step was to define a model that would optimize the OpenSees analysis in terms of run-time and stability of results. Foundation-soil behavior in the vertical direction is simulated using the Qz nonlinear springs developed by Boulanger et al. (1999). These elements are available in OpenSees as Qzsimple1 elements. We have explored various modeling options to identify an optimal number of springs that would be large enough to capture the soil-foundation stiffness interaction along the base of the footings, yet small enough to insure reasonable computer run-time. Based on numerous tests conducted using simplified models within OpenSees, we have concluded that a five spring assemblage was optimal (Fig. 5.22), which is consistent with results obtained by Harden and Hutchinson (2003).

To model the horizontal stiffness and damping associated with frictional resistance and lateral earth pressures, we used linear springs and dashpots. Nonlinear horizontal spring elements are not currently available in OpenSees for shallow foundations. The lateral foundation springs used for analysis in OpenSees are nonlinear p-y elements (Pysimple1), which are capable of combining stiffness and viscous damping. We attempted to adapt these nonlinear p-y elements for use with shallow foundations, but this was found to be impractical because intractable convergence problems occurred when running OpenSees. To avoid these convergence problems, we modified the spring properties to ensure that they would remain linear for the full range of force-displacement. Taking the springs as linear allowed us to use the equations summarized by Gazetas (1991) to define their stiffness and damping properties.

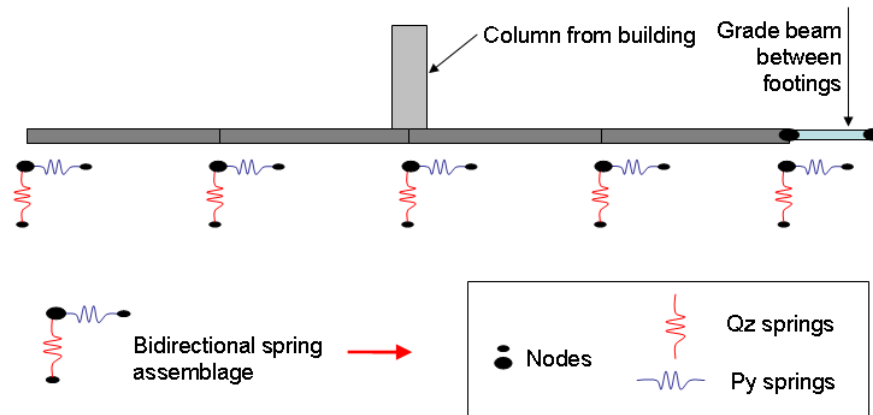


Fig. 5.22 Schematic diagram for inertial SSI modeling in OpenSees.

The nonlinear behavior of the foundation in the vertical direction is modeled with Q-z springs (Qzsimple1 element in OpenSees). This element has four input parameters: (1) the ultimate bearing capacity (Q_{ult}) of the soil, (2) the displacement at which the vertical foundation load is $0.5 \times Q_{ult}$ (z_{50}), (3) tensile (or suction) capacity of the foundation, which is not considered here because the foundation soils are dry and granular, and (4) the viscous damping term.

Q_{ult} is a function of the soil shear strength. The foundation soil is generally granular; hence its shear strength can be described by a friction angle (ϕ). The friction angle was estimated using correlations with penetration resistance values determined from standard penetration tests (SPT) at the site (N). We assumed that the energy ratio of the testing is 60% based on the method of hammer release and other factors, and hence the penetration resistance can be denoted N_{60} . After correcting to an effective overburden stress of $\sigma_v' = 1.0$ atm, the penetration resistance is denoted $(N_1)_{60}$.

We evaluated the expected distribution of penetration resistance for a given depth by assuming that the measured values of penetration resistance represent the mean. The coefficient of variation of SPT results has been found to be ~15% when the test rigorously follows the ASTM D 1586-99 standard and ~45% when there are deviations from the standard (Kulhawy and Trautmann 1996). As mentioned in Chapter 3, the field investigation was coordinated through the ROSRINE project, and appropriate control measures were taken to insure a high level of data quality. Therefore, we have used $COV = 15\%$ to estimate the standard deviation of $(N_1)_{60}$.

We then considered various correlation relationships between N_{60} and $(N_1)_{60}$ and friction angle (ϕ) as shown in Figure 5.23 (all summarized in Hatanaka and Uchida 1996). All of the relations shown in the figure, except for Hatanaka and Uchida (1996), use non-overburden corrected blow counts. The relations from Japan are generally considered to correspond to an energy level of 70%, whereas U.S. relations correspond more closely to 60%. The relation by Dunham (1954) relates ϕ to N_{60} conditional on soil type, but provided no dispersion estimate. The results are in the middle of the range from the other relationships considered. The relation of Oshaki et al. (1959) provides similar results (after correcting from N70 to N60), but also provides a standard deviation estimate of 3° . We used the Oshaki et al. relation to create a second distribution to characterize the (N_{60}) to ϕ relation. We then randomly sampled the N_{60} distribution, then for each N_{60} value, developed many possible ϕ values by randomly sampling the $\phi|N$ relation. From this synthetic data set, we have computed the first two moments of the ϕ distribution to be $\mu = 37.2$ and $\sigma = 4.1$. Sample results from the final ϕ distribution are presented in Table 5.4.

Q_{ult} is also a function of the foundation geometry and soil unit weight. It is important to note that bearing capacity ($q_{ult} = Q_{ult}/A$, where A = foundation area) is usually expressed in stress units, but for the Qzsimple1 input it is converted to an equivalent force applied on the whole footing area.

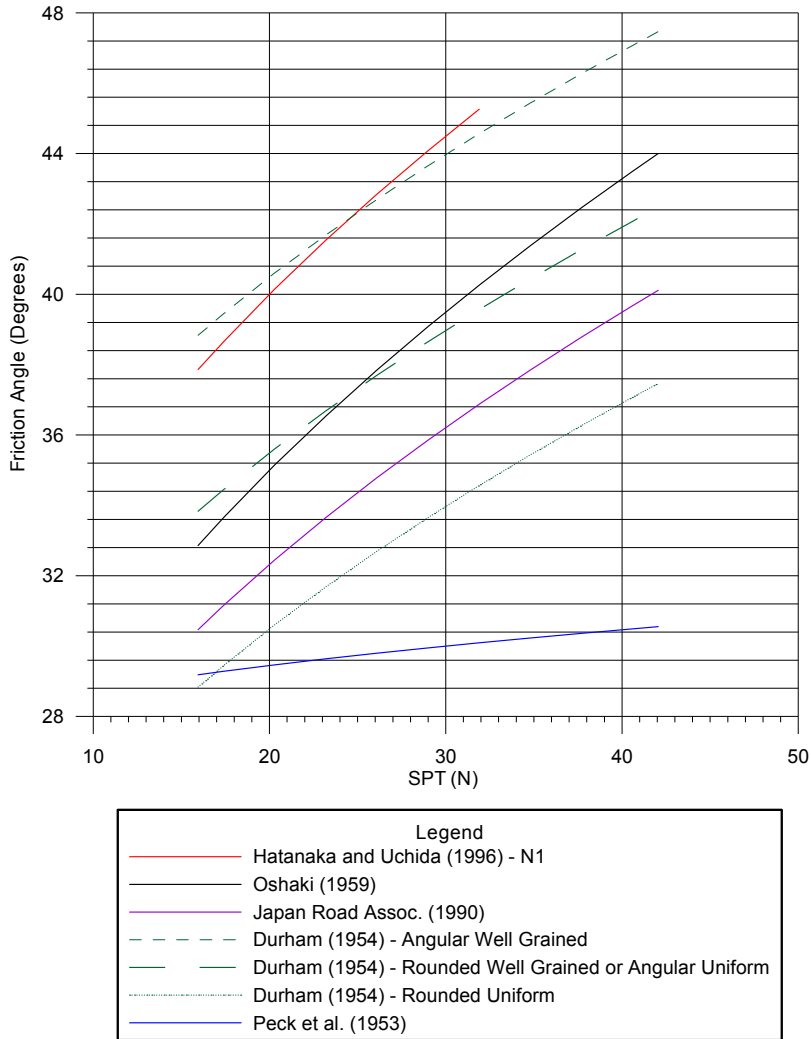


Fig. 5.23 Empirical relationships for SPT blow count and internal angle of friction for sandy soils, mean values. All SPT values made uniform to represent N60.

Table 5.4 Bearing capacity (Qult) properties utilized with Qzsimple1 elements. Qult computed with Vesic's bearing capacity equations (Coduto 2001).

Variant	ϕ (degrees)	Qult (ksf)
$\mu - 2^* \sigma$	28.9	183
$\mu - 1.73^* \sigma$	30	212
$\mu - 1^* \sigma$	33.1	327
μ	37.2	599
$\mu + 1^* \sigma$	41.3	1153
$\mu + 1.73^* \sigma$	44.4	1977
$\mu + 2^* \sigma$	45.5	2420

To define the Qzsimple element in OpenSees, parameter z_{50} is needed in addition to Q_{ult} . Vijayvergiya (1977) defines z_{50} for granular materials as:

$$z_{50} = 0.125 \times 0.05 \times B \quad (5.6)$$

where B = dimension of equivalent square footing ($B = \sqrt{A}$).

Once the properties were correctly defined, we distributed the computed stiffnesses on the springs following FEMA 356 recommendations; so that the external springs contribute to approximately nine times the stiffness of the internal springs (Fig. 5.24).

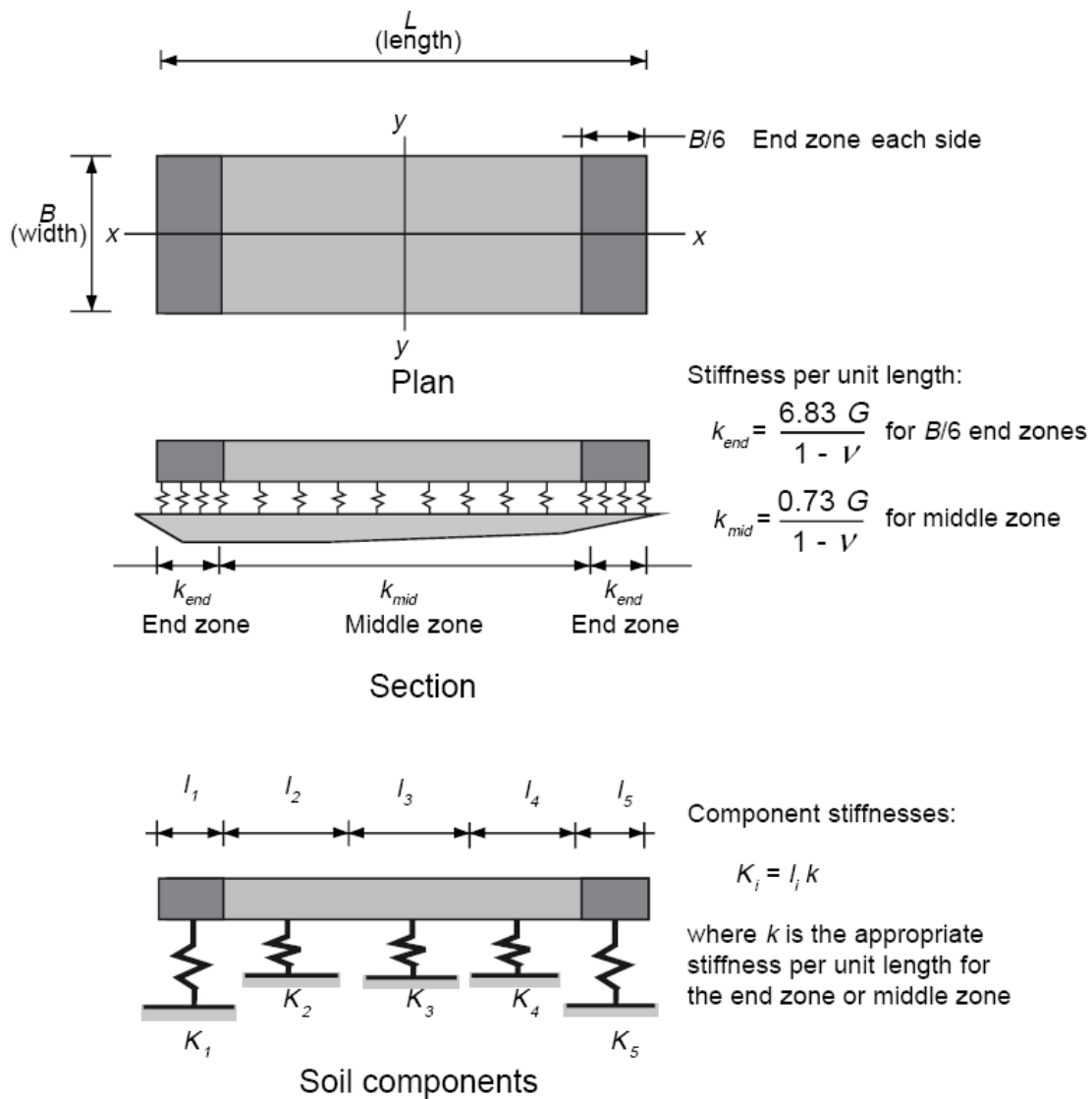


Fig. 5.24 Vertical stiffness modeling for shallow bearing footings (FEMA 356).

The viscous damping properties for the dashpot were computed using Gazetas (1991) equations. Simplified versions of the original equations that were used for stiffness are presented for reference in Figure 5.25. Equations for viscous damping properties are also presented in Gazetas (1991).

Stiffness Parameter	Rigid Plate Stiffness at Surface, K_i'
Vertical Translation, K_z'	$\frac{GL}{1-\nu} \left[0.73 + 1.54 \left(\frac{B}{L} \right)^{0.75} \right]$
Horizontal Translation, K_y' (toward long side)	$\frac{GL}{2-\nu} \left[2 + 2.5 \left(\frac{B}{L} \right)^{0.85} \right]$
Horizontal Translation, K_x' (toward short side)	$\frac{GL}{2-\nu} \left[2 + 2.5 \left(\frac{B}{L} \right)^{0.85} \right] - \frac{GL}{0.75-\nu} \left[0.1 \left(1 - \frac{B}{L} \right) \right]$
Rotation, $K_{\theta x}'$ (about x axis)	$\frac{G}{1-\nu} I_x^{0.75} \left(\frac{L}{B} \right)^{0.25} \left(2.4 + 0.5 \frac{B}{L} \right)$
Rotation, $K_{\theta y}'$ (about y axis)	$\frac{G}{1-\nu} I_y^{0.75} \left[3 \left(\frac{L}{B} \right)^{0.15} \right]$
Stiffness Parameter	Embedment Factors, e_i
Vertical Translation, e_z	$\left[1 + 0.095 \frac{D}{B} \left(1 + 1.3 \frac{B}{L} \right) \right] \left[1 + 0.2 \left(\frac{(2L+2B)}{LB} d \right)^{0.67} \right]$
Horizontal Translation, e_y (toward long side)	$\left[1 + 0.15 \left(\frac{2D}{B} \right)^{0.5} \right] \left\{ 1 + 0.52 \left[\frac{\left(D - \frac{d}{2} \right) 16 (L+B) d}{BL^2} \right]^{0.4} \right\}$
Horizontal Translation, e_x (toward short side)	$\left[1 + 0.15 \left(\frac{2D}{L} \right)^{0.5} \right] \left\{ 1 + 0.52 \left[\frac{\left(D - \frac{d}{2} \right) 16 (L+B) d}{LB^2} \right]^{0.4} \right\}$
Rotation, $e_{\theta x}$ (about x axis)	$1 + 2.52 \frac{d}{B} \left(1 + \frac{2d}{B} \left(\frac{d}{D} \right)^{-0.20} \left(\frac{B}{L} \right)^{0.50} \right)$
Rotation, $e_{\theta y}$ (about y axis)	$1 + 0.92 \left(\frac{2d}{L} \right)^{0.60} \left(1.5 + \left(\frac{2d}{L} \right)^{1.9} \left(\frac{d}{D} \right)^{-0.60} \right)$

Fig. 5.25 Simplified Gazetas equations as presented in ATC-40 (1996). Refer to Gazetas (1991) for complete and detailed procedure.

The linear properties of the PySimple1 spring were also defined using Gazetas (1991) equations. From Figure 5.25, K_y , the linear horizontal stiffness, is a function of (1) foundation geometry, (2) soil Poisson's ratio ($\nu=0.25$ as recommended per ATC-40 for dry granular material), (3) soil modulus G , which is ultimately a function of the soil's shear-wave velocity and unit weight. We have made the assumption that the foundation behaved like a mat with an area matching the building footprint for the purpose of horizontal frictional resistance. At the scale of the benchmark structure, this is consistent with the foundation design of footings interconnected with grade beams. We considered K_y for the whole footprint of the building (120 ft x 180 ft) and then divided by six to obtain K_y for the corresponding slice of the building used as the frame for OpenSees analyses. We have also used the effective shear modulus G , applying the proper shear modulus ratio based on PGA at the surface, following the FEMA 356 (2005) recommendations summarized in Table 5.3. Poisson's ratio has a relatively modest impact on the computed horizontal stiffnesses and was not varied, but G was varied for the sensitivity study. The summary of the values used for the inertial SSI simulations will be presented in Section 5.8.4.

5.8.3 Modeling Variants for OpenSees Analyses and Data Post-Processing

Having defined the key parameters controlling SFSI, we prepared a set of runs to investigate the effect of each parameter on *EDP* (bias and dispersion). The run combinations are schematized in Figure 5.26. There are a total of four types of ground motions, six variations of spring properties and seven hazard levels (totaling 212 ground motion records) for a total of 5088 simulations. Other simulations not presented in Figure 5.26 were also completed recently to further investigate modeling variabilities. It is important to note here that this does not represent a Monte Carlo experimental design where each possible combination of variants is processed. Instead, we varied one parameter at a time. The goal was originally to combine the results through a First-order second-moment (FOSM) statistical approximation as detailed in Baker and Cornell (2003). As it will be shown in the next section, we did not observe differences significant enough to justify the propagation of uncertainties to the damage estimation level and therefore, we decided not to integrate our results with FOSM.

It is important to note that when selecting the run variants, we regrouped them following the input parameter and not necessarily the physical mechanism. That is, the vertical viscous

damping (C_z) is varied at the same time as the horizontal elastic initial stiffness (K_y) and viscous damping (C_y) because all 3 parameters are computed using the Gazetas equations with the shear modulus G as the input variable. Q_z is varied separately, since it depends only on bearing capacity, which is ultimately a function of the shear strength (ϕ). This way, what we actually compute is the impact of variability of soil properties embedded within the models.

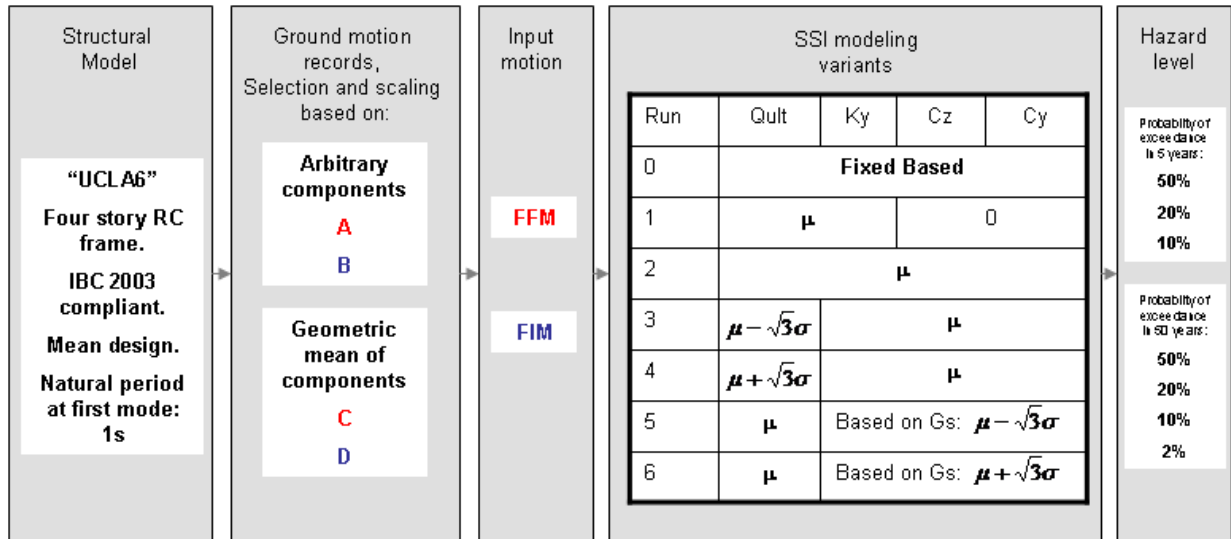


Fig. 5.26 Schematic of model variants for OpenSees simulations. Examples of run names: C0 would consider using FFM records with fixed-base building, while D2 would be FIM records applied to flexible-base system with mean valued parameters.

Table 5.5 EDPs tracked through incremental dynamic analysis (IDA).

<i>EDP</i>	Location
Peak Beam Plastic Rotation	Full Frame
Peak Column Plastic Rotation	Full frame
Peak Floor Acceleration	Floor 4 only
Peak Transient Drift	Floors 1, 2, 3 and 4

Through the OpenSees simulations, we have selected to track the *EDPs* listed in Table 5.5. The results were post-processed using an ensemble of MATLAB scripts. The *EDP* results were fit to a lognormal distribution for each hazard level (also called stripe), each point corresponding to the *EDP* response for a given ground motion and a given set of input parameters (soil properties). We then computed the sample mean and standard deviation of each *EDP* for each stripe. We also computed a 95% confidence interval (*CI*) for the sample mean using the following equation for each stripe:

$$CI = \exp \left[\log(\bar{x}) \pm t_{n-1,0.95} \frac{\log(\hat{S})}{\sqrt{n}} \right]$$

Where n is the sample size, \bar{x} is the sample (stripe) mean, \hat{S} is the sample standard deviation, $t_{n-1,0.95}$ is the two-tailed t distribution at significance level 95% with $n-1$ degrees of freedom. Although this definition of the confidence interval for a lognormal distribution is simplistic and could create a bias (Olsson 2005), it was compared to other approaches also presented in Olsson (such as the modified Cox method) and there was no appreciable difference in the results. The mean results with the corresponding 95% confidence intervals are presented on incremental dynamic analysis (IDA) plots (linear axis scales) in the following section.

5.8.4 Summary of Results from OpenSees Simulations

We have observed that for the current benchmark structure, the effects of SFSI on $EDPs$ are minimal. We expected these results given the structural design of the benchmark building and its long first-mode period (1 sec). This will be discussed in Section 5.8.5. Nevertheless, we have selected the following representative figures to illustrate our observations.

5.8.4.1 Fixed and Flexible Cases with and without Viscous Damping (Runs C0, C1, and C2)

Figure 5.27 shows the IDA EDP response plots for the fixed-based model (C0: solid black line) and two variants of the flexible base with spring parameters defined by mean soil properties. For the first flexible base model, no viscous damping was specified (C1: red dashed line) while the second model included damping based on the mean soil properties (C2: blue dashed line). None of the plots presented in Figure 5.27 shows a statistically significant difference between the three cases. Slight differences of the computed sample means are observed, mostly on the roof acceleration plot (Fig. 5.27g), but the mean lines are all constrained by the 95% confidence interval. We were expecting to observe a reduction of the mean $EDPs$ for the flexible case with damping, but the results are not conclusive.

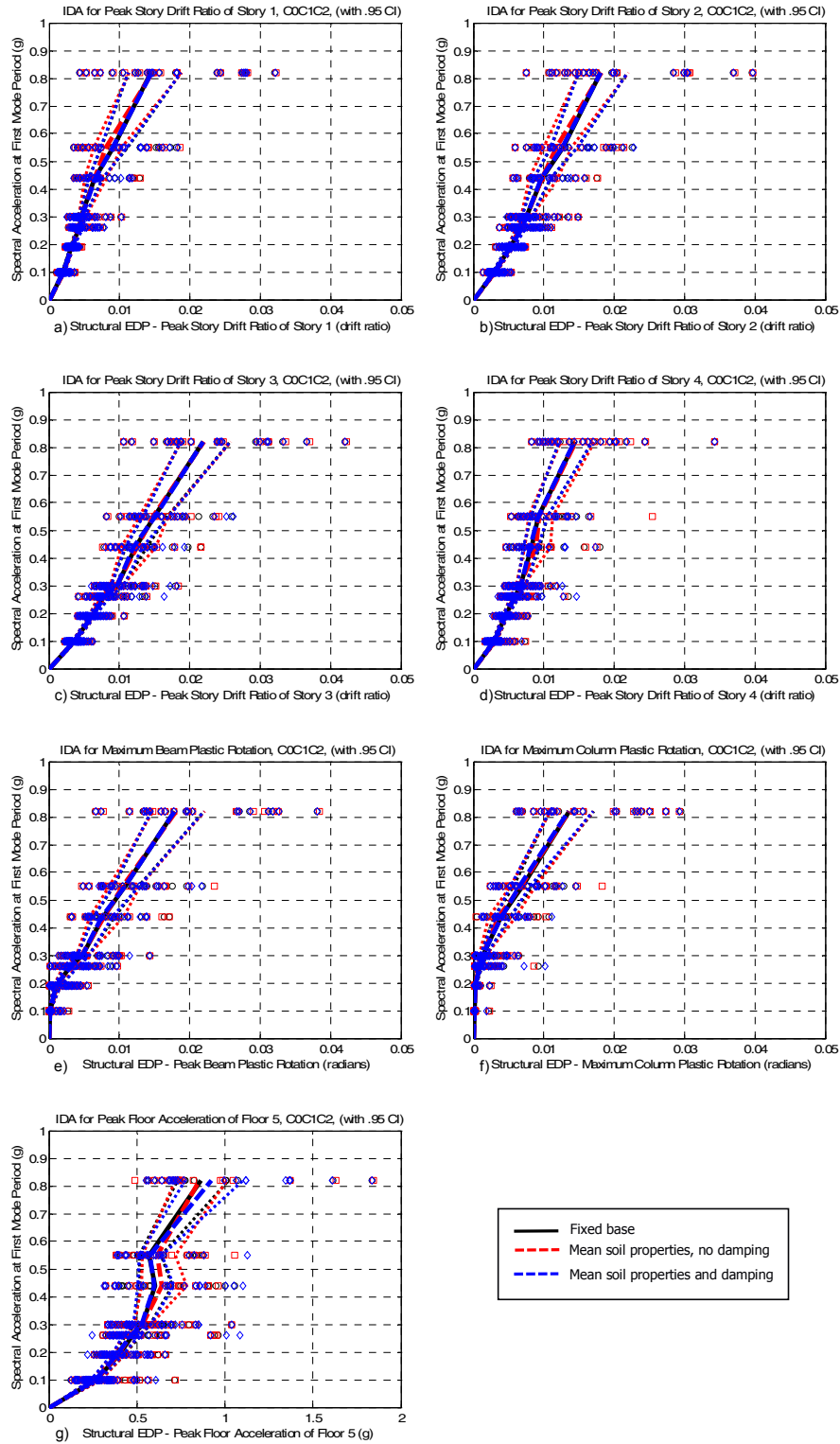


Fig. 5.27 IDA plots comparing EDP response for fixed-base and flexible models.

5.8.4.2 Flexible Cases with Varying Soil Strength Properties (Runs D2, D3, and D4)

This section compares the results for three set of runs, D2, D3, and D4 as presented in Figures 5.26 and 5.28. For these, only the strength parameter is varied from \bar{x} to $\bar{x} \pm \sqrt{3}\hat{S}$ while all the other parameter values remain constant at their mean value. The IDA results for all *EDPs* are similar to those presented above except for the roof acceleration, which is shown in Figure 5.28. For all other *EDPs*, the mean values and confidence interval limits almost perfectly overlap and are not presented here. In the cases presented in Figure 5.28, only one comparison is statistically different—for some stripes and only marginally—at the 95% level. The mean *EDP* response for the $\bar{x} - \sqrt{3}\hat{S}$ soil properties is outside the confidence interval for the $\bar{x} + \sqrt{3}\hat{S}$ soil properties. The trend observed is consistent with expected patterns of behavior—as the shear strength of the soil decreases, the *EDP* response increases and vice-versa.

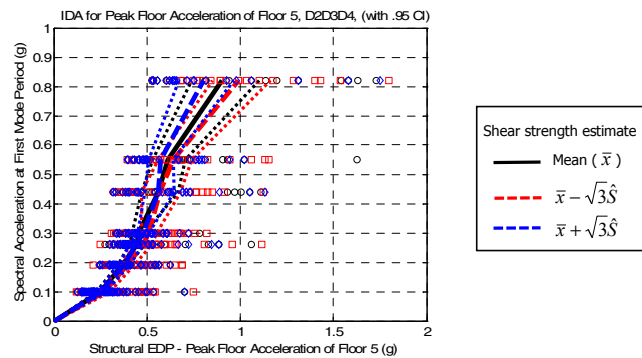


Fig. 5.28 IDA plots comparing maximum roof (floor 5) acceleration for 3 estimates of soil strength properties ϕ . Run D2: \bar{x} or mean soil strength (black), run D3: $\bar{x} - \sqrt{3}\hat{S}$ (red) and run D4: $\bar{x} + \sqrt{3}\hat{S}$ (blue). All analyses performed for FIM.

5.8.4.3 Flexible Cases with Varying Shear Modulus Properties (Runs D2, D5, and D6)

This section compares the results for another set of three runs, D2, D5, and D6 as presented in Figures 5.26 and 5.29. For these, the strength parameter is kept constant at its mean value while G (shear modulus) is varied from \bar{x} to $\bar{x} \pm \sqrt{3}\hat{S}$. The general observations are the same as for the above case. Only the maximum roof acceleration *EDP* is affected by the changes in the soil shear modulus G . The *EDP* response increases when the horizontal stiffness and damping are reduced (Fig. 5.29). It can further be observed that the effect of G does not seem to be as important as the effect of shear strength.

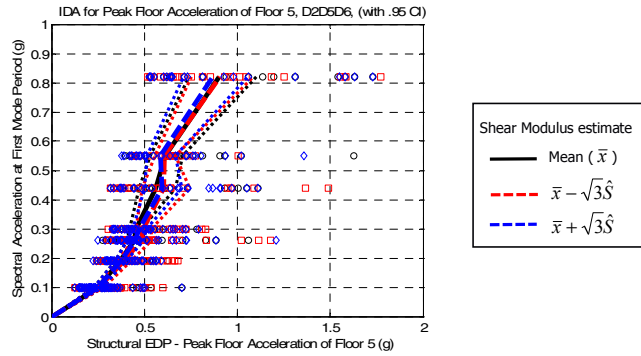


Fig. 5.29 IDA plots comparing maximum roof (floor 5) acceleration for 3 estimates of soil shear modulus G_s . Run D2: \bar{x} or mean G_s (black), run D3: $\bar{x} - \sqrt{3}\hat{S}$ (red) and run D4: $\bar{x} + \sqrt{3}\hat{S}$ (blue). All analyses performed for FIM.

5.8.4.4 Effect of Free-Field and Foundation Input Motions (Runs C0 and D0)

We have also isolated the impact of kinematic interaction by running the fixed-base case with both FFM and FIM records. We have observed a slight difference (although not statistically significant) for the maximum floor acceleration only. The general trend was consistent with our expectations, showing a lower response for the FIM motions. The IDA plots are shown in Figure 5.30.

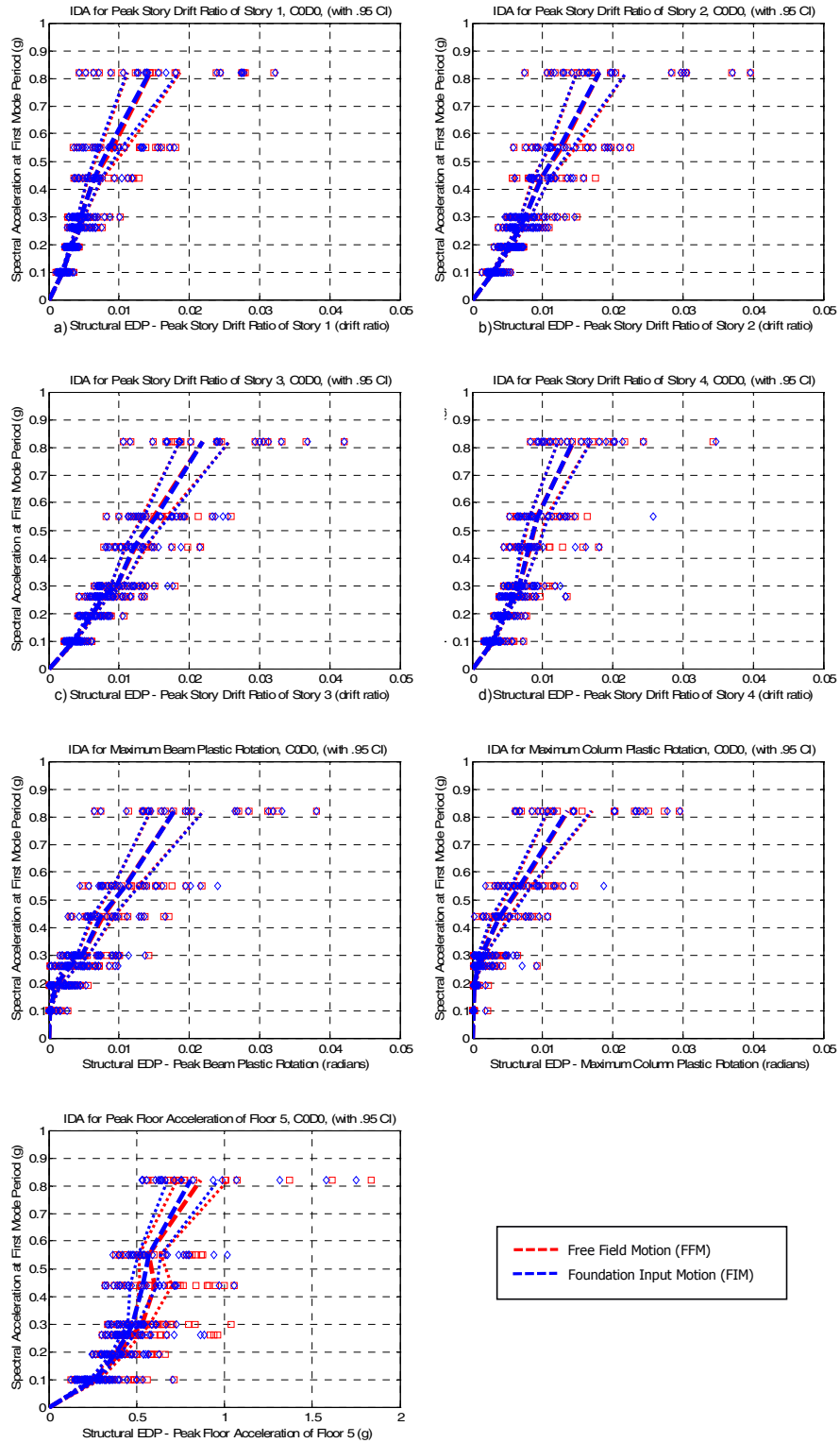


Fig. 5.30 IDA plots comparing response to FIM (blue) to FFM (red) as input motions.

5.8.4.5 Other Observations

We have also compared the *EDP* results for the records selected based on the arbitrary component parameters versus the ones selected using the parameters from the geometric mean of both horizontal components (Chapter 4). For this specific project, because we have selected a relatively large number of records for each stripe, we did not observe a statistically significant difference in the IDA plots. This result is expected to be different for studies where a limited number of records are utilized for the analysis. Although the selecting of records based on arbitrary components is not consistent with presently available attenuation relationships within PSHA codes, when a large number of records are selected, the average response tends to be similar, although the overall dispersion (sample standard deviation of the mean) might be different. When only a small number of records is selected, there is a stronger probability that a bias is introduced, especially regarding ϵ , when each record is scaled to the target S_a . Refer to Chapter 4 for considerations regarding consistency between PSHA and record selection.

5.8.5 General Interpretation and Discussion of Results

The relatively small impact of SFSI on the tracked *EDPs* can be explained by the properties of the structural system, especially by its relatively long natural first-mode period (flexibility).

First, as presented in Section 5.8.2.1, transfer functions for kinematic SFSI are acting as a high-frequency filter applied to the Fourier amplitude spectra. The transfer function computed for the benchmark building is presented in Figure 5.31. This transfer function does not significantly reduce the Fourier amplitudes near the natural frequency of the benchmark building.

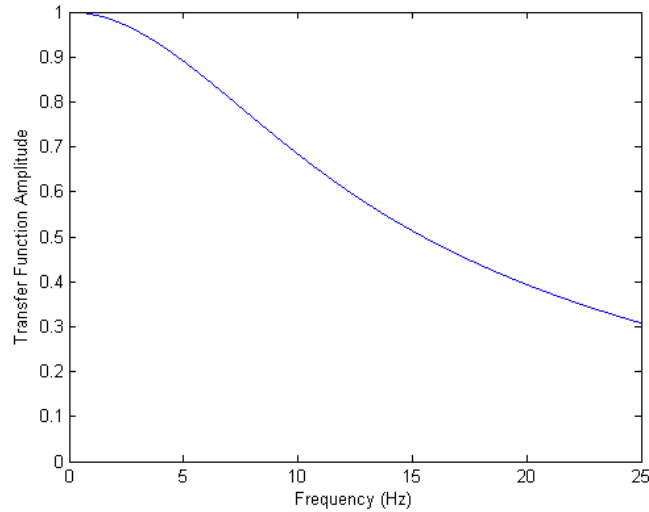


Fig. 5.31 Transfer function for kinematic SFSI computed using Kim and Stewart (2003), for mean benchmark building.

Secondly, we did not expect significant impact from inertial SFSI effects. Figure 5.32, shows the variations of \tilde{T}/T (period lengthening due to inertial SFSI) with $h/(V_s T)$ and h/r based on the analytical solution of Veletsos and Nair (1975), where h is the height of the building and r is the equivalent foundation radius. The results show that \tilde{T}/T increases with $h/(V_s T)$ and h/r . The computed value for $h/(V_s T)$ is around 0.1 for the benchmark building (h/r is 0.7), which results in an expected period lengthening of less than 10% (indicating no significant inertial interaction effect).

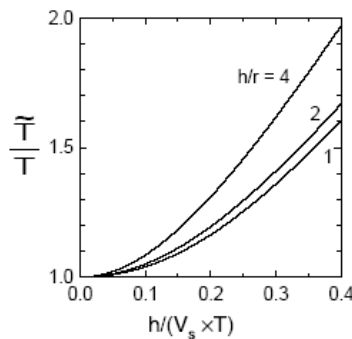


Fig. 5.32 Period-lengthening ratio for single-degree-of-freedom structure. Simplified case for rigid circular foundation on viscoelastic halfspace (Veletsos and Nair 1975).

5.9 NUMERICAL AND DAMPING CONSIDERATIONS

5.9.1 Numerical Solution Algorithm

Numerical solution convergence is particularly challenging for nonlinear degrading systems with a significant number of degrees of freedom. As part of this research, considerable time and effort was invested to develop numerical solution algorithms for static and dynamic analyses. These algorithms are a product of the work of many researchers: Frank McKenna of UC, Berkeley, created the initial algorithms, which were then modified by Paul Cordova of Stanford University, and then further modified as part of this project at Stanford University.

We designed these solution algorithms to automatically test alternative strategies before failing to converge. This is particularly important for the IDA collapse assessments, where it is important to establish that a real structural limit state is reached, rather than a premature numerical limit. Figure 5.33 summarizes the solution algorithm for a single time step of a dynamic time-history analysis. This solution algorithm uses the average acceleration option of the standard Newmark (Chopra 2001) time integration method. A key feature of the solution strategy is that at each step of the convergence algorithm, we gradually increase the convergence tolerance until convergence is obtained. The final convergence tolerance is saved in an output file for the analyst to decide if the tolerance is acceptable. In the analyses completed as part of this study, typical simulations converged within a maximum tolerance of 10^{-6} , which is considered to be acceptable. In addition, at each tolerance level, we try multiple solution algorithms if the first algorithm is unsuccessful. For each new time step of the analysis, the algorithm resets to the tightest convergence tolerance, and then the routine continually increases this tolerance until convergence is achieved. We found this to work much better than simply starting with a larger tolerance at the beginning of each step, because starting with the larger tolerance allows the solution to “converge” further away from the true solution, thus making convergence more difficult for subsequent analysis steps.

An outline of the solution algorithm for *a single time step* of a dynamic time-history analysis is as follows:

```

minimumTolerance = 1.0 * 10-7;
maximumTolerance = 1.0 * 10-1;
toleranceStepSize = 1.0 * 10-1;
currentTolerance = minimumTolerance;
while ( (currentTolerance <= maximumTolerance) AND (still non-converged) )
    currentTolerance = currentTolerance - toleranceStepSize;
    Try NewtonLineSearch to converge;
    if (still non-converged) Try Newton;
    if (still non-converged) Try ModifiedNewton;
    if (still non-converged) Try KrylovNewton;
end
if (still non-converged)
    Stop analysis and report non-convergence
else
    Save the final convergence tolerance to file (for use while post-processing)
    Convergence successful, so move to next step of analysis
end

```

Fig. 5.33 Pseudo-code for solution convergence algorithm for nonlinear dynamic analysis.

5.9.2 Other Numerical Issues

When trying to simulate structural collapse, the structural elements soften and have negative stiffness prior to collapse. This caused great difficulty and problems with singularity of the dynamic stiffness matrix. The primary solution to this problem was the robust solution algorithm presented in the last section, but this was not enough. In some cases, the analysis technically “converged” but the simulation results were unreasonable. Upon close investigation of the analysis results, we found that the dynamic stiffness matrix had become singular, but the analysis still “converged.”

We attempted many approaches to solve this problem. The best solution was to populate the mass matrix as uniformly as possible. Specifically, we divided the floor masses equally to all nodes at the floor level; each joint has four external nodes, so the mass from each floor was divided and placed equally over the 20 joint nodes. Additional nodes, such as those on the leaning column and the foundation springs, were also assigned a small amount of mass (the equivalent of one foot of beam) so those portions of the mass matrix were not empty. In addition, smaller rotation masses were also applied to every rotational degree of freedom.

To ensure that these additional masses did not adversely affect the results of the simulation, we compared results (for simulations that did not produce a singular dynamic stiffness matrix) before and after adding the masses and ensured that they were virtually identical.

5.9.3 Damping

Standard Rayleigh damping was utilized, proportional to the initial stiffness (as opposed to tangent stiffness) and mass matrices, with 6.5% of critical damping. Determination of this damping ratio is discussed in Appendix E.

5.10 NONLINEAR STATIC PUSHOVER ANALYSIS AND FUNDAMENTAL PERIOD FOR EACH DESIGN VARIANT

5.10.1 Fundamental Period

Table 5.6 presents the first-mode periods computed for each design variant using standard eigenvalue analyses in OpenSees (2006). These periods were computed after the application of gravity loads but before the application of any lateral loads; so in the fiber models most sections are uncracked. The lateral stiffness reduction due to axial loads (P-delta stiffness) is included and increases the periods slightly. The table gives three periods for the lumped-plasticity models, based on differing initial stiffness assumptions. The first value was computed from the model with the yield point secant stiffness (see Section 5.4.3) and the other two points are secant to 40% and 50% of the yield point, respectively. The majority of lumped-plasticity analyses were run using the yield point secant stiffness, which in retrospect is probably too flexible for accurate assessment of economic losses at low drift levels. For this reason, the performance for ground motions up to the 2%-in-50-years exceedance level was estimated using the fiber model. For future work, we suggest that the lumped-plasticity models with K_{str_2} (secant stiffness to 0.5 yield) would be a more appropriate choice to better model the full range of behavior.

Table 5.6 Fundamental periods for each of 8 design variants and various structural models (initial stiffness terminology defined in Fig. 5.12 of Section 5.4.3.1).

Design	Frame System	Fiber Model	Lumped Plasticity Models		
		Fundamental period with uncracked concrete (sec)	Fundamental period using element stiffness of K_{yld} (sec)	Fundamental period using element stiffness of K_{stf_1} (sec)	Fundamental period using element stiffness of K_{stf_2} (sec)
A	Perimeter	0.75	1.25	1.02	0.84
B	Perimeter	0.73	1.06	0.87	0.71
C	Perimeter	0.87	1.50	1.22	1.01
D	Perimeter	model not used	1.50	1.22	1.01
E	Space	model not used	0.78	0.64	0.53
F	Space	model not used	0.86	0.70	0.58
G	Space	model not used	0.78	0.64	0.53
H	Space	model not used	0.78	0.64	0.53

5.10.2 Static Pushover Analyses

Figure 5.34a presents the static pushover response for Design A, with and without the gravity frame, and using an inverted triangular pushover load distribution. The distributions of interstory drift, for a base shear of 1200 kips, is shown in Figure 5.34b. Figure 5.34a shows that the gravity system maintains strength up to a roof drift ratio of 2.5%, at which time the slab-column connections lose strength due to punching shear. Even after this loss in strength, the gravity columns continue to contribute lateral strength to the system until nearly 5% roof drift. Figure 5.34a shows that for this specific building, the gravity system causes final strain softening to initiate at a slightly lower roof drift (about 10% less), as compared to the model that excludes the gravity frame.

The interstory drift distribution in Figure 5.34b explains why the gravity system reduces the building displacement capacity. For the model without the gravity frame, the damage localizes in stories two and three. On the other hand, when the gravity frame is included in the model, the damage tends to localize in the first story. The columns in these lower stories have smaller plastic-rotation capacities, due to higher levels of axial load, and hence the building deformation capacity is reduced.

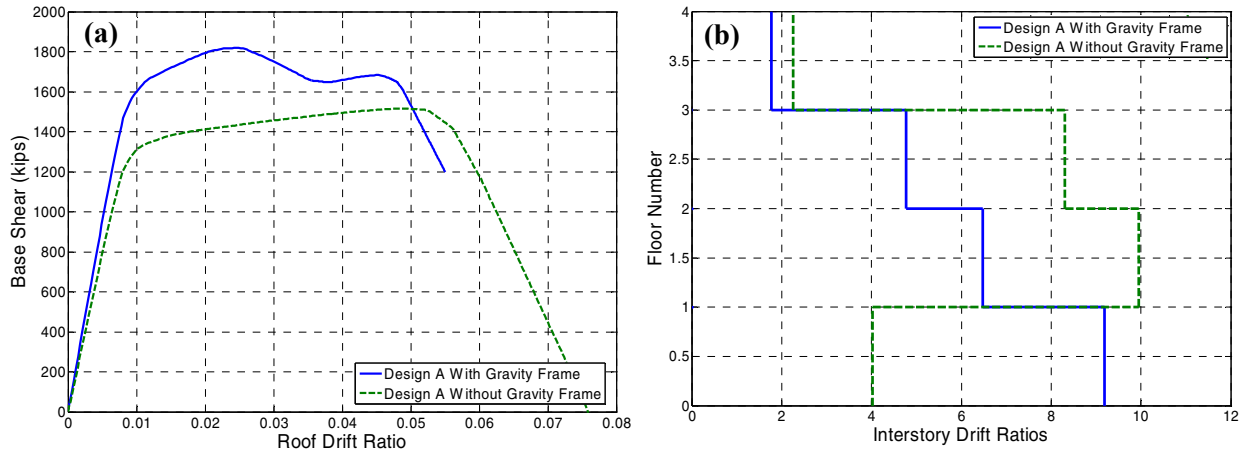


Fig. 5.34 (a) Static pushover curves, using an inverted triangular load pattern, for Design A with and without including gravity frame in structural model; (b) story drift profiles for each model at point building has degraded to 1200 kips base shear.

In some cases, the gravity system instead increases the building deformation capacity. Figure 5.35 shows the static pushover curves and drift distributions for Design D. This is the design that violates the strong-column weak-beam provision and could be considered as more representative of a non-conforming building. As shown in Figure 5.35b, in this design the deformations tend to concentrate in the first story. Here the gravity frame increases the building displacement capacity by about 30% by helping to strengthen the first story and distribute the damage into the second and third stories.

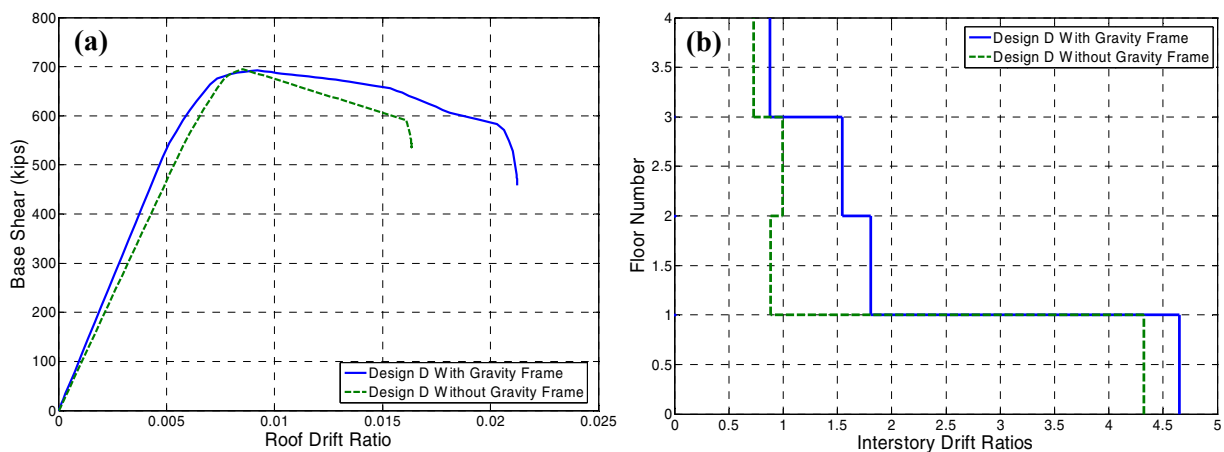


Fig. 5.35 (a) Static pushover curves, using an inverted triangular load pattern, for Design D with and without including gravity frame in structural model; (b) story drift profiles for each model at end of pushover shown in part (a).

Figure 5.36 compares the pushover curves for the fiber-spring model and the lumped-plasticity model of Design A, where the lumped-plasticity model is run with the yield point and 40% of yield point secant stiffnesses. This figure illustrates a few important differences in the model predictions:

- When comparing the fiber-spring model and the lumped-plasticity model with secant stiffness K_{stf_2} (40% of yield, per Fig. 5.12), the initial stiffness agrees well but the drift at yield is underestimated by about 20%.
- When comparing the fiber-spring model and the lumped-plasticity model with secant stiffness K_{yld} (at yield, per Fig. 5.12), the initial stiffness is underestimated, but the drift at yield agrees fairly well.
- The fiber-spring is less numerically stable and stops converging at a roof drift of just over 3%. Note that the negative slope seen in the fiber-spring model results, just before non-convergence, comes primarily from softening in the lumped plastic hinges of the gravity-frame slab system and not from the fiber elements. Note that these numerical problems are much less prevalent for dynamic analyses.
- The fiber-spring model can not capture the severe strain softening, usually caused by rebar buckling, which is simulated by the lumped-plasticity model. In this case, the severe strain softening begins at a roof drift ratio of about 0.045.

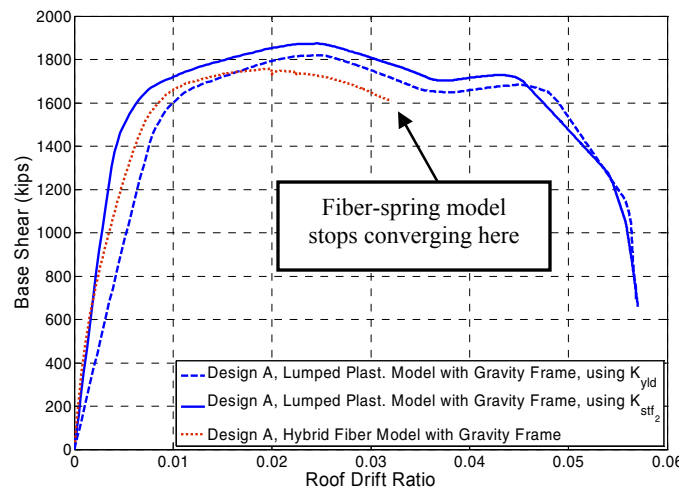


Fig. 5.36 Static pushover curves for both lumped-plasticity and fiber-spring models (using inverted triangular load pattern, for Design A including gravity frame in structural model).

The pushover responses of the four perimeter-frame design are compared in Figure 5.37. These pushover curves are for the lumped-plasticity model, including the gravity frame, and represent one four-bay frame of the building, which was designed for a base shear of 635 kips. Designs A, B, and C have overstrength factors of 2.7, 3.1, and 1.9, respectively. Design D, which is not code-conforming, has an overstrength factor of 1.1. These relative overstrength factors agree with what is expected based on the design assumptions (Section 3.3.6.1). The deformation capacity of frame B is smaller than the other code-conforming frames because the constant story strengths over the height cause the deformations to concentrate in fewer stories. The behavior of Design D is notably different and fails at much smaller displacements, because this design does not comply with the strong-column weak-beam provision (ACI 318-02, Section 21.4.2.2).

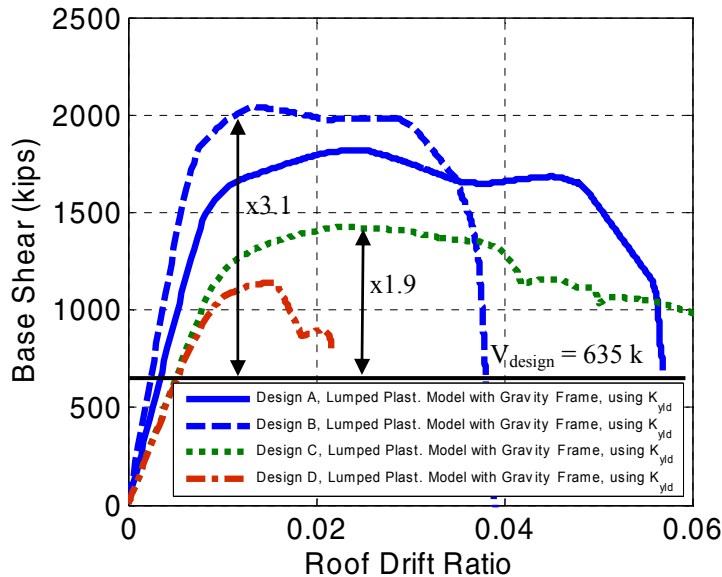


Fig. 5.37 Static pushover curves, using an inverted triangular load pattern and including P-delta effects. Curves are for perimeter-frame Designs A, C, and D, without including gravity frame in structural model.

The pushover curves for the space-frame designs (E–H) are compared in Figure 5.38. Most notable in this figure is that the overstrength factors for the space-frame buildings (ranging from 3.6 to 5.6) are almost double the counterpart values for the perimeter-frame buildings. This occurs primarily because of the larger overstrength in the beams due to gravity load effects. The space-frame plots in Figure 5.38 also exhibit a steeper negative post-yield stiffness, as compared to the perimeter-frame buildings. Both the perimeter and space-frame pushover results include

the additional negative stiffness from P-delta effects, but the beams of the space frames tend to have lower post-yield stiffness (average of $0.01K_e$) as compared to the perimeter frames (average of $0.04K_e$). As a result, the combined effects of strain softening and P-delta effects are more severe for the space-frame buildings. Consequently, the space-frame buildings tend to have lower drift capacities than the perimeter-frame buildings.

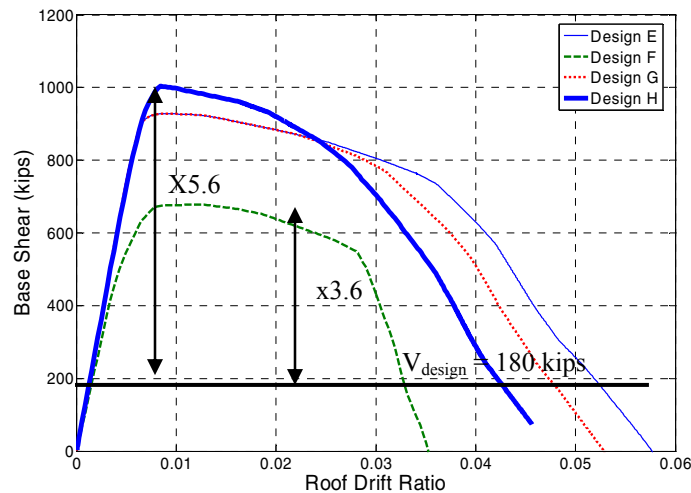


Fig. 5.38 Static pushover curves, using inverted triangular load pattern and including P-delta effects. Curves are for space-frame designs E, F, G, and H.

Comparing Designs E and F, we see a drastic strength difference and a slight difference in displacement capacity. This comes from the fact that Design E has stronger beams, since the slab steel was ignored in calculating the beam design strengths, whereas in Design F the slab steel is considered in the beam strength design (Section 3.3.6). Both designs equally meet the ACI 318-02 requirement that the slab steel be considered in proportioning the column to meet the strong-column weak-beam provision (ACI 2002, Section 21.4.2.2). Independent of how the slab steel was considered in the structural design, the slab steel is always included in the structural model (Section 5.3.3).

Comparing Designs E and G, we see that Design G has slightly lower strength at high levels of displacement. Design E was designed according to the 2003 IBC (ICC 2003); Design G was similarly designed except it used the strong-column weak-beam requirement from the 1997 UBC (Section 3.3.6). This design change made the columns weaker for Design G, so the difference in the pushover curves starts at the point that the columns begin to yield.

Comparing Designs G and H, we see that Design H has slightly higher strength but lower displacement capacity. This occurs because Design H has more slab steel than Design G (Section 3.3.6). This additional slab steel increases the beam strength and forces the plastic hinges into the columns at a lower displacement, thus reducing the displacement capacity.

The degree to which these differences are apparent in the pushover analyses affect the final loss, and collapse performance is investigated through the nonlinear time-history analyses, described next.

5.11 PREDICTION OF STRUCTURAL RESPONSES BEFORE COLLAPSE

5.11.1 Methodology

Nonlinear dynamic analyses were run for each of the buildings at eight different ground motion intensity levels. As described in Chapter 4, distinct sets of ground motions were selected for seven of these intensity levels to account for the differences in the expected ground motion properties at the various hazard levels. At each ground motion intensity, each pair of horizontal ground motions is scaled such that the geometric mean spectral acceleration (geometric mean S_a is the square-root of the product of the S_a values of the two horizontal components) matches the target intensity level. Between 10–30 ground motion pairs are utilized for each level of ground motion (depending on the number of motions available with the correct properties). For more details on the selection and scaling of the ground motions, see Chapter 4.

The following sections present the structural response predictions for Design A using a fiber-spring model. These same response predictions were completed for all design variants (using the fiber-spring and/or lumped-plasticity models) and each set of response predictions are used to complete damage and loss analyses (Chapter 6). For brevity, this section only presents the structural response predictions for Design A. The results are first shown for the fiber-spring model and then contrasted with the lumped-plasticity model. The collapse predictions are reported later in Sections 5.12 to 5.14.

5.11.2 Interstory Drift Predictions

The simulated roof drift ratios of Design A for eight ground motion intensities are shown in Figure 5.39. These are calculated using the fiber-spring model, including the gravity frame. The small dots represent the response predictions for a single ground motion component at a single S_a level, the solid line represents the median response, and the dashed lines represent the mean \pm one standard deviation (assuming a lognormal distribution). The median roof drift ratios are 1.0% and 1.4% for the 10%- and 2%-in-50-years ground motion levels, respectively, with dispersions on the order of $\sigma_{LN} = 0.27$ and $\sigma_{LN} = 0.31$, respectively. The corresponding story drift ratios are shown in Figure 5.40, where the largest drifts occur in the third story—with median values of 1.2% and 1.8%, and dispersions of $\sigma_{LN} = 0.29$ and $\sigma_{LN} = 0.35$, for the 10%- and 2%-in-50-years ground motion levels, respectively. Overall, the median response tends to exceed the design expectations, as compared to the inelastic story drift limit of 2% at the 10%-in-50-years ground motion level and maintaining fairly linear response up to 1.5 times the 2%-in-20-years ground motion hazard.

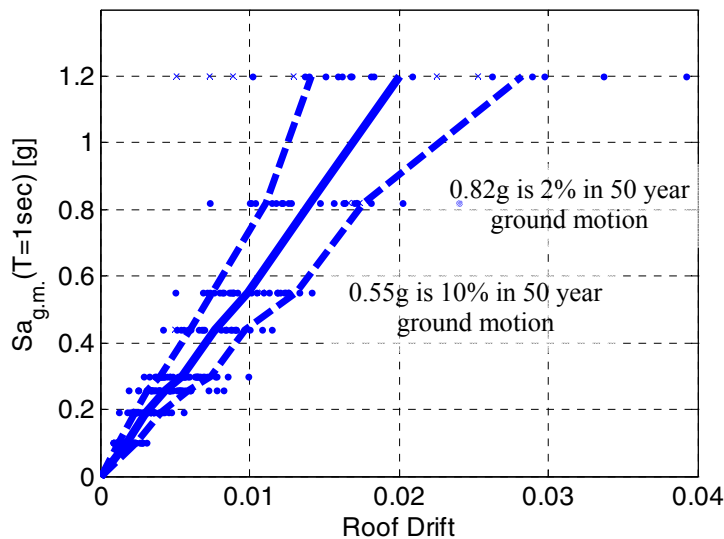


Fig. 5.39 Nonlinear dynamic analysis predictions of roof drift ratio for Design A; fiber-spring model with seven ground motion sets selected specifically for each of eight intensity levels.

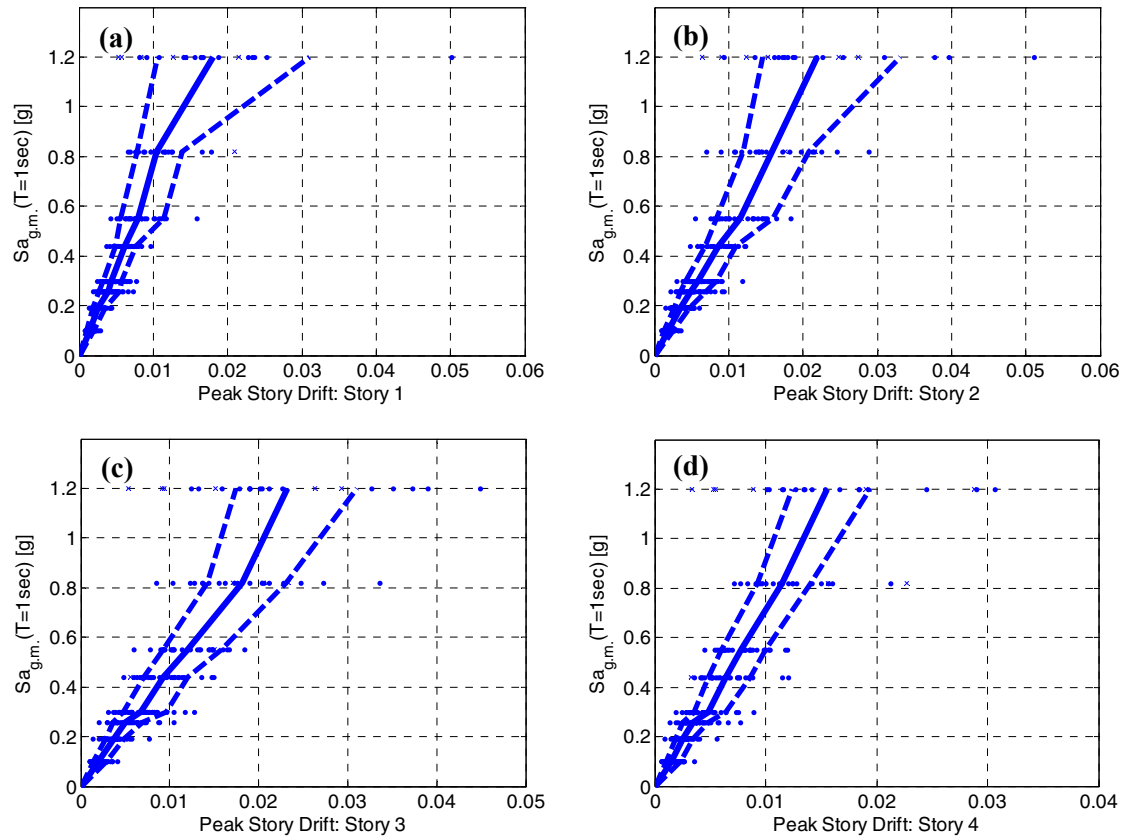


Fig. 5.40 Nonlinear dynamic analysis predictions of interstory drift ratios (stories 1–4) for Design A; fiber-spring model with seven ground motion sets selected specifically for each of eight intensity levels.

5.11.3 Residual Drift Predictions

Residual drifts are an important consideration for loss analysis (building repair), post-earthquake safety and building closure. Figure 5.41 shows the residual interstory drifts calculated using the fiber-spring model. The residual drifts are largest in the third story, with a median residual drift ratio of about 0.0015 for the 2%-in-50-years motion. This location of maximum residual drift is consistent with the location of the maximum transient drift ratio. Comparing Figure 5.41 to 5.40 also indicates that the dispersion of residual drifts ($\sigma_{LN} = 1.7$ and $\sigma_{LN} = 1.4$ for the third story and the 10%- and 2%-in-50-years motions, respectively) is much larger than the dispersion in peak drifts, which is consistent with previous studies of residual drifts (Ruiz-Garcia 2005). However, the residual drift ratios shown in Figure 5.41 should be interpreted with caution, since previous research has shown fiber-type models to underpredict residual displacements (Hachen et al.

2003; Lee 2007). Later, in Figure 5.47, we will compare residual deformation predictions between the fiber-spring and lumped-plasticity models and show that the predictions are quite variable, with the fiber-spring model predicting much lower residual displacements.

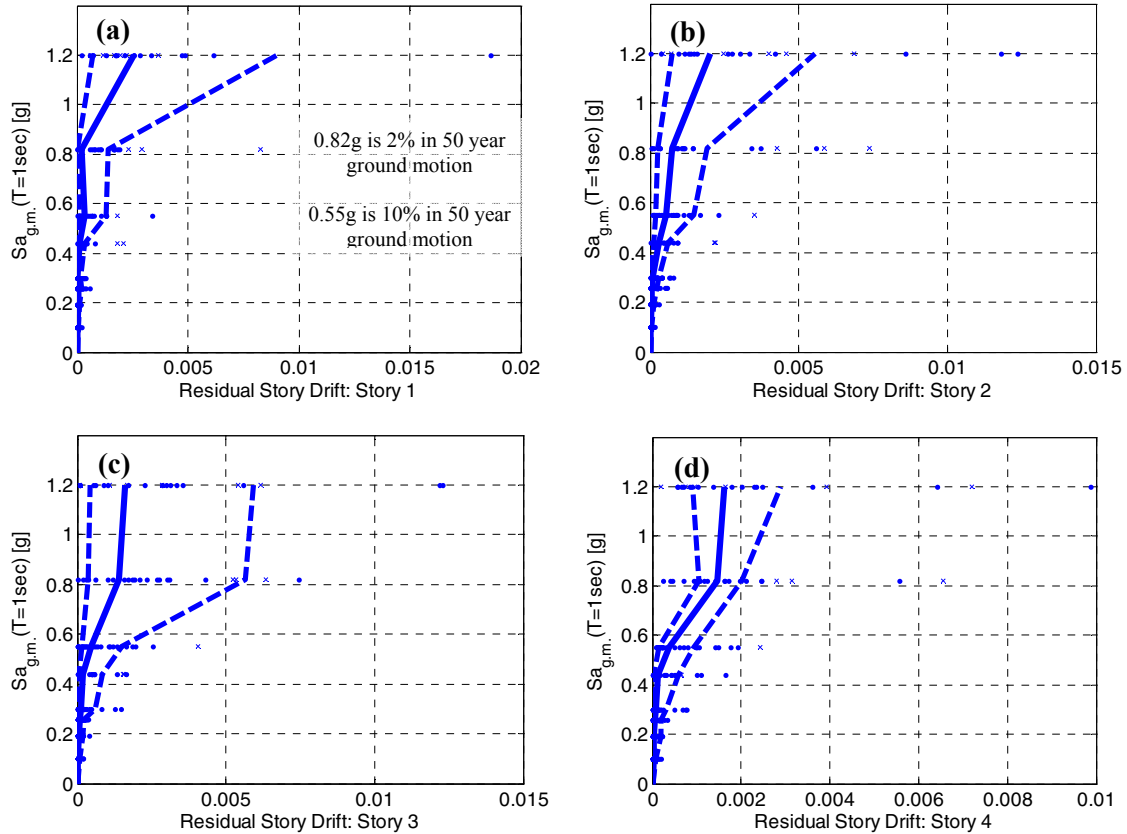


Fig. 5.41 Nonlinear dynamic analysis predictions of residual interstory drift ratios (stories 1–4) for Design A; fiber-spring model with seven ground motion sets selected specifically for each of eight intensity levels.

5.11.4 Peak Floor Acceleration Predictions

Figure 5.42 shows the peak absolute floor accelerations for each of the four elevated floors of the building. This shows that the median floor accelerations are approximately 0.5g–0.7g for the 10%-in-50-years event and 0.7g–0.9g for the 2%-in-50-years event. This dispersion of peak roof acceleration is $\sigma_{LN} = 0.27$ and $\sigma_{LN} = 0.38$, respectively, for the 10%- and 2%-in-50-years ground motions. This figure also shows that for high levels of ground motion (where the building response is strongly nonlinear) the dispersion is larger lower in the building where the nonlinear

behavior of the structure has less effect on filtering the ground motions. These peak floor acceleration demands are used in Chapter 6 for damage and loss analyses of building contents.

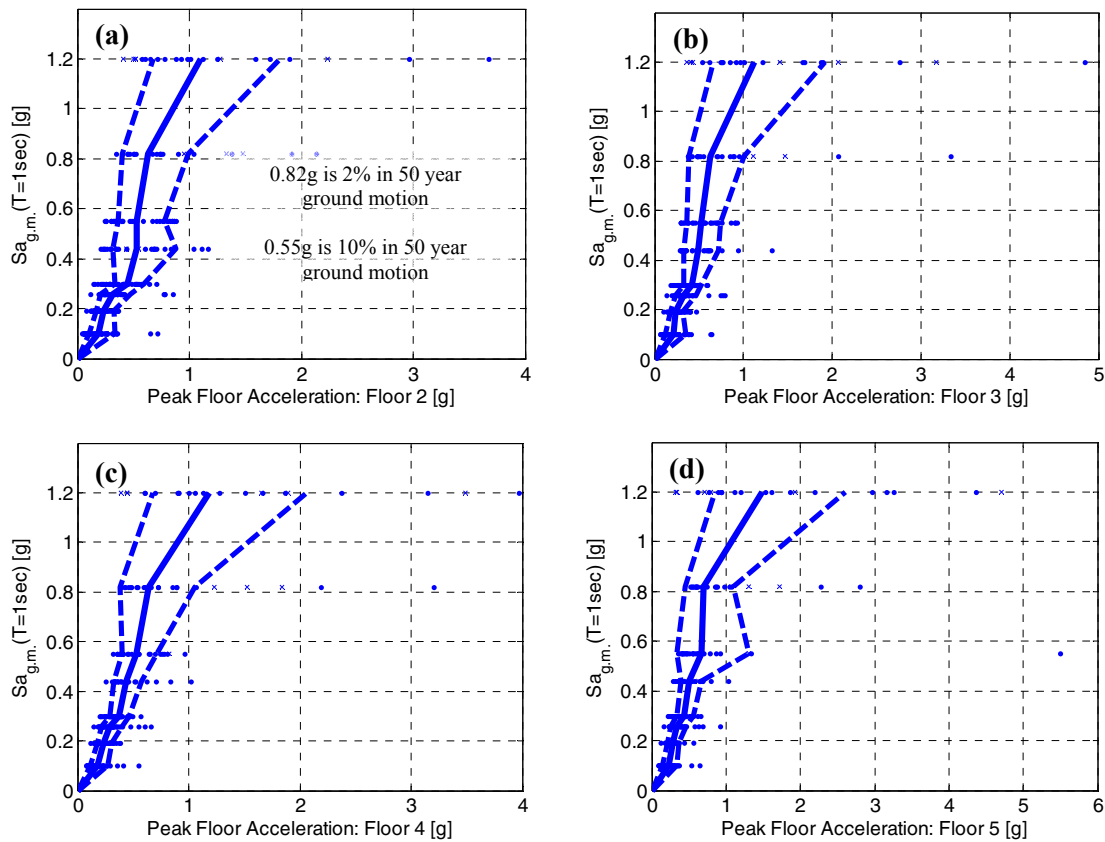


Fig. 5.42 Nonlinear dynamic analysis predictions of peak absolute floor accelerations (floors 2-roof) for Design A; fiber-spring model with seven ground motion sets selected specifically for each of eight intensity levels.

5.11.5 Element Plastic-Rotation Predictions

Figure 5.43 shows the column and beam plastic-rotation demands. These show the plastic rotations predicted using the fiber-element model, though the plastic-rotation predictions are also similar when using the plastic-hinge model (Section 5.11.7). When using the fiber-element model, the plastic-rotation demands are computed using the standard method included in the fiber beam-column element model (OpenSees 2006).

For the purposes of damage and loss analyses, the plastic-rotation demands are computed and reported for each element in the frame. For purposes of illustration, Figure 5.43 shows the plastic-rotation demand that is largest for any beam and for any column in the frame. The

median peak plastic-rotation demand for columns is 0.007 and 0.014 radians for the 10%- and 2%-in-50-years ground motion levels, respectively; and median values for the beams are: 0.011 and 0.019 radians. These values are below the demand levels of 0.03 radians that is sometimes associated with the 2%-in-50-years earthquake hazard. These data also show that while the strong-column weak-beam design provisions (ACI 2005, Section 21.4.2.2) limit hinging in the columns, they do not prevent column hinging. Also, one may expect the majority of column hinging at the foundation level; this is generally not the case with this building, and more column hinging occurs in the third story. Even though the third story tends to have most damage, the location of the maximum plastic-rotation demand depends heavily on the ground motion record, with many of the records causing higher plastic rotations in other floors.

Finally, the data in Figure 5.43 reveal a relatively large dispersion in the plastic-rotation demands, being approximately $\sigma_{LN} = 0.7$ for columns and a lower value for beams, showing that some records cause little damage in the 2%-in-50-years ground motion, and a few records cause relatively large plastic-rotation demands.

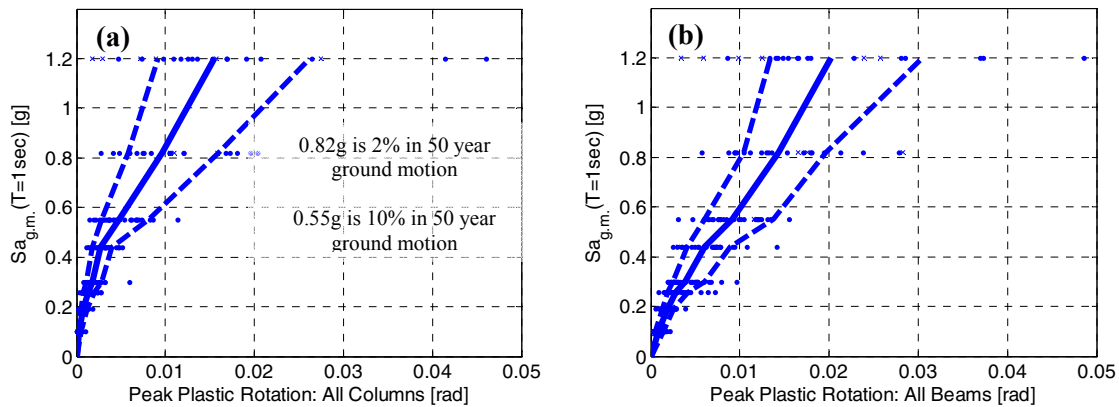


Fig. 5.43 Nonlinear dynamic analysis predictions of maximum column and beam plastic-rotation demands for Design A (fiber-spring model with eight ground motion sets selected specifically for each intensity level). Reported plastic-rotation demand is peak demand for any column or any beam in frame; element with maximum demand differs with ground motion input.

5.11.6 Damage Patterns for 2%-in-50-Years Ground Motion

Figure 5.44 illustrates damage patterns for six of the 20 ground motion components used for the 2%-in-50-years ground motion level. In contrast to the previous results, these results are based on the lumped-plasticity model. Data for all 20 ground motion components indicated that no

elements experience strain softening during the 2%-in-50-years event, which is consistent with the magnitude of maximum hinge rotations reported in Figure 5.43. This figure also shows that the damage patterns vary depending on the input ground motion. Most ground motions cause both beam and column hinging, while some (e.g., Fig. 5.44b) show small amounts of beam hinging and no column hinging, and others (e.g., Fig. 5.44e) show damage only in the upper stories.

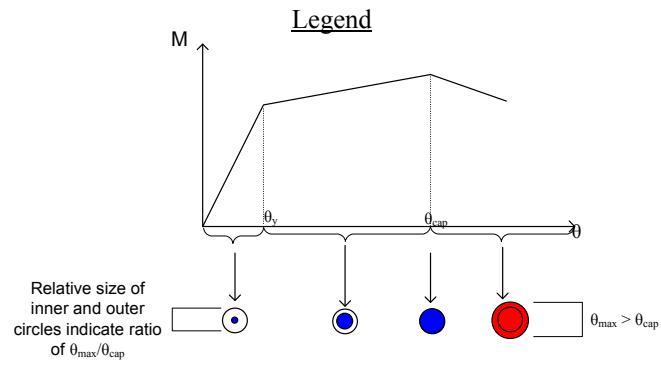
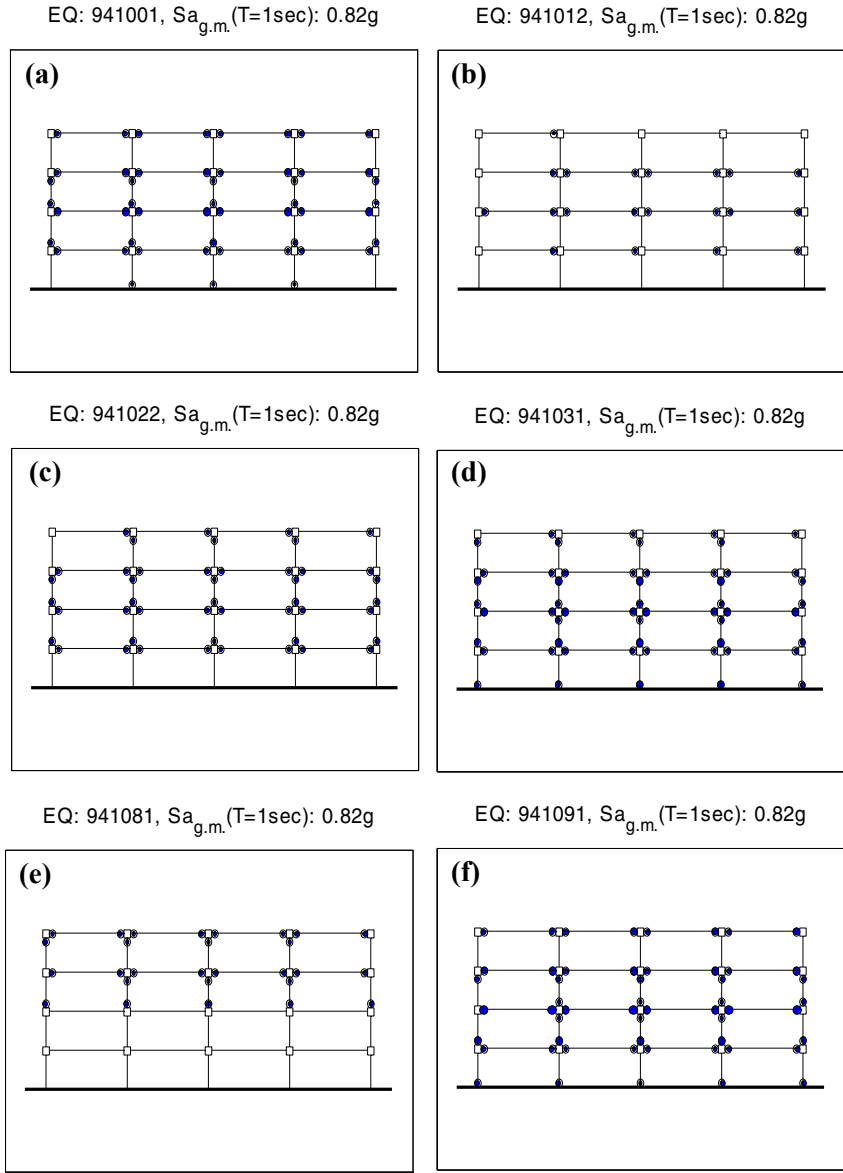


Fig. 5.44 Damage patterns for Design A subjected to 2%-in-50-yrs ground motion. Response predictions completed using lumped-plasticity model (legend by A.B. Liel of Stanford University).

5.11.7 Comparison of Response Predictions Using Fiber-Spring and Lumped-Plasticity Models

The fiber-spring and lumped-plasticity models have several differences that may result in differing response predictions. To investigate the difference in response prediction obtained from the two models, Figure 5.45 compares the mean roof drift responses predicted for Design A using the fiber-spring and two lumped-plasticity models with secant stiffnesses based on yield and 40% of yield. This shows that the lumped-plasticity model can predict roof drifts consistent with the fiber-spring model, if the effective initial stiffness is assumed to be fairly stiff (K_{stf_2} , based on 40% of yield). When the lumped-plasticity model is used with an initial stiffness that is secant through the yield point (K_{yld}), the drift demands are consistently about 20–25% larger than the fiber-spring results. These differences arise because the lumped-plasticity model is linear before yielding, while the fiber-element model accounts for the increased initial stiffness from the tension-stiffening effect (Section 5.3.3.1), as well as the nonlinearity in the bond-slip component of deformation (Section 5.5.2.4).

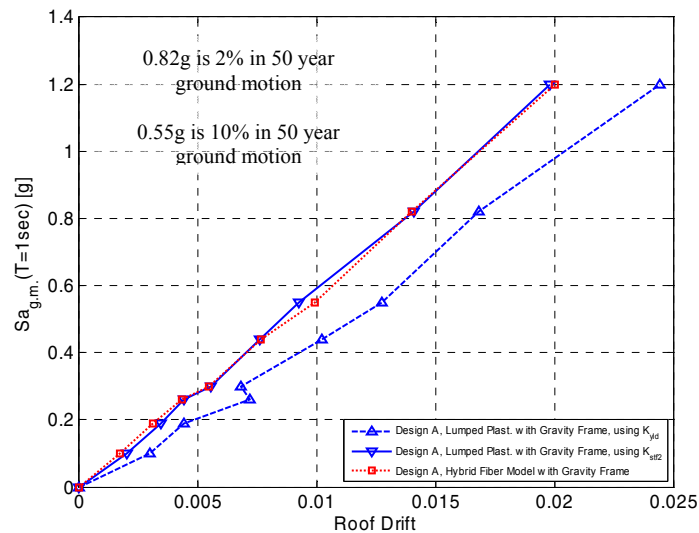


Fig. 5.45 Comparison of peak roof drift demand predictions using fiber-spring and lumped-plasticity models for Design A.

Figure 5.46 presents a comparison of the peak interstory drift ratios for each of the four stories. This shows similar trends as in Figure 5.45, but makes it clear that interstory drifts, as compared to roof drifts, are more variable and are affected more by subtleties of the structural model.

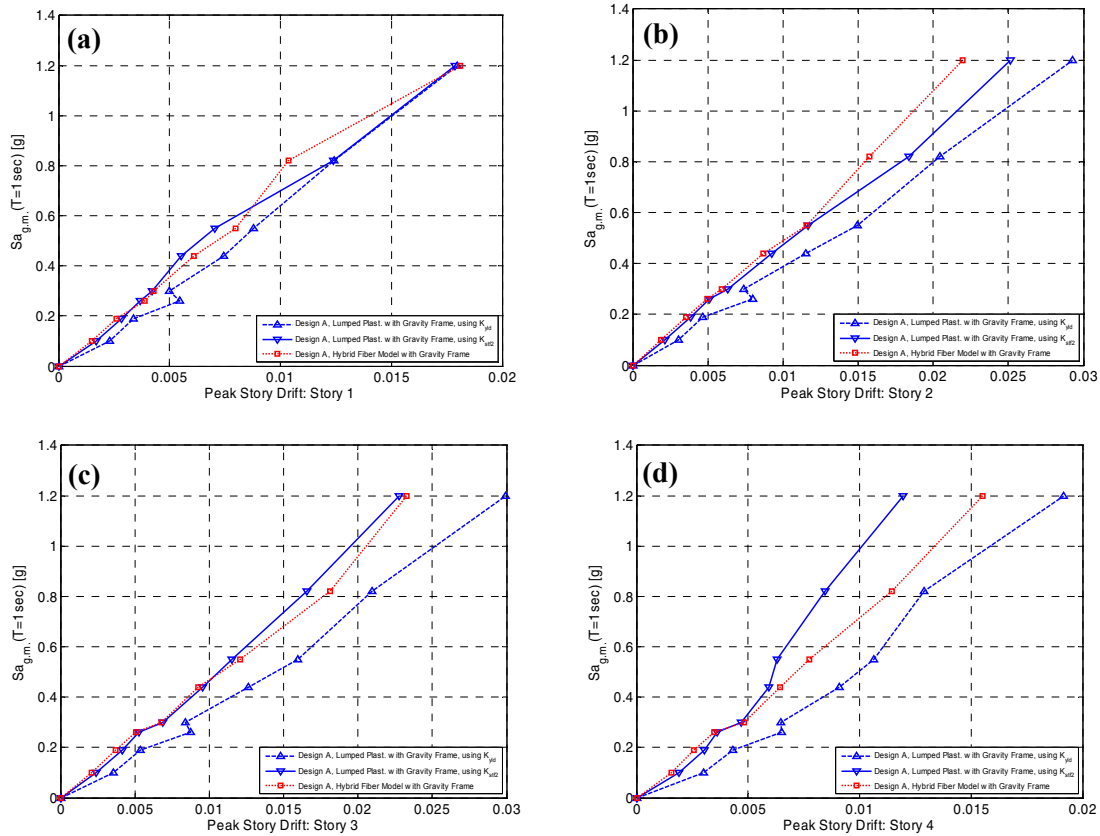


Fig. 5.46 Comparison of peak interstory drift demand predictions using fiber-spring and lumped-plasticity models for Design A.

Figure 5.47 compares the residual drifts predicted by each model. This shows that the fiber model tends to predict lower residual drifts in most stories. When normalized by the peak interstory drift, for $S_a = 0.55g$ (10%-in-50-years motion) the residual drift is only about 2–3% of the peak interstory drift. At $S_a = 1.2g$ (1.5x the 2%-in-50-years motion) level, this ratio increases to between 6–17% for all models and all stories. Overall, the residual drift ratios are quite small, e.g., at the 2%-in-50-years motion, the maximum median residual drift ratio is smaller than 0.2%, which is probably about the threshold at which the residual drift becomes a serviceability issue.

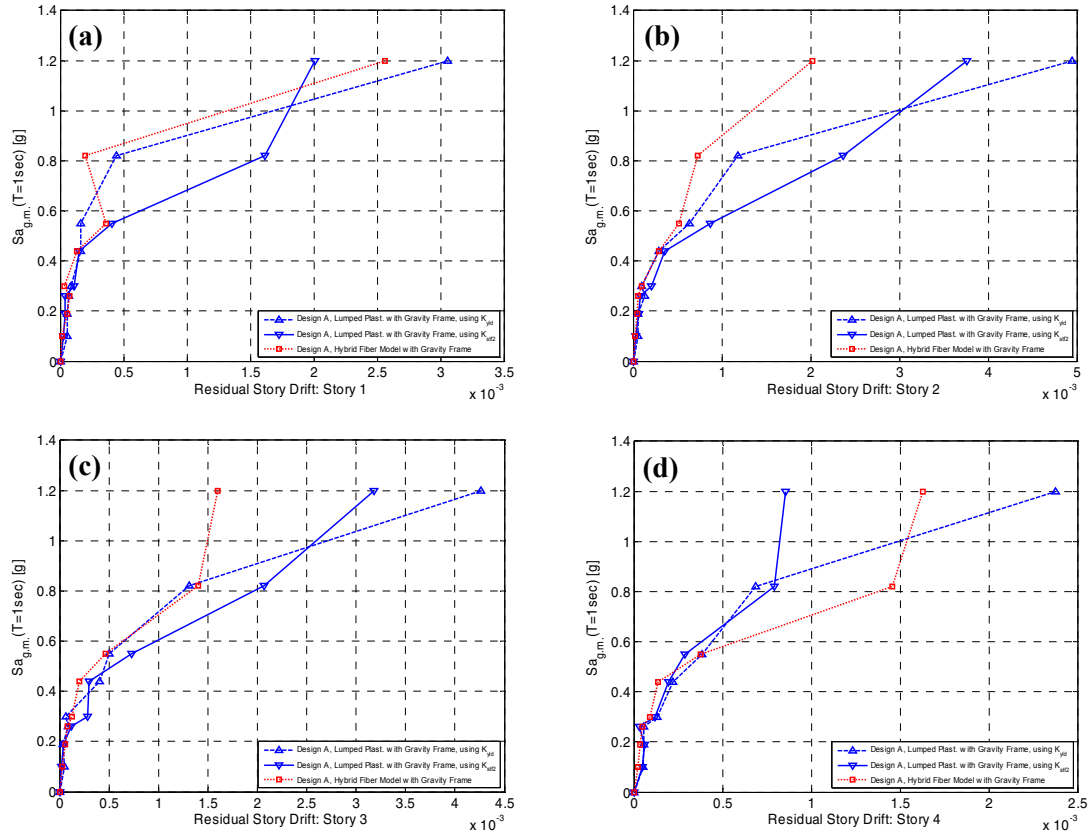


Fig. 5.47 Comparison of residual interstory drift demand predictions using fiber-spring and lumped-plasticity models for Design A.

Figure 5.48 compares the peak floor accelerations predicted using each of the three models. The predictions are surprisingly consistent. One exception is that the fiber-spring model predicts higher floor accelerations at the higher levels of ground motion, with the differences being most pronounced in the upper floors of the building. This is perhaps due to the fact that the fiber-spring model does not soften as quickly as the lumped-plasticity models.

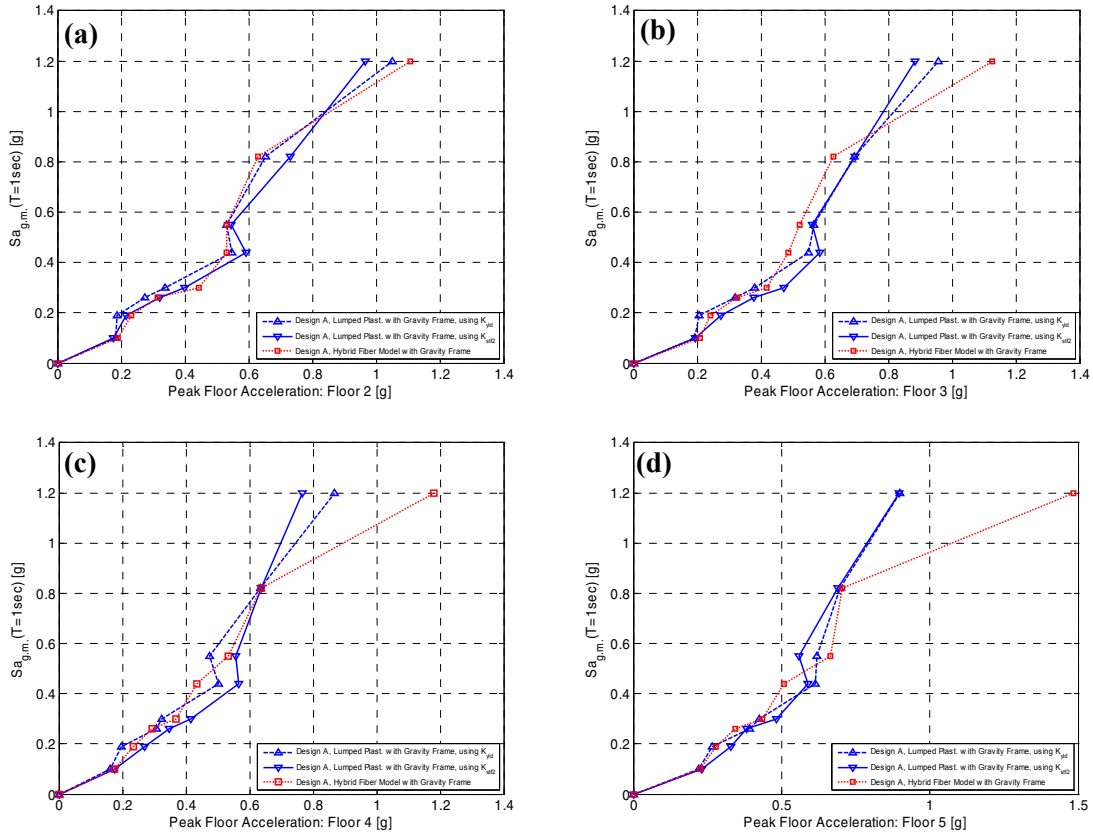


Fig. 5.48 Comparison of peak floor acceleration demand predictions using fiber-spring and lumped-plasticity models for Design A.

Figure 5.49 shows a similar comparison for maximum beam and column plastic-rotation demand. This shows that the peak plastic-rotation demand predictions agree fairly well and are even more consistent than the story drift demand ratios.

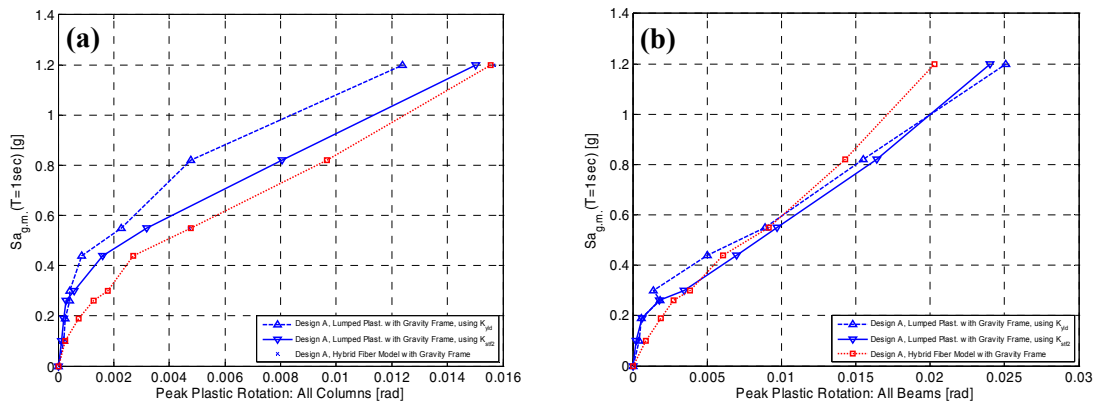


Fig. 5.49 Comparison of plastic-rotation demand predictions using fiber-spring and lumped-plasticity models for Design A; for (a) columns and (b) beams.

5.12 COLLAPSE CAPACITY PREDICTION

5.12.1 Collapse Methodology and Three-Dimensional Considerations

To quantify the collapse capacity of the RC frame structures used in this study, we employ the incremental dynamic analysis (IDA) procedure (Vamvatsikos 2002). The IDA procedure consists of running multiple nonlinear time-history analyses (NLTH) for the same ground motion record scaled to different intensity levels. Since collapse occurs above the 2%-in-50-years hazard level, ground motions from that bin (the largest intensity available) are used for the IDA procedure. The collapse point is defined as the point of dynamic instability (*not* numerical non-convergence) when any further increase in the intensity of the record causes the drifts to increase without bound. We observed that dynamic instability always occurred at interstory drifts less than 12% (which coincides with the roof drift at zero base shear strength of approximately 6%; see Fig. 5.37). Therefore, we stopped any analysis that produced an interstory drift larger than 12% since trying to solve for dynamic equilibrium is impossible for an unstable (i.e., collapsed) system.

A lumped-plasticity model is used for collapse simulation and was calibrated using past research from 30 experimental tests (Section 5.4). The fiber-spring model is not used for collapse simulation due to the material model limitations that were discussed in Section 5.3.2.

In predicting collapse, it is important to consider that building collapse may occur due to a local collapse (such as loss of vertical carrying capacity in a slab-column connection) or global side-sway collapse (Ibarra 2003). To date, we have considered only the global side-sway collapse mode, which is defined as occurring when one or more stories have a dynamic instability that causes the drift ratios in those stories to increase without limitation. We assume that vertical collapse due to punching shear of slab-column connections is unlikely due to the design requirements for continuous bottom bar reinforcement through the column. In addition, we assume that the minimum confinement of columns (ACI 318-02, Section 21.4.4.1) and capacity design for shear strength will be sufficient to prevent vertical collapse after flexural hinging.

Three-dimensional collapse behavior is a complex process. When the building is in a highly deteriorated state, the responses in the two orthogonal directions will be highly coupled. Clearly, the collapse behavior of a building is three dimensional in nature and research should

move toward three-dimensional collapse modeling. With that said, we chose to use a two-dimensional model in this research, for the following reasons:

- Direct collapse simulation is still a topic of current research even for two-dimensional problems. We decided to put effort into understanding and simulating two-dimensional collapse behavior before adding the complexities of three-dimensional collapse behavior.
- Two-dimensional modeling is less computationally demanding and takes less time, thus allowing us to design and assess a larger number of design variants. This was done with the goal of making the conclusions more general and not as specific to a single building design.
- The primary three-dimensional element model currently available in OpenSees is the fiber model. Section 5.3.2 previously discussed the difficulties of using this model to simulate collapse.
- Experimental data are limited for biaxial loading; such data would be necessary to accurately calibrate and verify three-dimensional element models.
- Finally, for the perimeter-frame designs, the lateral-load-resisting members will primarily respond in two-dimensional action (i.e., uniaxial bending of beams and columns).

To approximately account for the fact that side-sway collapse can occur in either or both of the two horizontal directions, we use a two-dimensional model and predict the collapse capacity for each horizontal component of the ground motion; we then take the minimum collapse capacities for the two ground motion components as the effective collapse capacity of the structure under that ground motion pair.

5.12.2 Collapse Predictions

Using the lumped-plasticity structural model (Section 5.4, with the secant stiffness defined at yield) and the collapse analysis method outlined in the previous section, we predicted structural collapse for Design A without the gravity frame using the 36 ground motions in Bins 4A and 4C. This section presents the predicted spectral accelerations at collapse, drifts at collapse, and collapse mechanisms.

5.12.2.1 Spectral Acceleration at Collapse

Figure 5.50 shows the IDA predictions for Design A without including beneficial effects of the gravity system. Figure 5.50a shows the collapse predictions for all 72 ground motion components (collapse capacity for 36 records, 2 horizontal components per record); and Figure 5.50b shows the collapse predictions for the critical (controlling) components that first cause collapse for each pair of ground motion records (collapse capacity for 36 components). By selecting the controlling horizontal ground motion component as the collapse spectral acceleration level (Section 5.12.1), the median calculated collapse capacity is reduced from 2.8g to 2.1g and the dispersion ($\sigma_{LN(Sa,col)}$) is reduced from 0.33 to 0.29.

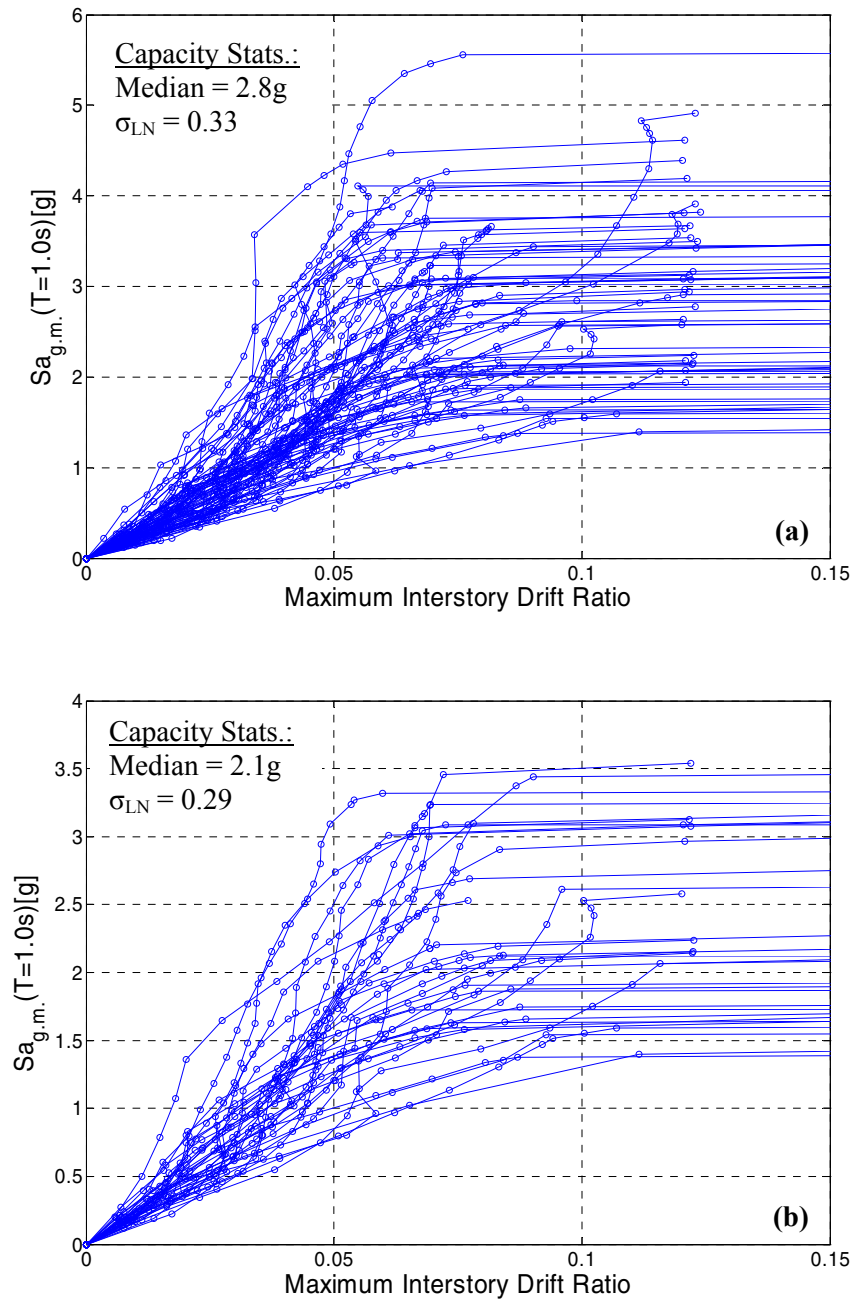


Fig. 5.50 Collapse IDAs for Design A not considering beneficial effects of gravity frame, using lumped-plasticity model and ground motion Bins 4A and 4C (36 ground motions with two components each). (a) All ground motion components (36x2) and (b) only ground motion components that first cause collapse for each record (36x1).

Figure 5.51 shows the cumulative density function of the results presented in Figure 5.50a–b. Each point shown on the x-axis of Figure 5.51 corresponds to the S_a level at which the IDA curve went flat, indicating dynamic instability of the structural system. This shows that when only accounting for record-to-record variability, the probability of collapse during the 2%-in-50-years ground motion is negligible. The next section will discuss the additional uncertainties that should be accounted for in collapse prediction.

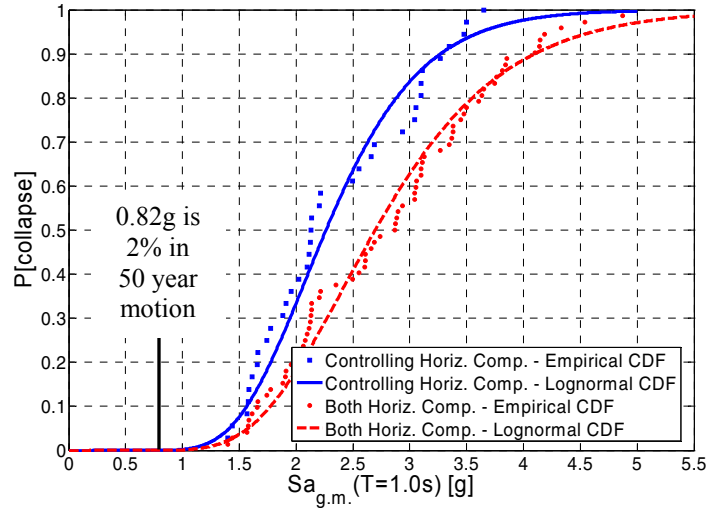


Fig. 5.51 Collapse CDFs for Design A.

Table 5.7 summarizes the collapse statistics for all eight design Variants (A–H) investigated in this study. For the perimeter-frame buildings A–D, the beneficial effects of the gravity frame are included in the structural model. Listed in the table are the median value of spectral acceleration at collapse, the collapse margin defined as the ratio of the collapse spectral acceleration to the 2%-in-50-years ground motion hazard, and the dispersion in response. This table shows that for the code-compliant designs, the collapse margin is 2.3–2.7 and $\sigma_{LN,RTR}$ is fairly consistent, varying between 0.30–0.39.

The *median* collapse capacities presented in Table 5.7 are higher than some may expect, though as will be presented in the next section, there are other uncertainties that should be accounted for in the collapse assessment. The *large* median collapse capacities are primarily due to the large *median* element plastic-rotation capacities of the conforming RC components (Section 5.4.6 and Appendix C). The calibrations included in Appendix C and continued research in calibration (Haselton et al. 2006, Chapter 4) have both shown that the plastic-rotation

capacities used in this study, albeit large, are *likely still conservative*. Note also that these large plastic-rotation capacities of the building columns used in this study are partially due to the low axial loads resulting from the building being only four stories tall.

Table 5.7 Summary of collapse capacity predictions for all design variants.

Design	Ground Motion Set	Median (Sa,col) [g]	Collapse Margin (median / Sa _{2/50})**	$\sigma_{LN,RTR}$ (Sa,col)
A	4A	2.19	2.7	0.36
B	4A	2.08	2.5	0.31
C	4A**	2.35	2.9	0.46
D*	4A	0.95	1.2	0.39
E	4A	1.95	2.4	0.32
F	4A	1.86	2.3	0.38
G	4A	1.88	2.3	0.34
H	4A	1.92	2.3	0.30

* Not a 2003 code conforming design (Chp. 3)
 ** Rec. 94103 and 94107 removed due to numerical prob.
 *** 2% in 50 year ground motion level: Sa(1sec) = 0.82g

It should also be noted that we are not modeling possible joint strength loss due to bond failure, and we are not modeling local collapse modes (such as loss of vertical load carrying capacity (LVCC) of slab-column connections, LVCC of a column, etc.). However, as discussed previously, these mechanisms are unlikely to control the collapse behavior of a code-conforming frame building. Further discussion of these topics can be found in Sections 5.5.2, 5.6.1, 5.6.2, and 5.12.1.

5.12.2.2 Modeling Uncertainty and Implications for Collapse Prediction

An important factor not included in the previous collapse analyses (Figs. 5.50–5.51 and Table 5.7) is the effect of *modeling uncertainty* on the response. Primarily, modeling uncertainty is associated with variability in the parameters that describe the nonlinear response of the structural components. In this research, considerable effort was spent to better understand the effects of

modeling uncertainty and to incorporate this into the collapse analyses. Appendix E explains how we quantified the variabilities and correlations of component response and integrated their effects through the first-order second-moment (FOSM) method to determine the resulting variability in the collapse capacity. Appendix E also includes the method of computing the mean annual frequency of collapse and includes a sensitivity study to show how various aspects of the performance assessment can affect the collapse prediction.

Using the FOSM approach employed in this study, modeling uncertainty increases the total uncertainty in collapse capacity, but does not affect the median collapse capacity. This effect of modeling uncertainty is illustrated in Figure 5.52, which shows two collapse capacity CDFs. The red solid CDF is the same as the blue solid CDF shown earlier in Figure 5.50 and is fit directly to the simulation data from the IDA procedure. As such, this plot includes only the record-to-record variability. The blue dashed CDF of Figure 5.50 has expanded uncertainty and includes the effects of both record-to-record variability and modeling uncertainty. In this example, the original dispersion due to record-to-record variability of $\sigma_{LN,RTR} = 0.29$ is increased to $\sigma_{LN,TOT} = 0.54$, based on the additional modeling uncertainty of $\sigma_{LN,MOD} = 0.45$.

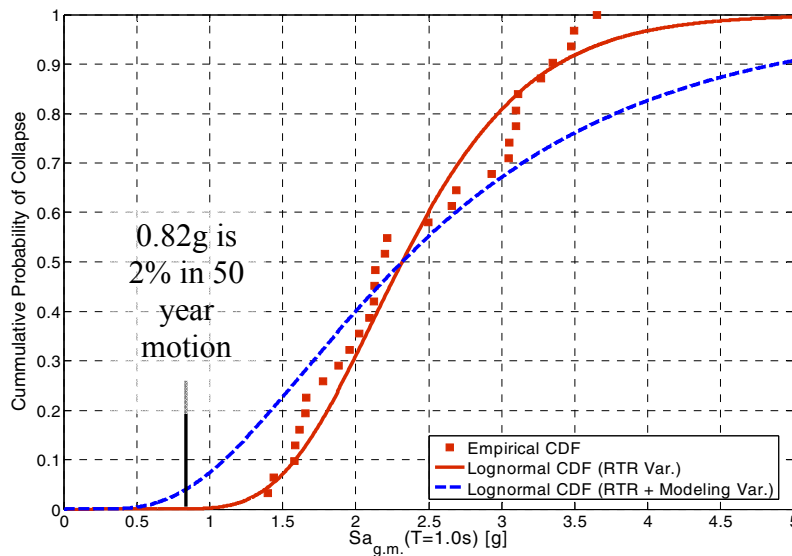


Fig. 5.52 Collapse CDFs for Design A, both excluding and including effects of modeling uncertainty.

Table 5.8 is an expansion of Table 5.7, and includes collapse statistics (median, margin, and dispersion) along with *mean estimates* of the collapse probability (conditioned on $Sa_{2/50}$) and the annual frequency of collapse. The significance of modeling uncertainty is reflected by reporting key data with and without the effect of modeling uncertainties. Comparing columns 7

and 8 to 11 and 12 indicates that inclusion of modeling uncertainty increases the $\lambda_{\text{collapse}}$ and $P[C | Sa_{2/50}]$ by almost an order of magnitude in some cases. Table 5.8 shows that for the code-conforming designs, when modeling uncertainty is included, the $P[C | Sa_{2/50}]$ is 0.02–0.07 and $\lambda_{\text{collapse}}$ is $[40 \text{ to } 140] \times 10^{-6}$.

Table 5.8 Summary of collapse predictions (mean estimates) for all design variants; showing probability of collapse, annual frequency of collapse, and effects of modeling uncertainty.

					With only record-to-record variability			With record-to-record and modeling uncertainty (mean estimate approach)			
Design	Ground Motion Set	Median (Sa,col) [g]	Collapse Margin (median / Sa _{2/50}) ^c	$\mu_{LN}(Sa,col)$	$\sigma_{LN,RTR}(Sa,col)$	$\lambda_{\text{collapse}} (10^{-6})$	$P[Col Sa_{2/50}]^a$	$\sigma_{LN,model}(Sa,col)$	$\sigma_{LN,Total}(Sa,col)$	$\lambda_{\text{collapse}} (10^{-6})$	$P[Col Sa_{2/50}]^a$
A	4A	2.19	2.7	0.86	0.36	9.2	0.00	0.45	0.58	69	0.03
B	4A	2.08	2.5	0.78	0.31	9.0	0.00	0.35	0.47	38	0.02
C	4A**	2.35	2.9	0.85	0.46	24.8	0.01	0.45	0.64	125	0.05
D ^b	4A	0.95	1.2	-0.038	0.39	663	0.34	0.35	0.52	1300	0.38
E	4A	1.95	2.4	0.71	0.32	14.5	0.00	0.35	0.47	55	0.03
F	4A	1.86	2.3	0.57	0.38	48.1	0.02	0.35	0.52	139	0.07
G	4A	1.88	2.3	0.67	0.34	20.6	0.01	0.35	0.49	71	0.04
H	4A	1.92	2.3	0.64	0.30	16.2	0.00	0.35	0.46	62	0.03

a - 2% in 50 year ground motion level: Sa(1sec) = 0.82g
b - columns designed for strength demand and not for SCWB; this is not a code-conforming design
c - collapse margin is ratio of median collapse capacity to Sa_{2/50}

The background for including structural modeling uncertainty using the so-called *mean estimate* approach is explained in Appendix E. The appendix also outlines the use of *prediction confidence levels* as an alternative way to incorporate uncertainty. Statistics using the prediction confidence method are briefly presented here, since this method has been applied in studies of nuclear power plant safety and in the building reliability investigation conducted as part of the SAC Joint Venture (Cornell et al. 2002). For reasons that will be shown, the authors strongly recommend interpretations using the mean estimate approach rather than the prediction confidence method.

Table 5.9 summarizes the collapse predictions at the 10% and 90% levels of prediction confidence. The mean estimate (or 50% confidence) without considering modeling uncertainty is also included for comparison. Comparing, for example columns 4-7-10 or 5-8-11, the data in Table 5.9 clearly show the significant impact that modeling uncertainty and the choice of

prediction confidence level have on the predictions of probability and rate of collapse. For example, between the 10–90% level of prediction confidence, the conditional collapse probability can change by a factor of 10–40 and the annual rate of collapse increases by a factor of 100–300. Section E.6.2 further shows that even small changes in the prediction confidence level (e.g., 80–95%) can drastically affect prediction. This is an important point since, while the prediction confidence seems to provide a reassuring way to present the results, for low-probability events the final result is very sensitive to the chosen value of prediction confidence level (which itself is a somewhat arbitrary decision).

Table 5.9 Summary of collapse predictions (at given levels of prediction confidence) for all design variants; showing probability of collapse and annual frequency of collapse.

Design	Ground Motion Set	10% Confidence Level			No Modeling Uncert.			90% Confidence Level		
		Shifted Median ¹ (Sa,col) [g]	$\lambda_{collapse}$ (10^{-6})	P[Col Sa _{2/50}] ^{**}	Shifted Median ¹ (Sa,col) [g]	$\lambda_{collapse}$ (10^{-6})	P[Col Sa _{2/50}] ^{**}	Shifted Median ¹ (Sa,col) [g]	$\lambda_{collapse}$ (10^{-6})	P[Col Sa _{2/50}] ^{**}
A	4A	4.2	4.3	0.00	2.36	9.2	0.00	1.1	370	0.23
B	4A ^{**}	4.0	2.6	0.00	2.34	24.8	0.01	1.0	800	0.33
C	4A	3.3	3.3	0.00	2.18	9.0	0.00	1.2	190	0.12
D*	4A	1.4	155	0.09	0.96	663	0.34	0.4	9400	0.95
E	4A	3.1	1.3	0.00	2.03	14.5	0.00	1.1	280	0.19
F	4A	2.6	6.2	0.00	1.77	48.1	0.02	0.9	830	0.41
G	4A	3.0	2.1	0.00	1.95	20.6	0.01	1.0	390	0.25
H	4A	3.0	1.4	0.00	1.90	16.2	0.00	1.0	310	0.22

* Not a 2003 code conforming design (strong-column weak-beam requirement not satisfied; Chp. 3)
** Rec. 94103 and 94107 removed due to numerical prob.
*** 2% in 50 year ground motion level: Sa(1sec) = 0.82g
¹ Actually the exponential of the shifted $\mu_{LN}(Sa,col)$

Whether evaluated by the mean estimate or confidence level approach, the reliability data show that the uncertainty in modeling collapse is large, and this large uncertainty has extreme effects on collapse safety predictions. More research in this area is needed to (a) better understand and model collapse behavior with more certainty and (b) better account for the uncertainties inherent in collapse assessment.

5.12.2.3 Maximum Drifts before Collapse

Using the median IDA data from Figure 5.48, the drifts corresponding to collapse are extracted and plotted in Figure 5.53. These reported values are the drifts at the highest spectral acceleration preceding collapse, which is typically 0.07g below the S_a level that causes collapse. Referring to Figure 5.53, the median peak interstory drift ratio at collapse is 0.086, with a COV of 15%. The median roof drift ratio is 0.060, with a COV of 15%; and the ratio of story drift at collapse to roof drift at collapse is about 1.5.

It is instructive to compare the displacement capacities at dynamic instability (Fig. 5.53) to those from the static pushover analysis (Fig. 5.34). As reported in Figure 5.34, the pushover analysis predicts the roof drift ratio of 0.075 and peak story drift of 0.12 at the point when the base shear capacity is zero. Comparing these values to the corresponding dynamic values indicates that the dynamic collapse drifts are about 0.7–0.8 of the pushover drift capacities.

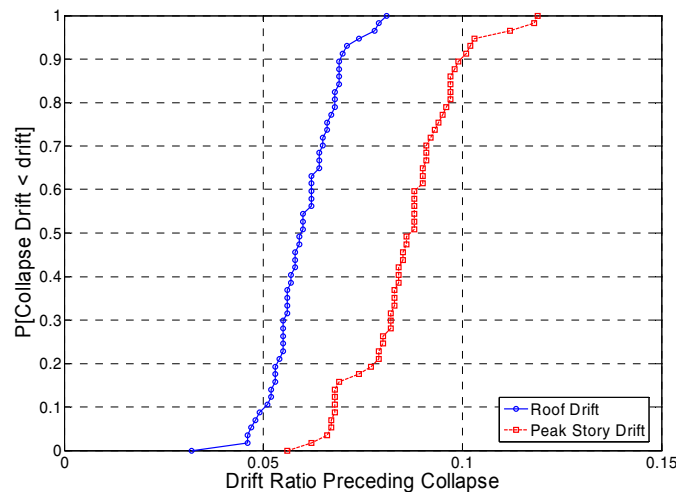


Fig. 5.53 Peak drifts just prior to side-sway collapse.

5.12.2.4 Collapse Mechanisms

Figure 5.54 illustrates the various collapse mechanisms predicted by nonlinear dynamic analyses. The mechanisms and component deformations are shown for the point just before the structure becomes dynamically unstable. This figure illustrates that there are many failure modes, which depend on the ground motion record. Note that a static pushover analysis, using an inverted

triangular load, predicts the collapse mode shown in Figure 5.54c, which was observed in less than 20% of dynamic collapses.

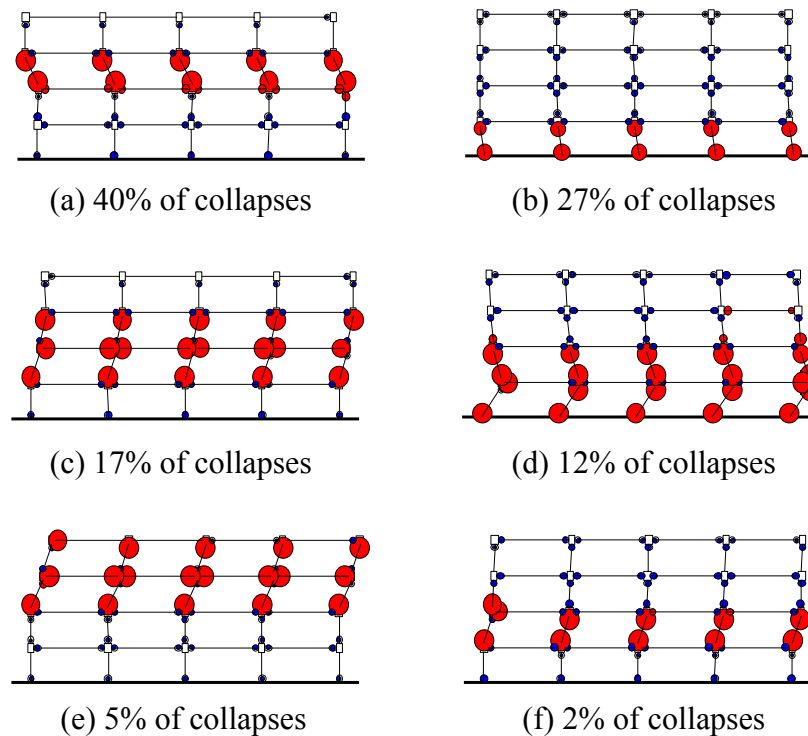


Fig. 5.54 Diagrams showing collapse modes for Design A, and percentage of ground motion records causing each collapse mode.

As observed previously, while the strong-column weak-beam design provision (ACI 318-02, Section 21.4.2.2) *delays* the plastic hinges forming in the columns, the data in Figure 5.54 clearly show that *the provision does not prohibit column plastic hinges from forming*. Furthermore, the provision does not prohibit the formation of a story collapse mechanism. Section 5.14 discusses an alternative design approach that may help further reduce the tendency for story collapse mechanisms and, thereby, improve the structural response.

5.13 ILLUSTRATION OF ELEMENT RESPONSES FROM LOW GROUND MOTION LEVELS TO COLLAPSE

The purpose of this section is to illustrate the behavior of the frame and its components for various levels of ground motion. This section uses time-history analysis results run with the 1986 North Palm Springs record ($M = 6.0$, N. Palm Springs recording station, record ID 941031)

to illustrate the element responses and progression of structural damage as the intensity of the ground motion increases.

Figure 5.55 shows the IDA diagram, the increase in drift demands for increasing spectral acceleration level, and the progression of plastic-hinge formation from low levels of ground motion to levels causing structural collapse. The legend for the hinge damage diagrams was shown previously in Figure 5.44.

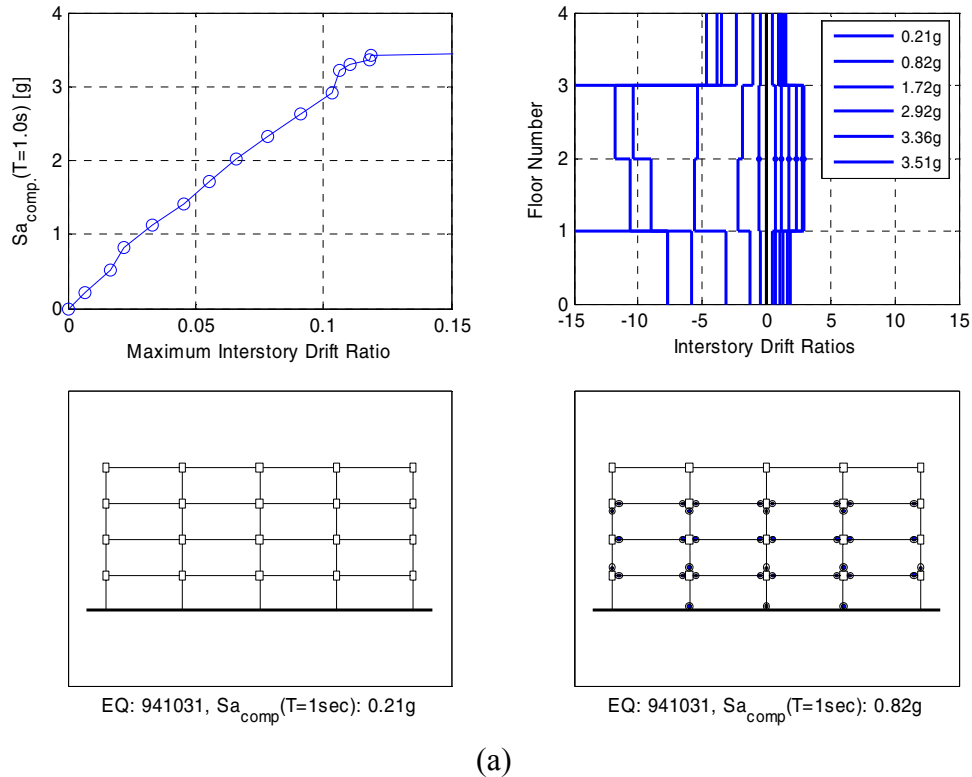


Fig. 5.55 Diagrams showing progression of peak interstory drift and damage from low levels of ground motion to collapse. Record causes damage to localize in second and third stories, and causing collapse at $S_a(T=1 sec) = 3.5g$.

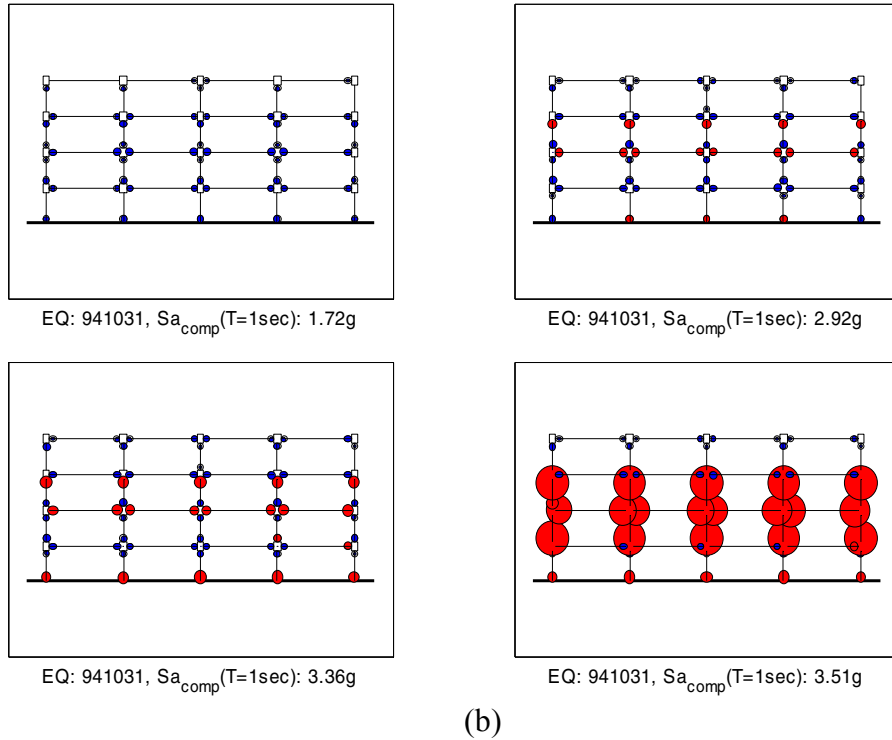


Fig. 5.55—Continued

Figure 5.56 shows the detailed responses of a third-story column for the same ground motion and spectral acceleration levels shown in Figure 5.55. The dot on the frame diagram indicates the column hinge being illustrated. At the 2%-in-50-years ground motion level (0.82g) the column yields but has only a 0.005 plastic-rotation demand; this is small compared to other earthquakes used to assess this building (Fig. 5.43a). Note that the column reaches the capping point (i.e., strain softens) well before the building collapses.

Figure 5.57 shows the response of a third floor beam for the same ground motion and spectral acceleration levels, and the dot on the frame diagram indicates the beam hinge being illustrated. At the 2%-in-50-years ground motion level (0.82g), the beam has a 0.013 plastic-rotation demand, which is also small compared to other earthquakes used for assessment (Fig. 5.43b). Similarly to the column behavior, the beam reaches the capping point (i.e., strain softens) well before the building collapses.

Figure 5.58 shows the joint response for the same ground motion and spectral acceleration levels, and the square on the frame diagram indicates the joint panel being

illustrated. This shows that the joint cracks in a pinched hysteretic response, but the joint never “yields” in shear due to the capacity design provisions of the 2003 IBC (ICC 2003).

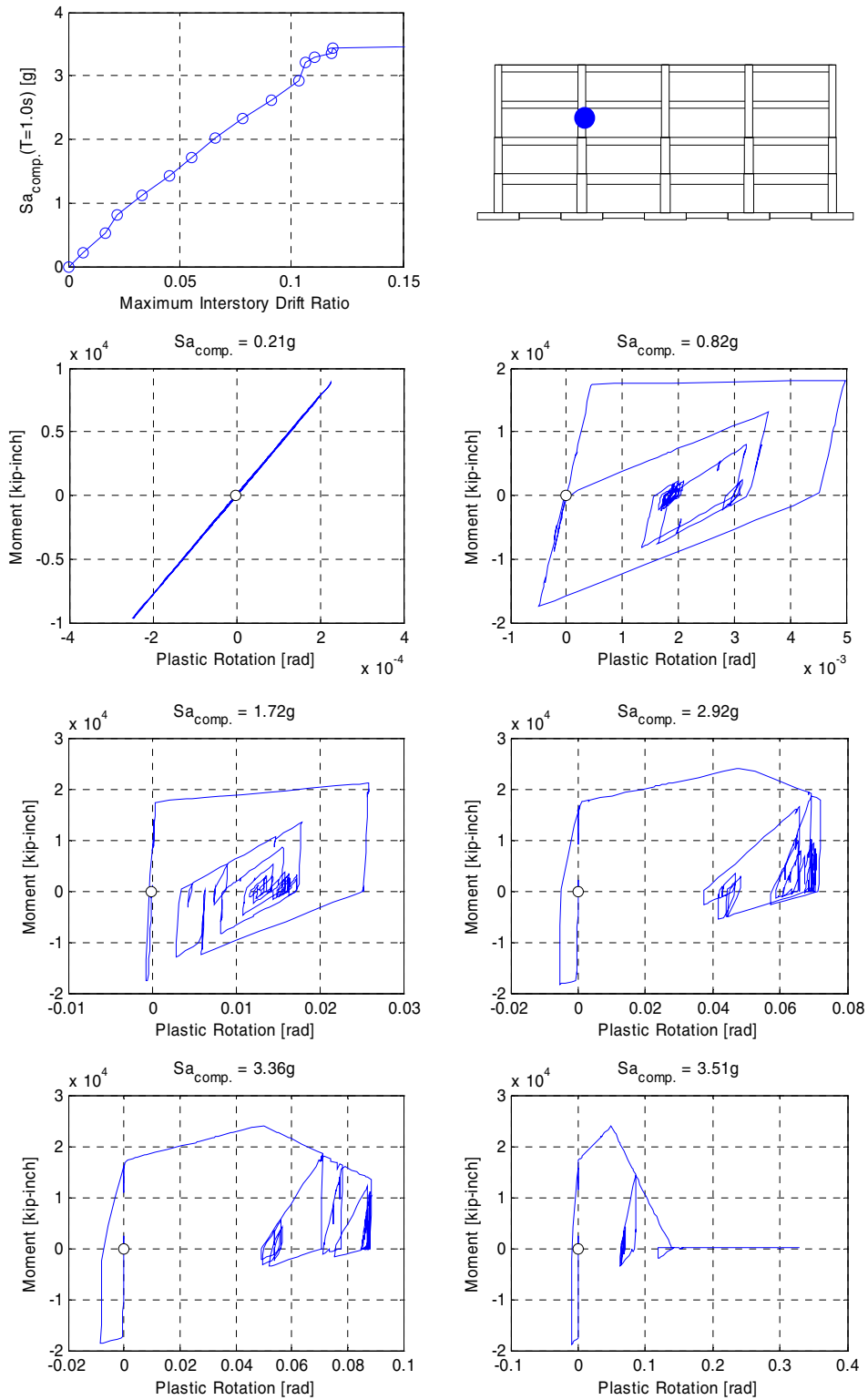


Fig. 5.56 Diagrams showing column responses for various levels of ground motion.

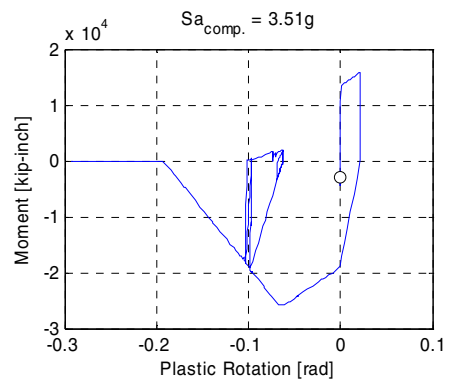
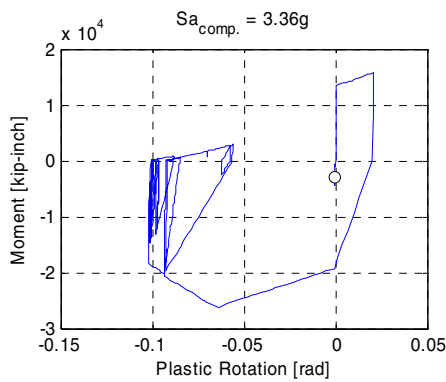
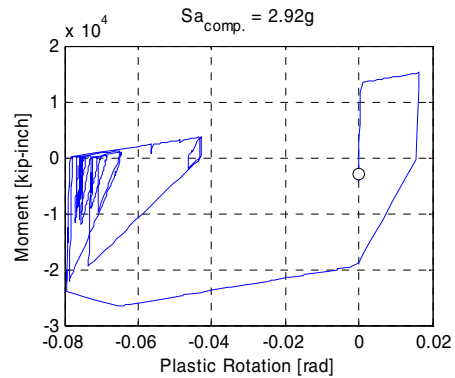
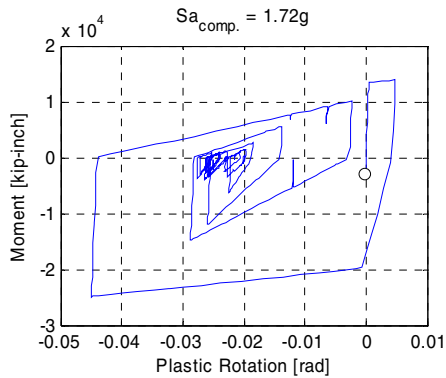
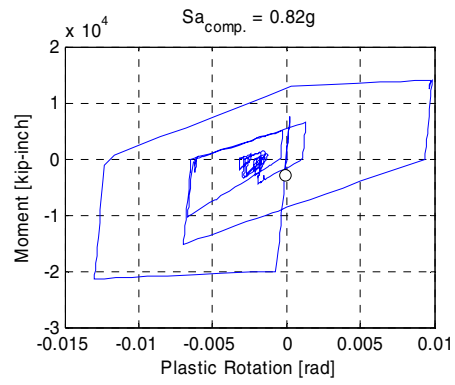
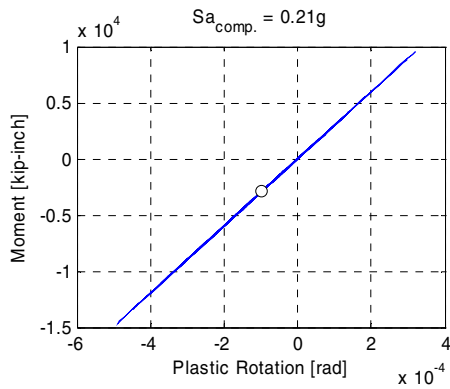
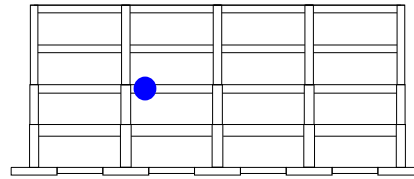
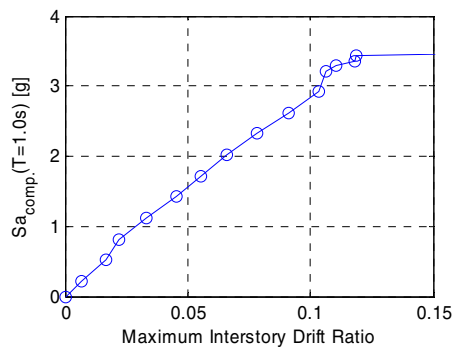


Fig. 5.57 Diagrams showing beam hinging responses for various levels of ground motion.

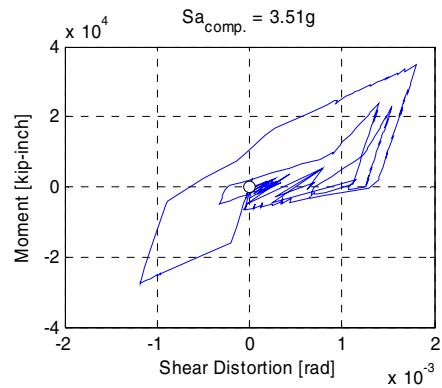
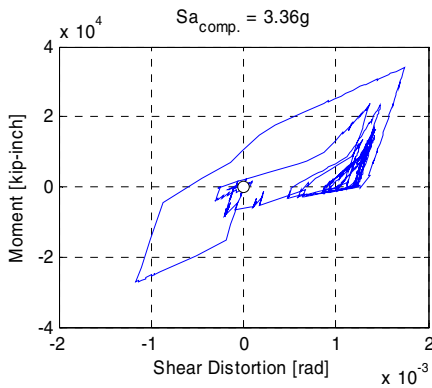
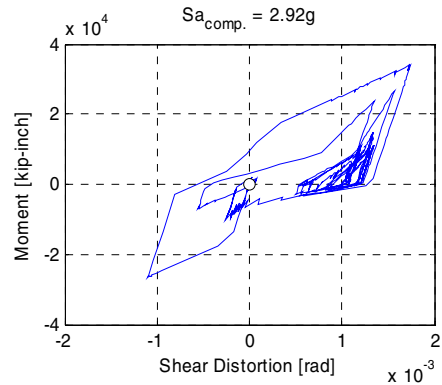
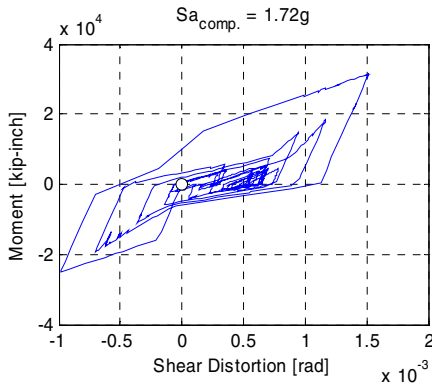
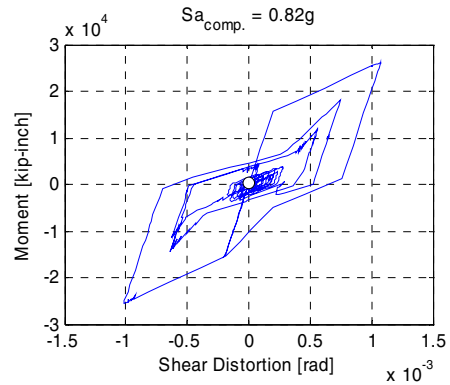
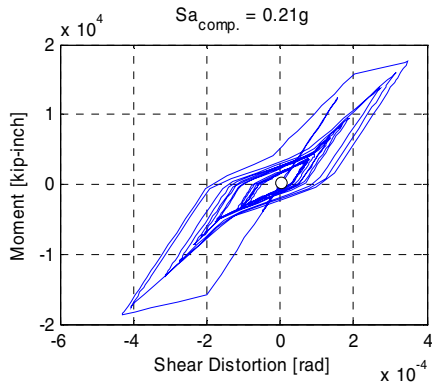
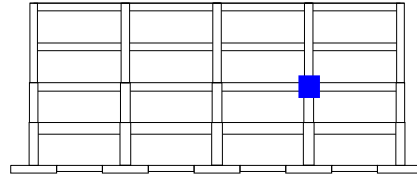
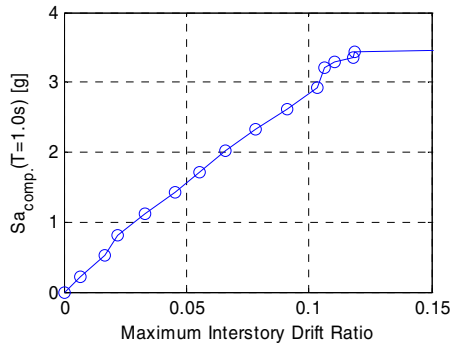


Fig. 5.58 Diagrams showing joint shear panel responses for various levels of ground motion.

5.14 PERFORMANCE-BASED DESIGN STUDY FOR BEAM TO COLUMN STRENGTH RATIO

As shown in the frame analyses, the current strong-column weak-beam design provision (ACI 318-05, Section 21.4.2.2) delays but does not prevent, column hinging and the formation of a story mechanism. Nonlinear dynamic analyses predict that the severe damage and strain softening is often concentrated in only one or two stories (Sections 5.13.2.3 and 5.12.2.4).

As the strong-column weak-beam provision recognizes, from the standpoint of safety and the energy absorption capacity of the building, it is more desirable for the damage to be concentrated primarily in the beams and distributed throughout the height of the building. Equipped with the simulation tools utilized in study, the question arises whether we can redesign the building to respond more in the desired fashion with fewer column hinges and more uniform beam hinging throughout the building.

If the objective is to limit column hinging, the column strengths will need to be increased with respect to the beam strengths. The typical approach to achieve this is by increasing the strength of the columns above the minimum strengths currently required. The Seismology and Structural Standards Committee of the Structural Engineering Association of California (SEAOC) has proposed this type of approach, effectively increasing the strong-column weak-beam ratio from 1.2 to around 2.0.

An alternative approach to strengthening the columns is to weaken the beams. Sections 5.12 and 5.13 have shown that despite the column hinging, the building still performs well in the 2%-in-50-years ground motion and has a mean collapse capacity several times larger than the 2% in 50 ground motion. Therefore, it appears that the frame has sufficient strength and stiffness to reduce the beam strengths and leave the column strengths unchanged (Takagi 2005). This approach effectively increases both the R-factor and the strong-column weak-beam ratio used in the building design. The goal of such an approach would be to reduce column hinging while saving material in the building construction.

Figure 5.59 shows static pushover curves for the original Design A (with 100% of beam strength) and a design with reduced beam strength (60% of the beam strengths provided in Design A). The pushover verifies the strength reduction and shows that this beam strength reduction caused the building to be only slightly more ductile in a static sense. An important point to remember, however, is that the static pushover analysis does not correctly predict the

dynamic failure modes. Therefore, even though the static pushover predicts only a slight increase in the building deformation capacity, the true effect on dynamic deformation capacity may be much more significant because the damage will distribute more throughout the building. In addition to deformation capacity, when the damage is more uniformly spread throughout the building, the building will be able to dissipate more energy.

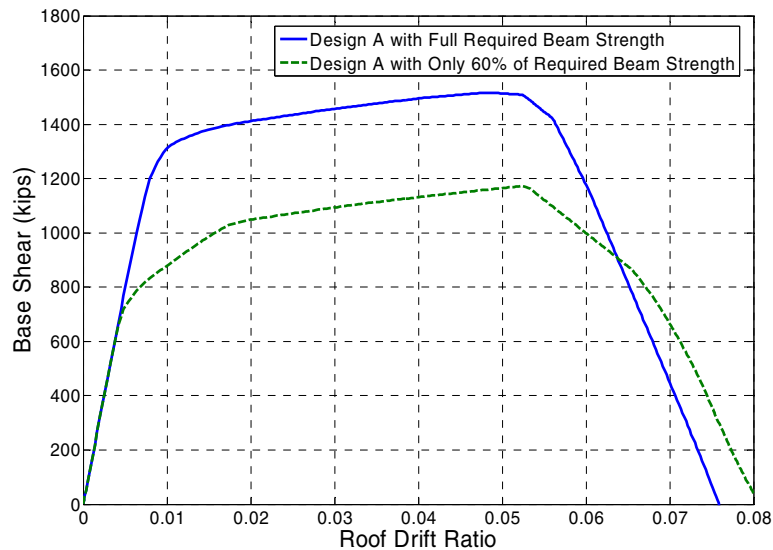


Fig. 5.59 Static pushover diagram (inverted triangular loading) showing effect of reducing beam strength in Design A by 40%.

To examine how reducing the beam strength will affect the damage pattern in the frame, we used ground motion record 941052 and predicted collapse for 100% of the design beam strength, 60% of beam strength, and 40% of beam strength. Figure 5.60 shows the collapse mechanisms predicted for each of these cases. This shows that for Design A with unreduced beam strength, this ground motion causes column hinging and a story mechanism in the first story. When the beam strength is reduced by 40%, the damage is distributed throughout the frame, with most hinging in beams but still some column hinging. When the beam strength is reduced by another 20%, a complete mechanism is reached with beam hinging and only column hinging at the foundation level. Also notice that a 40% reduction in beam strength (from 100% to 60%) does not change the predicted collapse capacity for this ground motion.

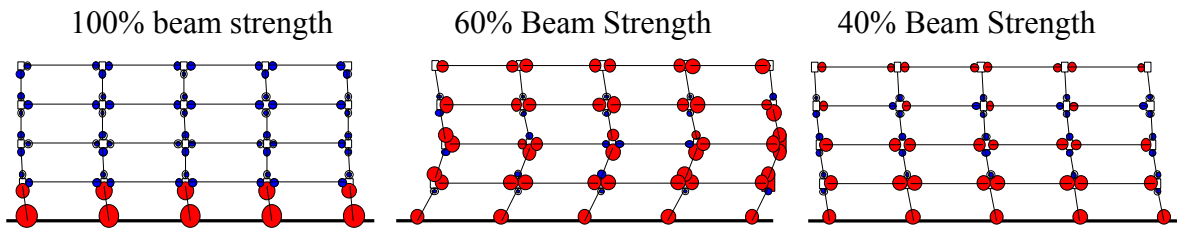


Fig. 5.60 Diagrams showing collapse mechanism for earthquake records 941052 for various levels of beam strength. This ground motion causes side-sway collapse at: 2.6g for 100% beam strength, 2.6g for 60% beam strength, and 2.2g for 40% beam strength.

In order to make these conclusions more general, we used 10 ground motion records selected from ground motion Bin 4A and predicted building collapse capacity for beam strengths ranging from 20% to 180%. Note that the column strengths are not changed; only the beam strengths are reduced or increased. Figure 5.61 shows the results of these analyses. For beam strengths of 60–100% of the design strength, the collapse capacity is relatively constant. This occurs due to a trade-off between the effects of lateral strength and the amount that the damage distributes throughout the building before collapse. When the beam strength goes lower than 60% of the design strength, the collapse capacity is decreased; when the beam strength is greater than 100%, the capacity is also decreased because the beams are as strong as or stronger than the columns.

If the beam strength design is governed primarily by the seismic demands, we can think of these beam strength changes as approximately equivalent to changes to the R-factor and the strong-column weak-beam ratio used in the design (which are 8 and 1.2 for 2003 IBC design, respectively). Figure 5.61 shows how these approximate design parameters relate to the beam strength. This figure shows that $R = 13$ and that a strong-column weak-beam ratio of 2.0 (i.e., 60% of current design beam strength) would result in similar performance as compared to the typical design values of 8 and 1.2. We see that the collapse capacity decreases for any further reduction in beam strength below 60% strength, so we could conservatively use $R = 12$ and a strong-column weak-beam ratio of 2.0.

An important note is that these analyses assume that reduction in beam strength does not adversely affect the plastic-rotation capacity of the beams. This will generally be true provided that the ratio of top and bottom steel areas remains consistent. Panagiotakos and Fardis (2001)

showed that the plastic-rotation capacity of beam-columns depends highly on the ratio of the steel areas in tension and compression. If there is significantly more steel in tension than compression, the plastic-rotation capacity will be substantially reduced.

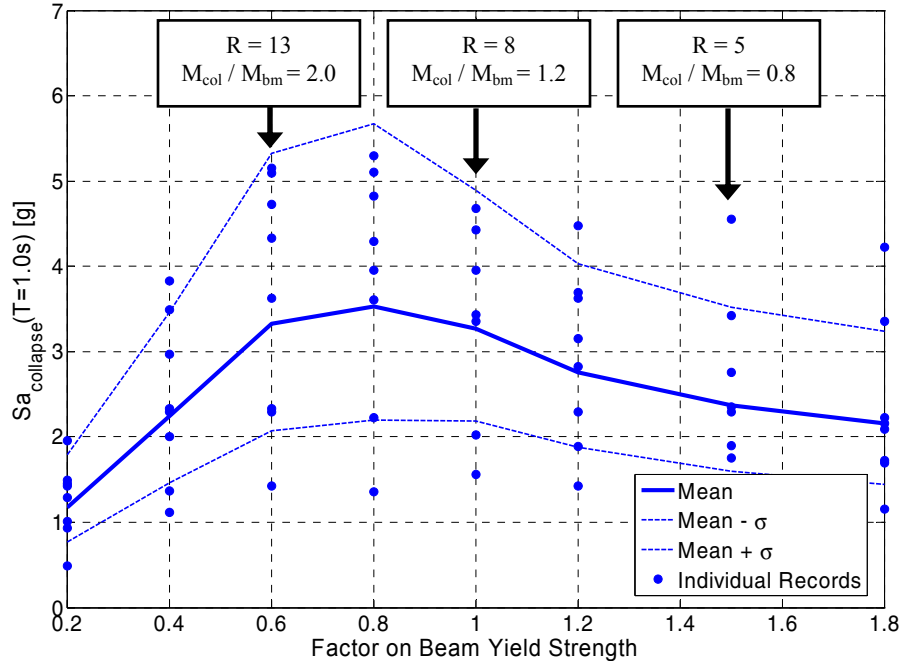


Fig. 5.61 Diagrams showing effects of beam strength on collapse capacity.

5.15 SUMMARY AND CONCLUSIONS

This chapter summarizes the structural modeling and simulation results. This section briefly summarizes the key points of the chapter and comes to appropriate conclusions.

5.15.1 Summary and Conclusions on Structural Modeling

As stated at the outset of the chapter, the overall goal is to accurately simulate response from small deformations (under frequent earthquakes) to collapse response (under rare earthquakes). A fiber-spring model is used to simulate the response from small to moderate deformations, where cracking, tension stiffening, and yield initiation are important. This model consists of fiber beam-column elements with an additional shear degree-of-freedom at each section, finite joint elements with panel shear and bond-slip springs, and column-base bond-slip springs.

Since the currently available fiber-spring model does not have a reliable way to accurately simulate strain-softening and degrading response due to reinforcing bar buckling and related effects, it is not capable of accurately simulating side-sway collapse. Therefore, a lumped-plasticity model is used for collapse simulation. This model is based on a trilinear hinge model developed by Ibarra and Krawinkler (2005) to simulate important modes of deterioration that precipitate side-sway collapse.

The most important parameter for collapse simulation is the element plastic-rotation capacity. Significant effort was spent determining the plastic-rotation capacities of conforming reinforced concrete components, which were found to have larger rotation capacities than commonly perceived. Previous research from two independent research groups and additional calibration to 30 experimental tests confirm that median plastic-rotation capacities of 0.04–0.07 radians are appropriate for conforming RC elements with relatively low levels of axial load.

5.15.2 Summary of Responses before Collapse

The four-story benchmark buildings performed extremely well at the 2%-in-50-years ground motion level. For Design A, no element experienced strain-softening in any of the 20 ground motions run at the 2%-in-50-years ground motion hazard. Mean roof drift demands were calculated as 1.8% and the mean plastic-rotation demands (for the most damaged element in the frame) were calculated as 0.014 radians for columns and 0.019 radians for beams.

5.15.3 Summary of Predicted Collapse Capacity

For the four-story benchmark buildings, the median spectral acceleration at collapse is 2.3–2.7 times larger than the 2%-in-50-years ground motion demand. When considering both record-to-record variability and structural modeling uncertainty (using the mean estimate approach), the probability of collapse at the 2%-in-50-years ground motion is 2–7% and the mean estimate of the mean annual frequency of collapse is $[38 \text{ to } 139] \times 10^{-6}$. These annual rates of collapse translate to collapse return periods of 7,000–25,000 years. The collapse estimates that do not account for modeling uncertainties are shown to significantly underestimate the likely collapse risk.

If we desired an estimate at a 90% confidence level, instead of using the mean estimate method, the conditional collapse probability increases to 12–41% and the mean annual frequency of collapse estimate increases to $[190 \text{ to } 830] \times 10^{-6}$. This shows that the high level of uncertainty associated with collapse simulation leads to high collapse probabilities and collapse rates when a high level of prediction confidence is specified. In addition to requiring the specification of a desired confidence level, the confidence approach requires the separation of epistemic and aleatory uncertainties. Since these reasons tend to introduce additional subjectivity to the collapse assessment, we recommend use of the mean estimate approach over the confidence level approach.

Nonlinear dynamic analyses show that the collapse mechanism is different for different ground motions. This simple four-story building displayed six distinct collapse mechanisms in the time-history analyses, whereas the static pushover analysis predicts only one mechanism, which was observed in only 20% of dynamic collapse simulations. Just prior to dynamic collapse, the median roof drift ratio is 0.06 and the median story drift ratio is 0.086, with COV of 15%. These drifts are about 70–80% of the maximum drift capacities as determined by the pushover response where the structural base shear capacity reduces to zero.

5.15.4 Generalizing Conclusions beyond Building Configurations Considered in Study

The overall goal of this ongoing research is to predict the performance of reinforced concrete buildings designed according to the 2003 IBC (ICC 2003). This study provides performance predictions for several different perimeter-frame and space-frame designs of a single four-story RC frame building. This provides some insight into the expected structural performance of newly designed buildings, but many more building designs and configurations need to be considered before we are able to make statements about the performance of new RC buildings in general.

6 Loss Analysis

6.1 FRAGILITY AND COST DISTRIBUTION FUNCTIONS

Fragility and cost distribution functions are created using experimental data, earthquake experience, analysis, expert opinion, or some combination of these. A review of loss estimation research shows that lognormal distributions are commonly used for fragility functions (e.g., Kennedy and Ravindra 1984; Beck et al. 2002; Aslani and Miranda 2004) and are reasonable to use for repair-cost distribution functions (e.g., Porter 2000). To fully describe a lognormal distribution, the median and logarithmic standard deviation are needed. Therefore, the median capacity and logarithmic standard deviations of capacity (defined as the *EDP* value that causes an assembly to reach or exceed a given damage state) are used to create the fragility functions, and then to estimate damage. Also, the corresponding median unit repair costs and logarithmic standard deviations of cost are used to create the cost distribution functions, to estimate the repair cost.

6.1.1 Structural Components: Beams and Columns

Various damage indices are used to quantify damage of reinforced concrete (RC) structural members. Williams et al. (1997) studied eight damage indices for concrete elements, using data from cyclic tests of beams and beam-column joints under combined shear and flexure. These authors introduce five damage states, shown in Table 6.1. They demonstrate that three indices: a modified Park-Ang damage index (*PADI*), ductility, and modified stiffness ratio, are consistently reliable indicators of severe damage to the beam and joint. They also show that the damage indices that most accurately represent the development of damage throughout the experiments are a modified *PADI*, ductility, a modified stiffness ratio, and an index calculated from increments in the plastic displacement. They conclude that the more sophisticated indices that

take into account the damage caused by repeated cycling gave no more reliable information of damage than the simpler indices such as ductility and stiffness degradation.

Table 6.1 Williams et al. (1997) damage states and consequences for concrete columns.

Damage State	Visible Damage	Likely Consequences
None	None or small number of light cracks, either flexural (90°) or shear (45°).	No loss of use or structural repair needed.
Light	Widespread light cracking; or a few cracks > 1mm; or light shear cracks tending to flatten towards 30°.	Only minimal loss of use, possible some minor repair needed to restore structure to its design strength.
Moderate	Significant cracking, e.g., 90° cracks > 2mm; 45° cracks > 2mm; 30° cracks > 1mm.	Structure closed for several weeks for major repairs.
Severe	Very large flexure or shear cracks, usually accompanied by limited spalling of cover concrete.	Structure damaged beyond repair and must be demolished.
Collapse	Very severe cracking and spalling of concrete; buckling, kinking or fracture of rebar.	Structure has completely or partially collapsed.

The modified PADI was first introduced with the release of IDARC version 3.0, a computer program created for the inelastic damage analysis of reinforced concrete structures (Kunnath et al. 1992):

$$PADI = \frac{\Phi_m - \Phi_r}{\Phi_u - \Phi_r} + \beta \left(\frac{A_t}{\Phi_u M_y} \right) \quad (6.1)$$

where

Φ_m = maximum curvature attained during seismic loading

Φ_u = curvature associated with nominal ultimate moment capacity of the section

Φ_r = recoverable curvature at unloading

β = strength deterioration parameter

A_t = total area contained in M- Φ loops

M_y = yield moment of section

This version of the software was heavily modified for a NIST study on the seismic performance of circular bridge columns designed in accordance with AASHTO/Caltrans standards (Stone and Taylor 1993). Stone and Taylor (1993) examined 82 spiral-reinforced bridge piers to estimate the threshold damage indices for yield, ultimate, and failure damage

states. These damage states are described in more detail in Table 6.2. These authors suggest that because the modified PADI is in non-dimensional format, comparisons may be made between columns of different sizes and of different loading histories.

Table 6.2 Stone and Taylor (1993) damage states and consequences for concrete columns.

Damage State	Likely Consequences
None	Light cracking may have occurred without compromising serviceability.
Repairable	Member has yielded and extensive spalling may have occurred. Inherent stiffness remains and member will likely need repair, not replacement.
Demolish	Member loaded beyond ultimate load, and will likely fail in another severe seismic event.
Collapse	Member has completely failed, implying additional collapse in structural system.

The above-mentioned studies (Williams et al. 1997; Stone and Taylor 1993), and a study by Williams and Sexsmith (1997) give clear definitions of damage states for reinforced concrete flexural members and appropriate empirical data to develop fragility functions (Beck et al. 2002). The fragility functions shown in Figure 6.1 were developed by Beck et al. (2002) and are used here to relate *EDP* values from the structural analysis to probabilities of exceeding each level of damage. These authors chose to use the deformation damage index (*DDI*) portion of the modified *PADI* in Equation (6.1) ($\beta = 0$), as the *EDP* for the fragility functions. Because rotation was a more readily available *EDP* from the present structural analyses, we assume that curvature is constant over the plastic-hinge length, and use *DDI* in terms of chord rotations:

$$DDI = \frac{\Phi_m - \Phi_r}{\Phi_u - \Phi_r} = \frac{(\theta_m - \theta_r)/L_p}{(\theta_u - \theta_r)/L_p} = \frac{\theta_{p_transient}}{\theta_u - \theta_r} \quad (6.2)$$

where

θ_m = maximum hinge rotation attained during seismic loading

θ_u = ultimate hinge rotation that is limited by hoop fracture or rebar buckling, and calculated from Fardis (2003), given in Section 5.4.6.3 and Appendix D

θ_r = recoverable rotation at unloading

L_p = plastic-hinge length

$\theta_{p_transient} (\theta_m - \theta_r)$ = peak transient plastic-hinge rotation

Beck et al. (2002) note that there is no consensus among researchers about the value for β in the energy term of *PADI*, and that in some cases this term might even have negative values. This and the lack of consistent data motivated us to use the fragility functions developed in Beck et al. (2002). Since the initiation of this study, the PEER Structural Performance Database of over 400 cyclic lateral-load tests of reinforced concrete columns has been made available to researchers via the World Wide Web (Berry et al. 2004). It would be beneficial in future work to create fragility functions from this database, and compare the loss results to those presented here.

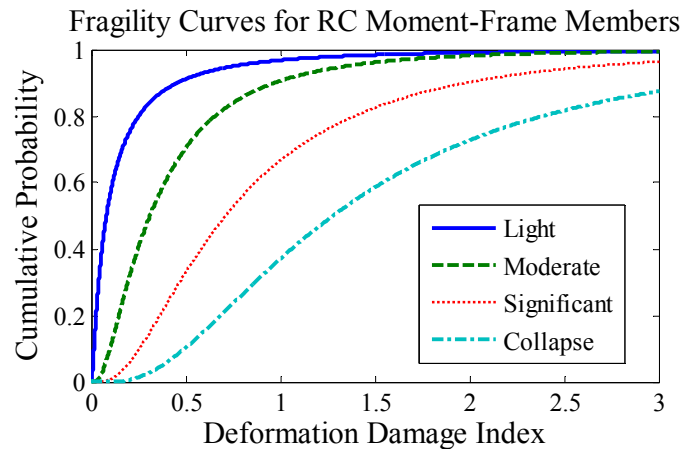


Fig. 6.1 Fragility curves for RC moment-frame members.

Each level of damage in Figure 6.1 corresponds to a specific repair effort. Beck et al. (2002) considered a variety of repair methods available to restore damaged concrete elements to an undamaged state: epoxy injection, replacement of damaged concrete, interior reinforcing, exterior reinforcing by reinforced concrete jacketing, exterior reinforcing by steel jacketing, exterior reinforcing by steel bracing, combined methods, fiber-reinforced polymers jacketing, and infill walls and wing walls. Based on their review of the use of these repair methods in industry, Beck et al. (2002) proposed the following repair efforts for the damage states considered in their fragility curves: the light damage state is repaired by epoxy injection; the moderate damage state corresponds to a jacketed repair; and the severe and collapse damage states correspond to replacement of the member. Note that no damage is also a damage state, known as “none.” These researchers used professional cost estimators to calculate repair costs. The details of this evaluation are available in their report (Beck et al. 2002); the results used in this study are summarized in Table 6.3. Note that a few years have passed since the repair costs

were estimated, and inflation is taken into account through the inflation factor, C_i , introduced in Chapter 2.

6.1.2 Structural Components: Column-Slab Connections

The fragility and repair of slab-column connections may depend on a number of parameters. Experimental results of column-slab damage reported by researchers (Aslani 2005, Kang 2006) were used to develop the fragility functions for this study, shown in Figure 6.2. The associated repair cost distributions were developed based on the recommendations of a professional cost estimator. The fragility functions relate the peak interstory drift ratio (but calculated as the average of peak transient interstory drift ratio in stories above and below the slab) to the probabilities of reaching or exceeding the following three damage states: (1) a “light cracking” damage state that is repaired using a surface coating of the affected area, (2) a “severe cracking” damage state that corresponds to epoxy injection repair of the affected area, and (3) a “punching shear (without collapse)” damage state that corresponds to replacing the concrete in the slab surface. The maximum value of IDR in either orthogonal direction (i.e., from the governing ground motion component) is the EDP chosen to estimate the damage of the column-slab connections. The details of the development of these fragility and cost distribution functions is given in Appendix I and summarized in Table 6.3.

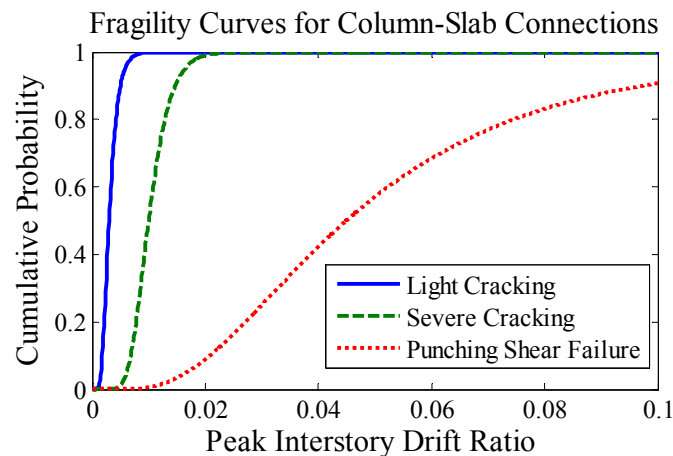


Fig. 6.2 Fragility curves for column-slab connections.

Beam-column joint fragility is not included in the present study, but the omission is not judged to make a material difference in the loss estimate for this building because the structural analyses showed that the rotations in the joints are very small. This is consistent with modern capacity design requirements that force damage to occur in adjacent columns and beams rather than in the joints. Furthermore, even if there is some damage in the joints, it is reasonable to expect that this damage would be less severe than that of the adjacent beam. Additionally, Brown and Lowes (2006) compiled results from 45 conforming beam-column connection tests and found that none exhibited damage requiring joint replacement. This suggests that the damage will be relatively greater in the adjacent columns and beams, as compared to the joint itself.

Repair costs for beam damage states were estimated for Beck et al. (2002) by a professional cost estimator. A literature review for that work indicated that the most likely mode of repair for the lowest damage state of a beam would be epoxy injection, that the next damage state would be repaired by jacketing the damaged element with new reinforced concrete, and that higher damage states would be repaired by demolition and replacement of the damaged member. A review of the detailed tasks involved in each repair indicates that the incremental costs to include a lesser damaged joint in any of these repairs would be small. It is therefore judged that any cost error introduced by ignoring possible damage in the beam-column joints in the perimeter moment frame is likely to be small and can be covered in the uncertainty associated with the adjacent beam repair costs.

6.1.3 Nonstructural Components: Drywall Partitions and Finish

The drywall partitions considered for the benchmark office building are 5/8" wallboard partitions on 3-5/8" metal studs with screw fasteners. The *EDP* used for the drywall partitions and finish is the peak transient drift ratio (*PTDR*). The fragility curves, shown in Figure 6.3, were developed by Porter (2000) and are based on Rihal's (1982) in-plane racking tests of 8'-0 x 8'-0 building partitions. These fragility functions are used to relate the *PTDR* values from the structural analysis to probabilities of exceeding the two levels of damage: visible and significant.

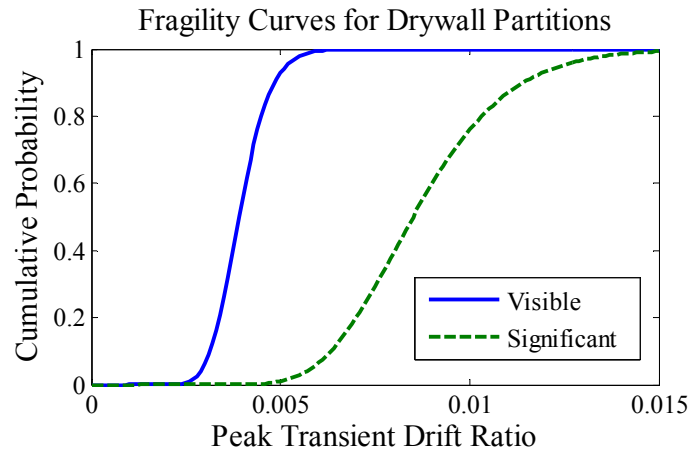


Fig. 6.3 Fragility curves for wallboard partitions.

Visible damage is repaired by patching cracks and possibly cutting out damaged pieces of wallboard and replacing them, then applying joint tape and joint compound to the cracks or seams, sanding, and repainting. Significant damage is repaired by demolishing and replacing the partition. Interior partitions with gypsum wallboard on both sides are treated as two separate assemblies: one that includes the framing and gypsum wallboard on one side, the other includes only the gypsum wallboard finish on the other side. Again, the cost associated with the repair effort to return the damaged wallboard partitions and finish to an undamaged state was calculated by professional cost estimators in Beck et al. (2002). The results used in this study are summarized in Table 6.3. Inflation is taken into account through the inflation factor, C_i , introduced in Chapter 2.

6.1.4 Nonstructural Components: Interior Paint

Researchers have shown that interior paint has a considerable contribution to the total repair costs of a damaged structure, especially for low levels of shaking (Beck et al. 2000). These researchers used a line-of-sight method to account for the needed interior painting of a damaged structure. This line-of-sight method assumes that damage on any wall of a room or hallway that requires repainting leads to the repainting of that entire room or hallway. Thus, they consider the need for owners to repaint areas that are not damaged, to achieve a reasonable uniform appearance. This approach works in a Monte Carlo simulation but not using FOSM or FOSM-

like approaches, so for present purposes an approximation is required. We propose a simplified formula for calculating the mean area requiring repainting:

$$ATP = DA + UA \cdot P(\text{paint } UA | DA) \quad (6.3)$$

where ATP = mean area to paint

DA = damaged area

UA = undamaged area

$P(\text{paint } UA | DA)$ = probability of needing to paint an entire floor as a function of the damaged area of wallboard partitions on the same floor

The fragility function in Figure 6.4 shows the cumulative lognormal distribution of painting an entire floor, based on the ratio of damaged area to total area of wallboard partitions on the same floor. The shape of this distribution, dictated by the median ($x_m = 0.25$) and the logarithmic standard deviation ($\beta = 0.5$), is based on our own judgment of the owner's tipping point to paint an entire floor based on the known damaged area. The cost associated with interior painting was calculated by professional cost estimators in Beck et al. (2002). The median and logarithmic standard deviation of cost to paint one square foot of interior wall space is \$1.52 and 0.2, respectively. Again, inflation is taken into account through the inflation factor, C_i , introduced in Chapter 2.

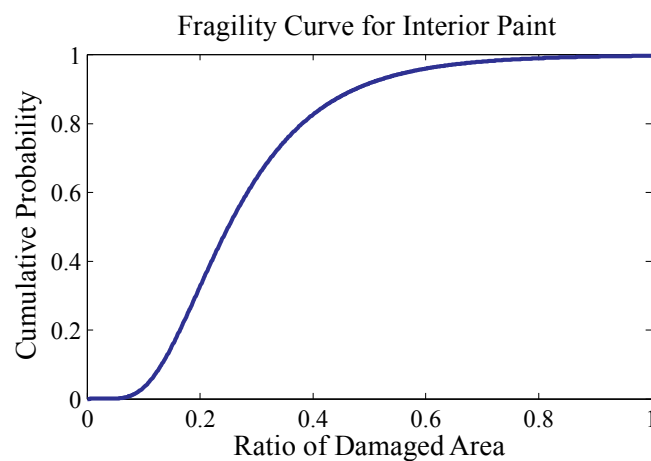


Fig. 6.4 Fragility curve for interior paint.

6.1.5 Nonstructural Components: Exterior Glazing

We used a fragility function for a particular type of glazing system (Horizon Wall glazing) as documented by Porter (2000). The *EDP* for the exterior glazing is the peak interstory drift ratio. The fragility functions developed by Porter (2000) are based on Behr and Worrell's (1998) laboratory test data for the in-plane cracking capacity of glazing systems. The two damage states for the glazing (cracked and fallout damage) require replacing the damaged glass pane.

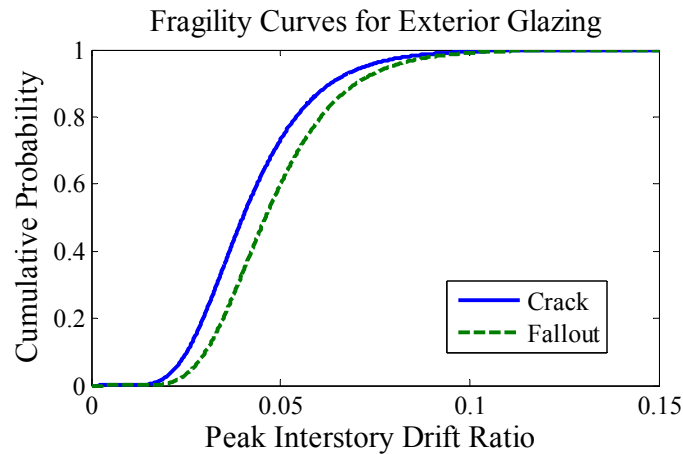


Fig. 6.5 Fragility curves for exterior glazing.

6.1.6 Nonstructural Components: Acoustical Ceiling

The *EDP* used for the acoustical ceilings is the maximum of the peak floor diaphragm accelerations in either orthogonal direction. The collapse fragility of these ceilings depends on the ceiling plan dimensions, which for this building were assumed to occur in square modules measuring 30 ft on a side. The collapse fragility and associated repair effort to replace the ceiling component, based on a theoretical approach, were developed by Porter (2001).

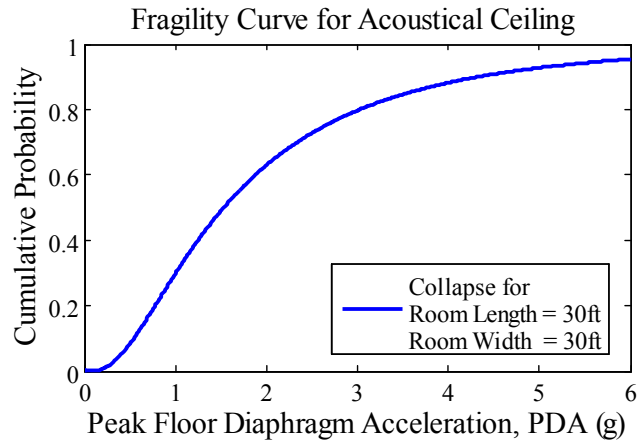


Fig. 6.6 Fragility curve for acoustical ceiling.

6.1.7 Nonstructural Components: Automatic Sprinklers

The *EDP* used for the sprinkler is the maximum of the peak floor diaphragm accelerations in either orthogonal direction. The fragility functions used here were developed by Porter (2001) and are based on the limited damage data for a few buildings affected by the 1989 Loma Prieta earthquake and compiled by Sprinkler Fitters U.A. Local 483 (1989). The damage state corresponds to the replacement of a 12-foot (3.7m) segment of pipe. A pressurized sprinkler that is fractured during a seismic event will lead to the wetting of exposed nonstructural components near the break of the sprinkler pipe. Since little data exist to determine the fraction of wetted items that should be considered worthless, it is assumed in Porter (2001) that all wetted ceiling tiles must be replaced, as well as all wetted computer equipment (2001). In addition, Porter (2001) assumes that repair cost to carpets and wall finishes amounts to 25% of their replacement cost. Therefore, the “fracture” damage state of the braced automatic sprinklers considered for this benchmark building corresponds to pipe replacement as well as the repair or replacement of wetted nonstructural components.

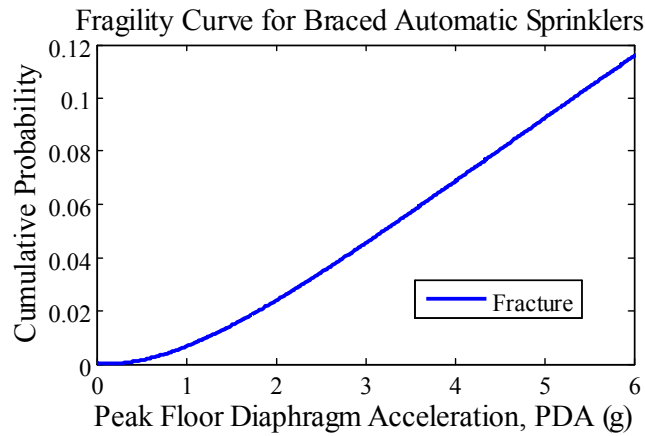


Fig. 6.7 Fragility curve for braced automatic sprinklers.

6.1.8 Nonstructural Components: Elevators

There are little data available about performance of hydraulic elevators from past seismic events or from experimental studies. Porter (2006) developed a fragility function for hydraulic elevators (reproduced as Fig. 6.8 below) based on data collected after the Loma Prieta and Northridge earthquakes. This fragility function lumps several damage scenarios into a single *failure* damage state, including “damage to car guide shoes, cab stabilizers, and cab interior, snagged ropes and traveling cables, and failure of equipment anchorage and hydraulic cylinder or piping” (Porter 2006). The repair effort includes inspection of the elevator and the materials and labor needed to repair the damage (Schiff 2006), which varies for the above-mentioned scenarios and is reflected by the coefficient of variation of the repair cost given in Table 6.3. The engineering demand parameter used for the fragility function is peak ground acceleration. This is the only case in this study where the *EDP* is independent of the building’s response; the loss associated with elevator damage is equal for all design variants.

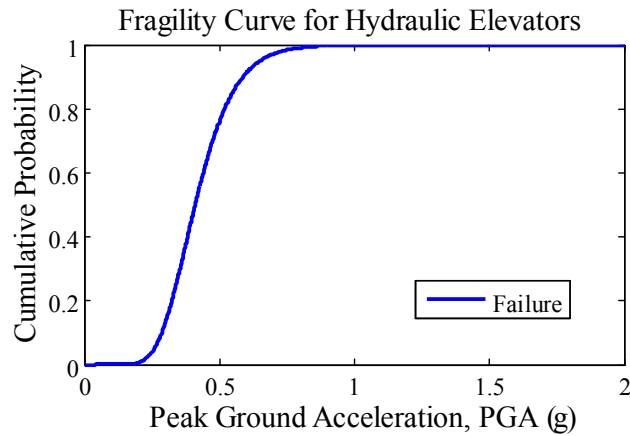


Fig. 6.8 Fragility curve for hydraulic elevators.

6.2 MDLA: MATLAB DAMAGE AND LOSS ANALYSIS TOOLBOX

The modular framework of the PEER methodology allows for straightforward software development. A MATLAB damage and loss analysis toolbox (MDLA) was created as part of this benchmark study to handle the damage and loss analyses portions of the PEER methodology. The input and output parameters for the program are shown graphically in Figure 6.9. The inputs into the toolbox are: a database of fragility and cost distribution functions, tables of the damageable components of the benchmark building, and the hazard and structural analysis results. The outputs of the toolbox are the probability of exceedance of damage states for all damageable components in the structure and the *DVs* of the methodology described above. The *DVs* considered in this study are the repair costs to restore the building to an undamaged state, collapse statistics, and losses due to fatalities.

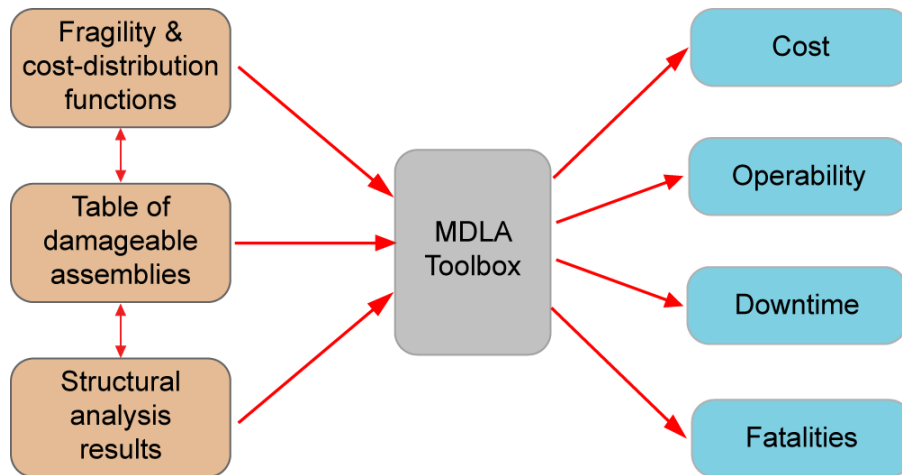


Fig. 6.9 Input and output parameters for MDLA toolbox.

6.2.1 MDLA Input: Table of Damageable Assemblies

The table of damageable assemblies is created by itemizing the components in a building that will contribute to earthquake losses. These tables are given in Chapter 3 (Tables 3.1–3.2) for the perimeter-frame and space-frame benchmark designs. The building’s damageable components are described using five categories: assembly type, assembly description, location, unit, and quantity. The assembly type is a unique identifying number for each component type. The taxonomy of building components used in this study was introduced by Porter (2000) and is based on the RS Means Corp. (RS Means, Corp. 1997) numbering format. The assembly description simply describes each unique building damageable component. The location number indicates the floor or story level where the components are located in the building. The unit of a damageable building component varies with assembly type and depends on the component’s fragility function used in the damage analysis. Finally, the quantity of components is used for bookkeeping purposes in the damage and loss analyses.

6.2.2 MDLA Input: Fragility and Cost-Distribution Functions

The table of damageable assemblies is used by MDLA to choose the fragility and cost-distribution functions from a library of available functions, to use in the damage and loss analyses. This library of functions is internal to the toolbox but can be edited as new ones

become available. The parameters of the fragility and the unit-repair-cost functions that are used in this study are in Table 6.3, where x_m is the median and β is the logarithmic standard deviation (*EDP*'s and corresponding units are given in the table footnotes).

Table 6.3 Summary of assembly fragility and cost distribution parameters.

Assembly Description	Unit	Damage State	Fragility Parameters		Repair Cost Parameters	
			x_m	β	x_m (\$)	β
Ductile CIP RC beams	ea	light	0.08 ^a	1.36	8,000	0.42
Ductile CIP RC beams	ea	moderate	0.31 ^a	0.89	22,500	0.40
Ductile CIP RC beams	ea	severe	0.71 ^a	0.80	34,300	0.37
Ductile CIP RC beams	ea	collapse	1.28 ^a	0.74	34,300	0.37
Ductile CIP RC columns	ea	light	0.08 ^a	1.36	8,000	0.42
Ductile CIP RC columns	ea	moderate	0.31 ^a	0.89	22,500	0.40
Ductile CIP RC columns	ea	severe	0.71 ^a	0.80	34,300	0.37
Ductile CIP RC columns	ea	collapse	1.28 ^a	0.74	34,300	0.37
Column-slab connections	ea	light cracking	0.3 ^b	0.40	35	0.20
Column-slab connections	ea	severe cracking	1.0 ^b	0.30	435	0.20
Column-slab connections	ea	punching shear failure	4.5 ^b	0.60	3,273	0.20
Drywall partition	64 ft ²	visible	0.0039 ^c	0.17	88	0.20
Drywall partition	64 ft ²	significant	0.0085 ^c	0.23	525	0.20
Drywall finish	64 ft ²	visible	0.0039 ^c	0.17	88	0.20
Drywall finish	64 ft ²	significant	0.0085 ^c	0.23	253	0.20
Exterior glazing	pane	crack	0.040 ^b	0.36	439	0.26
Exterior glazing	pane	fallout	0.046 ^b	0.33	439	0.26
Acoustical ceiling	ft ²	collapse	92/(l+w) ^d	0.81	2.21*A	0.50
Automatic sprinklers	12 ft	fracture	32 ^d	1.40	900	0.50
Hydraulic elevators	ea	failure	0.41 ^e	0.28	5,000	1.00

a. peak plastic-hinge rotation/(ultimate hinge rotation–recoverable hinge rotation) [rad/rad]
b. average of peak transient interstory drift ratio in stories above and below the slab [%]
c. peak transient drift ratio [in/in]
d. peak diaphragm acceleration [g]
e. peak ground acceleration [g]
l = room length; w = room width; A = room area

6.2.3 MDLA Input: Structural Analysis Results

The structural analysis step of the PEER PBEE methodology, described in detail in Chapter 5, results in structural responses, or *EDPs*. As mentioned in Chapter 2, the lognormal distribution is often used by researchers to fit structural analysis data. A lognormal distribution is used to fit the structural analysis data for every *EDP* at all hazards levels; we use the Kolmogorov-Smirnov (Massey 1951; Miller 1956) goodness-of-fit test at the 1% significant level to show that it is a

good fit (only 5% of fitted distributions fail the test for Variant 6 at one stripe level). Figure 6.10 shows the cumulative step function of raw data for peak roof acceleration in the EW-direction for four *IM* levels, and the corresponding fitted lognormal *cdf*'s. Note that the dashed lines in this figure correspond to the fitted distribution +/- the critical values associated with the Kolmogorov-Smirnov test at the 1% significance level.

There are 44 *EDPs* of interest identified for the perimeter-frame structural model based on the table of damageable assemblies in Table 3.1. These include 4 peak diaphragm accelerations (one per floor), 4 peak transient drifts (one per story), and 36 deformation damage indices (one per structural member). There are 60 *EDPs* of interest identified for the space-frame structural model based on the table of damageable assemblies in Table 3.2. These include 4 peak diaphragm accelerations (one per floor), 4 peak transient drifts (one per story), and 52 deformation damage indices (one per structural member).

Although the perimeter-frame and space-frame-designs have the same number of bays in the N-S and E-W directions, the space-frame design has additional structural members to consider in the loss analysis. These members include the beams in the exterior bays in the E-W direction and all the interior beams and columns of the building. For simplicity, the space-frame was designed only in the N-S direction of the building and similar structural behavior is assumed in the E-W direction if designed by the same practitioner (i.e., have similar strength and stiffness as the N-S direction). This is a fair assumption for strength (as practitioners would likely reduce element strengths in the E-W direction to benefit from the additional bays) but conservative for stiffness (as the building code stiffness requirements do not control the design, so the practitioners may use similar element dimensions in the N-S and E-W directions).

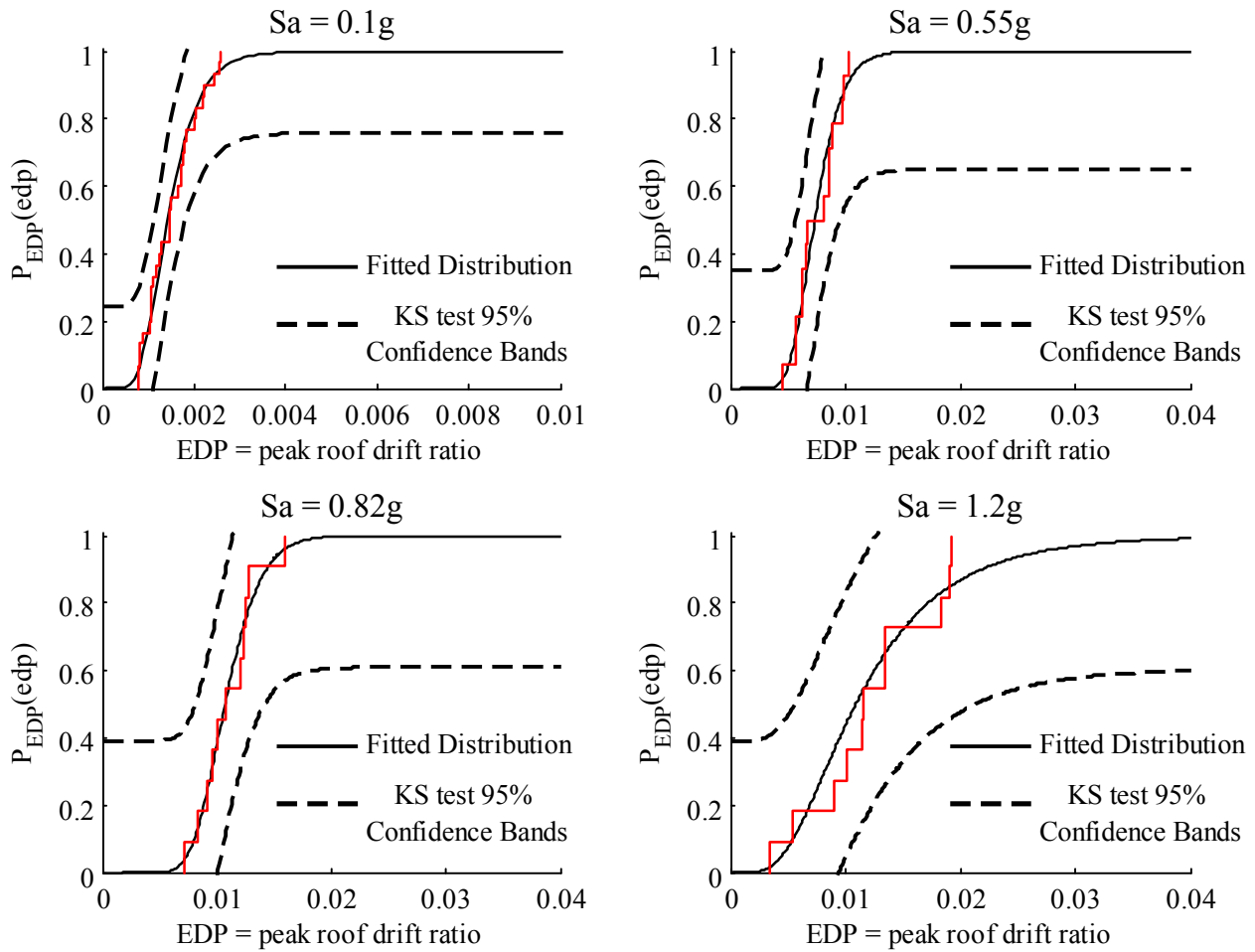


Fig. 6.10 Fitted probability and observed step-function distributions of peak roof drift ratio (EW-dir) results for four levels of IM.

Using the above assumptions, the same four-bay frame model is used to represent the behavior in both the N-S and E-W directions. The behavior of the extra members in the six-bay E-W frame is extrapolated from the structural analysis of the four-bay N-S frame. We assume that the interior beams and columns adjacent to one another will have similar levels of damage. Thus the *EDPs* for interior beams and columns from the four-bay structural model are replicated for the additional bays, as shown below in Figure 6.11.

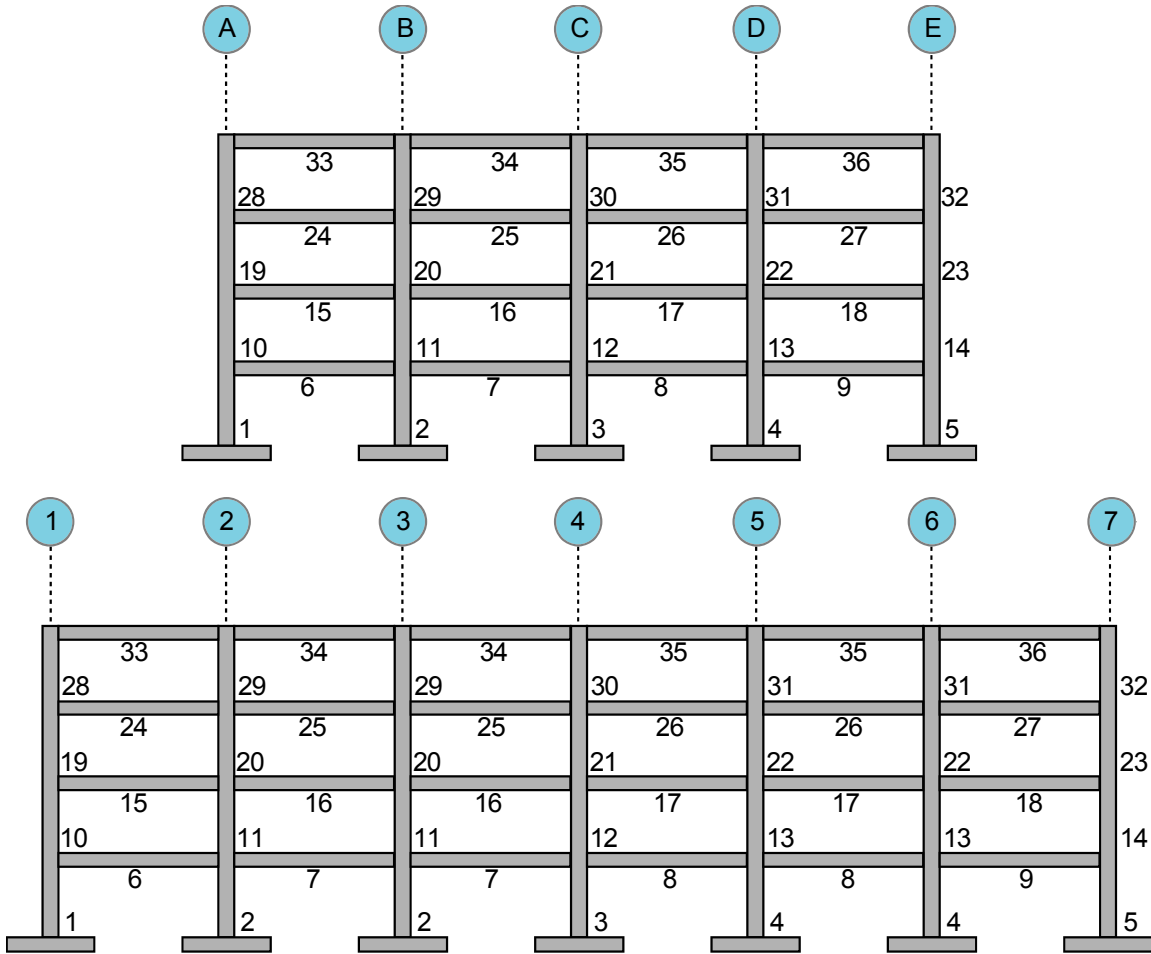


Fig. 6.11 EDP numbering for structural components in N-S and E-W directions.

The column members in the space-frame design are common to the lateral resisting frames in the N-S and E-W directions. The question arises then, if the fragility function is expressed in terms of *DDI* for one direction, how should one combine *DDIs* acting on the same column from two perpendicular directions? Three possible combinations were considered: simple maximum (*DDI* is taken as the larger of the two directions), absolute sum (*DDI* is taken as the sum of the *DDIs* from the two directions), and square root of the sum of the squares (SRSS). These are shown graphically in Figure 6.12 and are given by:

$$\begin{aligned}
 DDI_{SM} &= \max(DDI_i, DDI_j) \\
 DDI_{AS} &= DDI_i + DDI_j \\
 DDI_{SRSS} &= \sqrt{(DDI_i^2 + DDI_j^2)}
 \end{aligned}
 \tag{6.4}$$

In the figure, points along each line have the same combined *DDI*.

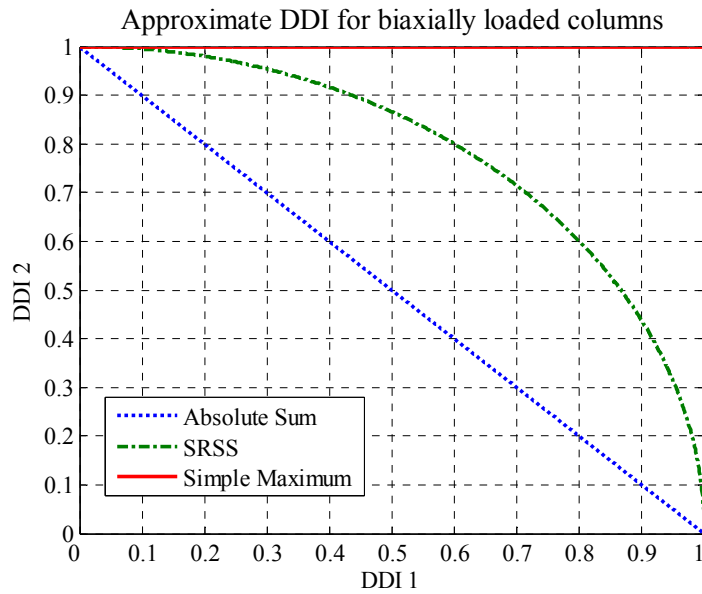


Fig. 6.12 Approximations for *DDI* for biaxially loaded columns.

The *ACI Design Handbook* for columns was consulted to determine which combination of *DDI* would be most appropriate to estimate the damage of the columns (ACI 1990). Figure 6.13 is from the *ACI Handbook* and shows the biaxial moment capacity relationship for a number of values of the biaxial bending constant. The biaxial bending design constant, $\beta = 0.5$, $\beta = 0.7071$, and $\beta = 1.0$, respectively, correspond to the absolute sum, the SRSS, and the simple maximum curves of Figure 6.12. The value of β depends on the design and nominal axial loads, the material and the geometric properties of the columns. Based on these criteria, the values of β range from 0.58 to 0.73 for the columns of the benchmark building. Thus, SRSS is a reasonable method to combine the *DDI* values of the N-S and E-W directions of the columns and was used in this study.

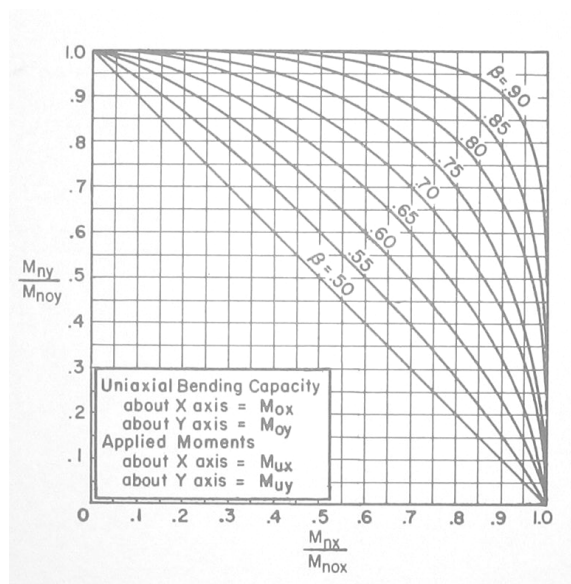


Fig. 6.13 Biaxial moment relationship for columns (ACI 1990).

6.2.4 MDLA Architecture

The software developed for this benchmark study is the MATLAB Damage and Loss Analysis (MDLA) toolbox. The flowchart for the program, shown in Figure 6.14, identifies the key modules of the software and the connections between these modules. The modularity of this program reflects the research coordination among the three schools involved with the benchmark study and the modularity of the PEER PBEE methodology. The umbrella module, “ANL_main” organizes the structural analysis results, extracts the fragility and cost-distribution function parameters of interest, fits the lognormal distributions to the transferred *EDP* data, calls the damage and loss analysis module, and calculates the repair costs moments. The “extract_EDP_matrix” module formats the structural responses and breaks up *EDP* vectors per structural simulation. The “generate_frag_cost_params” module chooses fragility and cost-distribution function parameters of interest from an internal library of these. The “Loss_Analysis” module performs the damage and loss analyses, as outlined in Sections 2.6 and 2.7. The results from this module are found in Sections 6.3–6.6. The “rc_moments” module computes the first four non-central moments of unit repair cost. The “generate_logn_pdf_params” module fits lognormal distributions to the raw *EDP* data. The “Loss_Analysis” module calls to other functions: “failure_prob” and “discrete_simpson”. The “failure_prob” module determines the failure probability, or the probability that the i^{th} assembly

is in damage state j . The “discrete_simpson” module performs numerical integration, using Simpson’s method.

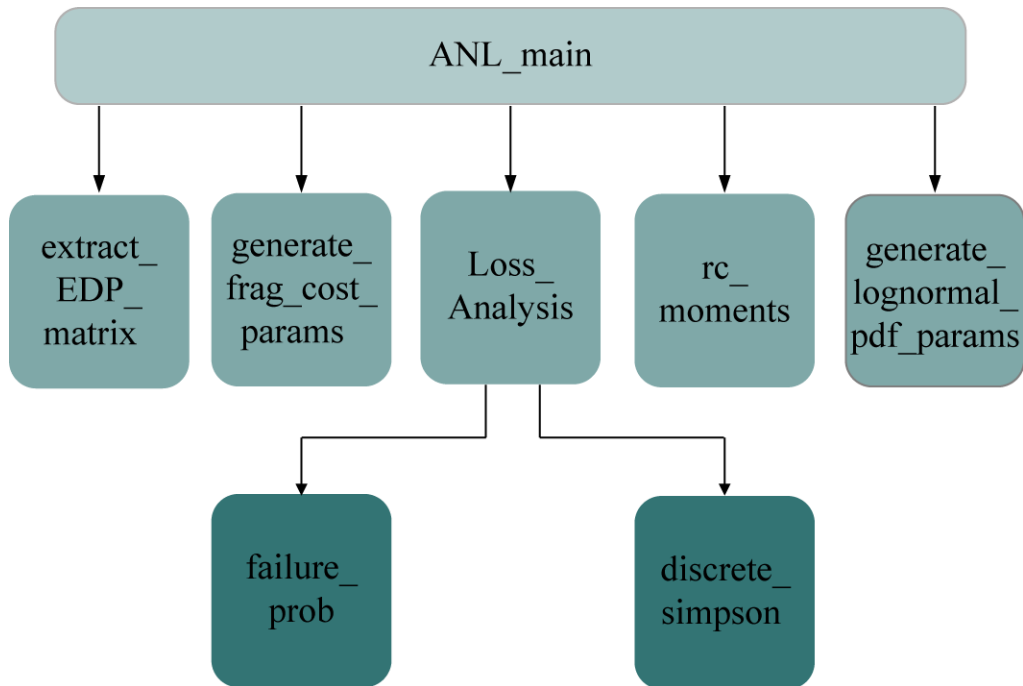


Fig. 6.14 Schematic of MDLA toolbox.

6.2.5 MDLA Output: Damage and Loss Results

The damage and loss analysis methodology is described in detail in Chapter 2. The results of the damage and loss analyses for the benchmark study are presented below in Sections 6.3–6.5 for the eight design variants of the benchmark building summarized in Table 6.4. These results include the average probability of damage for the mean design variants, vulnerability functions, and calculated *EAL* for these variants, some modeling and design comparisons of these variants, and finally a note on the probability of fatalities due to collapse of the benchmark building.

Table 6.4 Summary of benchmark building designs and structural models.

Design	Variant #	Design and Model Description
A	1	Perimeter frame, designed with expected over-strength; fiber model, concrete tensile strength modeled, gravity frame included.
B	3	Same as Design A, but designed with bare code-minimum strengths; modeled same as VID #1.
C	2	Same as Design A, but designed with uniform beams and columns over height; modeled same as VID #1.
D	9	Same as Design C, but no SCWB provision enforced (not code-conforming); modeled same as VID #1.
E	6	Baseline space frame; fiber model, concrete tensile strength modeled.
A	11	Same as Design A; modeled same as VID #1, but concrete tensile strength and stiffness not modeled.
A	12	Same as Design A; modeled same as VID #1, but gravity frame not modeled.
A	13	Same as Design A; lumped-plasticity model with secant stiffness through yield (K_{yld}).
A	14	Same as Design A; lumped-plasticity model, with secant stiffness through 60% of yield.
A	15	Same as Design A; lumped-plasticity model with secant stiffness through 40% of yield (K_{stf}).

6.3 DAMAGE RESULTS

The methodology for calculating the probability of the structural components being damaged is described in detail in Section 2.6. Some results of the damage analysis step are shown in Figures 6.15–6.24, showing plots against $IM=S_a$ of the average probability of reaching or exceeding each possible damage state for like components on each story level of the benchmark building. These plots show the average trend of damage of like components along the height of the structure and with increasing intensity level. As expected, these figures show that the probability of exceeding each damage state increases with increasing shaking intensity, and can be utilized to help predict the location in the building of greatest damage. The greatest damage to the columns occurs in the first story for all the variants, which is an anticipated behavior of reinforced concrete structures under seismic loading (Moehle 1991). These plots are also useful to compare with the figures showing collapse mechanisms in Chapter 5 (Fig. 5.53). This output from the toolbox will be a great asset to engineers who would like to optimize their design choices, and to their clients who will benefit from this information.

The damage results can be used to quickly compare various designs and to estimate what will likely control the repair cost in future earthquakes. The designs and models considered are summarized in Table 6.4. The variant that does not include code's strong-column weak-beam provision (Variant 9, Fig. 6.19) has the most damage (or smallest probability of "no damage") to its columns throughout the height of the structure and even at small hazard levels, as compared to the other perimeter-frame designs. The lowest probability of damage (or largest probability of "no damage") to the columns, beams, and partitions of the perimeter-frame designs occurs in the variant conservatively designed using the same beams and columns throughout (Variant 2, Fig. 6.16). The space-frame baseline design (Variant 6, Fig. 6.18) acquires a significant amount of damage to the columns in the first story, but it better withstands damage to the beams and partitions as compared to the perimeter-frame designs. This suggests that either Variant 2 or Variant 6 is likely to have the least expensive repairs. Also, all these damage plots show that significant damage to wallboard partitions has an early onset (at all story levels) for most of the variants considered in this study. As will be shown later, this early onset of damage in the nonstructural elements is a major contributor to the mean total repair costs for low levels of shaking and to *EAL*, since these lower-level ground motions are more likely to occur.

A more detailed comparison of Variants 1 (Fig. 6.15) and 2 (Fig. 6.16) demonstrates what is gained and lost with the more conservative design that uses the same beams and columns throughout the height of the building. The design of Variant 2 with the same structural members over the height of the building makes the building significantly stiffer and stronger than required by the minimum code requirements. This design change specifically causes the members to be larger and stronger in the upper stories. This results in lower interstory drifts in the upper two stories of Variant 2, causing the building to suffer less damage in these stories. However, the stiffening and strengthening of the upper stories causes the damage to concentrate more in the first-story columns, thus causing more structural and nonstructural damage in the first story. An alternative to the conservative design of Variant 2 is the design of Variant 9, which does not comply with the code's strong-column weak-beam (SCWB) provisions. The columns of stories 1–4 have lower probability of "no damage" (and have a higher probability of reaching the severe and collapse damage states in stories 1–2) for Variant 9 than for Variant 2; the beams in stories 2–4 for Variant 9 are also more damaged. Also, the partitions at the top three stories of this non-code-conforming design are more significantly damaged at lower levels of ground shaking.

These damage plots are also an effective way to compare modeling choices of the benchmark building. Some modeling assumptions can lead to over- (conservative) or under- (non-conservative) estimation of the structural response. Variant 11 assumes that all the concrete is pre-cracked and is not expected to perform as well as the perimeter-frame baseline model (Variant 1). A comparison of Figures 6.15 and 6.20 shows that the structural members of Variant 11 have a higher average probability of reaching more severe damage states throughout the height of the building; the partitions for Variant 11 have an earlier onset and a higher probability of reaching the significant damage state. This model is therefore a conservative representation of the baseline perimeter-frame design.

Another alternative to the baseline model is ignoring the effect of the gravity-load-resisting frames, which results in an overall loss of strength and stiffness and an overall increase in structural response. Variant 12, which does not model the gravity-load-resisting frames, has a higher average probability of its components being damaged for nearly all the hazard levels, when compared to the baseline design (Variant 1). The most notable difference between Figures 6.15–6.21 can be seen in the wallboard partitions, where the average probability of being damaged exceeds 0.50 and 0.85 (both occur at story level (3) at only the second and third smallest hazard levels, respectively). Again, this model overestimates the structural response.

All the above-mentioned variants have used fiber models for the structural analysis. Another type of model, the lumped-plasticity model is described in Section 5.4 and has been shown to better capture collapse behavior (Haselton 2006). The structural analysis results using the lumped-plasticity models are not realistic at low hazard levels and so the initial stiffness used in these models was adjusted to match the results of the fiber model at these hazard levels. The damage results in Figures 6.22–6.24 correspond to Variants 13–15 that use an initial stiffness defined as the secant stiffness through the yield point (K_{yld}), through 60% and through 40% of the yield moment (K_{stf}), respectively. Variant 13 underestimates the response of the structural components at low hazard levels, where there is little light or no damage until the 2%-in-50-years event ($S_a = 0.82g$); the behavior of the structural components is captured a little better with Variant 14 and is best portrayed with Variant 15. The lumped-plasticity models overestimate the response of the nonstructural components at low hazard levels (most notably in Variant 13, Fig. 6.22), but the damage results of Variant 15 are most similar to the baseline fiber model.

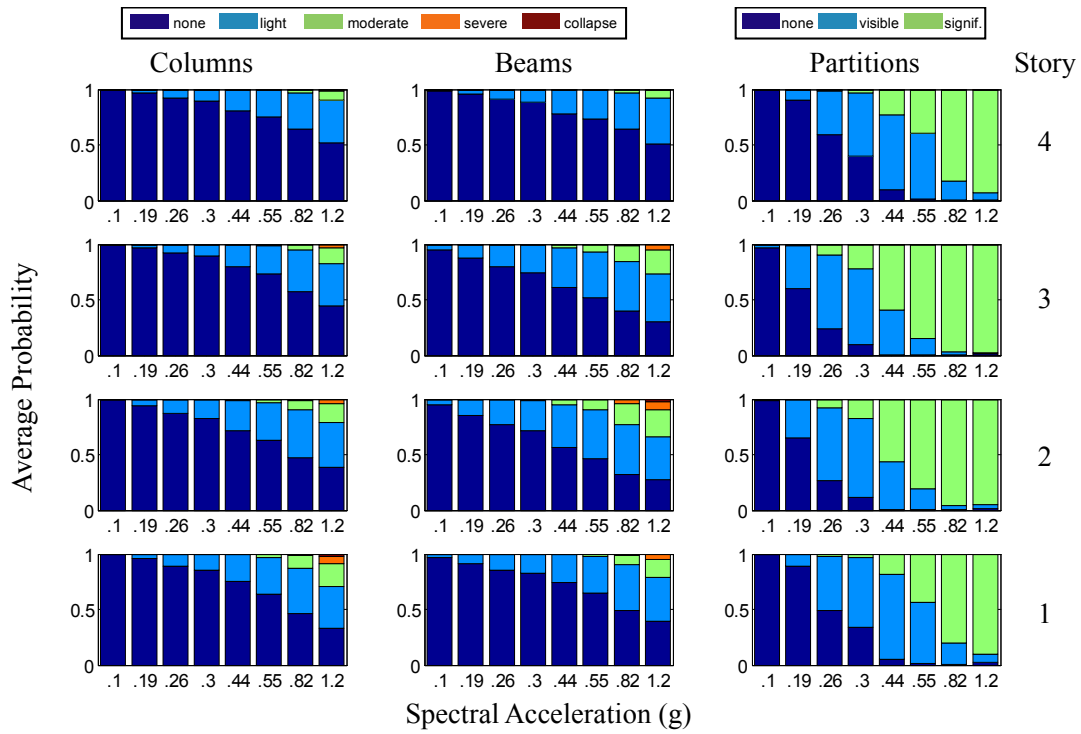


Fig. 6.15 Average probabilities of damage per story level for Variant 1.

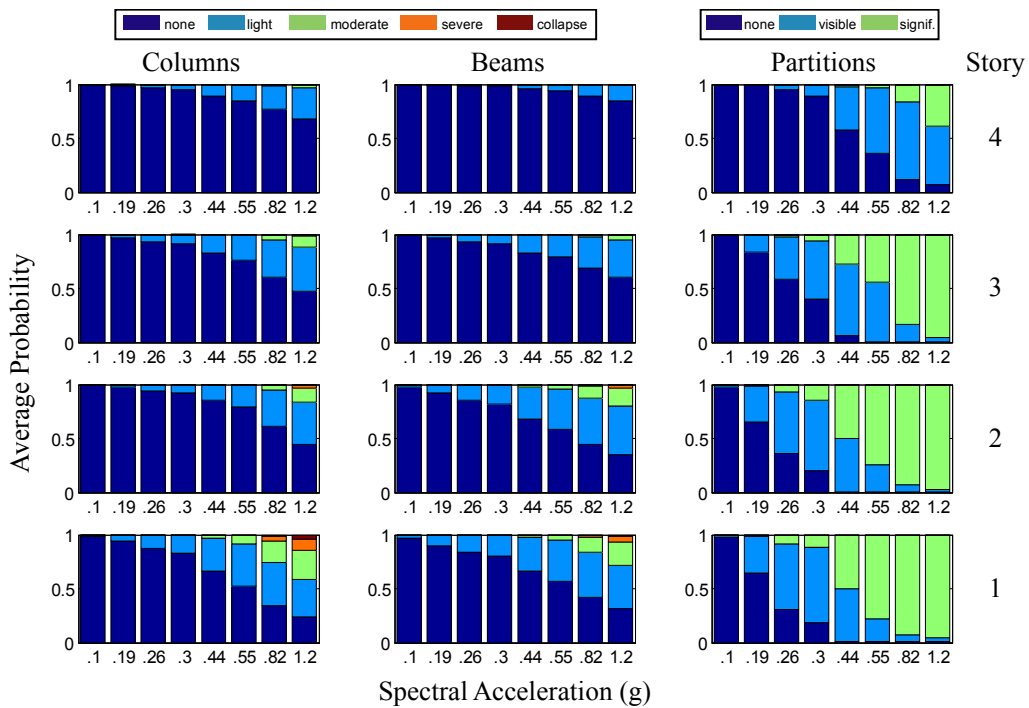


Fig. 6.16 Average probabilities of damage per story level for Variant 2.

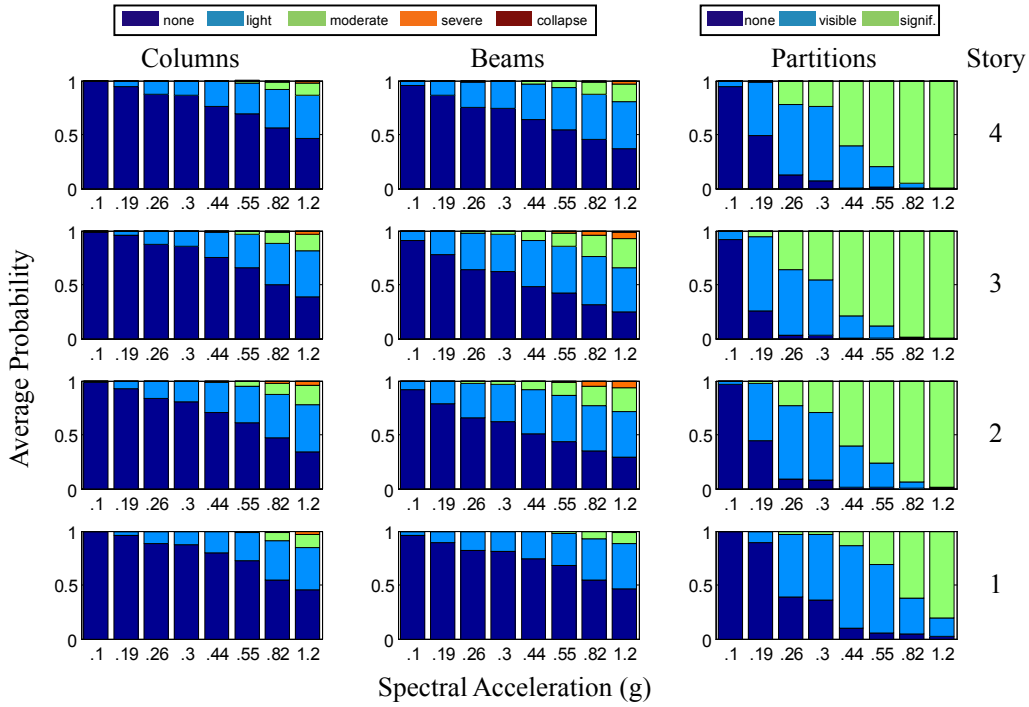


Fig. 6.17 Average probabilities of damage per story level for Variant 3.

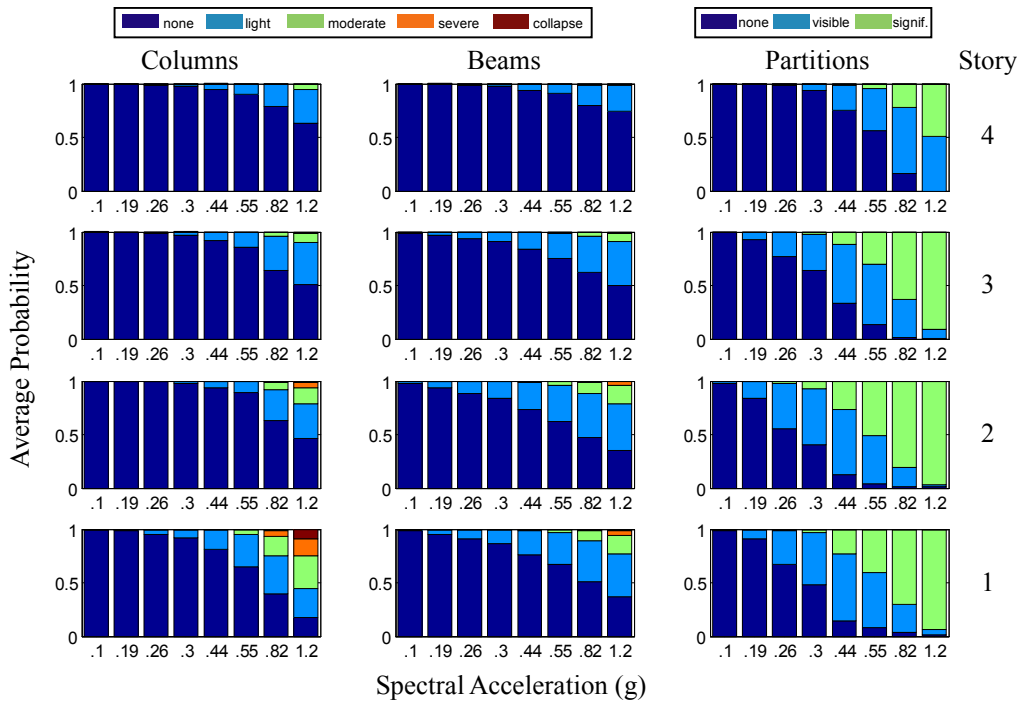


Fig. 6.18 Average probabilities of damage per story level for Variant 6.

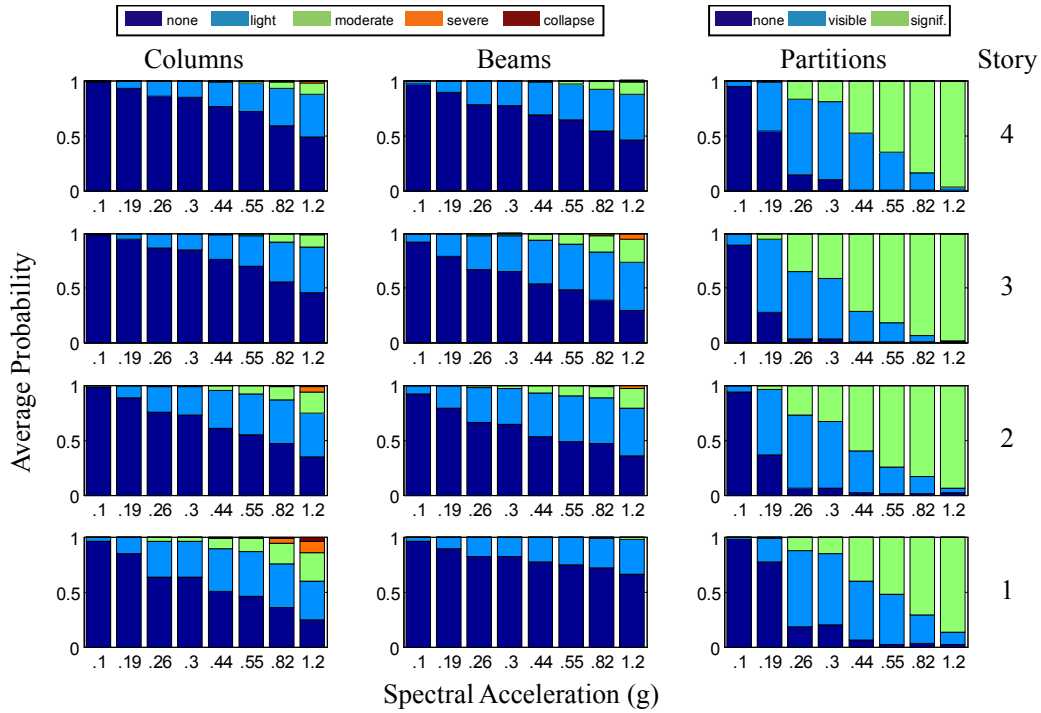


Fig. 6.19 Average probabilities of damage per story level for Variant 9.

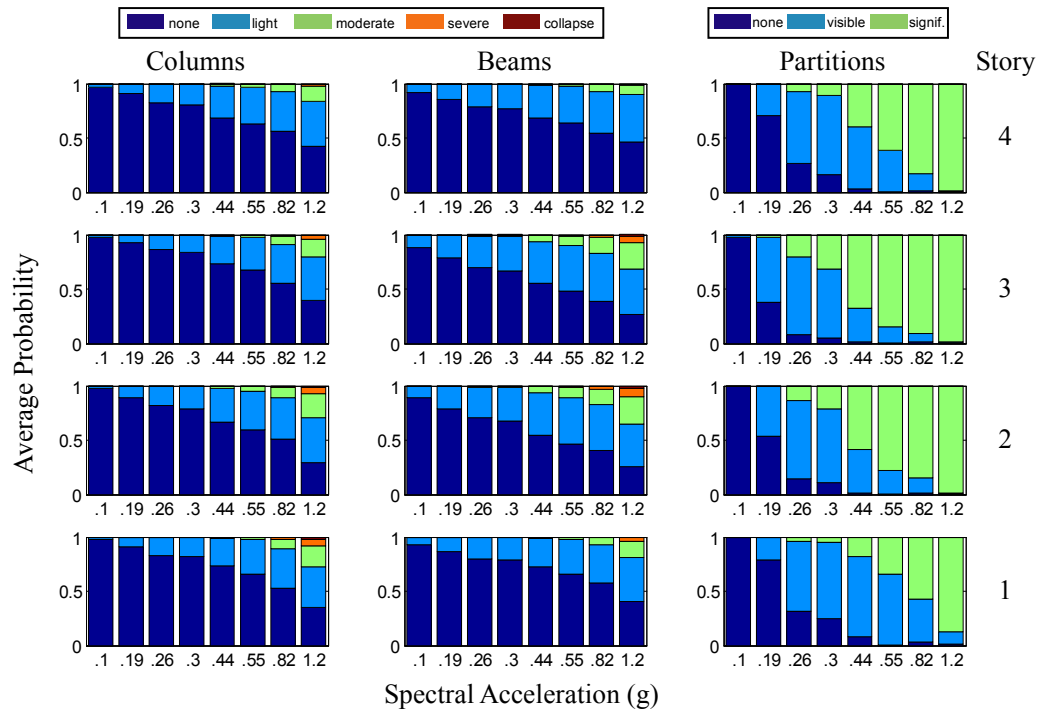


Fig. 6.20 Average probabilities of damage per story level for Variant 11.

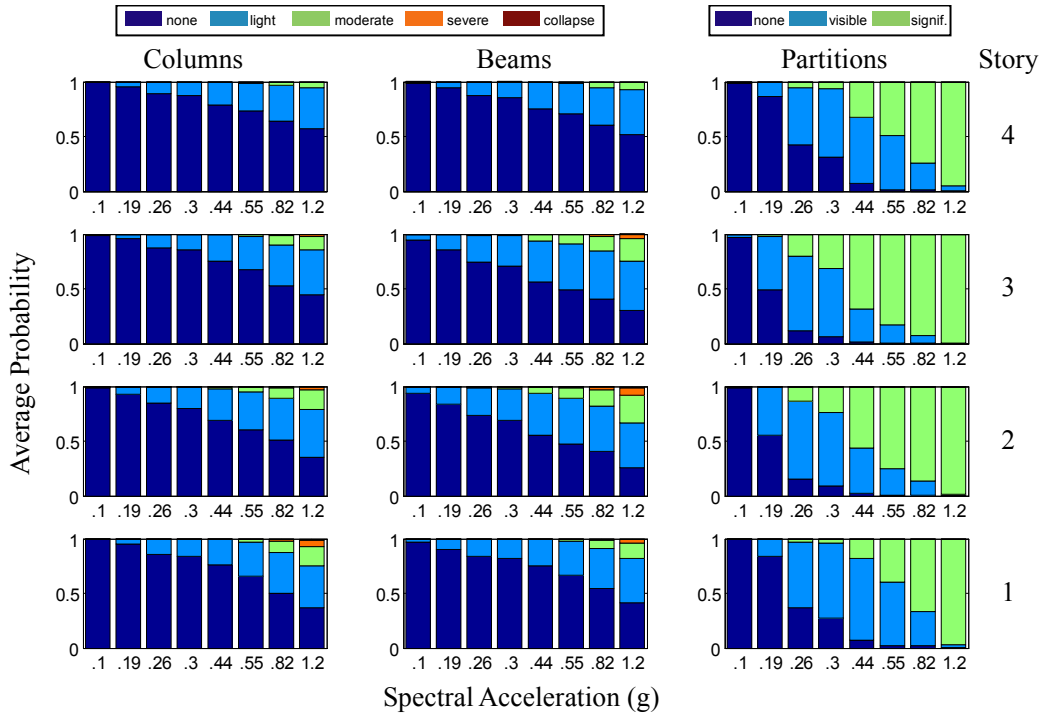


Fig. 6.21 Average probabilities of damage per story level for Variant 12.

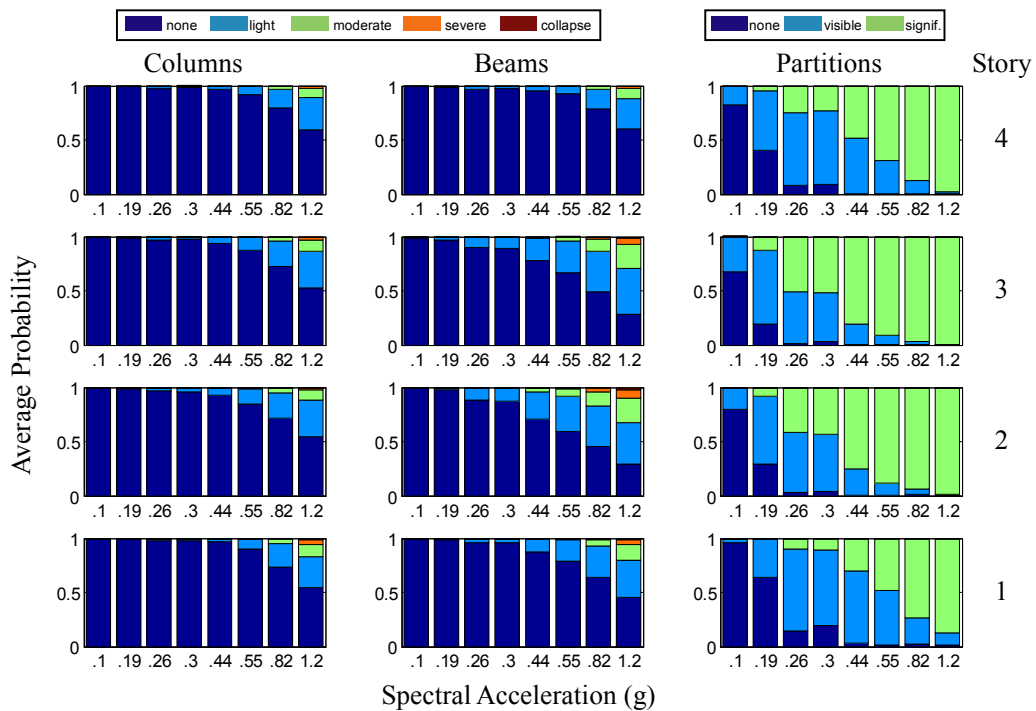


Fig. 6.22 Average probabilities of damage per story level for Variant 13.

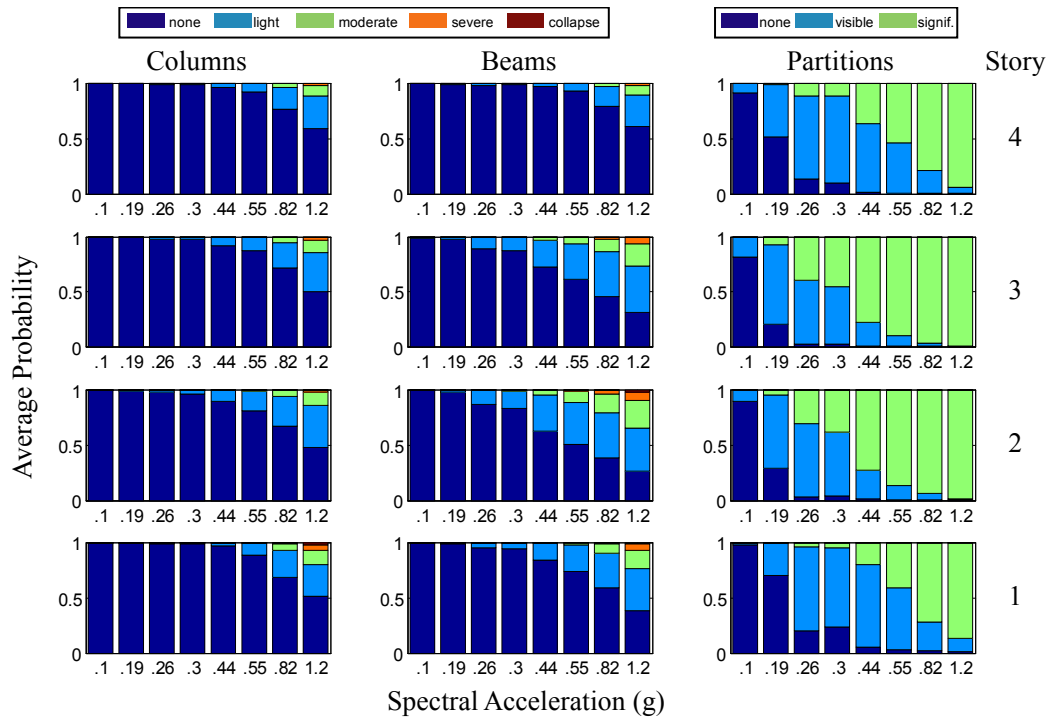


Fig. 6.23 Average probabilities of damage per story level for Variant 14.

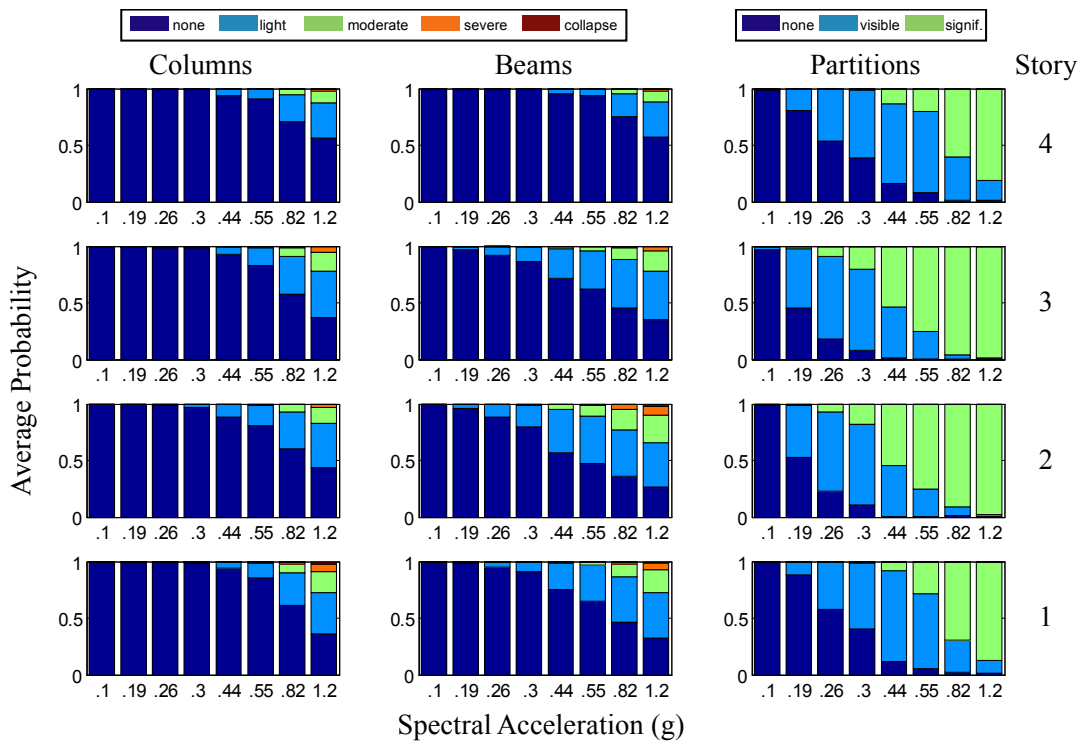


Fig. 6.24 Average probabilities of damage per story level for Variant 15.

6.4 LOSS RESULTS: SEISMIC VULNERABILITY FUNCTIONS

The methodology for calculating seismic vulnerability functions is described in detail in Section 2.7.1. The vulnerability functions for the design variants are shown and discussed in Sections 6.4.1 and 6.4.2 below. The mean total repair cost given no collapse is the sum of the mean repair costs of the considered structural and nonstructural assembly groups, which is then scaled by inflation, location, and overhead and profit factors. A breakdown for the mean total repair cost given no collapse against $IM=S_a$ is given in Figures 6.25–6.29.

The cost contribution curves in these figures increase monotonically with increasing S_a for all the building assembly groups except for one; the contribution of paint repair costs plateaus for all of the variants (occurring at about $S_a=0.26g$ for most variants), which is the result of needing to repaint undamaged areas to achieve a uniform appearance (Section 6.1.4). The cost to repair beams is greater than the cost to repair columns at most hazard levels for all the variants designed using the SCWB provision, except for Variants 2 (Fig. 6.25b). The additional axial load from the heavier structural members in the upper top stories for Variant 2 reduces the flexural capacity of the columns in the first story, which results in costlier repairs for the columns than for the beams. Variant 9, which ignores the SCWB provision, is expected to have more yielding and costlier repair efforts in its columns (rather than for its beams), which is shown to be true in Figure 6.27a.

The cost contribution figures shown below demonstrate that the contribution of wallboard partitions is significant for all hazards levels and that the contributions of glazing, column-slab connections, sprinkler piping, ceilings, and elevators do not play a major role in the total repair costs. The largest repair loss for nonstructural components corresponds to the minimum-code design (Variants 3, Fig. 6.26a) and the non-code-conforming design (Variant 9, Fig. 6.27a); the smallest repair loss for nonstructural components to the baseline perimeter- (Variant 1, Fig. 6.25a) and space-frame designs (Variant 6, Fig. 6.26b) and to the design that uses the same beams and columns throughout the height of the building (Variant 2, Fig. 6.25b). The lumped-plasticity models with a secant stiffness through the yield moment (Variant 13, Fig. 6.28b) and through 60% of the yield moment (Variant 14, Fig. 6.29a) do not accurately predict the structural response at low levels of ground shaking and leads to large economic losses for the nonstructural components, which are most likely damaged components at these levels. Note that the losses due to damaged wallboard partitions are comparable to the losses associated with structural damage

for the space-frame design (Variant 6, Fig. 6.26b) because the number of lateral resisting frames is greater in the space-frame design; this accounts for the increase in repair costs of beams and columns for this variant.

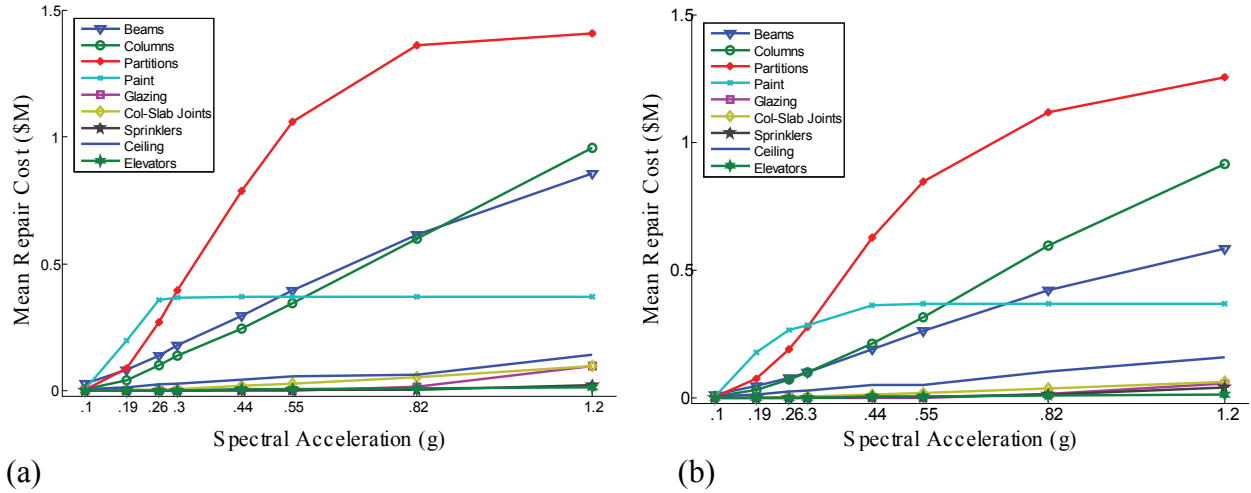


Fig. 6.25 Contributions to mean total repair cost for (a) Variant 1 and (b) Variant 2.

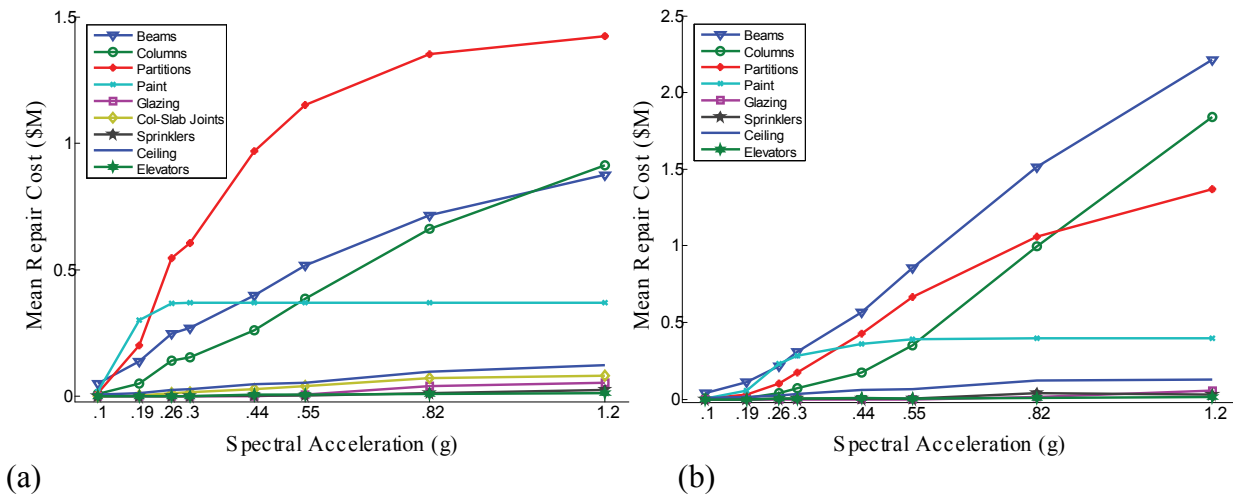


Fig. 6.26 Contributions to mean total repair cost for (a) Variant 3 and (b) Variant 6.

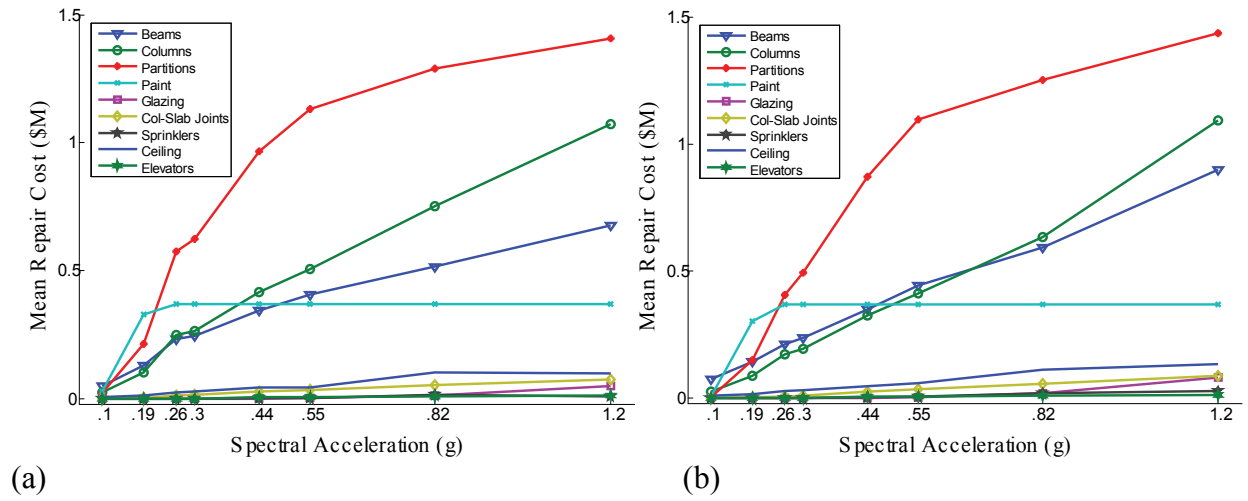


Fig. 6.27 Contributions to mean total repair cost for (a) Variant 9 and (b) Variant 11.

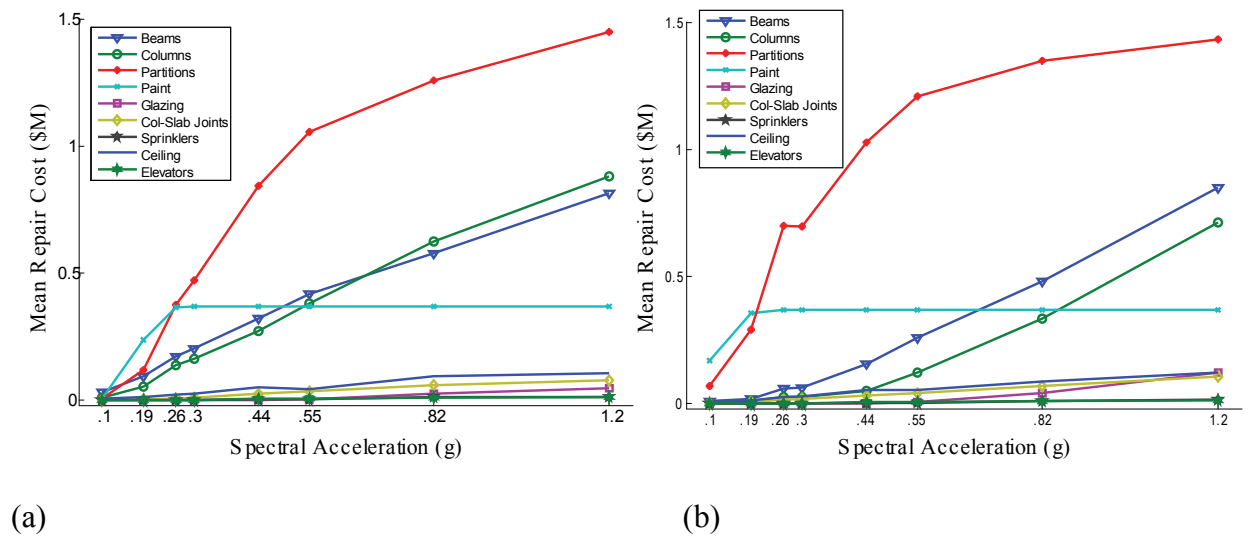


Fig. 6.28 Contributions to mean total repair cost for (a) Variant 12 and (b) Variant 13.

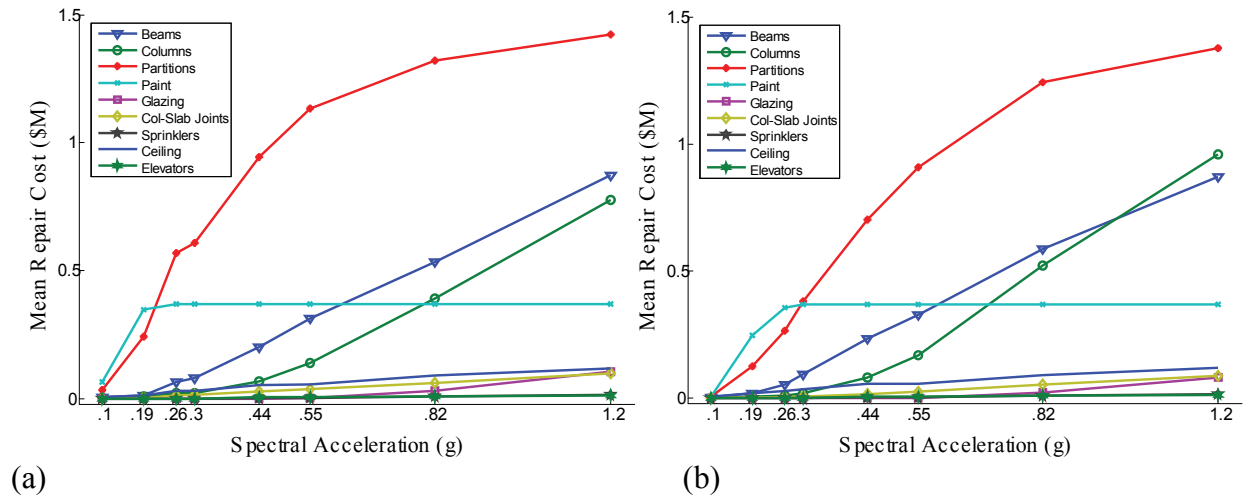


Fig. 6.29 Contributions to mean total repair cost for (a) Variant 14 and (b) Variant 15.

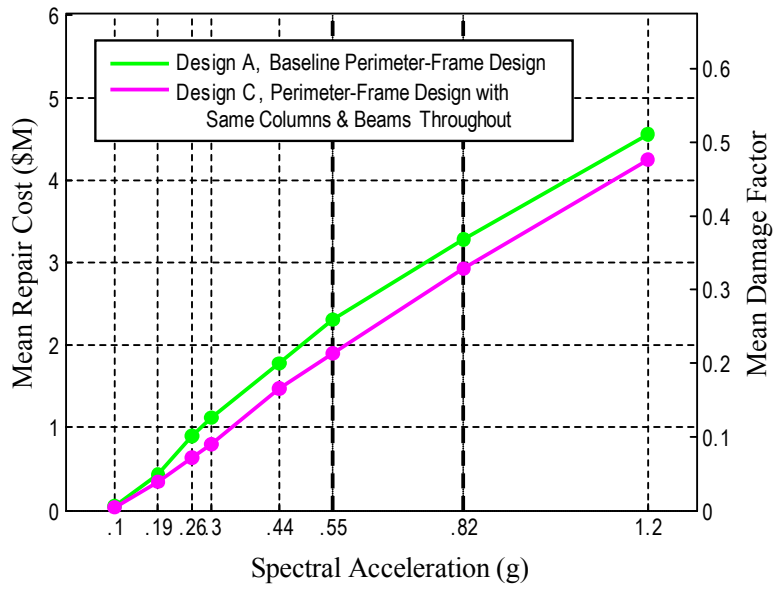
6.4.1 Vulnerability Functions: Design Comparisons

The vulnerability functions (using $C_{op}=0.175$; $C_i=1.13$; and $C_L=1.085$) for variants having different structural designs are shown in Figures 6.30 and 6.31, where the black dashed vertical lines at $S_a = 0.55g$ and $S_a = 0.82g$ correspond to the 10%-in-50-years event (475-year return period) and the 2%-in-50-years event (2475-year return period), respectively, for the site. The mean total repair cost is represented in these figures as \$USD and as a ratio over the mean building replacement cost, known as the *mean damage factor*. Some interesting comparisons of design and modeling choices are made from these results.

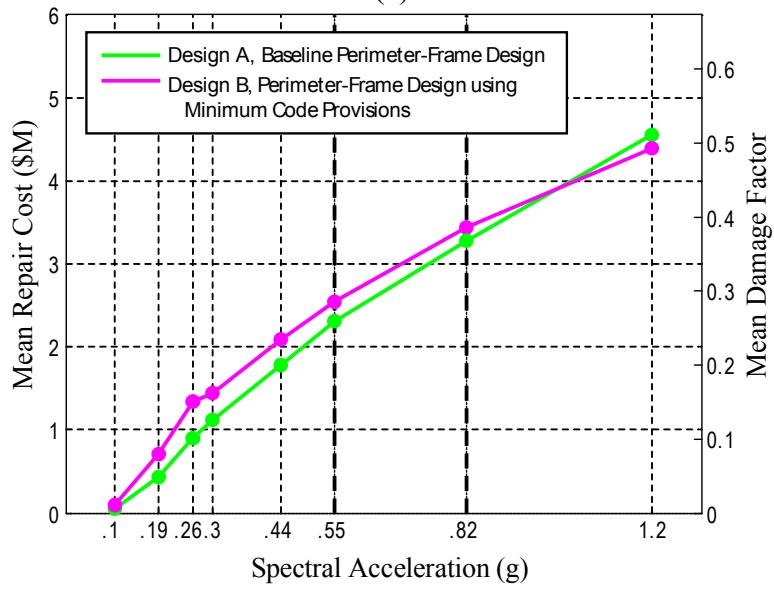
In Figure 6.30a, the curve for Variant 1 (green) corresponds to a perimeter-moment-frame design, considering the gravity frame and a flexible base; the curve for Variant 2 (magenta) corresponds to a similar structural model except that the structural design uses the same beams and columns throughout, which makes the structure stiffer and more conservative. This more conservative design variant has smaller structural responses and thus smaller mean losses at every level of S_a . Another interesting comparison in Figure 6.30b shows the vulnerability functions for Variants 1 (green) and 3 (magenta). These variants are both perimeter-frame designs, except that Variant 3 is a code-minimum design. The code-minimum design has higher losses for every level of S_a , except at $S_a=1.0g$ because losses associated with building collapse significantly contribute to mean total repair cost at this hazard level and because the probability of collapse for the code-minimum design is smaller than for the baseline design at this level.

In Figure 6.31a, the green curve again corresponds to Variant 1; the perimeter-moment-frame baseline design and the curve for Variant 6 (magenta) correspond to the space-frame baseline design. Since up-front costs are different for these designs, the vulnerability function is plotted using only the mean damage factor when comparing these two variants. The space-frame design should better withstand lateral motions, since it has lateral-force-resisting moment frames on every grid line, which is consistent with Figure 6.31a up until $S_a = 0.55g$. The beams and columns are heavily damaged at the two highest hazard levels for simulation ($S_a = 0.82g$ and $S_a = 1.2g$) and because there are more of them to repair in the space-frame design than in the perimeter-frame design, their contributions to the total repair cost dominate the contributions of the other damageable components. In fact, the contribution to mean total repair cost from the beams surpasses that of the partitions in the space-frame design at all levels of S_a , which does not occur in any of the perimeter-frame variants.

One building design, Variant 9, was chosen to investigate the importance of the strong-column weak-beam design provision (ACI 2002). Figure 6.31b shows this design in addition to its code-conforming counterpart, Variant 2. The losses increase at every hazard level when the SCWB provision is ignored. In fact, the largest value of mean repair cost is 1.5 times larger than the mean repair cost for any of the other designs considered in this section. This comparison is also significant to the expected annual loss, which is found in Section 6.5.

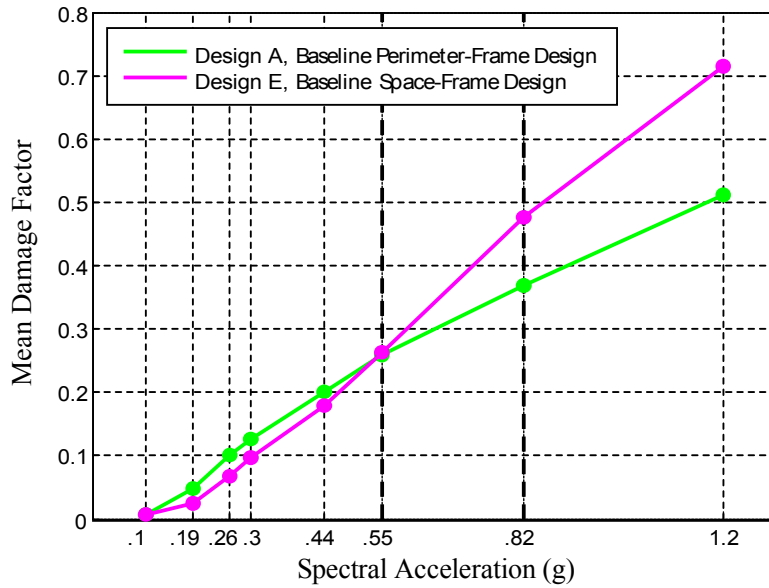


(a)

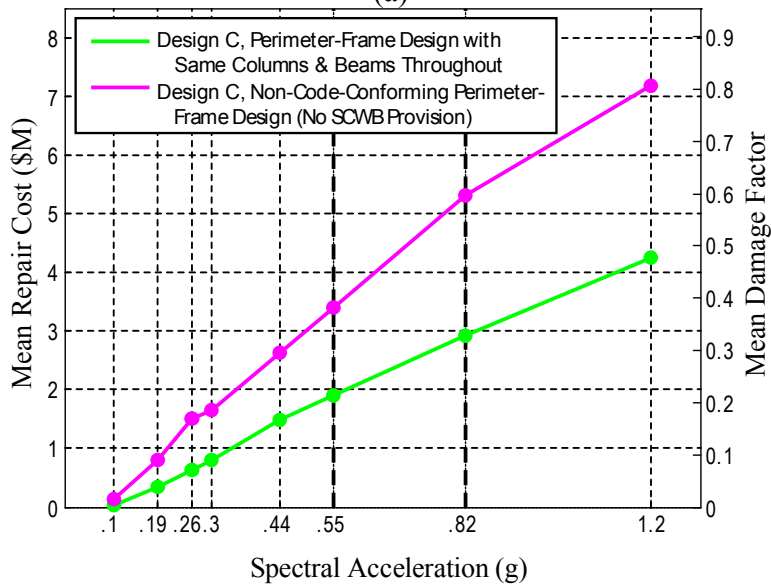


(b)

Fig. 6.30 Vulnerability functions for (a) Variants 1 and 2 and (b) Variants 1 and 3.



(a)



(b)

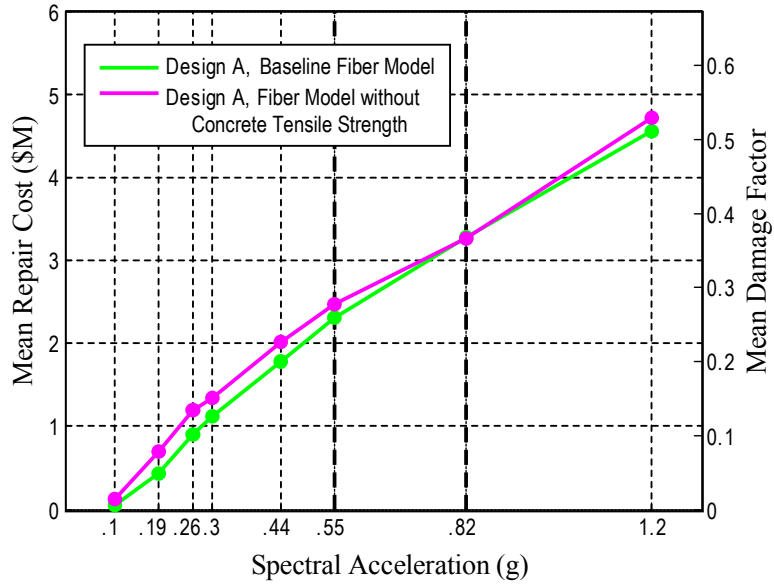
Fig. 6.31 Vulnerability functions for (a) Variants 1 and 6 and (b) Variants 2 and 9.

6.4.2 Vulnerability Functions: Modeling Comparisons

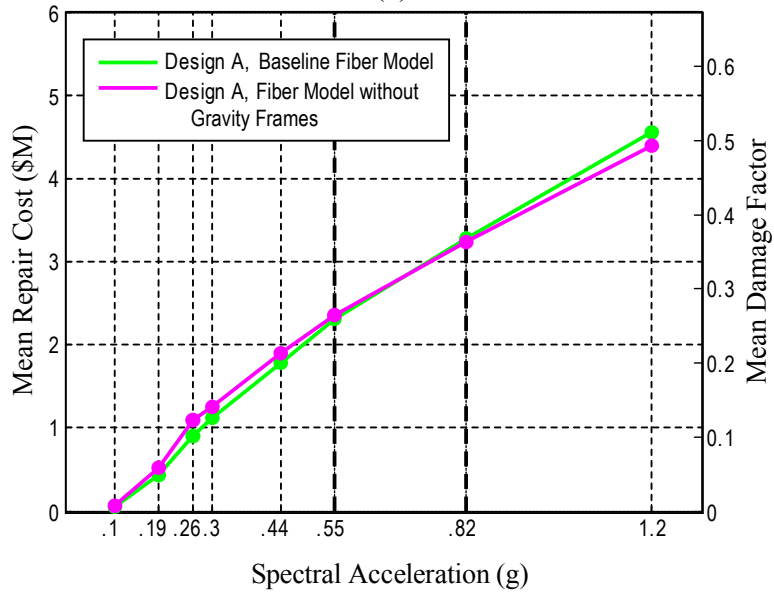
The vulnerability functions for variants having the same design (Design A), but different structural models are shown in Figure 6.32 and Figure 6.33, where, again the black dashed vertical lines correspond to the 10%-in-50-years and the 2%-in-50-years events. Some interesting comparisons are made from the results of variants with varied modeling choices.

In Figure 6.32a, the curve for Variant 11 (magenta) corresponds to a perimeter-moment-frame design excluding the tensile strength of the concrete. This structural model assumes that all the concrete is pre-cracked and therefore is expected not to perform as well as the perimeter-frame baseline model (Variant 1), which can be seen to have mean repair costs that are 5–40% smaller except at $S_a = 0.82g$, where they are very close numerically. A comparison of Variants 1 and 12 (Fig. 6.32b) shows the significance of modeling the gravity frame. Variant 1 (green) includes the gravity frame in the model, which adds stiffness and strength relative to Variant 12, which ignores the gravity frame. One would expect to see larger structural responses without the gravity frame (Variant 12), and thus larger mean losses; this expectation is borne out in Figure 6.32b, except at the largest hazard levels, but the differences are not significant.

In Figure 6.33, the curve for Variant 13 (magenta) corresponds to the baseline perimeter-moment-frame design using a lumped-plasticity model with initial stiffness defined as the secant stiffness through the yield point (K_{yld}); the curves for Variants 14 (blue) and 15 (black) correspond to a similar design except that the initial stiffness is defined as the secant stiffness that corresponds to 60% and 40%, respectively, of the yield moment (K_{stf}); Variant 1 (green) is given again in this plot to compare the baseline fiber model with these lumped-plasticity models. Note that the fiber model results are consistent with the ones from the lumped-plasticity model using K_{stf} until $S_a = 0.19g$, where the two curves diverge and the mean total repair costs become greater than for the fiber model for all values of $S_a > 0.19g$. This is consistent with the behavior shown in the static pushover curves of Chapter 5 (Fig. 5.33). The lumped-plasticity models using K_{yld} and a secant stiffness corresponding to 60% of the yield moment result in greater losses at low levels of ground shaking and lower losses at higher levels of ground shaking compared with the fiber model; this switch occurs near $S_a = 0.40g$.



(a)



(b)

Fig. 6.32 Vulnerability curves for (a) Variants 1 and 11 and (b) Variants 1 and 12.

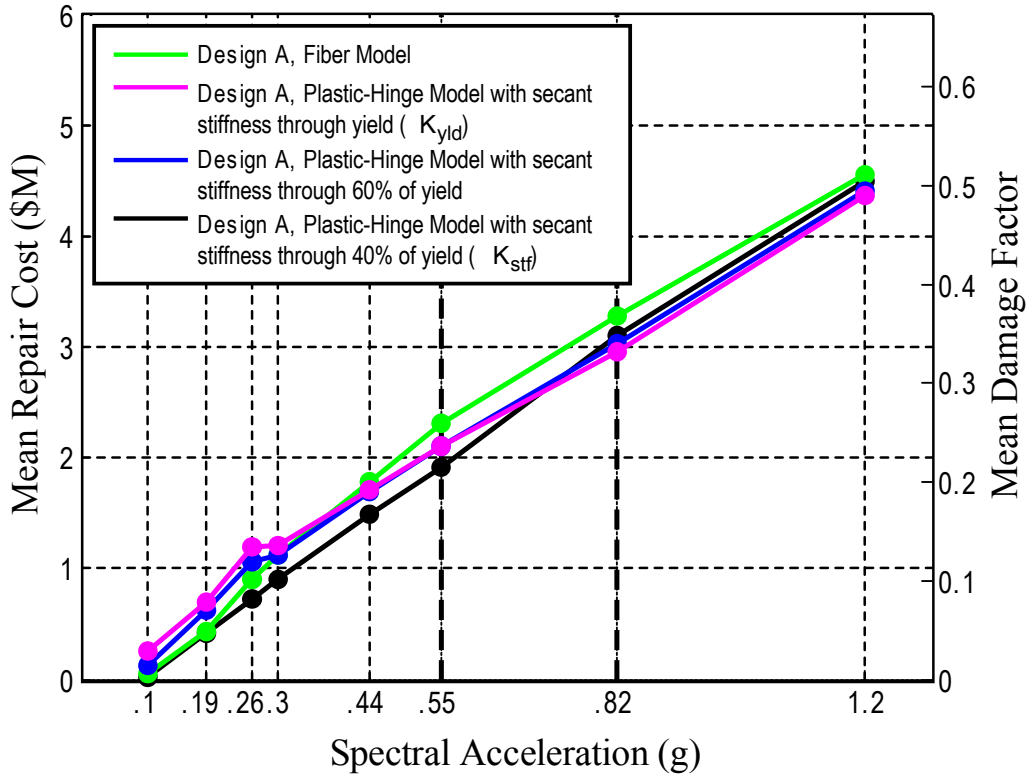


Fig. 6.33 Vulnerability curves for Variants 1, 13, 14, and 15.

6.5 LOSS RESULTS: MDF, PML, AND EAL

The vulnerability functions, the hazard function, and the uncertainty of the losses may be used to compute other loss results that are valuable to stakeholders, such as mean damage factor (MDF), probable maximum loss (PML), and expected annual loss (EAL). MDF is defined as the ratio of the expected value of repair cost to the replacement cost of the building for a given seismic intensity measure. PML is used to describe the amount of loss associated with a large, rare event. *EAL* is the average annual magnitude if loss, which is described in Section 2.3.5.1. The MDF, PML, and *EAL* results for all design variants are given in the following two sections.

6.5.1 MDF and PML for All Design Variants

The mean damage factor, or MDF, is simply calculated as the ratio of the mean loss to the replacement cost of the building for a given intensity measure. The MDF results for all design variants for the 10%-in-50-years event ($S_a(T_1)=0.55g$) are given in Table 6.5. These results range between 21–29% for code-conforming designs, and equal 38% for the non-code-conforming

design. The MDF values estimated in this study were compared with results estimated using three other predictive models: ATC-13 (1985), HAZUS (NIBS and FEMA 2003), and ST-Risk 4.1.1 (Risk Engineering Inc. 2004). The seismic intensity measures used in these models were converted (see Appendix K) to compare the mean damage factor results with those of Table 6.5. ATC-13 (1985) estimates that the damage factor is 8–25% for a building comparable to the benchmark building; ST-Risk 4.1.1 (Risk Engineering Inc. 2004) gives a mean damage factor of 11–16%; and HAZUS (NIBS and FEMA 2003) calculates MDF=36%. Although there is general agreement with the results calculated by all loss models, including the PEER method, the comparison is imperfect for various reasons, including: (1) the loss models use different *IMs*, (2) ATC-13 and HAZUS are category-based approaches, and (3) ATC-13 and ST-Risk use vulnerability information on pre-1982 earthquakes. The details of this comparison are given in Appendix K.

Although there is no one definition for PML that is agreed upon, this term is generally used to describe the amount of loss associated with a large, rare event such as a shaking with 10% probability of exceedance in 50 years (Porter et al. 2004). A lognormal distribution is used to model the total repair cost, and to estimate the loss with 10% exceedance probability at intensity $S_a(T_I)=0.55g$, taken here as PML. The PML results for all design variants are given in Table 6.5. These results range between 29–36% for code-conforming designs, and equals 69% for the non-code-conforming design. These results are double the PML results estimated using ST-Risk (approximately 15–20%). As stated above, remember that the comparison between the two loss models is not exact.

Table 6.5 Design variant descriptions and corresponding MDF results at IM having 10% exceedance probability in 50 yrs ($S_a = 0.55g$), and PML results.

Variant	Design	Design & Model Description	MDF _{$S_a=0.55g$}	PML
1	A	Perimeter frame, designed with expected overstrength; fiber model, concrete tensile strength modeled, gravity frame included.	0.26	0.34
2	C	Same as Design A, but designed with uniform beams and columns over height; modeled same as Index 1.	0.21	0.29
3	B	Same as Design A, but designed with bare code-minimum strengths; modeled same as Index 1.	0.29	0.33
6	E	Baseline space frame; fiber model, concrete tensile strength modeled.	0.26	0.32
9	D	Same as Design C, but no SCWB provision enforced (not code-conforming); modeled same as Index 1.	0.38	0.69
11	A	Same as Design A; modeled same as Index 1, but concrete tensile strength and stiffness not modeled.	0.28	0.36
12	A	Same as Design A; modeled same as Index 1, but gravity frame not modeled.	0.26	0.34
13	A	Same as Design A; plastic-hinge model with secant stiffness through yield (K_{yld}).	0.24	0.32
14	A	Same as Design A; plastic-hinge model, with secant stiffness through 60% of yield.	0.24	0.32
15	A	Same as Design A; plastic-hinge model with secant stiffness through 40% of yield (K_{st}).	0.21	0.30

6.5.2 EAL for All Design Variants

A table of *EAL* results for the four variants considered in the previous section is shown below in Table 6.6. The potential for financial loss is considerable. Loss modeling considering the moment-frame beams and columns, the column-slab connections, the wallboard partitions, the acoustical ceiling, the sprinkler piping, the exterior glazing, and the interior paint, indicates that

mean annual losses from earthquakes are likely in the range of \$52,000–\$97,100 for the various code-conforming benchmark building designs, or roughly 1% of the replacement cost of the building. Some important lessons learned from these simulations that may be transferable to other projects include the following:

- Expected annual loss (*EAL*) estimates are highly sensitive to the manner of estimating the initial stiffness of the structural elements. The *EAL* for the baseline perimeter-frame model using the fiber model is \$66,600 (0.75% of the assumed replacement cost of \$8.9M); the *EAL* for the same design using the lumped-plasticity model with secant stiffness through yield (K_{yld}) is \$97,100 (1.1 % of replacement cost); the *EAL* using a secant stiffness through 60% and 40% of yield (K_{stf}) is \$82,400, and \$57,400, (0.9%, and 0.6% of replacement cost), respectively. If a plastic-hinge approach is used to model structural behavior, the initial stiffness of the hinge element should be calibrated to test data and chosen carefully (similar to K_{stf}) to better model the building stiffness under frequent ground motions.
- Losses are sensitive to other modeling choices. If the tensile strength of the concrete is ignored by assuming all pre-cracked concrete (Variant 11) (this changes the initial stiffness of the element model), *EAL* increases almost 40%. If the gravity frame is ignored in the structural model (Variant 12), thus neglecting the contribution of its strength and stiffness, increases almost 15%.
- Variant 2 (Design C), a more conservative design than Variant 1 (Design A) because it uses the same beams and columns throughout the building, produces an *EAL* that is 22% smaller. Variant 3 (Design B), a code-minimum design, produces an *EAL* that is 44% larger.
- The strong-column weak-beam provisions are ignored for Variant 9 (Design D), which drastically increases the *EAL* of the baseline model (Variant 1, Design A) by 70%.

Table 6.6 Design variant descriptions and corresponding EAL results.

Variant	Design	Design & Model Description	$S_a(T_I)$	Mean: Mean Total Repair Cost for S_a (g) in \$M								EAL (\$)
				COV: Coefficient of Variation of Repair Cost for S_a (g)								
				0.1	0.19	0.26	0.3	0.44	0.55	0.82	1.2	
1	A	Perimeter frame, designed with expected overstrength; fiber model, concrete tensile strength modeled, gravity frame included.	Mean	0.06	0.43	0.9	1.12	1.78	2.31	3.28	4.56	66,585
			COV	0.52	0.17	0.15	0.16	0.2	0.24	0.33	0.36	
2	C	Same as Design A, but designed with uniform beams and columns over height; modeled same as Index 1.	Mean	0.04	0.35	0.64	0.8	1.48	1.9	2.92	4.25	51,933
			COV	0.62	0.18	0.16	0.17	0.21	0.27	0.41	0.46	
3	B	Same as Design A, but designed with bare code-minimum strengths; modeled same as Index 1.	Mean	0.1	0.71	1.34	1.44	2.09	2.54	3.43	4.39	95,656
			COV	0.37	0.13	0.12	0.12	0.11	0.13	0.23	0.35	
6	E	Baseline space frame; fiber model, concrete tensile strength modeled.	Mean	0.06	0.22	0.61	0.87	1.6	2.36	4.29	6.43	49,422
			COV	0.51	0.25	0.15	0.14	0.16	0.17	0.19	0.16	
9	D	Same as Design C, but no SCWB provision enforced (not code-conforming); modeled same as Index 1.	Mean	0.13	0.8	1.51	1.64	2.63	3.41	5.31	7.18	112,930
			COV	0.36	0.33	0.4	0.51	0.64	0.66	0.53	0.34	
11	A	Same as Design A; modeled same as Index 1, but concrete tensile strength and stiffness not modeled.	Mean	0.12	0.7	1.19	1.34	2.01	2.47	3.26	4.72	92,721
			COV	0.35	0.13	0.13	0.14	0.18	0.22	0.33	0.33	
12	A	Same as Design A; modeled same as Index 1, but gravity frame not modeled.	Mean	0.06	0.52	1.09	1.25	1.9	2.35	3.23	4.39	76,069
			COV	0.49	0.15	0.14	0.15	0.19	0.23	0.34	0.38	
13	A	Same as Design A; plastic-hinge model with secant stiffness through yield (K_{yld}).	Mean	0.26	0.69	1.20	1.20	1.71	2.11	2.96	4.37	97,066
			COV	0.18	0.16	0.15	0.16	0.21	0.26	0.38	0.39	
14	A	Same as Design A; plastic-hinge model, with secant stiffness through 60% of yield.	Mean	0.12	0.63	1.07	1.13	1.69	2.11	3.03	4.41	82,433
			COV	0.29	0.15	0.15	0.17	0.21	0.26	0.37	0.38	
15	A	Same as Design A; plastic-hinge model with secant stiffness through 40% of yield (K_{stf}).	Mean	0.03	0.42	0.72	0.91	1.49	1.91	3.11	4.50	57,363
			COV	0.75	0.17	0.17	0.19	0.25	0.3	0.36	0.37	

6.6 LOSS RESULTS: EXPECTED ANNUAL LOSS DUE TO FATALITIES

The safeguarding of human lives is a top priority for engineers when designing buildings. That said, the estimation of human fatalities and/or injuries during a seismic event has had a limited role in current and past design practice. This section proposes a methodology for estimating fatalities for a specific building that can be used as a decision variable (DV) in performance-

based earthquake engineering. The methodology presented incorporates many efforts toward this end from the past 30 years.

6.6.1 History of Fatality Modeling

The earliest publication (known to the authors) to propose estimates of earthquake casualties is a report by NOAA for the Office of Emergency Preparedness (1972). This report lays the groundwork for fatality modeling, and outlines several important factors that should be included in casualty and serious-injury models: (1) empirical data from relevant events, such as data from damaging U.S. earthquakes, or from comparable events in other countries; (2) building inventory (e.g., number of concrete versus number of steel frame buildings) and/or the physical properties of an individual building (e.g., material, height, gross area); and (3) population estimates including the population of a study area (e.g., a city or county), and the number of building occupants of a specific building. These factors as well as a few others highlighted in the earthquake morbidity/mortality literature are addressed in more detail in the following sections.

6.6.1.1 Empirical Data

The work by NOAA (1972) summarizes the casualties due to major U.S. earthquakes between 1886–1971; their empirical data are reproduced in Table 6.7. This table does not describe the injury mechanisms (e.g., crushed by fallen ceiling, head injured by fallen bricks from damaged masonry wall), which we and others (Wagner et al. 1994; Jones et al. 1990; Mahue-Giangreco et al. 2001) consider to be extremely important for accurate building-specific fatality modeling. However, the NOAA data do provide a means to forecast the numbers of fatalities and serious injuries in future events having similar attributes and comparable building stocks as those listed in Table 6.7. The last entry of this table contains the number of deaths per 100,000 people due to the Loma Prieta earthquake; this was calculated based on data from coroner and medical examiner reports (Eberhart-Phillips et al. 1994). Other prominent studies propose estimates for future earthquake casualties: (1) FEMA’s collaborative work with the National Security Council (FEMA 1980) provides numbers for deaths and hospitalized victims (categorized by occurrence times) for earthquakes occurring along four different Californian faults; (2) the Applied Technology Council (ATC 1985) provides estimates for fatalities, minor injuries, and serious

injuries based on building type and mean damage factor (including structural and nonstructural components); and (3) the technical manual for FEMA's HAZUS99-SR2 earthquake loss analysis software (HAZUS 2002) provides casualty estimates (ranging from injuries requiring basic medical aid to fatal injuries) for various levels of structural damage (from slight structural damage to complete structural damage with collapse) and based on building type (the extensive list includes 36 building types). The casualty ratios from (2) and (3) are given later in Table 6.8.

There is also vast knowledge of earthquake casualties due to disastrous seismic events from around the world, including studies of the 1976 Guatemala earthquake (Glass et al. 1977); several Japanese earthquakes (Ohta et al. 1986); the 1986 San Salvador, El Salvador earthquake (Durkin 1987); the 1988 Spitak, Armenia, earthquake (Murakami 1992); the 1999 Izmit, Turkey, earthquake (Shoaf and Seligson 2005); and a study of many international seismic events (Coburn et al. 1992). It is problematic to use casualty earthquake data from countries other than the U.S. because of the great differences in the seismic/geophysical characteristics (e.g., Peek-Asa et al. 2003), inconsistencies with construction practices² (e.g., Glass et al. 1977), differences in population density (e.g., Samardjieva and Badal 2002), and/or the disparate levels of earthquake preparedness³ (e.g., Tierney 1990). However, if a careful examination of the international data proves that in some cases similar characteristics may be established between the events in these countries and those in the U.S., it is reasonable to use the empirical data (in those cases) to better inform casualty models of future U.S. events. In cases where data have been categorized by injury mechanisms, damage extent, and/or by building construction type, it is possible to use these results from international events, together with the probabilities of these conditions occurring to estimate casualties for buildings in U.S. seismic regions.

² As an extreme example of the significance of these differences, all the deaths and serious injuries in the village of Santa Maria Cauque after the 1976 Guatemalan earthquake occurred in one-room adobe shelters (Glass et al., 1977).

³ After the 1998 Armenian earthquake, emergency care providers were unable to provide basic forms of treatment to many individuals, leading to deaths and severe injuries that would not have otherwise occurred (Tierney 1990).

Table 6.7 Death and injury ratios from some major U.S. earthquakes. [All entries but last modified from NOAA (1972). Last entry calculated from Loma Prieta mortality data (Eberhart-Phillips et al. 1994) and from 1980 population of seven Bay Area counties (U.S. Census 2006)].

Earthquake	Date	Time of Occurrence	Deaths per 100,000 Population	Injuries per 100,000 Population
Charleston, SC	08/31/1886	21:51	45 outright, 113 total	---
San Francisco, CA	04/18/1906	05:12	320	211
Santa Barbara, CA	06/29/1925	06:42	45	119
Long Beach, CA	03/10/1933	17:54	26	1300
Imperial Valley, CA	03/18/1940	20:37	18	40
Puget Sound, WA	04/13/1949	23:56	1	---
Kern County, CA	07/21/1952	04:52	500	---
Bakersfield, CA	08/22/1952	15:41	3	47
Anchorage, Alaska	03/27/1964	17:36	9	315
San Fernando, CA	02/09/1971	06:01	12 excl. VA Hosp., 64 incl. VA Hosp.	180
Loma Prieta, CA	10/17/1989	17:04	1.4	---

6.6.1.2 Building Characteristics and Occupancy

An extensive study of worldwide earthquakes between 1900–1992 (Coburn et al. 1992), shows that nearly 75% of earthquake-related deaths have been caused by building collapse, and specifically, 7% of total deaths have been caused by the collapse of RC buildings. Additionally, researchers found that 98% of direct earthquake fatalities were caused by structural failures in the 1989 Loma Prieta earthquake. It is therefore important to investigate the relationship between structural behavior and human casualties during earthquakes. Building properties such as type, material, height, and area have an impact on the collapse mechanism of the building due to future seismic events, and play a very important role in casualty modeling (NOAA 1972; Ohta et al. 1986; Jones et al. 1990; Coburn et al. 1992; Murakami 1992; Shoaf and Seligson 2005). However, most of the available empirical earthquake casualty data have not been collected with these characteristics in mind and are therefore not disaggregated by building characteristics. Further, it is difficult to reconstruct these data after the fact due to confidentiality of hospital records and the redistribution of the original population from a study area. Fatality ratios that have been determined with consideration to some characteristics applicable to the benchmark study are given in Table 6.8. This table does not reflect consistent terminology for building types

or the associated damage states, which is typical of the available empirical earthquake data since there is no existing standard for data collection. The fatality modeling effort would be greatly assisted if standardized post-event data collection forms, such as those developed by Choudhury and Jones (1996) would be adopted for U.S. reconnaissance efforts to ensure that valuable, perishable data are not lost.

The occurrence time of an earthquake greatly affects the casualty outcomes. FEMA (1980) describes residential buildings as the safest environment during a seismic emergency and so the safest (fewest casualties) time for a Californian earthquake is the night time. Additionally, FEMA (1980) reports that when an earthquake strikes in the daytime people are more at risk in the early afternoon because they are more vulnerable to the collapse of office buildings and failures of transportation systems. Several models take building occupancy at various times of the day directly into account when calculating earthquake casualties (NOAA 1972; Ohta et al. 1986; Coburn et al. 1992). NOAA's (1972) model uses the empirical data from Table 6.7 to estimate the number of deaths and victims with hospitalized injuries for future events occurring at three discrete times of day in the San Francisco Bay Area. Ohta et al. (1986) provide a periodic function, based on empirical data, to more accurately estimate the number of fatalities in Japanese homes through a 24-hour period. Coburn et al. (1992) propose the most comprehensive occupancy model for a 24-hour period, considering occupancy patterns of buildings in rural agricultural societies and in residential and commercial buildings of urban societies; a modified version of their commercial building occupancy curve is presented later in Figure 6.34.

6.6.1.3 Other Important Factors for Casualty Modeling

Several other important factors contribute to casualties in seismic events: damage to nonstructural building elements; location of occupant in the building and their gender, age, and behavior during and immediately after the event; search and rescue immediately following the event; and quality and efficiency of medical treatment.

Table 6.8 Comparison of fatality models disaggregated by building type and damage quantity (modified from Table 19 in Shoaf and Seligson 2005).

Building Characteristics	Fatality Model	Damage Description	Conditional Fatality Probability
For all construction types except light steel and wood frame.	ATC-13 ^a (1985)	“none”	0
		“light”	0.00001
		“moderate”	0.0001
		“heavy”	0.001
		“major”	0.01
		“destroyed”	0.20
Reinforced-concrete (non-near-field ground motions)	Coburn et al. ^b (1992)	“partial collapse (10% of volume”	0.082
		“partial collapse (50% of volume”	0.31
		“top down collapse”	0.41
		“bottom up collapse”	0.57
Mid-rise concrete moment frame	HAZUS 99-SR2 ^c (2002)	“moderate”	0
		“extensive”	0.00001
		“complete without collapse”	0.0001
		“complete with collapse”	0.1
Mid-rise non-ductile reinforced-concrete frame	Shoaf and Seligson ^d (2005)	“partial collapse”	0.015
		“total collapse”	0.131
^a Fatality ratios are based on NOAA’s report (1972) and expert opinion. ^b Fatality ratios are based on worldwide data from Coburn et al. (1990). ^c Fatality ratios are based on and revised from ATC-13 (1985). ^d Fatality ratios are based on population survey data from Golcuk, Turkey, after the 1999 Izmit earthquake (Shoaf and Seligson 2005).			

Although it is intuitive to attribute earthquake injuries to falling nonstructural elements and building contents, researchers (e.g., Durkin and Thiel 1992) found that there was a low probability of these elements causing fatal injuries and that they were responsible instead for numerous minor and moderate injuries. In addition to falling objects, it is believed that a person’s spatial location in a building during an event can also have an affect on their risk of injury. Wagner et al. (1994) show that a person has a higher risk of being injured if they occupy upper stories of a building instead of the first floor. Also, a study by Ohta et al. (1986) shows that small living spaces amplify the risk of casualty in a home.

Human characteristics can also play a role in the risk of people incurring injuries during seismic events. For example, the risk of injury is consistently greater for women than it is for men (Glass et al. 1977; Ohta et al. 1986). Also, several researchers demonstrate that children and elderly people are at a higher risk of being injured (Glass et al. 1977; Ohta et al. 1986; Mahue-Giangreco et al. 1994). Also, the behavior of people during and immediately following an event can affect the risk of injury. For example, people on a ground floor are more likely to run out of a building during an earthquake⁴, and Wagner et al. (1994) show that those people who stay inside a building during shaking have a higher risk (5 times more likely) of being injured than those who run outside. In addition, Durkin and Thiel (1992) found that in the absence of structural failure, peoples' behavior during and after the event contribute only in a small way to the probability of their being seriously injured, although it does contribute in a large way to minor injuries.

Most severe injuries and deaths are caused by entrapment in the structural debris of a damaged building. Wagner et al. (1994) found that being trapped by collapsing structures was the most significant risk for dying in the 1988 Armenian and the 1980 southern Italian earthquakes; these researchers estimate from empirical data that trapped people are 68–107 times more likely to die, and 5–11 times more likely to have non-lethal injuries than those who are not trapped. The Coburn et al. (1992) fatality model accounts for this in their “M3” factor. The time it takes to find victims in rubble and treat their injuries to prevent further deterioration is critical. Coburn et al. (1992) also include an “M5” factor in their earthquake injury model that accounts for the additional deaths of trapped victims that occur after an event. For example, after the 1998 Armenian earthquake, emergency care providers were unable to provide basic forms of treatment to many individuals that certainly would have prevented further deaths (Tierney 1990).

6.6.2 Methodology for Fatality Estimation

The literature on earthquake casualty modeling and earthquake epidemiology provides a number of factors that are likely to affect the risk of human injury during seismic events. In this report, the purpose of the casualty modeling is to inform the building design process. Therefore,

⁴ Statistical data on evacuation patterns are lacking, tests have shown that people cannot get out of a building above the first floor in less than 30 sec (based on Georgescu 1988, as cited in Coburn et al. 1992). It is reasonable to assume, as others have in their fatality models (Coburn et al. 1992; HAZUS 2002; Yeo and Cornell 2003), that 50% of people on a ground floor will run outside during ground shaking.

although all the factors mentioned above are important, only those that may be directly affected by a change in building design are considered here. These include collapse states of the building (partial or complete), building occupancy, and spatial location of building occupants.

The probability of side-sway collapse (C) comes from the structural analysis results in Chapter 5, whereas the probability of a local collapse (LC) comes from the damage analysis results; it is taken as the probability that any beam or column in the building is in a severe or collapse damage state. The next step in estimating fatalities in a building due to an earthquake is to determine the population at risk by considering the building occupancy and the spatial location of the occupants. The benchmark building is a hypothetical structure, and so in order to estimate a realistic value for building occupancy, the recommendations of ATC-13 (1985) were used. ATC-13 provides tables for estimating the mean building daytime and nighttime occupancies based on building type and square footage, but they do not provide information about the uncertainty (e.g., the variance) of these occupancy estimates (1985). The calculated mean number of occupants for the benchmark building using Table 4.12 of ATC-13 (1985) is 346 people. The floor plans of the building, given in Figures 3.6 and 3.7, are used to estimate the distribution of this population throughout the building. The top three stories have exactly the same floor plans and are thus assumed to have the same mean number of occupants (95 people). The ground floor has many areas that are not designated as desk/continued-usage areas (the cafeteria, mail room, and open lobby space), and so the ground floor is assumed to have about 2/3 of the mean number of occupants as in each of the stories above (61 people). Also, using the result the fact that people on the ground floor tend to run out of the building during seismic events, it is reasonable to assume that 50% of the ground floor occupants will evacuate during ground shaking and therefore, will not be injured by any resulting structural damage inside the building⁵. The mean number of occupants for the benchmark building minus the 50% of the first floor occupants assumed to evacuate at the first sign of an earthquake, O_N , is equal to 316. The occupancy patterns of Figure 6.34 must also be incorporated to account for the equal likelihood of earthquakes occurring at any hour of the day.

The proposed fatality model uses the non-residential (commercial) occupancy model of Coburn et al. (1992). It is reasonable to use this model for occupancy during weekdays; however, most typical businesses have many fewer employees on-site during weekends and holidays.

⁵ The assumption of 50% evacuees was first introduced by Coburn et al. (1992), and has been adopted by HAZUS (2002) and Yeo and Cornell (2003).

Therefore, the occupancy pattern during these times is reduced from the weekday occupancy (both occupancy patterns are shown in Fig. 6.34). It is assumed that an earthquake can occur at any time of any day with equal probability, and so the mean population at risk is calculated by:

$$n_{\text{weekday}} = O_N \cdot \int_0^{24} E[OF | \text{weekday}, t] \cdot p(t) dt$$

$$n_{\text{weekend/holiday}} = O_N \cdot \int_0^{24} E[OF | \text{weekend/holiday}, t] \cdot p(t) dt \quad (6.5)$$

$$n = n_{\text{weekday}} \cdot \left(\frac{\text{No. weekdays}}{365} \right) + n_{\text{weekend/holiday}} \cdot \left(\frac{\text{No. weekends/holidays}}{365} \right)$$

where n is the mean population at risk; $O_N = 316$, as determined above by assuming first floor evacuations during the earthquake and the estimated occupancy of ATC-13 (1985); n_{weekday} is the mean number of occupants in the building during the weekdays over a 24-hour period; mean $E[OF | \text{weekday}, t]$ is the mean occupancy factor for the building for weekdays at any given hour of the day; $n_{\text{weekend/holiday}}$ is the mean number of occupants in the building during weekends and holidays over a 24-hour period; mean $E[OF | \text{weekend/holiday}, t]$ is the mean occupancy factor for the building during weekends/holidays at a given hour; and $p(t)$ is a uniform distribution equal to $1/24$ for $t \in [0, 24]$. In calculating n , we use 251 weekdays and 114 weekend/holidays (accounting for the 10 observed U.S. national holidays), respectively. Equation (6.5) then gives $n=133.4$ for the mean population at risk in the benchmark building. In the discussion that follows, fatalities are estimated for $n=133$.

Human fatalities due to strong seismic events can be estimated as a function of the population at risk and the probability of building damage. The probability of fatalities occurring, given the damage state of the structure, can be modeled with the binomial distribution given by:

$$P_{Y_n|DM}(y | DM) = \frac{n!}{y!(n-y)!} p_{DM}^y (1-p_{DM})^{n-y} \quad (6.6)$$

where Y_n is the number of fatalities when there are n total occupants in the building at the time of the earthquake, $P_{Y_n|DM}(y | DM)$ is the probability of y deaths occurring given the damage state of the building, and p_{DM} is the fatality probability (also known as fatality rate in epidemiology literature) given the damage state of the building. The fatality probability, p_{DM} , is given in Table 6.8 for reinforced concrete buildings for various levels of damage. Note that the

number of building occupants is also uncertain; the mean value of n calculated in Equation (6.5) is used here as a simplification for design purposes.

The mean and the variance of the number of fatalities given the damage state of the building are computed as follows:

$$E[Y_n | DM] = (np_{DM}) \tag{6.7}$$

$$Var[Y_n | DM] = n \cdot p_{DM}(1 - p_{DM})$$

where $n=133.4$ for the benchmark building and the fatality probabilities are for local collapse and for global (side-sway) collapse. These probabilities are listed in Table 6.9 for various building construction types, where the damage states “local collapse” and “collapse” are assigned to the appropriate damage descriptions given in Table 6.8. In this table the “major” and “destroyed” damage states of ATC-13 (1985) are used for local collapse (LC) and collapse (C); the “partial collapse (50% volume)” damage state of Coburn et al. (1992) is used for LC. In Table 6.9 the average of the collapse damage states, “top down collapse” and “bottom up collapse,” is used for C in Table 6.9, the “complete without collapse” and “complete with collapse” damage states of HAZUS (2002) are used for LC and C, respectively, and the “partial collapse” and “total collapse” damage states Shoaf and Seligson (2003) are used for LC and C, respectively.

Event trees have been used in the past by researchers to model casualties caused by seismic events (Murakami 1992; HAZUS 2002; Yeo and Cornell 2003). The proposed event tree model to estimate earthquake fatalities for the example benchmark building in this work is given in Figure 6.35, which builds on the virtual inspector model of Mitrani-Reiser (2007). The first block in the event tree of Figure 6.35 corresponds to the population of a building that is at risk, which was calculated using Equation (6.5). The event-tree branches leaving this block correspond to the probability of damage states for the building conditioned on the hazard level and then the fatality probabilities associated with these damage states.

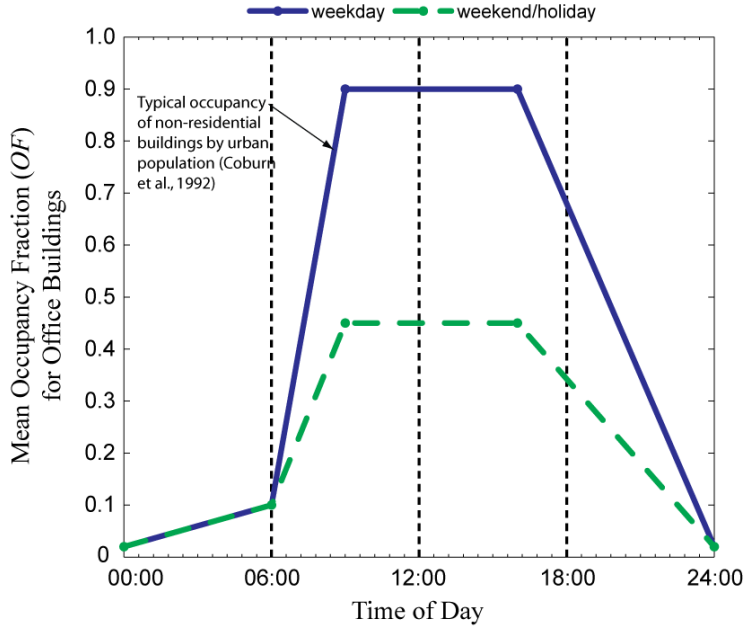


Fig. 6.34 Fractional office building occupancy throughout day. (Weekday modeled after Coburn et al. (1992) and weekend/holiday is modified version of it).

The results from the damage analysis of Section 6.3 may be used to determine the expected number of deaths and the variance of deaths for each hazard level, given the building's damage state. Using the terminology of the event tree, the mean and variance of fatalities for a given hazard level are given by:

$$\begin{aligned}
 E[Y_n | im] &= E[Y_n | C]P[C | im] + E[Y_n | NC]P[NC | im] \\
 &= E[Y_n | C]P[C | im] + E[Y_n | LC, NC]P[LC | im, NC]P[NC | im] \\
 &= (np_C) \cdot P[C | im] + ((np_{LC}) \cdot P[LC | im, NC]) \cdot (1 - P[C | im])
 \end{aligned}$$

$$\begin{aligned}
 E[Y_n^2 | im] &= E[Y_n^2 | C]P[C | im] + E[Y_n^2 | NC]P[NC | im] \\
 &= E[Y_n^2 | C]P[C | im] + E[Y_n^2 | LC, NC]P[LC | im, NC]P[NC | im] \\
 &= [np_C(1 - p_C + np_C)] \cdot P[C | im] + [np_{LC}(1 - p_{LC} + np_{LC})] \cdot P[LC | im, NC] \cdot (1 - P[C | im])
 \end{aligned} \tag{6.8}$$

$$Var[Y_n | im] = E[Y_n^2 | im] - (E[Y_n | im])^2$$

where $P[C|im]$ is the probability of collapse conditioned on the hazard level, which is estimated from the structural response simulated using the lumped-plasticity model described in Section 5.4; $E[Y_n | NC, im] = E[Y_n^2 | NC, im] = 0$ assuming that there are no fatalities if the building has no global or local collapse; $E[Y_n^2 | C, im] = Var[Y_n | C, im] + (E[Y_n | C, im])^2$ for global collapse and $E[Y_n^2 | NC, im] = Var[Y_n | NC, im] + (E[Y_n | NC, im])^2$ for no global collapse;

and $P[LC|im, NC]$ is the probability of a local collapse given the hazard level and that there is no global collapse, which is determined by calculating the probability that at least one beam or column is in a severe or collapse damage state.

The mean number of fatalities conditioned on the hazard level is calculated from Equation 6.8 and then combined with the hazard function to compute the expected annual number of fatalities:

$$EANF = \lambda_0 \int_{im} E[Y_n | im] p(im | im \geq im_0) dim \quad (6.9)$$

where im_0 refers to a value of IM below which repair cost is probably negligible (here taken as 0.1g), and λ_0 is the mean annual rate of events with $IM \geq im_0$.

Table 6.9 Mean and variance of fatality models for local collapse (LC) and global collapse (C) of building. [Calculated with Eq. (6.7)].

Building Characteristics	Fatality Model	Damage State (DM)	P_{DM}	$E[Y_n DM]$	$Var[Y_n DM]$
For all construction types except light steel and wood frame.	ATC-13 (1985)	LC	0.01	1.33	1.32
		C	0.20	26.68	21.34
Reinforced concrete (non-near-field ground motions)	Coburn et al. (1992)	LC	0.31	41.35	28.53
		C	$(0.57+0.41)/2$	65.37	33.2
Mid-rise concrete moment frame	HAZUS 99-SR2 ^c (2002)	LC	0.0001	0.01	0.01
		C	0.1	13.34	12.01
Mid-rise non-ductile reinforced concrete frame	Shoaf and Seligson (2005)	LC	0.015	2.00	1.97
		C	0.131	17.47	15.19

The expected annual number of fatalities has been calculated for the five benchmark building designs using the fatality probabilities of Shoaf and Seligson (2005) listed in Table 6.9 and the results are given in Table 6.10. The expected annual number of fatalities for Designs A, B, C, and E range between 0.0010–0.0016. The expected annual number of fatalities increases

drastically to 0.023 for Design D, which does not include the SCWB provision; this is numerically close to the annual number of fatalities equal to 0.024 for a post-Northridge steel moment-resisting-frame building reported by Yeo and Cornell (2003), assuming various occupancy values in a 24-hour period. The expected loss of life during a seismic event is perhaps the decision variable that owners and policymakers will be most interested in mitigating. The fatality estimation carried out for the benchmark building provides a methodology for comparing this important value for various building designs, and enables informed decision making during the design process.

6.6.3 Methodology for Loss Estimation due to Fatalities

Many people are uncomfortable with putting a price on human life, and the process is fraught with philosophical and economic challenges. However, public agencies routinely allocate scarce resources to improve life safety, and for the public good must assess the value of competing activities, regulations, and policies that cost money but save lives (FHWA 1994). Typically, the “value of a statistical life,” or *VSL*, is used in benefit-cost analyses of competing policies (or building designs in our case), where the main objective is to reduce the number of human fatalities. A quantitative, meta-analysis approach that was used to estimate the value of a statistical life based on labor-market data shows that \$1.5–\$2.5 million (in 1998 dollars) is a plausible range for *VSL* (Mrozek and Taylor 2002). The obvious worth of human life suggests that it is inappropriate to neglect it entirely in a comparison of economic benefits and costs.

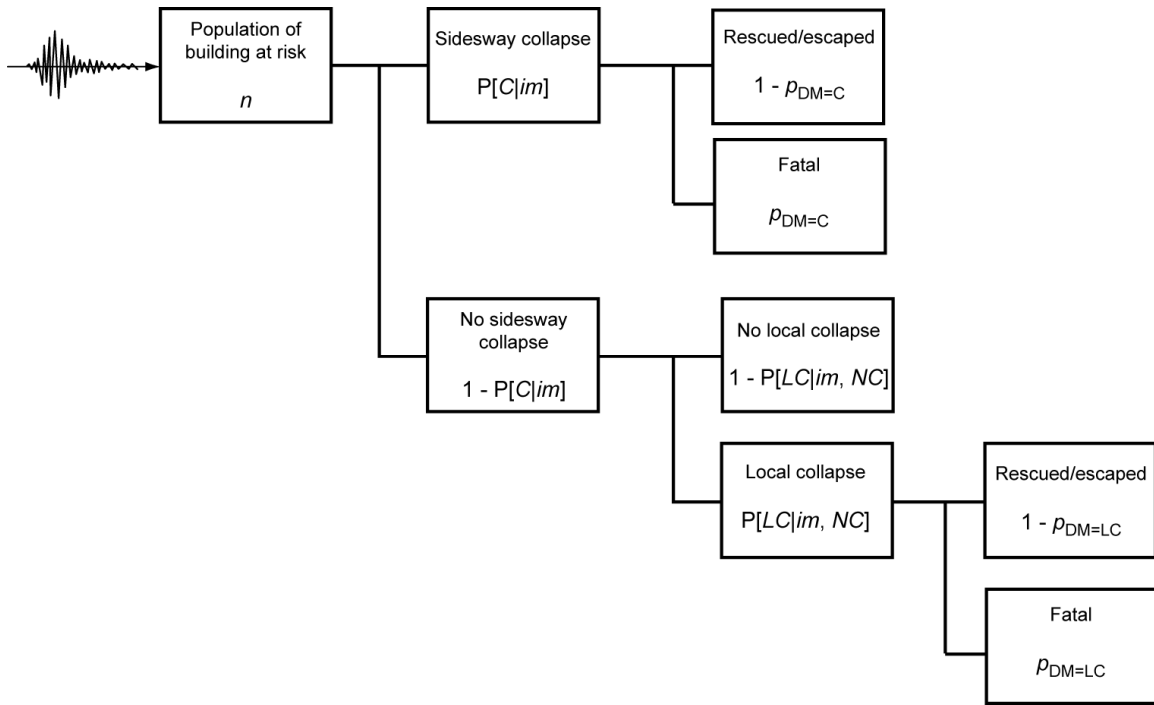


Fig. 6.35 Event tree model for fatality estimation of specific building, considering probabilities of local and global collapse at every hazard level im .

The expected annualized loss associated with fatalities ($EALF$), caused by building earthquake-damage may be estimated by multiplying the expected annual number of fatalities ($EANF$) calculated in Section 6.6.2, with a reasonable VSL . The Federal Highway Administration (FHWA 1994) approved using \$2.6 million as an acceptable cost to assign to regulations or safety measures that avoid one future statistical death. The FHWA figure in 1998 dollars equals \$2.8 million, which is comparable to Mrozek and Taylor’s suggested range of VSL (2002); a VSL of \$3.5 million (accounting for inflation) is used here. The values of $EALF$ for the five benchmark designs compared in this work are given in Table 6.10. The results of this table show that the expected annual losses due to fatalities are 5–11% of the annual losses due to repair cost. However, the value of $EALF = \$79,800^6$ estimated for the non-code-conforming Design D (VID 9) particularly stands out because it is an order of magnitude larger than the losses due to fatalities for the other designs.

⁶ This figure corresponds to the loss of one human life over the lifetime of the building, taken as 50 years for this example.

Table 6.10 Design variant descriptions and corresponding expected annual number of fatalities (*EANF*) and expected annual loss due to fatalities (*EALF*).

Design (VID): description	EANF (*10⁻³)	EALF (\$)
A (VID #1): Baseline perimeter-frame design.	1.4	4,900
B (VID #3): Same as A, but with code-min strengths.	1.3	4,550
C (VID #2): Same A, but with uniform beam/column throughout.	1.6	5,600
D (VID #9): Same as C, but no SCWB provision.	22.8	79,800
E (VID #6): Baseline space-frame design.	1.0	3,500

6.7 SUMMARY AND CONCLUSIONS

This chapter documents the significant results of the damage and loss analysis work conducted in pursuit of establishing a methodology for evaluating the performance of new reinforced concrete buildings in response to seismic hazards. The implementation of the MATLAB Damage and Loss Analysis (MDLA) toolbox, described in Section 6.3, enabled us to efficiently apply PEER's PBEE framework to the benchmark building. The work presented here estimates the first two of the three main decision variables (termed the *3 Ds*: dollars, deaths, and downtime), proposed by PEER and the ATC-58 Project for performance assessment of structures. The significant results and major contributions from each section of this chapter are outlined below.

- The structural and nonstructural components included in the damage and loss estimation of the benchmark building were selected to closely agree with those deemed as necessary for a detailed-level performance assessment by the ATC-58 guidelines for next-generation performance-based seismic design.
- An analytical methodology for damage and loss estimation was implemented using the MATLAB Damage and Loss Analysis (MDLA) toolbox. Although targeted to the benchmark study, the MDLA toolbox provides a clearly defined interface for the results of the hazard and structural analyses and the models of damageable building components, and can be adapted in future studies.

- In contrast to previous studies, the damage analysis of the benchmark building includes some three-dimensional effects in the performance of the structural and nonstructural building components. To implement this, the orthogonal building frames were modeled in a two-dimensional structural analysis, using the two horizontal components of the ground motion record. The geometric mean of the two horizontal components was considered for the selection of ground motion records.
- The MDLA toolbox was used to perform the damage analysis of ten variants (design and structural modeling) of the benchmark building. A damage visualization tool that presents the average probability of reaching or exceeding the damage states of like components in each story is useful for predicting probable locations of severe damage and is an intermediate means for the performance comparison of the various designs.
- The most severe damage to the reinforced concrete columns of the moment frames is likely to occur in the first story of all the building variants. The code-conforming designs resist structural damage at low levels of ground shaking, while the one design that does not enforce the SCWB provision has a significantly higher probability of suffering damage even at the lowest hazard levels.
- The damage results are used to make design comparisons; for instance, the space-frame design is shown to resist nonstructural damage to a greater extent than the perimeter-frame designs; in general, the damage is less severe and the onset occurs at higher levels of ground shaking. These differences in damage across the building designs anticipate the repair losses that are subsequently determined.
- The damage results are also used to compare modeling choices; for example, ignoring the added strength and stiffness of the gravity frames in the structural model is demonstrated to be a reasonable approximation with respect to structural damage, while it leads to a slightly higher level of nonstructural damage.
- The MDLA toolbox was used to perform the loss analysis of ten variants (design and modeling) of the benchmark building. The mean total repair cost and the contribution of individual damageable building components to this cost are calculated across all hazard levels. Subsequently, these repair costs are used to determine the expected annual loss, which is one of several economic performance metrics useful for building design comparisons.

- The potential for financial loss is significant when considering that the expected annual losses from earthquakes are roughly equal to 1% of the replacement cost of the building. The results show that the repair costs are quite sensitive to modeling choices; in particular, the choice of the initial stiffness of the structural elements significantly contributes to the expected annual loss. In addition, the findings of the loss analysis are consistent with those of previous chapters in that the non-code-conforming design fares much worse than its code-conforming counterparts.
- An event-tree-based fatality model was developed that accounts for the factors affecting fatalities that have been identified in epidemiological studies of earthquake-related injuries. The model considers human fatalities due to the partial and global collapse of buildings, using probabilities of fatality based on relevant empirical data of human injuries in historic seismic events. The mean number of fatalities is determined using the probabilities of partial and global collapse.
- The results of the fatality estimation demonstrate that there is no substantial life-safety risk in code-conforming building designs at all hazard levels; the expected annual number of fatalities does not exceed 0.002 for these designs. Although the fatality risk is considerably larger for the non-code-conforming design, the expected annual number of fatalities of this building is approximately 0.023, which is not alarming.

7 Summary and Conclusions

7.1 OVERVIEW

We have applied the PEER PBEE methodology to assess the seismic performance of a four-story reinforced concrete office building that is generally representative of low-rise office building construction in highly seismic regions of California. The so-called “benchmark” building was located at a site in the Los Angeles basin and had a ductile RC SMF seismic lateral system, designed according to modern building codes and standards. The building performance is quantified in terms of structural behavior up to collapse, structural and nonstructural damage and associated repair costs, and the risk of fatalities and their associated economic costs.

Eight structural design alternatives are investigated in order to assess the variation in performance that is likely to arise from so-called “design uncertainty,” i.e., variations in the structural design that are likely to exist for a certain configuration of building designed to meet a specified set of building code provisions. These design variants include (1) the choice between a perimeter-frame versus complete space-frame configuration, (2) variations in the degree of member size optimization and stepping of member sizes throughout the frame, and (3) variations in design according to the 2003 edition of the International Building Code (IBC 2003) and the 1997 edition of the Uniform Building Code (UBC 1997) and the associated standards. For comparison, the design variants also include a case where the capacity design requirements for columns (“strong-column weak-beam” provisions) are violated.

The performance assessment accounted for important sources of uncertainty in the ground motion hazard, the structural response, structural and nonstructural damage, repair costs, and life-safety risk. Ground motion hazard characterization employed a site-specific probabilistic seismic hazard assessment that considered disaggregation to develop seven bins of ground motions that reflect dominant earthquake scenarios over the range from frequent

earthquakes up through return periods of 2475 years. The ground motion hazard characterization also considered site effects and the influence of soil-foundation-structure interaction. Structural modeling uncertainty was incorporated through comparative assessments of alternative modeling approaches (“fiber” versus “concentrated hinge” analyses) and variations in structural component modeling parameters (stiffness, plastic deformation capacity, degradation). Structural and nonstructural damage (fragility) models are based on a combination of test data, observations from post-earthquake reconnaissance, and expert opinion. Structural damage and repair costs are modeled in the RC beams, columns, and slab-column connections. Nonstructural damage and repair costs are considered for major building components, including partition walls, exterior glazing, ceilings, sprinkler systems, and elevators. The risk of casualties and the associated economic costs are evaluated based on the risk of structural collapse, combined with recent models on earthquake fatalities in collapsed buildings and accepted economic modeling guidelines for the value of human life to be used in loss and cost-benefit studies.

Sections 7.2–7.4 summarize the major findings and conclusions regarding the structural performance, loss analysis, and fatality assessment. General observations about the performance-based methodology and suggestions for future research and development are summarized in Section 7.5.

7.2 COLLAPSE SAFETY

Accounting for uncertainties in structural modeling and record-to-record variability, the structural collapse probabilities of the various four-story RC SMF designs are in the range of 2–7% for earthquake ground motions with a 2% probability of exceedance in 50 years. The corresponding collapse margins (the ratio between the median collapse capacity and the spectral demand at the 2%-in-50-years hazard) range from 2.3 to 2.9. When integrated with the ground motion hazard for the southern California site, the mean annual frequency of collapse is in the range of $[0.4 \text{ to } 1.4] \times 10^{-4}$ for the various benchmark building designs.

Figure C1-23 from the FEMA 223 document (FEMA 1992) suggests that these computed collapse probabilities are high, compared with previous estimates on the order of 0.2% to 0.5% for a building subjected to 2%-in-50-years ground motions. However, the collapse assessment methodology of the Applied Technology Council Project 63 (ATC 2007) suggests that these

collapse probabilities are acceptable. The topic of acceptable collapse risk is worthy of substantial further study.

At ground motions compatible with typical design basis exceedance probabilities (10% probability of exceedance in 50 years), the peak interstory drift ratios range from 0.005 to 0.02, which are consistent with the limits imposed by building codes. Peak interstory drift ratios at collapse are on the order of 0.07–0.12 owing to the large deformation capacities of the structural components.

In the process of developing the above findings related to structural response and collapse, a number of additional observations were made that are of more general significance to structural performance assessment:

- For rare ground motion levels (i.e., that can cause collapse in well-designed modern buildings), it is critical to consider of spectral shape when selecting ground motion records structural analyses. Here, this was done using the parameter “ ϵ ” from the PSHA, which is a measure of the ground motion intensity relative to mean predicted values from attenuation functions. For coastal California, the high-intensity, infrequent (rare) ground motions are associated with positive ϵ values, on the order of $\epsilon = 1$ to 2. If ϵ had been neglected in the record selection for the low return periods (high intensities), the median predicted collapse capacities would have been reduced by about 20–40%, which in turn would have increased the mean annual rate of collapse by a factor of five to nine.
- The collapse analyses require accurate models that capture strength and stiffness degradation associated with large deformations of code-conforming RC elements. Additionally, according to the PEER PBEE approach where modeling uncertainties are explicitly considered, the component response models used for collapse analysis should be based on the characteristic (median) response properties, as opposed to lower-bound values that are often applied in design practice. Calibrations to test-data of code-conforming RC elements indicate that the median inelastic rotation capacities are significantly larger than those generally applied in modern practice (such as in FEMA 356, 2000). For example, calibrations of RC beam-columns for this study indicate that the members can sustain plastic rotations on the order of 0.04–0.07 prior to the onset of strain softening. For purposes of uncertainty assessment, the uncertainty in plastic-rotation capacity is $\sigma_{LN} = 0.54$ –0.60.

- Structural modeling uncertainties have a significant impact on the calculated collapse probabilities and mean annual rates. Sensitivity analyses conducted for this study substantiate previously published research that collapse capacity, as calculated by nonlinear response history analysis, is highly dependent on the component deformation capacity (the rotation capacity to the onset of strain softening) and the post-peak degrading stiffness. FOSM analyses conducted for this study showed that the variability introduced by structural modeling uncertainties ($\sigma_{LN} = 0.35$ to 0.45) is similar to that due to record-to-record variability of the ground motions (typically $\sigma_{LN} = 0.30$ to 0.40). Accounting for modeling uncertainty increased the mean annual collapse rates by roughly four to eight times relative to rates evaluated for the median structural model.
- The nonlinear response analyses of the four-story building revealed at least six distinct collapse mechanisms, which occurred for different ground motions. Three of the six involved single-story mechanisms, in spite of building code provisions (which were applied in design) intended to avoid such mechanisms. Moreover, the most prevalent of the six collapse modes was a story mechanism in the third story, which is in contrast to the multi-story mechanism predicted by nonlinear static pushover analysis. This reveals the extent to which inelastic dynamic response can differ from “equivalent” static response even for a low-rise building frame.
- Variations between collapse performance for the code-conforming design variants was not insignificant, with the collapse probabilities for the 2%-in-50-years hazard varying from 2% to 7% and the mean annual collapse rates varying from $[0.4$ to $1.4] \times 10^{-4}$ (a range of about three times for both statistics). Overall, the difference in performance between the perimeter and space-frame designs was less than differences arising from other design variants, such as the degree of modest overstrength in the designs. However, the design that did not enforce the strong-column weak-beam provision (design Variant D, which is not code-conforming) had a much reduced collapse capacity as compared to the code-conforming designs. For this design, the mean annual frequency of collapse was over ten times that of the conforming designs, with a mean annual frequency of 13×10^{-4} as compared $[0.3$ to $1.4] \times 10^{-4}$.
- Nonlinear analyses confirmed that soil-foundation-structure interaction effects do not have a significant effect on the structural response. This behavior was expected due to

the flexibility of the moment-frame superstructure, whose natural period of 0.7–1.0 sec is beyond the range where kinematic and inertial effects are typically significant for stiff soil sites.

7.3 DAMAGE AND REPAIR COSTS

The potential for financial loss is significant. Overall, the calculated expected annual losses (*EAL*) are in the range of \$52,000–\$97,000 for the various code-conforming benchmark building designs. For the assumed building replacement value of \$8.9M, these *EALs* amount to about 0.6–1.1% of the building replacement cost. Considered another way, the estimated repair costs for damage incurred under the design level ground motions (10% chance of exceedance in 50 years) ranged from about 21–29% of the building replacement cost. Additional findings and observations that are more general in nature and could apply to loss assessment for other buildings include the following:

- Economic losses are dominated by the expected costs of (1) repairing the wallboard partitions, (2) repairing the structural members, and (3) repainting the interior, in this order of importance. For example, for a typical design variant, the percentages of the *EAL* associated with these components are 30% (wallboard partitions), 31% (structural members), and 34% (repainting). Repainting and the wallboard partitions tend to dominate the loss under frequent (low-intensity) ground motions (up to about one half of the design earthquake motions). At less frequent (high-intensity) ground motions (above the design motions), repair of the wallboard partitions and structural members contribute about equally to the loss.
- Calculation of *EAL* is sensitive to the initial stiffness of the structural elements used in the analysis. For example, the *EAL* for the baseline perimeter-frame model using the fiber-type elements with concrete tension stiffening is \$67,000 (0.75% of replacement cost) versus \$97,000 (1.1 % of replacement cost) for the same design analyzed using the lumped-plasticity model with secant stiffness through yield (K_{yld}). Adjustment of the initial stiffness of the lumped-plasticity model by calculating the RC secant stiffness at 60% or 40% (K_{stf}) of the flexural yield point reduces the *EAL* values to \$82,000 and \$57,000, (0.9% and 0.6% of replacement cost), respectively. These results suggest that a secant stiffness calibrated to about 50% of the yield point may provide a reasonable

match to the deformations and *EAL* calculated from the analyses with fiber-type elements. The sensitivity of the *EAL* to the initial stiffness was also evident in other design variants where the initial stiffness was modified by altering the member sizes or modeling parameters.

- Similar to the collapse analyses, the repair cost losses are much larger for the design variant that did not adhere to the strong-column weak-beam provisions for column design. A comparison of this design with the baseline perimeter-frame design indicates that the *EAL* increases by 70% when the strong-column weak-beam design provision is not adhered to.
- The trends in mean repair costs for specific ground motion intensities do not necessarily follow the trend in *EALs*. Differences in the trends may affect the way that stakeholders view the loss results. The comparison of results between the perimeter-frame and space-frame design variants helps illustrate this. In this case, the space-frame variant has slightly lower repair costs than the perimeter frame for ground motion intensities below the design level earthquake, but much larger losses at intensities above the design earthquake. At the 2%-in-50-years hazard level, the losses for the space frame are about \$1M larger (about 30% larger) than the perimeter frame. However, when the losses are integrated over the hazard curve, the *EAL* for the space-frame design is about 25% less than for the perimeter-frame design. This is because the mean repair costs of the space frame are smaller for the more frequent events. This comparison also substantiates the general observation that in modern code-conforming buildings, the *EAL* is generally dominated by frequent low-intensity earthquakes as compared to less frequent severe earthquakes.
- The mean damage factor (MDF), or the ratio of the mean loss to the replacement cost of the building, was compared for each design variant at the 10%-in-50-years hazard level using four different loss estimation models (ATC-13, HAZUS, ST-Risk, and PEER). Using the methodology presented in this report, MDF ranges between 21–29% for code-conforming designs, and equals 38% for the non-code-conforming design. The MDF results from the other predictive models ranges between 8–36%. Although there is general agreement with the results calculated by all loss models, the comparison is imperfect for various reasons. The details of this comparison are given in Chapter 6 and Appendix K.

- The probable maximum loss (PML), defined here as the amount of loss with 10% exceedance probability associated with a large, rare event that has a shaking intensity with 10% probability of exceedance in 50 years. These results for PML range between 29–36% for code-conforming designs, and equals 69% for the non-code-conforming design. These values double when PML is estimated using ST-Risk (approximately 15–20%). Again, the comparison between the two loss models is not exact. The details of this comparison are given in Chapter 6.

7.4 LIFE-SAFETY RISKS AND COSTS

For the assumed mean building occupancy of 346 people, and the expected fatality rates of 0.015 and 0.131 in the event of local and global collapses, respectively, the mean annual rate of fatalities for the code-conforming buildings is 0.001–0.002 casualties/year. Assuming the value of a human life at \$3.5M, the fatality rates translates to expected annual losses due to fatalities of \$3,500–\$5,600. Compared to the *EAL* for repair costs on the order of \$66,000, the dollar loss associated with life lost is small, suggesting that the governing factor in this respect will be the maximum permissible life-safety risk deemed by the public (or its representative government) to be appropriate for buildings.

7.5 FUTURE RESEARCH NEEDS

While this study has successfully demonstrated a rigorous and comprehensive seismic performance assessment, it has also highlighted areas where further research and development is warranted. Some of the gaps will warrant further fundamental research, whereas others are more straightforward but will require large coordinated efforts for systematic data collection and model development/validation. The following summarizes the key outstanding needs identified through this benchmarking exercise:

1. The ground motion selection process was enormously time consuming due to inefficiencies associated with poor packaging of both hazard codes and ground motion databases. The OpenSHA effort is a major step forward in the packaging of state-of-the-art seismic hazard calculation routines, which we would use today in lieu of the Fortran

codes run for the present study. The need remains to organize the NGA ground motion dataset in a manner that facilitates the streamlining of acceleration history selection. This could be accomplished by creating a software tool for ground motion selection.

2. For the extreme hazard levels that were required to bring on collapse of the benchmark structures, it was necessary to exceed normal scaling limitations. There is a need to both understand the implications of this severe scaling for large hazard levels and to develop improved acceleration histories (perhaps drawing upon seismological simulations) to represent those hazard levels.
3. Validated structural component response models: One of the reasons for focusing on ductile RC moment frames in this study was the availability of a significant body of test data and knowledge to establish and validate statistically robust nonlinear force-deformation models. Similar idealized models to the ones described herein for RC components are required for other materials, members, and systems. To be widely accepted by the profession, such models should ideally be vetted through a professional consensus process in a similar manner to other existing design codes and standards.
4. The soil-structure interaction routines utilized in our response simulations were computationally inefficient and lead to significant convergence problems. There is a significant need for improved models and improved packaging. Moreover, there is a need to investigate the importance of soil-structure interaction for building performance levels when the structural system is one that will tend to produce notable SSI effects, such as shear wall systems.
5. Structural and nonstructural component fragility models: Similar to the case for structural response models, the proposed framework for fragility models needs to be broadly applied to develop models for structural and nonstructural components that are common to building construction. In addition to the models of individual components, further work is required to establish appropriate correlations between uncertainties in multiple components in buildings.
6. Loss assessment models: Current loss models (relating damage to repair measures and costs) rely heavily on expert judgment of cost estimators. Significant improvements to the process could be made by more systematic study of repairs and losses to buildings in

past and future earthquakes. The loss assessment process could be further enhanced by linking information from building information models to loss assessment tools.

7. Propagation of uncertainties in structural modeling, damage, and loss assessment: While inroads have been made on the challenge to propagate uncertainties in key response and loss parameters through the assessment process, this study has demonstrated the sensitivity of the final loss estimates to assumptions made regarding modeling uncertainties and correlation between these uncertainties. Future studies should seek to further establish which components of the loss assessment process have the largest impact on the estimated loss and then seek to develop models to assess those components.
8. Generalization to evaluate building codes and standards: While the current study provides insight on the likely performance of modern code-conforming office buildings, it is limited in scope to one general configuration and one location. The methods applied to this building study should be generalized to assess the performance associated with entire classes of structural and building systems.
9. Guidelines on appropriate performance targets: As confidence is developed in performance assessment methods, important questions arise as to what constitutes “acceptable” or “appropriate” performance. What is the minimum performance (maximum conditional collapse probability, maximum annual rate of collapse, maximum loss metrics, maximum casualty risk, etc.) that should be permitted by building codes? Is it appropriate to design all buildings to the same performance criteria? Are there societal benefits to enhanced performance, and if so, what incentives could be provided to examine cost-benefit studies in design? These and other related questions will require closer coordination between engineers, building officials, and public policy experts than has existed in the past.

Beyond these needs, convenient user friendly tools (computer software) will be necessary to promote widespread use of comprehensive seismic performance assessments. It is anticipated that commercial software can readily fill this need provided that a consistent methodology and specific modeling standards and criteria are established. This study has provided many of the modeling and simulation tools that are needed to achieve this goal.

REFERENCES

- Abrahamson, N. A.; Silva, W. J., 1997. "Empirical response spectral attenuation relations for shallow crustal earthquakes", *Seismological Research Letters*, 68, 1, Jan.-Feb. 1997, pages 94-127.
- Abrahamson, N. A., 2004. "Haz 3.6: Fortran computer code for probabilistic seismic hazard analysis", personal communication.
- Altoontash, A., 2004. *Simulation and Damage Models for Performance Assessment of Reinforced Concrete Beam-Column Joints*, Dissertation, Department of Civil and Environmental Engineering, Stanford University.
- American Concrete Institute (ACI), 2004. *546R-04 Concrete Repair Guide*, Farmington Hills, MI, 53 pp.
- American Concrete Institute (ACI), 2002. "*Building Code Requirements for Structural Concrete (ACI 318-02) and Commentary (ACI 318R-02)*". American Concrete Institute, Farmington Hills, MI.
- American Concrete Institute (ACI), 1998. *224.1R-93, Causes, Evaluation and Repair of Cracks in Concrete Structures*, Farmington Hills, MI, 22 pp.
- American Concrete Institute (ACI), 1990. "*Design Handbook Volume 2: Columns (ACI 340.2R-90)*", American Concrete Institute, Detroit, MI.
- American Society for Testing and Materials (ASTM) Standard Test Methods, 2004. "ASTM D1586-99 "Standard Test Method for Penetration Test and Split-Barrel Sampling of Soils." ASTM International. Book of Standards Volume: 04.08
- American Society of Civil Engineers (ASCE), 2000. FEMA 356, *Prestandard and Commentary for the Seismic Rehabilitation of Buildings*. Prepared for the Federal Emergency Management Agency FEMA, Washington, D.C.
- American Society of Civil Engineers (ASCE), 2002. ASCE-7-02: "*Minimum Design Loads for Buildings and Other Structures*". American Society of Civil Engineers, Reston, VA.
- American Society of Civil Engineers (ASCE), 2006. *Minimum Design Loads for Buildings and Other Structures*, SEI/ASCE 7-05. Reston, VA
- Applied Technology Council, 1985. ATC-13, "*Earthquake Damage Evaluation Data for California*". Redwood City, California.

- Applied Technology Council, 1989. ATC-20, "*Procedures for Post-Earthquake Safety Evaluation of Buildings*". Redwood City, California.
- Applied Technology Council, 1995. ATC 20-2, Addendum to the ATC-20 "*Post-Earthquake Building Safety Evaluation Procedures*". Redwood City, California.
- Applied Technology Council, 1996a. ATC-32, "*Improved Seismic De-sign Criteria for California Bridges: Provisional Recommendations*". Redwood City, California.
- Applied Technology Council, 1996b. ATC-40, "*Seismic Evaluation and Retrofit of Concrete Buildings*". Report No. SSC 96-01, *Seismic Safety Commission*, Applied Technology Council Project 40, Redwood City, California.
- Applied Technology Council, 2007. ATC-63, "Recommended Methodology for Quantification of Building System Performance and Response Parameters," ATC-63 90% Draft, Redwood City, CA, 2007.
- Aslani, H., 2005. *Probabilistic Earthquake Loss Estimation and Loss Disaggregation In Buildings*, Doctoral Thesis, Stanford University Department of Civil and Environmental Engineering, Stanford CA, 355 pp.
- Aslani, H. and Miranda, E., 2004. *Component-Level and System-Level Sensitivity Study for Earthquake Loss Estimation*. Proceedings, Thirteenth World Conference on Earthquake Engineering. Vancouver, B.C., Canada.
- Atkinson, G.M., and, Silva, W., 2000. "Stochastic modeling of California ground motions", *Bulletin of the Seismic Society of America* 2000, 90 (2), 255-274.
- Baker, J.W. and Cornell, C.A., 2003. *Uncertainty Specification and Propagation for Loss Estimation Using FOSM Methods*, Proceedings, Ninth International Conference on Applications of Statistics and Probability in Civil Engineering (ICASP9). San Francisco, California.
- Baker, J. and Cornell, C.A. 2003. "Uncertainty specification and propagation for loss estimation using FOSM methods" Report PEER 2003/07, Pacific Earthquake Engineering Research (PEER) Center, Richmond, CA.
- Baker, J.W. and Cornell, C.A., 2005a. A vector-valued ground motion intensity measure consisting of spectral acceleration and epsilon, *Earthquake Engr. & Structural Dynamics*, 34 (10), 1193-1217.
- Baker, J.W. and Cornell, C.A., 2005b. "Which Spectral Acceleration Are You Using?" *Earthquake Spectra* (under revision for publication).

- Bazzurro, P. and Cornell, A.C., 1999. "Disaggregation of Seismic Hazard," *Bull. Seism. Soc. Am.*, Vol. 89, no. 2, 501-520.
- Beck, J.L., A. Kiremidjian, S. Wilkie, A. Mason, T. Salmon, J. Goltz, R. Olson, J. Workman, A. Irfanoglu, and K. Porter, 1999. Decision Support Tools for Earthquake Recovery of Businesses. CUREE-Kajima Joint Research Program Phase III, Consortium of Universities for Earthquake Engineering Research, Richmond, CA.
- Beck, J.L., K.A. Porter, R. Shaikhutdinov, S. K. Au, T. Moroi, Y. Tsukada, and M. Masuda, 2002. *Impact of Seismic Risk on Lifetime Property Values*, Final Report, Consortium of Universities for Research in Earthquake Engineering, Richmond, CA.
- Behr, R.A., and Worrell, C.L., 1998. "Limit States for Architectural Glass Under Simulated Seismic Loadings," *Proc., Seminar on Seismic Design, Retrofit, and Performance of Nonstructural Components, ATC-29-1 January 22-23, 1998, San Francisco*, Redwood City, CA: Applied Technology Council, pp. 229-240.
- Berry, M., Parish, M., and Eberhard, M., 2004. *PEER Structural Performance Database User's Manual*, Pacific Engineering Research Center, University of California, Berkeley, California, 38 pp. Available at <http://nisee.berkeley.edu/spd/> and <http://maximus.ce.washington.edu/~peera1/>.
- Board on Earth Sciences and Resources (BESR), 1997. "Review of Recommendations for Probabilistic Seismic Hazard Analysis: Guidance on Uncertainty and Use of Experts", National Academies Press. Available online at: <http://www.nap.edu/books/0309056322/html/R1.html> (last accessed in July 2005)
- Baecher, G. B. and Christian, J. T., 2003. "Reliability and Statistics in Geotechnical Engineering". John Wiley and Sons, 605 pp.
- Boore, D.M., Joyner, W.B., and Fumal, T.E., 1997. "Equations for estimating horizontal response spectra and peak acceleration from western North American earthquakes: A summary of recent work," *Seism. Res. Letters*, 68(1), 128-153.
- Bryant, W. A. (compiler), 2005. Digital Database of Quaternary and Younger Faults from the Fault Activity Map of California, version 2.0: California Geological Survey Web Page, http://www.consrv.ca.gov/CGS/information/publicatons/QuaternaryFaults_ver2.htm; (last accessed December 2007)
- Building Seismic Safety Council, BSSC, 2001. NEHRP Recommended Provisions for Seismic Regulations for New Buildings and Other Structures, Part 1 . Provisions and Part 2 . Commentary, Federal Emergency Management Agency, Washington D.C., February.

- Cao, T, Petersen, M.D. and Frankel, A.D., 2005. "Model Uncertainties of the 2002 Update of California Seismic Hazard Maps." *Bull. Seism. Soc. Am.*
- Campbell, K.W., 1997. "Empirical near-source attenuation relations for horizontal and vertical components of peak ground acceleration, peak ground velocity, and pseudo-absolute acceleration response spectra," *Seism. Res. Letters*, 68(1), 154-179.
- Celebi, M., Sanli, A., Gallant, S., and Radulescu, D., 2004. Real-Time Seismic Monitoring Needs of a Building Owner—and the Solution: A Cooperative Effort. *Earthquake Spectra* 20 (2). Earthquake Engineering Research Institute, pp. 333-346.
- Chen, T., Morris, J., and Martin, E., 2004. Particle Filters for the Estimation of a State Space Model. *Proceedings of the 14th European Symposium on Computer Aided Process Engineering (ESCAPE-14)*, pp. 613-618.
- Ching, J., Beck, J.L., Porter, K.A., and Shaikhutdinov, R.V., 2004a. Real-Time Bayesian State Estimation of Uncertain Dynamical Systems. *Earthquake Engineering Research Library*. Pasadena, CA.
- Ching, J., Porter, K.A., and Beck, J.L., 2004b. Manuscript in progress for submission to *Earthquake Spectra*.
- Coduto, Donald P., 2001. "Foundation Design, Principles and Practice.", Second Edition, Prentice Hall, New Jersey. 883.pp.
- Cornell, C. A., Jalayer, F., Hamburger, R. O., and Foutch, D. A., 2002. "Probabilistic Basis for 2000 SAC Federal Emergency Management Agency Steel Moment Frame Guidelines," *Journal of Structural Engineering*, Vol. 128, No. 4, April 2002, pp. 526-533.
- Deierlein, G., 2006. Personal communication 1 Mar 2006.
- Ellingwood, B., Galambos, T.V., MacGregor, J.G., and Cornell, C.A., 1980. *Development of a Probability-Based Load Criterion for American National Standard A58*, National Bureau of Standards, Washington, DC, 222 pp.
- Fang, Hsai-Yang, ed., 1991. *Foundation Engineering Handbook*, Van Nostrand Reinhold, New York. 923 pp.
- Fardis, M. N. and Biskinis, D. E., 2003. "Deformation Capacity of RC Members, as Controlled by Flexure or Shear," *Otani Symposium*, 2003, pp. 511-530.
- Federal Emergency Management Agency, FEMA, 2005. Improvement of inelastic seismic analysis procedures, FEMA 440, Federal Emergency Management Agency, Washington, D.C.

- Federal Emergency Management Agency (FEMA), 2004. Hazus. <http://www.fema.gov/hazus/>.
- Federal Emergency Management Agency (FEMA), 2000. FEMA 356, Prestandard and Commentary for the Seismic Rehabilitation of Buildings. Washington, D.C.
- Federal Emergency Management Agency (FEMA), 1998. *FEMA-310: Handbook for the Seismic Evaluation of Buildings—A Prestandard*, Washington, DC, 364 pp.
- Federal Emergency Management Agency (FEMA), 1997a. FEMA 273, NEHRP Guidelines for Seismic Rehabilitation of Buildings. Washington, D.C.
- Federal Emergency Management Agency (FEMA), 1997b. FEMA 274, NEHRP Commentary on the Guidelines for Seismic Rehabilitation of Buildings. Washington, D.C.
- Federal Emergency Management Agency (FEMA), 1992. *FEMA 222: NEHRP Recommended Provisions for the Development of Regulations for New Buildings and NEHRP Maps, Part 1, 1991 Edition*, Federal Emergency Management Agency, Washington, DC.
- Federal Emergency Management Agency (FEMA), 1992. FEMA 223: NEHRP Recommended Provisions for the Development of Regulations for New Buildings, Part 2, Commentary, 1991, Federal Emergency Management Agency, Washington, DC.
- Federal Highway Administration (FHWA), 1994. Motor Vehicle Accident Costs, Technical Advisory #7570.2, Federal Highway Administration U.S. Department of Transportation, Washington, D.C.
- Frankel, A.D., M.D. Petersen, C.S. Muller, K.M. Haller, R.L. Wheeler, E.V. Leyendecker, R.L. Wesson, S.C. Harmsen, C.H. Cramer, D.M. Perkins, and K.S. Rukstales, 2002. “Documentation for the 2002 Update of the National Seismic Hazard Maps.”, U.S. Geological Survey, Open-file Report 02-420, 33 pp.
- Gazetas G., 1991. Chapter 15: Foundation Vibrations, *Foundation Engineering Handbook*, H.-Y. Goulet, C., Haselton, C., Mitrani-Reiser, J., Stewart, J.P., Taciroglu, E., and Deierlein, G., 2006. Evaluation of the Seismic Performance of a Code-Conforming Reinforced-Concrete Frame Building - Part I: Ground Motion Selection and Structural Collapse Simulation. Proceedings of Eighth U.S. National Conference on Earthquake Engineering. San Francisco, California
- Hamburger, R.O. and Moehle, J.P., 2000. State of Performance Based-Engineering in the United State. Proceedings of the Second US-Japan Workshop on Performance-Based Design Methodology for Reinforced Concrete Building Structures. Sapporo, Japan.
- Harden C. and Hutchinson, T., 2003. “Numerical Modeling of the Non-Linear Cyclic Response of Shallow Foundations.”, Master’s thesis. University of California at Irvine.

- Hart, G. C. and Vasudevan, R., 1975. "Earthquake Design of Buildings: Damping," *Journal of the Structural Division*, Vol. 101, No. ST1, January, 1975, pp. 11-20.
- Haselton, C.B. and G.G. Deierlein (2007). Assessing Seismic Collapse Safety of Modern Reinforced Concrete Frame Buildings, Blume Earthquake Engineering Research Center Technical Report No. 156, Stanford University, 313 pp.
- Haselton, C.B. (2006). *Assessing Seismic Collapse Safety of Modern Reinforced Concrete Moment Frame Buildings*, Ph.D. Dissertation, Department of Civil and Environmental Engineering, Stanford University, 313 pp.
- Haselton, C.B. and Baker, J.W., 2006a. "Ground motion intensity measures for collapse capacity prediction: Choice of optimal spectral period and effect of spectral shape", *8th National Conference on Earthquake Engineering*, San Francisco, California, April 18-22, 2006.
- Haselton, C.B., Liel A.B., Taylor Lange S. and G.G. Deierlein, 2006/7. *Beam-Column Element Model Calibrated for Predicting Flexural Response Leading to Global Collapse of RC Frame Buildings*, PEER Report 2006/7, Pacific Engineering Research Center, University of California, Berkeley, California.
- Ibarra, L.F., Medina, R.A., and Krawinkler, H., 2005. "Hysteretic models that incorporate strength and stiffness deterioration," *Earthquake Engr. and Structural Dynamics*, Vol. 34, pp. 1489-1511.
- Ibarra, L., 2003. *Global Collapse of Frame Structures Under Seismic Excitations*, Ph.D. Dissertation, Department of Civil and Environmental Engineering, Stanford University.
- International Code Council (ICC), 2003. *International Building Code 2003*, International Conference of Building Officials. Falls Church, VA.
- Julier, S.J. and Uhlmann, J.K., 1997. A new extension of the Kalman filter to nonlinear systems. International Symposium Aerospace/Defense Sensing, Simulation and Controls. Orlando, Florida.
- Kang, T.H.K., and J.W. Wallace, 2006. Drift capacity models and shear strength degrading models for slab-column connections. *Proc 8th National Conference on Earthquake Engineering 8NCEE*, April 2006, San Francisco, CA <http://www.seas.ucla.edu/~tkang/radAFBCF.pdf> [02 Mar 2006],
- Kang, T.H.K., J.W. Wallace, and K.J. Ellwood, 2006a. Dynamic tests and modeling of RC and PT slab-column connections. *Proc 8th National Conference on Earthquake Engineering 8NCEE*, April 2006, San Francisco, CA <http://www.seas.ucla.edu/~tkang/rad4ACCE.pdf> [02 Mar 2006]

- Kang, T.H.K., S.H. Kee, S.W Han, L.H. Lee, and J.W. Wallace, 2006b. Interior post-tensioned slab-column connections, subjected to cyclic lateral loading. *Proc 8th National Conference on Earthquake Engineering 8NCEE*, April 2006, San Francisco, CA
<http://www.seas.ucla.edu/~tkang/rad38846.pdf> [02 Mar 2006]
- Kang, T.H.K., and J.W. Wallace, 2005. Dynamic responses of flat plate systems with shear reinforcement. *ACI Structural Journal*, Sept-Oct 2005, 763-773
- Kim S and Stewart JP., 2003. Kinematic soil-structure interaction from strong motion recordings, *J. Geotech. & Geoenv. Engrg.* 129, 323-335
- Kramer, S.L., 1996. *Geotechnical Earthquake Engineering*, Prentice Hall, Upper Saddle River, NJ.
- Krawinkler, H., Editor, 2005. "Van Nuys Hotel Building Testbed Report: Exercising Seismic Performance Assessment", PEER Report 2005/11, Oct. 2005.
- Krawinkler, H., and Miranda, E., 2004. "Performance-based earthquake engineering," Chapter 9 of *Earthquake engineering: from engineering seismology to performance-based engineering*, Y. Bozorgnia and V.V. Bertero, Editors, CRC Press.
- Kulhawy, F.H. and Trautmann, C. H., 1996. "Estimation of in-situ uncertainty.", *Uncertainty in the Geologic Environment*, Madison, ASCE:49-75.
- Luco, N. and Cornell, C.A., 2007. "Structure-Specific Scalar Intensity Measures for Near Source and Ordinary Earthquake Ground Motions," *Earthquake Spectra* 23 (2) pp. 357-392, Earthquake Engineering Research Institute, Oakland, CA.
- Mathworks, 2004. <http://www.mathworks.com/>.
- McGuire, R.K., 1995. "Probabilistic seismic hazard analysis and design earthquakes: closing the loop," *Bull. Seism. Soc. Am.*, 86, 1275-1284.
- McGuire, R.K., 2004. *Seismic hazard and risk analysis*, Earthquake Engineering Research Institute, MNO-10, 240 p.
- Melchers, R. E., 1999. *Structural Reliability Analysis and Prediction*, John Wiley and Sons Inc., New York.
- Miranda, E., 2005. Personal communication regarding damping in buildings.
- Porter, K. A., Beck, J. L., Shaikhutdinov, R. V., 2002. Sensitivity of Building Loss Estimates to Major Uncertain Variables, *Earthquake Spectra* 18 (4) pp. 719-743, Earthquake Engineering Research Institute, Oakland, CA.

- Mitrani-Reiser, J., Haselton, C., Goulet, C., Porter, K., Beck, J., and Deierlein, G., 2006. Evaluation of the Seismic Performance of a Code-Conforming Reinforced-Concrete Frame Building - Part II: Loss Estimation. Proceedings of Eighth U.S. National Conference on Earthquake Engineering. San Francisco, California.
- National Fire Protection Association (NFPA), 2002. *Standard for the Installation of Sprinkler Systems, NFPA-13*, National Fire Protection Association, Quincy, MA. Sprinkler Fitters U.A. Local 483, 1989, untitled, San Carlos, CA
- National Institute of Building Sciences and Federal Emergency Management Agency (NIBS and FEMA), 2003. *Multi-hazard Loss Estimation Methodology, Earthquake Model, HAZUS^{®MH} Technical Manual*, Federal Emergency Management Agency, Washington, DC, 690 pp.
- OpenSees, 2006. Open System for Earthquake Engineering Simulation, Pacific Earthquake Engineering Research Center, Univ. of California, Berkeley, <http://opensees.berkeley.edu/>.
- Pacific Coast Building Officials (PCBO), 1927. Uniform Building Code, Whittier, California.
- Pacific Earthquake Engineering Center (PEER), 2005. *PEER Structural Performance Database*, University of California, Berkeley, Available at <http://nisee.berkeley.edu/spd/> and <http://maximus.ce.washington.edu/~peera1/>.
- Pacific Earthquake Engineering Center (PEER), 2005. *PEER Strong Motion Database*, University of California, Berkeley, <http://peer.berkeley.edu/smcat/>.
- Panagiotakos, T. B. and Fardis, M. N., 2001. "Deformations of Reinforced Concrete at Yielding and Ultimate," *ACI Structural Journal*, Vol. 98, No. 2, March-April 2001, pp. 135-147.
- Pinelli, J.P., Subramanian, C., Zhang, L., Gurley, K., Cope, A., Simiu, E., Diniz, S., and Hamid, S., 2003. A Model to Predict Hurricanes Induced Losses for Residential Structures. Proceedings of the European Safety and Reliability Conference. Maastricht, the Netherlands.
- Porter, K.A., 2000. Assembly-Based Vulnerability of Buildings and Its Uses in Seismic Performance Evaluation And Risk-Management Decision-Making, Doctoral Dissertation, Stanford University, Stanford, CA, published by ProQuest Co., Ann Arbor, MI.
- Porter, K.A., A.S. Kiremidjian, and J.S. LeGrue, 2001. Assembly-based vulnerability of buildings and its use in performance evaluation. *Earthquake Spectra*, 17(2), 291-312
- Porter, K.A., 2002. Preliminary *EDP* List. Pacific Earthquake Engineering Center. Richmond, California. <http://www.peertestbeds.net/Crosscutting.htm>.

- Porter, K.A., J.L. Beck, and R.V. Shaikhutdinov, 2002. Investigation of Sensitivity of Building Loss Estimates to Major Uncertain Variables for the Van Nuys Testbed. Report to Pacific Earthquake Engineering Research Center. Richmond, California.
- Porter, K.A., 2003. *An Overview of PEER's Performance-Based Earthquake Engineering Methodology*. Proceedings of Ninth International Conference on Applications of Statistics and Probability in Civil Engineering. San Francisco, California.
- Porter, K.A., J.L. Beck, and R.V. Shaikhutdinov, 2002. Investigation of Sensitivity of Building Loss Estimates to Major Uncertain Variables for the Van Nuys Testbed. Report to Pacific Earthquake Engineering Research Center. Richmond, California.
- Porter, K.A., Beck, J.L., Shaikhutdinov, R.V., Au, S.K., Mizukoshi, K., Miyamura, M., Ishida, H., Moroi, T., Tsukada, Y. and Masuda, M., 2004. Effect of Seismic Risk on Lifetime Property Value, *Earthquake Spectra* 20(4), 1211-1237.
- Porter, K.A., C.R. Scawthorn, and J.L. Beck, 2006. Cost-effectiveness of stronger woodframe buildings. *Earthquake Spectra*, 22(1), February 2006, 239-266
- Rihal, S.S., 1982. *Behavior of Nonstructural Building Partitions During Earthquakes*. Proceedings of the Seventh Symposium on Earthquake Engineering, Department of Earthquake Engineering, University of Roorke, India, November 10-12, 1982, Dehli: Sarita Prakashan, pp. 267-277.
- Risk Engineering Inc., 2004. *ST-Risk Version 4.1*. Boulder, CO. <http://www.st-risk.com/> [07 March 2006]
- RSMeans Corp., 2001, *Means Construction Cost Data*, Kingston, MA: RS Means Co.
- ROSRINE, 2005. Resolution of Site Response Issues from the Northridge Earthquake, *Website by Earthquake Hazard Mitigation Program & Caltrans*. <http://geoinfo.usc.edu/rosrine/>.
- Saatcioglu, M and Grira, M., 1999. "Confinement of Reinforced Concrete Columns with Welded Reinforcement Grids," *ACI Structural Journal*, American Concrete Institute, Vol. 96, No. 1, January-February 1999, pp. 29-39.
- Sadigh, K., Chang, C.-Y., Egan, J.A., Makdisi, F., and Youngs, R.R., 1997. "Attenuation relations for shallow crustal earthquakes based on California strong motion data," *Seism. Res. Letters*, 68(1), 180-189.
- Silva, W., 2000. PEER Strong Motion Database, Pacific Earthquake Engineering Research (PEER) Center, Berkeley, CA, <http://peer.berkeley.edu/smcat/index.html>

- Shoaf, K., Seligson, H., Ramirez, M., and Kano, M., 2003. *Fatality Model for Non-ductile Concrete Frame Structures Developed from Golcuk Population Survey Data*, PEER Report 2006, University of California, Berkeley, California.
- Shome, Nilesh, Cornell, Allin C., 1998. "Normalization and Scaling Accelerograms for Nonlinear Structural Analysis", Proceedings of the 6th U.S. National Conference on Earthquake Engineering, Paper 243, Seattle, Washington.
- Southern California Earthquake Data Center (SCEDC), 2005. "Clickable fault map.", <http://www.data.scec.org/faults/lafault.html>; (last accessed August 2005)
- Somerville, P. and Collins, N., 2002. Ground Motion Time Histories For The Van Nuys Building, Prepared for the PEER Methodology Testbeds Project, URS Corporation, Pasadena, CA. <http://www.peertestbeds.net/VNY/PrelimVanNuysHazardReport.pdf>
- Somerville, P.G., Smith, N.F., Graves, R.W. and Abrahamson, N.A., 1997. "Modification of empirical strong ground motion attenuation relations to include the amplitude and duration effects of rupture directivity," *Seismological Research Letters* 68, 199-222.
- Steinbrugge, K.V., 1982. *Earthquakes, Volcanoes, and Tsunamis, An Anatomy of Hazards*, Skandia America Group, New York, 392 pp.
- Stewart, J. P., Fenves, G.L., and Seed, R.B., 1999. "Seismic soil-structure interaction in buildings. II: Empirical findings" *J. Geotech. & Geoenviron. Engrg.*, ASCE, 125, 38-48.
- Stewart, J.P., Chiou, S.-J., Bray, J.D., Somerville, P.G., Graves, R.W., and Abrahamson, N.A., 2001. "Ground motion evaluation procedures for performance based design," Rpt . No. PEER-2001/09, Pacific Earthquake Engineering Research Center, University of California, Berkeley, 229 pgs.
- Stewart, J.P., Comartin, G. and Moehle, J.P., 2004. "Implementation of soil-structure interaction models in performance based design procedures. Proc. 13th World Conference on Earthquake Engineering, Vancouver, Canada, 15 pp.
- Swiss Re., 2004. Sigma 1/2004: Natural Catastrophes and Man-Made Disasters in 2003. Swiss Reinsurance Company Economic Research and Consulting. Zurich, Switzerland. <http://www.swissre.com/sigma>
- Structural Engineers Association of California (SEAOC), 1995. Vision 2000, A Framework for Performance-Based Engineering. Structural Engineers Association of California. Sacramento, California.

- Trifunac, M. D. and A.G. Brady, 1975. On the correlation of seismic intensity scales with the peaks of recorded ground motion, *Bulletin of the Seismological Society of America*, 65(1), February 1975, 139-162
- UBC, 1997. *Uniform Building Code*, International Conference of Building Officials, Whittier, California.
- Vamvatsikos, D. and Cornell, C.A., 2002. "Incremental Dynamic Analysis," *Earthquake Engr. and Structural Dynamics*, Vol. 31, Issue 3, pp. 491-514.
- Veletsos AS and Prasad AM., 1989. "Seismic interaction of structures and soils: Stochastic approach," *J. Struct. Engrg.*; 115(4): 935-956.
- Veletsos AS, Prasad AM, and Wu WH., 1997. "Transfer functions for rigid rectangular foundations," *J. Earthquake Engrg. Struct. Dynamics*; 26(1): 5-17.
- Vijayvergiya, V.N., 1977. "Load-Movement Characteristics of Piles." Proceedings, Ports 77, Fourth Annual Symposium of the Waterway, Port, Coastal and Ocean Division of the ASCE. Long Beach, California. Vol. II, pp. 269-284.
- Wallace, J.W., ND. *Slab-column frames*. Presentation to EERI.
- Wang, P.T., Shah, S., Naaman, P., and Antoine, E., 1978. "High-Strength Concrete in Ultimate Strength Design," *Journal of the Structural Division*, ST11, November 1978, pp. 1761-1773.
- Williams, M.S., Villemure, I. and Sexsmith, R.G., 1997. Evaluation of Seismic Damage Indices for Concrete Elements Loaded in Combined Shear and Flexure, *ACI Structural Journal* 94 (3), 315-322.
- Whittaker, A., Hamburger, R.O., Comartin, C., Mahoney, M., and Bachman, R., 2004. Performance-Based Engineering of Buildings and Infrastructure for Extreme Loadings. Technical paper submitted to the ATC, relating to the ATC-58 Project. <http://www.atcouncil.org/ATC58TechnicalPapers.shtml>.
- Working Group on California Earthquake Probabilities, 1995. "Seismic hazards in southern California: Probable earthquakes, 1994-2024," *Bull. Seism. Soc. Am.*, 85, 379-439.
- Zareian, F., 2006. *Simplified Performance-Based Earthquake Engineering*, Dissertation, Department of Civil and Environmental Engineering, Stanford University.

Appendix A: Review of Practitioner Designs

A.1 INTRODUCTION AND PURPOSE OF APPENDIX

A.1.1 Introduction

This appendix summarizes our review of two practitioner-designed buildings used to better understand the variability in how such a building can be designed within the context of current code provisions. These buildings are used in the design of the benchmark buildings to ensure that the benchmark frame designs are “representative of current design.”

A.1.2 Purpose in Reviewing Practitioner Designs

The primary purpose of reviewing the practitioner-designed buildings is simply to ensure that we design the benchmark buildings in agreement with what is done in current practice. In addition, we use the practitioner designs to try to get a rough idea about the variability in how a building can be designed based on the code provisions.

When we reviewed the practitioner designs, we tried to quantify the design parameters in the following list. Where possible, we try to quantify the design parameters numerically (as in the case of flexural overstrength) but this is not possible for many design traits (like foundation layout), so many of the design traits are qualitative. The following is a summary of the key design variables and traits that we looked at for each practitioner building design:

- Design criteria and modeling assumptions
 - Sense of what code-requirements drove design decisions
 - Governing non-code constraints that influenced the design
 - Modeling assumptions used in design and analysis

- Structural design parameters
 - Reserve strength values (i.e., ratios of $R_u / \phi R_n$, where ϕR_n is the design strength and R_u is the required strength, based on elastic design calculations)
 - Degree of conservatism in applying the strong column–weak beam (SCWB) provisions
 - Degree of conservatism in applying the code-specified drift criteria
 - Ratio of beam flexural capacities for positive and negative moments (comparison to SMRF provision of $M_{u, \text{pos}} > 0.5 * M_{u, \text{neg}}$)
 - Application of seismic detailing requirements for SMRFs
 - Frequency of column changes over the building height (changes in column size, reinforcement, and f_c')
 - Framing layouts (bay widths, floor heights, floor framing systems, etc.)
 - Typical foundation systems
- Nonstructural parameters—for use with loss modeling
 - Type of curtain wall system and possible impact on drift criteria used in design
 - Building occupancy type—to determine contents information
 - Information on nonstructural components and contents that are important to the seismic performance assessment

A.2 PRACTICAL CONSIDERATIONS FOR ASSESSMENT OF PRACTITIONER DESIGNS

The goal of this review of the practitioner designs is to approximately determine the values of the design variables listed previously (and uncertainty in these values when possible). To realize this goal within the time frame of this effort, several decisions and approximations were necessary.

In the specific building designs that we reviewed, due to architectural considerations many of the members of the exterior frames were designed with capacities up to three or four times larger than the demand on such members. The additional strength and stiffness provided by members being oversized based on architectural considerations will likely be drastically different for each specific building design. Therefore, this is impossible to quantify using only

two building designs. To avoid this problem, we based the assessment of design variables primarily on structural members whose designs were controlled by demands due to code-prescribed loading and not controlled by architectural considerations. This simplification will lead to results that underpredict the true capacity of the building and underpredict the variability in the design.

Since each of these designs is a real existing building, many irregularities and three-dimensional effects exist that we treated with caution in order to make the results of the review not be entirely specific to only two building designs. In the effort to avoid the specific effects of these irregularities and to allow the results of this review to be general and applicable to the widest possible range of buildings, one lateral-force-resisting frame in each direction is used from each design. The frames chosen for review are those that are the most regular throughout the building. In addition, when one standard frame is used for many bays, we use the frame with the highest lateral load demands.

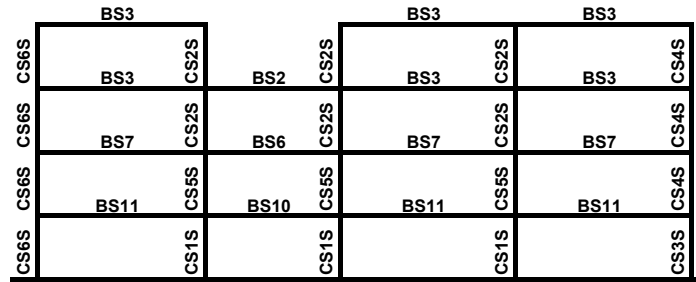
A.3 INTRODUCTION TO PRACTITIONER-DESIGNED BUILDINGS

Two San Francisco Bay Area practitioners contributed to this process by supplying their knowledge and experience, as well as building plans for two buildings. These buildings are considered to be generally representative of current practice for the design of reinforced concrete SMRFs, yet Design 2 shows some unusual levels of overstrength, so we interpret those results with conservative caution. For reasons of confidentiality, the identity of the practitioners and details regarding the building location and use are withheld from the following discussion.

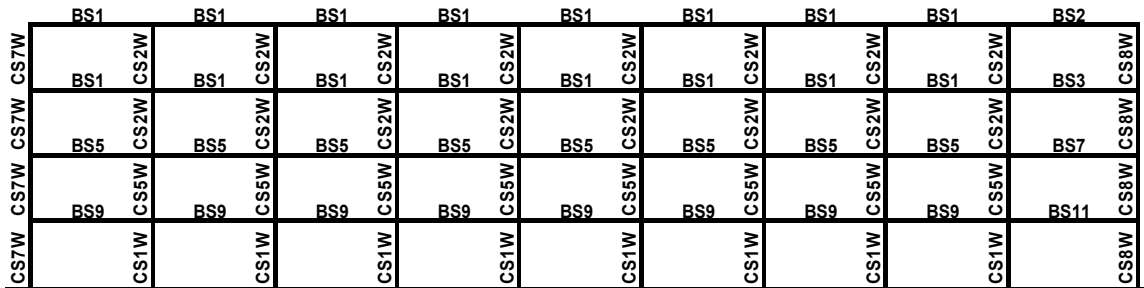
A.3.1 Practitioner Design 1

A.3.1.1 Introduction to Practitioner Design 1

Building One consists of a four-story nine-bay by four-bay reinforced concrete special moment-resisting space frame. Figure A.1 shows schematic diagrams of the two frames assessed from Building One.



(a)



(b)

Fig. A.1 Elevation view from Practitioner Design 1 of (a) frame A and (b) frame B.

In the above figure, each of the labels corresponds to the reinforced concrete section that is present in the specified location of the frame. Note that “BS” and “CS” simply stand for “beam section” and “column section” while “W/S” represent the weak or strong axis of the column section.

Regarding placement of these frames within the building, frame A is located along the column of frame B that is fourth from the right; frame B is located along the column of frame A that is second from the right.

A.3.1.2 Design Observations for Practitioner Design 1

This building was designed according to the 1997 Uniform Building Code (UBC) and the 2001 California Building Code (CBC) provisions. Limited site and design information are as follows:

- Seismic zone three
- Soil Type S_c
- Seismic source Type B

- Portion of design base shear resisted by each frame:
- frame A–V = 110 kips
- frame B–V = 220 kips

The design base shear is based upon the provisions in the 1997 UBC Section 1630.2. In computing the first-mode period of the structure, method B (of the 1997 UBC) was used because this is judged to be consistent with current engineering practice. For this design review, the equation for method B was not explicitly used, but instead an eigenvalue analysis was used to determine the first-mode period of the structural model.

In the mathematical model created for each frame (in order to review the designs), we used pins at the bases of each column. This was done because the practitioner informed us that this was done in the design of the building, and we wanted to assess the building in the same manner in which it was designed to more clearly see how the practitioner applied the code criteria in the design.

Using the same justification as above, the cross-section stiffnesses are based on the recommendations of FEMA 356 (FEMA 2000).

Design 1 is a fairly regular building, but has a few irregularities, as are present in any building. A list of the notable irregularities is as follows:

- The missing beam at the roof level of frame A is due to a stairwell that proceeds to the roof of the building. This would have been avoided if possible but, despite the missing beam, this was the most regular frame of all the frames parallel to frame A.
- The left column of frame A (CS6S) is extremely oversized due to architectural considerations. Therefore, no results are used that directly relate to this column.
- The beams in the right bay of frame B are larger than the other beams in the frame due to higher floor loading in this bay.
- The right column of frame B is oversized due to gravity loading that is not modeled in this assessment. Therefore, the results for this column that relate to the level of axial load are excluded.

A.3.2 Introduction to Practitioner Design 2

Practitioner Design 2 consists of a two-story building that has three seismically separated units. For the building portion considered here, there are three SMRFs in one direction and four in the

other direction. The design seemed to be driven heavily by architectural constraints causing the exterior exposed columns to be much larger than the interior columns. Due to this observation, we selected only one interior column to review from this design, which is depicted in Figure A.2.

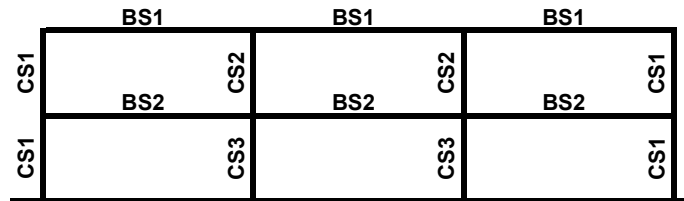


Fig. A.2 Elevation view of frame C from practitioner Design 2.

It should be noted that the columns are spliced at mid-height of the lower floor, thus making column section three exist only over the first half of the first story.

A.3.2.1 Design Observations for Practitioner Design 2

This building was designed according to the 1997 UBC provisions. Site and design information are as follows:

- Seismic zone four
- Soil Type S_D
- Seismic source Type B
- Portion of design base shear resisted by frame C–V = 140 kips

As will be discussed later, columns section two is larger than column section three, which would not be common in a building that is taller than this one. Due to this irregularity, and due to this design being representative of a two-story building rather than a four-story building, we extrapolate these results to a taller building with care.

The mathematical model we created in reviewing this design is similar to that described for Design 1. The difference for this design is that the column bases were not considered to be pinned, but given some rotational restraint consistent with the effects of the grade beams.

A.4 RESULTS OF PRACTITIONER DESIGN REVIEWS

A.4.1 General Observations on Columns Sizes

Column sizes are “stepped down” at each floor of frames A and B, with the exception of the top floor. Each column is typically spliced at the column base. The column size change between stories one and two is the largest change, with both the size of the column and the amount of reinforcing being changed. In the upper floors, the column dimension changes, but the number of reinforcing bars and size of reinforcing bars remain the same. We replicated this general frequency of stepping down the column size changes when designing the benchmark frames. For the practitioner designs, the exterior columns are generally held constant over the height of the building. Even so, we did not mimic this in the design of the benchmark buildings because this was done for architectural reasons in the practitioner designs, and this may be specific to these designs.

A.4.2 Framing Layouts

The benchmark building was designed to represent an office building. These practitioner-designed buildings are not offices, so the framing layouts from these practitioner designs give no useful information regarding the layouts we should use for the benchmark frames. Therefore, we talked with the practitioners and their ideas regarding typical framing layout for office usage are summarized as follows:

- 30' typical bay width
- 8-8.5" flat plate, with column capitals as needed

A.4.3 Typical Foundation Systems

Both practitioner designs have similar foundations systems which include column spread footings linked together by tie beams. The sizes of these tie beams are similar to the sizes of other beams in the frame, with some tie beams being smaller. We designed the foundation system of the benchmark building to be similar to the foundations of these practitioner designs. Note that the only way that the foundation design enters the design and performance assessment of the benchmark building is that it affects the foundation rotational stiffness used in the assessment model.

A.4.4 Material Strengths

The material strengths used for each frame were fairly consistent. The nominal concrete strength of columns is 5000 psi in all frames. The nominal beam concrete strength is 4000 psi or 5000 psi (both allowed by the plans) for frames A and B and 5000 psi for frame C. To be consistent, the benchmark frames were designed using a nominal concrete strength of 5000 psi for both columns and beams. As would be expected, the nominal yield strength of rebar is 60,000 psi, complying with ASTM A615 Low Alloy A706, and we use this in the benchmarking frame designs.

A.4.5 Geometry of Structural Sections

In both designs, the beams sections are typically 24" wide and 30" deep, with some beams having depths of 28" or 33". The beam sections of Design 1 consist of a single layer of #8-#10 bars at the top and bottom of the section, with intermediate #4 side bars spaced at 12" on center. The beams of Design 2 are similar, with the intermediate #4 bars not being spaced at 12", but simply having two sets of intermediate bars equally spaced in each beam.

The columns of Design 2 are all 30" by 30". The columns of Design 1 were typically 24" wide with a height of 30" or 33". CS1 is an exception, having a dimension of 33" by 33". The external columns (CS7 and CS8) are also deeper, with depths of approximately 40" to 70". These higher depths for the exterior columns are due to architectural consideration, so the larger size is not mimicked in the design of the benchmarking frames. Notice that the larger depths of the exterior columns don't heavily effect this assessment, as the bending in these columns is about the weak axis in frame B. The columns of Design 1 have 12–20 #9 or #10 bars that are evenly spaced around the perimeter of the column section. Each of the longitudinal bars are supported with a lateral ties. The column sections of Design 2 are similar, with the only difference being that the longitudinal bars are not always evenly spaced. The median of the reinforcing ratios for the columns is 0.016 with a COV of 0.13. In the design of the benchmark frames, we loosely stayed in this range of reinforcing ratios, but in some cases allowed deviations from these numbers.

The geometry of the sections is generally designed to be exactly what is required in the 1997 UBC Section 1907.7, which is a clear cover distance of 2" to the longitudinal bars or 1 ½"

to the stirrups. As these designs exactly follow the code requirements, the similar code requirements of the 2002 ACI will be used in the design of the benchmarking frames.

A.4.6 Application of Seismic Detailing Requirements for SMRFs

We compared the detailing requirements (1997 UBC Section 1921.3.3.2 and 1921.4.4.2) to what was provided in each design and found that all frame detailing was very close to the code minimum requirements, with a few exceptions of additional conservatism in the detailing.

Based on this observation, we detailed the benchmark frames based strictly on the detailing requirements included in the code provisions, with no variations or additional conservatism in the application of detailing requirements.

A.4.7 Application of Code Drift Criteria

Drifts were computed for each frame and show that the frames were not significantly controlled by drift constraints, so the review of these practitioner buildings did not give any useful information regarding application of code drift requirements. Therefore, we simply ensured that the benchmark frame designs met drift requirements.

A.4.8 Beam Reserve Strength Ratios

An important design parameter relates to how conservative the practitioner is when proportioning members to resist the strength demands. We computed the reserve strength ratios ($\phi M_n / M_u$, where M_u is the required flexural strength based on elastic design calculations of the 1997 UBC and M_n is the nominal flexural design strength) for the three practitioner frames; the results follow in Figures A.3(a)–(c) (for positive bending) and A.4(a)–(c) (for negative bending):

	3.17		3.42	3.48
1.84	3.40	2.04	2.04	
2.00	3.96	2.23	2.19	
2.62	2.76	2.92	2.83	

(a)

Fig. A.3a Reserve strength ratios for positive bending for frame A.

4.55	2.88	2.98	5.11	4.96	4.94	5.17	2.91	2.72
1.96	2.09	2.00	1.99	2.00	2.00	2.00	1.81	2.59
2.02	2.24	2.15	2.16	2.15	2.16	2.16	2.15	3.33
1.80	2.07	2.05	2.04	2.04	2.04	2.04	2.06	2.77

(b)

Fig. A.3b Reserve strength ratios for positive bending for frame B.

4.91	3.84	3.16
2.62	3.06	2.62

(c)

Fig. A.3c Reserve strength ratios for positive bending for frame C.

2.25		2.23	2.32
(1.48)	(2.92)	1.53	1.56
(1.49)	(1.93)	1.57	1.59
(1.78)	(1.73)	1.85	1.84

(a)

Fig. A.4a Reserve strength ratios for negative bending for frame A.

2.10	1.55	1.56	2.18	2.33	2.31	2.23	1.64	(2.01)
1.09	1.06	1.09	1.09	1.09	1.09	1.09	(1.03)	(1.89)
(1.26)	1.31	1.31	1.31	1.31	1.31	1.31	1.30	(1.86)
(1.15)	1.18	1.19	1.19	1.19	1.19	1.19	1.19	(1.67)

(b)

Fig. A.4b Reserve strength ratios for negative bending for frame B.

3.06	2.08	(1.99)
(1.99)	2.20	2.10

(c)

Fig. A.4c Reserve strength ratios for negative bending for frame C.

The circled demand is what controls the design for the given beam section. As Figures A.3 and A.4 show, the flexural design of the beams is controlled by negative bending demands, as would be expected. Therefore, we only utilize the factors associated with negative bending. Figure A.4 shows that the demand-capacity ratios are fairly consistent at each floor level, with the exception of the beams in the shorter span (due to the difference in the section and load effects). Note that the factors are different for the beams in the right bay of frame B because there is higher floor loading on these beams causing the beams of this bay to be designed differently (and more conservatively) from the beams of the other bays. Additionally, the beam with the 1.03 factor has additional flexural demands due to a high asymmetric roof load in the second bay from the right.

In determining how to use these results in designing the benchmark building, we made several observations:

- With the exception of more heavily loaded areas or unequal spans, the beams are the same for each floor level and are reduced in size at each floor, with the exception that the roof beam is the same as the beam at floor four. We step down the beam sizes in the benchmark building in the same manner.
- The design for the positive moment capacity of the beams seems to be controlled more by the ratio of the positive to negative moment capacities (discussed later) rather than the positive moment demand. Therefore, in proportioning the beams of the benchmark frames to resist positive moment, the ratio of positive to negative moment capacity is used rather than the positive moment demand. Note that the ratio of positive to negative moment capacity is likely not explicitly decided by the practitioner, but results from making the beam reinforcement somewhat symmetric.

The final conclusion we draw from these observations is that a *conservative* estimate for mean and dispersion of the beam reserve strength ratio is a mean of 1.25 with a COV of 0.20.

A.4.9 Ratio of Beam Flexural Capacities

Section 1921.3.2.2 of the 1997 UBC requires that the ratio of positive moment capacity to negative moment capacity be a minimum of one half, in seismic zones three and four. This ratio was computed for all of the sections of the three frames that were assessed. The median ratio is 0.8 with a coefficient of variation of 0.1. We see that the design of the beam sections for positive

bending was not controlled by this provision, but was likely simply controlled by the designer providing reasonable amounts of reinforcing for positive bending as compared to negative bending. Even though this ratio did not control the design, it is surprisingly precise in describing what positive moment capacity is provided, given the negative moment capacity. Given this precision, this factor could be used to proportion the beams for positive flexural capacity; however to not include additional strength that other practitioners may not include, we simply design the benchmark frames for the code-required ratio of 0.5.

A.4.10 Degree of Conservatism in Applying SCWB Provision

For each of the three frames, we compared the required SCWB ratio from the code provision (1997 UBC Section 1921.4.2.2) to that provided in the design. To fulfill the related provision of the 1997 UBC, this factor must be at minimum 1.2. Figure A.5 shows these ratios for the three frames we reviewed.

2.82	0.89	0.89	0.52	0.78
5.75	1.21	1.22	1.07	1.60
5.53	1.13	1.18	1.14	1.54
4.79	1.26	1.25	1.20	1.38

(a)

1.82	0.69	0.70	0.68	0.67	0.67	0.67	0.68	0.61	1.86
3.68	1.44	1.47	1.41	1.41	1.41	1.41	1.41	0.98	2.42
2.67	1.35	1.37	1.32	1.31	1.31	1.31	1.32	1.05	2.27
2.34	1.93	1.94	1.87	1.86	1.87	1.86	1.87	1.48	1.98

(b)

1.83	1.32	1.32	1.89
3.70	2.64	2.64	3.70

(c)

Fig. A.5 SCWB ratios for (a) frame A, (b) frame B, and (c) frame C.

Observations from the data presented in Figure A.5 are follows:

- A few SCWB ratios in frames A and B are below the 1.2 threshold (right side of frame). This was caused by the beams sizes adjacent to these joints being increased due to higher floor loads. Even with these few “non-code-conforming” SCWB ratios, the conservatism in the column sizes over the story level cause that *average* ratio of column strength to beam strength over the floor to be well above the required ratio of 1.2.

Table A.1 summarizes the SCWB ratios shown in the above figures. We do not include the results from frame C because of the unrepresentatively large values. For comparison purposes, the values computed using the ACI 318-02 provisions are presented along with the 1997 UBC.

Table A.1 SCWB factors.

Frame	Median		Coef. Of Variation	
	1997 UBC	ACI 318-02	1997 UBC	ACI 318-02
Frame A	1.20	0.90	0.05	0.04
Frame B	1.36	0.94	0.20	0.25

Observations from the data presented in Table A.1:

- For the design of the benchmark frames, a reasonable estimate of the mean SCWB ratio is 1.3 with a COV of 0.15. The previous figures show that this estimate may be low for some designs (frame C), but since we only reviewed at two practitioner designs, we do not want any peculiarities of these designs to cause us to design the benchmark frames too conservatively.
- Factors computed using the ACI 318-02 provisions are approximately 25–35% more conservative as compared to the factors computed using the 1997 UBC provisions. This difference is based on the effects of slab steel and summing the moments at the faces of the joint rather than at the center of the joint. It is noted that frames A and B, especially frame B, has more slab steel than common in building design. Therefore, this difference may be a bit lower for other designs. For comparison purposes, the ratio of frame C is 25% lower when computed using the ACI 318-02 provisions as compared to the 1997 UBC provisions.

- The new provisions being more conservative will cause a higher proportion of column designs to be controlled by the SCWB provision instead of being controlled by force demands.

A.5 SUMMARY AND CONCLUSIONS

These reviews gave us useful information about how practitioners design buildings in current engineering practice. We used this information in the design of the benchmark buildings, in order to ensure the designs are “representative of current design.”

Due to the limited information (only two designs) we could only quantitatively estimate two of the design variables. The beams were typically designed with 25% additional strength (above the code minimum requirements), with a 20% COV. The strong-column weak-beam ratio was 1.3 on average (as compared to the code minimum of 1.2), with a 15% COV.

Appendix B: Design Documentation for Each Design Variant

B.1 INTRODUCTION AND PURPOSE OF APPENDIX

This appendix summarizes the member proportions and reinforcement of the eight structural design variants. It contains diagrams of the buildings, diagrams of the beam and column cross sections, and beam and column schedules. This appendix also includes more detailed design information for Design A, including beam design strengths, strong-column weak-beam ratios, and the design drift demands (computed using the equivalent lateral force procedure of ASCE7-02 with a simple elastic centerline model).

B.2 BEAM AND COLUMN CROSS-SECTIONAL DESIGNS

Figure B.1 shows the cross-sectional design for the columns. This diagram applies to all design variants, except for smaller columns where there are fewer intermediate rebar.

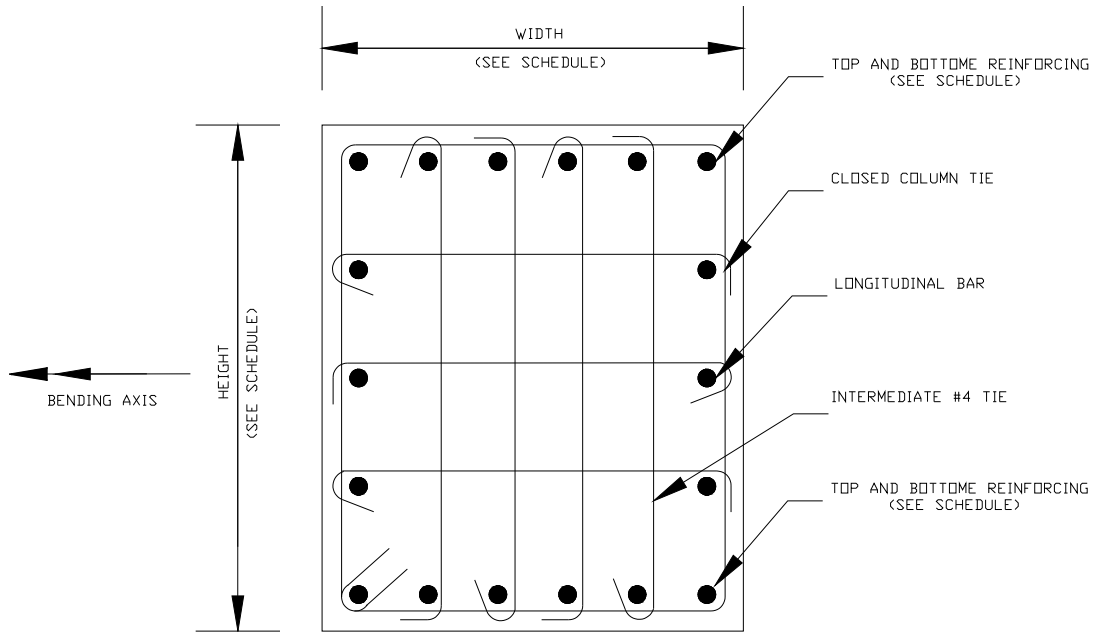


Fig. B.1 Cross-sectional diagram for columns.

The column confinement consists of closed #4 column ties with each longitudinal bar laterally supported by a #4 tie. The lateral support of each top and bottom longitudinal bar is provided by the hoop reinforcement area requirements of ACI 318-02, Section 21.4.4.1. The number of top and bottom bars varies and the resulting reinforcing ratios are given in the column schedule (Table B.1). Intermediate bars and related cross-ties are required to be less than 14" apart, by ACI 318-02, Section 21.4.4.3, so the number of intermediate ties varies dependent on the column depth. Each column is oriented such that the bending axis is perpendicular to the direction of the frame.

Figure B.2 shows the beam cross section for the perimeter frames. The intermediate bars consist of #4 bars. Note that Section 7.10.5.3 of ACI 318-02 requires at least one intermediate tie in the beam section to provide lateral support to the longitudinal bars. The slab consists of 8" of concrete with #4 rebar on both the top and bottom of the slab, spaced at 12" on center (note that design H has more slab steel than is shown here).

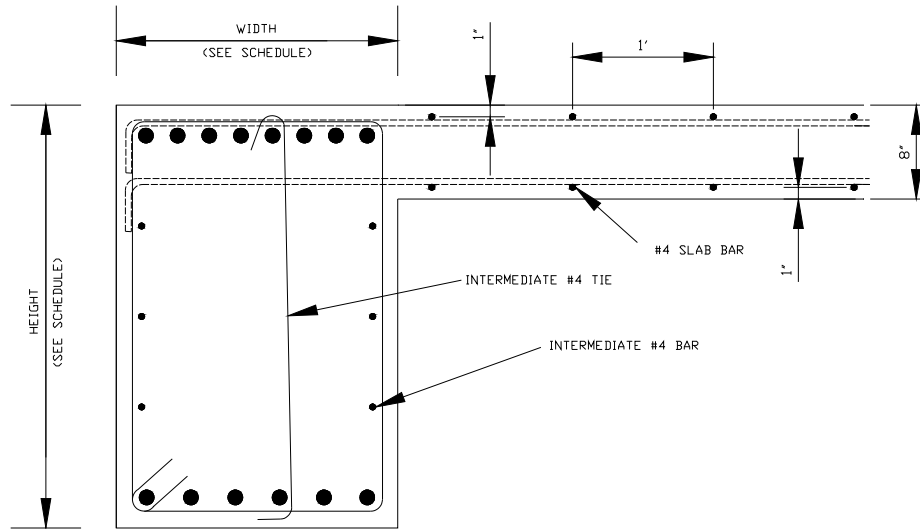


Fig. B.2 Cross-sectional diagram for perimeter-frame beams.

Figure B.3 shows the beam cross section for the space frames. The space-frame beams are the same as those of the perimeter, with the exception that the interior frames have a slab on both sides on the beam.

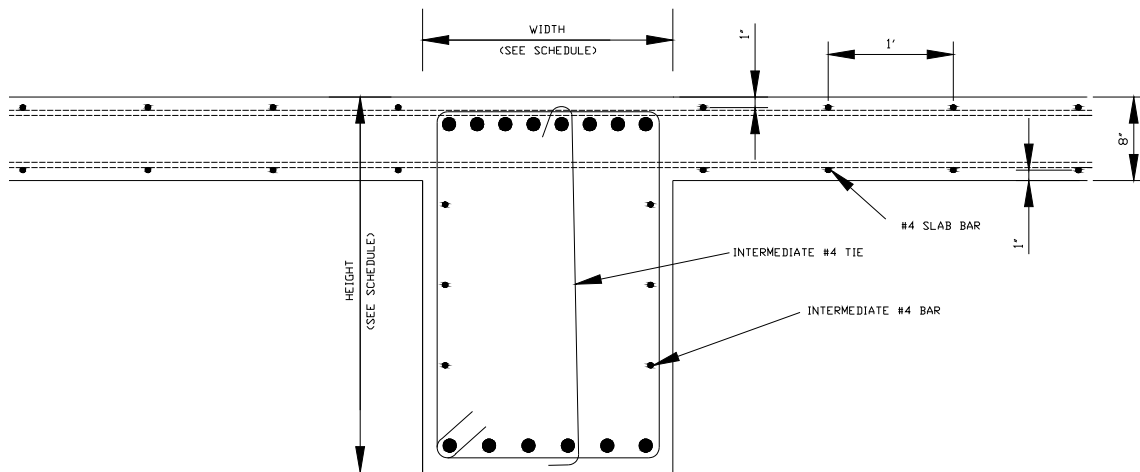


Fig. B.3 Cross-sectional diagram for space-frame beams.

B.3 MEMBER SCHEDULES FOR EACH DESIGN VARIANT

Table B.1 shows the beam and column schedule for all of the design variants. The labels for each section are shown in the frame elevation view in Figure B.4. Some of the large section

sizes for the perimeter frame are proportioned to meet the joint shear provision (ACI 318-02 Section 21.5.3).

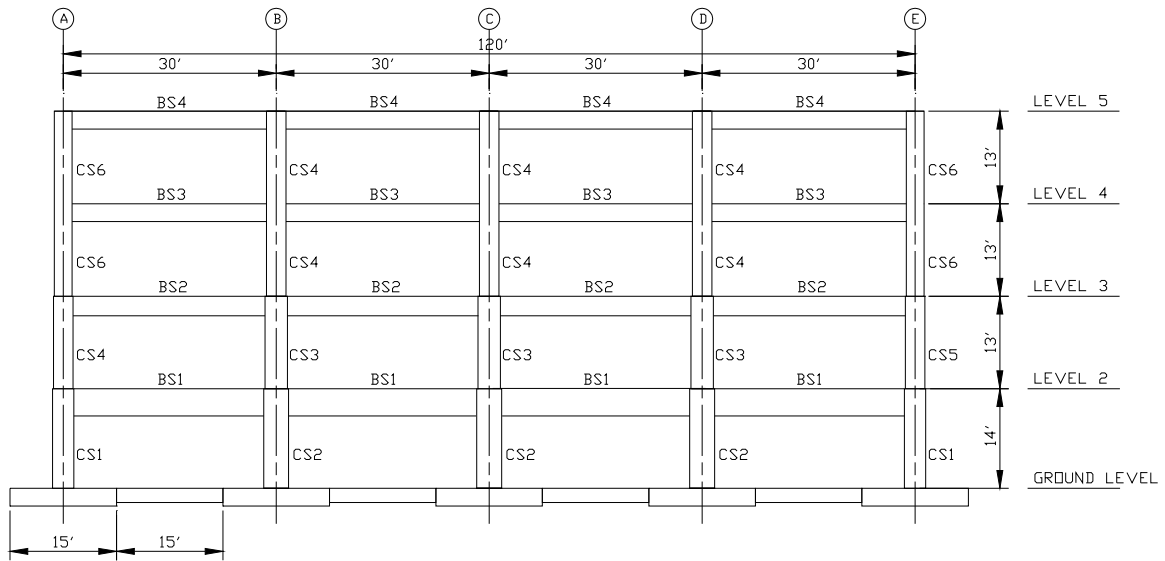


Fig. B.4 Elevation view of frame along column line 1.

Table B.1 Beam and column schedule for all design variants.

Section Tag	Section Property	Design A	Design B	Design C	Design D	Design E	Design F	Design G	Design H
CS1	h (inch)	30	30	30	Same as Design B, but simply with column strengths reduced to meet the code required force demand (+20% for material overstrength and $\Phi = 0.9$).	30	24	26	26
	b (inch)	30	30	30		24	18	24	24
	Long. Bar #	9	8	9		8	8	8	8
	ρ_g	0.027	0.021	0.027		0.017	0.022	0.010	0.010
CS2	h (inch)	40	36	40		30	25	26	26
	b (inch)	30	30	30		24	18	24	24
	Long. Bar #	10	9	10		9	9	8	8
	ρ_g	0.018	0.024	0.018		0.019	0.031	0.010	0.010
CS3	h (inch)	33	30	40		28	25	26	26
	b (inch)	30	30	30		24	18	24	24
	Long. Bar #	9	8	10		9	9	8	8
	ρ_g	0.024	0.019	0.018		0.021	0.027	0.010	0.010
CS4	h (inch)	34	30	40		27	25	26	26
	b (inch)	30	30	30		24	18	24	24
	Long. Bar #	8	8	10		9	8	8	8
	ρ_g	0.012	0.012	0.018		0.025	0.028	0.015	0.015
CS5	h (inch)	30	28	30		30	24	26	26
	b (inch)	30	30	30		24	18	24	24
	Long. Bar #	9	8	9		8	8	8	8
	ρ_g	0.018	0.017	0.027		0.015	0.015	0.010	0.010
CS6	h (inch)	28	26	30		30	24	26	26
	b (inch)	24	24	30		24	18	24	24
	Long. Bar #	8	8	9		8	8	8	8
	ρ_g	0.016	0.015	0.027		0.015	0.018	0.010	0.010
BS1	h (inch)	42	36	42		38	38	38	38
	b (inch)	24	24	24		18	18	18	18
	Long. Bar #	9	9	9		9	9	9	9
	$\rho_{tensile, top}$	0.010	0.012	0.010		0.009	0.009	0.009	0.009
	$\rho_{tensile, bottom}$	0.008	0.009	0.008		0.004	0.004	0.004	0.004
BS2	h (inch)	36	30	42		33	33	33	33
	b (inch)	24	24	24		18	18	18	18
	Long. Bar #	9	8	9		9	9	9	9
	$\rho_{tensile, top}$	0.010	0.011	0.0099		0.010	0.010	0.010	0.010
	$\rho_{tensile, bottom}$	0.008	0.007	0.0079		0.005	0.005	0.005	0.005
BS3	h (inch)	32	26	42		33	33	33	33
	b (inch)	24	24	24		18	18	18	18
	Long. Bar #	9	8	9		9	8	9	9
	$\rho_{tensile, top}$	0.009	0.011	0.010		0.010	0.010	0.010	0.010
	$\rho_{tensile, bottom}$	0.006	0.006	0.008		0.005	0.005	0.005	0.005
BS4	h (inch)	32	24	42		33	33	33	33
	b (inch)	24	24	24		18	18	18	18
	Long. Bar #	9	8	9		9	8	9	9
	$\rho_{tensile, top}$	0.008	0.010	0.010		0.008	0.008	0.008	0.008
	$\rho_{tensile, bottom}$	0.005	0.005	0.008		0.005	0.005	0.005	0.005

B.4 DETAILED SUMMARY OF DESIGN VARIABLE VALUES FOR DESIGN A

As discussed previously, each variant of the benchmark building was designed by the current building codes (2003 IBC, ACI 318-02, and ASCE7-02) but each variant was designed slightly differently to investigate specific aspect of the code requirements. Chapter 3 presents a summary of the designs including discussion on the design variables that were varied in each design. Summarized below are additional details for Design A. For brevity, this additional detail is not given for the other design variants; however, the data for the other variants can be calculated from the design information given previously.

For Design A, the beam strengths were set to have 25% overstrength, as is representative of the practitioner designs reviewed (Appendix A). Figure B.5 shows the additional strengths provided in Design A.

1.54	1.59	1.59	1.54
1.20	1.22	1.22	1.20
1.19	1.19	1.19	1.19
1.21	1.29	1.29	1.21

Fig. B.5 Additional negative flexural beam strength: $M_u/\phi M_n$.

In addition to the beam design strengths, another important design variable is the SCWB ratio, which has a mean value of 1.3 (Appendix A). Figure B.6 shows the SCWB values provided in Design A.

0.77	0.72	0.70	0.72	0.77
1.40	1.28	1.26	1.28	1.40
1.38	1.33	1.33	1.33	1.38
1.36	1.30	1.30	1.30	1.36

Fig. B.6 SCWB ratios for Design A.

The story drifts for Design A, computed using the equivalent lateral force method in ASCE 7-02 with a simple elastic centerline model, are shown in Table B.2. For comparison, the drift value from the practitioner design was 1.6%.

Table B.2 Story drift ratios for Design A, as computed by ASCE 7-02 procedure.

<u>Story</u>	<u>Drift ratio (%)</u>
Story 4	0.9
Story 3	1.4
Story 2	1.5
Story 1	1.6

Appendix C: Calibration of Beam-Column Element Model

This appendix summarizes the results of calibrating the beam-column element model to 30 experiments of reinforced concrete columns under cyclic loading.

In order to calibrate the beam-column element model for use in analyzing a low-rise conforming special reinforced concrete frame building, we selected tests from the PEER Structural Performance Database (PEER 2005; Eberhard 2005) that met the following criteria, which resulted in 30 experimental tests meeting the criteria.

- ρ_{sh} (area confinement ratio) > 0.006 (ACI 318-05 Eq. 21-4 requires $\rho_{sh} > 0.0075$)
- $P/A_g f'_c < 0.30$
- $f'_c < 40$ MPa

Table C.1 summarizes the results of calibration, including the mean and dispersion for each calibration parameter.

Table C.1 Results of calibration study for 30 experimental tests.

Test Number (Eberhard Database)	Physical Column Properties					Calibrated Data										Comparison to Fardis		
	P/A _y f _c	P/P _b	ρ _{sh}	s (mm)	f _c (Mpa)	θ _y	EI _{eff} / EI _g	EI _{stiff} / EI _g	α _s	α _c	θ _{cap,pl} (rad)*	1 if cap is observed*	λ	c	Fardis θ _{u,mono} ^{pl} (rad)	θ _{cap,pl} computed with Fardis θ _u ^{pl} (rad)	θ _{cap,pl} - Fardis / Calibrated	
1	0.26	0.65	0.0071	80	23.1	0.008	0.25	0.47	0.01	--	0.028	0	136	1.0	0.032	0.010	0.36	
6	0.21	0.55	0.0087	90	25.0	0.009	0.31	0.83	0.04	--	0.036	0	64	1.0	0.045	0.023	0.63	
11	0.22	0.58	0.0067	117	28.3	0.010	0.34	0.75	0.07	--	0.078	0	74	1.0	0.046	0.024	0.31	
18	0.20	0.58	0.0106	80	25.6	0.010	0.30	0.65	0.02	--	0.083	0	114	1.0	0.050	0.028	0.33	
19	0.20	0.58	0.0106	80	25.6	0.009	0.33	0.77	0.02	--	0.069	0	89	1.0	0.050	0.028	0.40	
20	0.20	0.58	0.0106	80	25.6	0.009	0.34	1.92	0.02	--	0.065	0	41	1.0	0.050	0.028	0.42	
21	0.20	0.58	0.0106	80	25.6	0.009	0.32	1.14	0.01	--	0.073	0	159	1.0	0.050	0.028	0.38	
22	0.10	0.30	0.0075	110	32.0	0.010	0.18	0.35	0.03	--	0.038	0	132	1.0	0.075	0.053	1.41	
23	0.10	0.30	0.0075	110	32.0	0.010	0.19	0.40	0.03	--	0.070	0	145	1.0	0.075	0.053	0.76	
24	0.30	0.89	0.0091	90	32.1	0.010	0.28	0.79	0.04	--	0.050	0	105	1.0	0.057	0.035	0.69	
25	0.30	0.89	0.0091	90	32.1	0.011	0.27	0.73	0.01	--	0.046	0	127	1.0	0.057	0.035	0.75	
26	0.10	0.26	0.0106	80	26.9	0.008	0.27	0.61	0.04	--	0.055	0	200	1.0	0.079	0.057	1.03	
88	0.10	0.27	0.0061	76	29.1	0.010	0.34	0.55	0.05	--	0.016	0	123	1.0	0.060	0.038	2.37	
90	0.10	0.27	0.0061	76	29.2	0.010	0.30	0.54	0.06	--	0.022	0	127	1.0	0.060	0.038	1.73	
92	0.20	0.56	0.0061	76	29.4	0.014	0.30	0.64	0.02	--	0.019	0	82	1.0	0.052	0.030	1.58	
94	0.26	0.72	0.0061	76	33.3	0.012	0.36	0.61	0.06	--	0.026	0	44	1.0	0.047	0.025	0.98	
96	0.28	0.76	0.0061	76	31.0	0.010	0.43	0.67	0.01	--	0.028	0	45	1.0	0.045	0.023	0.83	
102	0.21	0.63	0.0093	102	39.3	0.011	0.31	0.43	0.20	--	0.038	0	182	1.0	0.046	0.024	0.62	
106	0.15	0.43	0.0090	50	32.0	0.016	0.20	0.35	0.06	--	0.125	0	91	1.0	0.076	0.054	0.43	
107	0.13	0.39	0.0085	65	37.3	0.021	0.15	0.37	0.07	--	0.072	0	118	1.0	0.076	0.054	0.75	
108	0.13	0.38	0.0085	65	39.0	0.021	0.15	0.35	0.07	-0.08	0.070	1	100	1.0	0.077	0.055	0.78	
167	0.20	0.59	0.0080	76	34.0	0.014	0.31	1.12	0.02	--	0.078	0	127	1.0	0.086	0.064	0.83	
181	0.00	0.00	0.0092	76	37.9	0.017	0.10	0.13	0.07	--	0.095	0	60	1.0	0.101	0.079	0.83	
182	0.00	0.00	0.0090	77	37.9	0.018	0.09	0.13	0.07	--	0.095	0	55	1.0	0.101	0.079	0.83	
187	0.11	0.32	0.0063	50	24.9	0.018	0.17	0.37	0.07	--	0.088	0	67	1.0	0.080	0.058	0.66	
188	0.16	0.45	0.0063	50	26.7	0.017	0.19	0.42	0.07	--	0.095	0	79	1.0	0.075	0.053	0.55	
189	0.22	0.61	0.0063	50	26.1	0.015	0.25	0.42	0.04	--	0.083	0	135	1.0	0.068	0.046	0.55	
190	0.11	0.32	0.0061	52	25.3	0.020	0.15	0.36	0.07	-0.07	0.070	1	78	1.0	0.080	0.058	0.82	
191	0.16	0.44	0.0061	52	27.1	0.013	0.24	0.41	0.06	-0.14	0.110	1	160	1.0	0.074	0.052	0.48	
192	0.21	0.60	0.0061	52	26.8	0.016	0.21	0.43	0.07	-0.07	0.055	1	115	1.0	0.068	0.046	0.84	
Median:	0.20	0.55	0.0078	76	29.2	0.011	0.27	0.50	0.04	-0.08	0.070	0.00	109	1.0	0.064	0.042	0.75	
Mean:	0.17	0.48	0.0079	76	30.0	0.013	0.25	0.59	0.05	-0.09	0.063	0.13	106	1.0	0.065	0.043	0.80	
C.O.V.:	0.45	0.45	0.21	0.24	0.16	0.32	0.32	0.59	0.76	0.37	0.46	2.59	0.39	0.00	0.27	0.41	0.57	

* The plastic rotation is a lower bound if a cap (i.e. a strain-softening slope) was not observed in the data.

It is important to note that the column was only pushed far enough to see a post-capping slope in only four of the 30 tests. For the tests in which a negative strain-softening slope was not observed in the test results, the calibrated value of plastic-rotation capacity represents a lower bound of what the true value might be. In future experimental work, tests should be continued to larger levels of deformation, to determine the true plastic-rotation capacity and post-capping stiffness.

The preceding table shows that the process of using Fardis' prediction of plastic-rotation capacity to compute an approximate capping point leads to predictions that are approximately 25% lower than observed values. Since most of these observed values represent a lower bound on the true plastic-rotation capacity, then the true plastic-rotation capacity is more than 25% larger than the estimate. The structural models used in this report are based on the estimates of

plastic-rotation capacity from Fardis' equation (Fardis 2003), so these structural models are slightly conservative.

It should be noted that, for elements with non-conforming detailing, Fardis' equation is unconservative by about 20% (Fardis 2003, page 526).

Sample comparisons between the experimental and calibrated results are shown in the following figures. For brevity, all 30 calibration figures are not included. The effects of P-delta are removed in each figure, according to the geometry of each test setup. The calibrated values shown in the legend on each figure may not be accurate, so please use the calibrated values shown in the table above.

After this benchmark project was completed, we expanded this calibration research to include calibration to 255 experimental tests. From these calibrations, we developed empirical equations to predict modeling parameters. We refer the reader to the paper and report of this work (Haselton, Liel, Taylor Lange, Deierlein 2007; two references).

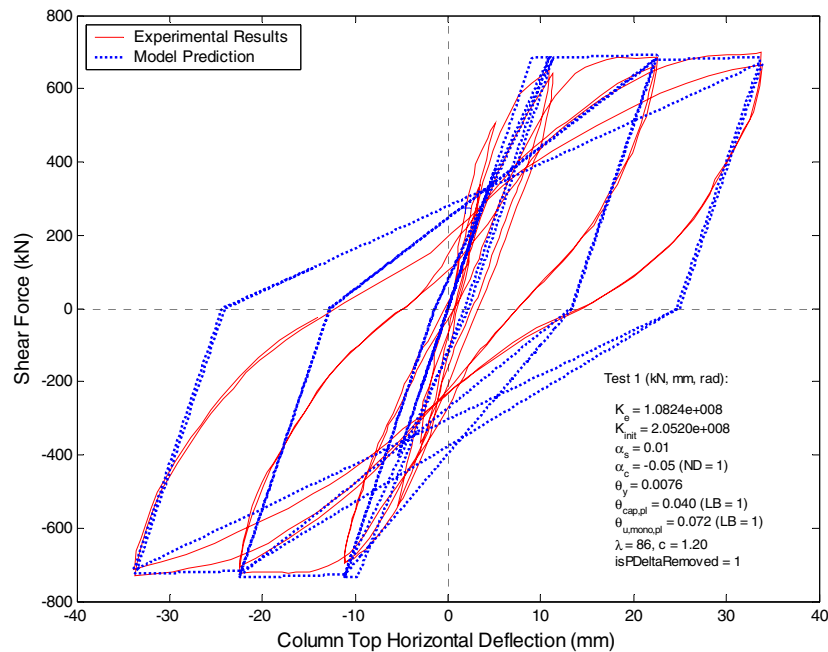


Fig. C.1 Comparison of model calibration and experimental results from Gill et al. (Gill 1979), specimen 1 (TestID 1) (PEER 2005; Eberhard 2005).

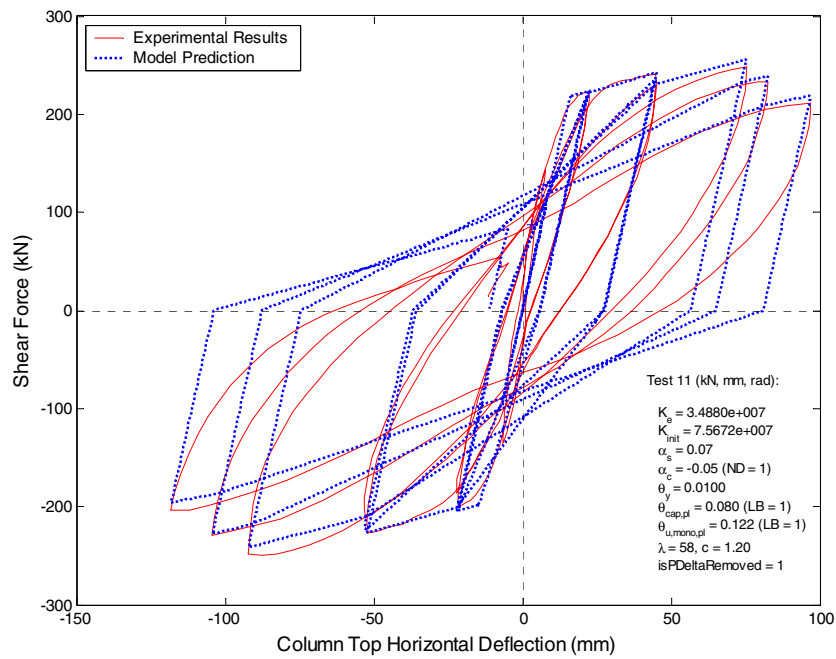


Fig. C.2 Comparison of model calibration and experimental results from Zahn et al. (Zahn 1986), specimen 7 (TestID 11) (PEER 2005; Eberhard 2005).

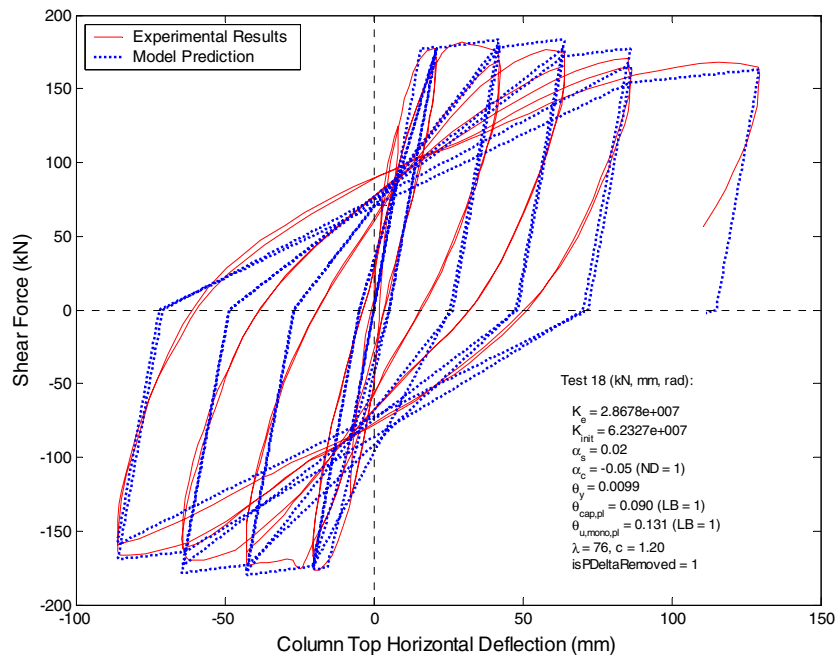


Fig. C.3 Comparison of model calibration and experimental results from Tanaka and Park (Tanaka 1990), specimen 1 (TestID 18) (PEER 2005; Eberhard 2005).

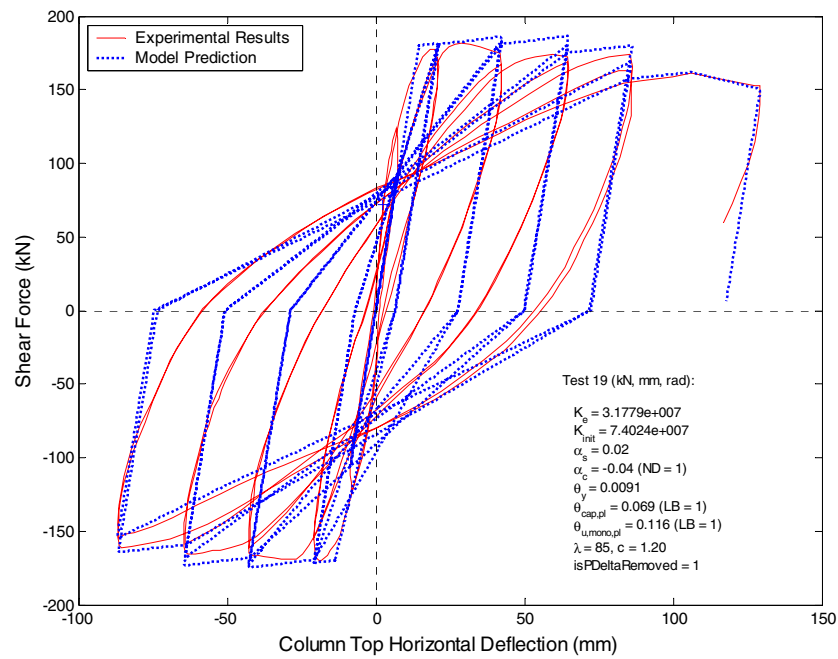


Fig. C.4 Comparison of model calibration and experimental results from Tanaka and Park (Tanaka 1990), specimen 2 (TestID 19) (PEER 2005; Eberhard 2005).

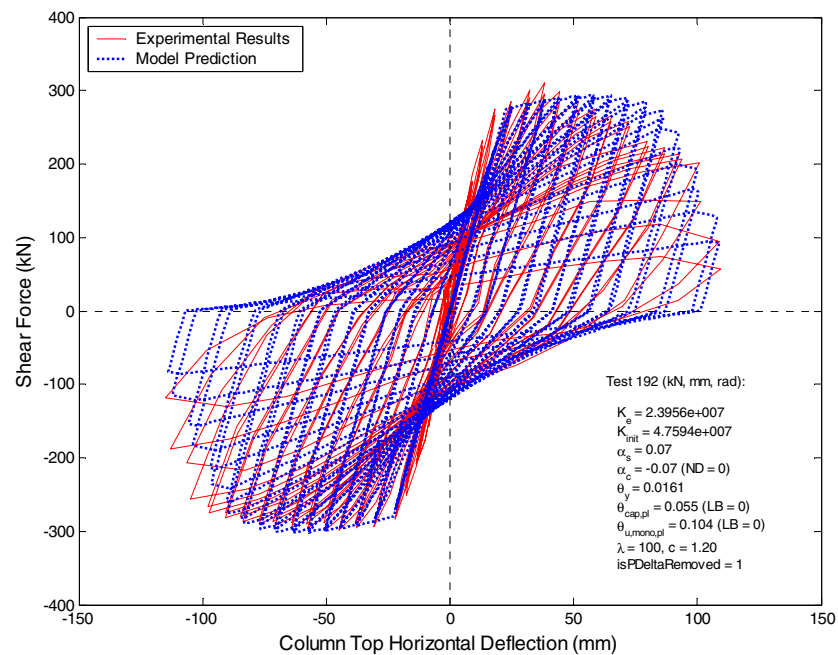


Fig. C.5 Comparison of model calibration and experimental results from Mo and Wang (Mo 2000), specimen C2-3 (TestID 192) (PEER 2005; Eberhard 2005).

Appendix D: Documentation of Element Plastic-Rotation Capacities for Each Design Variant

The purpose of this appendix is to document the plastic-rotation capacities used in the structural models for each design variant. Table D.1 lists these plastic-rotation capacities for each design variant. The relationship between section identifiers and their locations in the building is shown the building elevation view in Chapter 3.

Table D.1 Element plastic-rotation capacities for each design variant.

Section	Design A		Design B*		Design C		Design D**		Design E		Design F		Design G		Design H	
	Expected Axial Load (kips)	$\theta_{cap,pl}$														
CS1	-218	0.047	-218	0.047	-218	0.047	-218	0.047	-436	0.043	-436	0.042	-436	0.037	-436	0.037
CS2	-410	0.047	-410	0.047	-410	0.047	-410	0.047	-820	0.031	-820	0.026	-820	0.027	-820	0.027
CS3	-298	0.043	-298	0.047	-298	0.043	-298	0.043	-596	0.033	-596	0.033	-596	0.030	-596	0.030
CS4	-190	0.047	-190	0.047	-190	0.047	-190	0.047	-380	0.039	-380	0.044	-380	0.035	-380	0.035
CS4	-87	0.050	-87	0.047	-87	0.050	-87	0.050	-174	0.046	-174	0.055	-174	0.042	-174	0.042
CS5	-156	0.047	-156	0.047	-156	0.047	-156	0.047	-312	0.044	-312	0.048	-312	0.040	-312	0.040
CS6	-99	0.049	-99	0.047	-99	0.049	-99	0.049	-198	0.048	-198	0.054	-198	0.043	-198	0.043
CS6	-45	0.051	-45	0.047	-45	0.051	-45	0.051	-90	0.052	-90	0.061	-90	0.046	-90	0.046
BS1	0	0.067	0	0.067	0	0.067	0	0.067	0	0.071	0	0.072	0	0.071	0	0.071
BS2	0	0.067	0	0.067	0	0.067	0	0.067	0	0.071	0	0.073	0	0.071	0	0.071
BS3	0	0.070	0	0.067	0	0.070	0	0.070	0	0.070	0	0.072	0	0.070	0	0.070
BS4	0	0.070	0	0.067	0	0.070	0	0.070	0	0.070	0	0.071	0	0.070	0	0.070

* In this design, the bottom columns and beam were used throughout the height of the building; the rotation capacities do not reflect the slight changes that should come from changes in axial load.
** Rotation capacities are assumed to be the same as Design C; only strength were changed between these designs.

Appendix E: Structural Sensitivity Study and Propagation of Structural Uncertainties Affecting Collapse Capacity

E.1 INTRODUCTION AND PURPOSE OF CHAPTER

The question of uncertainty is at the heart of robust performance-based earthquake engineering assessment and design. The goal of seismic performance assessment is to quantify the building performance probabilistically, accurately quantifying the mean and variability of building response parameters such as peak interstory drift ratio, peak floor acceleration, element plastic rotation, and global or local collapse. This probabilistic description of response is needed in order to estimate probabilities of “failure” (i.e., reaching or exceeding some predefined limit state). In addition, once we have a distribution of response, we can combine the response information with the site hazard to obtain yearly rates of the “failure” events of interest.

This probabilistic approach is starkly different than approaches currently used in engineering practice, even when advanced nonlinear dynamic time-history analyses are employed. For example, the most advanced nonlinear dynamic procedure (FEMA 2000a) requires the use of three to seven earthquake ground motions scaled to a single design hazard level, and considers only the mean *EDP* response (or maximum response when less than seven motions are used). This approach neglects the variability in response due to record-to-record variations and the variability in the structural modeling (FEMA 2000a). The method used in this study is quite different, as it uses between 10–30 earthquake ground motions, scales the ground motions to seven different hazard levels, and estimates both the mean and the variability in

response due to the variability between different earthquake ground motions. In addition to accounting for effects of record-to-record variability, uncertainty in the structural model is recognized and accounted for, in order to achieve a probabilistic estimate of *EDP* response that is as complete as practically possible. The method to account for the effects of the uncertainty in the structural design and structural modeling is the subject of this chapter.

It should be noted that there is good reason that current engineering practice uses a more simplified method; the more complete probabilistic method is extremely time consuming and computationally expensive. In creating a mathematical structural model and trying to quantify all of the uncertainty that is inherent in the model, it quickly becomes apparent that there are numerous uncertainties that must be included in order to obtain a full probabilistic description of the *EDP* responses and collapse behavior. The number of random variables can quickly become unreasonable, even from a research perspective, so we discuss the many random variables and select a subset of these variables that we judge to be most important.

E.2 UNCERTAINTY CONSIDERED IN STUDY

The uncertainty and variability considered in this work is broken into three categories: record-to-record variability, design uncertainty, and modeling uncertainty. The record-to-record variability comes from variations between the properties of different ground motions; this variability is quantified directly by using nonlinear dynamic time-history analysis with a sufficiently large number of ground motions. Design uncertainty accounts for the variability in the engineer's design choices, given the prescriptive code requirements that govern the design (each possible design is termed a design realization). Design uncertainty is essentially the variation in how an engineer applies the code criteria in building design. Modeling uncertainty accounts for the variability of the physical properties and behavior of a structure for a *given design realization*. An example of an important design variable is the amount of additional strength that the engineer provides in a beam (above the code required strength), and an example of an important modeling variable is the seismically effective mass of the building.

E.2.1 Important Uncertainty Not Considered in Study: Human Error

This study does not address all important uncertainties. Some of these may be associated with construction and human error (Melchers 1999, Chapter 2). Melchers shows that the majority of failures are caused by human error and not by mere randomness in loading and structural response.

Melchers reviewed the causes of over 100 documented structural failures before 1980 and summarized the primary causes of each failure¹. Table E.1 presents the results of the work by Melchers. This table shows that the majority of structural failures involve human error.

Even though human error is a primary contributor to many structural failures, this study does not consider the effects of human error. The reason for this exclusion is that the understanding of human error is limited, and most information regarding human error is qualitative and difficult to incorporate (Melchers 1999). The effects of human error could be incorporated using a judgmental increase in the final estimate of uncertainty; this was not done in this study but may be included in future work.

Table E.1 Primary cause of structural failures (after Melchers 1999).

Primary Cause of Failure	%
Inadequate appreciation of loading conditions or structural behavior	43
Inadequate execution of erection procedures	13
Random variation in loading, structure, materials, workmanship, etc.	10
Violation of requirements in contract documents or instructions	9
Mistakes in drawings or calculations	7
Unforeseeable misuse, abuse/sabotage, catastrophe, deterioration	7
Inadequate information in contract documents or instructions	4
Other	7

E.2.2 Design Variables

When an engineer applies the code criteria in structural design, conservatism and architectural and constructability constraints typically lead to a structural design that is above the code minimum level. For example, higher than average floor loading in one span of a floor system

¹ Note that these failures were of many types and are not limited to seismically induced failures.

can easily cause the engineer to increase the beam strength for the full floor, thus adding additional strength to the design.

When benchmarking the performance of new construction, this conservatism and uncertainty in design is important to quantify, as this conservatism can create a great deal of additional strength and stiffness above the code minimum requirements. This design conservatism may be one of the important reasons that we seldom observe catastrophic failures of new buildings that are correctly designed.

Table E.2 gives a partial list of the code provisions that are used by practitioners in the design of new buildings; each of these will have uncertainty in how they are applied in the building design.

Table E.2 Partial list of design variables.

<u>Uncertain Structural Design Parameters</u>	
1	Strong-column weak-beam ratio (code limit of 1.2)
2	Member strength
3	Structural system: Exterior vs. interior frame
4	Beams: Designed as T-beams, or excluding slab effects
5	Maximum story drifts allowed in design
6	Member stiffness assumed in design
7	Column footing rotational stiffness assumed in design
8	Element shear force demands allowed in design
9	Joint shear force demands allowed in design
10	Slab column joints: Stress levels allowed in design
11	Column axial load ratio
12	Detailing: Confinement ratio and stirrup spacing
13	Column spacing for lateral system
14	Bay spacing for gravity system

As can be seen from Table E.2, there can be much variability in the building design, even though the design is based on the exact same code design provisions. The uncertain application of these design provisions can cause significant variability in the resulting performance of the building. The complete quantification of all the design variables in Table E.2 would involve reviewing a great number of practitioner-designed buildings, which is beyond the scope of this study. We focus on the first four items of Table E.2 in this study.

In order to quantify the first two items of Table E.2, we reviewed two practitioner-designed buildings (details in Appendix A). Table E.3 shows some of the quantitative

information from these reviews. Note that the mean and COV estimates are highly judgmental due to the limited number of designs reviewed.

Table E.3 Design variables used in study.

<u>Uncertain Structural Design Parameters</u>	<u>Mean</u>	<u>Coefficient of Variation</u>
Strong-column weak-beam ratio	1.3 (code limit of 1.2)	0.15
Member strength	25% above code required minimum	0.2

As evident when comparing Tables E.2 and E.3, much additional work is required to better quantify variability in design. Note that accurately quantifying design uncertainties using only two practitioner designs was a difficult to impossible task. Therefore, the values shown in Table E.3 reflect the fact that we removed some additional overstrength that came from the architectural considerations in the designs, so these values represent a *conservative estimate* of the design variables.

Even though the amount of quantitative information that we could extract from the review of the practitioner designs was minimal, reviewing these designs provided a great deal of qualitative information regarding how the practitioner designed each of the buildings. Both the qualitative and quantitative information was used in the design of the benchmark buildings, to make the benchmark buildings “representative of current practice.”

In addition to the design variables in Table E.3, we investigated the third item in Table E.2 by designing several perimeter and space-frame buildings. We addressed item four in Table E.2 by designing a space-frame building both including and excluding the slab steel effects in the beam design strength (Designs F and E, respectively). All of these designs are described in detail in Section 3.3.6.

E.2.3 Modeling Variables

In contrast to design variables, much previous research has focused on quantifying modeling variables. Table E.4 presents the mean and coefficient of variation (c.o.v.) of each of the basic design and modeling variables. In addition, the table shows the references used to quantify each of the uncertainties, and the level of accuracy of the COV estimates. Note that some of the

variables in Table E.4 are not used in the uncertainty analysis to follow in Section E.4; even so, they are documented here for use in future uncertainty studies.

Table E.4 Summary of modeling and design random variables.

Random Variable	Mean	c.o.v.	Level of Accuracy of RV Value	Reference(s)
Design Variables:				
Strong-column weak-beam design ratio	1.3	0.15	2	This study
Beam design strength	1.25	0.20	2	This study
System Level Variables:				
Dead load and mass	1.05(computed)	0.10	1	Ellingwood (1980)
Live load (arbitrary point in time load)	12 psf	--	1	Ellingwood (1980)
Damping ratio	0.065	0.60	1	Miranda (2005), Porter et al. (2002), Hart et al. (1975)
Beam-Column Element Variables:				
Element strength	1.0(computed)	0.12	1	Ellingwood (1980)
Element initial stiffness	1.0(computed)	0.36	1	Panagiotakos (2001), Fardis (2003)
Element hardening stiffness	0.5(computed)*	0.50	2	Wang (1978), Melchers (1999), Fardis (2003)
Plastic rotation capacity	1.0(computed)	0.60	1	Panagiotakos (2001), Fardis (2003)
Hysteretic energy capacity (normalized)	110-120	0.50	2	This study, Ibarra (2003)
Post-capping stiffness	0.08(-K _{elastic})	0.60	2	This study, Ibarra (2003)
Concrete tension softening slope	1.0(computed)	0.25	2	Kaklauskas et al. (2001), Torres et al. (2004)
Beam-Column Material Variables (note that these only contribute to element-level variables):				
Rebar yield strength	66.8 ksi	0.04--0.07	1	Melchers (1999)
Rebar strain hardening	0.018E _s	--	1	Wang (1978)
Rebar stiffness (E _s)	29,000 ksi	0.033	1	Melchers (1999)
Concrete strength	4030 ksi	0.21	1	Ellingwood (1980)
Gravity System Variables:				
Slab strength (effective width)	1.0(computed)	0.2	1	Ellingwood (1980), Enomoto (2001)
Drift at slab-beam capping	4.5% drift	0.6	1	This study (Appendix 7a)
Other Variables:				
Column footing rotational stiffness	1.0(computed)	0.3	2	This study
Joint shear strength	1.40**	0.1	2	Altoontash (2004), Meinheit (1981)
Level of Accuracy of Random Variable Quantification:				
1: Coefficient of variation computed from a relatively large amount of data and/or from a computed value stated in the literature				
2: Coefficient of variation computed from a relatively small amount of data or estimated from a figure in a reference				
Notes:				
-- the RV was treated deterministically or another model variable accounts for the same uncertainty				
* value is a fraction of the value computed using fiber analysis with expected values of material parameters				
** value is a fraction of the value computed from ACI 318-02 provisions				

The detailed explanation of how we quantified each of the important random variables in Table E.4 is given in Appendix F.

After the sensitivity study and the propagation of uncertainty were completed, further research yielded improved estimates for some random variable values. Further calibrations to experimental data (Haselton et al. 2007) verified that the coefficient of variation of the plastic-rotation capacity should be 0.54. The same study verified that the coefficient of variation of

energy-dissipation capacity should be 0.47 and showed that the coefficient of variation of post-capping stiffness should be increased to 0.72. Recent work by Miranda (2005) shows that a mean damping ratio of 6–7% and a coefficient of variation of 0.60 are more appropriate than what was used in this study. This new information was discovered after the current sensitivity study was completed, so these improvements were not used in this study but will be used for future uncertainty studies.

E.3 CORRELATIONS BETWEEN VARIABLES

The correlations between each of the modeling and design variables are difficult to quantify but prove to be one of the most important aspects in quantifying the uncertainty in structural response. To our knowledge, these correlations have not been significantly investigated in previous research. However, Section E.8.4 will show that the assumptions regarding these correlations will *significantly affect* our final predictions of structural response. This is particularly true for predictions of low probabilities of collapse and for the predictions of the mean annual frequency of collapse.

We completed sensitivity analyses for both fiber and lumped-plasticity models, but for brevity, only the results for the collapse analyses using the lumped-plasticity model are presented in this report. Table E.5 presents the ten random variables used in the sensitivity study and uncertainty propagation with the lumped-plasticity model. These variables were selected based on preliminary analyses to determine which variables could be excluded.

Table E.5 Ten random variables used for uncertainty propagation.

Random Variable Number	RV Name
RV1	Plastic rotation capacity
RV2	Hysteretic energy capacity (normalized)
RV3	Post-capping stiffness
RV4	Element strength
RV5	Strong-Column Weak-Beam design ratio
RV6	Element initial stiffness
RV7	Element hardening stiffness
RV8	Damping ratio
RV9	Dead load and mass
RV10	Beam design strength

In order to use each of these random variables and propagate the combined effects of their uncertainties, we need to quantify the correlations between the variables. These correlations are of two basic types, each of which are described in the next two sections:

- (a) Correlations between parameters of a given element
- (b) Correlations between parameters of different elements

E.3.1 Correlations for a Single Element (Type A Correlation)

An example of the correlations between random variables for a single element is the correlation between the strength of a column and the stiffness of that same column. This correlation comes from the fact that the strength and stiffness of an element are affected by some of the same things such as member dimensions, rebar placement, and quality of construction.

In this study, we calibrated to only 30 column tests, so we did not try to estimate these correlations from the test data. Therefore, we simply used judgment to decide which random variables we expect to be correlated, and then assumed full correlation between these variables. Table E.6 shows the resulting correlation matrix for the ten random variables of a single element.

Later, for estimates of uncertainty in collapse capacity, Section E.5.2 presents uncertainty estimates assuming no Type A correlation, full Type A correlation, and expected Type A correlation (expected correlations are reflected in Table E.6). Section E.8.4 then shows how the range of possible uncertainties translate into ranges of predictions for $P[C | Sa_{2/50}]$ and $\lambda_{collapse}$.

Table E.6 Correlation matrix used for correlations for a single element.

	RV1	RV2	RV3	RV4	RV5	RV6	RV7	RV8	RV9	RV10
RV1	1									
RV2	1	1								
RV3	-1	-1	1							
RV4	0	0	0	1						
RV5	0	0	0	0	1					
RV6	0	0	0	1	0	1				
RV7	0	0	0	0	0	1	1			
RV8	0	0	0	0	0	0	0	1		
RV9	0	0	0	1	0	1	0	0	1	
RV10	0	0	0	0	1	0	0	0	0	1

E.3.2 Correlations for Random Variables of Different Elements (Type B)

An example of the correlations between random variables for different elements is the correlation between the strength of the bottom floor column and the stiffness of the beam at the roof level. This correlation is difficult to quantify and is affected by many factors. For example, the contractor may fabricate a large number of stirrups at the same time and systematically make the stirrups larger than what is called for in the plans. In this case, when the longitudinal rebar are placed into the elements with larger stirrups, the effective depth of the rebar will tend to be systematically larger than expected. This will cause a high positive correlation between the strengths of all of the affected elements.

To completely solve this problem, we would need to accurately quantify all of these correlations between elements, then use unique RVs for each element, while maintaining the proper correlation structure for all of the elements of the frame. This is a prohibitive task when using nonlinear dynamic time-history analysis for performance assessment. If we do not assume full correlation between elements then we will need to have a separate random variable for each element, resulting in a total of 360 random variables for the 36 elements of a single frame. If we assume full correlation between the random variables of different elements we can reduce the total number of random variables to 10 (i.e., one strength variable for the full frame rather than one strength variable for each element). Therefore, when running the sensitivity analysis, we assumed that the parameters between each element are fully correlated, as shown in the correlation matrix in Table E.7.

Note that this full Type B correlation assumption is not a conservative assumption. The possible impacts of this assumption are mentioned at the end of this section.

Table E.7 Correlation matrix used for correlations for multiple elements.

		Element _i										Element _j									
		RV1	RV2	RV3	RV4	RV5	RV6	RV7	RV8	RV9	RV10	RV1	RV2	RV3	RV4	RV5	RV6	RV7	RV8	RV9	RV10
Element _i	RV1	1										(Symmetric)									
	RV2	1	1																		
	RV3	-1	-1	1																	
	RV4	0	0	0	1																
	RV5	0	0	0	0	1															
	RV6	0	0	0	1	0	1														
	RV7	0	0	0	0	0	1	1													
	RV8	0	0	0	0	0	0	0	1												
	RV9	0	0	0	1	0	1	0	0	1											
	RV10	0	0	0	0	1	0	0	0	0	1										
Element _j	RV1	1	1	-1	0	0	0	0	0	0	0	1									
	RV2	1	1	-1	0	0	0	0	0	0	0	1	1								
	RV3	-1	-1	1	0	0	0	0	0	0	0	-1	-1	1							
	RV4	0	0	0	1	0	1	0	0	1	0	0	0	0	1						
	RV5	0	0	0	0	1	0	0	0	0	1	0	0	0	0	1					
	RV6	0	0	0	1	0	1	1	0	1	0	0	0	0	1	0	1				
	RV7	0	0	0	0	0	1	1	0	0	0	0	0	0	0	1	1				
	RV8	0	0	0	0	0	0	0	1	0	0	0	0	0	0	0	0	1			
	RV9	0	0	0	1	0	1	0	0	1	0	0	0	0	1	0	1	0	0	1	
	RV10	0	0	0	0	1	0	0	0	0	1	0	0	0	0	1	0	0	0	0	1

To investigate the effects of this correlation assumption, we developed a simple approximate method for quantifying the effect of partial correlation between parameters of different elements. This approximate method is only appropriate for elements in parallel (e.g., two columns of the same story) and for responses that are global in nature (e.g., drift and floor acceleration); this will not work for *EDPs* like plastic rotation in a single element. Appendix G explains this approximate method and shows the effects that the correlation assumptions have on the estimated uncertainty in collapse capacity. Depending on Type B correlation assumptions, the final uncertainty in collapse capacity can change by a *factor of 2.0* (Section E.5.2).

One *extremely important point* that was not considered in this study is the possibility of partial correlation between elements at different story levels. In this work, we assume that the variables (like strength, ductility, etc.) are *perfectly correlated* from story to story. This was done to reduce the number of random variables, and thus the computational expense, since the sensitivity study presented in this report took several weeks to be completed using five 2004-era desktop computers. However, use of this simplifying assumption does not allow the sensitivity analysis to account for the fact that partial correlation may cause one story to be weaker or less ductile than adjacent stories, thus causing the damage to concentrate unequally in that story. Future research needs to look more closely at these uncertainty issues to better understand the impacts of simplifying assumptions, such as those made in this study.

E.4 SENSITIVITY STUDY: COLLAPSE CAPACITY

In order to learn how the previously discussed uncertainties affect the uncertainty in collapse capacity, we vary the value of each random variable (RV) individually, rerun the collapse analysis, and then observe how the RV affects the collapse capacity. This section discusses this sensitivity of collapse capacity to each RV. As previously mentioned, when varying each RV value, we assume full Type B correlation to reduce computational burden and to make the problem tractable.

To find the total uncertainty in collapse capacity that results from the uncertainty in all of the RVs, we use the first-order second-moment (FOSM) method to combine the effects of each RV with information regarding correlations. Section E.5 presents these calculations and the final estimated uncertainty in collapse capacity.

E.4.1 Sensitivity of Collapse Capacity to Each Random Variable

To determine the sensitivity of the collapse capacity to each of the ten RVs listed in Table E.5, we took each RV individually, set the RV value to $\mu_{RV} \pm \sqrt{3} \sigma_{RV}$, and then ran the collapse analysis for ten ground motions. We used Design A for the sensitivity analysis and used the records from Bin 4A (one random component from each record pair) because these are the records selected for the highest *IM* level that are closest to those that may cause collapse. We used $\mu_{RV} \pm \sqrt{3} \sigma_{RV}$ because these values are needed for the moment-matching method that we were considering for uncertainty propagation; however in the course of this project, we decided to instead use the FOSM approximation (Section E.5.1). When moment matching is not used, $\mu_{RV} \pm \sigma_{RV}$, is more appropriate (Baker 2003).

Figure E.2 shows the collapse cumulative density functions (CDFs) for the plastic-rotation capacity (RV1) set to $\mu_{RV1} \pm \sqrt{3} \sigma_{RV1}$ ². Similar graphs for the other random variables are given in Figure E.1(a)–(h). Note that these sensitivity analysis results use a slightly different structural model and set of ground motions than for other collapse results presented elsewhere in this report, so the collapse capacities will not precisely match other presented values. Even so,

² When we computed the altered random variable values used in the sensitivity study, we inadvertently used a normal standard deviation; a lognormal standard deviation should be used in future sensitivity analyses of this type (Ibarra 2003, Chapter 6).

the differences in the structural models are relatively minor, so we believe that the sensitivity of the collapse capacity predictions is similar for the different models used.

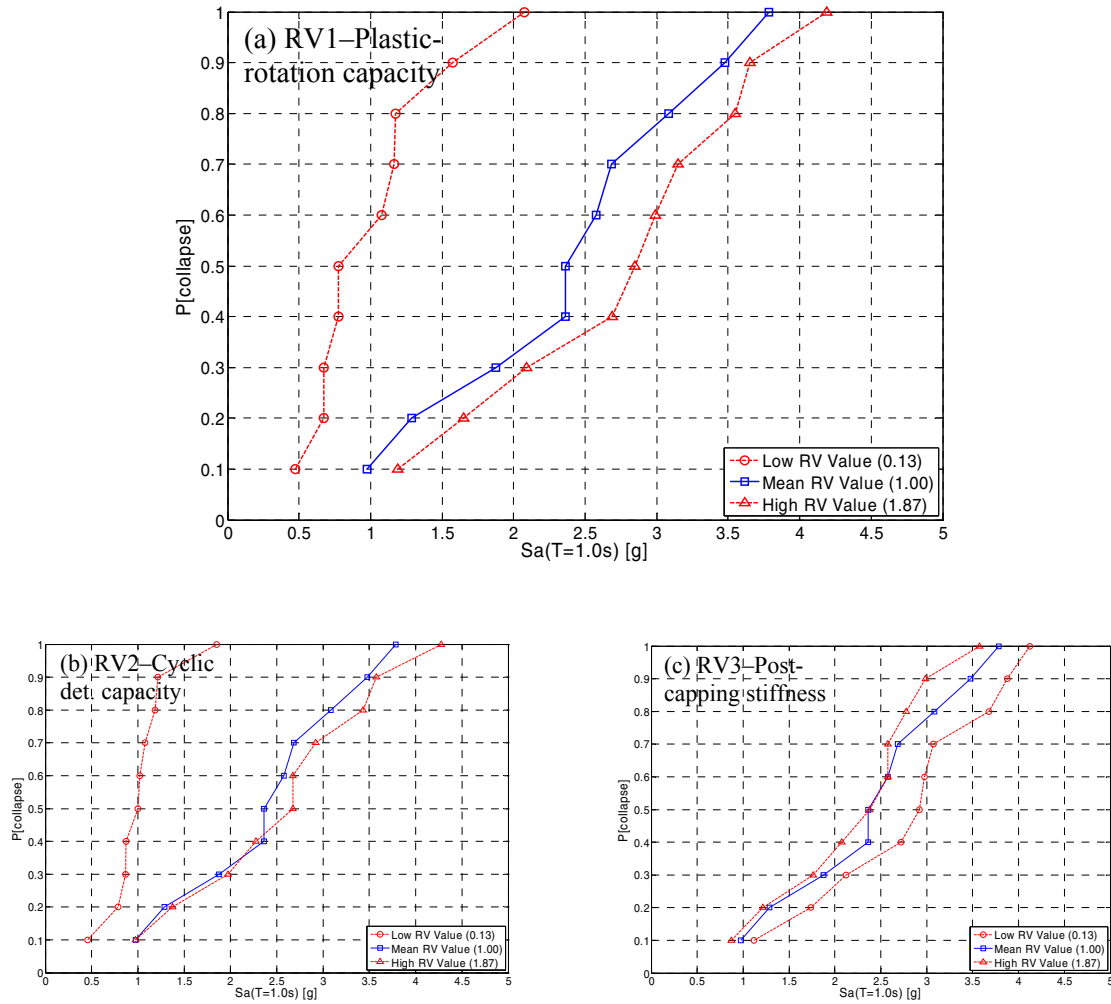


Fig. E.1 Variation in collapse cumulative distribution function (CDF) with individual RV values varied to $\mu_{RV} \pm \sqrt{3} \sigma_{RV}$. Note that Table E.5 defines RV indices. Spectral acceleration shown that of ground motion component.

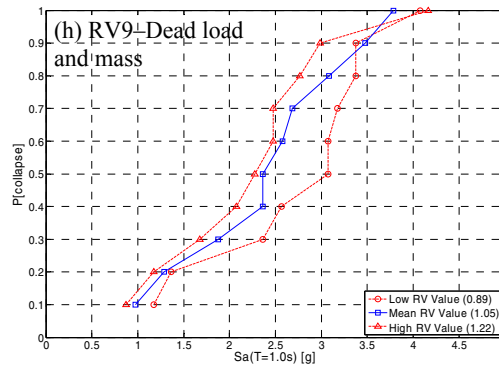
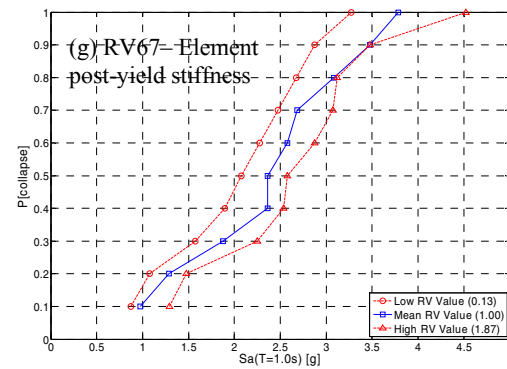
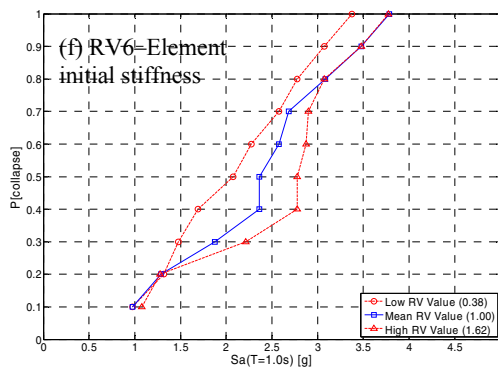
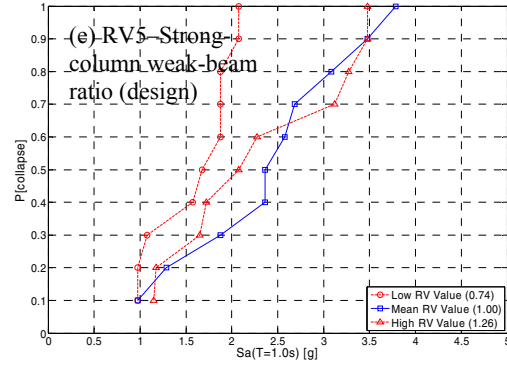
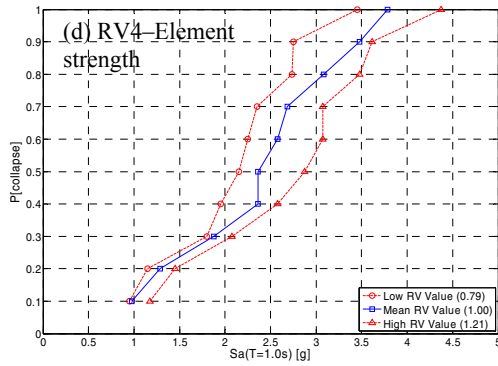


Figure E.1—Continued

Figure E.1 shows how the RVs affect the full collapse cumulative distribution function (CDF). A tornado diagram may also be used to show only the change in the mean collapse capacity (Porter 2003). Figure E.2 shows a tornado diagram derived from the information in Figure E.1. This tornado diagram shows only the *mean* collapse capacities from each of the above figures, and the variables are ordered by relative importance (note that the tornado diagram uses the mean of a fitted lognormal distribution).

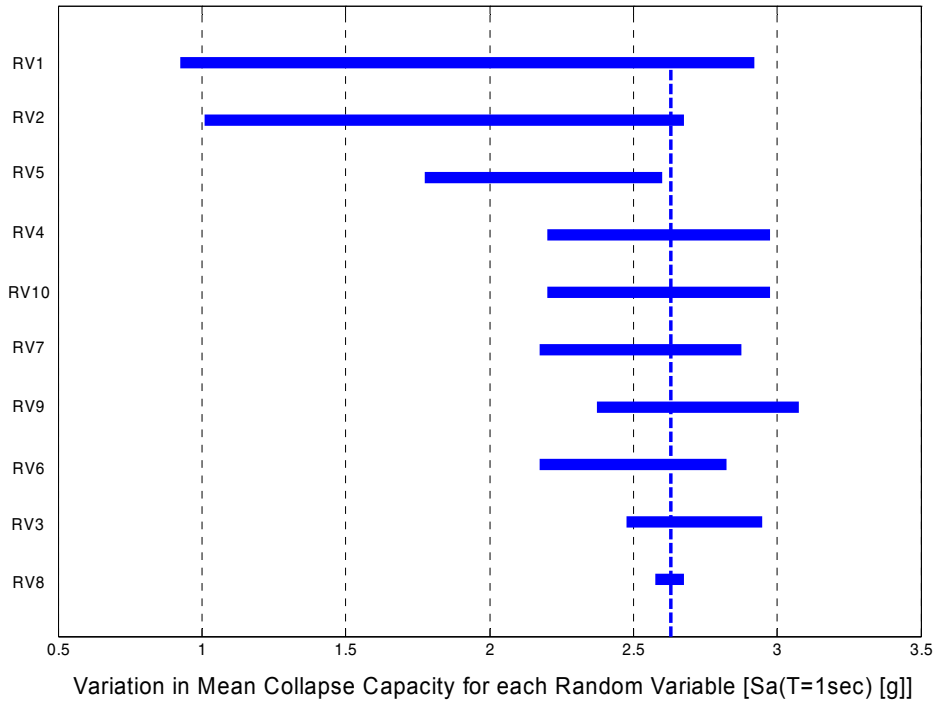


Fig. E.2 Tornado diagram showing sensitivity of mean collapse capacity to each RV. RVs varied to $\mu_{RV} \pm \sqrt{3} \sigma_{RV}$, and values displayed are means of fitted lognormal distribution. Note that Table E.5 defines RV indices.

Figures E.1–E.2 show the relative importance of each random variable. Observations from these figures are as follows:

- Element plastic-rotation capacity (RV1) most influences the collapse capacity. This agrees with findings by Ibarra (2003). Note that the apparent insignificance of increasing the plastic-rotation capacity comes from the fact that for large increases in plastic-rotation capacity, the element hardens enough to cause the joints to fail in shear. Figure E.3 will show this in more detail.
- Cyclic deterioration capacity (RV2; λ) is shown to be the second most influential variable, but this is not consistent with findings from Ibarra (2003). Ibarra found that the effects of cyclic deterioration are not important for conforming elements with slow deterioration rates. The apparent importance of the cyclic deterioration in Figure E.1(b) is related to the fact that we used $\mu_{RV} \pm \sqrt{3} \sigma_{RV}$ for the sensitivity study, and $\lambda = \mu_{\lambda} - \sqrt{3} \sigma_{\lambda}$ with a normal distribution is an unreasonably low value to use for assessing sensitivity. The following section looks into this issue more closely and shows that for

more reasonable values, λ is not as significant as suggested by Figure E.1(b). The following section shows that the final findings regarding cyclic deterioration agree well with the findings of Ibarra.

- Reducing the strong-column weak-beam ratio (RV5) causes the collapse capacity to decrease (Fig. E.1(e)). Increasing the strong-column weak-beam ratio causes no systematic change to the collapse capacity, and with the ground motion randomness the mean collapse capacity actually decreases slightly.
- The post-capping stiffness ratio (RV3; α_c) is shown to be almost insignificant. Ibarra has previously shown for single-degree-of-freedom systems that the post-capping stiffness is of critical importance when α_c is changed from -10% to -30%, but almost insignificant when α_c is changed from -30% to -50% (Ibarra 2003, Fig. 4.13). The mean element-level α_c is -8% (Table E.4), but Figure 5.23 shows that the static pushover analysis indicates damage localizing in two stories, causing the system-level post-capping stiffness to be nearly -30% of the initial stiffness. Therefore, the effective building-level α_c is -30%, so our findings about the unimportance of post-capping slope agree with findings of Ibarra (2003).
- The sensitivity to damping ratio (RV8: ξ) is not shown here because the damping values used in the sensitivity study differ from those used in other analyses presented in this report. Not reporting these values is warranted because the damping value does not have large impacts on the collapse capacity. However, continued studies have indicated that the damping *formulation* may be an important factor in collapse simulation; this is a topic of continued study.

This section showed the sensitivity of the collapse capacity for each RV individually. This information, combined with the correlations between random variables, can be used with the FOSM approximation to determine the total uncertainty in collapse capacity. However, before computing the final uncertainty in collapse capacity, the next section takes a closer look at the two RVs that this section showed to be most critical to the prediction of collapse capacity.

E.4.1.1 Closer Look at Sensitivity to Important Random Variables

Figures E.1–2 showed that the plastic-rotation capacity and the cyclic energy-dissipation capacity are the two variables that most influence the collapse capacity estimate. Part of the reason that these variables appear so significant is the fact that the sensitivity study was completed using $\mu_{RV} \pm \sqrt{3} \sigma_{RV}$ (Section E.4.1). These points represent extremely large changes to the RV values and this may not be appropriate when assuming that each variable linearly affects the collapse capacity (see FOSM explanation in Section E.5.1). Ibarra found that using such extreme changes to random variable values can skew the uncertainty predictions when using the FOSM approximation (Ibarra 2003).

In order to check the linearity assumption of the FOSM method, Figures E.3 and E.4 show how the two most important random variables (plastic-rotation capacity and hysteretic energy-dissipation capacity) affect the collapse capacity for earthquake number 941082 (Loma Prieta E-W motion from the 58235 Saratoga station). Note that trends for a single ground motion record may not accurately reflect trends for a larger set of ground motion records, so the following is primarily for illustration. Therefore, it is important to note that the information used from this single record changed only the final modeling uncertainty estimates (σ_{LN}) by 16%, which is small in comparison to many of the other uncertainties. If the effect would have been more significant, it would have been wise to do the following comparisons for ten or more records and use average results for the multiple ground motions.

Figure E.4 shows that the relationship between plastic-rotation capacity and collapse capacity is linear for reductions in plastic-rotation capacity. Since reducing the plastic-rotation capacity will lead to earlier collapse, we used the leftward gradient for the FOSM calculations. Since the leftward gradient is linear, the gradient estimate is not sensitive to the amount of change to the random variable, so we did not adjust the gradient estimate based on results shown in Figure E.4.

For increases in plastic-rotation capacity, the elements strain harden significantly and the predicted failure mode of the building is changed to joint shear failure; therefore the predicted collapse capacity does not increase with increases in plastic-rotation capacity. This alteration of the failure mode for larger plastic-rotation capacities is likely only an artifact of the model, as the strain-hardening stiffness will likely reduce at large levels of plastic rotation. The current element model does decrease the strain hardening based on cyclic deterioration, but this

reduction is typically too low in comparison to experimental results (see calibrations in Appendix C).

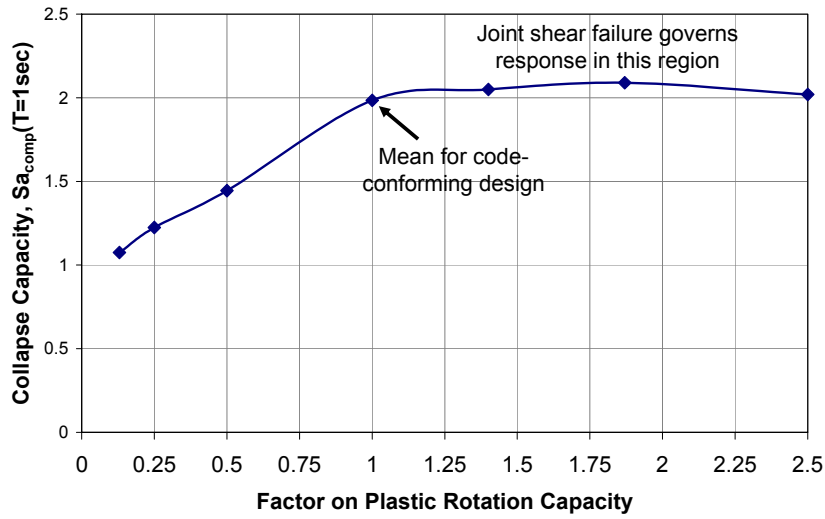


Fig. E.3 Effect of plastic-rotation capacity on collapse capacity for earthquake number 941082.

Figure E.4 shows that for reductions in hysteretic energy-dissipation capacity, the effect on collapse capacity is highly nonlinear. The original gradient estimate (earlier in Fig. E.1(a) and E.2) was based on a large reduction in the random variable value. Figure E.4 shows that this gradient reduces by a factor of 2.5 if a random variable alteration of $\mu_{RV} - \sigma_{RV}$ is used rather than $\mu_{RV} - \sqrt{3} \sigma_{RV}$. This reduction in the gradient reduced the final predicted uncertainty in the collapse capacity by 16%.

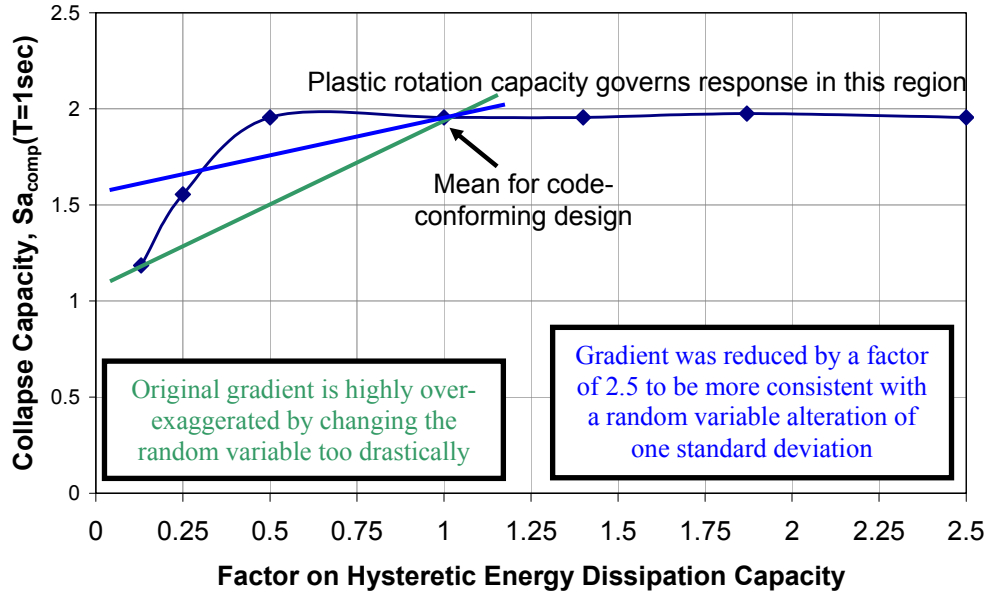


Fig. E.4 Effect of hysteretic energy-dissipation capacity on collapse capacity for earthquake number 941082.

E.5 PROPAGATION OF UNCERTAINTY: COLLAPSE CAPACITY

The previous two sections discussed the correlations between RVs and the sensitivities of the collapse capacity to these random variables. This section takes this information and uses the first-order second-moment (FOSM) approximation to estimate the total uncertainty in collapse capacity that is caused by the uncertainty in the random variables. This same method can be used for pre-collapse responses (e.g., drift, floor acceleration, etc.) but was not done in this study.

E.5.1 First-Order Second-Moment Method

This section explains the FOSM method (Baker 2003; Cornell and Baker 2002); to clarify this method, Appendix H presents a sample FOSM calculation. The FOSM method assumes that each random variable linearly affects the collapse capacity. This allows us to predict how the standard deviation of collapse capacity is increased by the structural modeling uncertainties. However, the FOSM method is incapable of predicting how the mean (or median) collapse capacity may be affected by structural modeling uncertainties.

To begin the FOSM method, we assume that a function, g , relates the random variables to the response of interest, which here is the collapse capacity³. The g -function simply represents the structural analysis, which relates the structural random variables to the collapse capacity.

$$S_{a_{collapse}} = g(X_1, X_2, \dots, X_n) + X_{RTR} \quad (E.1)$$

where X_1, \dots, X_n are random variables (e.g., plastic-rotation capacity, etc.) and X_{RTR} is a zero-mean random residual representing the record-to-record variability of $S_{a_{collapse}}$.

To determine the mean and the record-to-record variability of the collapse capacity, we simply set all random variables to their respective mean values and perform the collapse analysis with a sufficiently large number of records (10–30 used in this study).

$$\mu_{S_{a_{collapse}}} \cong g(M_x) \quad (E.2)$$

where M_x is the vector of mean values of the random variables.

Equation E.3 is used to determine the total variance in collapse capacity. The correlation coefficients and standard deviations of each random variable were discussed in Sections E.3 and E.2.3, respectively. The gradients are obtained from the sensitivity analyses presented in Section E.4.1.

$$\sigma^2 [S_{a_{collapse}}] \cong \left[\sum_{i=1}^n \sum_{j=1}^n \left[\frac{\partial g(X)}{\partial x_i} \cdot \frac{\partial g(X)}{\partial x_j} \right]_{X=M_x} \rho_{ij} \sigma_i \sigma_j \right] + \sigma^2 [X_{RTR}] \quad (E.3)$$

where $\frac{\partial g(X)}{\partial(x_i)}$ is the gradient of the $S_{a_{collapse}}$ with respect to random variable I ,

ρ_{ij} is the correlation coefficient between RV_i and RV_j , and σ_i is the standard deviation of RV_i .

Figure E.5 shows a schematic of how the FOSM method approximates the effect of each RV on $S_{a_{collapse}}$.

³ The notation used in this section is written for propagating uncertainty in collapse capacity, but the same equations can be applied to other values of interest, such as drift ratio, by simply replacing $S_{a_{collapse}}$ by whichever term for which one wishes to estimate the uncertainty.

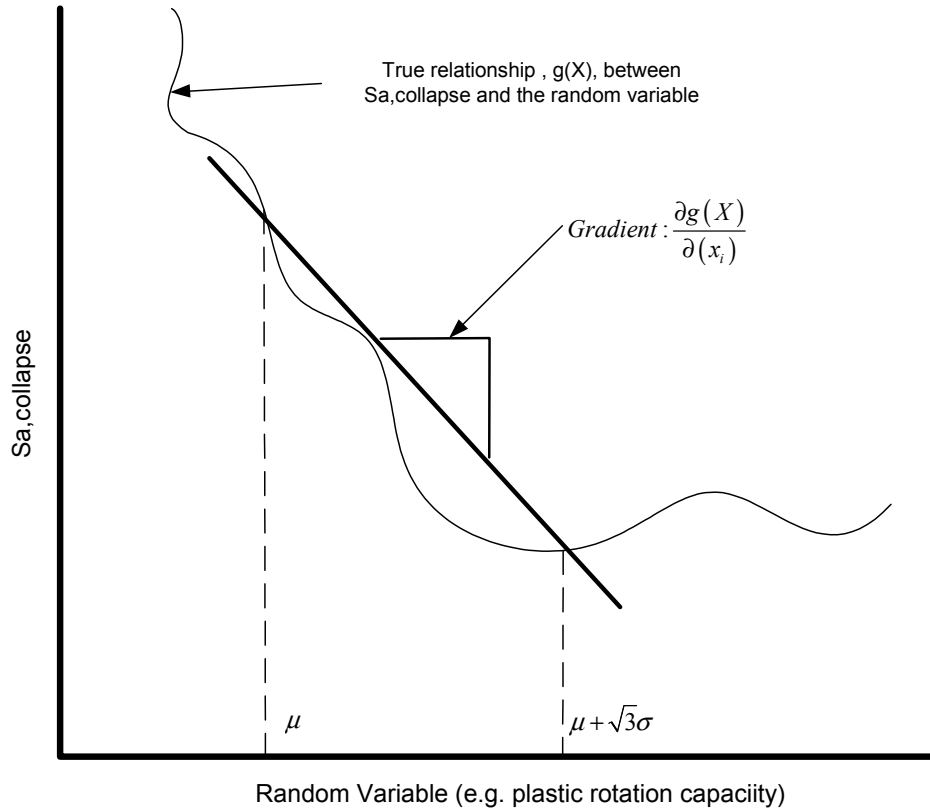


Fig. E.5 Schematic diagram of true nonlinear relationship, $g(x)$, and FOSM linear approximation.

E.5.2 Estimated Variability of Collapse Capacity

We used the FOSM method to estimate the total variability in the collapse capacity estimate. We performed all FOSM calculations in the log-domain of the data based on recommendations from previous research (Ibarra 2003, Chapter 6). As correlation assumptions have a large effect on estimated collapse capacity variability, we completed the FOSM calculations for three levels of both Type A and Type B correlations (correlations discussed in Sections E.3.1–2).

Table E.8 presents the estimated collapse capacity variability when considering all ten variables shown earlier in Table E.5 (i.e., both modeling uncertainties and design uncertainties). These values represent the standard deviation of a lognormally distributed random variable (numerically similar to the coefficient of variation). Also, note that the values of Table E.8 do not include the contribution of record-to-record variability (i.e., they include only the first term in Eq. E.3); the record-to-record variability is incorporated later in Section E.7.1 individually for each structural design. Table E.8 shows that the estimates depend heavily on correlation

assumption, with Type A correlations changing predictions by a factor of two to three, and Type B correlations changing predictions by a factor of two. In later calculations for Design A, to account for both design and modeling uncertainties, 0.45 is used as the “best estimate” of the log-standard deviation of $S_{a \text{ collapse}}$ (note that this value does not include record-to-record variability).

The results shown in Table E.8 result from the FOSM approximation being completed using the data transformed by using the natural logarithm (because the relationships between the random variables and the collapse capacity are typically more linear after the data are transformed using the natural logarithm) (Cornell and Baker 2002). For comparison, the FOSM approximations were also completed without transforming the data by the natural logarithm for a select few sets of correlation assumptions; this resulted in values of 0.67 and 0.52 in place of 0.54 and 0.38, respectively, in Table E.8. Differences of similar magnitude have been documented by Ibarra (Chapter 6, 2003).

Table E.8 Estimated variability in collapse capacity. Both modeling variability (RVs 1–4 and 6–9) and design variability (RVs 5 and 10) are included and computations completed for three levels of Types A and B correlations.

$\sigma_{LN, modeling\&design}$ with various correlations		Type B Correlations - Between Parameters of Element _i and Element _j		
		Full Correlation	Partial ($\rho_{ij} = 0.5$) - approx. method	No Correlation
Type A Correlations - Between Different Parameters of the Same Element	Full Correlation	1.00	0.79	0.56
	Full Correlation between Variables Expected to be Correlated	0.54	0.43	0.28
	No Correlation	0.38	0.30	0.21

Table E.8 showed the estimates that include both modeling and design uncertainties. This is appropriate for assessing *future construction* when how the building may be designed is still uncertain. For a situation in which the design is fully specified, only the modeling uncertainties should be included. To facilitate this, Table E.9 presents similar predictions that include only the contributions of the modeling variables (i.e., only variables 1–4 and 6–9). IN situations where design uncertainties should not be included, 0.35 is used as the “best estimate” of the log-standard deviation of $S_{acollapse}$ (note that this value does not include record-to-record

variability). Table E.10 is similar, but shows predictions when only design variables are included (i.e., only variables 5 and 10).

Table E.9 Estimated variability in collapse capacity. Only modeling variability (RVs 1–4 and 6–9) included (design variability not accounted for) and computations completed for three levels of Types A and B correlations.

$\sigma_{LN,modeling}$ (no design uncert.) with various correlations		Type B Correlations - Between Parameters of Element _i and Element _j		
		Full Correlation	Partial ($\rho_{ij} = 0.5$) - approx. method	No Correlation
Type A Correlations - Between Different Parameters of the Same Element	Full Correlation	0.68	0.54	0.40
	Full Correlation between Variables Expected to be Correlated	0.43	0.34	0.23
	No Correlation	0.30	0.24	0.18

Table E.10 Estimated variability in collapse capacity. Only design variability (RVs 5 and 10) is included (modeling variability not accounted for) and computations completed for three levels of Types A and B correlations.

$\sigma_{LN,design}$ (no modeling uncert.) with various correlations		Type B Correlations - Between Parameters of Element _i and Element _j		
		Full Correlation	Partial ($\rho_{ij} = 0.5$) - approx. method	No Correlation
Type A Correlations - Between Different Parameters of the Same Element	Full Correlation	0.33	0.26	0.16
	Full Correlation between Variables Expected to be Correlated	0.33	0.26	0.16
	No Correlation	0.24	0.19	0.12

E.6 METHODS TO ACCOUNT FOR UNCERTAINTIES

E.6.1 Introduction and Types of Uncertainties

There are two primary ways to consider the impacts that uncertainties have on structural response. We can either separate uncertainties into two abstract categories (aleatory and epistemic, which are defined below), or we can make no distinction between different types of uncertainty. The recent SAC effort (Cornell 2002) separated uncertainties into categories, while our work makes no distinction between types of uncertainties.

Uncertainty is often categorized into two conceptual types. The first type of uncertainty is “randomness.” This is uncertainty that comes from something that is inherently random, in which case we will never be able to reduce this uncertainty by researching the phenomenon in more detail; this is often called *aleatory* uncertainty. The other type of uncertainty comes from lack of knowledge (ignorance) or modeling error; this is often called *epistemic* uncertainty. Epistemic uncertainty can always be reduced by further research that leads to better understanding and better modeling of the phenomenon.

The remainder of this section discusses the two methods (separating uncertainties or putting them all together) and explains why we chose to not separate uncertainties by type in this study. The example used in this section is for Design A without considering the gravity-frame contribution, and subjected to the ground motions from Bins 4A and 4C.

E.6.2 Estimates at a Given Level of Prediction Confidence: Separating Uncertainties by Conceptual Type

The motivation to separate uncertainties is to be able to make statements regarding prediction confidence, (e.g., “At 90% prediction confidence, the probability of collapse is only 25%”). In order to make such statements, we need to separate the uncertainties and categorize them into “randomness” (aleatory) or “lack of knowledge” (epistemic). There is much debate about how to separate variability, so in this illustration, we will say that ground motion variability is *aleatory* and all the modeling uncertainties (as computed in Section E.5.2) are *epistemic*.

Figure E.6 shows the distribution of the building collapse capacity and illustrates how these uncertainties are utilized after they are separated.

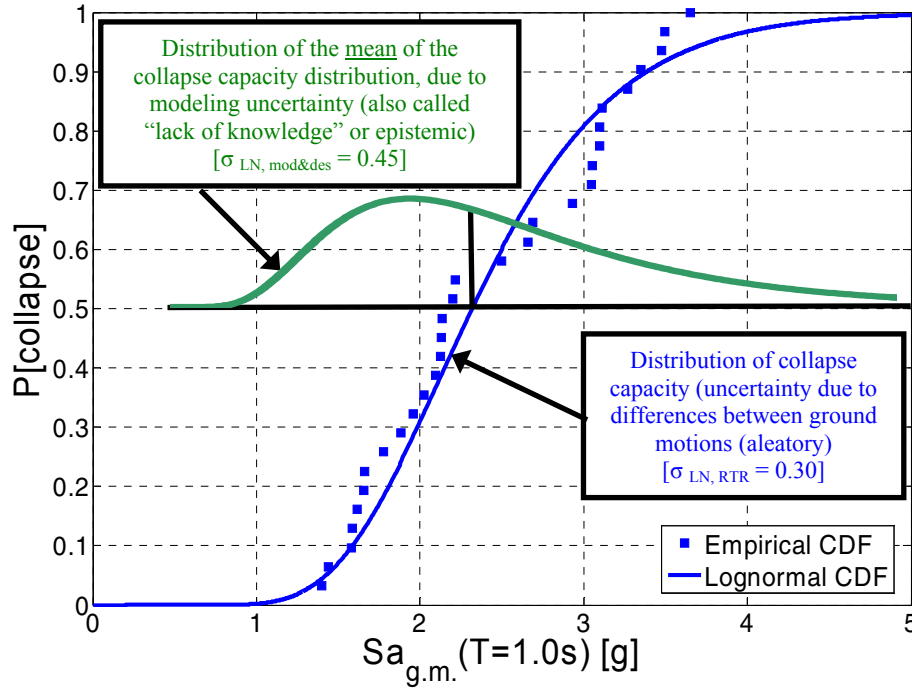


Fig. E.6 Collapse capacity distributions showing variability coming from ground motion randomness and uncertainty coming from modeling uncertainty.

Figure E.6 shows how the two types of uncertainty are assumed to interact. We commonly say that the “randomness” causes an inherent uncertainty on the collapse capacity, which is shown as the blue record-to-record (RTR) CDF. We then continue by saying that the “lack of knowledge” causes an additional *uncertainty on the mean* of the blue RTR CDF; the uncertainty is shown by the green modeling PDF. Figure E.6 currently shows the RTR CDF at this position of 50% prediction confidence, since the mean of the RTR collapse CDF is at the 50th percentile of the modeling PDF.

To make predictions at a given prediction confidence level, the RTR collapse CDF must be shifted to the appropriate percentile of the modeling PDF. Figure E.7 shows an example for 90% prediction confidence. The left-shifted RTR CDF (red dotted line) is the same as the original blue CDF on the right but the mean has been shifted to the 10th percentile of the green PDF. This figure shows that at a 90% prediction confidence level the probability of collapse for the 2%-in-50-years motion ($S_d(T=1s) = 0.82g$) is 18%.

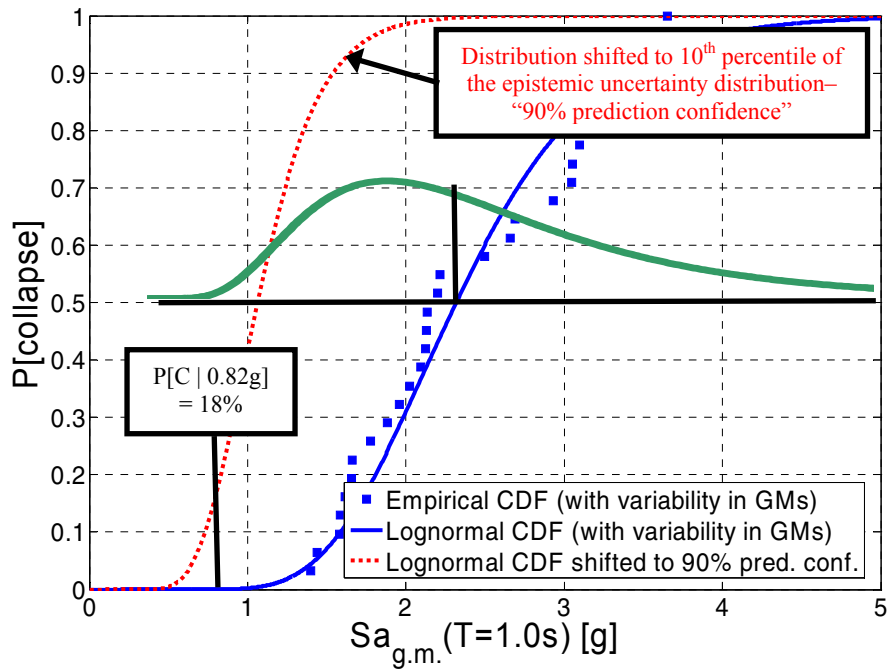


Fig. E.7 Collapse capacity distributions showing collapse capacity CDF shifted to 90% prediction confidence.

Figure E.8 follows by showing the $P[C | Sa_{2/50}]$ for a range of prediction confidence levels. Notice that the probability is 18% at 90% prediction confidence, in agreement with Figure E.7. Figure E.8 shows that the probability estimates at high levels of prediction confidence are unstable; at 80% prediction confidence $P[C | Sa_{2/50}] = 4\%$, while at 95% prediction confidence $P[C | Sa_{2/50}] = 45\%$.

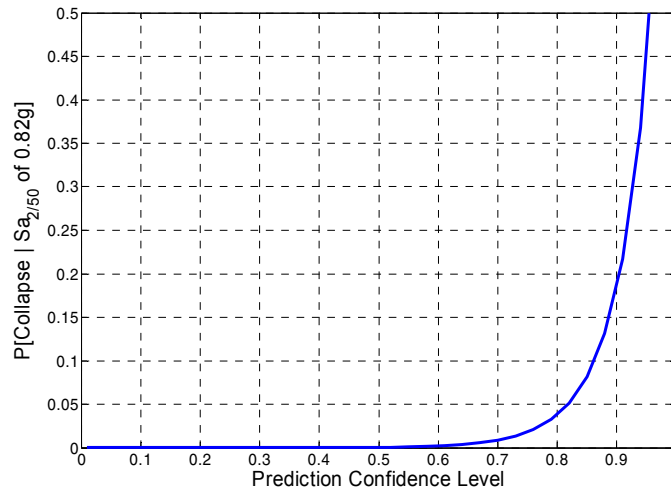


Fig. E.8 Effect of prediction confidence level on estimate of probability of collapse for 2%-in-50-yrs event.

Making performance predictions at high levels of prediction confidence is attractive because it makes it possible to make concluding statements that are based on high levels of statistical confidence. Even so, this approach has two primary drawbacks:

- (a) The estimates of $P[C | S_{a_{2/50}}]$ (and similarly $\lambda_{\text{collapse}}$) are highly unstable for high levels of prediction confidence. This causes slight variations in the prediction confidence level to have extreme impacts on performance predictions. This is undesirable because the choice of prediction confidence level is somewhat arbitrary, yet the choice will result in large changes in the performance predictions.
- (b) Making predictions with a level of prediction confidence requires separation of uncertainty into “randomness” and “lack of knowledge.” This separation is quite difficult and quickly becomes a philosophical debate (Cornell 2005).

Based on these two drawbacks of the prediction confidence approach, we use the “mean estimate” approach in this research; this method is discussed in this next section.

E.6.3 Mean Estimates: Not Separating Uncertainties by Conceptual Type

The mean estimate approach avoids the question of “randomness” as opposed to “lack of knowledge” and considers all uncertainties to be the same. This avoids the philosophical debate

required to separate the uncertainties and also makes the performance prediction more stable and not dependent on an arbitrary decision regarding the appropriate level of prediction confidence.

Figure E.6 showed the distribution of collapse capacity due to ground motion variability and also the variability in the mean collapse capacity due to modeling variability. If we assume that these two distributions are independent and assume that both are well described by lognormal distributions, we can obtain the mean estimate by simply combining all uncertainties using the square-root-of-sum-of-squares (SRSS) and doing all computations using a new distribution with this combined variance.

Figure E.9 illustrates the mean estimate approach. The solid red line is the lognormal distribution fitted to the predicted collapse capacities ($\sigma_{LN,RTR(Sa,col)} = 0.30$). The dashed blue line shows the collapse capacity CDF that includes the contributions of both RTR variability and modeling/design uncertainty ($\sigma_{LN,Total(Sa,col)} = [(0.45)^2 + (0.30)^2]^{0.5} = 0.54$). Using this approach, the mean estimate of the $P[C | Sa_{2/50}]$ is 3%.

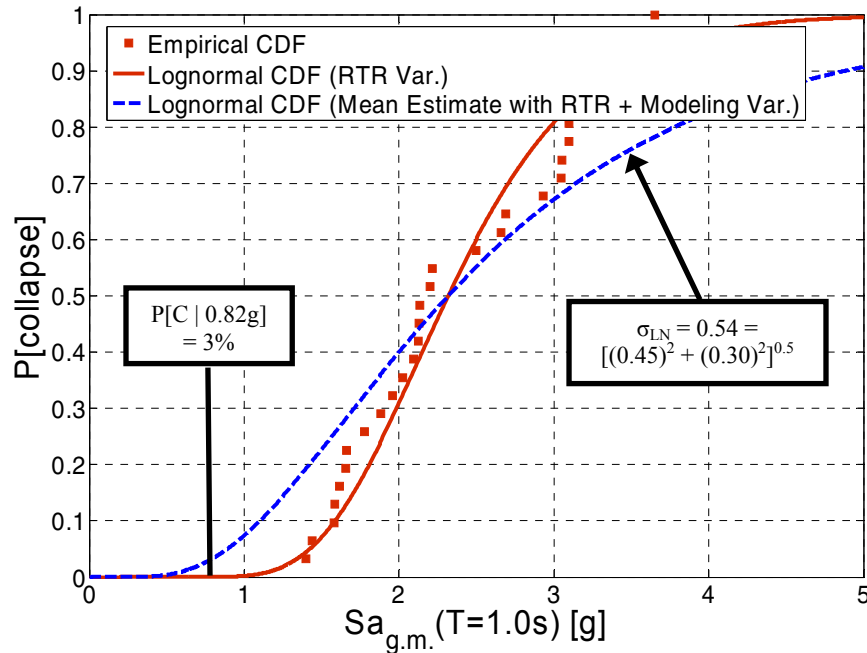


Fig. E.9 Collapse distributions showing distribution considering only variability between ground motion records (solid red) and distribution with variance expanded to include effects of modeling uncertainty (dashed blue).

E.6.4 Summary

This work uses the mean estimate approach when making performance predictions, as opposed to making predictions at a given level of prediction confidence. Using the mean estimate approach avoids philosophical debates regarding whether uncertainty should be considered as “randomness” (aleatory) or “lack of knowledge” (epistemic). The mean estimate approach also results in predictions that are more stable because predictions at a given level of prediction confidence are highly dependent on the arbitrary choice of prediction confidence level.

In addition, we decided to use the mean estimate approach because it is simpler. This will be a great benefit when working to get this methodology adopted into engineering practice (Cornell 2005).

E.7 RESULTS FOR PROBABILISTIC PREDICTION OF COLLAPSE PROBABILITY AND RATE

This section combines all of the collapse simulation results of Chapter 5 with the collapse uncertainty analysis results presented in this chapter to compute collapse probabilities and yearly collapse rates for each design variant considered in this study. The collapse uncertainty was computed by the FOSM method for Design A only; we assume that all other models have similar levels of modeling uncertainty.

E.7.1 Mean Estimates of Probability and Annual Frequency of Collapse

This study primarily uses the *mean estimates* (Section E.6.3) of the mean annual frequency of collapse ($\lambda_{\text{collapse}}$) and the probability of collapse given the 2%-in-50-years event ($P[\text{Col} | \text{Sa}_{2/50}]$). The *mean estimate* is used in contrast to computing values at a certain prediction confidence level, as has been done in some recent studies (Cornell et al. 2002; Yun et al. 2002; Jalayer 2003).

Figure E.10 shows the collapse CDF (from Fig. E.9) and the ground motion hazard curve for the site at a period of 1.0 secs. This section discusses how these two figures are used to compute the mean estimate of the mean annual frequency of collapse ($\lambda_{\text{collapse}}$). The estimates of $\lambda_{\text{collapse}}$ and $P[\text{Col} | \text{Sa}_{2/50}]$ are then presented at the end of this section for all design variants used in this study.

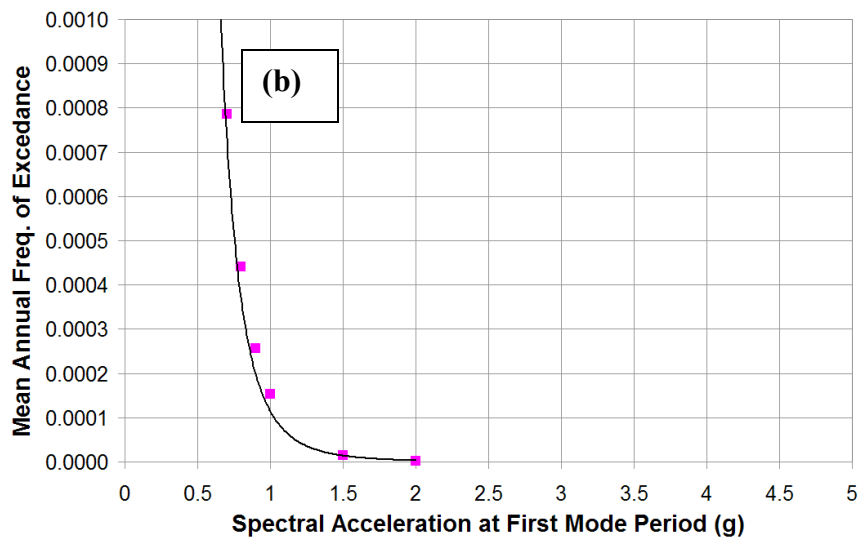
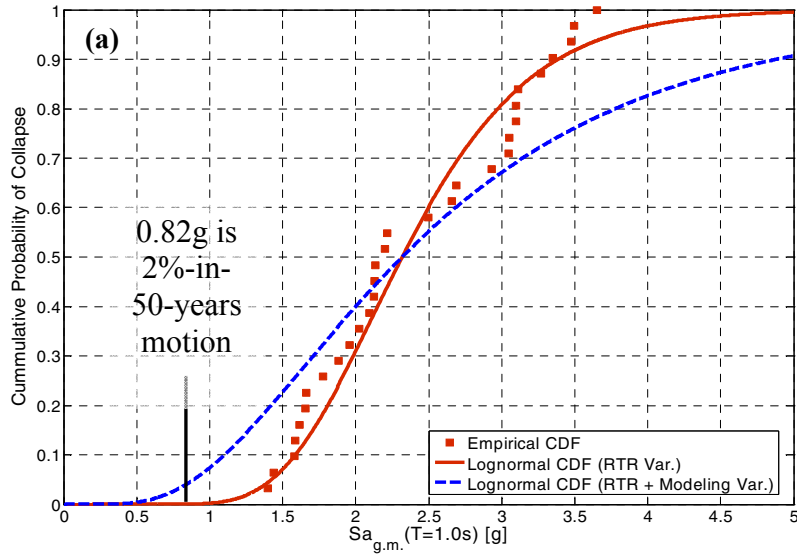


Fig. E.10 (a) Collapse predictions for Design A, ground motion Bins 4A and 4C, showing collapse capacity CDF with only RTR variability and with modeling/design variability included; (b) ground motion hazard curve used to compute $\lambda_{collapse}$.

The mean annual frequency of collapse ($\lambda_{collapse}$) is computed using Equation E.4 (Ibarra 2003, Eq. 7.10).

$$\lambda_{collapse} = \int P[Sa_{collapse} \leq x] \cdot |d\lambda_{IM}(x)| \quad (E.4)$$

where $\lambda_{collapse}$ is the mean annual frequency of collapse, $P[Sa_{collapse} \leq x]$ is the probability that x exceeds the collapse capacity (i.e., the probability that the building is collapsed

when the ground motion intensity is x), and $\lambda_{IM}(x)$ is the mean annual frequency of the ground motion intensity exceeding x (i.e., a point on the ground motion hazard curve).

There are many ways to approximate Equation E.4. Baker provides a closed-form solution that involves fitting the hazard function (Baker 2003; Eq. 3.66). To avoid error induced by fitting an exponential function to the hazard curve, we used numerical integration and used the PCHIP (piecewise cubic Hermite interpolating polynomial) function in Matlab (Matlab 2005). Section E.8.6 discusses the sensitivity of the $\lambda_{collapse}$ to the method of approximating Equation E.4.

Table E.11 presents the estimated $\lambda_{collapse}$ and $P[Col | Sa_{2/50}]$ for all design variants considered in this study. This table also shows the median collapse capacity, $\sigma_{LN,RTR}(Sa,col)$, collapse capacity margin, and parameters for the fitted lognormal distributions.

Table E.11 Summary of collapse predictions (mean estimates) for all design variants; including probability of collapse, annual frequency of collapse, and effects of modeling uncertainty.

					With only record-to-record variability			With record-to-record and modeling uncertainty (mean estimate approach)			
Design	Ground Motion Set	Median (Sa,col) [g]	Collapse Margin (median / Sa _{2/50}) ^c	$\mu_{LN}(Sa,col)$	$\sigma_{LN,RTR}(Sa,col)$	$\lambda_{collapse}(10^{-6})$	$P[Col Sa_{2/50}]^a$	$\sigma_{LN,model}(Sa,col)$	$\sigma_{LN,Total}(Sa,col)$	$\lambda_{collapse}(10^{-6})$	$P[Col Sa_{2/50}]^a$
A	4A	2.19	2.7	0.86	0.36	9.2	0.00	0.45	0.58	69	0.03
B	4A	2.08	2.5	0.78	0.31	9.0	0.00	0.35	0.47	38	0.02
C	4A**	2.35	2.9	0.85	0.46	24.8	0.01	0.45	0.64	125	0.05
D ^b	4A	0.95	1.2	-0.038	0.39	663	0.34	0.35	0.52	1300	0.38
E	4A	1.95	2.4	0.71	0.32	14.5	0.00	0.35	0.47	55	0.03
F	4A	1.86	2.3	0.57	0.38	48.1	0.02	0.35	0.52	139	0.07
G	4A	1.88	2.3	0.67	0.34	20.6	0.01	0.35	0.49	71	0.04
H	4A	1.92	2.3	0.64	0.30	16.2	0.00	0.35	0.46	62	0.03

a - 2% in 50 year ground motion level: Sa(1sec) = 0.82g
b - columns designed for strength demand and not for SCWB; this is not a code-conforming design
c - collapse margin is ratio of median collapse capacity to Sa_{2/50}

Table E.11 shows that the probability of collapse for the 2%-in-50-years ground motion, even including additional uncertainties for structural modeling, is only 2–7% for the various code-conforming buildings. For these same buildings, the mean annual frequency of collapse ($\lambda_{collapse}$) ranges from 40–140x10⁻⁶.

E.7.2 Disaggregation of Mean Annual Frequency of Collapse

To better understand the spectral acceleration levels contributing most to the $\lambda_{\text{collapse}}$, Figure E.11 shows a disaggregation of $\lambda_{\text{collapse}}$ (Baker 2005). This disaggregation diagram is simply created by keeping track of each term of Equation E.4 during the process of numerical integration. Each term is then normalized by $\lambda_{\text{collapse}}$, so the area of the disaggregation diagram is one. These figures show the results for Designs A and D, and are based on the hazard curve shown in Figure E.11(b). These figures show that for Design A (expected perimeter code-conforming design), ground motions with $S_{ag,m}(T=1\text{sec})$ from 0.8g to 2.0g dominate the collapse hazard, while 0.3–1.5g dominate the collapse hazard for Design D (perimeter non-code-conforming design that does not comply with the strong-column weak-beam design requirements).

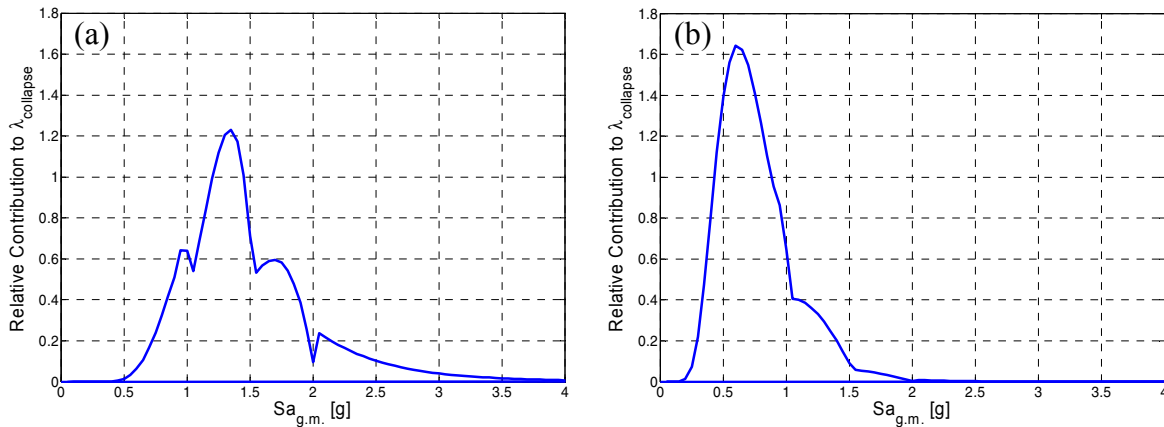


Fig. E.11 Annual frequency of collapse disaggregation. $\lambda_{\text{collapse}}$ computed with fitted lognormal distribution considering only record-to-record variability and using ground motion Bin 4A; (a) for Design A and (b) for Design D.

E.7.3 Estimates of Probability and Annual Frequency of Collapse at a Given Level of Prediction Confidence

Section E.2 discussed the approach where collapse probability and mean rate of collapse are computed at a given level of prediction confidence. Table E.12 is similar to Table E.11 but presents predictions at the 10% and 90% levels of prediction confidence, instead of using the mean estimate approach.

Table E.12 Summary of collapse predictions for all design variants at 10% and 90% levels of prediction confidence, including probability of collapse, annual frequency of collapse, and effects of modeling uncertainty.

Design	Ground Motion Set	Counted Median (Sa,col) [g]	$\mu_{LN}(Sa,col)$	$\sigma_{LN,RTR}(Sa,col)$	$\sigma_{LN,model}(Sa,col)$	10% Confidence Level			No Modeling Uncert.			90% Confidence Level		
						Shifted Median ^a (Sa,col) [g]	$\lambda_{collapse}(10^{-6})$	P[Col Sa _{2/50}] ^b	Shifted Median ^a (Sa,col) [g]	$\lambda_{collapse}(10^{-6})$	P[Col Sa _{2/50}] ^b	Shifted Median ^a (Sa,col) [g]	$\lambda_{collapse}(10^{-6})$	P[Col Sa _{2/50}] ^b
A	4A	2.19	0.86	0.36	0.45	4.2	4.3	0.00	2.36	9.2	0.00	1.1	370	0.23
B	4A	2.08	0.78	0.31	0.35	3.3	3.3	0.00	2.18	9.0	0.00	1.2	190	0.12
C	4A ^c	2.35	0.85	0.46	0.45	4.0	2.6	0.00	2.34	24.8	0.01	1.0	800	0.33
D ^d	4A	0.95	-0.04	0.39	0.35	1.4	155	0.09	0.96	663	0.34	0.4	9400	0.95
E	4A	1.95	0.71	0.32	0.35	3.1	1.3	0.00	2.03	14.5	0.00	1.1	280	0.19
F	4A	1.86	0.57	0.38	0.35	2.6	6.2	0.00	1.77	48.1	0.02	0.9	830	0.41
G	4A	1.88	0.67	0.34	0.35	3.0	2.1	0.00	1.95	20.6	0.01	1.0	390	0.25
H	4A	1.92	0.64	0.30	0.35	3.0	1.4	0.00	1.90	16.2	0.00	1.0	310	0.22

a - Actually the exponential of the shifted $\mu_{LN}(Sa,col)$
b - 2% in 50 year ground motion level: Sa(1sec) = 0.82g
c - Records 94103 and 94107 removed due to numerical problems
d - columns designed for strength demand and not for SCWB; this is not a code-conforming design

E.8 SENSITIVITIES OF COLLAPSE CAPACITY PREDICTIONS TO ADDITIONAL ASPECTS OF PERFORMANCES ASSESSMENT METHODOLOGY

E.8.1 Effects of Considering Gravity System in Structural Model

To better understand the effects of the gravity system on the collapse capacity, we completed collapse analysis for Designs A and D with and without including the gravity system in the structural model. Design A is a code-conforming perimeter-frame building, so this comparison with and without the gravity frame will show how the gravity system will increase the collapse capacity of a newly designed building. Design D is a similar design but is not code-conforming, as the strong-column weak-beam design provision (ACI 318-05, 21.4.2) is not enforced. The comparison with and without the gravity frame for Design D is more representative of how the gravity system may increase the collapse capacity of an older existing building or a building designed for a non-seismic region that requires lower lateral force demands and does not need to abide by the strong-column weak-beam requirement.

Figure E.12 presents the collapse capacities for Designs A and D with and without including the gravity system in the structural model. These analyses used ground motions from

Bin 4A and the results from both horizontal components of each ground motion are shown in the following figures.

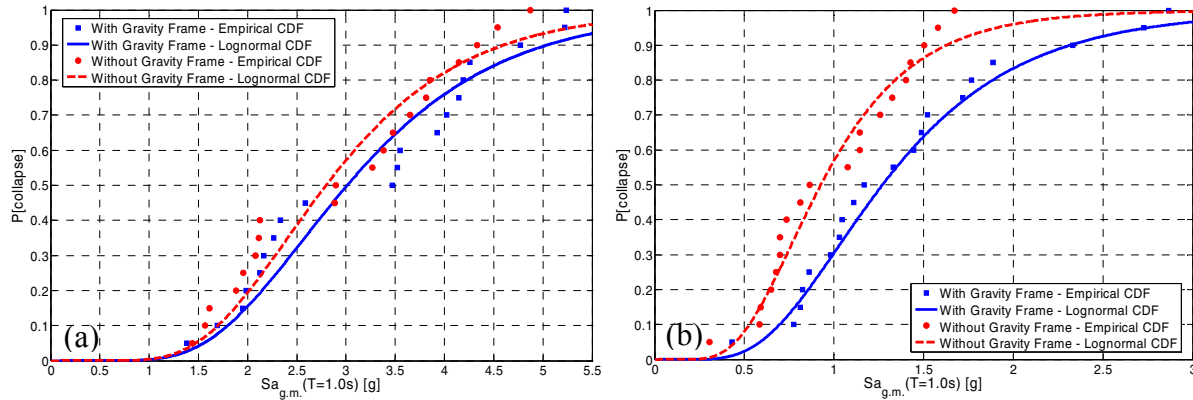


Fig. E.12 Effects of gravity frame on predicted collapse capacity for (a) Design A (mean perimeter-frame design) and (b) Design D (perimeter-frame design without enforcing strong-column weak-beam code provisions).

Table E.13 gives the summary statistics for the data presented in Figure E.12. This shows that the gravity system increases the collapse capacity by about 10% for Design A (code-conforming design) and about 25% for Design D (design without enforcing the strong-column weak-beam requirements). This shift in the collapse capacity distribution resulted in a change to the $\lambda_{collapse}$ of 30% and 500% for Designs A and D, respectively.

Table E.13 Summary statistics showing effects of gravity system on predicted collapse capacity for two structural designs (Designs A and D).

Building Design	Gravity System Included	Mean Sa_{col} [g]	Median Sa_{col} [g]	$\sigma_{LN,RTR}$ (Sa_{col})	$\lambda_{collapse}$ (10^{-6}) (RTR Var.)	$P[Col Sa_{2/50}]^*$
A	Yes	3.2	3.5	0.40	3.8	0.00
A	No	3.0	2.9	0.39	4.9	0.00
% Difference:		-8%	-17%	-3%	29%	0%
Building Design	Gravity System Included	Mean Sa_{col} [g]	Median Sa_{col} [g]	$\sigma_{LN,RTR}$ (Sa_{col})	$\lambda_{collapse}$ (10^{-6}) (RTR Var.)	$P[Col Sa_{2/50}]^*$
D	Yes	1.4	1.2	0.47	357	17.5
D	No	1.0	0.8	0.44	2000	57.1
% Difference:		-28%	-33%	-6%	460%	226%

* 2% in 50 year ground motion level: $Sa(1sec) = 0.82g$

E.8.2 Effects of Considering Collapse in Either Horizontal Direction of Building

Section 5.11.1 discusses an approximate method for accounting for the possibility of structural collapse in either of the two horizontal directions of the building. This method simply consists of predicting the collapse capacity for the two horizontal components of ground motion and then systematically selecting the lower of the two component collapse capacities as the building collapse capacity. Figure E.13 compares the results of this method to the method of simply using a single horizontal ground motion component and considering collapse in only a single direction. Figure E.13 shows results for Design A and Design D, which are highly ductile and less ductile designs, respectively.

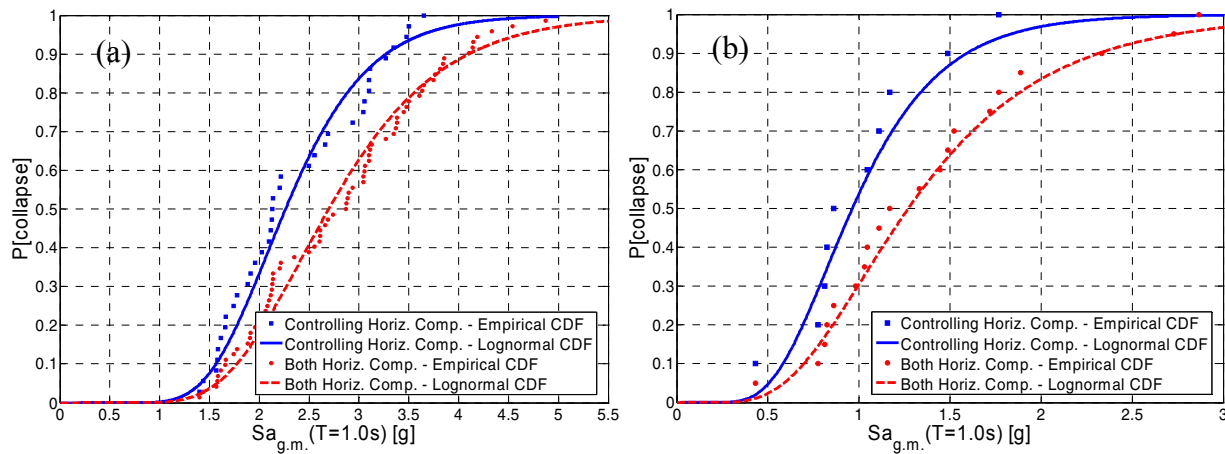


Fig. E.13 Effects of approximately considering collapse in both horizontal direction of building for (a) Design A (mean perimeter-frame design) with ground motion Bins 4A and 4C and (b) Design D (perimeter-frame design without enforcing strong-column weak-beam code provisions) with ground motion Bin 4A.

Table E.14 shows the results from Figure E.13 with additional information regarding collapse probability and rate. Table E.13 shows that systematically selecting the lower collapse capacity of the two horizontal components reduces the mean (or median) collapse capacity by 20–35%, reduces $\sigma_{LN,RTR}(Sa,col)$ by 15–20%, and increases $\lambda_{collapse}$ by about 45% and increases $P[\text{Col} | Sa_{2/50}]$ by 0–45%. Notice that the $P[\text{Col} | Sa_{2/50}]$ is not changed when $Sa_{2/50}$ is on the tail of the collapse capacity distribution, causing $P[\text{Col} | Sa_{2/50}]$ to be nearly 0.0%. However, when $Sa_{2/50}$ is not on the extreme tail, then the $P[\text{Col} | Sa_{2/50}]$ and $\lambda_{collapse}$ are both affected by the same amount of 45%. This shows that $\lambda_{collapse}$ is a more stable indicator of collapse risk, as compared to $P[\text{Col} | Sa_{2/50}]$ because the change in $\lambda_{collapse}$ is not affected by where $Sa_{2/50}$ lies with respect to the tail of the collapse capacity distribution.

Table E.14 Summary statistics showing effects of considering collapse in both horizontal direction of building for two structural designs (Designs A and D).

Building Design	Ground Motion Bins	Ground Motion Components	Mean $S_{a,col}$ [g]	Median $S_{a,col}$ [g]	$\sigma_{LN,RTR}$ ($S_{a,col}$)	$\lambda_{collapse}$ (10^{-6})	P[Col $S_{a,2/50}$]*
Design A, no gravity frame	4A, 4C	Controlling	2.36	2.13	0.29	5.8	0.00
Design A, no gravity frame	4A, 4C	All	2.84	2.87	0.33	3.1	0.00
		% Difference:	20%	35%	14%	-47%	0%
Building Design	Ground Motion Bins	Ground Motion Components	Mean $S_{a,col}$ [g]	Median $S_{a,col}$ [g]	$\sigma_{LN,RTR}$ ($S_{a,col}$)	$\lambda_{collapse}$ (10^{-6})	P[Col $S_{a,2/50}$]*
Design D	4A	Controlling	1.03	0.95	0.39	663	0.34
Design D	4A	All	1.41	1.25	0.47	357	0.18
		% Difference:	37%	32%	21%	-46%	-47%

* 2% in 50 year ground motion level: $S_a(1sec) = 0.82g$

E.8.3 Effects of FOSM Approximations and Correlation Assumptions

Section E.5.2 discusses how the correlation assumptions and FOSM approximation can *significantly alter* the estimated uncertainty in collapse capacity coming from uncertainty in the structural modeling ($\sigma_{LN,modeling}(S_{a,col})$). Table E.8 showed that when considering modeling and design uncertainties, the $\sigma_{LN,modeling\&design}(S_{a,col})$ can range from 0.21 for the uncorrelated case to 0.54 for the case of full correlation between variables where high correlation is reasonable. In addition, the value can range between 0.54 and 0.67 depending on if the FOSM approximation is done with the original data of the natural logarithm of the data. This shows that a precise estimate of modeling uncertainty is difficult.

This section discusses how the large variability in the value of $\sigma_{LN,modeling\&design}(S_{a,col})$ carries over to a large variability in the estimates of the P[Col | $S_{a,2/50}$] and $\lambda_{collapse}$. Figure E.15 shows the relationship between modeling (and/or design) uncertainty and the mean estimate of $\lambda_{collapse}$ for Design A using ground motion set 4A. This shows that for the range of 0.21–0.67 for modeling (and/or design) uncertainty, the mean estimate of the $\lambda_{collapse}$ ranges from 9.2×10^{-6} to 300×10^{-6} , a change of more than an order of magnitude. Figure E.16 similarly shows the effect on the estimate of P[Col | $S_{a,2/50}$]. For the same range of modeling (and/or design) uncertainty, 0.21–0.67, the P[Col | $S_{a,2/50}$] varies by an order of magnitude, from 0.6% to 8.0%.

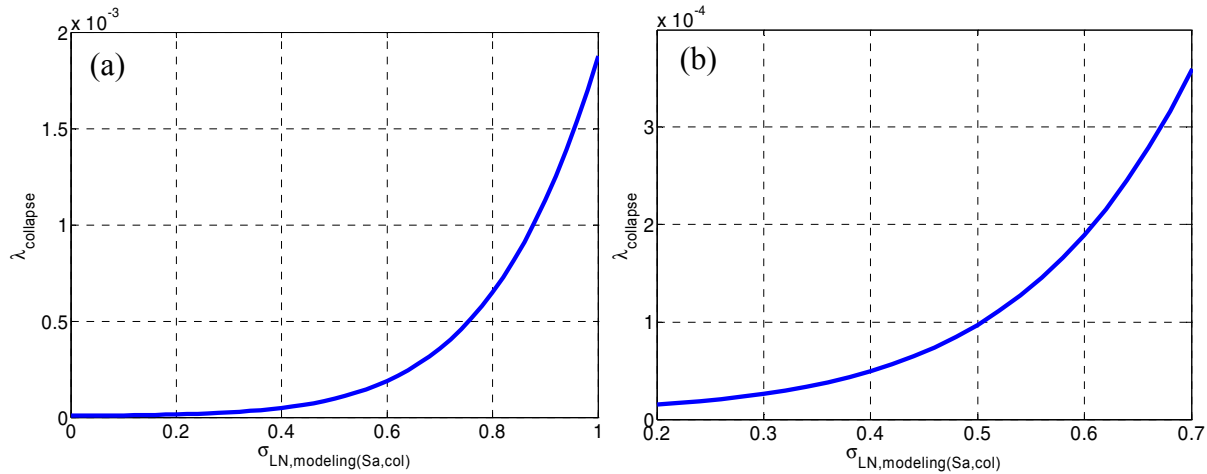


Fig. E.14 Effect of modeling (and/or design) uncertainty on mean estimate of $\lambda_{\text{collapse}}$, for Design A using ground motion Bin 4A; (a) full view of graph and (b) zoomed-in for important values of uncertainty.

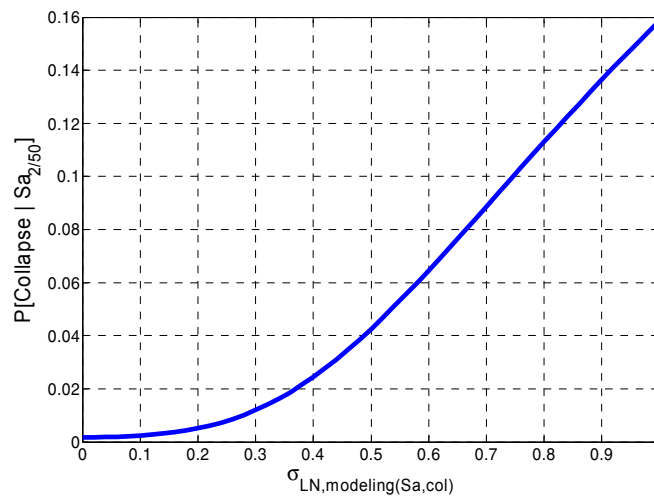


Fig. E.15 Effect of modeling (and/or design) uncertainty on mean estimate of $P[\text{Col} | \text{Sa}_{2/50}]$, for Design A using ground motion Bin 4A.

E.8.4 Effects of Fitting Lognormal Distribution to Collapse CDF

This section looks at the variability in predictions resulting from the fit of the collapse capacity distribution. Table E.15 compares using an empirical (counted) distribution and fitting a lognormal distribution to the collapse capacities for Designs A and D. This shows that the fitting method can change the mean annual frequency of collapse ($\lambda_{\text{collapse}}$) estimate by a factor of two; this occurs for Design A when the $\lambda_{\text{collapse}}$ is a small value and a smaller number of ground motions are used. The $\lambda_{\text{collapse}}$ being small indicates that the tail of the collapse capacity

distribution is an important contributor to the collapse hazard, and accurately estimating this tail is difficult when using 10, and even 36, ground motions. Table E.15 shows that the $\lambda_{\text{collapse}}$ for Design D is much less sensitive to the collapse capacity distribution fit, because Design D collapses at much lower ground motion intensities, causing the tail of the collapse capacity distribution to be less important. All of the results shown in Table E.15 are based on using the controlling horizontal ground motion component, as discussed in Section 5.12.1.

Table E.15 Summary statistics showing effects of how collapse capacity distribution is fit.

Building Design	Ground Motion Bins	Number of Ground Motions	Method of Fitting Collapse CDF	$\lambda_{\text{collapse}}$ (10^{-6})	Percent change in $\lambda_{\text{collapse}}$
Design A, no gravity frame	4A	10	Lognormal	11.8	-55%
Design A, no gravity frame	4A	10	Empirical (counted)	5.3	
Design A, no gravity frame	4A, 4C	36	Lognormal	5.8	-28%
Design A, no gravity frame	4A, 4C	36	Empirical (counted)	4.2	
Design D	4A	10	Lognormal	357	4%
Design D	4A	10	Empirical (counted)	371	

E.8.5 Effects of Hazard Curve Fit

To check the effects of the hazard curve fit, this section looks at several different methods to fit the hazard curve and shows the effects on the estimate of $\lambda_{\text{collapse}}$. The comparisons in this section are based on Designs A and D with ground motion Bin 4A, using the controlling horizontal ground motion component.

In this research, the hazard curve is fit using the piecewise cubic Hermite interpolating polynomial (PCHIP) function in Matlab (2005); this method gives a good fit to the hazard curve without needing to assume a functional form. We then numerically integrate the fitted hazard curve with the collapse capacity distribution using Equation E.4 to obtain the $\lambda_{\text{collapse}}$. Figure E.16 shows the fit to the hazard curve using the PCHIP function; this shows that the PCHIP function fits the hazard values well.

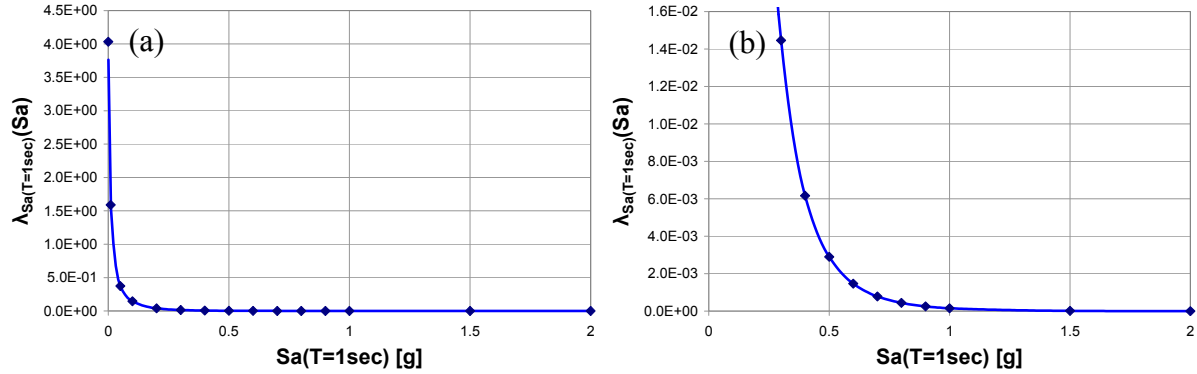


Fig. E.16 Fit to hazard curve using PCHIP function; (a) full view and (b) zoomed-in for important spectral acceleration values.

The PCHIP function is not typically used in the literature for fitting hazard curves. The hazard curve is typically fit using a functional form shown in Equation E.5 (Krawinkler et al. 2004, Baker et al. 2003; Ibarra 2003):

$$\lambda_{Sa}(Sa) = k_o Sa^{-k} \quad (E.5)$$

If the functional form above is fit to the hazard curve, then Equation E.6 can be used in place of Equation E.4 to compute the expected value of the annual collapse rate. If the functional form for the hazard curve is not used, then Equation E.4 can be used with numerical integration to estimate the annual collapse rate from the hazard curve and the collapse capacity distribution.

$$E[\lambda_{collapse}] = k_o \eta_c^{-k} e^{(0.5k^2 \beta_{RC}^2)} \quad (E.6)$$

where η_c is the median collapse capacity predicted from collapse analyses, and β_{RC} ($= \sigma_{LN,RTR}$) is the standard deviation of the natural logarithms of the collapse capacities.

Using Equations E.5–6 to estimate the $\lambda_{collapse}$ requires the analyst to decide over what ranges of spectral acceleration to fit the hazard curve. If the collapse rate is being estimated, then the hazard curve should be fit in the spectral acceleration range that contributes most significantly to the annual collapse rate, as shown earlier in Figure E.11 (Cornell 2005). The rest of this section shows compares the $\lambda_{collapse}$ estimated from using the PCHIP function and various methods of fitting the hazard curve with the form of Equation E.5.

As mentioned above, when fitting the hazard curve, one must determine which portion of the hazard curve to fit. In order to illustrate the potentially large error that may occur due to inaccurately fitting the hazard curve, this section computes the mean annual frequency of

collapse for Designs A and D (since they have much different S_a levels that contribute to the collapse hazard) using various fits to the hazard curve:

- Interpolate hazard curve using Matlab PCHIP function. This has already been illustrated in Figure E.16.
- Fit hazard curve using Equation E.5 and using full range of hazard data (0.01g–2.0g).
- Fit hazard curve using Equation E.5 and using full range of hazard data that are most important for Design A (0.8g–2.0g). Figure E.11(a) shows these ranges of S_a that most contribute to annual collapse rate for Design A.
- Fit hazard curve using Equation E.5 and using full range of hazard data that are most important for Design D (0.3g–1.5g). Figure E.11(b) shows these ranges of S_a that most contribute to annual collapse rate for Design D.

The following figures illustrate how each of the methods provides a fit to the hazard curve.

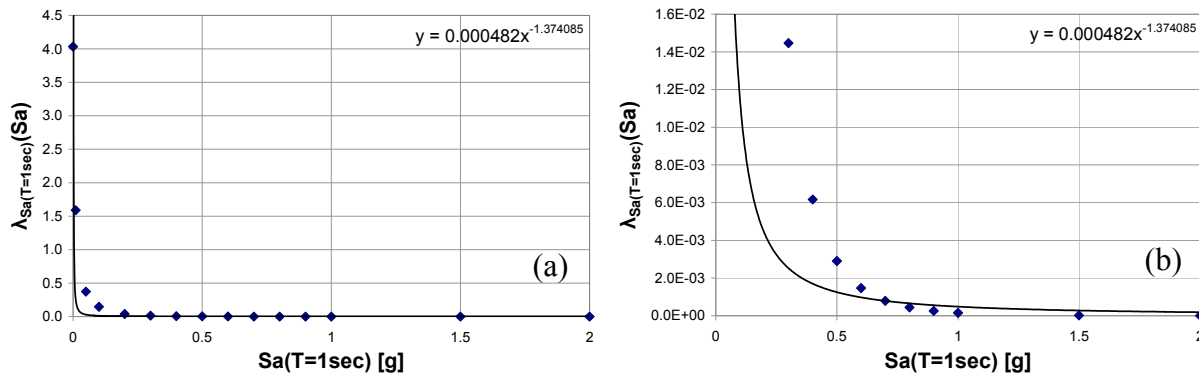


Fig. E.17 Fit to hazard curve using Eq. E.5 and for hazard point for $0.01\text{g} < S_a(T=1\text{sec}) < 2.0\text{g}$; (a) full view of region of fit and (b) zoomed-in for important spectral acceleration values. This shows that hazard curve fit is not good for any level of ground motion.

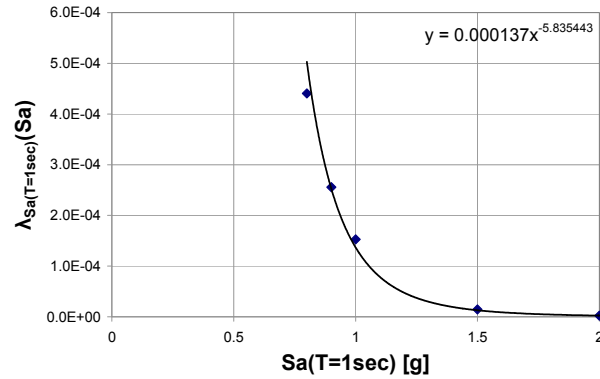


Fig. E.18 Fit to hazard curve using Eq. E.5 and for hazard point for $0.8g < S_a(T=1sec) < 2.0g$ (i.e., those important for collapse of Design A).

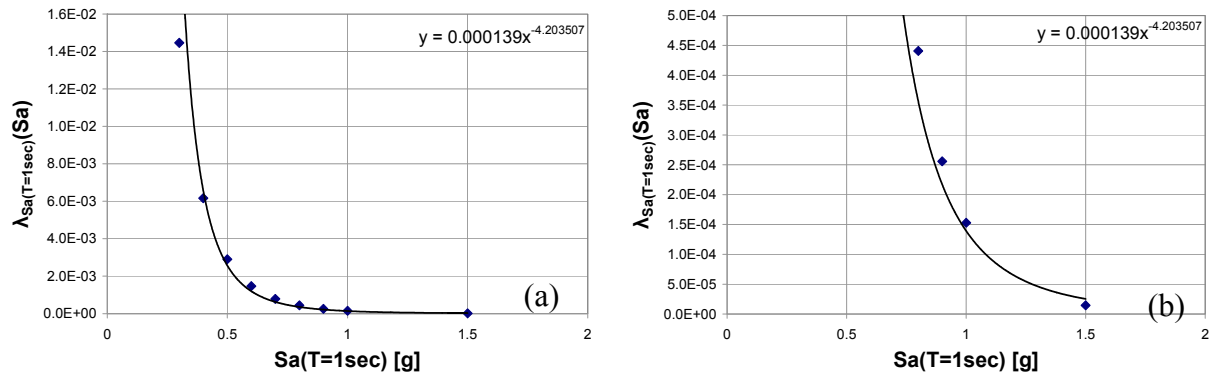


Fig. E.19 Fit to hazard curve using Eq. E.5 and for hazard point for $0.3g < S_a(T=1sec) < 1.5g$ (i.e., those important for collapse of Design D); (a) full view of region of fit and (b) zoomed-in for important spectral acceleration values.

The mean annual frequency of collapse was computed for Designs A and D using each of the hazard curve fitting methods listed previously. Table E.16 presents the results of these computations; conclusions can be drawn as follows:

- The exponential fit to the full hazard curve overpredicts the mean annual frequency of collapse for Design A by a factor of 20 (2000%). This occurs because the fitting method significantly overpredicts hazard level for $S_a > 0.7g$ (see Fig. E.19(b)).
- The exponential fit to the full hazard curve only slightly underpredicts the mean annual frequency of collapse for Design D by a factor of 11%. This is not a general conclusion, but comes from compensating errors, as the hazard is overpredicted for $S_a > 0.7g$ and underpredicted for $S_a < 0.7g$ (see Fig. E.19(b)).

- The most accurate estimate comes when the exponential fit is done over the spectral acceleration range that contributes most to the mean annual frequency of collapse for each respective building. For Design A, this range is 0.8–2.0g and the fit over this range results in a 39% error. For Design D, this range is 0.3–1.5g and the fit over this range results in only a -1% error.

Table E.16 Estimates of mean annual frequency of collapse using various methods of fitting hazard curve.

Building Design	Method of Fitting Hazard Curve	k_o	k	$\lambda_{collapse}$ (10^{-6})	Percent difference in $\lambda_{collapse}$ (PCHIP baseline)
Design A	Matlab PCHIP fit	n/a	n/a	9.2	0%
Design A	Exponential fit to full hazard curve	0.000482	1.34	189.4	1959%
Design A	Exponential fit for 0.8g > Sa > 2.0g (important region for Des. A)	0.000137	5.84	12.8	39%
Design A	Exponential fit for 0.3g > Sa > 1.5g (important region for Des. D)	0.000139	4.20	16.2	76%
Design D	Matlab PCHIP fit	n/a	n/a	663	0%
Design D	Exponential fit to full hazard curve	0.000482	1.34	592	-11%
Design D	Exponential fit for 0.8g > Sa > 2.0g (important region for Des. A)	0.000137	5.84	2473	273%
Design D	Exponential fit for 0.3g > Sa > 1.5g (important region for Des. D)	0.000139	4.20	659	-1%

E.9 SUMMARY AND CONCLUSIONS

This chapter looked at the question of uncertainties in structural modeling, focusing specifically on the resulting uncertainty in the predicted collapse capacity. This study accounted for uncertainties in structural design, uncertainties in structural behavior and modeling, and ground motion variability. This study did not address the question of other important uncertainties such as human error.

In the effort to predict the final uncertainty in collapse capacity resulting from uncertainty in design and modeling, we (a) quantified the uncertainties using results from previous research and additional model calibrations, (b) used judgment to establish reasonable correlations between variables, then (c) used the first-order second-moment approximation to propagate the uncertainties. In this process, we found that element plastic-rotation capacity is the variable that most significantly impacts collapse capacity for this building (note that Ibarra shows that the strain-softening slope is also important in general, but it was not for this building). In addition, we found that the correlation between variables is the single most important factor when

estimating the effects of uncertainties; correlations can easily change the mean annual frequency of collapse estimates by an *order of magnitude*.

The uncertainty propagation concluded that the best estimate of modeling collapse uncertainty (not including effects of record-to-record variability) is $\sigma_{LN} = 0.45$ when considering modeling and design uncertainty, and $\sigma_{LN} = 0.35$ when only considering modeling uncertainty.

We use the mean estimate approach when computing $P[C | Sa_{2/50}]$ and $\lambda_{collapse}$. This approach is in contrast to the approach where predictions are made at a level of prediction confidence. Using the mean estimate approach, we conclude that for the six code-conforming building designs evaluated, the $P[C | Sa_{2/50}] = 0.02\text{--}0.07$ and $\lambda_{collapse} = 40 \times 10^{-6} - 140 \times 10^{-6}$; these estimates include design uncertainty (as appropriate), modeling uncertainty, and effects of ground motion variability. For comparisons, if we instead would have made predictions at a 90% prediction confidence level, the $P[C | Sa_{2/50}] = 0.12\text{--}0.41$ and $\lambda_{collapse} = 190 \times 10^{-6} - 830 \times 10^{-6}$.

The final section of this chapter contains a sensitivity study that quantifies the effects of many of the aspects of this performance assessment methodology. Many conclusions are made in this section. One important conclusion is that the manner in which the hazard curve is fit can cause significant errors in the $\lambda_{collapse}$ estimate of up to 20. An additional noteworthy conclusion is that many aspects of the performance assessment change estimates of $\lambda_{collapse}$ by 30–80%, so care should be taken when computing and reporting results for $\lambda_{collapse}$.

Appendix F: Quantification of Structural Modeling Uncertainties for Lumped-Plasticity Model

F.1 INTRODUCTION AND PURPOSE OF APPENDIX

The purpose of the Appendix is to provide a detailed explanation of how we quantified the modeling uncertainty (uncertainty in the modeling of building behavior for a given design). This appendix is designed to complement the discussion of uncertainty in Appendix E and give more detail to the quantification of the variables.

This appendix describes the quantification of the random variables shown in Table E.4. This Appendix focuses on the variables used in the lumped-plasticity model, as this is the model that was used more extensively for sensitivity analyses. To quantify many of the structural uncertainties, we utilize the statistical work of Ellingwood et al. (1980) that was done in the development of the load and resistance factor design (LRFD) guidelines.

F.2 MODELING VARIABLE VALUES

Table F.1 shows the values that we used for modeling variables and is the same table presented in Appendix E.2.4; we presented this table again here for the convenience of the reader.

Table F.1 Summary of modeling random variables.

Random Variable	Mean	c.o.v.	Level of Accuracy of RV Value	Reference(s)
Design Variables:				
Strong-column weak-beam design ratio	1.3	0.15	2	This study
Beam design strength	1.25	0.20	2	This study
System Level Variables:				
Dead load and mass	1.05(computed)	0.10	1	Ellingwood (1980)
Live load (arbitrary point in time load)	12 psf	--	1	Ellingwood (1980)
Damping ratio	0.065	0.60	1	Miranda (2005), Porter et al. (2002), Hart et al. (1975)
Beam-Column Element Variables:				
Element strength	1.0(computed)	0.12	1	Ellingwood (1980)
Element initial stiffness	1.0(computed)	0.36	1	Panagiotakos (2001), Fardis (2003)
Element hardening stiffness	0.5(computed)*	0.50	2	Wang (1978), Melchers (1999), Fardis (2003)
Plastic rotation capacity	1.0(computed)	0.60	1	Panagiotakos (2001), Fardis (2003)
Hysteretic energy capacity (normalized)	110-120	0.50	2	This study, Ibarra (2003)
Post-capping stiffness	0.08(-K _{elastic})	0.60	2	This study, Ibarra (2003)
Concrete tension softening slope	1.0(computed)	0.25	2	Kaklauskas et al. (2001), Torres et al. (2004)
Beam-Column Material Variables (note that these only contribute to element-level variables):				
Rebar yield strength	66.8 ksi	0.04--0.07	1	Melchers (1999)
Rebar strain hardening	0.018E _s	--	1	Wang (1978)
Rebar stiffness (E _s)	29,000 ksi	0.033	1	Melchers (1999)
Concrete strength	4030 ksi	0.21	1	Ellingwood (1980)
Gravity System Variables:				
Slab strength (effective width)	1.0(computed)	0.2	1	Ellingwood (1980), Enomoto (2001)
Drift at slab-beam capping	4.5% drift	0.6	1	This study (Appendix 7a)
Other Variables:				
Column footing rotational stiffness	1.0(computed)	0.3	2	This study
Joint shear strength	1.40**	0.1	2	Altoontash (2004), Meinheit (1981)
Level of Accuracy of Random Variable Quantification: 1: Coefficient of variation computed from a relatively large amount of data and/or from a computed value stated in the literature 2: Coefficient of variation computed from a relatively small amount of data or estimated from a figure in a reference Notes: -- the RV was treated deterministically or another model variable accounts for the same uncertainty * value is a fraction of the value computed using fiber analysis with expected values of material parameters ** value is a fraction of the value computed from ACI 318-02 provisions				

The remainder of this appendix gives additional detail and justification for why we are using the modeling variable values shown in the table above.

F.2.1 Live Load Present in Building during Seismic Event

The typical design live load for office occupancy is 50 psf. This live load is a *design* load that represents the infrequent live load that could be experienced during the life of the building and not the expected live load at the time of a seismic event (Ellingwood 1980). Ellingwood (1980) separates live load into an “arbitrary point-in-time load” (L_{apt}) and a maximum live load during a

50-years reference period. For office occupancy and the floor geometry of the benchmark building, the procedure proposed by Ellingwood (1980) leads to a mean L_{apt} of 12 psf; this was used in this study to represent the expected live load present in the building at the time of the seismic event.

F.2.2 Mass and Dead Load

In agreement with other research reviewed by Ellingwood, Ellingwood (1980) proposed that the random variable used for dead load and mass be a normal distribution with the mean value being 5% greater than the nominal dead load and the coefficient of variation being 0.10.

Regarding the spatial correlation of the mass throughout the building, we assume that the masses are perfectly correlated in the building throughout all floors and stories. This perfect correlation assumption comes from the basic assumption that if a contractor tends to put more or less concrete in one portion of the building, then that same contractor will do the same thing in other portions of the building. We make this assumption for two reasons: to simplify the analysis and because there are no data regarding the spatial correlations of building mass.

In addition, we include 25% of the live load (the L_{apt} as described in the last subsection) in the seismically effective mass. In retrospect, due to the low value of L_{apt} , it may be appropriate to include a greater percentage of L_{apt} in the seismically effective mass. However, including a large percentage of the live load would not have significantly changed the results because the live load is small as compared to the dead load.

F.2.3 Viscous Damping: Damping Ratio

Total damping in a building during a seismic event is a complicated phenomenon and comes from a wide range of contributors. Multiple researchers have listed the important contributors to damping as follows (Fajfar et al. 1993, Fang et al. 1999, Bernal 1994):

- (a) Hysteretic energy dissipation from damage to structural elements
- (b) Hysteretic energy dissipation from damage to nonstructural elements (partition walls, etc.)
- (c) Energy dissipation due to friction between elements in the building
- (d) Energy dissipation in the soil-foundation system
- (e) Intrinsic internal material damping

In this work, the nonlinear structural model accounts for the contribution of item (a) and we use viscous damping to roughly account for the contributions of items (b)–(e). For a more rigorous treatment of damping, damping from items (b) and (d) could be explicitly incorporated into the structural model; this was not done due to project time constraints.

For example, to include the additional damping from gypsum drywall partitions, one could include in the structural model an accurate representation of the contribution of the gypsum drywall partitions, including the nonlinear behavior. Deierlein and Kanvinde (2003) proposed a nonlinear model that can be used for gypsum drywall partitions.

Miranda (2005) recently completed an extensive study of the response of instrumented buildings. In his study, he quantified the mean and variability of the viscous damping ratio and found that these values strongly depend on the building height. For our four-story RC frame building, Miranda estimates a mean damping ratio of 6.5%, with a log standard deviation of 0.6.

Other useful studies on damping were done by Hart and Vasudevan (1975) and Porter et al. (2002).

F.2.4 Viscous Damping: Damping Formulation

Medina (2002) and Bernal (1994) have shown that the damping formulation can have an important effect on the response prediction. Medina (Appendix A of Medina 2002) shows that improper damping formulation can cause static equilibrium to be violated. We tried various damping formulations in this study, and decided that Medina's approach is best in the context of a lumped-plasticity model in OpenSees. Damping formulation can have relatively important effects on response predictions; however due to time limitations, this added uncertainty was not accounted for in this study. In future studies on modeling uncertainty, we recommend that the effects of damping formulation be included.

F.2.5 Element Variability

There is much variability in the structural element models. Figure F.1 shows the backbone of the lumped-plasticity element model and indicates several of the random input parameters. Note that for the fiber model, these same uncertainties are can be accounted for by changing the input parameters appropriate for the fiber model (as shown in Table E.4).

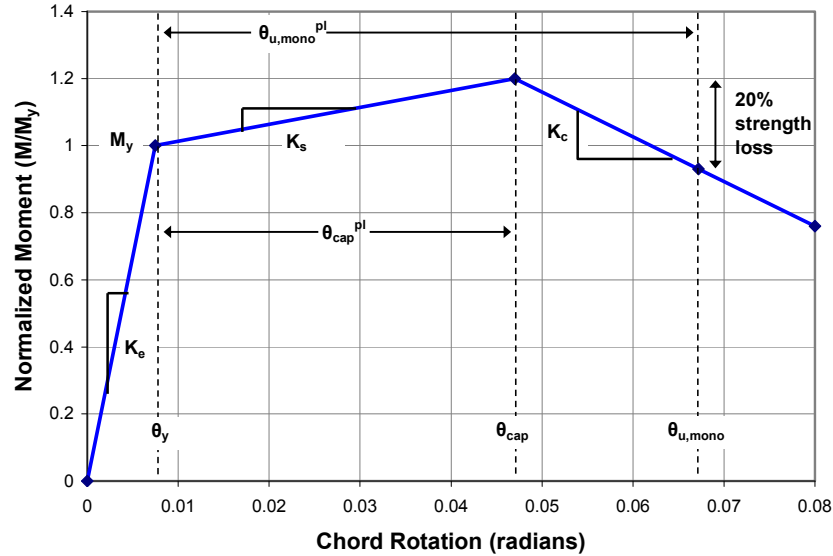


Fig. F.1 Backbone curve of element model.

As Figure F.1 indicates, there are many parameters of the element model, all of which are uncertain. The following list shows the six parameters of the lumped-plasticity model; the remainder of this section discusses the uncertainty of each of these parameters.

- Flexural strength, M_y
- Secant stiffness to yield point, $K_e (= 3 * EI_{eff} / L_s)$
- Hardening stiffness, $K_s (= \alpha_s * K_e)$
- Post-capping stiffness, $K_c (= \alpha_c * K_e)$
- Plastic-rotation capacity to cap point, θ_{cap}^{pl}
- Hysteretic energy-dissipation capacity (normalized) (not shown in figure)

F.2.5.1 Element Variability: Flexural Strength

The flexural strength of an element is affected by many uncertain parameters such as rebar yield strength, concrete compressive strength, rebar placement, member dimensions, axial load, and construction quality (not fully addressed). Ellingwood (1980) aggregated these contributors and estimated that for beams and short columns that exhibit tension controlled failure, the mean flexural strength is 5% above the nominal strength and the coefficient of variation is 11–12%. In this study we use the coefficient of variation for element strength, but compute the mean strength using fiber moment-curvature analysis, as described below.

To compute the mean strength of each member (for lumped-plasticity modeling), we conduct fiber moment-curvature analyses using the expected values of all element properties, as detailed below.

- Axial load: We use the expected value of building dead load and live load (as described earlier in this chapter) to compute the expected gravity induced axial load level of each member.
- Steel yield strength: For nominally 60 ksi rebar, Melchers (1999) found that the expected yield strength is 66.8 ksi.
- Concrete compressive strength: For $f'_c = 5000$ ksi concrete, Ellingwood (1980) found that the expected concrete strength is 4030 ksi (this value is comparable to $0.85 f'_c$ of 4250 ksi).

Figure F.2 shows an example moment-curvature diagram for the outer column of the first story for Design A:

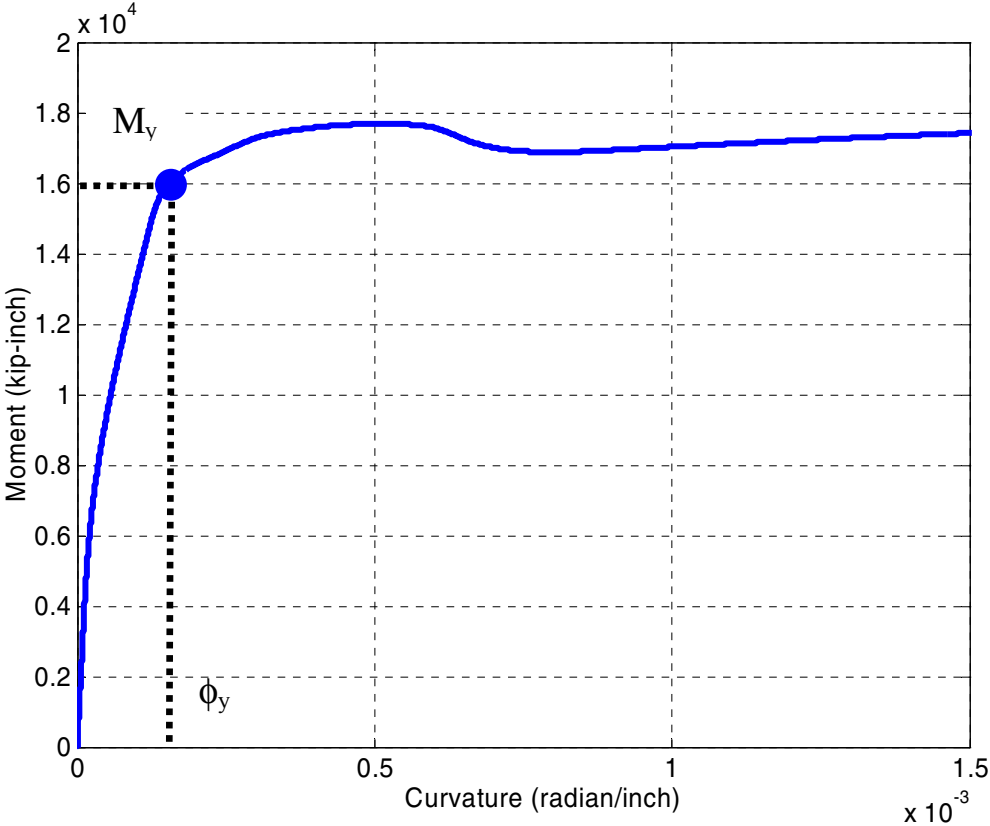


Fig. F.2 Moment-curvature diagram for CS1 of Design A.

F.2.5.2 Element Variability: Initial Stiffness

Stiffness of concrete elements has been a topic of research for years and is still not completely resolved because it is a complicated issue. The factors affecting the pre-yield deformation and stiffness characteristics of a concrete element can be divided into three categories (Fardis et al. 2003; Panagiotakos et al. 2001):

- Deformation due to flexure
 - Element dimensions—Shear span length, cross-sectional dimensions
 - Material stiffnesses
 - Concrete tensile behavior and tension-stiffening effect (Kaklauskas et al. 2001)
 - Contribution of slab (in this work, we included slab contribution to the beam stiffness but did not account for how this affects the uncertainty in stiffness)
- Deformation due to bond-slip
 - Rebar size and placement
 - Concrete placement quality
 - Embedment conditions beyond the end of the element
- Deformation due to shear distortion
 - Ratio of shear demand to shear capacity (level of diagonal cracking) (Mehanny 1999)

As indicated in the above list, we include the slab contribution to the beam stiffness, but do not increase the variability in the slab-beam member stiffness to account for the fact that the stiffness of a slab-beam will likely be more uncertain than the stiffness of a simple beam-column element without an attached slab.

Fardis, Panagiotakos, and Biskinis (Fardis et al. 2003; Panagiotakos et al. 2001) propose a function for the mean chord rotation at member yield (θ_y) that account for all three categories of deformation. In this study, we use this function to predict the contributions of flexure and bond-slip to θ_y , but for predicting the shear contribution we use recommendations by Mehanny (1999). In retrospect, it would be more consistent to use the prediction of the shear contribution from Fardis, so this will be done in future work of this type.

Panagiotakos et al. (2001) also finds that the coefficient of variation of θ_y is 36% for a database of test results for more than 1000 tests. In later work by the same researchers (Fardis et al. 2003) they used an expanded database for 1802 tests and estimated the coefficient of variation

to be 40% for members with bond-slip. In this study, we use a coefficient of variation of 36% for θ_y .

Sensitivity analyses for pre-collapse responses (note that these sensitivity results are not shown in this report) show that the uncertainty in element stiffness significantly affects drift predictions, so better quantifying this uncertainty is an important topic of future research. Specific topics of future research should include the following:

1. Taking a closer look at the appropriate definition of initial stiffness (see Fig. 5.15 of Section 5.4.3.1). Fardis' work was focused on the deformation at yielding, but a stiffer initial stiffness, that better represents the stiffness from zero load to yield, is appropriate for structural modeling; this is especially true when using results of structural analyses to predict nonstructural damage and monetary losses (Chapter 6). The uncertainty in initial stiffness should also be adjusted to account for both the variability in the yield deformation and the fact that the stiffness is not constant from zero load to yield load.
2. Investigating the effects that the slab has on both the mean and variability in initial stiffness. In this study, the mean initial stiffness accounted for the slab, but the variability in initial stiffness was not altered.

F.2.5.3 Element Variability: Hardening Stiffness

The stiffness in the post-yield regime is also complicated and is affected by many things similar to those that affect the stiffness in the pre-yield regime. We use the common approach where the post-yield stiffness is estimated by combining the section-level post-yield stiffness $(M/\phi)_{\text{tangent}}$ from the moment-curvature analysis with an effective plastic-hinge length.

We use the plastic-hinge length expression proposed by Paulay and Priestley (1992), and estimate the post-yield $(M/\phi)_{\text{tangent}}$ between the yield curvature and a curvature of 0.003 (which approximately corresponds to the curvature at which the element starts to have negative stiffness). When completing the moment-curvature, we use the steel strain-hardening modulus of $0.0184 E_s$ from work by Wang (1978).

We found no data on the uncertainty in post-yield stiffness, so a coefficient of variation of 0.5 was assumed. A continued calibration study (Haselton et al. 2006) is working to quantify this variability based on experimental test data.

Representing post-yield flexibility when using a fiber model is more difficult. The model automatically captures the plastic-hinge length through modeling the spread of plasticity, but has no simple way to account for the additional flexibility due to shear and bond-slip. In order to try to determine the relative contributions to post-yield flexibility from flexure, bond-slip, and shear, we refer again to the work by Fardis (2003). The empirical equations that Fardis (2003) developed for ultimate rotation capacity of concrete members (this will be discussed in a later section) indicate that at high ductility levels, bond-slip deformation accounts for approximately 35% of the deformation. Fardis does not similarly separate the shear contribution from flexural contribution. To account for these flexibilities, we tried to add nonlinear springs in series with the fiber element, but this proved problematic due to strain localizations. Therefore, to account for all of these effects within the limitations of the fiber model, we simply use a steel strain-hardening modulus in the model that is $\frac{1}{2}$ of the true material hardening modulus.

F.2.5.4 Element Variability: Plastic-Rotation Capacity

The section on collapse modeling provides a detailed discussion regarding the predictions of the mean and the uncertainty for plastic-rotation capacity (Section 5.4.6). To provide a quick summary of the more detailed discussion: the mean estimate of plastic-rotation capacity comes from the empirical expressions that Fardis proposed and the coefficient of variation is given as 54%. In this work, we expand the coefficient of variation to 60% to account for the variability in predicting the model parameters from the equations proposed by Fardis.

F.2.5.5 Element Variability: Hysteretic Energy Capacity and Post-Capping Stiffness

The section on collapse modeling (Sections 5.4.7–8) also provides discussion of how we quantify the hysteretic energy-dissipation capacity and the post-capping stiffness. To provide a quick summary of the more detailed discussion:

- Hysteretic energy-dissipation capacity (normalized): Mean $\gamma = 120$, with a coefficient of variation of 50%.
- Post-capping stiffness ratio: Mean of $-0.08 K_o$, with a coefficient of variation of 60%.

F.2.5.6 Element Variability: Correlations

This section discussed the variability of modeling parameters for a single element. A more difficult question is regarding the correlations between the behaviors of each element in the building. Appendix E.3 discusses this issue.

F.2.6 Drift at Slab-Beam Capping

We assume that the capping of the slab-beam will coincide with the onset of punching shear. Appendix 7a discusses the fragility models for punching shear failure.

Appendix G: Approximate Method for Estimating Effects of Correlations between Elements

G.1 INTRODUCTION AND PURPOSE OF APPENDIX

This appendix explains an approximate method to quantify the impacts of assumptions of correlations between the element parameters for different elements in the frame (as discussed in Appendix E.3). The approach that we use here is to try to adjust the element-level standard deviations by a factor, in order to approximate the effect of partial correlations between the element parameters for different elements.

This approximation shows that for n elements in parallel (e.g., n beams or columns in parallel over a story), we can scale the element-level standard deviations by the factor $1/\sqrt{n}$ in order to use a model with full correlation between the element parameters for difference elements in the frame, and try to approximate the results that we would obtain by using a model with partial correlation of this type.

It is important to note that this approximate method is only useful for predicting global responses such as interstory drift or floor acceleration. This approximation is not appropriate for trying to estimate variability in more local responses, such as element plastic-rotation demands.

G.2 APPROXIMATION METHOD

To estimate the effects of the assumption of perfect correlation between the parameters of different elements, we try in this section to find a way to estimate what the total uncertainty in structural response would be assuming partial correlation between the parameters of different elements. As discussed above, to completely solve this problem, we would need to use 360

random variables instead of 10, so the approach that we take here is to still use perfect correlation between parameters of different elements, but reduce the variance on each element random variable to try to estimate the final variance of structural response that we would obtain if we used partial correlation between the parameters of different elements.

In making this approximation, we restrict ourselves to the prediction of global response parameters such as roof drift ratio and global collapse. We do this because if the parameters of different elements are uncorrelated, the local response quantities (such as element plastic rotation) will be more variable and more difficult to predict. For example, if the stiffness of adjacent columns are uncorrelated and one column is much stiffer than the adjacent column, the damage will begin in the stiffer column and will cause the estimates of plastic-rotation demands to be much different than estimated when assuming perfect correlation between element stiffnesses.

To make this approximation, we assume that the following two models will provide the same final variance in the estimate of global structural response parameters:

- A model with partial correlation between parameters of different elements and that uses the original variances, σ_{ele}^2 , for all of the element-level random variables (uses the variances as shown in Table E.4)
- A model with full correlation between parameters of different elements and that uses reduced variances, $\kappa\sigma_{ele}^2$, for all of the element-level random variables (variances reduced by the factor κ)

To equate the final variances in global response, call it σ_{EDP}^2 , we will look at a single story of the frame and approximately equate the total variance in the stiffness of the story. Figure G.1 depicts this story deformation and stiffness:

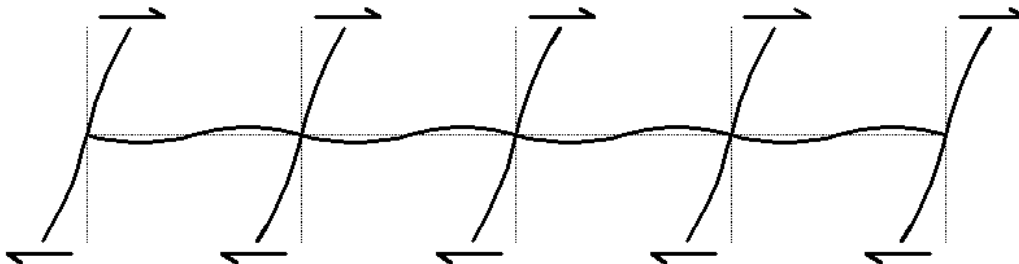


Fig. G.1 Illustration of story stiffness approximately composed of 4–5 elements in parallel.

If we assume that the story stiffness can be approximated by n elements in parallel (actually a combination of four beams and five columns in this case), we can compute the story stiffness by simply summing the stiffnesses of the individual components:

$$K_{story} = \sum_i K_i$$

To find the variance in the story stiffness due to the variances in the individual element stiffnesses, we can use the equation for the variance of a linear function of random variables:

$$\sigma_{K_{story}}^2 = \sum_{i=1}^n \sum_{j=1}^n \rho_{ij} \sigma_i \sigma_j$$

We now can compute the variances for the story stiffness for the two cases listed above.

Case 1:

$$0.0 < \rho_{ij} < 1.0 \text{ for } i \neq j$$

$$\sigma_{K_{story}}^2 = n\sigma_{ele}^2 + (n^2 - n)\rho_{ij}\sigma_{ele}^2$$

Case 2:

$$\rho_{ij} = 1.0 \text{ for all } i \text{ and } j$$

$$\sigma_{K_{story}}^2 = n^2 (\kappa\sigma_{ele})^2$$

Now that we have the variances computed for both cases, we can simply equate the variances of the story stiffness and solve for the effective reduction in element-level standard deviation, κ .

$$\sigma_{K_{story}}^2 = n\sigma_{ele}^2 + (n^2 - n)\rho_{ij}\sigma_{ele}^2 = n^2 (\kappa\sigma_{ele})^2$$

$$\kappa = \sqrt{\frac{1 + \rho_{ij}(n-1)}{n}}$$

This approximation shows that if we assume zero element correlation and that the story stiffness is approximately equivalent to four element stiffnesses in parallel, then we can decrease the element-level standard deviations by a factor of $1/\sqrt{4} = 0.5$ in order to approximate the effects of zero correlation between the parameters of different elements. If we instead assume that the story is composed of five elements in parallel, then the factor is $1/\sqrt{5} = 0.45$. This is essentially showing the averaging effect that causes the final uncertainty to be reduced by a factor of 2.0 when there are several uncorrelated random variables in parallel.

In order to look at a more general result for partial correlations, Figure G.2 shows the relationship between ρ_{ij} and κ when using the above equation and assuming $n = 4$:

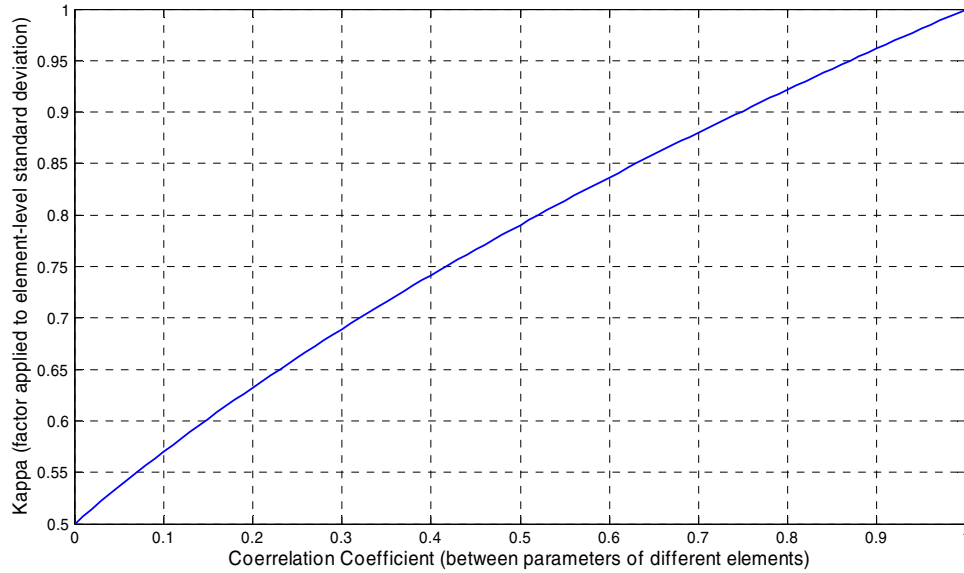


Fig. G.2 Effects of partial correlation between element parameter of different elements.

If we assume an average correlation of 0.5 between the parameters of different elements, this leads to $\kappa=0.78$. In all the modeling uncertainty calculations shown in this report (Appendix E.5.2), we keep track of the full range of possible correlations, but we use this kappa factor of 0.78 to approximate what we think to be the approximate “central value” of the level of correlation.

Appendix H: Sample First-Order Second-Moment Calculation for Collapse Capacity of Design A

H.1 INTRODUCTION AND PURPOSE OF APPENDIX

This appendix presents an example of applying the first-order second-moment (FOSM) method to estimate the uncertainty of collapse capacity that comes from uncertainties in model and design variables. This example is for Design A with full Type B correlations, expected Type A correlations (correlation explanation can be found in Appendix E.3), and uses a subset of the ground motions in the sensitivity analyses. The example includes the contribution of all ten random variables considered (i.e., both modeling and design variables). For simplicity, the first example FOSM calculation is completed with the data not transformed by logarithms (i.e., in the non-Ln-domain). At the end of this Appendix, a comparison is made to the results that would be obtained if the computation was done in the Ln-domain. These examples follow directly from the first-order second-moment (FOSM) procedure introduced in Appendix E.5.1.

H.2 EXAMPLE IN THE NON-LN-DOMAIN

The mean and record-to-record variability are simply estimated from the structural collapse analysis. Figure 5.49 in Chapter 5 shows results of IDA analyses that are used to estimate the collapse capacities for each ground motion record. From these analyses, we can establish the mean and record-to-record standard deviation. Note that this is a subset of the records, so the median collapse capacity is slightly higher than the median of the full set (as compared to Table 5.15 in Chapter 5).

$$\mu_{Sa_{collapse}} \cong g(M_X) = 2.63g \quad (H.1)$$

$$\sigma^2[X_{RTR}] = 0.86, \quad \sigma[X_{RTR}] = 0.93 \quad (H.2)$$

We need to solve Equation H.3. To do this, we will need information about standard deviations of each random variables, the correlations between the variables, and the gradients of collapse capacity with respect to each random variable.

$$\sigma^2[Sa_{collapse}] \cong \left[\sum_{i=1}^n \sum_{j=1}^n \left[\frac{\partial g(X)}{\partial x_i} \cdot \frac{\partial g(X)}{\partial x_j} \right]_{X=M_X} \rho_{ij} \sigma_i \sigma_j \right] + \sigma^2[X_{RTR}] \quad (H.3)$$

where $\frac{\partial g(X)}{\partial(x_i)}$ is the gradient of the $Sa_{collapse}$ with respect to random variable i ,

ρ_{ij} is the correlation coefficient between RV_i and RV_j , and σ_i is the standard deviation of RV_i .

The standard deviation of each random variable must be determined using test data and past research. Table H.1 gives the standard deviations of each random variable, while Appendices 5c and 5d give the detail regarding how these values were determined. Note that Table H.1 defines the random variable numbers.

Table H.1 Uncertainty (standard deviation) for each random variable.

Random Variable Number	Random Variable Name	σ_i
1	Plastic rotation capacity	0.60
2	Hysteretic energy capacity	0.50
3	Post-capping stiffness	0.60
4	Element strength (modeling)	0.12
5	Strong-col. weak-beam design ratio	0.15
6	Initial stiffness	0.36
7	Post-yield stiffness	0.50
8	Damping ratio	0.60
9	Dead load	0.10
10	Element design strength	0.20

We also must estimate the correlations between the variables (Type A correlations), which is difficult and requires significant judgment. These correlations can be determined if large amounts of test data are available, though this was not pursued in this study (an ongoing study by the authors is hoped to provide some insight into Type A correlations for the beam-column element model). Note that we are assuming full Type B correlation (see Appendix E.3

for definition of types of correlations). Table H.2 shows the correlation matrix assumed for this example, which is based solely on judgment.

Table H.2 Correlation matrix for correlations within single element (Type A).

	RV1	RV2	RV3	RV4	RV5	RV6	RV7	RV8	RV9	RV10
RV1	1									
RV2	1	1								
RV3	-1	-1	1							
RV4	0	0	0	1						
RV5	0	0	0	0	1					
RV6	0	0	0	1	0	1				
RV7	0	0	0	0	0	1	1			
RV8	0	0	0	0	0	0	0	1		
RV9	0	0	0	1	0	1	0	0	1	
RV10	0	0	0	0	1	0	0	0	0	1

(Symmetric)

We next need to estimate the gradients of the collapse capacity to each random variable. To do this, we must alter each random variable value individually, rerun the collapse analysis, observe how much the collapse capacity changed, then compute the gradient. Appendix E.4.1 shows the results of such a sensitivity study; the results were used to create this example. If we are interested in computing a probability or annual frequency of some failure event (i.e., collapse in this case), the gradients used in the FOSM computation should be the gradients in the direction of the failure domain. Table H.3 displays this gradient for each random variable. This example uses the median for gradient computations (as this is hopefully more stable than the mean), though typically the mean is used. It is expected that using either the mean or median should yield similar results.

Table H.3 Gradients of collapse capacity with respect to each random variable; estimated from collapse sensitivity study presented in Appendix E.4.1.

Random Variable Number	Gradient ($\Delta\text{Median}_{\text{SaCol}} / \Delta\text{RV}$)
1	1.96
2	0.74
3	-0.18
4	2.05
5	3.29
6	0.73
7	0.52
8	0.08
9	-1.50
10	2.05

We now need to compute the remaining components of Equation H.3. This is done in multiple steps, as follows, so the numerical example will be more complete.

Table H.4 Term used to solve Eqs. H.3.

$\rho_{ij}\sigma_i\sigma_j$										
	RV1	RV2	RV3	RV4	RV5	RV6	RV7	RV8	RV9	RV10
RV1	0.36	0.30	-0.36	0.00	0.00	0.00	0.00	0.00	0.00	0.00
RV2	0.30	0.25	-0.30	0.00	0.00	0.00	0.00	0.00	0.00	0.00
RV3	-0.36	-0.30	0.36	0.00	0.00	0.00	0.00	0.00	0.00	0.00
RV4	0.00	0.00	0.00	0.01	0.00	0.04	0.00	0.00	0.01	0.00
RV5	0.00	0.00	0.00	0.00	0.02	0.00	0.00	0.00	0.00	0.03
RV6	0.00	0.00	0.00	0.04	0.00	0.13	0.18	0.00	0.04	0.00
RV7	0.00	0.00	0.00	0.00	0.00	0.18	0.25	0.00	0.00	0.00
RV8	0.00	0.00	0.00	0.00	0.00	0.00	0.00	0.36	0.00	0.00
RV9	0.00	0.00	0.00	0.01	0.00	0.04	0.00	0.00	0.01	0.00
RV10	0.00	0.00	0.00	0.00	0.03	0.00	0.00	0.00	0.00	0.04

Table H.5 Term used to solve Eqs. H.3.

(Gradient)_i * (Gradient)_j										
	RV1	RV2	RV3	RV4	RV5	RV6	RV7	RV8	RV9	RV10
RV1	3.84	1.46	-0.35	4.01	6.44	1.44	1.02	0.16	-2.94	4.01
RV2	1.46	0.55	-0.13	1.53	2.45	0.55	0.39	0.06	-1.12	1.53
RV3	-0.35	-0.13	0.03	-0.36	-0.59	-0.13	-0.09	-0.01	0.27	-0.36
RV4	4.01	1.53	-0.36	4.19	6.73	1.50	1.07	0.16	-3.07	4.19
RV5	6.44	2.45	-0.59	6.73	10.81	2.41	1.72	0.26	-4.93	6.73
RV6	1.44	0.55	-0.13	1.50	2.41	0.54	0.38	0.06	-1.10	1.50
RV7	1.02	0.39	-0.09	1.07	1.72	0.38	0.27	0.04	-0.78	1.07
RV8	0.16	0.06	-0.01	0.16	0.26	0.06	0.04	0.01	-0.12	0.16
RV9	-2.94	-1.12	0.27	-3.07	-4.93	-1.10	-0.78	-0.12	2.25	-3.07
RV10	4.01	1.53	-0.36	4.19	6.73	1.50	1.07	0.16	-3.07	4.19

Table H.6 Term used to solve Eqs. H.3.

$\rho_{ij}\sigma_i\sigma_j$ * (Gradient)_i * (Gradient)_j										
	RV1	RV2	RV3	RV4	RV5	RV6	RV7	RV8	RV9	RV10
RV1	1.38	0.44	0.13	0.00	0.00	0.00	0.00	0.00	0.00	0.00
RV2	0.44	0.14	0.04	0.00	0.00	0.00	0.00	0.00	0.00	0.00
RV3	0.13	0.04	0.01	0.00	0.00	0.00	0.00	0.00	0.00	0.00
RV4	0.00	0.00	0.00	0.06	0.00	0.06	0.00	0.00	-0.04	0.00
RV5	0.00	0.00	0.00	0.00	0.24	0.00	0.00	0.00	0.00	0.20
RV6	0.00	0.00	0.00	0.06	0.00	0.07	0.07	0.00	-0.04	0.00
RV7	0.00	0.00	0.00	0.00	0.00	0.07	0.07	0.00	0.00	0.00
RV8	0.00	0.00	0.00	0.00	0.00	0.00	0.00	0.00	0.00	0.00
RV9	0.00	0.00	0.00	-0.04	0.00	-0.04	0.00	0.00	0.02	0.00
RV10	0.00	0.00	0.00	0.00	0.20	0.00	0.00	0.00	0.00	0.17

Using the results shown in Table H.6, the terms of Equation I.3 can be computed with a simple summation, then the results of modeling/design uncertainty can be combined with record-to-record variability to get the total uncertainty in collapse capacity.

$$\left[\sum_{i=1}^n \sum_{j=1}^n \left[\frac{\partial g(X)}{\partial x_i} \cdot \frac{\partial g(X)}{\partial x_j} \right]_{X=M_x} \rho_{ij} \sigma_i \sigma_j \right] = \sigma_{FOSM}^2 = 3.89 \quad (H.4)$$

$$\sigma_{FOSM} = 1.97 \quad (H.5)$$

$$\sigma^2 [Sa_{collapse}] \cong 3.89 + 0.86 = 4.75 \quad (H.6)$$

$$\sigma[Sa_{collapse}] \cong 2.18 \quad (\text{H.7})$$

H.3 COMPARISON TO RESULTS OBTAINED IN LN-DOMAIN

We can now compare this result with the results by completing the FOSM approximation in the Ln-domain. To make this comparison, we can first transform the predicted standard deviation into an equivalent ln-standard deviation, as shown in Equation H.8.

$$\sigma_{LN,FOSM} = \sqrt{\text{Ln} \left[\left(\frac{\sigma_{FOSM}}{\text{median}(Sa_{collapse})} \right)^2 + 1 \right]} = \sqrt{\text{Ln} \left[\left(\frac{1.97}{2.63} \right)^2 + 1 \right]} = 0.67 \quad (\text{H.8})$$

Table E.8 of Appendix E shows that this value would be 0.54 if the FOSM approximation was done in the Ln-domain; showing a 25% difference in results. Similar differences have been documented by Ibarra (2003).

Performing this approximation in the Ln-domain is considered to be more correct because the relationships should be more linear in the Ln-domain of the data, thus making the FOSM approximation more accurate.

Appendix I: Fragility Functions and Cost of Column-Slab Connection Damage

I.1 INTRODUCTION AND PURPOSE OF APPENDIX

The following text addresses the fragility functions and repair of column-slab connections. The fragility and repair of slab-column connections may depend on a number of parameters: code era (with the 1976 UBC marking an important dividing line), type of slab, post-tensioning (denoted by PT, as opposed to reinforced concrete, RC), shear reinforcement, the ratio of gravity to seismic shear, and possibly others. A partial topology of these connections is shown in Figure I.1. The variants of the benchmark building considered here are those with a post-1976, flat-plate system with post-tensioning and no shear reinforcement. They have an internal gravity frame comprising 18-in.-sq columns and 8-in. flat post-tensioned reinforced concrete slabs.

To address the issue of fragility and repair of the types of connection at issue, this text draws on three sources: Aslani's (2005) doctoral thesis; tests reported by Kang et al. (2006a, b) of slab-column connections; and post-earthquake damage observations by Wallace (ND). Repairs are described and quantified, but costs and repair durations are not calculated here.

I.2 FRAGILITY FUNCTIONS

Aslani's (2005) doctoral thesis develops punching-shear fragility functions and cost distributions for older slab-column connections, i.e., cast-in-place slab-column connections built prior to 1976 that have no shear reinforcement and that typically do not have continuous slab bars passing through the column cage. Four damage states are defined, from cosmetic to loss of gravity support (Table I.1). The repairs associated with each are qualitatively described, and fragility functions are developed for each damage state in terms of peak transient interstory drift. Cost estimates are provided for each repair effort. Eighteen sets of laboratory tests on 82 specimens

are employed in developing the fragility functions. A number of ACI publications are cited in support of the recommended repair efforts, e.g., ACI 224.1R-93 (1998) and ACI 546 (2004). Cost estimates are developed using RS Means cost manuals. It is noteworthy that Aslani equates yielding of top bars with damage state 2 (denoted by DS2), which occurs at drifts on the order of 0.9%, a point that will be relevant later.

Kang et al. (2006a) report on laboratory tests of post-tensioned interior slab-column joints in flat-plate frames subjected to cyclic lateral loading. The emphasis is on strength and force-deformation behavior and on drift at yield and at the onset of punching shear, rather than on other damage states, repair efforts, and fragility functions. In the tests that involved modern code-conforming reinforced concrete and post-tensioned slabs, yielding of top steel occurred at drifts of approximately 1%, a level similar to that proposed by Aslani for pre-1976 UBC connections for DS2, which he equates with yielding. This suggests that code era and post-tensioning may have limited relevance to DS2. Punching shear (Aslani's DS3) occurred in RC and PT specimens at 3.5–4% and 4–5% drift, respectively, with logarithmic standard deviation ≈ 0.3 (Fig. I.2). These levels are substantially higher than that suggested for DS3 by Aslani (2005) for pre-1976 connections.

The performance differences between RC and PT slabs observed by Kang et al. (2006a) is significant, enough that separate fragility functions are reasonable for each slab type, but perhaps not so great that one must distinguish between them in a loss analysis; a third set of fragility functions is reasonable for undifferentiated post-1976 flat-plate slab-column connections.

It is supposed here that the provision of continuous bars through the slab-column joint would prevent loss of vertical load-carrying capacity before a collapse mechanism occurred in the LFRS (Deierlein 2006) so Aslani's (2005) DS4 would not be applicable in the present study. Based on this limited literature review, the fragility functions shown in Table I.2 are employed for the interior slab-column joints of the benchmark building. For use in other applications with post-1976 RC flat-plate slabs, Table I.3 could be used, while undifferentiated (PT or RC) post-1976 slab-column connections for flat-plate slabs could be represented by the fragility functions shown in Table I.4. In the three tables, peak interstory drift ratio is defined as the displacement of the mid-height of the column above the slab relative to that of the column below, divided by the vertical distance between the two points. Where unavailable (as would be common), it seems that

this *EDP* could reasonably be approximated as the average of the interstory drift ratios of the stories above and below the slab.

Regarding uncertainty, Tables I.2–3 use the greater logarithmic standard deviations suggested by Aslani (2005), under the assumptions that: (1) the tests reported by Kang et al. (2006a) are a limited sample; (2) that diversity of conditions beyond that sample would produce greater uncertainty; and (3) that Aslani’s literature review of 18 sets of tests and 82 experiments could reasonably be judged to indicate a proper logarithmic standard deviation for a representatively diverse set of conditions. The logarithmic standard deviation of capacity for DS3 in Table I.4 reflects the greater uncertainty resulting from an equiprobable mix of the two types of connections shown in Tables I.2–3.

I.3 REPAIRS

There appears to be no strong reason to suppose that repairs for a code-conforming slab-column joint in DS1 through 3 would be substantially different than in a pre-1976 connection, so Aslani’s (2005) suggested repairs are employed here, with minor but potentially costly additions. In addition to the efforts suggested by Aslani (2005), repair involves removal and replacement of finishes. In the case of DS1 and DS2, these include floor finishes and partitions on the story above the damaged slab. In the case of DS3, it also includes shoring to the slab below of the damaged slab, to the extent of twice as far from the column face as severe cracking appears, and removal and replacement of affected ceiling finishes and above-ceiling services.

Third, it is worthwhile to quantify the extent of cracking and therefore repairs, as this could also affect the cost estimate. Wallace (ND) provides images of slab-column joint damage to a four-story reinforced concrete frame building in Sherman Oaks, CA, after the 1994 Northridge earthquake. The joint has a drop panel (a thicker section near the column), so the critical section for shear above the edge of the drop panel is away from the column face. In the image, damage takes the form of concrete spalling over the edge of a drop panel, with the spalled area on the slab surface extending approximately $\frac{1}{2}$ to 1 times the depth of the slab to either side of the edge of the drop panel (Fig. I.3).

Kang et al. (2006b) report cracks initiating at the column face at drifts less than 1% (assumed to be DS2), and extending 2.5 times the slab depth from the column face by the onset of DS3. No evidence was readily available to quantify the extent of cracking in DS1 and DS2, so

it will be assumed here that at DS1, surface coating is required within 1.0 times the slab thickness of the column face, and at DS2, 2.0 times the slab thickness. It appears from Kang and Wallace (2005, 2006) that the damage at DS3 would be substantially less for post-1976 slab-column connections *with* shear-reinforced slabs, so the costs and possibly the fragility functions proposed here should not be used for shear-reinforced connections without further study.

I.4 COSTS

Aslani (2005) proposes repair costs for each damage state, but ignores finishes, shoring, dust protection, etc. His estimates are replaced in the present study with those of a professional cost estimator.

Table I.1 Aslani’s (2005) fragility functions for pre-1976 UBC slab-column connections in terms of peak interstory drift ratio (*IDR*) and repair efforts.

Damage State	IDR ^(a)	$\sigma_{\ln IDR}^{(b)}$	Repair
DS1: Light cracking	0.33	0.39	Surface coating for moisture protection
DS2: Severe cracking	0.90	0.25	Epoxy injection
DS3: Punching shear failure	2.00	0.62	Chip out and replace spalled concrete
DS4: Loss of vertical capacity	4.28	0.36	Demolish building

(a) median value in the lognormal CDF used as the fragility functions, expressed as percent

(b) $\sigma_{\ln IDR}$ is the logarithmic standard deviation in the lognormal CDF used as the fragility functions

Table I.2 Fragility of post-1976 flat-plate PT slab-column connections without shear reinforcement.

Damage State	IDR ^(a) (%)	$\sigma_{\ln IDR}^{(b)}$	Repair description
DS1: Light cracking	0.3	0.4	Remove and replace floor and wall finishes and move tenants away from work area, as necessary. Apply 5–10 sf surface coating to top of slab to conceal cracks and inhibit water infiltration. Partitions may or may not abut column. No work required on story below damaged slab.
DS2: Severe cracking	1.0	0.3	Remove and replace finishes and move tenants away from work area, as necessary. Epoxy injection of cracks over 10–20 sf of slab near column face. Partitions may or may not abut column. No work required on story below damaged slab.
DS3: Punching shear failure	4.5	0.6	Shore slab all around within 2–3 ft of column to floor below. Remove and replace finishes, including ceiling finishes and above-ceiling systems affected by shoring. Chip out and replace 15–25 sf of loose concrete at slab surface to a depth of 1–2 in. Dust and noise control. Partitions may or may not abut column.

(a) Average of peak transient interstory drift ratio in stories above and below the slab. For 3D analyses, use the maximum direction. Value shown here is the median for use in lognormal CDF fragility function

(b) logarithmic standard deviation for use in lognormal CDF fragility function

Table I.3 Fragility of post-1976 flat-plate RC slab-column connections without shear reinforcement.

Damage State	IDR ^(a) (%)	$\sigma_{\ln IDR}^{(b)}$	Repair description
DS1: Light cracking	0.3	0.4	Remove and replace floor and wall finishes and move tenants away from work area, as necessary. Apply 5–10 sf surface coating to top of slab to conceal cracks and inhibit water infiltration. Partitions may or may not abut column. No work required on story below damaged slab.
DS2: Severe cracking	1.0	0.3	Remove and replace finishes and move tenants away from work area, as necessary. Epoxy injection of cracks over 10–20 sf of slab near column face. Partitions may or may not abut column. No work required on story below damaged slab.
DS3: Punching shear failure	3.8	0.6	Shore slab all around within 2–3 ft of column to floor below. Remove and replace finishes, including ceiling finishes and above-ceiling systems affected by shoring. Chip out and replace 15–25 sf of loose concrete at slab surface to a depth of 1–2 in. Dust and noise control. Partitions may or may not abut column.

- (a) Average of peak transient interstory drift ratio in stories above and below the slab. For 3D analyses, use the maximum direction. Value shown here is the median for use in lognormal CDF fragility function
(b) logarithmic standard deviation for use in lognormal CDF fragility function

Table I.4 Fragility of post-1976 flat-plate RC or PT slab-column connections, without shear reinforcement.

Damage State	IDR ^(a) (%)	$\sigma_{\ln IDR}^{(b)}$	Repair description
DS1: Light cracking	0.3	0.4	Remove and replace floor and wall finishes and move tenants away from work area, as necessary. Apply 5–10 sf surface coating to top of slab to conceal cracks and inhibit water infiltration. Partitions may or may not abut column. No work required on story below damaged slab.
DS2: Severe cracking	1.0	0.3	Remove and replace finishes and move tenants away from work area, as necessary. Epoxy injection of cracks over 10–20 sf of slab near column face. Partitions may or may not abut column. No work required on story below damaged slab.
DS3: Punching shear failure	4.2	0.7	Shore slab all around within 2–3 ft of column to floor below. Remove and replace finishes, including ceiling finishes and above-ceiling systems affected by shoring. Chip out and replace 15–25 sf of loose concrete at slab surface to a depth of 1–2 in. Dust and noise control. Partitions may or may not abut column.

- (a) Average of peak transient interstory drift ratio in stories above and below the slab. For 3D analyses, use the maximum direction. Value shown here is the median for use in lognormal CDF fragility function
(b) logarithmic standard deviation for use in lognormal CDF fragility function

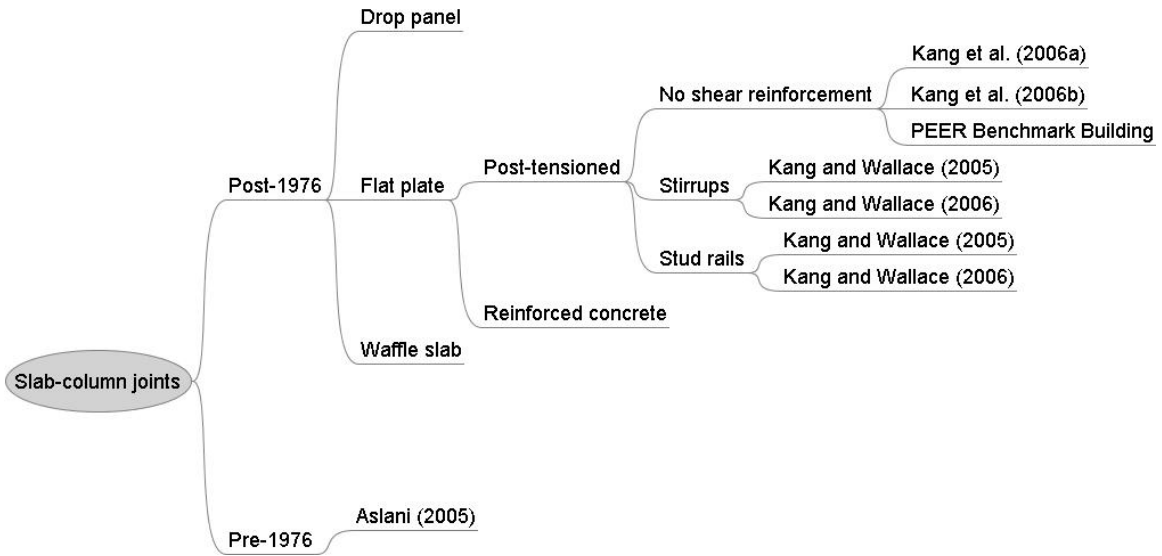
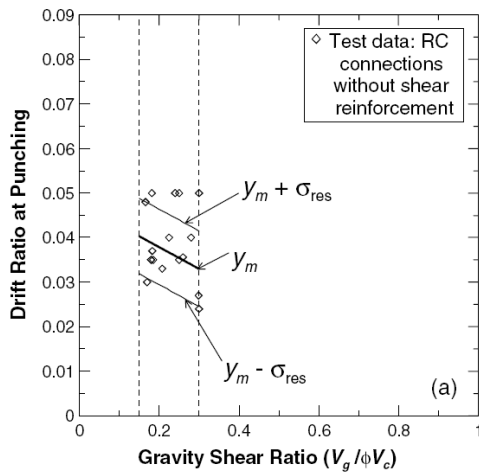
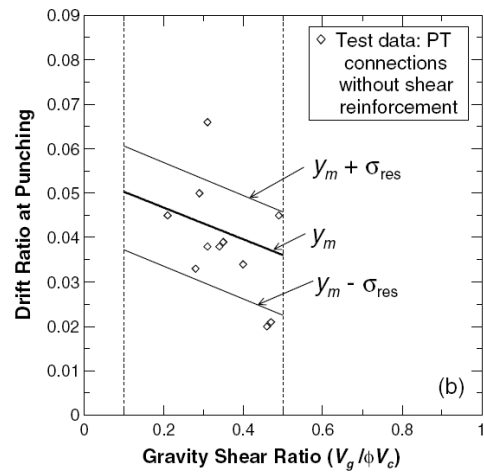


Fig. I.1 Partial topology of slab-column joints and related literature.



(a) RC slab-column connections



(b) PT slab-column connections

Fig. I.2 Onset of punching shear in code-conforming slab-column connections (Kang et al. 2006a).

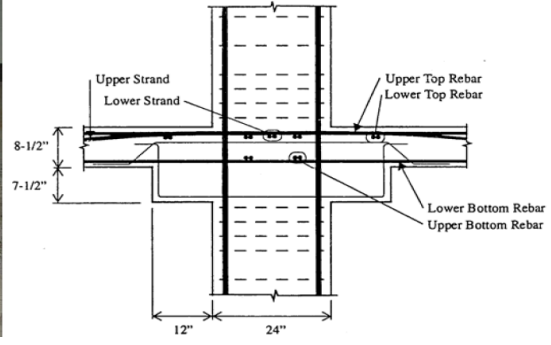


Fig. I.3 Damage to four-story reinforced concrete frame in Sherman Oaks due to 1994 Northridge earthquake (Wallace ND).

Appendix J: Tables of Damageable Assemblies

Table J.1 Table of damageable assemblies for perimeter-frame buildings.

Assembly Type	Assembly Description	Location (story/floor)	Unit	Quantity
3.5.190.1102.01	Ductile cast-in-place reinforced concrete beam, NS-dir	2	ea	8
3.5.190.1102.01	Ductile cast-in-place reinforced concrete beam, NS-dir	3	ea	8
3.5.190.1102.01	Ductile cast-in-place reinforced concrete beam, NS-dir	4	ea	8
3.5.190.1102.01	Ductile cast-in-place reinforced concrete beam, NS-dir	5	ea	8
3.5.180.1101.01	Ductile cast-in-place reinforced concrete column, NS-dir	1	ea	10
3.5.180.1101.01	Ductile cast-in-place reinforced concrete column, NS-dir	2	ea	10
3.5.180.1101.01	Ductile cast-in-place reinforced concrete column, NS-dir	3	ea	10
3.5.180.1101.01	Ductile cast-in-place reinforced concrete column, NS-dir	4	ea	10
6.1.500.0001.01	Drywall partition, 5/8-in., 1 side, on metal stud, screws, NS-dir	1	64 sf	134
6.1.500.0001.01	Drywall partition, 5/8-in., 1 side, on metal stud, screws, NS-dir	2	64 sf	181
6.1.500.0001.01	Drywall partition, 5/8-in., 1 side, on metal stud, screws, NS-dir	3	64 sf	181
6.1.500.0001.01	Drywall partition, 5/8-in., 1 side, on metal stud, screws, NS-dir	4	64 sf	181
6.1.500.0002.01	Drywall finish, 5/8-in., 1 side, on metal stud, screws, NS-dir	1	64 sf	134
6.1.500.0002.01	Drywall finish, 5/8-in., 1 side, on metal stud, screws, NS-dir	2	64 sf	181
6.1.500.0002.01	Drywall finish, 5/8-in., 1 side, on metal stud, screws, NS-dir	3	64 sf	181
6.1.500.0002.01	Drywall finish, 5/8-in., 1 side, on metal stud, screws, NS-dir	4	64 sf	181
3.5.190.1102.01	Ductile cast-in-place reinforced concrete beam, EW-dir	2	ea	8

Table J.1—Continued

Assembly Type	Assembly Description	Location (story/floor)	Unit	Quantity
3.5.190.1102.01	Ductile cast-in-place reinforced concrete beam, EW-dir	3	ea	8
3.5.190.1102.01	Ductile cast-in-place reinforced concrete beam, EW-dir	4	ea	8
3.5.190.1102.01	Ductile cast-in-place reinforced concrete beam, EW-dir	5	ea	8
3.5.180.1101.01	Ductile cast-in-place reinforced concrete column, EW-dir	1	ea	10
3.5.180.1101.01	Ductile cast-in-place reinforced concrete column, EW-dir	2	ea	10
3.5.180.1101.01	Ductile cast-in-place reinforced concrete column, EW-dir	3	ea	10
3.5.180.1101.01	Ductile cast-in-place reinforced concrete column, EW-dir	4	ea	10
6.1.500.0001.01	Drywall partition, 5/8-in., 1 side, on metal stud, screws, EW-dir	1	64 sf	175
6.1.500.0001.01	Drywall partition, 5/8-in., 1 side, on metal stud, screws, EW-dir	2	64 sf	181
6.1.500.0001.01	Drywall partition, 5/8-in., 1 side, on metal stud, screws, EW-dir	3	64 sf	181
6.1.500.0001.01	Drywall partition, 5/8-in., 1 side, on metal stud, screws, EW-dir	4	64 sf	181
6.1.500.0002.01	Drywall finish, 5/8-in., 1 side, on metal stud, screws, EW-dir	1	64 sf	175
6.1.500.0002.01	Drywall finish, 5/8-in., 1 side, on metal stud, screws, EW-dir	2	64 sf	181
6.1.500.0002.01	Drywall finish, 5/8-in., 1 side, on metal stud, screws, EW-dir	3	64 sf	181
6.1.500.0002.01	Drywall finish, 5/8-in., 1 side, on metal stud, screws, EW-dir	4	64 sf	181

Table J.2 Table of damageable assemblies for space-frame buildings.

Assembly Type	Assembly Description	Location (story/floor)	Unit	Quantity
3.5.190.1102.01	Ductile cast-in-place reinforced concrete beam, NS-dir	2	ea	28
3.5.190.1102.01	Ductile cast-in-place reinforced concrete beam, NS-dir	3	ea	28
3.5.190.1102.01	Ductile cast-in-place reinforced concrete beam, NS-dir	4	ea	28
3.5.190.1102.01	Ductile cast-in-place reinforced concrete beam, NS-dir	5	ea	28
3.5.180.1101.01	Ductile cast-in-place reinforced concrete column, NS-dir	1	ea	35
3.5.180.1101.01	Ductile cast-in-place reinforced concrete column, NS-dir	2	ea	35
3.5.180.1101.01	Ductile cast-in-place reinforced concrete column, NS-dir	3	ea	35
3.5.180.1101.01	Ductile cast-in-place reinforced concrete column, NS-dir	4	ea	35
6.1.500.0001.01	Drywall partition, 5/8-in., 1 side, on metal stud, screws, NS-dir	1	64 sf	134
6.1.500.0001.01	Drywall partition, 5/8-in., 1 side, on metal stud, screws, NS-dir	2	64 sf	181
6.1.500.0001.01	Drywall partition, 5/8-in., 1 side, on metal stud, screws, NS-dir	3	64 sf	181
6.1.500.0001.01	Drywall partition, 5/8-in., 1 side, on metal stud, screws, NS-dir	4	64 sf	181
6.1.500.0002.01	Drywall finish, 5/8-in., 1 side, on metal stud, screws, NS-dir	1	64 sf	134
6.1.500.0002.01	Drywall finish, 5/8-in., 1 side, on metal stud, screws, NS-dir	2	64 sf	181
6.1.500.0002.01	Drywall finish, 5/8-in., 1 side, on metal stud, screws, NS-dir	3	64 sf	181
6.1.500.0002.01	Drywall finish, 5/8-in., 1 side, on metal stud, screws, NS-dir	4	64 sf	181
3.5.190.1102.01	Ductile cast-in-place reinforced concrete beam, EW-dir	2	ea	30
3.5.190.1102.01	Ductile cast-in-place reinforced concrete beam, EW-dir	3	ea	30
3.5.190.1102.01	Ductile cast-in-place reinforced concrete beam, EW-dir	4	ea	30
3.5.190.1102.01	Ductile cast-in-place reinforced concrete beam, EW-dir	5	ea	30
3.5.180.1101.01	Ductile cast-in-place reinforced concrete column, EW-dir	1	ea	35
3.5.180.1101.01	Ductile cast-in-place reinforced concrete column, EW-dir	2	ea	35
3.5.180.1101.01	Ductile cast-in-place reinforced concrete column, EW-dir	3	ea	35

Table J.2—Continued

Assembly Type	Assembly Description	Location (story/floor)	Unit	Quantity
3.5.180.1101.01	Ductile cast-in-place reinforced concrete column, EW-dir	4	ea	35
6.1.500.0001.01	Drywall partition, 5/8-in., 1 side, on metal stud, screws, EW-dir	1	64 sf	175
6.1.500.0001.01	Drywall partition, 5/8-in., 1 side, on metal stud, screws, EW-dir	2	64 sf	181
6.1.500.0001.01	Drywall partition, 5/8-in., 1 side, on metal stud, screws, EW-dir	3	64 sf	181
6.1.500.0001.01	Drywall partition, 5/8-in., 1 side, on metal stud, screws, EW-dir	4	64 sf	181
6.1.500.0002.01	Drywall finish, 5/8-in., 1 side, on metal stud, screws, EW-dir	1	64 sf	175
6.1.500.0002.01	Drywall finish, 5/8-in., 1 side, on metal stud, screws, EW-dir	2	64 sf	181
6.1.500.0002.01	Drywall finish, 5/8-in., 1 side, on metal stud, screws, EW-dir	3	64 sf	181
6.1.500.0002.01	Drywall finish, 5/8-in., 1 side, on metal stud, screws, EW-dir	4	64 sf	181

Appendix K: Comparing Loss Predictions to Other Standard Methodologies

K.1 COMPARISON WITH OTHER PREDICTIVE TOOLS

While little empirical data are available to compare the estimated performance of the benchmark building with earthquake experience, it may be valuable to examine how the PEER methodology compares with other predictive estimates of performance. Three standard methodologies are commonly used. ATC-13 (1985), HAZUS (NIBS and FEMA 2003), and ST-Risk 4.11 (Risk Engineering, Inc. 2004) offer loss estimates that can be compared with results from this study. Provided here is an examination of the mean damage factor (*MDF*, the expected value of repair cost as a fraction of replacement cost) for the shaking intensity with 10% exceedance probability in 50 years, using the PEER methodology and these three authorities. (*MDF* is not the same as *PML*, which commonly refers to the loss with 10% exceedance probability, conditioned on shaking with 10% exceedance probability in 50 years, i.e., an upper-bound loss at the same level of shaking considered here.)

K.2 INTENSITY MEASURE

Some *IM* conversion is necessary. ST-Risk uses the US Geological Survey's National Seismic Hazard Maps to determine hazard, but converts to Modified Mercalli Intensity (*MMI*) for use with its seismic vulnerability functions. ATC-13 uses *MMI*. HAZUS's *IM* can be considered to be its input spectrum (an idealized 5%-damped elastic response spectrum on site class B) adjusted to account for site soil conditions and hysteretic damping. The adjusted spectrum is referred to as the demand spectrum, and is a function of *PGA*, $S_a(0.3s,5\%)$, $S_a(1.0s,5\%)$, $S_a(T_{VD},5\%)$, moment magnitude, NEHRP site class, and structure type, where T_{VD} denotes the

period at which the constant-velocity and constant-displacement portions of the input spectrum. The 10%/50-years shaking is estimated here to have $S_a(1s,5\%) = 0.55g$. To estimate MMI from $S_a(1s,5\%)$, one can apply the rule of thumb that $PGA \approx S_a(1s,5\%)$, and convert to MMI using Trifunac and Brady (1975), yielding $MMI = IX$.

K.3 DECISION VARIABLE

Loss is measured here in terms of damage factor (DF), defined as the repair cost as a fraction of the expected value of the replacement cost. The present study finds that the mean damage factor (MDF) varies between 21–29% for the code-conforming designs, and equals 38% for the non-code-conforming design.

ATC-13 expresses DF by model building type (denoted here by MBT), which here would be mid-rise moment-resisting ductile concrete frame. Seven experts each provided their best estimate for MDF at $MMI = IX$ for this MBT ; their responses varied between 8 and 25%. (See ATC-13 Table G.1.).

HAZUS estimates MDF in terms of MBT , code design level, occupancy type, and IM , but the documentation does tabulate DF against these parameters. In unpublished work, Porter set the ratios $PGA: S_a(0.3s, 5\%)$ and $PGA: S_a(1.0s, 5\%)$ to values offered by the HAZUS technical manual, and then calculated MDF as a function of PGA by MBT , code design level, and occupancy using the HAZUS methodology. For mid-rise concrete frames with high design level and professional/technical/business services occupancy, he found that $MDF = 36\%$. (HAZUS' building-specific module requires the user to apply expert judgment on various performance parameters, so the comparison would not be independent and is therefore not employed here.)

Comparison with ST -Risk is somewhat more valuable but more problematic than HAZUS or ATC-13: more valuable because ST -Risk addresses a range of building-specific features (while ATC and HAZUS apply to broad classes of buildings), and more problematic because ST -Risk is a proprietary model with limited available documentation and because it appears to reflect insurance losses in excess of a 5% deductible. ST -Risk conditions its loss estimates on a large number of parameters including MBT , occupancy type, and 67 facility-specific parameters (collectively denoted here by E) based on building features identified in FEMA 310 (1998). $MBTs$ are the Insurance Services Office (ISO) classifications, mapped to

FEMA 310 for use with the modifiers. ST-Risk employs base-class seismic vulnerability functions constructed by a straight line fit through ($MMI=V$, $DF = 0$) and ($MMI = IX$, $DF = x$), where x appears to be Steinbrugge's (1982) figure for the 90th percentile of loss in excess of 5% deductible. The base-class seismic vulnerability function is factored by a function $f(E)$. There is a modifier for each component of E , assigned by expert opinion. The function $f(E)$ sums these modifiers and constrains the sum to reasonable limits for combinations of FEMA 310 features, with constraints set by expert opinion. In the present application, the MBT used is C1, concrete moment frames, or 4A by ISO classification. With all modifiers set to their best value (i.e., lowest vulnerability), ST-Risk gives a 6% mean loss. Correcting for the deductible, this equates with $MDF = 11\%$. (This is not simply 6% + 5% deductible, but because of an apparently low-enough coefficient of variation, the simple sum gives the same answer.) Had all modifiers in E been set default values, MDF would have been 16%.

K.4 CONCLUSIONS

Table K.1 summarizes the results of the comparison. comparison of the mean damage factor (MDF) in 10%/50-years shaking by four methods. The loss estimates from ATC-13, ST-Risk, and HAZUS span half an order of magnitude, from 8 to 36% of replacement cost. The PEER results, $MDF = 21\text{--}29\%$, are bracketed by these other estimates, indicating general agreement. Note that the comparison is imperfect, for at least three reasons:

- Three different IMs are used, with attendant conversion uncertainty;
- ATC-13 and HAZUS are generic, category-based approaches, while PEER's is building-specific; and
- ATC-13 and ST-Risk depend for their basic vulnerability information on pre-1982 earthquakes, while the benchmark building reflects modern design.

Nonetheless, these other approaches authoritative and are widely recognized, so the general agreement with PEER's estimate tends to validate the PEER results.

Table K.1 Comparison of mean damage factor (MDF) in 10%/50-yr shaking by four methods.

Method	<i>IM</i>	<i>MDF</i>	Comment
PEER	$S_d(1s,5\%) = 0.55g$	21–29%	For code-conforming design variants
ATC-13	$MMI = IX$	8–25%	Varies by ATC expert
HAZUS	$PGA = 0.55g$	36%	Uses unpublished work
ST-Risk 4.11	$MMI = IX$	11–16%	Range reflects best and default conditions and some inference

PEER REPORTS

PEER reports are available from the National Information Service for Earthquake Engineering (NISEE). To order PEER reports, please contact the Pacific Earthquake Engineering Research Center, 1301 South 46th Street, Richmond, California 94804-4698. Tel.: (510) 665-3405; Fax: (510) 665-3420.

- PEER 2008/02** *Treatment of Uncertainties in Seismic-Risk Analysis of Transportation Systems.* Evangelos Stergiou and Anne S. Kiremidjian. July 2008.
- PEER 2008/01** *Seismic Performance Objectives for Tall Buildings.* William T. Holmes, Charles Kircher, William Petak, and Nabih Youssef. August 2008.
- PEER 2007/12** *An Assessment to Benchmark the Seismic Performance of a Code-Conforming Reinforced Concrete Moment-Frame Building.* Curt Haselton, Christine A. Goulet, Judith Mitrani-Reiser, James L. Beck, Gregory G. Deierlein, Keith A. Porter, Jonathan P. Stewart, and Ertugrul Taciroglu. August 2008.
- PEER 2007/11** *Bar Buckling in Reinforced Concrete Bridge Columns.* Wayne A. Brown, Dawn E. Lehman, and John F. Stanton. February 2008.
- PEER 2007/10** *Computational Modeling of Progressive Collapse in Reinforced Concrete Frame Structures.* Mohamed M. Talaat and Khalid M. Mosalam. May 2008.
- PEER 2007/09** *Integrated Probabilistic Performance-Based Evaluation of Benchmark Reinforced Concrete Bridges.* Kevin R. Mackie, John-Michael Wong, and Božidar Stojadinović. January 2008.
- PEER 2007/08** *Assessing Seismic Collapse Safety of Modern Reinforced Concrete Moment-Frame Buildings.* Curt B. Haselton and Gregory G. Deierlein. February 2008.
- PEER 2007/07** *Performance Modeling Strategies for Modern Reinforced Concrete Bridge Columns.* Michael P. Berry and Marc O. Eberhard. April 2008.
- PEER 2007/06** *Development of Improved Procedures for Seismic Design of Buried and Partially Buried Structures.* Linda Al Atik and Nicholas Sitar. June 2007.
- PEER 2007/05** *Uncertainty and Correlation in Seismic Risk Assessment of Transportation Systems.* Renee G. Lee and Anne S. Kiremidjian. July 2007.
- PEER 2007/04** *Numerical Models for Analysis and Performance-Based Design of Shallow Foundations Subjected to Seismic Loading.* Sivapalan Gajan, Tara C. Hutchinson, Bruce L. Kutter, Prishati Raychowdhury, José A. Ugalde, and Jonathan P. Stewart. May 2008.
- PEER 2007/03** *Beam-Column Element Model Calibrated for Predicting Flexural Response Leading to Global Collapse of RC Frame Buildings.* Curt B. Haselton, Abbie B. Liel, Sarah Taylor Lange, and Gregory G. Deierlein. May 2008.
- PEER 2007/02** *Campbell-Bozorgnia NGA Ground Motion Relations for the Geometric Mean Horizontal Component of Peak and Spectral Ground Motion Parameters.* Kenneth W. Campbell and Yousef Bozorgnia. May 2007.
- PEER 2007/01** *Boore-Atkinson NGA Ground Motion Relations for the Geometric Mean Horizontal Component of Peak and Spectral Ground Motion Parameters.* David M. Boore and Gail M. Atkinson. May. May 2007.
- PEER 2006/12** *Societal Implications of Performance-Based Earthquake Engineering.* Peter J. May. May 2007.
- PEER 2006/11** *Probabilistic Seismic Demand Analysis Using Advanced Ground Motion Intensity Measures, Attenuation Relationships, and Near-Fault Effects.* Polsak Tothong and C. Allin Cornell. March 2007.
- PEER 2006/10** *Application of the PEER PBEE Methodology to the I-880 Viaduct.* Sashi Kunnath. February 2007.
- PEER 2006/09** *Quantifying Economic Losses from Travel Forgone Following a Large Metropolitan Earthquake.* James Moore, Sungbin Cho, Yue Yue Fan, and Stuart Werner. November 2006.
- PEER 2006/08** *Vector-Valued Ground Motion Intensity Measures for Probabilistic Seismic Demand Analysis.* Jack W. Baker and C. Allin Cornell. October 2006.
- PEER 2006/07** *Analytical Modeling of Reinforced Concrete Walls for Predicting Flexural and Coupled-Shear-Flexural Responses.* Kutay Orakcal, Loenardo M. Massone, and John W. Wallace. October 2006.
- PEER 2006/06** *Nonlinear Analysis of a Soil-Drilled Pier System under Static and Dynamic Axial Loading.* Gang Wang and Nicholas Sitar. November 2006.
- PEER 2006/05** *Advanced Seismic Assessment Guidelines.* Paolo Bazzurro, C. Allin Cornell, Charles Menun, Maziar Motahari, and Nicolas Luco. September 2006.

- PEER 2006/04** *Probabilistic Seismic Evaluation of Reinforced Concrete Structural Components and Systems.* Tae Hyung Lee and Khalid M. Mosalam. August 2006.
- PEER 2006/03** *Performance of Lifelines Subjected to Lateral Spreading.* Scott A. Ashford and Teerawut Juirnarongrit. July 2006.
- PEER 2006/02** *Pacific Earthquake Engineering Research Center Highway Demonstration Project.* Anne Kiremidjian, James Moore, Yue Yue Fan, Nesrin Basoz, Ozgur Yazali, and Meredith Williams. April 2006.
- PEER 2006/01** *Bracing Berkeley. A Guide to Seismic Safety on the UC Berkeley Campus.* Mary C. Comerio, Stephen Tobriner, and Ariane Fehrenkamp. January 2006.
- PEER 2005/16** *Seismic Response and Reliability of Electrical Substation Equipment and Systems.* Junho Song, Armen Der Kiureghian, and Jerome L. Sackman. April 2006.
- PEER 2005/15** *CPT-Based Probabilistic Assessment of Seismic Soil Liquefaction Initiation.* R. E. S. Moss, R. B. Seed, R. E. Kayen, J. P. Stewart, and A. Der Kiureghian. April 2006.
- PEER 2005/14** *Workshop on Modeling of Nonlinear Cyclic Load-Deformation Behavior of Shallow Foundations.* Bruce L. Kutter, Geoffrey Martin, Tara Hutchinson, Chad Harden, Sivapalan Gajan, and Justin Phalen. March 2006.
- PEER 2005/13** *Stochastic Characterization and Decision Bases under Time-Dependent Aftershock Risk in Performance-Based Earthquake Engineering.* Gee Liek Yeo and C. Allin Cornell. July 2005.
- PEER 2005/12** *PEER Testbed Study on a Laboratory Building: Exercising Seismic Performance Assessment.* Mary C. Comerio, editor. November 2005.
- PEER 2005/11** *Van Nuys Hotel Building Testbed Report: Exercising Seismic Performance Assessment.* Helmut Krawinkler, editor. October 2005.
- PEER 2005/10** *First NEES/E-Defense Workshop on Collapse Simulation of Reinforced Concrete Building Structures.* September 2005.
- PEER 2005/09** *Test Applications of Advanced Seismic Assessment Guidelines.* Joe Maffei, Karl Telleen, Danya Mohr, William Holmes, and Yuki Nakayama. August 2006.
- PEER 2005/08** *Damage Accumulation in Lightly Confined Reinforced Concrete Bridge Columns.* R. Tyler Ranf, Jared M. Nelson, Zach Price, Marc O. Eberhard, and John F. Stanton. April 2006.
- PEER 2005/07** *Experimental and Analytical Studies on the Seismic Response of Freestanding and Anchored Laboratory Equipment.* Dimitrios Konstantinidis and Nicos Makris. January 2005.
- PEER 2005/06** *Global Collapse of Frame Structures under Seismic Excitations.* Luis F. Ibarra and Helmut Krawinkler. September 2005.
- PEER 2005/05** *Performance Characterization of Bench- and Shelf-Mounted Equipment.* Samit Ray Chaudhuri and Tara C. Hutchinson. May 2006.
- PEER 2005/04** *Numerical Modeling of the Nonlinear Cyclic Response of Shallow Foundations.* Chad Harden, Tara Hutchinson, Geoffrey R. Martin, and Bruce L. Kutter. August 2005.
- PEER 2005/03** *A Taxonomy of Building Components for Performance-Based Earthquake Engineering.* Keith A. Porter. September 2005.
- PEER 2005/02** *Fragility Basis for California Highway Overpass Bridge Seismic Decision Making.* Kevin R. Mackie and Božidar Stojadinović. June 2005.
- PEER 2005/01** *Empirical Characterization of Site Conditions on Strong Ground Motion.* Jonathan P. Stewart, Yoojoong Choi, and Robert W. Graves. June 2005.
- PEER 2004/09** *Electrical Substation Equipment Interaction: Experimental Rigid Conductor Studies.* Christopher Stearns and André Filiatrault. February 2005.
- PEER 2004/08** *Seismic Qualification and Fragility Testing of Line Break 550-kV Disconnect Switches.* Shakhzod M. Takhirov, Gregory L. Fenves, and Eric Fujisaki. January 2005.
- PEER 2004/07** *Ground Motions for Earthquake Simulator Qualification of Electrical Substation Equipment.* Shakhzod M. Takhirov, Gregory L. Fenves, Eric Fujisaki, and Don Clyde. January 2005.
- PEER 2004/06** *Performance-Based Regulation and Regulatory Regimes.* Peter J. May and Chris Koski. September 2004.
- PEER 2004/05** *Performance-Based Seismic Design Concepts and Implementation: Proceedings of an International Workshop.* Peter Fajfar and Helmut Krawinkler, editors. September 2004.
- PEER 2004/04** *Seismic Performance of an Instrumented Tilt-up Wall Building.* James C. Anderson and Vitelmo V. Bertero. July 2004.

- PEER 2004/03** *Evaluation and Application of Concrete Tilt-up Assessment Methodologies.* Timothy Graf and James O. Malley. October 2004.
- PEER 2004/02** *Analytical Investigations of New Methods for Reducing Residual Displacements of Reinforced Concrete Bridge Columns.* Junichi Sakai and Stephen A. Mahin. August 2004.
- PEER 2004/01** *Seismic Performance of Masonry Buildings and Design Implications.* Kerri Anne Taeko Tokoro, James C. Anderson, and Vitelmo V. Bertero. February 2004.
- PEER 2003/18** *Performance Models for Flexural Damage in Reinforced Concrete Columns.* Michael Berry and Marc Eberhard. August 2003.
- PEER 2003/17** *Predicting Earthquake Damage in Older Reinforced Concrete Beam-Column Joints.* Catherine Pagni and Laura Lowes. October 2004.
- PEER 2003/16** *Seismic Demands for Performance-Based Design of Bridges.* Kevin Mackie and Božidar Stojadinović. August 2003.
- PEER 2003/15** *Seismic Demands for Nondeteriorating Frame Structures and Their Dependence on Ground Motions.* Ricardo Antonio Medina and Helmut Krawinkler. May 2004.
- PEER 2003/14** *Finite Element Reliability and Sensitivity Methods for Performance-Based Earthquake Engineering.* Terje Haukaas and Armen Der Kiureghian. April 2004.
- PEER 2003/13** *Effects of Connection Hysteretic Degradation on the Seismic Behavior of Steel Moment-Resisting Frames.* Janise E. Rodgers and Stephen A. Mahin. March 2004.
- PEER 2003/12** *Implementation Manual for the Seismic Protection of Laboratory Contents: Format and Case Studies.* William T. Holmes and Mary C. Comerio. October 2003.
- PEER 2003/11** *Fifth U.S.-Japan Workshop on Performance-Based Earthquake Engineering Methodology for Reinforced Concrete Building Structures.* February 2004.
- PEER 2003/10** *A Beam-Column Joint Model for Simulating the Earthquake Response of Reinforced Concrete Frames.* Laura N. Lowes, Nilanjan Mitra, and Arash Altoontash. February 2004.
- PEER 2003/09** *Sequencing Repairs after an Earthquake: An Economic Approach.* Marco Casari and Simon J. Wilkie. April 2004.
- PEER 2003/08** *A Technical Framework for Probability-Based Demand and Capacity Factor Design (DCFD) Seismic Formats.* Fatemeh Jalayer and C. Allin Cornell. November 2003.
- PEER 2003/07** *Uncertainty Specification and Propagation for Loss Estimation Using FOSM Methods.* Jack W. Baker and C. Allin Cornell. September 2003.
- PEER 2003/06** *Performance of Circular Reinforced Concrete Bridge Columns under Bidirectional Earthquake Loading.* Mahmoud M. Hachem, Stephen A. Mahin, and Jack P. Moehle. February 2003.
- PEER 2003/05** *Response Assessment for Building-Specific Loss Estimation.* Eduardo Miranda and Shahram Taghavi. September 2003.
- PEER 2003/04** *Experimental Assessment of Columns with Short Lap Splices Subjected to Cyclic Loads.* Murat Melek, John W. Wallace, and Joel Conte. April 2003.
- PEER 2003/03** *Probabilistic Response Assessment for Building-Specific Loss Estimation.* Eduardo Miranda and Hesameddin Aslani. September 2003.
- PEER 2003/02** *Software Framework for Collaborative Development of Nonlinear Dynamic Analysis Program.* Jun Peng and Kincho H. Law. September 2003.
- PEER 2003/01** *Shake Table Tests and Analytical Studies on the Gravity Load Collapse of Reinforced Concrete Frames.* Kenneth John Elwood and Jack P. Moehle. November 2003.
- PEER 2002/24** *Performance of Beam to Column Bridge Joints Subjected to a Large Velocity Pulse.* Natalie Gibson, André Filiatrault, and Scott A. Ashford. April 2002.
- PEER 2002/23** *Effects of Large Velocity Pulses on Reinforced Concrete Bridge Columns.* Greg L. Orozco and Scott A. Ashford. April 2002.
- PEER 2002/22** *Characterization of Large Velocity Pulses for Laboratory Testing.* Kenneth E. Cox and Scott A. Ashford. April 2002.
- PEER 2002/21** *Fourth U.S.-Japan Workshop on Performance-Based Earthquake Engineering Methodology for Reinforced Concrete Building Structures.* December 2002.
- PEER 2002/20** *Barriers to Adoption and Implementation of PBEE Innovations.* Peter J. May. August 2002.

- PEER 2002/19** *Economic-Engineered Integrated Models for Earthquakes: Socioeconomic Impacts.* Peter Gordon, James E. Moore II, and Harry W. Richardson. July 2002.
- PEER 2002/18** *Assessment of Reinforced Concrete Building Exterior Joints with Substandard Details.* Chris P. Pantelides, Jon Hansen, Justin Nadauld, and Lawrence D. Reaveley. May 2002.
- PEER 2002/17** *Structural Characterization and Seismic Response Analysis of a Highway Overcrossing Equipped with Elastomeric Bearings and Fluid Dampers: A Case Study.* Nicos Makris and Jian Zhang. November 2002.
- PEER 2002/16** *Estimation of Uncertainty in Geotechnical Properties for Performance-Based Earthquake Engineering.* Allen L. Jones, Steven L. Kramer, and Pedro Arduino. December 2002.
- PEER 2002/15** *Seismic Behavior of Bridge Columns Subjected to Various Loading Patterns.* Asadollah Esmaeily-Gh. and Yan Xiao. December 2002.
- PEER 2002/14** *Inelastic Seismic Response of Extended Pile Shaft Supported Bridge Structures.* T.C. Hutchinson, R.W. Boulanger, Y.H. Chai, and I.M. Idriss. December 2002.
- PEER 2002/13** *Probabilistic Models and Fragility Estimates for Bridge Components and Systems.* Paolo Gardoni, Armen Der Kiureghian, and Khalid M. Mosalam. June 2002.
- PEER 2002/12** *Effects of Fault Dip and Slip Rake on Near-Source Ground Motions: Why Chi-Chi Was a Relatively Mild M7.6 Earthquake.* Brad T. Aagaard, John F. Hall, and Thomas H. Heaton. December 2002.
- PEER 2002/11** *Analytical and Experimental Study of Fiber-Reinforced Strip Isolators.* James M. Kelly and Shakhzod M. Takhirov. September 2002.
- PEER 2002/10** *Centrifuge Modeling of Settlement and Lateral Spreading with Comparisons to Numerical Analyses.* Sivapalan Gajan and Bruce L. Kutter. January 2003.
- PEER 2002/09** *Documentation and Analysis of Field Case Histories of Seismic Compression during the 1994 Northridge, California, Earthquake.* Jonathan P. Stewart, Patrick M. Smith, Daniel H. Whang, and Jonathan D. Bray. October 2002.
- PEER 2002/08** *Component Testing, Stability Analysis and Characterization of Buckling-Restrained Unbonded Braces™.* Cameron Black, Nicos Makris, and Ian Aiken. September 2002.
- PEER 2002/07** *Seismic Performance of Pile-Wharf Connections.* Charles W. Roeder, Robert Graff, Jennifer Soderstrom, and Jun Han Yoo. December 2001.
- PEER 2002/06** *The Use of Benefit-Cost Analysis for Evaluation of Performance-Based Earthquake Engineering Decisions.* Richard O. Zerbe and Anthony Falit-Baiamonte. September 2001.
- PEER 2002/05** *Guidelines, Specifications, and Seismic Performance Characterization of Nonstructural Building Components and Equipment.* André Filiatrault, Constantin Christopoulos, and Christopher Stearns. September 2001.
- PEER 2002/04** *Consortium of Organizations for Strong-Motion Observation Systems and the Pacific Earthquake Engineering Research Center Lifelines Program: Invited Workshop on Archiving and Web Dissemination of Geotechnical Data, 4–5 October 2001.* September 2002.
- PEER 2002/03** *Investigation of Sensitivity of Building Loss Estimates to Major Uncertain Variables for the Van Nuys Testbed.* Keith A. Porter, James L. Beck, and Rustem V. Shaikhutdinov. August 2002.
- PEER 2002/02** *The Third U.S.-Japan Workshop on Performance-Based Earthquake Engineering Methodology for Reinforced Concrete Building Structures.* July 2002.
- PEER 2002/01** *Nonstructural Loss Estimation: The UC Berkeley Case Study.* Mary C. Comerio and John C. Stallmeyer. December 2001.
- PEER 2001/16** *Statistics of SDF-System Estimate of Roof Displacement for Pushover Analysis of Buildings.* Anil K. Chopra, Rakesh K. Goel, and Chatpan Chintanapakdee. December 2001.
- PEER 2001/15** *Damage to Bridges during the 2001 Nisqually Earthquake.* R. Tyler Ranf, Marc O. Eberhard, and Michael P. Berry. November 2001.
- PEER 2001/14** *Rocking Response of Equipment Anchored to a Base Foundation.* Nicos Makris and Cameron J. Black. September 2001.
- PEER 2001/13** *Modeling Soil Liquefaction Hazards for Performance-Based Earthquake Engineering.* Steven L. Kramer and Ahmed-W. Elgamel. February 2001.
- PEER 2001/12** *Development of Geotechnical Capabilities in OpenSees.* Boris Jeremi . September 2001.
- PEER 2001/11** *Analytical and Experimental Study of Fiber-Reinforced Elastomeric Isolators.* James M. Kelly and Shakhzod M. Takhirov. September 2001.

- PEER 2001/10** *Amplification Factors for Spectral Acceleration in Active Regions.* Jonathan P. Stewart, Andrew H. Liu, Yoojoong Choi, and Mehmet B. Baturay. December 2001.
- PEER 2001/09** *Ground Motion Evaluation Procedures for Performance-Based Design.* Jonathan P. Stewart, Shyh-Jeng Chiou, Jonathan D. Bray, Robert W. Graves, Paul G. Somerville, and Norman A. Abrahamson. September 2001.
- PEER 2001/08** *Experimental and Computational Evaluation of Reinforced Concrete Bridge Beam-Column Connections for Seismic Performance.* Clay J. Naito, Jack P. Moehle, and Khalid M. Mosalam. November 2001.
- PEER 2001/07** *The Rocking Spectrum and the Shortcomings of Design Guidelines.* Nicos Makris and Dimitrios Konstantinidis. August 2001.
- PEER 2001/06** *Development of an Electrical Substation Equipment Performance Database for Evaluation of Equipment Fragilities.* Thalia Agnanos. April 1999.
- PEER 2001/05** *Stiffness Analysis of Fiber-Reinforced Elastomeric Isolators.* Hsiang-Chuan Tsai and James M. Kelly. May 2001.
- PEER 2001/04** *Organizational and Societal Considerations for Performance-Based Earthquake Engineering.* Peter J. May. April 2001.
- PEER 2001/03** *A Modal Pushover Analysis Procedure to Estimate Seismic Demands for Buildings: Theory and Preliminary Evaluation.* Anil K. Chopra and Rakesh K. Goel. January 2001.
- PEER 2001/02** *Seismic Response Analysis of Highway Overcrossings Including Soil-Structure Interaction.* Jian Zhang and Nicos Makris. March 2001.
- PEER 2001/01** *Experimental Study of Large Seismic Steel Beam-to-Column Connections.* Egor P. Popov and Shakhzod M. Takhirov. November 2000.
- PEER 2000/10** *The Second U.S.-Japan Workshop on Performance-Based Earthquake Engineering Methodology for Reinforced Concrete Building Structures.* March 2000.
- PEER 2000/09** *Structural Engineering Reconnaissance of the August 17, 1999 Earthquake: Kocaeli (Izmit), Turkey.* Halil Sezen, Kenneth J. Elwood, Andrew S. Whittaker, Khalid Mosalam, John J. Wallace, and John F. Stanton. December 2000.
- PEER 2000/08** *Behavior of Reinforced Concrete Bridge Columns Having Varying Aspect Ratios and Varying Lengths of Confinement.* Anthony J. Calderone, Dawn E. Lehman, and Jack P. Moehle. January 2001.
- PEER 2000/07** *Cover-Plate and Flange-Plate Reinforced Steel Moment-Resisting Connections.* Taejin Kim, Andrew S. Whittaker, Amir S. Gilani, Vitelmo V. Bertero, and Shakhzod M. Takhirov. September 2000.
- PEER 2000/06** *Seismic Evaluation and Analysis of 230-kV Disconnect Switches.* Amir S. J. Gilani, Andrew S. Whittaker, Gregory L. Fenves, Chun-Hao Chen, Henry Ho, and Eric Fujisaki. July 2000.
- PEER 2000/05** *Performance-Based Evaluation of Exterior Reinforced Concrete Building Joints for Seismic Excitation.* Chandra Clyde, Chris P. Pantelides, and Lawrence D. Reaveley. July 2000.
- PEER 2000/04** *An Evaluation of Seismic Energy Demand: An Attenuation Approach.* Chung-Che Chou and Chia-Ming Uang. July 1999.
- PEER 2000/03** *Framing Earthquake Retrofitting Decisions: The Case of Hillside Homes in Los Angeles.* Detlof von Winterfeldt, Nels Roselund, and Alicia Kitsuse. March 2000.
- PEER 2000/02** *U.S.-Japan Workshop on the Effects of Near-Field Earthquake Shaking.* Andrew Whittaker, ed. July 2000.
- PEER 2000/01** *Further Studies on Seismic Interaction in Interconnected Electrical Substation Equipment.* Armen Der Kiureghian, Kee-Jeung Hong, and Jerome L. Sackman. November 1999.
- PEER 1999/14** *Seismic Evaluation and Retrofit of 230-kV Porcelain Transformer Bushings.* Amir S. Gilani, Andrew S. Whittaker, Gregory L. Fenves, and Eric Fujisaki. December 1999.
- PEER 1999/13** *Building Vulnerability Studies: Modeling and Evaluation of Tilt-up and Steel Reinforced Concrete Buildings.* John W. Wallace, Jonathan P. Stewart, and Andrew S. Whittaker, editors. December 1999.
- PEER 1999/12** *Rehabilitation of Nonductile RC Frame Building Using Encasement Plates and Energy-Dissipating Devices.* Mehrdad Sasani, Vitelmo V. Bertero, James C. Anderson. December 1999.
- PEER 1999/11** *Performance Evaluation Database for Concrete Bridge Components and Systems under Simulated Seismic Loads.* Yael D. Hose and Frieder Seible. November 1999.
- PEER 1999/10** *U.S.-Japan Workshop on Performance-Based Earthquake Engineering Methodology for Reinforced Concrete Building Structures.* December 1999.
- PEER 1999/09** *Performance Improvement of Long Period Building Structures Subjected to Severe Pulse-Type Ground Motions.* James C. Anderson, Vitelmo V. Bertero, and Raul Bertero. October 1999.

- PEER 1999/08** *Envelopes for Seismic Response Vectors.* Charles Menun and Armen Der Kiureghian. July 1999.
- PEER 1999/07** *Documentation of Strengths and Weaknesses of Current Computer Analysis Methods for Seismic Performance of Reinforced Concrete Members.* William F. Cofer. November 1999.
- PEER 1999/06** *Rocking Response and Overturning of Anchored Equipment under Seismic Excitations.* Nicos Makris and Jian Zhang. November 1999.
- PEER 1999/05** *Seismic Evaluation of 550 kV Porcelain Transformer Bushings.* Amir S. Gilani, Andrew S. Whittaker, Gregory L. Fenves, and Eric Fujisaki. October 1999.
- PEER 1999/04** *Adoption and Enforcement of Earthquake Risk-Reduction Measures.* Peter J. May, Raymond J. Burby, T. Jens Feeley, and Robert Wood.
- PEER 1999/03** *Task 3 Characterization of Site Response General Site Categories.* Adrian Rodriguez-Marek, Jonathan D. Bray, and Norman Abrahamson. February 1999.
- PEER 1999/02** *Capacity-Demand-Diagram Methods for Estimating Seismic Deformation of Inelastic Structures: SDF Systems.* Anil K. Chopra and Rakesh Goel. April 1999.
- PEER 1999/01** *Interaction in Interconnected Electrical Substation Equipment Subjected to Earthquake Ground Motions.* Armen Der Kiureghian, Jerome L. Sackman, and Kee-Jeung Hong. February 1999.
- PEER 1998/08** *Behavior and Failure Analysis of a Multiple-Frame Highway Bridge in the 1994 Northridge Earthquake.* Gregory L. Fenves and Michael Ellery. December 1998.
- PEER 1998/07** *Empirical Evaluation of Inertial Soil-Structure Interaction Effects.* Jonathan P. Stewart, Raymond B. Seed, and Gregory L. Fenves. November 1998.
- PEER 1998/06** *Effect of Damping Mechanisms on the Response of Seismic Isolated Structures.* Nicos Makris and Shih-Po Chang. November 1998.
- PEER 1998/05** *Rocking Response and Overturning of Equipment under Horizontal Pulse-Type Motions.* Nicos Makris and Yiannis Roussos. October 1998.
- PEER 1998/04** *Pacific Earthquake Engineering Research Invitational Workshop Proceedings, May 14–15, 1998: Defining the Links between Planning, Policy Analysis, Economics and Earthquake Engineering.* Mary Comerio and Peter Gordon. September 1998.
- PEER 1998/03** *Repair/Upgrade Procedures for Welded Beam to Column Connections.* James C. Anderson and Xiaojing Duan. May 1998.
- PEER 1998/02** *Seismic Evaluation of 196 kV Porcelain Transformer Bushings.* Amir S. Gilani, Juan W. Chavez, Gregory L. Fenves, and Andrew S. Whittaker. May 1998.
- PEER 1998/01** *Seismic Performance of Well-Confined Concrete Bridge Columns.* Dawn E. Lehman and Jack P. Moehle. December 2000.

ONLINE REPORTS

The following PEER reports are available by Internet only at http://peer.berkeley.edu/publications/peer_reports.html

- PEER 2008/101** *Seismic Performance Objectives for Tall Buildings*. William T. Holmes, Charles Kircher, William Petak, and Nabih Youssef. August 2008.
- PEER 2007/101** *Generalized Hybrid Simulation Framework for Structural Systems Subjected to Seismic Loading*. Tarek Elkhoraibi and Khalid M. Mosalam. July 2007.
- PEER 2007/100** *Seismic Evaluation of Reinforced Concrete Buildings Including Effects of Masonry Infill Walls*. Alidad Hashemi and Khalid M. Mosalam. July 2007.